



**HAL**  
open science

# Simulation du rayonnement de l'entree atmospherique sur les planètes gazeuses geantes

Chris James

► **To cite this version:**

Chris James. Simulation du rayonnement de l'entree atmospherique sur les planètes gazeuses geantes. Autre. Université Paris Saclay (COMUE); University of Queensland, 2018. Français. NNT : 2018SACLCO85 . tel-01998442

**HAL Id: tel-01998442**

**<https://theses.hal.science/tel-01998442>**

Submitted on 29 Jan 2019

**HAL** is a multi-disciplinary open access archive for the deposit and dissemination of scientific research documents, whether they are published or not. The documents may come from teaching and research institutions in France or abroad, or from public or private research centers.

L'archive ouverte pluridisciplinaire **HAL**, est destinée au dépôt et à la diffusion de documents scientifiques de niveau recherche, publiés ou non, émanant des établissements d'enseignement et de recherche français ou étrangers, des laboratoires publics ou privés.

# Radiation from Simulated Atmospheric Entry into the Gas Giants

Thèse de doctorat de The University of Queensland et l'Université Paris-Saclay  
préparée à CentraleSupélec

Ecole doctorale n°579 Sciences mécaniques et énergétiques, matériaux et  
géosciences (SMEMaG)  
Spécialité de doctorat: thermique

Thèse présentée et soutenue à Brisbane, Australia, le 20 septembre 2018, par

**M. CHRISTOPHER JAMES**

Composition du Jury :

M. Mário LINO DA SILVA Professeur, Technical University of Lisbon (Institute for Plasma Research and Nuclear Fusion)	Président et Rapporteur
M. Aaron DUFRENE Senior Research Scientist, CUBRC	Rapporteur
Denis PACKAN Ingénieur de Recherche, ONERA (Equipe Foudre et Plasma)	Examineur
Arnaud BULTEL Associate Professor, CORIA, Université de Rouen (UMR CNRS 6614)	Examineur
M. Richard MORGAN Professor, The University of Queensland (Centre for Hypersonics)	Directeur de thèse
M. Christophe LAUX Professeur, CentraleSupélec (La Laboratoire EM2C, EM2C-UPR288)	Directeur de thèse
M. David GILDFIND Senior Lecturer, The University of Queensland (Centre for Hypersonics)	Co-Directeur de thèse
M. Timothy MCINTYRE Associate Professor, The University of Queensland (Centre for Hypersonics)	Co-Directeur de thèse





**THE UNIVERSITY OF QUEENSLAND**  
Australia

**Radiation from Simulated Atmospheric Entry into the Gas Giants**

Christopher Matthew James

BEng (Hons IIB) - Extended Major in Mechanical Engineering

*A thesis submitted for the degree of Doctor of Philosophy at*

*The University of Queensland in 2018*

School of Mechanical and Mining Engineering





---

# Résumé

---

La recherche sur les planètes géantes gazeuses se concentre sur l'étude des effets aerothermodynamiques lors du vol dans les atmosphères des plus grandes planètes du système solaire - Jupiter, Saturne, Neptune et Uranus - appelées « les géantes gazeuses ». La majorité des études sur les géantes gazeuses menées dans le passé étaient liées à la conception et à l'analyse des résultats de la sonde atmosphérique de Galileo, qui a pénétré l'atmosphère de Jupiter le 7 décembre 1995. Plus récemment, il y a eu un regain d'intérêt pour les futures sondes atmosphériques des géantes gazeuses. Dans l'enquête « Vision and Voyages for Planetary Science in the Decade 2013-2022 » du conseil national de la recherche des États-Unis, les futures missions spatiales vers Uranus et vers Saturne ont été identifiées comme grandement prioritaires.

Les vitesses d'entrée proposées sont de 22.3 km/s pour Uranus et de 26.9 km/s pour Saturne. Les géantes gazeuses sont quatre grandes planètes gazeuses dans les régions externes de notre système solaire, qui sont principalement composées d'hydrogène moléculaire avec de l'hélium de dix à vingt pour cent (en volume), et quelques oligo-éléments, principalement du méthane. Bien que leur poids moléculaire atmosphérique est minuscule, ce qui signifie que le gaz peut être accéléré plus facilement, les grandes vitesses d'entrée provoquées par leur taille ont traditionnellement rendu leurs entrées difficiles à simuler dans les installations d'essais au sol. Les expériences réalisées lors de la conception de la sonde atmosphérique de Galileo ont pu recréer le flux thermique prédit, mais aucune d'entre elles n'a pu recréer la vitesse d'entrée de 47.5 km/s. Les vitesses d'entrée plus lentes associées à l'entrée dans Uranus et Saturne impliquent que les entrées sont plus susceptibles d'être réalisables. Pour cette raison, cette thèse se concentre sur la génération de conditions d'essai pour l'étude de ces entrées dans le tube d'expansion X2, un tube d'expansion à piston libre à l'Université du Queensland.

Pour permettre la prédiction rapide de la réponse de l'installation X2 pour la génération de nouvelles conditions d'essai utilisées pour simuler l'entrée dans les géantes gazeuses, un nouveau code de simulation de tube d'expansion appelé PITOT a été conçu. Le code isole les processus importants qui se produisent lors d'une expérience dans le tube d'expansion et les simule en utilisant des relations isentropiques et compressibles d'écoulement de gaz et l'équilibre chimique. Pour tester la précision du code par rapport à la réalité, PITOT a été testé contre

deux cas test expérimentaux utilisant comme gaz d'essai de l'air. On a constaté qu'il pouvait bien prédire des données expérimentales lorsque certaines variables d'ajustement empiriques étaient ajustées pour s'assurer qu'il correspondait aux mesures expérimentales des vitesses de choc et aux dépressions aux parois et dans la section d'essai.

PITOT a ensuite été utilisé pour générer des cartographies de performance théoriques pour la simulation de l'entrée d'Uranus et de Saturne dans X2. En théorie, avec une enceinte amont secondaire utilisée pour augmenter la performance de l'installation, X2 pourrait recréer la vitesse requise de 22.3 km/s pour simuler l'entrée d'Uranus proposée. Cependant, dans l'expérience actuelle, les pertes causées par la membrane secondaire ont légèrement réduit la performance, et les vitesses de choc au-dessus de 20 km/s dans le tube d'accélération étaient difficiles à mesurer sans grandes incertitudes. Une condition de test plus lente sans enceinte amont secondaire, avec une vitesse de vol équivalente de 19 km/s, a été conçue, ce qui n'était pas assez rapide pour simuler l'entrée. Une autre analyse théorique a révélé qu'avec une enceinte amont à piston libre plus puissante, une installation de la même taille que X2 pourrait simuler plus facilement l'entrée dans Uranus ou être capable de simuler l'entrée dans Saturne proposée. Il a également été proposé qu'un système de détection de choc avec un temps de réponse plus rapide serait nécessaire pour réduire les incertitudes sur les vitesses de choc dans des ces conditions au-dessus de 20 km/s.

Puisque X2 n'a pas été capable de simuler directement l'entrée dans Uranus ou Saturne, d'autres pistes ont été explorées. Dans la littérature, il a été proposé que pour la simulation de les entrées balistiques dans les géantes gazeuses, le pourcentage d'hélium dans le gaz d'essai pouvait être supérieur à la vraie composition atmosphérique (en substituant quelque  $H_2$  pour He), ou l'hélium pouvait être remplacé par du néon, un gaz plus lourd. Ces deux changements augmentent la force de l'arc de choc sur le modèle d'essai, permettant de reproduire d'importants phénomènes de vol de conditions de vol qui ne peuvent pas être simulés directement à des vitesses réalisables dans l'installation X2. Ceci a été exploré théoriquement en utilisant à la fois des gaz d'hélium et de néon, et la condition d'essai de vitesse de vol équivalente à 19 km/s conçue au cours de l'analyse précédente. Il a été trouvé théoriquement que l'entrée d'Uranus et de Saturne pouvait être facilement recrée dans X2 en utilisant soit un pourcentage molaire accru d'hélium, soit un pourcentage molaire similaire de néon à la place de l'hélium dans l'entrée réelle. Du point de vue de la dynamique des gaz, l'hélium produisait des écoulements d'essais de la même enthalpie de stagnation quel que soit le pourcentage utilisé, ce qui est une conclusion intéressante, permettant de choisir des températures en post-choc différentes tout en maintenant l'enthalpie de stagnation. Cela ne s'est pas produit pour le néon, avec des conditions qui se sont considérablement ralenties même lorsque les températures de la couche de choc du modèle d'essai ont augmenté, en raison des changements beaucoup plus

grands du poids moléculaire du gaz d'essai associé au néon. On a vérifié expérimentalement que l'enthalpie de stagnation d'écoulement d'essai restait constante dans les pourcentages molaires d'hélium testés (de 15 à 70%) et qu'on observait plus de rayonnement de couche de choc avec des pourcentages plus élevés d'hélium.

Actuellement, le rayonnement associé à l'entrée dans Uranus et Saturne n'a été simulé que dans des tubes à choc non réfléchis, où, en raison des temps d'essai courts, les modèles d'essai ne peuvent généralement pas être utilisés. Les tubes d'expansion comme X2 sont capables de simuler les conditions d'essai d'entrée planétaire avec des temps d'essai plus longs et des écoulements aérothermodynamiques plus réalistes. C'est ce qui rend la possibilité de simuler des conditions post-choc expérimentales lors de l'entrée dans Uranus et Saturne dans X2 si importante. X2 permet non seulement pour l'étude du rayonnement associé à ces entrées, mais aussi pour la simulation expérimentale des phénomènes liés à ces entrées qui nécessitent des modèles d'essais, tels que les taux de flux thermique, les études de la couche limite du modèle d'essai, ou en utilisant un modèle d'essai avec un mur chauffé, pour étudier l'interaction entre l'écoulement et la surface chaude.

---

## Abstract

---

Gas giant research focuses on the study of the aerothermodynamic effects during flight into the atmospheres of the solar system's largest planets - Jupiter, Saturn, Neptune and Uranus - called "the gas giants". The majority of gas giant studies conducted in the past were related to the design and analysis of results from the Galileo atmospheric probe, which entered Jupiter's atmosphere on 7 December 1995. More recently, there has been renewed interest in future gas giant entry probes. The United States National Research Council's survey "Vision and Voyages for Planetary Science in the Decade 2013-2022" identified future space missions to Uranus and Saturn as a high priority.

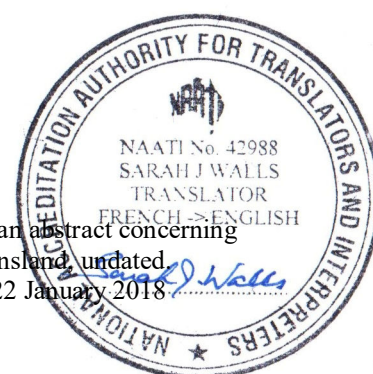
The proposed entry velocities are 22.3 km/s for Uranus and 26.9 km/s for Saturn. The gas giants are four large gaseous planets in the outer regions of our solar system, which are mainly composed of molecular hydrogen with ten to twenty per cent helium (by volume), and some trace elements, mainly methane. Although their atmospheric molecular weight is minuscule, which means that the gas can be more easily accelerated, the high entry velocities caused by their size have traditionally made their entries difficult to simulate in ground testing facilities. The experiments carried out during design of the Galileo atmospheric probe were able to recreate the predicted heat flow, but none was able to recreate the entry velocity of 47.5 km/s. The slower entry velocities associated with entry into Uranus and Saturn imply that the entries are more likely to be achievable. For this reason, this thesis focuses on the generation of test conditions for studying these entries in the X2 expansion tube, a free-piston-driven expansion tube at the University of Queensland.

To allow prompt prediction of the X2 facility response for generating new test conditions used to simulate gas giant entry, a new expansion tube simulation code called PITOT was designed. The code isolates the important processes that occur during an experiment in the expansion tube, and simulates them using isentropic and compressible gas flow relationships and equilibrium chemistry.

xiv

### CERTIFICATION

I certify that this is a true and accurate translation from French to English of a copy of an abstract concerning gas giant entry research conducted on the X2 expansion tube at the University of Queensland, undated, Sarah J. Walls - Professional translator from French to English - NAATI No: 42988 - 22 January 2018.



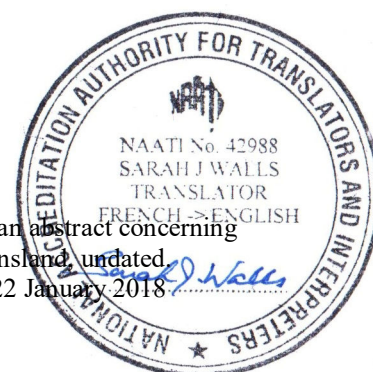
In order to test the accuracy of the code compared with reality, PITO<sup>T</sup> was tested against two experimental test cases using air as the test gas. PITO<sup>T</sup> was found to predict the experimental data well once certain empirical adjustment variables were adjusted to ensure that it matched the experimental shock-speed measurements and the wall and test-section pressures.

PITO<sup>T</sup> was then used to generate theoretical performance maps for simulating the Uranus and Saturn entries in X2. In theory, with a secondary driver used to increase the facility's performance, X2 could recreate the required velocity of 22.3 km/s to simulate the proposed Uranus entry. However, in the current experiment, the losses caused by the secondary diaphragm slightly reduced performance, and shock speeds above 20 km/s in the acceleration tube were difficult to measure without substantial uncertainties. A slower test condition was designed with no secondary driver and with a flight velocity equivalent to 19 km/s, which was not fast enough to simulate entry. Another theoretical analysis revealed that with a more powerful free-piston driver, a facility the same size as X2 could simulate the Uranus entry more easily or be capable of simulating the proposed Saturn entry. It was also proposed that a shock detection system with a faster response time would be necessary in order to reduce the uncertainties concerning shock speeds above 20 km/s under these conditions.

Since X2 was not capable of directly simulating Uranus or Saturn entry, other avenues were explored. In the literature, it was proposed that for blunt-body simulation of gas giant entry, the percentage of helium in the test gas could be increased above the real atmospheric composition (by substituting some H<sub>2</sub> for He), or the helium could be replaced by neon, a heavier gas. These two changes increase the strength of the bow shock over the test model, allowing important flight condition phenomena to be reproduced, which cannot be simulated directly at the velocities achievable in the X2 facility. This was explored theoretically using both helium and neon gases, and the flight speed test condition equivalent to 19 km/s designed during the previous analysis. It was found theoretically that Uranus and Saturn entry could easily be recreated in X2 using either an increased molar percentage of helium, or a similar molar percentage of neon instead of helium in the real entry. From the gas dynamic point of view, helium produced test flows with the same stagnation enthalpy regardless of the percentage used; this is an interesting conclusion, as it allows various post-shock temperatures to be selected while maintaining the same stagnation enthalpy.

#### CERTIFICATION

I certify that this is a true and accurate translation from French to English of a copy of an abstract concerning gas giant entry research conducted on the X2 expansion tube at the University of Queensland, undated.  
Sarah J. Walls - Professional translator from French to English - NAATI No: 42988 - 22 January 2018

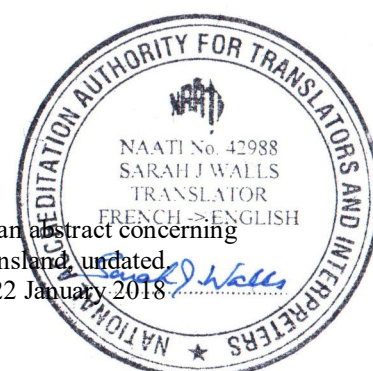


This did not occur for neon, with conditions that slowed considerably even when the temperatures of the test model shock layer increased, due to the much greater changes in the molecular weight of the test gas associated with neon. It was verified experimentally that the test flow stagnation enthalpy remained constant across the helium molar percentages tested (from 15% to 70%), and that more shock layer radiation was observed with higher percentages of helium.

Currently, the radiation associated with Uranus and Saturn entry has only been simulated in non-reflected shock tubes, where, due to the short test times, test models generally cannot be used. Expansion tubes such as X2 are capable of simulating planet entry test conditions with longer test times and more realistic aerothermodynamic flows. This is what makes the possibility of simulating experimental post-shock conditions during Uranus or Saturn entry in X2 so important. X2 enables not only study of the radiation associated with these entries, but also experimental simulation of phenomena related to these entries which require test models, such as heat transfer rates, studies of the test model boundary layer, or using a test model with a heated wall to study the interaction between the flow and the hot surface.

#### CERTIFICATION

I certify that this is a true and accurate translation from French to English of a copy of an abstract concerning gas giant entry research conducted on the X2 expansion tube at the University of Queensland, undated.  
Sarah J. Walls - Professional translator from French to English - NAATI No: 42988 - 22 January 2018



---

# Declaration By Author

---

This thesis is composed of my original work, and contains no material previously published or written by another person except where due reference has been made in the text. I have clearly stated the contribution by others to jointly-authored works that I have included in my thesis.

I have clearly stated the contribution of others to my thesis as a whole, including statistical assistance, survey design, data analysis, significant technical procedures, professional editorial advice, financial support and any other original research work used or reported in my thesis. The content of my thesis is the result of work I have carried out since the commencement of my higher degree by research candidature and does not include a substantial part of work that has been submitted to qualify for the award of any other degree or diploma in any university or other tertiary institution. I have clearly stated which parts of my thesis, if any, have been submitted to qualify for another award.

I acknowledge that an electronic copy of my thesis must be lodged with the University Library and, subject to the policy and procedures of The University of Queensland, the thesis be made available for research and study in accordance with the Copyright Act 1968 unless a period of embargo has been approved by the Dean of the Graduate School.

I acknowledge that copyright of all material contained in my thesis resides with the copyright holder(s) of that material. Where appropriate I have obtained copyright permission from the copyright holder to reproduce material in this thesis and have sought permission from co-authors for any jointly authored works included in the thesis.



---

# Publications During Candidature

---

## Journal Articles

Gildfind, D., James, C., Toniato, P., and Morgan, R., “Performance considerations for expansion tube operation with a shock-heated secondary driver,” *Journal of Fluid Mechanics*, Vol. 777, 2015, pp. 364–407. doi:10.1017/jfm.2015.349

Gildfind, D., James, C., and Morgan, R., “Free-piston driver performance characterisation using experimental shock speeds through helium,” *Shock Waves*, Vol. 25, No. 2, 2015, pp. 169–176. doi:10.1007/s00193-015-0553-8

Lewis, S. W., James, C., Morgan, R. G., McIntyre, T. J., Alba, C. R., and Greendyke, R. G., “Carbon Ablative Shock-Layer Radiation with High Surface Temperatures,” *Journal of Thermophysics and Heat Transfer*, Vol. 31, No. 1, 2017, pp. 193–204. doi:10.2514/1.T4902

James, C., Cullen, T., Wei, H., Lewis, S., Gu, S., Morgan, R., and McIntyre, T., “Improved test time evaluation in an expansion tube,” *Experiments in Fluids*, Vol. 59, No. 5, 2018, pp. 59–87. doi:10.1007/s00348-018-2540-1

Parekh, V., Gildfind, D., Lewis, S., and James, C., “X3 Expansion Tube Driver Gas Spectroscopy and Temperature Measurements,” *Shock Waves*, Vol. 28, No. 4, 2018, pp. 851–862. doi:10.1007/s00193-017-0754-4

Sheikh, U., Wei, H., Lewis, S., James, C., Leyland, P., Morgan, R., and McIntyre, T., “Spectrally Filtered Imaging and VUV Spectroscopy of Preheated Models in X2,” *AIAA Journal*, Vol. 55, No. 12, 2017, pp. 4167–4180. doi:10.2514/1.J056021

Lewis, S. W., James, C., Ravichandran, R., Morgan, R. G., and McIntyre, T. J., “Carbon Ablation in Hypervelocity Air and Nitrogen Shock Layers,” *Journal of Thermophysics and Heat Transfer*, Vol. 32, No. 2, 2018, pp. 449–468. doi:10.2514/1.T5270

James, C., Bourke, E., and Gildfind, D., “Calculating shock arrival in expansion tubes and shock tunnels using Bayesian changepoint analysis,” *Experiments in Fluids*, Vol. 59, No. 6, 2018, pp. 59–92. doi:10.1007/s00348-018-2546-8

## Conference Papers

James, C. and Morgan, R., “Radiation from simulated atmospheric entry into the gas giants,” *18th Australasian Fluid Mechanics Conference*, Launceston, Tasmania, Australia, December 3-7, 2012

James, C., Gildfind, D., Morgan, R., Jacobs, P., and Zander, F., “Designing and Simulating High Enthalpy Expansion Tube Conditions,” *5th Asia-Pacific International Symposium on Aerospace Technology*, Takamatsu, Japan, November 20-22, 2013

James, C., Gildfind, D., Morgan, R., and McIntyre, T., “Working Towards Simulating Gas Giant Entry Radiation in an Expansion Tube,” *Proceedings of the 29th International Symposium on Shock Waves*, Madison, WI, U.S.A., July 14-19, 2013. doi:10.1007/978-3-319-16835-7\_89

James, C., Gildfind, D., Morgan, R., and McIntyre, T., “Theoretical Validation of a Test Gas Substitution for Expansion Tube Simulation of Gas Giant Entry,” *44th AIAA Thermophysics Conference*, San Diego, California, U.S.A., 2013. doi:10.2514/6.2013-2506

James, C., Gildfind, D., Morgan, R., Lewis, S., Fahy, E., and McIntyre, T., “On the limits of simulating gas giant entry at true gas composition and true flight velocities in an expansion tube,” *6th International Workshop on Radiation of High Temperature Gases in Atmospheric Entry*, St Andrews, Scotland, United Kingdom, November 24-28, 2014

James, C., Gildfind, D., Morgan, R., and McIntyre, T., “The limits of simulating gas giant entry at true gas composition and true flight velocities in an expansion tube,” *19th Australasian Fluid Mechanics Conference*, Melbourne, VIC, Australia, 2014

James, C., Gildfind, D., Morgan, R., Lewis, S., Fahy, E., and McIntyre, T., “Limits of Simulating Gas Giant Entry at True Gas Composition and True Flight Velocities in an Expansion Tube,” *8th European Symposium on Aerothermodynamics for Space Vehicles*, Lisbon, Portugal, March 2-6, 2015

James, C., Gildfind, D., Morgan, R., Lewis, S., Fahy, E., and McIntyre, T., “On the Current Limits of Simulating Gas Giant Entry Flows in an Expansion Tube,” *20th AIAA International Space Planes and Hypersonic Systems and Technologies Conference*, Glasgow, Scotland, July 6-9, 2015. doi:10.2514/6.2015-3501

James, C., Gildfind, D., Morgan, R., Lewis, S., and McIntyre, T., “Simulating Gas Giant Entry with Increased Helium Diluent in an Expansion Tube,” *30th International Symposium on Shock Waves*, Tel Aviv, Israel, 2015. doi:10.1007/978-3-319-44866-4\_104

James, C., Gildfind, D., Morgan, R., Lewis, S., Fahy, E., and McIntyre, T., "Simulating gas giant entry in an expansion tube," *7th Asia-Pacific International Symposium on Aerospace Technology*, Cairns, Australia, November 25-27, 2015

Morgan, R., Rees, B., Rutherford, J., Jefferey, M., Sollart, M., Morris, N., Basore, K., James, C., Wei, H., Gu, S., Lewis, S., and Landsberg, W., "Advanced hypersonic vehicle component testing using pre-heated models and infrared scanning," *7th Asia-Pacific International Symposium on Aerospace Technology*, Cairns, Australia, November 25-27, 2015

James, C., Gildfind, D., Morgan, R., Lewis, S., and McIntyre, T., "Experimentally Simulating Gas Giant Entry in an Expansion Tube," *21th AIAA International Space Planes and Hypersonic Systems and Technologies Conference*, Xiamen, China, March 6-9, 2017. doi:10.2514/6.2017-2152

James, C., Smith, D., McLean, C., Morgan, R., Lewis, S., and Toniato, P., "Improving High Enthalpy Expansion Tube Condition Characterisation Using High Speed Imagery," *2018 AIAA Aviation and Aeronautics Forum and Exposition*, Atlanta, GA, U.S.A., June 25-29, 2018. doi:10.2514/6.2018-3805

Liu, Y., James, C., Morgan, R., and McIntyre, T., "Experimental Study of Saturn Entry Radiation with Higher Amount of Diluent in an Expansion Tube," *2018 AIAA Aviation and Aeronautics Forum and Exposition*, Atlanta, GA, U.S.A., June 25-29, 2018. doi:10.2514/6.2018-4070

Gildfind, D., Smith, D., Lewis, S., Kelly, R., James, C., Wei, H., and McIntyre, T., "Expansion Tube Magnetohydrodynamic Experiments with Argon Test Gas," *2018 AIAA Aviation and Aeronautics Forum and Exposition*, Atlanta, GA, U.S.A., June 25-29, 2018. doi: 10.2514/6.2018-3754

Smith, D., Gildfind, D., James, C., McIntyre, T., and Wheatley, V., "Magnetohydrodynamic Drag Force Measurements in an Expansion Tube," *2018 AIAA Aviation and Aeronautics Forum and Exposition*, Atlanta, GA, U.S.A., June 25-29, 2018. doi:10.2514/6.2018-3755

## Publications Included in This Thesis

As allowed by the University of Queensland Policy PPL 4.60.07, this thesis partly consists of two journal papers which were published in the peer reviewed journals *Shock Waves* and *Journal of Spacecraft and Rockets*. The first paper is incorporated into Chapters 4 and 5, with an extended version of the paper’s introduction included in Chapter 4 and the rest of the paper included as Chapter 5. The second paper is incorporated as Chapter 7 with the text in Australian English, some of the repeated introductory paragraphs removed, and references added to earlier chapters. Citation and contribution details for the papers can be found below.

James, C., Gildfind, D., Lewis, S., Morgan, R., and Zander, F., “Implementation of a state-to-state analytical framework for the calculation of expansion tube flow properties,” *Shock Waves*, Vol. 28, No. 2, 2018, pp. 349–377. doi:10.1007/s00193-017-0763-3

Contributor	Statement of Contribution
Christopher James	Conception and design (50%)
	Analysis and interpretation (80%)
	Drafting and production (80%)
David Gildfind	Conception and design (10%)
	Analysis and interpretation (5%)
	Drafting and production (5%)
Richard Morgan	Conception and design (20%)
	Analysis and interpretation (5%)
	Drafting and production (5%)
Steven Lewis	Conception and design (0%)
	Analysis and interpretation (5%)
	Drafting and production (5%)
Fabian Zander	Conception and design (20%)
	Analysis and interpretation (5%)
	Drafting and production (5%)

James, C., Gildfind, D., Morgan, R., Lewis, S., and McIntyre, T., “Simulating Gas Giant Atmospheric Entry Using Helium and Neon Test Gas Substitutions,” *accepted for publication in Journal of Spacecraft and Rockets, 2018*

Contributor	Statement of Contribution
Christopher James	Conception and design (50%)
	Analysis and interpretation (80%)
	Drafting and production (80%)
David Gildfind	Conception and design (10%)
	Analysis and interpretation (5%)
	Drafting and production (5%)
Richard Morgan	Conception and design (40%)
	Analysis and interpretation (5%)
	Drafting and production (5%)
Steven Lewis	Conception and design (0%)
	Analysis and interpretation (5%)
	Drafting and production (5%)
Timothy McIntyre	Conception and design (0%)
	Analysis and interpretation (5%)
	Drafting and production (5%)

## Contributions by Others to the Thesis

None.

## Statement of Parts of the Thesis Submitted to Qualify for the Award of Another Degree

None.

## Research Involving Human or Animal Subjects

No animal or human participants were involved in this research.

---

# Acknowledgements

---

I don't think that I would have survived this thesis without the aid of myriad supporters, both from inside and outside of the university. A few words on paper can't really do justice to the amount of knowledge, guidance, and levelling out that everyone was able to give to me, but a series of words is all that I have here, so I hope that they appreciate it, and that I manage to do everyone justice.

Firstly, to Richard Morgan, my brilliant primary supervisor, who has taken a lot of chances on me over the last seven years. I was a fairly ordinary undergraduate student when I stumbled into his office overdressed for my first Final Year Thesis meeting at the start of 2011, and I'd like to hope that I'm a lot more than that now. Richard is always happy to offer assistance when you need it, while also being hands off enough to let you get your work done in your own way. I think that makes him a perfect supervisor, and I'm glad to have him in my corner. While everyone loves to joke about Richard not reading anything, when everything came down to the wire at the end, he read almost everything in this thesis in the week before submission, provided some very insightful feedback, as he always does, and then went fishing for a week.

To Timothy McIntyre for always being supportive of the project, even as I went further and further away from the original plan to just do spectroscopic measurements.

To my tertiary supervisor, David Gildfind, for stopping to help me every time I bugged him, and calming me down during the times when I really needed it. You are alright, mate, and it is great that you are a lecturer here now, even if it means that you have less time for all of us. If my thesis is a tenth of the thesis yours is, I'll be proud of it. An extra special thanks to David for dropping everything to read the final thesis document when everything came down to the wire at the end.

To Christophe Laux, for going out of his way to get me to Paris and welcoming me warmly to his group when I arrived. It was a big deal for me to move half-way around the world, and I could not have done that without your help. Thanks to Megan MacDonald and Carolyn Jacobs for helping me on the plasma torch while I was there too.

To Peter Jacobs and Rowan Gollan, who took the time to get me started with using their codes and put up with all of my stupid questions as I dove into Linux and the cfcfd code collection. I hope that I contributed enough to the collection to make up for some of the time they wasted getting me started.

To Hadas Porat, for being the poor person who had to teach me how to operate X2 all those years ago. She's always been patient with me, she's taught me a lot, and she put up with sitting next to me for a long time, thank you.

To Umar Sheikh and Fabian Zander, who worked me hard on the tunnel and never expected anything less than 110%. I can remember the day that Umar asked me if I felt comfortable on the tunnel yet, and not realising it was a trick question, I answered with a quick "*yes*". He told me to never get comfortable on the tunnel, because that is when you get lazy and things go wrong. I try to keep that in mind every day now, and I have tried to instil that same attitude into the generation of students which I have trained.

To Troy Eichmann for allowing me to ask him stupid questions about optics and spectroscopy about a hundred times until it all finally started to make sense... sometimes.

To Elise Fahy, for being the other cool young person in the lab, and always being down for a chat or a walk somewhere. You're a good partner in crime. I am very thankful that the stars aligned and that yourself and Nik could come to my thesis defence.

To Brad Wheatley, for keeping everyone grounded, always coming up with the best nicknames (except the ones aimed at me), and for being hilarious after he drinks about half a beer.

To Steven Lewis, for being generally level headed, always being happy to talk ideas through when it is needed, and for reading everyone's work when they can't get their own supervisors to do it.

To Yu Liu, whose successful initial experiments using test conditions from this thesis makes this work feel extremely worthwhile. Thank you for helping to fix the bicycle. I am sorry for sometimes being a harsh mentor, it is only because I want you to become the best researcher that you can be, and that I believe that you can get there.

To everyone else who has passed through the xlabs in my time here, Han, Gueric, Sangdi, Randy, Augustin, Tim, Jorge, Noel, Sam Stennett, Andreas, Pierpaolo, Sam Vella, Ranjith, Daniel, Rory, Matt, Steve, Ranjini, Nils, Theo, and Robert, thank you for all of your help, your ideas, and for putting up with me. As a group, we are stronger together than we could ever be on our own. We may like to say that there is a rivalry, but thank you to everyone from T4 as well, mainly, Sam, Keith, Kevin, Tristan, Wilson, and Zac, but there have been many others.

To all of our related technical stuff, mainly Frans de Beurs, Neil Duncan, Keith Hitchcock, Brian Loughrey, and Barry Allsop, who taught me about the difference between an engineering drawing and reality many times. Our whole group would be lost without them, and they are an amazing resource whenever we need to make or fix anything.

To my older sister, Samantha James, for starting a PhD before me, which gave me the guts to throw away a boring, normal engineering career and chase the only thing in engineering which has ever made me excited, even if it doesn't pay as well. (Sorry mum.)

To my younger sister, Rachel James, who I try and be an inspiration to every day. How about we make that 3 PhD's in the family?

To Emily Bourke, who seems to think that I am some sort of inspiration to her, when, in reality, it is the other way around. An even bigger thank you to her for doing many final read throughs of various parts of this document before the first submission as well.

I think that having a great group of friends doing interesting things is a measure of a strong and fulfilling life, and I consider myself lucky to have the group of friends that I have, and that they are so numerous that I could never possibly try to name them all without leaving someone very important out, but let's try anyway: Jacob, TJ, Daniel, Nick, Nat, Stuart, CJ, Duffy, Blaine, Sean, Sasha, Dan, Scrad, Cass, Alice, Alex, Fin, Michelle, Maddie, Emma, Fran, Peers, Alex, Jeremy, Victoria, James, Luke, Tay, Allan, Bex, Jaz, Dave Bloye, Matt, Grace, Owen, Dakota, Rob, Annalise, Elliot, Chris P., and Nath P. They remain excited about me doing this project, and keep telling me I'm awesome for doing it, even if it means that I can't always see them as much as I'd like. I would be lost without you all, thank you for putting up with me.

Enfin, à tout mes amis en France, Erwan, Wassim, Abigail, Nadine, Théa, Davy, Megan, Carolyn, Aurélie, Natalia, Augustin, et Claire, et à tout mes collègues à École Centrale Paris. Vous me manquez ! C'était avec une grande tristesse que j'ai quitté la France. Merci une mille fois pour votre amitié durant mon séjour en France. Ce n'est pas facile commencer une vie dans un autre pays et ça aurait été plus difficile sans vous. Je pense que mon année en France a changé complètement comment je vois le monde et je chéris mes souvenirs de ma vie là.

Merci beaucoup à Augustin d'avoir lu mon résumé et de m'aider avec la structure et des mots.



---

# Financial Support

---

This project was supported by the University of Queensland through a UQ Research Scholarship (UQRS), Campus France (the French agency promoting French higher education) through the Eiffel Excellence Scholarship Programme, and the Australian Research Council.

## **Keywords**

hypersonic, experimental, ground testing, expansion tube, shock tunnel, planetary entry, gas giant entry

## **Australian and New Zealand Standard Research Classifications (ANZSRC)**

ANZSRC 090107 Hypersonic Propulsion and Hypersonic Aerodynamics 100%

## **Field of Research (FoR) Classification**

FoR 0901 Aerospace Engineering 100%

---

# Dedication

---

To my parents, Karen Anne James and Norman Joseph James.

My mother has always been, and probably will always be, the strongest person that I've ever known. I've never met someone so selfless and so loving in my life. I know I'm not always the son she imagined, and I know that I haven't always been the easiest son to have around, but she loves me all the same, and that is all that matters. I hope this document, and the work that I have done over the last few years to produce it, make her proud.

My father has always been both a thousand times smarter and a thousand times more practical than the author. I hope that with all the work I have completed here, maybe I'll feel confident enough to say that I'm in his league now, or maybe just the league below.

*“Carry the lantern high.”*

---

# Contents

---

Résumé	i
Abstract	iii
Declaration By Author	vii
Publications During Candidature	viii
Acknowledgements	xiii
Dedication	xvii
Contents	xviii
List of Figures	xxv
List of Tables	xxxiii
Nomenclature	xliv

<b>1</b>	<b>Introduction</b>	<b>1</b>
1.1	Chapter Overview . . . . .	1
1.2	Space Exploration . . . . .	1
1.3	The Gas Giants . . . . .	3
1.3.1	What are they? . . . . .	3
1.3.2	Jupiter . . . . .	4
1.3.3	Gas Giant Exploration . . . . .	5
1.3.4	Gas Giant Entry in the Past: The Galileo Probe . . . . .	6
1.3.5	Gas Giant Entry in the Future . . . . .	10
1.3.6	Ground Testing of Gas Giant Entry at UQ . . . . .	11
1.4	Objectives of this Thesis . . . . .	13
1.5	Structure of this Thesis . . . . .	14
<b>2</b>	<b>Literature Review of Hypervelocity Flow Simulation</b>	<b>16</b>
2.1	Chapter Overview . . . . .	16
2.2	Ground Testing of Hypervelocity Flows . . . . .	16
<b>3</b>	<b>Literature Review of Gas Giant Entry</b>	<b>23</b>
3.1	Chapter Overview . . . . .	23
3.2	Where it all Started . . . . .	23
3.3	The Galileo Probe . . . . .	31
3.4	Stalker Substitution . . . . .	38
3.5	Modern Resurgence in the Study of Gas Giant Entry . . . . .	43

<b>4</b>	<b>The X2 Free Piston Driven Expansion Tube</b>	<b>47</b>
4.1	Chapter Overview . . . . .	47
4.2	The Expansion Tube . . . . .	47
4.3	The X2 Expansion Tube . . . . .	52
4.4	Proposed Test Models for the Project . . . . .	58
4.4.1	The Eichmann Cylinder . . . . .	59
4.4.2	The Pitot rake . . . . .	61
4.4.3	Pitot Rake Cylinders . . . . .	62
4.4.4	Standalone Pitot Probe Mount Models . . . . .	62
4.5	Physical Upgrades to the X2 Expansion Tube . . . . .	65
4.5.1	New Wall Pressure Transducer Mounts . . . . .	65
4.5.2	Improved Shock Speed Measurements . . . . .	68
4.6	The Shot Class . . . . .	69
<b>5</b>	<b>Simulating the X2 Expansion Tube</b>	<b>71</b>
5.1	Chapter Overview . . . . .	71
5.2	Introduction . . . . .	72
5.3	The X2 Expansion Tube . . . . .	74
5.4	Simulating an Expansion Tube with PITOT . . . . .	76
5.4.1	Driver Simulation . . . . .	77
5.4.2	Secondary Driver Simulation . . . . .	80
5.4.3	Shock Tube Simulation . . . . .	81

5.4.4	Secondary / Tertiary Diaphragm Modelling . . . . .	82
5.4.5	Acceleration Tube Simulation . . . . .	88
5.4.6	Nozzle Simulation . . . . .	91
5.4.7	Simulation of Various Basic Test Models . . . . .	94
5.5	Quantifying Experimental Data using PITOT . . . . .	95
5.5.1	Experimental Calibration of the Shock Tube . . . . .	95
5.5.2	Experimental Calibration of the Acceleration Tube . . . . .	96
5.5.3	Experimental Calibration of the Nozzle . . . . .	96
5.5.4	Examples . . . . .	97
5.6	Conclusions . . . . .	115
<b>6</b>	<b>True Gas Composition Gas Giant Entry Simulation</b>	<b>117</b>
6.1	Chapter Overview . . . . .	117
6.2	Introduction . . . . .	117
6.3	Theoretical Condition Analysis . . . . .	120
6.3.1	Conditions Without a Secondary Driver . . . . .	122
6.3.2	Conditions With a Secondary Driver . . . . .	124
6.3.3	Chosen Conditions . . . . .	127
6.4	Experimental Results . . . . .	127
6.4.1	Test Condition without Secondary Driver (X2-GG-UE-2.5 mm) . . . . .	128
6.4.2	Test Condition with Secondary Driver (X2-GG-UE-2.5 mm-SD) . . . . .	136
6.5	Theoretical Expansion Tube Compression Ratio Analysis . . . . .	143

6.5.1	Maximum Stagnation Enthalpy . . . . .	146
6.5.2	Density Requirements . . . . .	147
6.5.3	Higher Acceleration Tube Fill Pressures . . . . .	149
6.6	Conclusions . . . . .	151
<b>7</b>	<b>Using Higher Amounts of Diluent for Gas Giant Entry Simulation</b>	<b>154</b>
7.1	Chapter Overview . . . . .	154
7.2	Introduction . . . . .	154
7.3	The Stalker Substitution . . . . .	158
7.4	Theoretical Analysis for Helium and Neon Diluents . . . . .	162
7.4.1	Effect on the Test Conditions in the Driven Tubes . . . . .	162
7.4.2	Effect on the Final Test Flow (states 8 and 10) . . . . .	165
7.4.3	Using a Higher $p_5$ Value with the Helium Diluent . . . . .	172
7.4.4	Effect on the Post-shock Radiation . . . . .	173
7.4.5	Effect on the Stagnation Point Heat Flux . . . . .	175
7.5	Experimental Results . . . . .	177
7.5.1	Test Condition Analysis . . . . .	177
7.5.2	High Speed Imagery Analysis . . . . .	184
7.6	Conclusions . . . . .	189

<b>8</b>	<b>Conclusions and Recommendations</b>	<b>192</b>
8.1	Chapter Overview . . . . .	192
8.2	Conclusions . . . . .	192
8.3	Recommendations . . . . .	194
	<b>Bibliography</b>	<b>199</b>
	<b>Appendices</b>	<b>227</b>
A	Eichmann Cylinder Drawings	227
B	Original Standalone Pitot Mount Drawing	240
C	Standalone Three Pitot Mount Drawings	242
D	Mini-cylinder Drawings	247
E	New wall PCB Mount Drawings	255
F	Photodiode Mount PCB Mount Drawings	263
G	Calculating Experimental Shock Speed Uncertainty	272
H	Setting Up and Running PITOT	276



<b>I</b>	<b>Extra Information About PITOT</b>	<b>277</b>
I.1	State Details in PITOT . . . . .	278
I.2	PITOT Configuration Details . . . . .	279
I.3	Sample PITOT Configuration File . . . . .	281
I.4	Sample of PITOT scripted in Python . . . . .	284
<b>J</b>	<b>Hydrogen Safety</b>	<b>286</b>
<b>K</b>	<b>Stagnation Point Heat Flux Correlation Selection</b>	<b>291</b>

---

# List of Figures

---

1.1	“Light Echo” illuminating dust around the supergiant star, V838 Monocerotis . . .	2
1.2	Comparative size of the four Gas Giants . . . . .	3
1.3	Jupiter’s Great Red Spot photographed by Voyager 1 on February 25, 1979 . . .	4
1.4	Jupiter’s Great Red Spot photographed by Juno on July 10, 2017, during its seventh close flyby of Jupiter [51]. . . . .	5
1.5	Jupiter’s four Galilean moons . . . . .	6
1.6	Maximum stagnation point heat flux for various entry vehicles. . . . .	8
1.7	Ablation of the Galileo probe’s heat shield during its entry into Jupiter . . . . .	9
1.8	How stagnation enthalpy increases with increasing planetary entry velocity. . . .	12
3.1	Variation of concentrations and T behind a 15.5 km/s shock in a 21% $H_2$ /79%He gas mixture (by volume) with an initial pressure of 1.0 torr (0.133,3 kPa) . . . .	25
3.2	Comparison between theoretical and experimental electron density profiles from Belozarov and Measures [158] . . . . .	26
3.3	Relaxation downstream of an oblique shock over a flat plate in a simulated gas giant entry test gas . . . . .	27
3.4	Schematic of a conical arc driver for an electric arc shock tube . . . . .	28

3.5	Comparison between conical arc driven shock tube facilities for gas giant entry simulation . . . . .	28
3.6	Schematic of the ANAA shock tube from Leibowitz [161] . . . . .	29
3.7	Figure showing the performance of the ANAA shock tube for simulating gas giant entry scenarios . . . . .	30
3.8	Galileo probe schematic from Lundell [60] showing the two types of carbon phenolic composites used on the probe's heat shield . . . . .	32
3.9	Comparison of the emission spectra of argon and an 89% $H_2$ /11% He mixture . .	33
3.10	Comparison of carbon-phenolic ablation rates measured in different types of facilities . . . . .	34
3.11	Schematic showing the instrumentation in the Galileo probe's heat shield . . . .	35
3.12	Comparison of the final shape of the Galileo entry probe compared to various theoretical predictions . . . . .	35
3.13	Comparison between simulated and measured recession of the Galileo probe's heat shield . . . . .	37
3.14	Comparison between simulated and measured recession of the Galileo probe's stagnation point . . . . .	38
3.15	How diluent and diluent concentration affect ionising relaxation behind a strong shock . . . . .	40
3.16	Sample electron concentration calculation from the work of Higgins [63] . . . . .	42
3.17	Comparison of shock standoff between nonequilibrium CFD, experiment and an analytical solution from Higgins [63] . . . . .	42
3.18	Ionisation time and ionisation distance from the work of Furudate [176] . . . . .	44

3.19	Comparison between reaction rate coefficients from Kim et al.'s [179] study, experiments, and other theoretical calculations . . . . .	44
3.20	Spectral Irradiance at 10 mm downstream for 174 second point in Jits et al.'s [189] Neptune entry trajectory . . . . .	45
4.1	How changing shock tube shock speed ( $V_{s,1}$ ) changes the post-shock temperature ( $T_2$ ) in air for both perfect gas and equilibrium conditions. . . . .	48
4.2	Maximum stagnation enthalpy ( $H_t$ ) achievable in air with changing shock tube shock speed ( $V_{s,1}$ ) for both a shock tube and an expansion tube . . . . .	49
4.3	Representation of a basic free piston driven expansion tube. . . . .	51
4.4	Representation of the original X2 configuration with a two-stage free piston driver. . . . .	53
4.5	Driver pressure simulations from L1d2 [237, 238] for the three tuned driver conditions shown in Table 4.1 and X2's original 35 kg piston condition from Gildfind [231] . . . . .	55
4.6	Schematics of the X2 expansion tube in various current configurations . . . . .	56
4.7	Current X2 wall pressure transducer locations . . . . .	58
4.8	CAD representation of the Eichmann cylinder and full X2 model mounting system from Appendix A. . . . .	60
4.9	X2's Pitot rake during experimental set up to measure pressures at the same axial location as the entrance to X2's nozzle from McLean [245]. . . . .	61
4.10	False colour sample high speed image from experiment x2s3119 testing argon test condition x2-mhd-lwp-02. . . . .	63
4.11	Photo of the second iteration of the standalone Pitot probe mount model mounted underneath a 3D printed scaled Hayabusa test model. . . . .	64

4.12	Section view of Gildfind’s new wall transducer mount from Gildfind [249] and Appendix E. . . . .	66
4.13	Section view of the photodiode mount pressure transducer mounts from Appendix F. . . . .	67
4.14	X2 PCB diagram with secondary driver section and ‘at7’ and ‘at8’ . . . . .	68
5.1	Schematic and position-time (‘x-t’) diagram of the X2 expansion tube . . . . .	75
5.2	Driver after rupture representation . . . . .	78
5.3	Secondary driver representation . . . . .	80
5.4	Shock tube representation . . . . .	81
5.5	Partial shock and acceleration tube representation showing how an inertial diaphragm model simulates secondary or tertiary diaphragm rupture . . . . .	83
5.6	L1d3 [237, 238] one-dimensional CFD results showing how different diaphragm hold times (‘dt_hold’) affect the shock speed of the test condition. . . . .	85
5.7	Shock tube representation with a reflected shock at the secondary or tertiary diaphragm . . . . .	87
5.8	Effect of reflected shock Mach number ( $M_{r,st}$ ) on flow variables in the shock tube and test section . . . . .	88
5.9	Acceleration tube representation without over-expansion . . . . .	89
5.10	Acceleration tube representation with over-expansion . . . . .	90
5.11	X2 nozzle representation . . . . .	92
5.12	Nozzle exit representation showing an example of the boundary layer . . . . .	93
5.13	Effect of changing nozzle area ratio on flow variables at the nozzle exit . . . . .	93

5.14	Representation of flow over a blunt body test model . . . . .	94
5.15	Experimentally measured shock tube shock speeds ( $V_{s,1}$ ) from Table 5.6 compared to the theoretical equilibrium result from PITOT. . . . .	100
5.16	Experimentally measured acceleration tube shock speeds ( $V_{s,2}$ ) compared to various semi-experimental equilibrium PITOT simulations . . . . .	101
5.17	Measured acceleration tube wall pressure traces for two experiments compared to the unsteadily expanded test gas (state 7) pressures for the semi-experimental equilibrium PITOT simulations shown in Fig. 5.16. . . . .	102
5.18	Measured acceleration tube wall pressure traces for two experiments compared to equilibrium PITOT simulations performed using experimentally measured shock speeds from experiment x2s2902 . . . . .	103
5.19	Measured 15° half-angle cone pressure traces in the test section ( $p_{10c}$ ) for two experiments compared to theoretical values from equilibrium PITOT simulations using shock speeds from experiment x2s2902 . . . . .	104
5.20	Experimentally measured shock speeds from Table 5.9 compared to PITOT results.	109
5.21	Measured acceleration tube wall pressure traces compared to equilibrium PITOT simulations performed using experimentally measured shock speeds from experiment x2s3232 . . . . .	111
5.22	Measured 15° half-angle cone pressure traces in the test section ( $p_{10c}$ ) compared to equilibrium PITOT simulations performed using measured experimental shock speeds from experiment x2s3232 . . . . .	112
6.1	Effect of shock tube fill pressure ( $p_1$ ) on conditions without a secondary driver. .	123
6.2	Effect of secondary driver fill pressure ( $p_{sd1}$ ) on performance for different test conditions with a set $p_5$ value of 0.5 Pa. . . . .	125

6.3	Effect of secondary driver fill pressure ( $p_{sd1}$ ) on $\rho_{10e}$ for both drivers when $p_1 = 2$ kPa. Results are shown both with and without X2's nozzle. . . . .	126
6.4	Experimental shock tube shock speeds ( $V_{s,1}$ ) for condition X2-GG-UE-2.5 mm. .	129
6.5	Experimental acceleration tube shock speeds ( $V_{s,2}$ ) for condition X2-GG-UE-2.5 mm from both the first and second experimental campaigns. . . . .	131
6.6	Experimental test section $15^\circ$ half-angle cone pressures ( $p_{10c}$ ) from experiment x2s3244. . . . .	135
6.7	Experimental secondary driver shock speeds ( $V_{s,sd}$ ) for condition X2-GG-UE-2.5 mm-SD from the first and second experimental campaigns. . . . .	137
6.8	Experimental shock tube shock speeds ( $V_{s,1}$ ) for condition X2-GG-UE-2.5 mm-SD from the first and second experimental campaigns. . . . .	138
6.9	Experimental acceleration tube shock speeds ( $V_{s,2}$ ) for condition X2-GG-UE-2.5 mm-SD from the first and second experimental campaigns. . . . .	139
6.10	Experimental test section $15^\circ$ half-angle cone pressures ( $p_{10c}$ ) from experiment x2s3249. . . . .	142
6.11	Performance of different conditions with set driver rupture pressures ( $p_4$ ), when compression ratio ( $\lambda$ ) is varied from 0 to 100, and $p_5 = 0.5$ Pa. . . . .	146
6.12	$\rho_{10e}$ for the conditions shown in Fig. 6.11 <i>with</i> a nozzle expansion performed at the end of the acceleration tube. . . . .	148
6.13	$\rho_{10e}$ for the conditions shown in Fig. 6.11 <i>without</i> a steady expansion through a nozzle performed at the end of the acceleration tube. . . . .	149
6.14	$\rho_{10e}$ of different conditions with set driver rupture pressures ( $p_4$ ), $\lambda = 100$ , <i>with</i> a nozzle expansion, when $p_5$ is varied from 0.1 to 10 Pa. . . . .	150

6.15	$\rho_{10e}$ of different conditions with set driver rupture pressures ( $p_4$ ), $\lambda = 100$ , <i>without</i> a nozzle expansion, when $p_5$ is varied from 0.1 to 10 Pa. . . . .	151
7.1	Effect of diluent fraction on the performance of the condition. Normalised by 10% diluent. . . . .	163
7.2	Effect of diluent fraction on the test gas fill condition (state 1). Normalised by 10% diluent. . . . .	164
7.3	Effect of diluent fraction on the post-shock test gas condition (state 2). Normalised by 10% diluent. . . . .	165
7.4	Effect of diluent fraction on the frozen and equilibrium post-normal shock temperatures in the stagnation region over the test model (state 10) . . . . .	166
7.5	Effect of diluent fraction on the equilibrium composition of the test gas in the stagnation region over the test model (state 10). . . . .	168
7.6	Effect of diluent fraction on the test gas in the test section both before (state 8) and immediately after (state 10fr) the normal shock over the test model. Normalised by 10% diluent. . . . .	170
7.7	Effect of diluent fraction on the immediate post-shock modified binary scaling parameter ( $\Omega$ ) for different test conditions. . . . .	171
7.8	Effect of diluent fraction and $p_5$ on the frozen and equilibrium post-normal shock temperatures in the stagnation region over the test model (state 10) . . . . .	173
7.9	Effect of diluent fraction on the theoretical total power density in the Balmer and Lyman series from a 1 cm tangent slab in thermochemical equilibrium. . . .	174
7.10	Effect of diluent fraction on the stagnation point heat flux to a spherical test model. . . . .	176
7.11	Experimental shock tube shock speeds ( $V_{s,1}$ ). . . . .	180



7.12	Experimental acceleration tube shock speeds ( $V_{s,2}$ ).	181
7.13	Comparing theoretical and experimental results for how changing helium diluent affects the stagnation enthalpy of the test condition.	183
7.14	Comparing theoretical and experimental results for how helium diluent fraction affects the post-shock temperature of the test gas along the stagnation streamline over the test model.	185
7.15	Time-resolved integrated high speed camera intensity over a Pitot pressure probe for different percentages of helium diluent (by volume).	186
7.16	False colour high speed camera images around 100 $\mu$ s after flow arrival for experiments with helium diluent fractions of 15 and 70% (by volume).	187
7.17	Effect of aluminium secondary diaphragm contamination on the theoretical total power density in the same wavelength region as the Balmer series from a 1 cm tangent slab in thermochemical equilibrium.	189
G.1	Representation of a moving shock wave about to pass wall pressure sensors ‘at1’ and ‘at2’ in the X2 expansion tube. (Not to scale.)	273
K.1	Comparing the convective heat transfer coefficient ( $K$ ) in a $H_2/He$ mixture between a simplified equation from Sutton [296] and the original work of Sutton and Graves [289].	293

---

# List of Tables

---

1.1	Atmospheric compositions of the four Jovian planets . . . . .	3
2.1	Ranges of application of hypersonic wind tunnels, adapted from Smelt [96] . . . . .	19
4.1	Current tuned X2 expansion tube lightweight piston driver conditions from Gildfind et al. [231, 230] . . . . .	54
4.2	X2 wall transducer and diaphragm locations from Gildfind et al. [239]. . . . .	57
5.1	Details of the 1/5 scale Hayabusa 13:52:20UTC trajectory point condition de- signed by Fahy et al. [81]. . . . .	77
5.2	State 4 values for X2-LWP-2mm-0 from Gildfind et al. in 2015 [2]. . . . .	78
5.3	Driver rupture conditions for two ‘cold driver’ conditions designed by Gu [87]. The rupture values ( $p_4$ and $T_4$ ) were found by the authors. . . . .	79
5.4	Comparison between expansion of the shocked test gas to the gas velocity behind the shock ( $V_6$ ) or the acceleration tube shock speed ( $V_{s,2}$ ) . . . . .	91
5.5	Facility configuration details for the ‘cold driver’ air test condition used by the authors and Gu [267]. . . . .	99
5.6	Experimentally measured quantities from the two experiments performed by the authors and Gu [267]. Analysis was performed by the authors. . . . .	99

5.7	Final result of the condition analysis of the ‘cold driver’ air test condition from Table 5.5. . . . .	106
5.8	Facility configuration details for the free piston driven air test condition designed by Zander et al. [90]. . . . .	107
5.9	Experimentally measured shock speeds for the free piston driven air test condition detailed in Table 5.8 from experiment x2s3232. . . . .	107
5.10	Filtered experimentally measured pressure data for the free piston driven air test condition detailed in Table 5.8 from experiment x2s3232. . . . .	110
5.11	Final result of the condition analysis of the free piston driven air test condition from Table 5.8. . . . .	113
6.1	X2 driver conditions used for this study. Driver conditions are from [231, 230], except operated with a 100%He driver gas and a 65 mm orifice plate [2]. . . . .	120
6.2	Final details of the chosen test conditions. . . . .	127
6.3	Facility configuration details of condition X2-GG-UE-2.5 mm. . . . .	129
6.4	Computed test section freestream and post-shock state ranges for experiment x2s3244. . . . .	135
6.5	Facility configuration details of condition X2-GG-UE-2.5 mm-SD. . . . .	136
6.6	Computed test section freestream and post-shock state ranges for experiment x2s3249. . . . .	142
6.7	Gas giant entry points from the literature used for comparison in this paper. Significant figures from the sources have been maintained. . . . .	145
7.1	Uranus and Saturn entry points from Tables 4 and 8 in Palmer et al. [71] used for comparison in this chapter. Significant figures from Palmer et al. [71] have been maintained. . . . .	167

7.2	Facility configuration details of the test condition used. . . . .	178
7.3	Experimental and theoretical unsteadily expanded test gas pressure ( $p_7$ ) results for all of the experiments. . . . .	182
7.4	Experimental and theoretical test section $15^\circ$ half-angle cone pressure ( $p_{10c}$ ) re- sults for all of the experiments. . . . .	183
I.1	Description of the notation for PITOT . . . . .	278
I.2	Configuration details for PITOT . . . . .	279
K.1	Comparison between stagnation point convective heat flux calculated by Palmer et al's CFD [71] and calculations performed here using the correlation from Sutton and Graves [289]. . . . .	294

---

# Nomenclature

---

---

## Acronyms

---

ANAA ANnular Arc Accelerator

ANU Australian National University

ANZSRC Australian and New Zealand Standard Research Classifications

CAD Computer-aided design

CEA NASA's Chemical Equilibrium with Applications code

CFD Computational Fluid Dynamics

CI confidence interval

CMA Charring Materials Ablation code

COLTS COupled Laminar and Turbulent Solutions program

DAQ data acquisition system

EAST Electric Arc Shock Tube

ESA European Space Agency

FAI Fédération Aéronautique Internationale

FoR Field of Research

JAXA Japan Aerospace Exploration Agency

JPL NASA's Jet Propulsion Laboratory

NASA National Aeronautics and Space Administration

NEQAIR Nonequilibrium Air Radiation program

NRST non-reflected shock tube

RASLE Radiating Shock Layer Environment code

TOPIC Thermodynamic Outer Planets Insulation Code

UQ The University of Queensland

VUV vacuum ultraviolet

X1 X1 expansion tube

X2 X2 expansion tube

X3 X3 expansion tube

---

### Subscripts

---

$\infty$  freestream condition

1 pre-shock Condition

1 shock tube fill state

10 post-shock state in the test section

10c equilibrium post conical shock of a specified angle state in the test section

10e equilibrium post normal-shock state in the test section

10f frozen post normal-shock state in the test section

10w	equilibrium post wedge shock of a specified angle state in the test section
2	post-shock Condition
2	post-shock state in the shock tube
2r	twice shocked test gas state in the shock tube to simulate shock reflection off the secondary diaphragm
3	unsteadily expanded driver gas or secondary driver gas state
4	driver rupture state
4''	driver throat state
5	acceleration tube fill state
6	post-shock state in the acceleration tube
7	unsteadily expanded test gas state / test section state when nozzle is not used
8	test section state when nozzle is used
conv	convective
cs	contact surface
fill	primary driver fill state before piston compression
n	nose
rad	radiative
s	shock
s	stagnation value at the edge of the boundary layer
sd	secondary driver

sd1	secondary driver fill state
sd2	secondary driver post-shock state in the shock tube
sd3	unsteadily expanded driver gas state when secondary driver is used
sx	steady expansion
usx	unsteady expansion
w	wall value

---

**Greek**

---

$\beta$	shock angle for a conical or oblique shock
$\chi$	binary reaction variable, $\text{Ns}/\text{m}^2$
$\delta_S$	shock standoff
$\gamma$	specific heat ratio
$\gamma_2$	shock tube post-shock specific heat ratio
$\gamma_4$	shock tube / tunnel driver specific heat ratio
$\gamma_D$	driver specific heat ratio
$\lambda$	compression ratio
$\lambda$	wavelength
$\lambda_1$	lower wavelength limit
$\lambda_2$	upper wavelength limit
$\Omega$	modified binary scaling parameter
$\Omega$	solid angle



$\Omega_I$	ionisation reaction rate parameter
$\rho$	density, kg/m <sup>3</sup>
$\rho_{10e}$	equilibrium post-normal shock density in the test section
$\rho_\infty$	freestream density
$\theta$	wedge or ('body') angle for an oblique shock and conical half angle for a conical shock
$\varepsilon$	inverse shock density ratio, $\rho/\rho_s$

---

**Variables**

---

$A$	area
$a$	sound speed
$A^*$	throat area
$A_{driven}$	driven section area
$C_p$	heat capacity at constant pressure
$p_{fill}$	primary driver fill pressure before piston compression
$T_{fill}$	primary driver fill temperature before piston compression
$u$	velocity
$a$	sound speed
$a_2$	post-shock sound speed in the shock tube
$a_3$	unsteadily expanded primary or secondary driver sound speed
$a_4$	shock tube / tunnel driver gas sound speed
AR	nozzle area ratio

$c_0$	freestream mass fraction of a species
$D_{exit, reduced}$	reduced nozzle exit diameter to take into account boundary layer growth
$D_{exit}$	nozzle exit diameter
$D_{inlet, reduced}$	reduced nozzle inlet diameter to take into account boundary layer growth
$D_{inlet}$	nozzle inlet diameter
$h$	static (or ‘chemical’) enthalpy
$h_0$	reference static (or ‘chemical’) enthalpy
$h_s$	stagnation enthalpy at the edge of the boundary layer
$H_t$	stagnation (or ‘total’) enthalpy
$h_w$	wall enthalpy
$I$	radiance, $W/cm^2-sr$
$K$	convective heat transfer coefficient
$L$	characteristic length scale for binary scaling
$M$	Mach number
$M_{2r}$	Mach number of the reflected shock at the secondary diaphragm
$M_{4''}$	driver ‘throat’ Mach number when an orifice plate is used and the throat is effectively supersonic
$M_{throat}$	throat Mach number
$MW$	molecular weight
$p$	pressure

$p_{10c}$	cone pressure in the test section
$p_1$	shock tube fill pressure
$p_2$	post-shock pressure in the shock tube
$p_3$	unsteadily expanded primary or secondary driver pressure
$p_4$	shock tube / tunnel driver pressure, diaphragm rupture / supply pressure for a free piston driven facility
$p_5$	acceleration tube fill pressure
$p_6$	post-shock pressure in the acceleration tube
$p_7$	unsteadily expanded test gas pressure
$p_{sd1}$	secondary driver fill pressure
$p_{sd2}$	post-shock pressure in the secondary driver
$p_{sd3}$	unsteadily expanded driver pressure when the secondary driver is used
$p_s$	stagnation pressure at the edge of the boundary layer
$q$	streamline velocity, m/s
$q_{conv}$	stagnation point convective heat flux
$q_{rad}$	stagnation point radiative heat flux
$q_{total}$	stagnation point total heat flux
$R$	specific gas constant
$r$	mole fraction of $H_2$
$R_4$	shock tube / tunnel driver gas specific gas constant

$R_B$	nose radius
$R_n$	vehicle or test model nose radius
$s$	distance along streamline, m
$T$	temperature, K
$T_2$	post-shock temperature
$T_4$	shock tube / tunnel driver temperature, diaphragm rupture / supply temperature for a free piston driven facility
$T_\infty$	freestream temperature
$T_t$	stagnation (or 'total') temperature, K
$U_\infty$	freestream velocity
$U_e$	flight equivalent velocity
$V_2$	post-shock velocity in the shock tube
$V_3$	unsteadily expanded primary or secondary driver velocity
$V_4$	driver gas velocity
$V_6$	post-shock velocity in the acceleration tube
$V_7$	unsteadily expanded test gas pressure velocity
$V_{r,st}$	shock speed of the reflected shock at the secondary diaphragm
$V_{s,1}$	shock tube (or 'primary') shock speed
$V_{s,2}$	acceleration tube (or 'secondary') shock speed
$V_{s,sd}$	secondary driver shock speed

$V_{sd2}$  post-shock velocity in the secondary driver

$V_{sd3}$  unsteadily expanded driver velocity when the secondary driver is used

# 1

## Introduction

*We set sail on this new sea because there is new knowledge to be gained, and new rights to be won, and they must be won and used for the progress of all people. For space science, like nuclear science and technology, has no conscience of its own. Whether it will become a force for good or ill depends on man... The great British explorer George Mallory, who was to die on Mount Everest, was asked why did he want to climb it. He said because it is there. Well, space is there, and we're going to climb it. And the moon and the planets are there. And new hopes for knowledge and peace are there. And therefore, as we set sail, we ask God's blessing, on the most hazardous, and dangerous, and greatest adventure, on which man has ever embarked.*

– President John F. Kennedy, *Sept. 12, 1962, Rice University, Houston* [27]

### 1.1 Chapter Overview

This chapter introduces the thesis. It gives some basic context for the thesis by discussing space exploration in general, and then more specifically, exploration of the four gas giants: Jupiter, Saturn, Uranus, and Neptune. Gas Giant entry research in expansion tubes is then briefly discussed, before the proposed original scientific contributions are presented. A summary of each chapter in the overall thesis document is also presented.

### 1.2 Space Exploration

In 1942, Germany launched a V2 rocket vertically and broke the 100 km altitude barrier which we call the boundary of space<sup>1</sup>. Since then, space continues to capture the hearts and minds of many. During the Cold War, the space race was seen as a show of power and supremacy by the

---

<sup>1</sup>This is the ‘Kármán line’ that the Fédération Aéronautique Internationale (FAI) accepts as the boundary between Earth’s atmosphere and outer space [28].

competing U.S.A. and U.S.S.R.. During times of peace, the International Space Station, built as a co-operative effort between the American, Russian, Canadian, European, and Japanese Space Agencies, shines as an example of what human beings can achieve when they work together.

To this day, countless experiments and missions have been undertaken to try to further understand our solar system, and the vast expanse of space surrounding it. We have sent people to the moon and back during the Apollo Program [29]. We have flown by and photographed every planet in our solar system during many missions. We have sent probes to land on and explore Venus and Mars. We have landed on an asteroid, taken a sample, and brought it home during the Japan Aerospace Exploration Agency's (JAXA) Hayabusa mission [30]. We have sent a probe to rendezvous with a distant comet, orbit its nucleus, and place a lander there during the European Space Agency's (ESA) Rosetta mission [31]. We have sent the Voyager probes to the edge of our solar system, and they are still going [32, 33]. We have the Hubble Space Telescope which allows us to see deep into the space surrounding us [34]. An example image taken by the Hubble Space Telescope can be seen in Figure 1.1.



Figure 1.1: “Light Echo” illuminating dust around the supergiant star, V838 Monocerotis, taken on February 8, 2004, by the Hubble Space Telescope [35].

## 1.3 The Gas Giants

### 1.3.1 What are they?

The four outermost planets in our solar system (Jupiter, Saturn, Uranus, and Neptune, all shown together in Figure 1.2) are known collectively as ‘the gas giants’ or ‘the Jovian planets’ [36]. They are large gaseous planets, with densities close to that of the sun [37], which together comprise 99.56% of the planetary mass in our solar system [37].

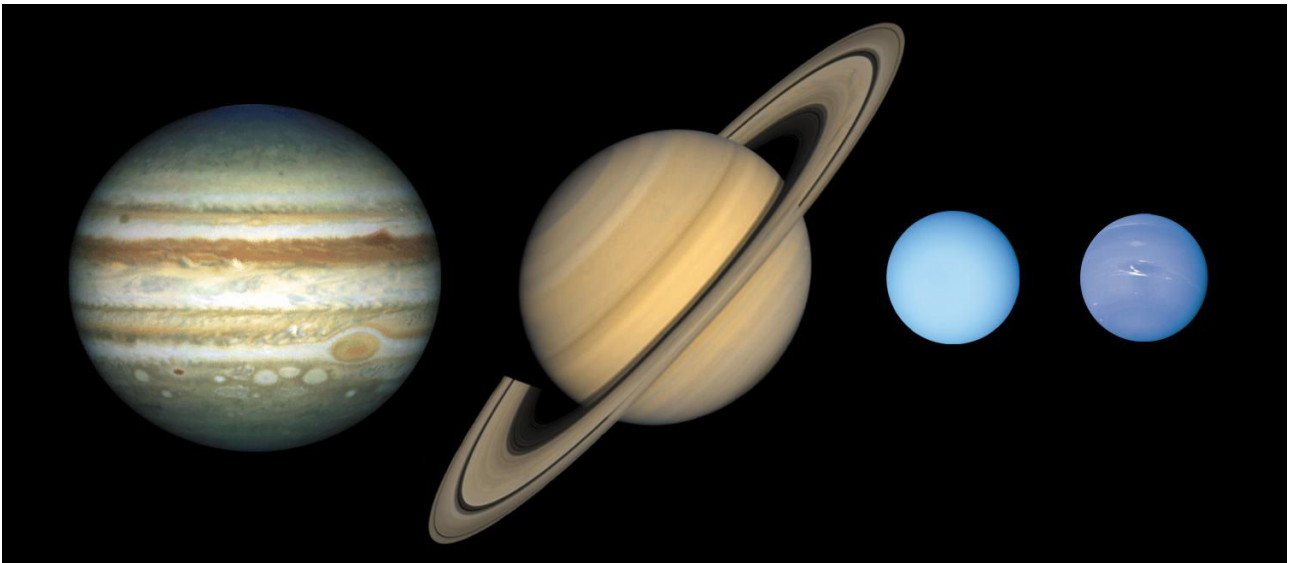


Figure 1.2: Comparative size of the four Gas Giants L–R: Jupiter, Saturn with its ring system, Uranus, and Neptune [38].

As shown in Table 1.1, all four gas giants are made up of primarily molecular  $\text{H}_2$  and He, with small amounts of other trace elements.

Planet	% $\text{H}_2$	% He	Trace Components	Mean MW (g/mol)
Jupiter	89.8 ( $\pm 2.0$ )	10.2 ( $\pm 2.0$ )	$\text{CH}_4$ , $\text{NH}_3$	2.22
Saturn	96.3 ( $\pm 2.4$ )	3.25 ( $\pm 2.4$ )	$\text{CH}_4$ , $\text{NH}_3$	2.07
Uranus	82.5 ( $\pm 3.3$ )	15.2 ( $\pm 3.3$ )	$\text{CH}_4$ (2.3%)	2.64
Neptune	80.0 ( $\pm 3.2$ )	19.0 ( $\pm 3.2$ )	$\text{CH}_4$ (2.3% ( $\pm 0.5$ ))	2.53 – 2.69

Table 1.1: Atmospheric compositions of the four Jovian planets (by volume, uncertainties in brackets) from the NASA Planetary Fact Sheets [39].



### 1.3.2 Jupiter

The most famous gas giant is Jupiter, the largest planet in our solar system. It is named after Jupiter, the king of the Roman gods, and astronomer and astrophysicist Carl Sagan once said of Jupiter that “*The cloud patterns are distinctive and gorgeous. No painter trapped on Earth ever imagined a world so strange and lovely*” [40]. Due to the fact that it can be seen by the naked eye in the night sky, Jupiter has been known to humanity since pre-biblical times, being first identified by Babylonian astronomers around the 7th and 8th century B.C [41]. However, it took another 2,500 years for detailed observations to be made of Jupiter. On January 7, 1610, using his own primitive telescope, Galileo discovered Jupiter’s four largest moons, now separately named Io, Europa, Ganymede and Callisto, and collectively known as the ‘Galilean moons’ in his honour [42]. In 1831, the pharmacist Heinrich Schwabe produced the earliest known drawing showing details of Jupiter’s Great Red Spot (shown photographed by Voyager 1 in Figure 1.3) [43].



Figure 1.3: Jupiter’s Great Red Spot photographed by Voyager 1 on February 25, 1979, when Voyager 1 was 9.2 million kilometres from Jupiter. [44]

### 1.3.3 Gas Giant Exploration

Humans have already commenced exploration of the gas giants. Various missions have examined the gas giants from afar (including Pioneer 10 and 11, Voyager 1 and 2, Ulysses, and Cassini [42, 45]) and missions have entered planetary bodies in the Jovian system (the Galileo probe's entry into Jupiter's atmosphere [42] and the Huygens probe's entry into Titan's atmosphere [46]). At the time of writing, the National Aeronautics and Space Administration's (NASA) Juno spacecraft is currently in orbit around Jupiter, after arriving in July 2016 [47]. The Juno mission is conducting a detailed study of Jupiter's origin, interior, atmosphere, and magnetosphere. It is hoped that clues to the origin of our solar system, and other systems like it, will be found [48]. It was originally planned that Juno would be slowly de-orbited over 5.5 days starting on February 20, 2018, causing it to burn up in Jupiter's atmosphere [49]. However, the mission has now been extended until 2021, partially due to an issue with a thruster placing it in a more elliptical orbit around Jupiter than had been planned [50]. A processed image from Juno's JunoCam created by Björn Jónsson can be seen in Figure 1.4. The image was taken on July 10, 2017, during Juno's seventh close flyby of Jupiter, and it shows what Jupiter's Great Red Spot would look like to the human eye from Juno's position.

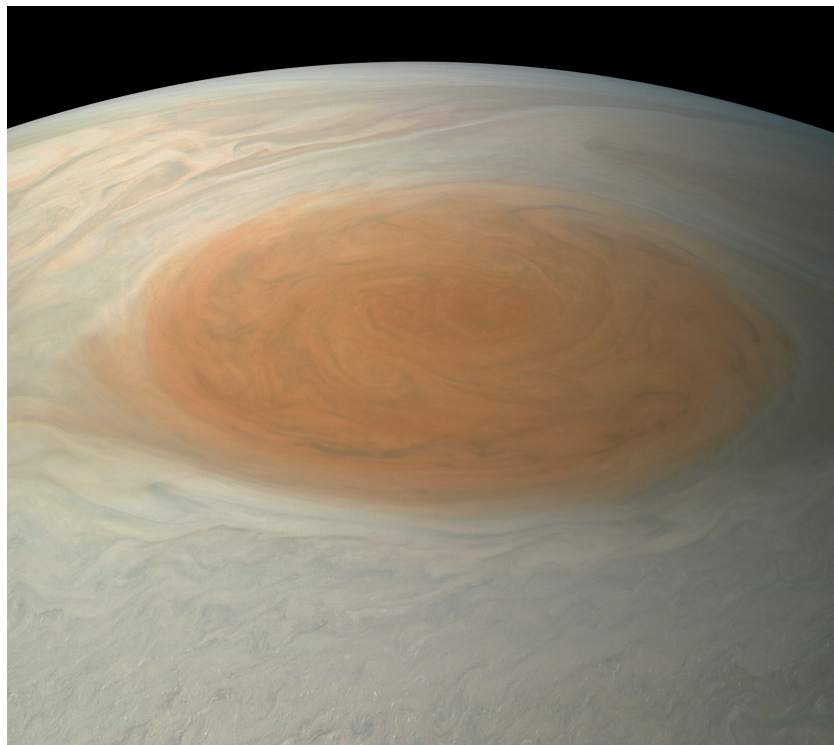


Figure 1.4: Jupiter's Great Red Spot photographed by Juno on July 10, 2017, during its seventh close flyby of Jupiter [51]. The processed image was created by Björn Jónsson and shows what Jupiter's Great Red Spot would look like to the human eye from Juno's position.

However, despite the research effort so far, there is still a lot which we do not know about the Jovian planets. The gas giants contain matter produced during the birth of the solar system which may hold valuable clues about the origins of life in the universe, and solar system formation and evolution [48]; the gas giants provide a valuable link to extrasolar planetary systems, where gas giant planets are common; Saturn's moon Titan (which the Huygens probe visited in 2005 [46]) is the only moon in our solar system with its own atmosphere, and Jupiter's four Galilean moons (shown in Figure 1.5) are all worthy of exploration: Io has over four hundred active volcanoes, and the other three moons, Europa, Ganymede, and Callisto, are all believed to house oceans of liquid water below their surfaces.

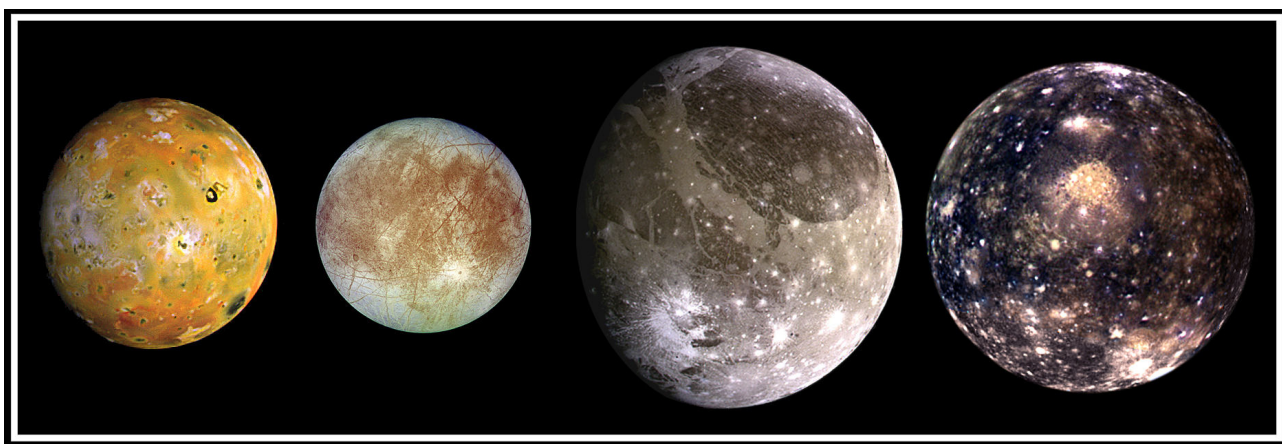


Figure 1.5: Jupiter's four Galilean moons, L-R: Io, Europa, Ganymede, and Callisto, photographed by the Galileo spacecraft. [52]

### 1.3.4 Gas Giant Entry in the Past: The Galileo Probe

*Note: a more comprehensive study of gas giant entry research can be found in Chapter 3.*

The entry of the Galileo probe into the atmosphere of Jupiter on December 7, 1995 is the only gas giant entry which humankind has ever performed. Being the largest of the four gas giants, entry into Jupiter presented the biggest challenge to engineers, with Jupiter's *inertial* entry speed being a massive 60 km/s [39]. However, it was the probe's speed *relative* to the atmosphere which needed to be minimised, rather than the *inertial* speed, and the probe's designers were able to reduce the atmospheric entry speed to a more manageable 47 km/s by entering the planet travelling due East, with Jupiter's rotation, and along the equator where Jupiter's rotational speed is at its maximum (roughly 13 km/s) [53]. The probe was designed for an entry speed of less than 47.8 km/s [53].

The Galileo probe entered Jupiter at a relative velocity of 47.5 km/s, and took less than 100 seconds to decelerate to 1 km/s [54]. Generally, even for ballistic Earth entries, the heat

load is principally convective and only partially radiative<sup>2</sup>. However, in these harsh conditions, radiation was the primary driver of the heat flux to the surface of the Galileo probe [54], contributing 99% of the total heating load, and constituting the most extreme heating environment ever experienced by a planetary entry probe. This is shown in Figure 1.6, where the magnitude of the engineering design problem can be seen when the Galileo probe's maximum stagnation point heat flux is compared to other planetary entries. At around  $34,000 \text{ W/cm}^2$ , the maximum stagnation point heat flux for the Galileo probe was a thousand times larger than the Space Shuttle's peak stagnation point heat flux (based on the experimental stagnation point heat flux from Space Shuttle flight STS-5 of  $34 \text{ W/cm}^2$  from Curry et al. [56]), and more than twenty times larger than the maximum stagnation point flux of faster Earth entries such as Hayabusa ( $1,800 \text{ W/cm}^2$ ) and Stardust ( $1,330 \text{ W/cm}^2$ ) (data from Davies [57]).

Behind the bow shock on the front of the Galileo probe during its entry, significant dissociation and ionisation would have occurred. The  $\text{H}_2$  in the flow would have dissociated directly behind the shock, before collisions with the heavier He atoms in the flow field would have started to ionise the H. Due to the much higher electronic excitation level of He (20 eV, compared to 10 eV for H), any He ionisation would probably have been fairly negligible in comparison, and the He would have acted as an inert diluent. As the partial ionisation created more free electrons, they would have become the primary driver of further ionisation, and the flow would have existed as a partially ionised plasma.

In ballistic planetary entry situations, ablative heat shields are generally used to manage surface heating and protect entry vehicles from destruction. This is especially important for harsh environments such as the entry which the Galileo probe encountered. However, heat shields comprise a large portion of the weight of a planetary entry vehicle, and as such, it is important that the uncertainties in the tools used to design the craft are minimised, so that safety margins can be adjusted accordingly. Due to the fact that radiative heat flux is still difficult to study, and uncertainties remain high, this is especially important for entries where radiative heat flux is significant, such as entry into Jupiter. The work of Milos [58] stated that, in relation to the Galileo probe heat shield, *"This thickness distribution provided a 50% safety margin against conservative predictions of heat shield recession for the nominal axisymmetric entry ... this margin was believed to be adequate for probable survival of the probe under a worst-case scenario of steep entry..."*. However, even with these conservative safety factors, analysis of the heat shield recession after the entry found that the heat shield had been bulky, inefficient, and unsafe.

---

<sup>2</sup>*Convection* is heat flux which occurs between a moving fluid and a surface when they are at different temperatures (i.e. heat flux to the heat shield from the hot, shocked gas flowing over it), and *radiation* is heat exchange between two surfaces at different temperatures, *in the absence of an intervening medium* (i.e. heat flux directly from the hot, shocked gas to other particles and the heat shield) [55].

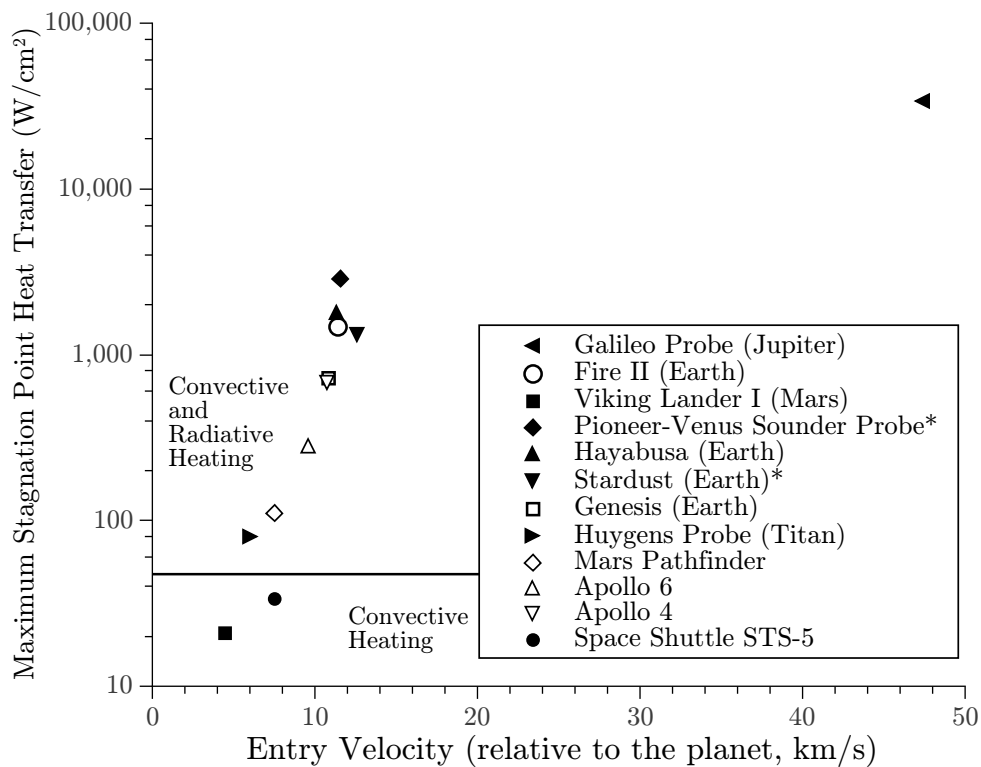


Figure 1.6: Maximum stagnation point heat flux for various entry vehicles. All data is from Davies [57] except for the Space Shuttle STS-5 data, which is experimental data from Curry et al. [56]. If the entry includes radiation, the heat flux value includes both the convective and radiative heat flux values from [57]. Where a range of radiative heat flux was given, the middle value has been taken. A \* next to a vehicle indicates data which is labelled in Davies [57] with a note saying “Heating rates and loads are probably for non-ablating conditions.” This figure was inspired by a similar figure by Gnoffo [54].

The Galileo probe was designed using the best computational aerothermodynamic methods available in the 1970’s and early 1980’s [59], with supporting experiments performed using a gas dynamic laser [60], a ballistic range [61], and an arc-jet [62], and its survival was an engineering triumph. However, the actual heat shield ablation did not agree well with the predictions [54]. In-flight measurements showed that only half of the sphere-cone heat shield actually ablated during entry [58]. Figure 1.7 shows that 100 mm of material thickness was left at the stagnation point of the probe, but that on the frustum<sup>3</sup> the heat shield ablated to within 10 mm of its base. This was different from the computational fluid dynamics (CFD) predictions which expected more recession at the stagnation point, and less on the frustum [58]<sup>4</sup>. These disagreements between the simulations and the flight test data indicated that improvements to both experimental and simulated modelling could be made.

<sup>3</sup>The conical sides of the probe’s sphere-cone heat shield.

<sup>4</sup>This is explained further in Section 3.3.

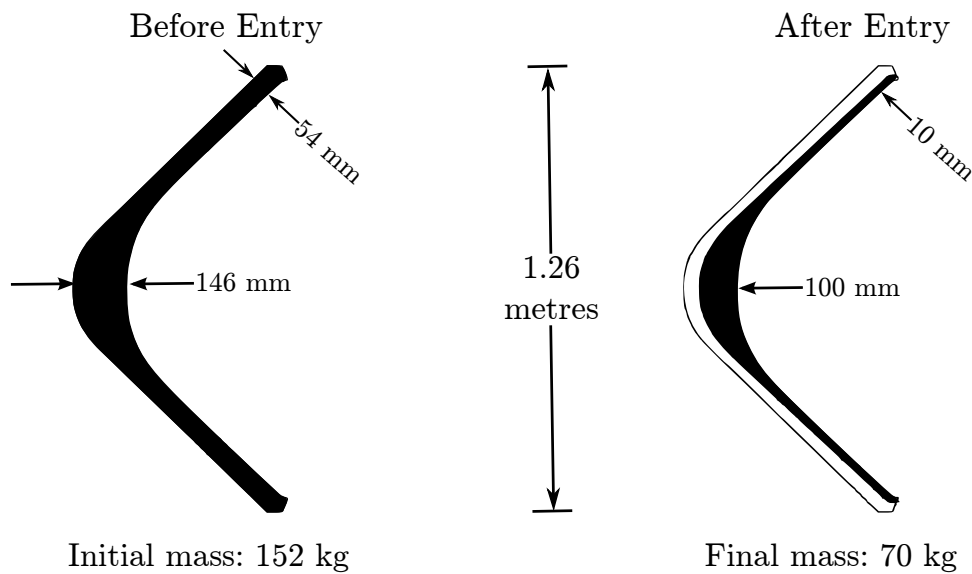


Figure 1.7: Ablation of the Galileo probe’s heat shield during its entry into Jupiter. (Adapted from NASA Ames photo ACD96-0313-13 [63])

In 2005, Matsuyama et al. [64] used the injection-induced turbulence model proposed by Park [65], as well as the actual atmospheric composition which the craft experienced (designers had expected Jupiter’s atmosphere to be the nominal value of 89% $\text{H}_2$ /11% $\text{He}$ , by volume, but where the probe entered was actually 86.4% $\text{H}_2$ /13.6% $\text{He}$ , 24% more  $\text{He}$  than was expected) in a radiating and ablating CFD model of the Galileo probe’s entry into Jupiter. They were able to closely reproduce the actual ablation on the frustum of the vehicle, but they largely overestimated the recession at the stagnation point.

A study by Park in 2009 [66] was able to recreate the stagnation point recession “*fairly closely*” by implementing a model which was focused on correctly modelling the interaction between the flow-field and the spallating carbon particles from the heat shield. Park’s model calculated the thermochemical state of the gas more accurately than had been achieved previously, and included the effects of vacuum ultraviolet (VUV) radiation absorption and spallation.

The fact that it is still difficult for CFD simulations to fully recreate the heat shield recession seen during the Galileo probe’s entry into Jupiter is motivation for the creation of techniques which would allow ground testing of gas giant entry radiation to be performed at velocities which are generally achievable in current impulse facilities (10 to 15 km/s) [67], hopefully leading to a greater understanding of gas giant entry phenomena.

### 1.3.5 Gas Giant Entry in the Future

While the majority of gas giant entry research in the past was either performed for the design of the Galileo probe, or to analyse issues associated with it, there is currently renewed interest in future gas giant entry probe missions. The US National Research Council ‘Vision and Voyages for Planetary Science in the Decade 2013-2022’ report identified probes to Uranus [68] and Saturn [69, 70] as high priorities for future space missions due to the aforementioned large scientific questions which remain unanswered, and the fact that Jupiter and Saturn are fundamentally different planets to Neptune and Uranus. The latter planets are known as ‘ice giants’ due to heavy elements trapped in their atmospheres in an ice-like state. It is hoped that by entering the atmosphere of an ice giant planet, humankind can then better understand the differences between gas giant and ice giant planets. The proposed probe entry velocities were 22.3 km/s for Uranus [68] and 26.9 km/s for Saturn [69, 70].

The expected aeroheating uncertainties of the aforementioned Uranus and Saturn entries, as well as a third steeper descent angle Saturn entry at 28.2 km/s, were analysed by Palmer et al. [71] in 2014 by performing a Monte Carlo study on the input parameters to their CFD model. They found that radiative heating for Uranus entry was negligible but at the highest velocity examined for Saturn entry, radiative heating contributed up to 20% of the heat load. In general, they found that the uncertainty in convective heating for Uranus and Saturn entry was “*no more than a few percent*”, but that for Saturn entry, where the post-shock temperatures are higher, that “*the uncertainty in radiative heating was substantial*”. The strongest contributor to the radiative heating variation was found to be the H<sub>2</sub> dissociation reaction rates, because the radiative heating seen at the wall is strongly influenced by the chemistry which occurs just behind the bow shock.

More recent work by Cruden and Bogdanoff [72, 73] has experimentally examined the expected radiation for parts of the three entry trajectories examined by Palmer et al. [71] in the Electric Arc Shock Tube (EAST) facility at NASA Ames Research Centre [74, 75, 76]. EAST is a non-reflected shock tube (NRST) capable of re-creating planetary entry shock waves at the true flight velocity and density. A suite of different spectrometers are then used to examine the relaxation behind the shock wave as it moves past a set axial location in the test section. Cruden and Bogdanoff used an 89%H<sub>2</sub>/11%He (by volume) simulated Saturn entry test gas, and examined freestream pressures from 13 to 66 Pa and velocities from 20 to 30 km/s. Consistent with Palmer et al.’s [71] conclusion that radiative heating for Uranus entry was “*negligible*”, Cruden and Bogdanoff found that, within their measurement limits, no shock layer radiation was detectable below 25 km/s. Above 25 km/s, radiation was observed, and they found that their shocks did not reach equilibrium over several centimetres, and that in many cases, the

state distributions were non-Boltzmann. Due to the fact that Nonequilibrium Air Radiation (NEQAIR) [77], NASA's in-house radiation code, is only able to simulate H<sub>2</sub>/He gas flows in Boltzmann states, NEQAIR currently over-predicts the radiation of the conditions by up to a factor of 10.

### 1.3.6 Ground Testing of Gas Giant Entry at UQ

Within this new context, which may see the design of two new gas giant probe missions in the foreseeable future, it is worth considering how the ground testing facilities at The University of Queensland (UQ) can further aid the development of this next generation of gas giant entry probes.

The large cost of performing flight experiments makes ground testing essential for the design of planetary entry vehicles. However, there are limitations: Due to the extreme total pressures and total temperatures encountered in planetary entry, it is impossible, in practice, to run continuous duration wind tunnel experiments at these speeds. Figure 1.8 shows how stagnation enthalpy, a parameter which correlates with total pressure and total temperature<sup>5</sup>, increases with increasing entry velocity. Stagnation enthalpy is a function of velocity squared, so an 8 km/s Earth entry has a stagnation enthalpy of 32 MJ/kg, but for an 11 km/s entry it is 61 MJ/kg, almost 100% higher. When gas giant entry is considered, the gases become lighter and it becomes easier to accelerate them to higher velocities, however, the stagnation enthalpies again get much larger. The aforementioned Uranus and Saturn entries at 22.3 and 26.9 km/s have related stagnation enthalpies of 249 and 362 MJ/kg respectively, and the Galileo probe's entry had a stagnation enthalpy of 1,130 MJ/kg. Due to these extreme energy requirements, decisions must be made about what to simulate. Many test facilities used to simulate planetary entry are relatively low velocity and long duration (i.e. arc-jets and plasma torches) where often neither the velocity nor the stagnation enthalpy of the true flight are re-created. In these facilities, the test times are long enough for the model to reach sufficient temperatures at which hot-wall and ablation tests can be performed. Others are high velocity, impulse facilities (i.e. shock tunnels and expansion tubes) where the velocity and Reynolds number of the true flight condition can be re-created, but the test times are generally extremely short (10's to 1000's of microseconds, depending on the size and type of facility) and experiments are performed on a 'cold' model.

The aforementioned three sets of experiments performed for the design of the Galileo probe all fell into the low velocity and long duration category [60, 61, 62]. None of the experiments

---

<sup>5</sup>Stagnation enthalpy ( $H_t$ ), is equal to  $C_p T + \frac{U_\infty^2}{2}$ , involving the static temperature ( $T$ ) and the entry velocity, and is also equal to  $C_p T_t$  because total temperature ( $T_t$ ) takes into account the velocity term.



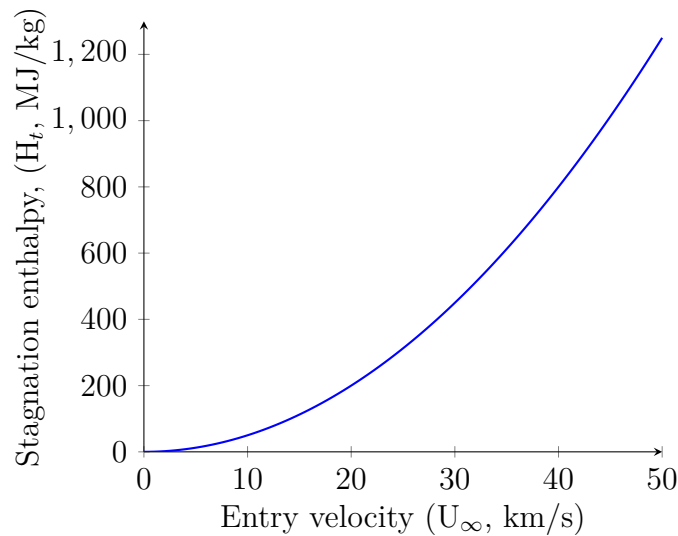


Figure 1.8: How stagnation enthalpy increases with increasing planetary entry velocity.

were able to re-create the velocity of the Galileo probe’s entry, but in various ways, and at various velocities, each experiment aimed to re-create the heating environment for a duration long enough to study the recession of an ablating model.

This thesis instead focuses on the use of an impulse facility, and it examines the opportunities and limitations of studying gas giant entry in an expansion tube, namely the X2 expansion tube at UQ. Expansion tubes are mainly used for studying planetary entry phenomena from around 3 to 12 km/s, but this thesis examines whether they are able to simulate the flow conditions of planned missions to Uranus and Saturn, and potentially faster gas giant entries, such as entry into Jupiter. This should be possible due to the high performance available from their high-powered free-piston drivers, and the extra speed gained by using a light hydrogen/helium test gas.

While an NRST facility like EAST has the ability to simulate and capture the relaxation behind a shock wave at true flight conditions, test time limitations generally preclude performing more complex experiments using test models. For most NRST facilities, this is a fundamental limitation. An expansion tube is a more versatile facility for several reasons. For a very short period of time (usually of the order of a hundred microseconds for the X2 facility) an expansion tube is capable of generating a realistic aerothermodynamic test flow, meaning that it can be used to simulate scaled test models. This opens X2 up to a series of different possibilities, including the use of quasi two-dimensional cylinder models [78, 79, 80], scaled aeroshell models [81, 82], instrumented models [83, 84, 85], wedge models to study expanding post-shock flows [86, 87], Mach disk models which produce standing normal shocks to study radiation over long relaxation distances [88, 89], and even resistively heated models to re-create the surface

temperatures of planetary entry vehicles [90, 91, 3, 7]. This added versatility means that re-creating gas giant entry flows in the X2 expansion tube would be very useful.

Previous work by Stalker and Edwards [67] showed that the inert diluent in gas giant entry flows, He, could be replaced by the heavier Ne to achieve significant shock layer dissociation and ionisation at much lower speeds. This is possible because He and Ne have similar excitation energies (21 and 17 eV, respectively). Their analytical and computational analysis showed that unless the post-shock temperature was above 60,000 K (where the Ne itself starts to ionise) the ionising relaxation of H<sub>2</sub>/Ne test flows was the same as H<sub>2</sub>/He ones. They also found that the similarity was not very sensitive to the *amount* of diluent used for the test gas substitution. This is helpful because Ne weighs five times as much as He, and therefore, if it is used in significant concentrations, it will increase the molecular weight of the test gas mixture by such a factor that the related decrease in  $C_p$  will cause the post-shock temperature to be much hotter for the same flow enthalpy. This means that test flows with shock layers containing significant levels of dissociation and ionisation could be produced at velocities of the order of 10 to 15 km/s compared to the more than 20 km/s velocities required to reproduce the real flight conditions. This means that the shock layers of conditions beyond the current stagnation enthalpy limitations of the X2 expansion tube could be simulated at slower velocities by using either a larger amount of He diluent, or the heavier diluent, Ne.

Previous studies in X2 [92, 63] used the test gas substitution to investigate shock standoff on blunt bodies with a H<sub>2</sub>/Ne test gas which was correlated to Damköhler numbers for the ionisation process and confirmed using an analytical ionisation model. Good reproduction of shock standoff was seen between experiment, CFD, and analytical results for cylinders and spheres. A test gas utilising 85%Ne diluent (by volume) was used to maximise dissociation and ionisation in the shock layer. However, no radiation measurements were taken, and it is not yet known how the substitution of He for Ne will affect the post-shock radiative emission, or if this substitution provides a valid platform for studying it. Due to the opportunities available for performing radiating gas giant entry experiments using test models if the substitution proves to be valid, this is worth investigating.

## 1.4 Objectives of this Thesis

The overall aim of this thesis is to establish the feasibility and practical limitations of simulating gas giant entry with a free piston driven expansion tube in UQ's X2 facility. The specific objectives required to do this are:

1. **Develop fast condition modelling capability.** To facilitate the design of new test conditions for simulating gas giant entry in the X2 expansion tube, it is necessary to have

tools which can quickly and easily perform parametric studies of facility performance with a reasonable level of accuracy.

2. **Investigate the feasibility of simulating Uranus and Saturn entry at true gas composition and true flight velocity in X2.** The recently proposed entry probe missions to Uranus and Saturn give new context for the study of gas giant entry. Due to their 22.3 km/s and 26.9 km/s entry velocities being much slower than Jupiter's 47.5 km/s, there is the potential that these entries could be simulated at true gas composition and true flight velocity. Using fast condition modelling tools, performance of the facility can be theoretically ascertained and then tested against experimental results.
3. **Investigate the possibility of using the Stalker substitution to simulate Uranus and Saturn entry at flow stagnation enthalpies more easily achievable in the X2 facility.** There are issues with simulating such high speed conditions, such as large shock speed uncertainties. For this reason, it is important to consider simulating these proposed entries at lower stagnation enthalpies than the true flight conditions using the established Stalker substitution. This substitution can also be used to investigate gas giant entries which cannot be simulated directly.

## 1.5 Structure of this Thesis

This thesis is organised as follows:

*Chapter 2* provides a brief introduction to the ground testing of hypervelocity flow and how it is generally simulated. It briefly discusses the limitations of a shock tunnel and how these limits can be circumvented by using an expansion tube facility. A brief literature review of the different types of experimental facilities used to simulate planetary entry is also presented.

*Chapter 3* presents a comprehensive literature review of the history of gas giant entry research starting from when it was first considered in the 1960's, through to the design and flight of the Galileo probe, and then the research still being conducted today. It aims to start from the very first experiments and continue until the present day, showing how the canon of gas giant entry knowledge has expanded over time.

*Chapter 4* is dedicated to a discussion of the X2 expansion tube at the University of Queensland, the facility which this thesis is built around. It expands on the short introduction to expansion tubes discussed in Chapter 2 and aims to give the reader a good understanding of the tube and its related hardware. Upgrades to analysis procedures and to the facility itself conducted by the author are also discussed.

*Chapter 5* discusses simulation of the X2 expansion tube. It begins by explaining what occurs during an X2 expansion tube experiment and then how PITOT, an equilibrium expansion tube analysis code written by the author, simulates the real experiment. How the PITOT code works is explained, including any issues related to a state-to-state analysis of some sections of the facility. Two examples of how to use the code to help analyse an actual experiment are provided.

*Chapter 6* presents the analysis of the performance limitations of the X2 expansion tube in its current configuration. It uses the PITOT code discussed in Chapter 5 to perform a parametric study of the facility for the simulation of gas giant entry at true flight velocity and true gas composition for the simulation of Uranus entry conditions. Experimental results are presented to validate the theoretical predictions, with discrepancies and issues associated with the high shock speeds also discussed. A theoretical analysis of how faster gas giant entries could be simulated with a more powerful free piston driver is also presented.

*Chapter 7* presents the theoretical analysis related to using higher amounts of helium diluent or the heavier neon diluent to simulate gas giant entry shock layers inside the current theoretical performance envelope of the X2 expansion tube. Experiments are then presented to validate the theoretical predictions using a helium diluent.

*Chapter 8* provides the conclusions and recommendations of the thesis.

## 2

# Literature Review of Hypervelocity Flow Simulation

*Ce que nous connaissons est peu de chose, ce que nous ignorons est immense.*

– mathematician and astronomer Pierre-Simon Laplace, *on his deathbed*, 1827

## 2.1 Chapter Overview

This chapter presents an overview of hypervelocity flow and how it is simulated. It begins by describing hypervelocity flow before moving on to the challenges of simulating it and the various types of facilities used for this purpose. This section does not claim to be completely comprehensive, but aims to give the reader a reasonable idea of the types of facilities which exist and what they are typically used for.

## 2.2 Ground Testing of Hypervelocity Flows

In a general sense, any gas flow above Mach 5 is considered to be not just supersonic, but *hypersonic*. However, this is a very loose definition. As Anderson states in the introduction to his textbook on hypersonic flow [93]:

*“There is a conventional rule of thumb that defines hypersonic aerodynamics as those flows where the Mach number  $M$  is greater than 5. However, this is no more than just a rule of thumb; when a flow is accelerated from  $M = 4.99$  to  $5.01$ , there is no ‘clash of thunder,’ and the flow does not ‘instantly turn from green to red.’ Rather, hypersonic flow is best defined as that regime where certain physical flow phenomena become progressively more important as the Mach number is increased*

*to higher values. In some cases, one or more of these phenomena might become important above Mach 3, whereas in other cases they may not be compelling until Mach 7 or higher.*

The reader is referred to the rest of Section 1.3 of Anderson [93] for a broader discussion of what constitutes hypersonic flow.

When dealing with an entry or re-entry scenario, a very applicable scenario for this thesis, the flow is generally not simply hypersonic, but *hypervelocity*. According to Stalker [94]:

*“Hypervelocity’ is a term that was originally coined to describe flows that are both hypersonic and high velocity, rather than merely hypersonic, and it is used in that context here. Hypervelocity aerodynamics arose as a field of research in fluid dynamics when it became necessary to understand the aerodynamics of vehicles entering the Earth’s atmosphere. The velocities involved in such re-entry manoeuvres ensure that the enthalpy of air, after crossing the strong bow shock that is formed ahead of the vehicle, is sufficient to cause dissociation of the air molecules.”*

In a hypervelocity flow-field, a strong bow shock envelops the vehicle, and the energy in the flow-field is high enough for intermolecular collisions to cause the flow to dissociate and potentially ionise behind the bow shock. These collisions also distribute energy amongst the internal energy modes of the atoms and molecules. In a general sense, until the flow reaches an equilibrium state, this is what is referred to as a ‘non-equilibrium flow-field’: the distribution of species and the distribution of energy among their internal modes, in any small part of the gas in the flow-field, are a function of the collisional history of atoms and the molecules [54]. Often it is not a simple task to simulate and analyse these hypervelocity flow-fields, and this is a theme which will be expanded upon in this chapter.

In the 19th century, the wind tunnel replaced the earlier, but somewhat more questionable, ‘whirling arm’ of the 18th century<sup>1</sup> as the aerodynamic test facility of choice, revolutionising aeronautical science with it. According to Baals and Corliss [95]:

*“This utterly simple device consists of an enclosed passage through which air is driven by a fan or any appropriate drive system. The heart of the wind tunnel*

---

<sup>1</sup>The ‘whirling arm’ was just like the name says, a sort of ‘aeronautical centrifuge’ where a model was mounted at the end of an arm, and the centre was rotated, spinning the model around in circles. This design has many obvious flaws (the spinning complicates the analysis, the model was constantly flying into its own wake, among others), but was used to successfully test early airfoil models, and Sir George Cayley used whirling arm test data to build and fly the world’s first successful heavier-than-air vehicle in England in 1804. [95]

*is the test section, in which a scale model is supported in a carefully controlled airstream, which produces a flow of air about the model, duplicating that of the full-scale aircraft. The aerodynamic characteristics of the model and its flow field are directly measured by appropriate balances and test instrumentation. The wind tunnel, although it appears in myriad forms, always retains the five identifying elements italicized above. The wind tunnel's great capacity for controlled, systematic testing quickly rendered the whirling arm obsolete.*

*The unique role and capabilities of a wind tunnel can best be appreciated by recognizing the aerodynamic forces and moments acting on an aircraft in flight. The three basic forces are lift, drag, and side force as measured in an axis system referenced to the direction of flight of the aircraft. The drag force is along (but reversed to) the flight path; the lift and side forces are at right angles to it. In a wind tunnel the axial centerline of the test section defines the direction of the oncoming wind - the aerodynamic equivalent of the flight path. The ease of measuring aerodynamic forces relative to the tunnel axis on a model held stationary in the airstream opened a new era in aerodynamic experimentation."*

With the advent of wind tunnel testing, aerodynamic theory accelerated very quickly, and such concepts as angle of attack, aspect ratio, and Reynolds number scaling are all concepts from the 19th century. The now famous Wright Brothers built a wind tunnel in 1901 which informed the design of their 1903 Wright Flyer, the first ever powered flight vehicle [95].

The wind tunnel was then, and still is today, an important subsonic aerodynamic testing device. Even when supersonic flight testing began in the 1940's, the wind tunnel was still considered the facility of choice [95]. However, in the 1950's, when hypersonic flow testing was beginning, the limits of wind tunnel testing started to become apparent, and it was generally accepted that normal supersonic wind tunnels could not simulate gas flows above Mach 5. In 1955, Smelt [96] stated that:

*"It is well known that ordinary supersonic wind tunnels, operating from an air supply at approximately room temperature, have an upper limit in Mach number which is determined by the commencement of liquefaction of the air around the model in the test section. For a wind tunnel with a supply pressure of one atmosphere and a supply temperature of 80° F (≈300 K), the air in the test section reaches the liquefaction point at a Mach number of 5."*

Smelt [96] went on to detail both the engineering and physical limits of hypersonic wind tunnel testing, before discussing the other types of facilities which could be used to perform hypersonic testing. Smelt stated that the maximum wind tunnel Mach number could be extended

to about 10 or 11 by heating the supply air but this could only occur “*at the expense of a considerable increase in the complexity of the wind tunnel*”. However, the practical engineering limit of needing to contain a high temperature and pressure supply chamber for long periods of time prevents hypersonic wind tunnels from operating past this limit. The physical limits of hypersonic wind tunnel applicability arrive due to the departure of hypersonic air from perfect gas behaviour as the flow Mach number increases. This occurs because traditional supersonic and hypersonic wind tunnels operate at low freestream temperatures close to the liquefaction temperature of air, meaning that the related post-shock temperatures are much lower than they would be in flight. Smelt identified three different regimes of hypersonic wind tunnel testing, and summarised his results in a table which has been reproduced below as Table 2.1 with the temperature unit converted from °R to K. Table 2.1 shows that by using corrections for vibration effects which would not be present in the wind tunnel post-shock flow, wind tunnels could be used up to around Mach 12, but beyond that, larger differences would be seen between tunnel and flight.

Table 2.1: Ranges of application of hypersonic wind tunnels, adapted from Smelt [96]. Temperature units have been converted from °R to K.

	<b>Range 1</b> Results applicable to flight without correction	<b>Range 2</b> Corrections for Vibration Effects Required	<b>Range 3</b> Large Differences between Tunnels and Flight
Maximum local temperature (K)	Up to 550	550 – 1,900	Above 1,900
Corresponding Stagnation temperature (K)	Up to 1,550	1,550 – 6,900	Above 6,900
Flight Mach number in stratosphere (T = 220 K)	Up to 5.5	5.5 – 12	Above 12

Smelt mentions the idea of short-duration high Mach number facilities as a solution to the cooling problem at the tunnel throat. He states that “*One possibility is to reduce the time of operation of the high-temperature flow to such an extent that the heat transfer to the critical parts of the wall is not large enough to do damage*” [96]. Following that, both reflected and non-reflected shock tubes are discussed as a type of impulse facility which could be used.

In another section, Smelt details the concept of simulating individual phenomena as a way to simplify the process of simulating complex hypersonic flow phenomena [96], a technique which is still carried out today for the study of hypersonic and hypervelocity gas flows.



In the 60 years since Smelt's paper was published, the simulation of hypervelocity flows has very much followed what Smelt discussed. Due to the extreme costs of performing flight experiments, ground tests have been essential to the design of planetary entry vehicles. Because of the aforementioned issues discussed by Smelt, it is impossible in practice to run continuous duration planetary entry wind tunnel experiments on a test model, and decisions must be made about what to simulate. Two different fields of planetary entry simulation have developed, and test facilities used to simulate planetary entry generally either choose to simulate a scaled version of the real flight condition for a very short period of time, or some specific phenomena of the real flight condition for a longer period of time.

Impulse facilities based on some variation of the shock tube and shock tunnel concept have been very popular for hypersonic and hypervelocity testing because even if the test times are extremely short (from 10's of microseconds to 100's of milliseconds depending on the scale and type of facility), and because of this, experiments are performed on a 'cold' model, they allow the stagnation enthalpy and Reynolds number of a true flight condition to be re-created.

The other types of ground testing facilities used to study hypersonic phenomena are generally relatively low velocity and long duration, such as arc-jets [97, 98], plasma torches [99, 100], and plasma wind tunnels [101, 102]. These are high enthalpy test facilities which have test times long enough for the test model to reach temperatures at which hot-wall and ablation tests can be performed. However, while they can re-create flow stagnation enthalpy, they do not re-create the velocity or a real aerodynamic flow-field, and due to the high freestream temperatures, the test flows are often subsonic. For this reason, these long duration facilities are often used for materials testing, because they allow representative heat loads to be re-created and the test model to be measured before and after the experiment, allowing the material lost through surface recession to be quantified<sup>2</sup>. Due to how their test flow is generated, arc jets and plasma wind tunnels can generally only produce test flows with low Reynolds numbers and low stagnation pressures. This also results in high levels of thermal non-equilibrium in the test flow. Conversely, plasma torches generally operate at much higher pressures, and the work of Laux [99] showed that the test flow generated by the plasma torch which he was using was in thermochemical equilibrium, allowing it to be used for the validation of radiation modelling codes. Many modern studies in these types of facilities focus on the interaction of an ablating test model with the test flow, such as the work of MacDonald et al. in a plasma torch [100], and the work of Hermann et al. in a plasma wind tunnel [103].

Shock tubes and shock tunnels also have their limitations. Because all of the energy is added to the flow using shock waves, both reflected and non-reflected shock tubes are limited

---

<sup>2</sup>This is not something which can be done in a shock tube type facility, because the driving gases flow over the test model after the experiment

in the stagnation enthalpy which they can simulate. This is because at very high shock speeds, the flow exists as a highly dissociated plasma, which is useful for studying post-shock planetary entry radiation, but not for aerothermodynamic testing. Such facilities are generally limited to speeds up to, and including, Earth orbit velocities ( $\approx 8$  km/s) [104].

Non-reflected shock tubes, such as the EAST facility at NASA Ames [74, 75, 76] and the currently under construction European Shock-Tube for High Enthalpy Research (ESTHER) in Portugal [105], are generally used for the study of planetary entry radiation, due to their ability to generate the real post-shock conditions of planetary entries. However, due to low density shock tube ('Mirels' [106, 107, 108]) effects, the separation distance between the moving shock wave and the contact surface travelling behind it decreases with distance, meaning that they often generate very short test gas slugs. This can make it difficult to establish flow over a test model. Even if flow over a model can be established, because the freestream flow generated is the condition directly behind a shock wave, its flow stagnation enthalpy is often highly chemical. In spite of this, experiments with test models have been performed in non-reflected facilities, and the 'prior steady flow' technique developed by Mudford and Stalker [109, 110, 111], wherein a flow was generated in a hypersonic nozzle before arrival of the shocked test gas, was able to start nozzles in high speed non-reflected shock tunnels, which could then be used to generate flows over test models.

One of the most common impulse facility configurations is the reflected shock tunnel, where the initially shocked test gas is reflected off a wall, generating a reservoir of twice shocked gas at high pressure and temperature. This reservoir can itself be probed to study high temperature gas behaviour, such as dissociation, or it can be slowly bled out through a de Laval nozzle to generate hypersonic test flows. One benefit of reflected shock tunnels is that because the test flow is generated by bleeding gas out of a reservoir, they produce much longer test times than non-reflected facilities. However, they also require different nozzles to generate different flow Mach numbers, and if the facility is driven too quickly, the stagnated test gas can become highly dissociated, and even if the temperature drops through the nozzle expansion, the test gas may not recombine [112, 113]. Reflected shock tunnels have been used for many different types of hypersonic testing. The list provided here is not exhaustive, but for example, they have been used to study planetary entry heat transfer [114, 115, 116, 117, 118, 119], scramjet flight [120, 121, 122], as well as many different fundamental studies of hypersonic flow-fields [123, 124, 119, 121].

The expansion tube, an idea which was originally proposed in the 1950's [125], refers the freestream chemistry issues to higher enthalpies by only adding part of the energy to the flow using a shock wave. The rest of the energy is added by accelerating the flow through an unsteady expansion. At the expense of test time (compared to a reflected shock tunnel), total

enthalpy and total pressure can be added to the flow without the dissociation which would occur if the conditions were generated in a traditional shock tube or shock tunnel [126]. Since this allows expansion tubes to simulate much higher enthalpy conditions, they are often used to simulate planetary entry. At UQ, the X2 expansion tube has been used to study entry into Earth [81, 127, 86, 103, 128, 129], Mars [78, 79, 87], Venus [80, 130], and Titan [79]. The LENS-XX expansion tube at CUBRC has been used to extensively study Mars entry test conditions [131, 132, 133, 134, 135]. Expansion tubes have also been used to simulate scramjet flight [136, 137, 138], the interaction between planetary entry flight conditions and an ablating wall using resistively heated test models [90, 91, 3, 7, 6, 139], and to study supersonic combustion phenomena at lower enthalpy conditions [140, 141, 142].

The first expansion tube experiments at UQ were performed in 1987 [143, 144, 145]. Throughout the 1990's, UQ developed, designed and commissioned three separate free piston driven expansion tube facilities, X1, X2, and X3, each larger than its predecessor. The X2 and X3 superorbital expansion tube facilities are both still operational to this day. A history of expansion tube research at UQ can be found in Gildfind et al. [146] and X2 is discussed further in Chapter 4.

# 3

## Literature Review of Gas Giant Entry

*The world is still a weird place, despite my efforts to make clear and perfect sense of it.*

– Hunter S. Thompson, *Songs of the Doomed*, 1990 [147]

### 3.1 Chapter Overview

This chapter presents a literature review of the history of gas giant entry. The review begins by discussing some of the work published in the late 1960's and 1970's by NASA when they were first considering the idea of sending a probe to enter a gas giant. The next section talks about the research done to transform that idea into a reality with the design of the Galileo probe, the first human-made object to enter a gas giant. A test gas substitution proposed in the literature is then presented, which allows gas giant entry conditions to be approximated in hypersonic ground testing facilities at lower velocities than in flight, before some of the research carried out using the substitution is discussed. Finally, the section concludes by discussing some of the recent research which has been completed and how it contributes to an increased understanding of gas giant entry.

### 3.2 Where it all Started

The very first mention of entry into a gas giant that the author could find was in a NASA paper titled '*Progress and Problems in Atmosphere Entry*', presented at the XVIth IAF International Congress in Athens in 1965 [148]. The paper discusses the issues facing NASA in the longer term, including the issues involved in sending unmanned probes to Mars and Venus. However, Jupiter, with an entry speed listed as approximately 60 km/s, is dismissed in a single paragraph:

*“Also listed in the figure is the entry velocity associated with atmosphere probes of Jupiter, provided that no propulsive braking is utilized. Today’s entry technology clearly does not permit such an entry and much work must be done if such a mission is to be attempted. Because Jupiter entry probes are so far in the future, no further consideration will be given to them here.” [148]*

However, with the technological leaps which led to humankind setting foot on the moon in 1969, came similar leaps in other areas, and during the final years of the 1960’s NASA researchers were starting to analyse gas giant entry. The first study of the heating environment and potential trajectories related to the once dismissed Jupiter atmospheric entry was performed by Tauber in 1969 [149]. Other early studies of gas giant entry heating environments, include the work of Stickford and Menard in 1968 [150]; Tauber and Wakefield in 1970 [151]; and Tauber [152] and Page [153] in 1971. All of these early studies made the assumption that the dissociation and ionisation of the  $\text{H}_2/\text{He}$  gas mixture was complete *immediately* after the shock; meaning that the whole flow-field in the shock layer was assumed to be in chemical equilibrium.

In 1973, Leibowitz [154] performed shock tunnel experiments in the new electric arc driven shock tube at NASA’s Jet Propulsion Laboratory (JPL) in Pasadena, California, U.S.A. [155] from 13 to 20 km/s with fill pressures of 33, 133, and 267 Pa, all using a 21% $\text{H}_2$ /79% $\text{He}$  test gas mixture (by volume). The work examined the relaxation of Hydrogen line and continuum emission intensities behind the incident shock in the shock tube. He found that dissociation of the  $\text{H}_2$  took place behind the shock in a region which was small compared to the ionisation, and that the ionisation process was governed by 2 different regions; one which was dominated by the excitation of H due to atom-atom collisions; and a second region which was dominated by H excitation due to collisions with electrons. Leibowitz found that when ionisation started, the electron temperature of the flow was significantly different to the heavy particle temperature, but that the two temperatures began to converge during the later part of the reaction. (This is shown in Figure 3.1.)

Leibowitz’ work in 1973 [154], along with a short theoretical paper by Howe in 1974 [156], showed that the assumption made in the initial gas giant entry papers had been wrong: dissociation and ionisation did not occur instantly. This meant that researchers needed to consider non-equilibrium flow and see if its effect was significant.

In 1976 Leibowitz and Kuo analysed results from shock tube experiments, flow-field calculations, and trajectory analysis to build an analytical tool which enabled the impact of ionisational non-equilibrium to be studied [157]. They found that during segments of simulated entries into Saturn and Jupiter, the ionisational non-equilibrium region behind the bow shock was of significant size, and would result in a reduction of the overall entry heat load. However, the

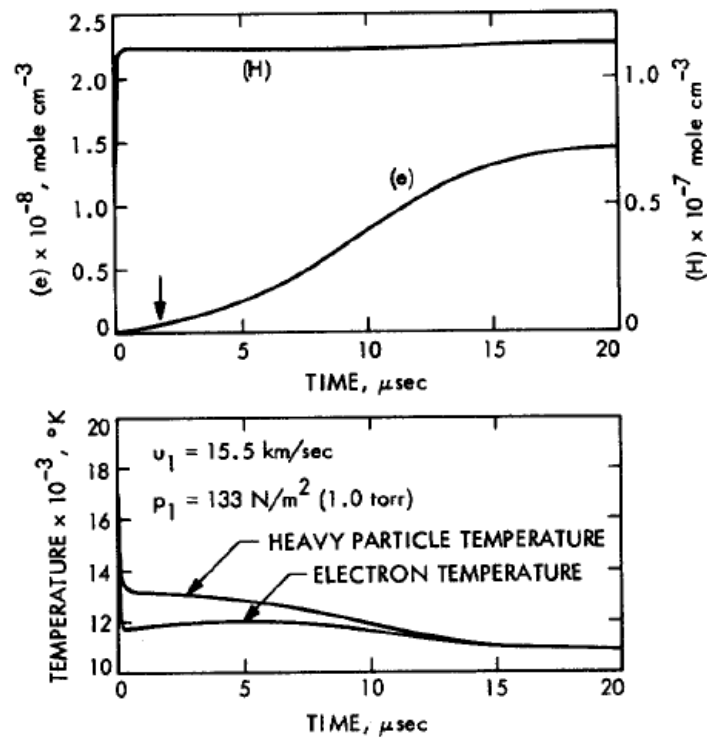


Figure 3.1: Variation of concentrations and temperature behind a 15.5 km/s shock in a 21% $\text{H}_2$ /79% $\text{He}$  gas mixture (by volume) with a fill pressure of 1.0 torr (133 Pa), calculated by Leibowitz [154].

non-equilibrium regions were found to be thin during the peak heating parts of the trajectories, so the overall reduction was typically less than 15%.

The first measurements of the ionisation rate of H were taken by Belozarov and Measures in 1969 [158] using an electric arc driven shock tube at the Institute for Aerospace Studies at the University of Toronto, Canada. They had estimated that shock speeds greater than 25 km/s would be required to complete dissociation of a pure hydrogen test gas and produce a ‘measurable’ electron concentration behind the shock. As such, they performed experiments from 28 to 35 km/s at between 1.5 to 3 torr (200 to 400 Pa) using an ‘*ultra-pure hydrogen with the specified impurity level 5 parts per million*’ [158] test gas. Electron concentration changes were observed using interferometry as the increase of electrons changed the refractive index of the gas. Experimental measurements were compared to their own theoretical relaxation model, and in Figure 3.2 it can be seen that good agreement was seen.

The previously mentioned shock tube work by Leibowitz in 1973 [154] presented new reaction rates which were smaller than the rates measured by Belozarov and Measures. Leibowitz and Kuo’s work in 1976 [157] included further shock tube measurements at higher shock speeds (26 to 27 km/s with an initial fill pressure of 4 torr [533 Pa] and 29 to 38 km/s with an initial fill

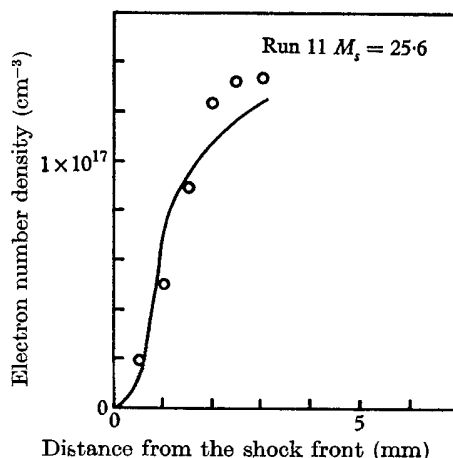


Figure 3.2: Comparison between theoretical (curve) and experimental (circles) electron density profiles from Belozarov and Measures [158].

pressure of 1 torr [133 Pa]) using a 85% $\text{H}_2$ /15% $\text{He}$  mixture (by volume) test gas, and the rates were again reduced.

In 1980, Stalker compared both sets of Leibowitz' data to experiments carried out in a non-reflected free piston driven shock tunnel at the Australian National University (ANU) in Canberra, Australia using an inclined flat plate and a test gas mixture of 60% $\text{H}_2$ /40% $\text{Ne}$  (by volume) [159]. He found good agreement between the set of reaction rates obtained by Leibowitz and Kuo in 1976, and his own experimental data. The results of the experiments can be seen in Figure 3.3. (The 'A' rate constants referred to in Figure 3.3 are the reaction rates obtained by Leibowitz in 1973 [154], and the 'B' rate constants are the reaction rates obtained by Leibowitz and Kuo in 1976 [157].)

In 1971, in an attempt to simulate Saturn and Jupiter atmospheric entry in a shock tube at NASA's JPL, Menard used an electric arc shock tube with a new lower volume, conical arc driver to improve facility performance from previous configurations [155]. (A diagram of a conical arc driver from Dannenberg [160] can be seen in Figure 3.4.)

Using a hydrogen driver gas and a very low pressure 0.05 torr (6.7 Pa) pure hydrogen test gas, Menard [155] was able to produce a shock velocity of 45 km/s 3.66 m away from the diaphragm separating the driver and driven sections, and a shock velocity of 39.5 km/s 10.67 m away from the diaphragm. With an 20% $\text{H}_2$ /80% $\text{He}$  (by volume) gas giant entry test gas at the same pressure, he was able to produce a shock velocity of 41.3 km/s 3.66 m away from the diaphragm, and 40.4 km/s 10.67 m away. Performance was considerably lower when a helium driver gas was used, dropping to around 30 km/s for the 20% $\text{H}_2$ /80% $\text{He}$  (by volume) condition. The following year in 1972, similar experiments were performed with the same type of driver at NASA Ames

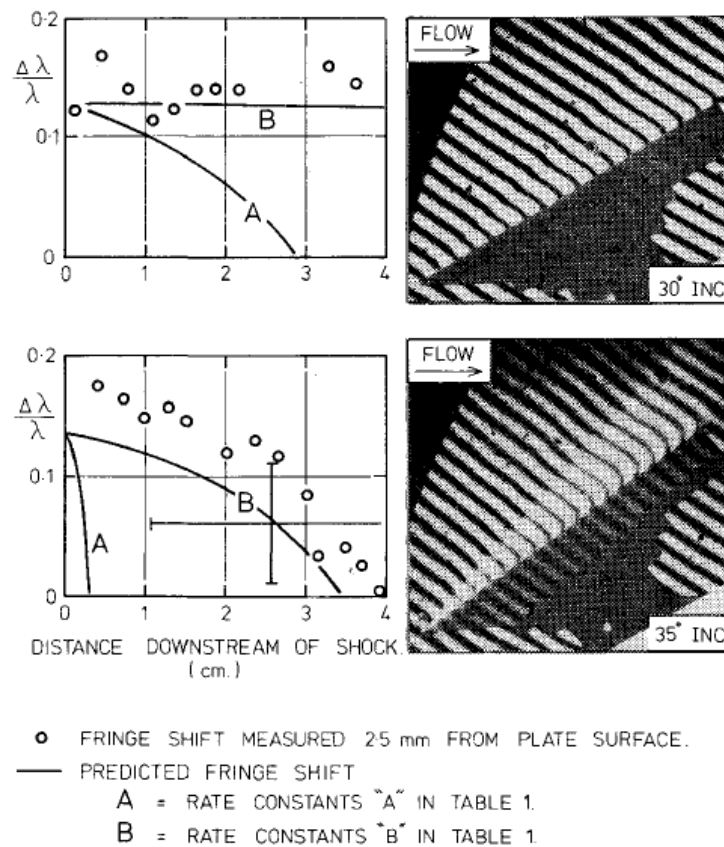


Figure 3.3: Relaxation downstream of an oblique shock over a flat plate from the work of Stalker [159]. The 'A' rate constants were obtained by Leibowitz in 1973 [154], and the 'B' rate constants were obtained by Leibowitz and Kuo in 1976 [157]. The test gas is 60% $H_2$ /40%Ne (by volume), and the primary shock speed is 11.4 km/s.

Research Center by Dannenberg and very similar results were seen [160]. A comparison plot between the two studies (taken from Dannenberg [160]) can be seen in Figure 3.5.

Looking at Figure 3.5, it can be seen that for both the work of Menard [155] and Dannenberg [160], with a driven gas mixture of 20% $H_2$ /80%He (by volume) and a 1.0 torr (133 Pa) shock tube fill pressure (labelled 'driven tube loading pressure' on the figure), both facilities cannot drive a shock faster than 20 km/s. It is only with a very low 0.05 torr (6.7 Pa) shock tube fill pressure, that they can manage to drive a shock at 40 km/s.

In 1975, while discussing previous gas giant entry shock tube research, Leibowitz [161] stated that the conical arc drivers used by Menard [155] and Dannenberg [160] had allowed the simulation of some of the variables for Jupiter entry but that "*performance has fallen short of the goal of 40 km/s shock velocities in hydrogen-helium mixtures with initial pressures of 1.0 torr or greater*" [161]. Leibowitz went on to show that the shock velocities required to study entry into Jupiter or Saturn could be established at higher pressures than the earlier



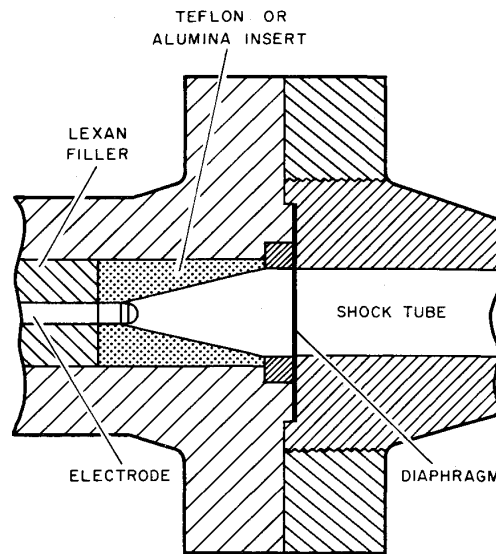


Figure 3.4: Schematic of a conical arc driver for an electric arc shock tube from Dannenberg [160]. The section to the left of the diaphragm is the driver.

Symbol	DRIVER		DRIVEN GAS
	GAS	kJ/g	
○ (AMES)	H <sub>2</sub>	850	0.2 H <sub>2</sub> - 0.8 He
● (JPL Ref 2)	He	250	0.2 H <sub>2</sub> - 0.8 He
□ (a,b,c)	He	375, 150, 75	0.2 H <sub>2</sub> - 0.8 He
◇	He	250	DRY AIR
◆	He	415	DRY AIR
▨ (AMES)	He	VARY	0.2 H <sub>2</sub> - 0.8 He
▩ (JPL)	He	PRESET VOLTAGE	0.2 H <sub>2</sub> - 0.8 He

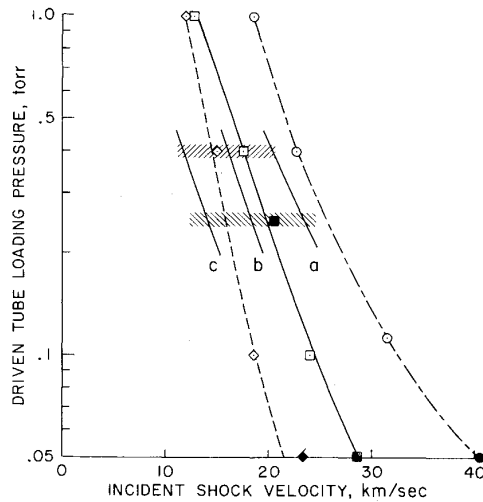


Figure 3.5: Comparison between conical arc driven shock tube facilities for gas giant entry simulation from Dannenberg [160]. The data labelled AMES is from the experiments performed by Dannenberg [160] and the data labelled JPL is from Menard [155].

work of Menard [155] and Dannenberg [160] using the newly developed ANAA (ANnular Arc Accelerator) driven shock tube [161].

Unlike traditional electric arc driven shock tubes like those used by Menard [155] and Dannenberg [160] (a version of which is shown in Figure 3.4), the ANAA shock tube used a more complex design where energy was deposited into an already moving gas to avoid the energy losses and radiative cooling generally associated with diaphragm opening in traditional electric arc driven shock tubes. The facility (a schematic of which can be seen in Figure 3.6) consisted of a cold gas driver, followed by an expansion section, several electrode sections, and then the shock tube test section. When the experiment starts, the driver gas accelerates into the expansion section with a shock wave being driven in front of it. As this gas flow passes through the electrode sections, a high voltage capacitor bank is used to discharge energy into the gas, creating an arc heated plasma that immediately expands and cools, driving a shock wave through the shock tube. Leibowitz stated that *“this immediate expansion greatly reduces the opportunity for the gas to lose energy by radiative cooling during the diaphragm opening process”* [161].

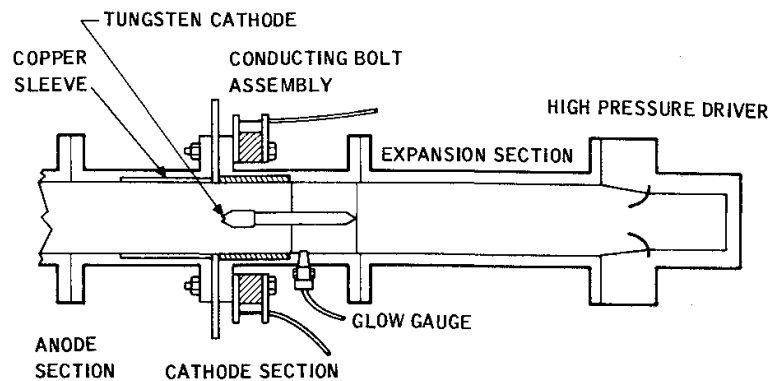
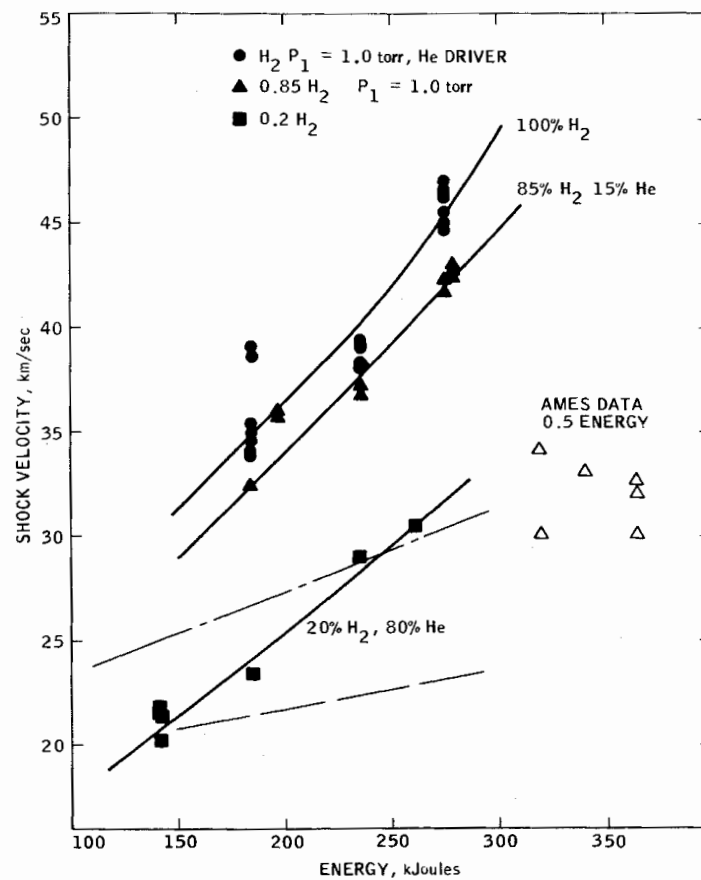


Figure 3.6: Schematic of the ANAA shock tube from Leibowitz [161]. Flow looks to be from right to left.

The ANAA facility was capable of achieving the 47 km/s required to simulate Jupiter entry conditions with a 1.0 torr (133 Pa) shock tube fill pressure, but only with a pure hydrogen test gas. The facility was limited to 40 km/s when using an 85% $\text{H}_2$ /15%He mixture<sup>1</sup>. The performance of the ANAA shock tube for various configurations can be seen in Figure 3.7. Leibowitz used radiation emission measurements of the Hydrogen Beta line at 486.1 nm to identify the test time and quality of the test conditions. For the slower 85% $\text{H}_2$ /15%He conditions (the diagram

<sup>1</sup>Leibowitz [161] does not specify whether the mixtures discussed in the paper are by volume or by mass, but due to the fact that in Fig. 2 in the paper (which is re-created here as Figure 3.7), Leibowitz has compared his own experiments to earlier experiments by Livingston and Menard [162] which *were* specified as by volume, Leibowitz’s mixture is probably by volume also.

in the paper is for a shock speed of 35.8 km/s) the intensity of the Hydrogen Beta line has an initial non-equilibrium rise, followed by a steady region, before a sharp decay which indicates the end of the test time. However, for the faster pure hydrogen conditions (the diagram in the paper is for a shock speed of 45.5 km/s) Liebowitz states that *“the initial jump in intensity is very rapid and is followed immediately by the decay of the continuum and line intensities”* [161]. No steady region can be seen in the diagram. Further on it is stated that it is difficult to ascertain the test time for these conditions, and that further investigation would be required to discover if these conditions were producing a usable amount of test time.



**Fig. 2 Shock tube performance as a function of energy. The curves -.- and -- represent data from the JPL conical arc driver<sup>3</sup> with 0.5 torr, 10% H<sub>2</sub>, 90% He test gas using hydrogen and helium driver gas, respectively.**

Figure 3.7: Figure taken from Liebowitz [161] showing the performance of the ANAA shock tube for simulating gas giant entry scenarios. Data comparing the ANAA facility to the conical arc driven shock tubes at NASA Ames and NASA's JPL which were used by Menard [155], Dannenberg [160], and Livingston and Menard [162] are also shown.

### 3.3 The Galileo Probe

From the end of the 1970's, and for most of the 1980's, the design of the Galileo probe was the primary driver for further gas giant entry research. Two separate codes were developed to design heat shields for outer planetary entry probes, such as the Galileo probe: 'COLTS' (COupled Laminar and Turbulent Solutions), a viscous shock layer code developed at the NASA Langley Research Centre [163]; and 'TOPIC' (Thermodynamic Outer Planets Insulation Code), an engineering code which combined computations and correlations of CFD and experimental data for a large number of flow factors [164].

A series of computational studies were completed in the early 1980's to try and understand the heating environment that the Galileo probe would encounter. These included, Balakrishnan and Nicolet in 1980 [165]; Green and Davy in 1981 [166]; Moss and Simmonds in 1982 [167]; and the analysis done by the General Electric Re-entry Systems Division in 1984, the group commissioned to design the heat shield [59].

Three different types of experiments were also performed to validate the aforementioned simulations and some of the parameters used. As can be seen in Figure 3.8, the Galileo probe's heat shield was built using two different carbon phenolic composites. The nose cap was made from a reinforced chopped-molded carbon phenolic, with the material molded normal to the centreline. The conical frustum section on the sides of the probe was made by tape wrapping carbon phenolic at an angle of  $30^\circ$ . To investigate the response of the materials to the expected entry heating, Lundell performed experiments in 1982 on the two materials with a 45 kW gas dynamic laser at NASA Ames Research Center [60]. The laser system used had several different parameters which could be adjusted to vary the laser power, allowing Lundell to achieve laser intensities from 8.5 to 32 kW/cm<sup>2</sup>, which were focused on 1 cm<sup>2</sup> sections of larger material samples, effectively boring a hole through the samples. It was found that both materials had a threshold intensity below which the material did not spallate. This was found to occur at 14.5 kW/cm<sup>2</sup> for the chopped-molded carbon phenolic, and 8.5 kW/cm<sup>2</sup> for the tape wrapped carbon phenolic. For both materials, correlations relating total and spallated mass loss to intensity were made and then applied to flight heating models of the Galileo probe.

In 1982, Park proposed a method by which gas giant entry heating rates could be simulated at velocities currently achievable in ground testing facilities [168]. He said that the ballistic ranges used at the time for measuring surface recession rates on scaled models were limited to velocities of around 5 km/s. While this provided shock layer temperatures of around 8,000 K which were suitable for studying the behaviour of heat shield materials subjected to a large *convective* heat load, radiation emission was relatively small. Park proposed that argon could be used as the test gas instead of air, as the shock layer temperatures become much higher

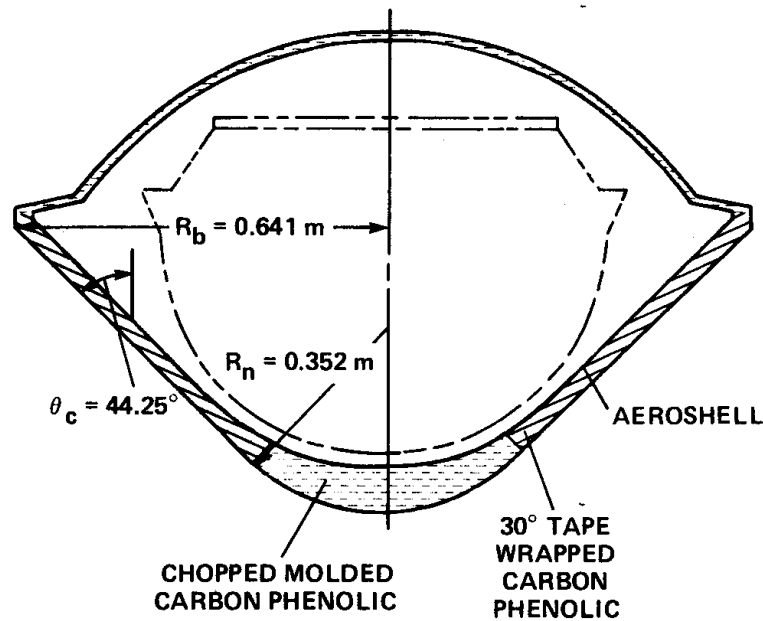


Figure 3.8: Gaileo probe schematic from Lundell [60] showing the two types of carbon phenolic composites used on the probe's heat shield, and where they were each located.

(around 15,000 K), where the radiative heating becomes much higher. He showed that by using an argon test gas, ballistic range facilities could produce radiative heat fluxes of the order of  $100 \text{ kW/cm}^2$  and claimed that radiative heat transfer in an  $89\% \text{H}_2/11\% \text{He}$  (by volume) gas giant atmosphere could be approximated by the heat transfer from Argon due to the theoretical similarity between the spectral lines of each gas. (This is shown in Figure 3.9.) While Park did not mention any specific entry velocity which this simulated, the heat transfer rates shown in Figure 3.9 ( $34.1 \text{ kW/cm}^2$  for Argon and  $42.1 \text{ kW/cm}^2$  for  $89\% \text{H}_2/11\% \text{He}$ , by volume) are similar to ground testing heat fluxes show below in Figure 3.10, and where the Galileo probe heat flux is marked as below  $25 \text{ kW/cm}^2$ .

In 1983, Park [169, 170] performed preliminary stagnation point ablation studies on flat disks of carbon-carbon and carbon phenolic materials in radiation dominated environments using an argon test gas in the AEDC-VKF 1000-ft Hyberballistic Range G at the Arnold Engineering Development Center [171]. The average wall heat flux ranged from  $30$  to  $35 \text{ kW/cm}^2$ , comparable to the laser irradiation experiments performed by Lundell [60]. However, Park found that the spallation contributed more to the thermochemical ablation rate in his experiments than had occurred in Lundell's.

To continue these experiments, Park and Balakrishnan flew  $1/24$  scale ablating Galileo probe models at  $4$  to  $5 \text{ km/s}$  [61] in the AEDC-VKF 1000-ft Hyberballistic Range G [171]. An air test gas was used to test convective heating and an argon test gas was used to test radiative heating.

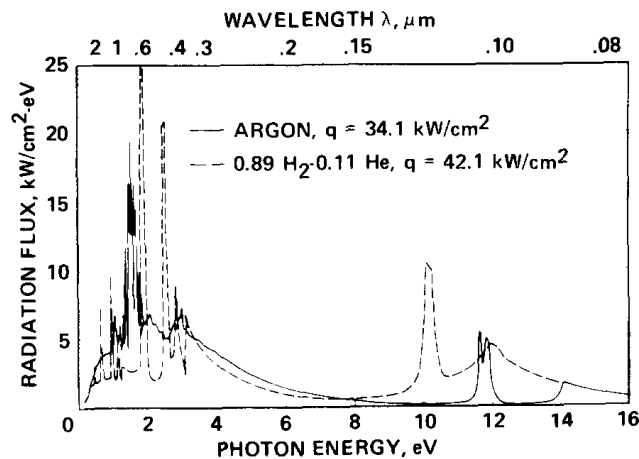


Figure 3.9: Comparison of the emission spectra of argon and an 89% $\text{H}_2$ /11% He mixture (by volume) from a uniform 1 cm thick slab with a temperature of 16,000 K and a pressure of 5.61 atm from Park [168].

The experimental argon results were found to agree “*approximately*” with theoretical conditions made using two different computer codes, radiating shock layer environment (RASLE) and charring materials ablation (CMA). For the air experiments which were used to examine the convective heating, the data was only found to agree “*approximately*” with the computer codes when turbulence and surface roughness effects were accounted for, because turbulence can greatly increase the ablation rate. Park concluded that the Galileo probe’s heat shield was “*adequately designed*” because he predicted an overall recession enhancement of around 10% on the stagnation point (where the safety margin was nearly 50% [166]) and an overall recession enhancement of around 20% on the frustum section (where the safety margin was 30% [61]).

Ablating models were also tested in a 50% $\text{H}_2$ /50%He (by volume) arc-jet flow by Park et al. [62] on NASA Ames’ Giant Planets Facility. The test condition velocity was between 15 and 16 km/s and had a total enthalpy of  $\approx 400$  MJ/kg (a static enthalpy of 260 MJ/kg due to the gas temperature of almost 11,000 K, and another  $\approx 130$  MJ/kg from the gas velocity). The carbon phenolic data was compared to other radiative heating data from the same era (see Figure 3.10) including the laser irradiation data of Lundell [60] and the stagnation point ballistic range ablation data from Park [169, 170] and it was said that “*the three sets of data are consistent and form a continuous trend*” [62]. Heat transfer rates and spectral data were found to agree well with theory, but compared to the aforementioned RASLE and CMA computer codes, the measured ablation rates were 15% higher, which was attributed to spallation phenomena. Once again the experiments indicated that the probe design was suitable.

Figure 3.12 shows the comparison between the predicted heat shield ablation using both COLTS and TOPIC, and the actual heat shield ablation which was measured by ten ablation

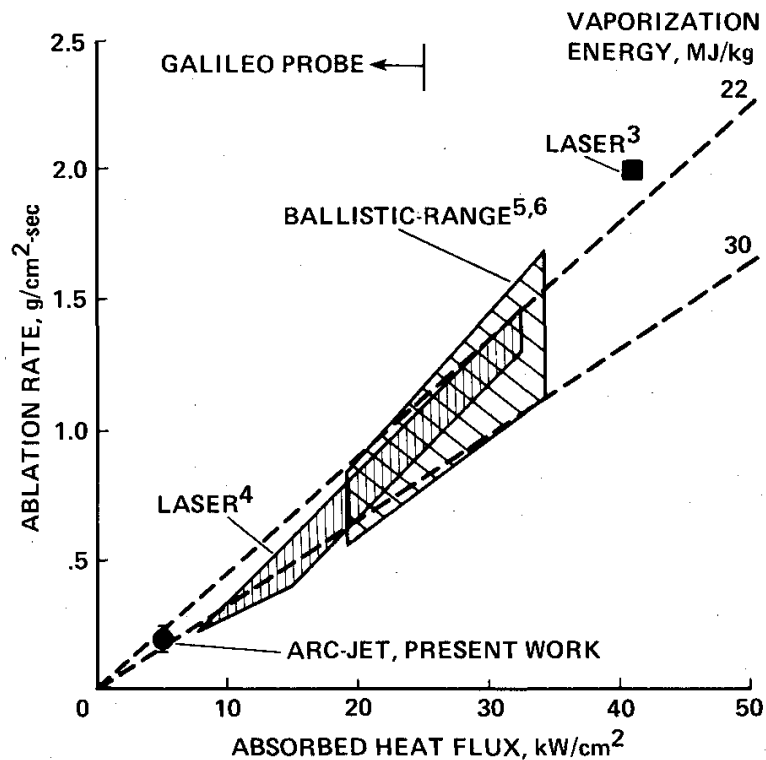


Figure 3.10: Comparison of carbon-phenolic ablation rates measured in an arc-jet (Park et al. [62]), a gas dynamic laser (the data marked '4' is from Lundell [60], and a ballistic range (the ballistic range data is the stagnation point data from Park [169, 170]) from Park et al. [62].

sensors embedded in the probe's surface [58] when the probe entered Jupiter's atmosphere on the 7th of December 1995. (A schematic of the locations of the ten ablation sensors from Milos et al. [172] can be seen in Figure 3.11.) It should be noted that Figure 3.12 shows results from the NASA analysis by Moss and Simmonds [167] as well as results from the analysis done by General Electric [59]. TOPIC was used as the primary design tool to design the heat shield for the Galileo probe [58].

The two predictions from the General Electric analysis used a non-reflecting surface, whereas the prediction from Moss and Simmonds (the dashed line) used a less conservative assumption of 10% surface reflectance [58]. The TOPIC prediction assumed abrupt transition to turbulent flow at a Reynolds number on the boundary-layer edge of  $10^5$ , whereas the COLTS predictions assumed turbulent flow on the nose of the vehicle at all times [58].

From Figure 3.12 it can be seen that all three predictions overestimated heat shield recession on the stagnation point of the vehicle, while underestimating recession on the frustum. Milos, who analysed the ablation data from the ablation sensors mounted on the surface of the probe in 1997 [58], said that "The TOPIC design prediction shows recession of 8.75 cm at the nose, which is 96% high, and 3.27 cm at the end of the frustum, which is 18% low. The less

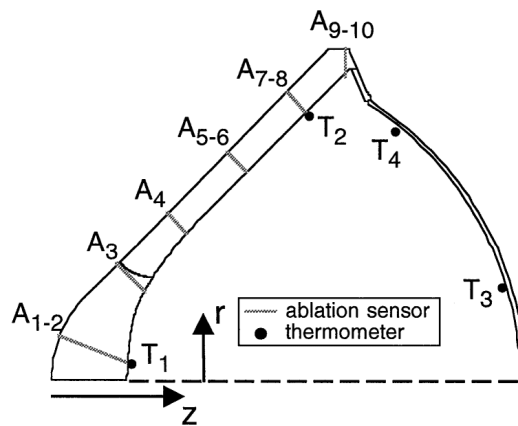


Figure 3.11: Schematic showing the locations of the ten ablation sensors ( $A_1 - A_{10}$ ) in the Galileo probe's heat shield, and the four resistance thermometers ( $T_1 - T_4$ ) inside the structure, from Milos et al. [172].

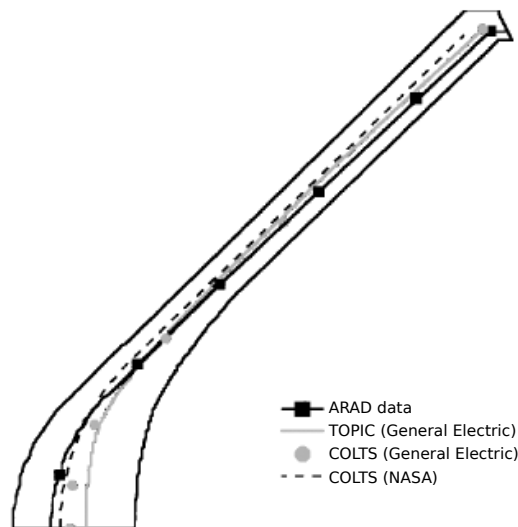


Figure 3.12: Comparison of the final shape of the Galileo entry probe compared to various theoretical predictions [58]. The solid black line shows the actual surface ablation (with the solid blocks showing where the ablation sensors were located on the heat shield surface), the other 3 lines show results obtained by both NASA [167] and General Electric [59] using two different CFD codes, COLTS and TOPIC.

*conservative COLTS calculation shows 5.84 cm at the nose (31% high) and 2.29 cm at the end of the frustum (43% low). The ratio of frustum end to nosetip recession was less than 0.4 in these two calculations, but the measured ratio was 0.9."*

Milos found that the ablation was axisymmetric and that the final shape of the heat shield was well defined. Only 10 mm of heat shield thickness remained on the end of the frustum of the heat shield after ablation. He theorised that the under-prediction of frustum recession may



have been a direct consequence of the greater than expected helium mole fraction in Jupiter's atmosphere, but he also said that explaining the over-prediction of recession near the stagnation point of the heat shield was "*more problematic*" [58].

A follow up paper by Milos et al. in 1999 [172] compared the heat shield recession data to data from temperature sensors mounted underneath the heat shield by performing a one-dimensional analyses of the heat shield ablation, pyrolysis, and heat conduction at the thermometer locations. Comparing the ablation data at ablation sensors A<sub>7</sub> and A<sub>8</sub> to thermometer T<sub>2</sub> which was located on the surface of the structure in the same plane (see Figure 3.11), the temperature and recession data were found to be very consistent. The estimated peak heat flux and heat load at the point were found to be  $13.4 \pm 0.5 \text{ kW/cm}^2$  and  $161 \pm 6 \text{ kJ/cm}^2$ . On the aft heat shield, Milos et al. were not able to find a theoretical solution which matched the recession of the two thermometers mounted there (see Figure 3.11). They said that "*The data seem to indicate an unexpected low heat conduction into the aft heat shield. Whether this discrepancy should be attributed to excessively high heating estimates, deficiencies of the material modelling, or other factors is unknown at this time.*" [172].

Following the Galileo probe mission, several CFD studies have aimed to re-create the ablation of the Galileo probe's heat shield, but no experimental campaigns have been performed. The pre-flight CFD studies had assumed an atmospheric composition of 89% $\text{H}_2$ /11% $\text{He}$  (by volume), whereas the measured mole fraction from the Galileo probe's mass spectrometer was 86.4% $\text{H}_2$ /13.6% $\text{He}$  [173, 174]. In 2005, a study by Matsuyama et al. [64] used this fact, Park's injection-induced turbulence model [65], and a radiative energy transfer calculation which was tightly coupled to the flow-field solver to examine the Galileo probe's heat shield ablation. Their study was able to re-create the recession of the frustum region of the probe closely but like the pre-flight CFD, stagnation point recession was still overestimated. This is shown below in Figure 3.13, where the work of Matsuyama et al. [64] is compared to the flight data [58, 172] and the pre-flight CFD performed by Moss and Simmons [167]. The x-axis has been normalised by the nose radius of the heat shield ( $R_n$ ), so 0 on the x-axis is the stagnation point, and 4 is the end of the frustum. The result from Matsuyama et al. [64] is the curve shown as 'Present' on the figure, and it can be seen to roughly follow the pre-flight CFD by Moss and Simmons [167] near the stagnation point, before changing and closely following the flight data [58, 172] for the whole frustum region.

A paper by Park in 2009 [66] was able to re-create the stagnation point recession "*fairly closely*" by implementing a model which was focused on correctly modelling the interaction between the flow-field and the spallating carbon particles from the heat shield, Park's model calculated the thermochemical state of the gas more accurately than had been done before, included the effects of VUV radiation absorption, and the effects of spallation. Park found

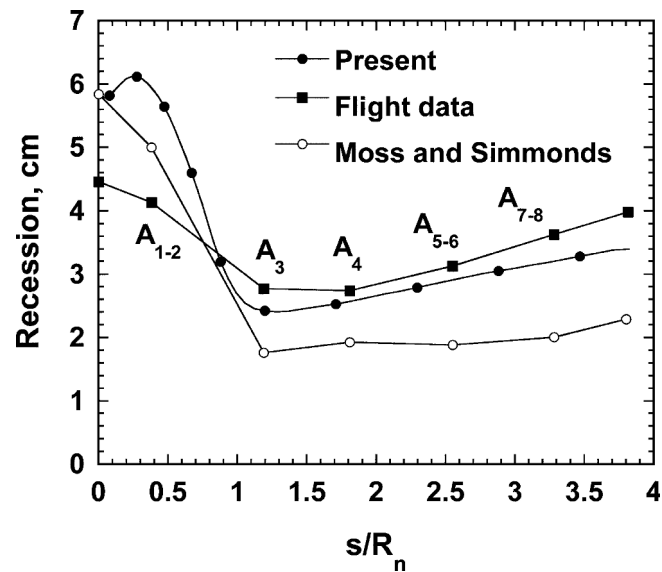


Figure 3.13: Figure from Matsuyama et al. [64] comparing the computed forebody recession profile from their own study, the study by Moss and Simmonds used to design the heat shield [167], and the actual flight data from Milos [58] and Milos et al. [172].

that when the radiative heat flux reaching the wall exceeded  $14.5 \text{ kW/cm}^2$  (the heat flux at which spallation of the material at the stagnation point begins [60]) spalled particles create a ‘radiation shield’ which prevents the surface heat flux from rising much further than this value. Park’s result is shown in Figure 3.14, where a figure from Park [66] has been reproduced. The curve labelled ‘present model’ follows the ‘flight data (ARAD1)’ (the stagnation point ablation data from Milos [58] and Milos et al. [172]) curve very closely.

While Park [66] did not study the surface recession in the frustum region downstream of the stagnation point, he theorised that a couple of different phenomena could have contributed to the larger than expected surface recession seen there. He stated that the heat shield material used on the frustum section was not the same as the material on the stagnation point and had been found experimentally to start spallating when the heat flux was  $8.5 \text{ kW/cm}^2$ , instead of the  $14.5 \text{ kW/cm}^2$  for the material at the stagnation point [60]. Therefore it would be expected that many more spalled particles would exist downstream than in the stagnation region. Park also stated that the spalled particles released in the stagnation region would have to flow downstream and over the frustum region, potentially causing strong turbulence in that area and increasing the convective heating rate.

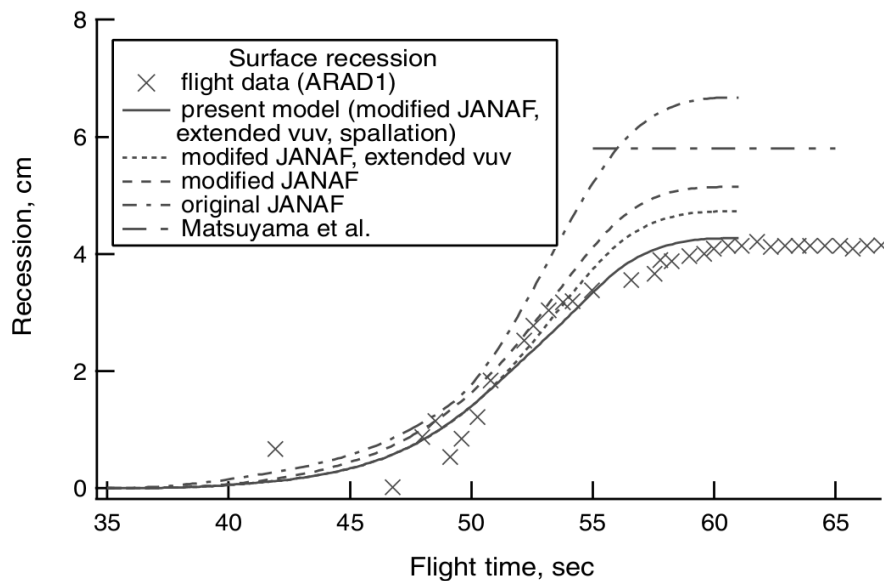


Figure 3.14: Figure from the work of Park [66] showing the progression of surface recession at the stagnation point (ARAD1) of the Galileo probe compared between the flight data [58, 172] and many different computational methods (including the work of Matsuyama et al. [64]).

### 3.4 Stalker Substitution

The velocities involved with entry into the gas giants are generally of the order of 20 to 50 km/s, well beyond the limits of what can be simulated in impulse facilities designed for use with test models. To overcome this issue, Stalker and Edwards [67] proposed a test gas substitution for the study of gas giant entry conditions at velocities currently achievable in ground testing facilities. Their theoretical analysis for inviscid gas giant entry flows showed that, due to its large ionisation energy, the helium in the hydrogen/helium flow-field acted as an ‘inert diluent’ and collision partner for the hydrogen molecules and atoms. They started their analysis with a completely dissociated shock layer (because for very fast gas giant entries they believed the dissociation distance was short enough to justify this) and they found that the amount of inert diluent in the flow-field, and even the *type* of inert diluent, did not affect the ionising relaxation of the test flow. They examined both hydrogen/helium test flows, and test flows with a heavier diluent, neon, across all diluent fractions (1 to 99%, by volume). Due to the much higher ionisation potentials of both He and Ne (21.6 and 24.6 eV, respectively) compared to H (13.6 eV), they expected that little He or Ne in the flow would ionise, and that the He or Ne would only act as an inert diluent and collision partner in the flow-field. They found that until the post-shock temperature became so hot that the neon itself began to ionise, the substitution held.

Stalker and Edwards [67] adapted the results of a previous blunt-body flow similarity study

[175] to the simulation of gas giant entry. The original study had investigated how, for a generalised shape at an given angle of incidence, different freestream and model parameters could be varied to produce similar shock layer flows. It was found that if appropriate freestream and model parameters were chosen, the distribution of flow variables in one shock layer could be obtained from another one, allowing conditions which cannot be simulated in test facilities to be simulated by testing similar flows.

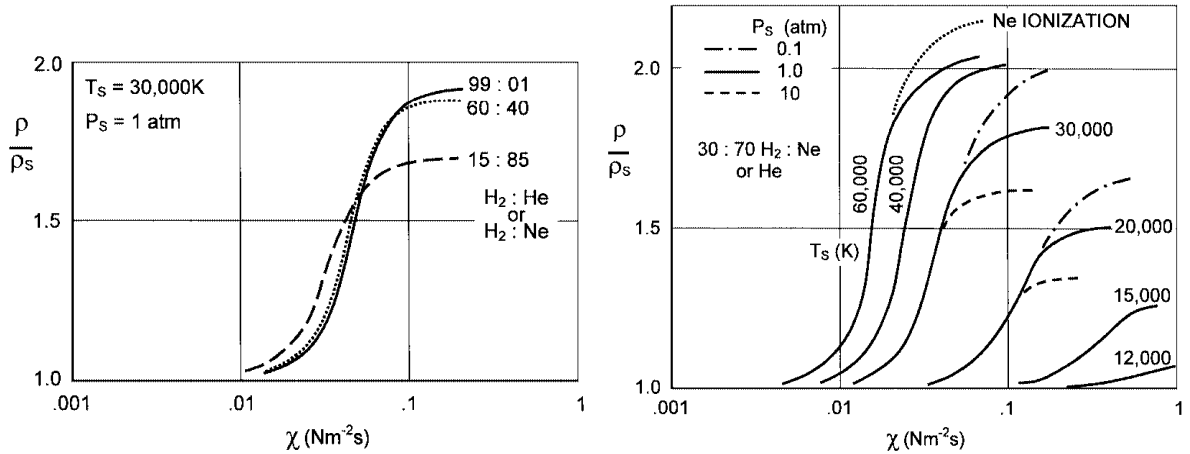
Four requirements were required for the similarity to be valid. These are discussed in depth by Stalker and Edwards [67], and therefore only a small summary is provided here. Requirements 1, 2, and 3 related mainly to the flow geometry, principally the angle of incidence between the model and the freestream flow, and the slope of the body surface. Both the angle of incidence with the flow and the slope of the body surface must be small, and the angle of incidence must be adjusted to take into account the change in normal shock density ratio between the two flows. This thesis only considers stagnation line flows at zero angle of attack (i.e. angle of incidence = 90 degrees), so these requirements do not need to be considered currently.

Requirement 4 is more complicated to satisfy: Variation of density along post-shock flow streamlines must be the same for the two flows. For frozen or equilibrium flow-fields this requirement is easily satisfied because the density remains effectively constant, but for non-equilibrium flows where the gas composition is changing along the streamline, it is not so simple. By examining computationally the relaxation behind strong shocks in both H<sub>2</sub>/He and H<sub>2</sub>/Ne test gases with differing concentrations of diluent, Stalker and Edwards found that if the reactions were binary it could hold, and then it was shown that for a set post-shock temperature, the non-equilibrium variation of the density ratio was independent of whether helium or neon was used as a diluent, and “*to a good approximation*” was independent of the amount of diluent used. Two figures from their paper which illustrate this can be seen in Figure 3.15, with the x-axes shown in terms of the binary reaction variable:

$$\chi = \int \frac{rp}{q} ds \quad (3.1)$$

where  $r$  is the mole fraction of H<sub>2</sub> in the gas mixture before dissociation and ionisation,  $p$  is the post shock pressure,  $q$  is the streamline velocity, and  $s$  is the distance along the streamline.

Examining Figure 3.15 it can be seen that they found no detectable difference between the relaxation of the He and Ne diluent, except when approaching equilibrium at the highest post shock temperature in Figure 3.15b, where the Ne started to ionise. The results shown in Figures 3.15a and 3.15b confirmed that not only did the type of diluent not matter, but neither



(a) Effect of diluent concentration on ionising relaxation (b) Effect of temperature and pressure on ionising relaxation

Figure 3.15: Two figures from the work of Stalker and Edwards [67] showing the effect that the two different diluents (He and Ne), and differing concentrations of those diluents, have on the ionising relaxation of the flow behind a strong shock.

did the *concentration of diluent*. From this conclusion, they stated that Requirement 4 would be satisfied by a modified binary scaling parameter term taking into account the molecular hydrogen partial pressure. This can be found below as Equation 3.2.

$$\Omega = \frac{rp_n L[\varepsilon_n(1 - \varepsilon_n)]^{-0.5}}{U_\infty} \quad (3.2)$$

where  $r$  is the fraction of molecular hydrogen (H<sub>2</sub>, by volume) in the gas mixture before dissociation and ionisation <sup>2</sup>,  $p$  is the post-shock pressure for the flow,  $L$  is an appropriate length scale to compare,  $\varepsilon$  is the inverse shock density ratio,  $\rho/\rho_s$ , for the flow,  $n$  represents each flow-field, and  $U_\infty$  is the freestream velocity of the flow.

What this means in practice, is that with appropriate selection of experimental parameters the limits of a shock tube facility can be circumvented for blunt body flow simulation because the shock layers of faster entries can be simulated at slower speeds using either an increased amount of helium diluent or a heavier neon diluent. Both of these substitutions produce stronger shock waves in the test flow, producing a hotter post-shock region, and allowing faster entry shock layers to be simulated when the facility is not able to produce enough stagnation enthalpy to reproduce the conditions directly. This also means that large concentrations of Ne diluent

<sup>2</sup>For an experiment, this is the hydrogen fraction in the test gas when the shock tube is filled, and for a real entry flow, this is the hydrogen fraction in the atmosphere

(40%, 60%, or even 85%), can be used to create test conditions with very significant levels of dissociation and ionisation behind the shock over the test model<sup>3</sup>.

Stalker and Edwards [67] performed experiments in the T3 shock tunnel at ANU in non-reflected shock tunnel mode with a 60% $\text{H}_2$ /40%Ne (by volume) test gas on a hemispherically blunted cone model, producing flows which re-created the frozen post-shock temperatures of gas giant entries from 24 to 28 km/s. They noted that because the experiments were performed using a non-reflected shock tunnel driven very quickly (from 8.3 to 11.1 km/s) a large source of error was added to their results because the test gas was fully dissociated before it flowed over the model. They estimated that up to around 30% of their flow stagnation enthalpy was chemical, whereas in the true flight situation the freestream flow would have no chemical enthalpy at all. They stated that expansion tubes, where only part of the flow energy is added to the flow using a shock wave, would potentially allow these errors to be minimised.

In 1999 Herbrig, a UQ final year thesis student, expanded Stalker and Edward's [67] work using the X2 expansion tube. He completed a small pilot study investigating gas giant entry in the X2 expansion tube at the University of Queensland [92], using a test condition which took advantage of the test gas substitution from Stalker and Edwards [67]. Herbrig designed a test condition utilising a 15% $\text{H}_2$ /85%Ne (by volume) test gas and used it to conduct experiments on a series of spherical blunted cones examining shock shape and shock standoff using schlieren.

The work which Herbrig started was then greatly expanded upon by Higgins in 2004 [63]. Higgins used the test condition which Herbrig had developed to conduct a much more comprehensive study on simulated gas giant entry [63]. She measured shock standoff and electron concentration along the stagnation streamline using both two-wavelength and near-resonant holographic interferometry on cylinders and spheres in the X2 expansion tube. Higgins demonstrated that nonequilibrium flow effects could be re-created in a ground testing facility using the Stalker substitution. A sample result can be seen in Figure 3.16.

Higgins also developed a one-dimensional inviscid analytical model to calculate properties along the stagnation line behind a blunt body shock in ionising nonequilibrium flow. This model was compared to both analytical and experimental results for shock standoff and Higgins found that CFD results were qualitatively similar to experimental data but generally 10% to 28% greater. This is shown in Figure 3.17.

However, comparing Higgins' work [63] to the original work by Stalker and Edwards [67], it could be argued that Higgins' work was at the edge of the validity of the substitution. Higgins'

---

<sup>3</sup>An 85% $\text{H}_2$ /15%He (by volume) Uranus gas mixture has a molecular weight of 2.31 g/mol, while a 15% $\text{H}_2$ /85%Ne (by volume) mixture (the maximum amount of Ne diluent discussed by Stalker and Edwards) has a molecular weight of 17.5 g/mol, more than seven times greater.

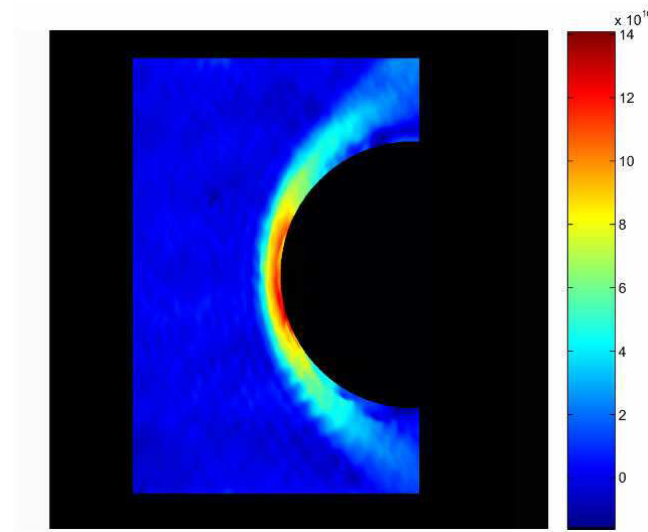


Figure 3.16: Sample electron concentration calculation (per  $\text{cm}^3$ ) from the work of Higgins [63], with a freestream velocity of 11.8 km/s.

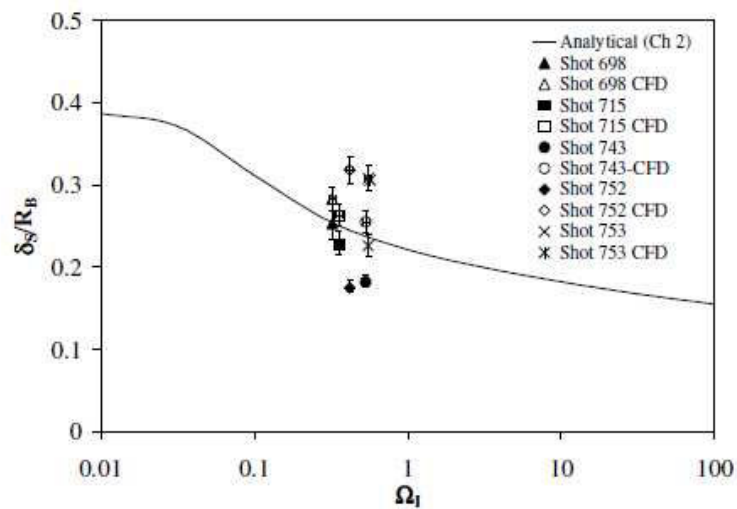


Figure 3.17: Comparison of shock standoff between nonequilibrium CFD, experiment and an analytical solution from Higgins [63]. The shock standoff distance ( $\delta_S$ ) has been normalised by the nose radius of the cylinder ( $R_B$ ).

analysis showed (and the author predicted, using the same input parameters as Higgins and the PITOT code<sup>4</sup>) that depending on the condition, the hydrogen gas in the freestream flow for the experiments was either almost fully dissociated or partially ionised at equilibrium, with a large amount of chemical enthalpy in the freestream. An equilibrium PITOT run for Higgins' shot 674 found a stagnation enthalpy which was 8% chemical, a fairly normal percentage for

<sup>4</sup>PITOT is an equilibrium gas shock tunnel and expansion tube analysis code written by the author. It is discussed in Chapter 5.

expansion tube conditions. However, Higgins' shot 752 has a stagnation enthalpy which is expected to be 21% chemical, a value approaching the amount of stagnation enthalpy error predicted for the original non-reflected shock tunnel experiments performed by Stalker and Edwards [67], and effectively cancelling out the benefits they believed expansion tubes would bring to research with the substitution.

Higgins also mentioned that the neon was a 'partially ionised' diluent for the experiments. Using PITOT, the author confirmed this, and found that it was expected that for shot 674 almost half of the ions in the post-shock stagnation line flow at equilibrium were produced by ionising neon, and over a third was produced by ionising neon for shot 752. This goes against the conclusions of Stalker and Edwards [67] where it was stated that *"it was found that there was no detectable difference in the use of neon or helium as diluent, except when approaching equilibrium at the highest temperature ... where the ionization of neon took place."* This fact adds more potential uncertainty to the experiments, and shows that potentially the substitution was used beyond its limits.

### 3.5 Modern Resurgence in the Study of Gas Giant Entry

In 2009, Furudate [176] developed a chemical kinetic model for re-creating a one-dimensional flow-field behind a shock wave in a high temperature  $\text{H}_2/\text{He}$  gas mixture. He used dissociation rate coefficients from the work of Leibowitz in 1973 [154], and new ionisation rate coefficients from the work of Park [177]. The model was found to reproduce shock tube data of ionisation time in  $\text{H}_2/\text{He}$  gas mixtures reasonably well. Figure 3.18 shows a comparison between the ionisation distance and time found from Furudate's model and the experimental work done by Leibowitz in 1973 [154] and Leibowitz and Kuo in 1976 [157].

Over two separate papers (one examining  $\text{H} + \text{H}_2$  and  $\text{He} + \text{H}_2$  collisions, and the other examining  $\text{H}_2 + \text{H}_2$  collisions) Kim et al. derived a comprehensive model describing dissociation of  $\text{H}_2$  in a  $\text{H}_2/\text{He}$  mixture [178, 179]. Part of the deliverables of the study were a set of rate coefficients for  $\text{H}_2$  dissociation and recombination from collisions with  $\text{H}_2$ ,  $\text{H}$ , and  $\text{He}$ . Both single temperature model reaction rates, and two-temperature reaction rates based on separate translational and vibrational temperatures are included. The rate coefficients were validated by comparison with various experimentally measured rate coefficients with good comparison seen. An example reaction rate coefficient comparison between experiment and theory from the  $\text{H}_2 + \text{H}_2$  collision paper [179] can be seen in Figure 3.19.

In 2012, Park [187] collected modern data on the physical properties of  $\text{H}_2/\text{He}$  mixtures and developed a new theoretical model for describing the non-equilibrium processes which occur behind a normal shock in a  $\text{H}_2/\text{He}$  mixture. The theoretical model was validated by



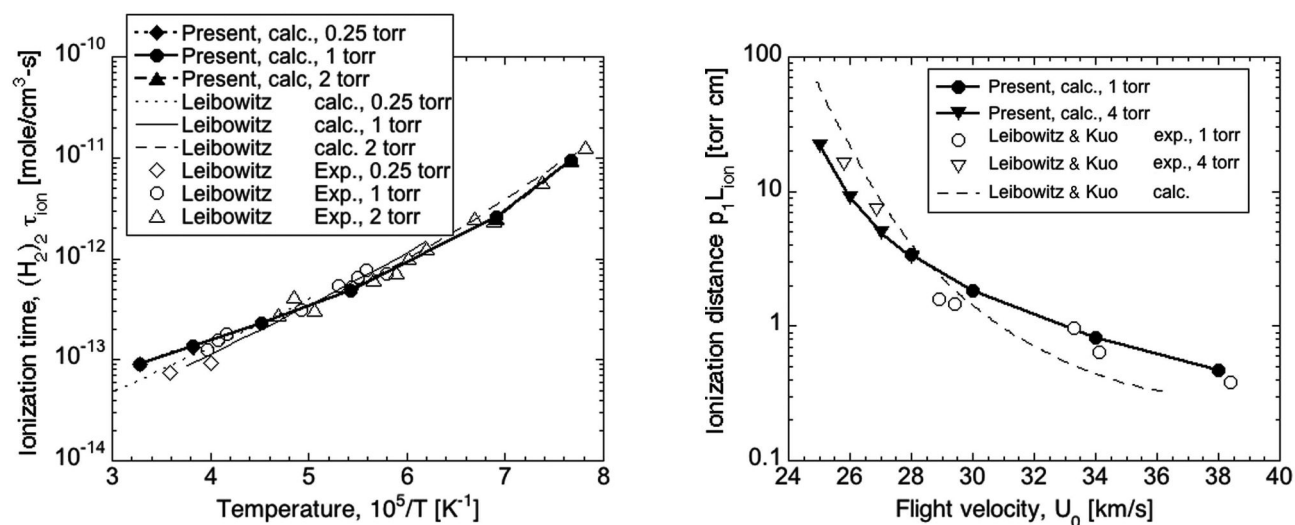
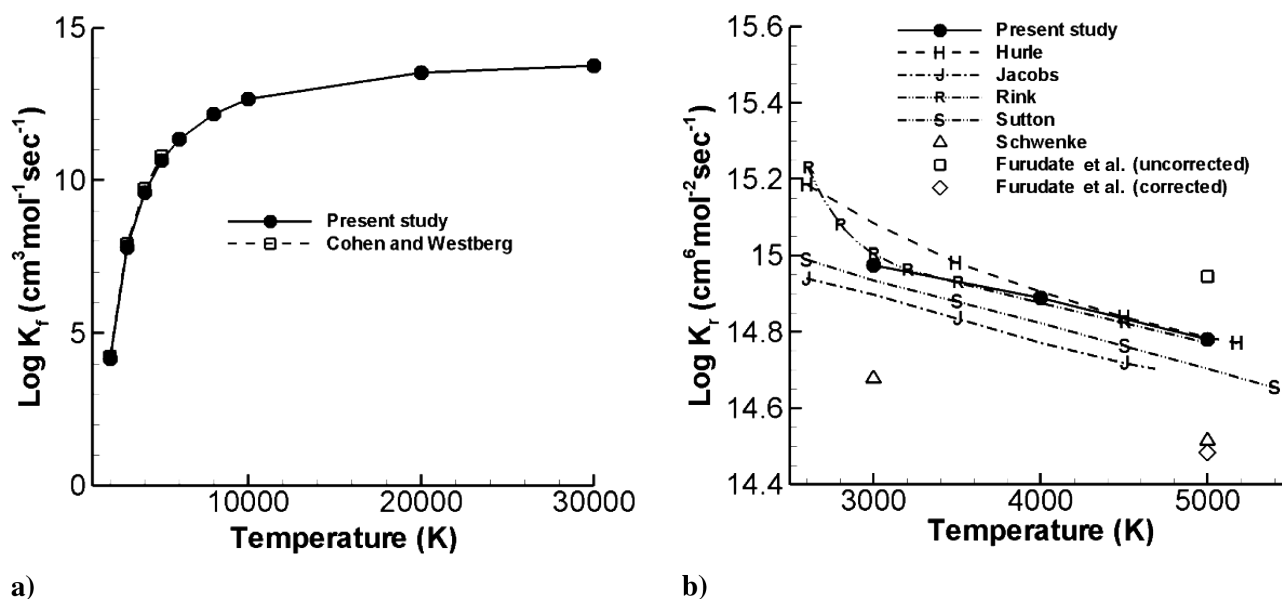
a) 21% H<sub>2</sub>-79% Heb) 85% H<sub>2</sub>-15% He

Figure 3.18: Ionisation time and ionisation distance from the work of Furudate [176] compared to measurements and calculations done by Leibowitz in 1973 [154] and Leibowitz and Kuo in 1976 [157].



a)

b)

Figure 3.19: Comparison between reaction rate coefficients for H<sub>2</sub> + H<sub>2</sub> collisions from Kim et al.'s study [179], experiments, and other theoretical calculations: a) dissociation rate coefficients compared with the experiments by Cohen and Westberg [180], and b) recombination rate coefficients compared with the experiments by Hurle [181], Jacobs et al. [182], Rink [183], and Sutton [184], as well as theoretical calculations performed by Schwenke [185] and Furudate et al. [186].

comparison with two sets of experiments carried out in the 1970's. The first set were collected by Leibowitz [154] in 1973, and the second set were collected by Livingston and Poon [188] in 1976. The model includes a full dissociation reaction scheme, a complex ionisation model and a radiation model which Park uses to calculate the spectral intensity at the surface of a Neptune entry vehicle and trajectory proposed by Jits et al. [189]. Park's result showing radiation in both the Lyman and Balmer Series' of H can be seen in Figure 3.20.

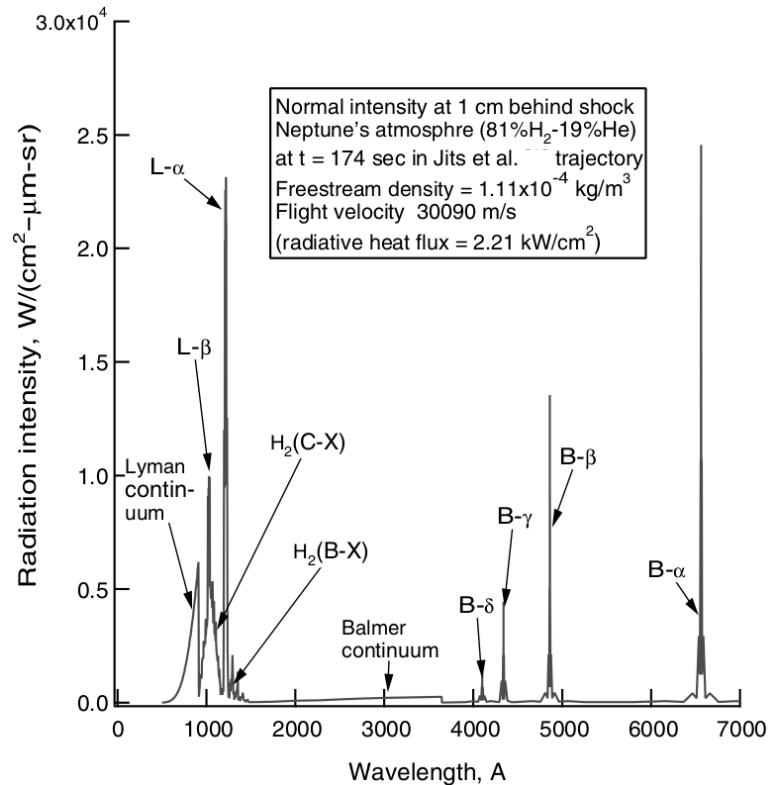


Figure 3.20: Spectral intensity at 10 mm downstream for 174 second point in Jits et al.'s Neptune entry trajectory [189] from the work of Park [187].

Neptune's atmosphere is believed to contain between 1 and 2% hydrocarbons (by volume), mainly CH<sub>4</sub> [190]. There are two other related Park [191, 192] papers in which the effect of these hydrocarbons on the shock layer radiation are examined theoretically for both shock tunnel data from Livingston and Poon [188], the proposed Jits et al. [189] trajectory and another proposed trajectory from Hollis et al. [193]. Park assumed a CH<sub>4</sub> percentage of 1.5% (by volume). The addition of CH<sub>4</sub> was found to appreciably shorten the ionisation equilibration distance, and the carbon atoms added to the flow-field were found to contribute significantly to the total radiative heat flux.

In 2010, the US National Research Council 'Vision and Voyages for Planetary Science in the Decade 2013-2022' report identified probes to Uranus [68] and Saturn [69, 70] as high priorities

for future space missions, and several studies have been performed to examine the proposed entries discussed in the report. The proposed probe entry velocities were 22.3 km/s for Uranus [68] and 26.9 km/s for Saturn [69, 70].

The expected aeroheating uncertainties of the aforementioned Uranus and Saturn entries, as well as a third steeper descent angle Saturn entry at 28.2 km/s, were analysed by Palmer et al. [71] in 2014 by performing a Monte Carlo study on the input parameters to their data parallel line relaxation computational fluid dynamics code. They found that radiative heating for Uranus entry was “*negligible*” but at the highest velocity examined for Saturn entry, radiative heating contributed up to 20% of the heat load. In general, they found that the uncertainty in convective heating for Uranus and Saturn entry was “*no more than a few percent*”, but that for Saturn entry, where the post-shock temperatures are higher, that “*the uncertainty in radiative heating was substantial*”. The strongest contributor to the radiative heating variation were found to be the H<sub>2</sub> dissociation reaction rates, because the radiative heating seen at the wall is strongly influenced by the chemistry which occurs just behind the bow shock.

A study by Cruden and Bogdanoff [72] in 2015 experimentally examined the expected radiation for parts of the three entry trajectories examined by Palmer et al. [71] in the EAST facility at NASA Ames Research Center [76]. A study by Bogdanoff and Park in 2002 [194] had brought heritage H<sub>2</sub>/He experiments in the EAST facility into question by showing that the radiation from the electric arc driver could be essentially ‘overheating’ the test gas to well above what would be expected from equilibrium shock wave theory. For Cruden and Bogdanoff’s experiments, a buffer section was added to the facility to protect the test gas from the driver radiation. After this addition, they stated that “*Somewhat surprisingly, no direct evidence of driver gas preheating was seen during any of the tests*”. Cruden and Bogdanoff used an 89%H<sub>2</sub>/11%He (by volume) simulated Saturn entry test gas, and examined freestream pressures between 13 and 66 Pa and velocities from 20 to 30 km/s. Consistent with Palmer et al.’s [71] conclusion that radiative heating for Uranus entry was “*negligible*”, Cruden and Bogdanoff found that, within their measurement limits, no shock layer radiation was detected below 25 km/s. Above 25 km/s, radiation was observed, and they found that their shocks did not reach equilibrium over several centimetres, and that in many cases, the state distributions were non-Boltzmann. Due to the fact that NEQAIR [77], NASA’s in-house radiation code, is only able to simulate H<sub>2</sub>/He gas flows in Boltzmann states, NEQAIR currently over-predicts the radiation of these conditions by up to a factor of 10. This work was published in the Journal of Spacecraft and Rockets in 2017 [73].

## 4

# The X2 Free Piston Driven Expansion Tube

*Nothing is built on stone; all is built on sand, but we must build as if the sand were stone.*

– Jorge Luis Borges, *The Book of Sand*, 1977 [195]

## 4.1 Chapter Overview

This chapter primarily discusses the facility which has been used for the experiments in this thesis, the X2 Expansion Tube at the University of Queensland. It begins with a short general discussion of expansion tubes, before providing a more specific introduction to the X2 facility and what it has been used for. The section closes with a discussion of both the physical and operational facility upgrades performed by the author during this thesis. For a larger discussion of the history of expansion tube research at UQ, the reader is directed to Gildfind et al. [146].

Section 4.2 is a slightly extended version of Section 1 of the final submitted version of the journal paper James et al. [25].

## 4.2 The Expansion Tube

Since spaceflight research began, shock tubes and shock tunnels have been widely used for the study of hypervelocity flows. However, they have generally been limited to the study of Earth orbit velocities up to around 8 km/s [104] because of a fundamental limitation: These facilities can only add energy to the flow through shock waves, and at sufficiently high shock speeds there can be significant dissociation and potentially even ionisation of the test gas. This makes the conditions suitable for the study of plasmas behind planetary entry shock waves, and shock speeds up to 47.5 km/s have been generated in non-reflected shock tubes [161], but unsuitable

for aerodynamic testing [196]. This can be seen in Figure 4.1 where the related post shock temperature ( $T_2$ ) in air for different shock tube shock speed ( $V_{s,1}$ ) values are shown for both the perfect gas condition, and equilibrium gas conditions with different representative shock tube fill pressures ( $p_1$ ) found using NASA's CEA program [197, 198]. It can be seen that above a shock speed of around 2,000 m/s all three equilibrium conditions start to diverge from perfect gas behaviour as dissociation of the molecules (mainly nitrogen and oxygen) begins. At a shock speed of 9,000 m/s, the upper limit of the data shown on the plot, the molecules in the air are almost fully dissociated, and the perfect gas model over-predicts the post-shock temperature ( $T_2$ ) by around a factor of four.

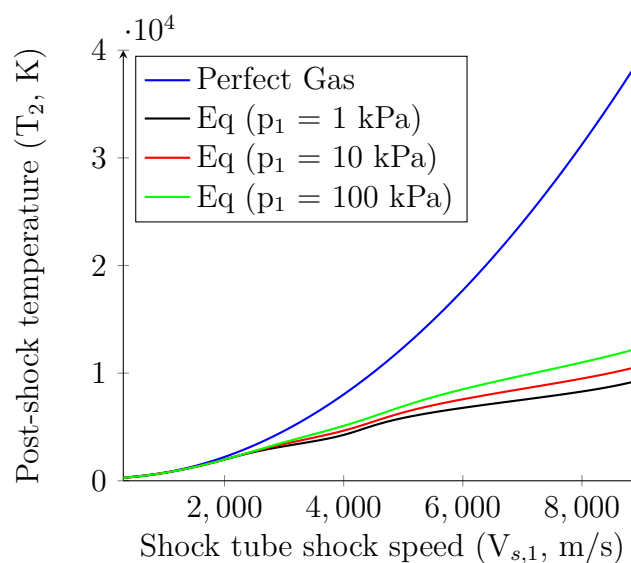


Figure 4.1: How changing shock tube shock speed ( $V_{s,1}$ ) changes the post-shock temperature ( $T_2$ ) in air for both perfect gas and equilibrium conditions.

Reflected shock tunnels have been used to study a wide variety of hypersonic phenomena, but also suffer from the same limitation as non-reflected ones: The twice shocked test gas feeding the nozzle may not recombine through the expansion, and this only gets worse for higher enthalpy conditions [113].

The expansion tube, a concept first proposed by Resler and Bloxson in the 1950s [125], is a modified shock tube which uses a second downstream low pressure shock tube to circumvent the enthalpy limitation by adding only part of the required energy to the flow using a shock wave. After initial shock processing of the test gas in the shock tube, more energy is added to the final test flow by processing it with an unsteady expansion, where total enthalpy and total pressure are added to the shocked test gas as it unsteadily expands, without ever having to stagnate the gas at these conditions during the operational cycle. At the expense of test time, this extra total enthalpy and total pressure are added to the flow without the dissociation which would occur

in a shock tunnel, and therefore much higher enthalpy conditions can be reached [196]. The expansion tube is therefore particularly suitable for the study of planetary entry flow-fields. Due to the two modes of energy addition available, the final test flow can be controlled by balancing energy addition between these two modes, without the need for changes in physical hardware, such as nozzles, making the expansion tube a very versatile type of test facility. An example of the extra stagnation enthalpy ( $H_t$ ) available in an expansion tube is shown in Figure 4.2 below, where the maximum  $H_t$  achievable in a non-reflected shock tube compared to an expansion tube can be seen. An equilibrium unsteady expansion from the shocked condition in the shock tube to a pressure of 100 Pa has been performed to simulate the maximum enthalpy situation where almost all of the pressure gained in the shock tube is converted to velocity in the acceleration tube. Using a shock tube shock speed ( $V_{s,1}$ ) of 5,000 m/s as an example, the stagnation enthalpy in the shock tube is 23 MJ/kg, but the maximum stagnation enthalpies achievable for an expansion tube are 80 MJ/kg with a shock tube fill pressure ( $p_1$ ) of 1 kPa, and 99 MJ/kg with a shock tube fill pressure of 10 kPa. These are increases of around 400 and 500%, respectively. For a perfect gas case, it is a function of the unsteadily expanded test gas Mach number only, asymptoting to a factor of around 3 [196].

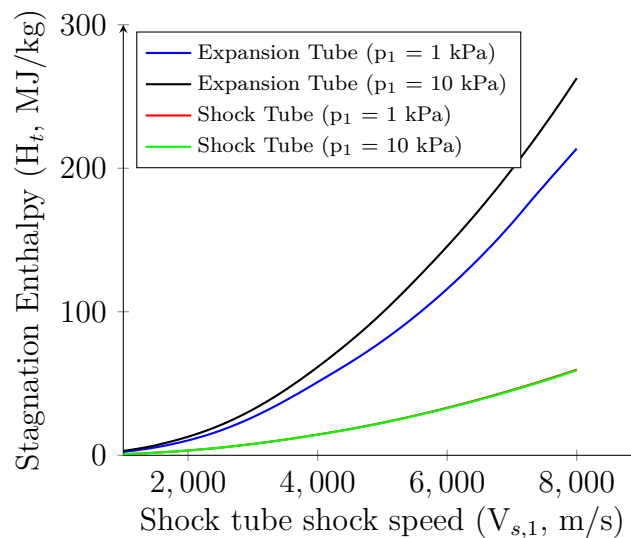


Figure 4.2: The maximum stagnation enthalpy ( $H_t$ ) achievable in air with changing shock tube shock speed ( $V_{s,1}$ ) for both a shock tube and an expansion tube. The expansion tube flow has been unsteadily expanded to 100 Pa to simulate the maximum situation where almost all of the pressure gained in the shock tube is converted to velocity in the acceleration tube.

The first detailed theoretical analysis of an expansion tube was presented by Trimpi in 1962 [199], who was the first to call the facility an expansion tube. Other theoretical work followed, such as Trimpi and Callis [200], Trimpi [201], and Norfleet and Loper [202]. Around this time, preliminary experimental expansion tube work was beginning, such as the work of Jones [203],

Givens et al. [204], Norfleet et al. [205], and Spurk [206], all published in 1965. Over the next twenty years, expansion tube research was pioneered at NASA Langley on two different facilities. The first facility, which is discussed in Jones [203] and Jones and Moore [207], was a pilot cold hydrogen driven facility converted from an existing shock tube. The second facility, called the Langley 6-inch expansion tube [208], was a purpose built expansion tube facility which could be run with either an arc heated driver [209], or a heated [210] or unheated [211] helium driver. While previous work had focused on trying to understand the expansion tube as a concept, the Langley 6-inch expansion tube was the first instance where one was used as a facility, and many studies were performed using blunt models, including Miller and Moore [212], and Shinn [213], where the pressure on the nose-cap of the space shuttle was analysed. Due to *“financial and manpower constraints and to diminished programmatic needs”*, the facility was decommissioned in 1983 [208]. A more comprehensive history and reference list of the work performed on the Langley 6-inch expansion tube can be found in [208], where it is also stated that *“contrary to theory, only a single flow condition, in terms of Mach number and Reynolds number, acceptable for model testing was found with the expansion tube for a given test gas”*, something which would have severely limited the usefulness of the facility. This facility was later recommissioned as HYPULSE at GASL [214]. Similar issues had also been seen for other facilities such as in Norfleet et al. [205], where it was stated that *“the steadiness of the resulting flow leaves much to be desired and the definition of accurate flow conditions remains in serious doubt”*.

In 1987, the first free piston driven expansion tube, later slightly modified and named X1, was built by converting the University of Queensland’s existing TQ shock tube into an expansion tube using a grant from NASA Langley [145]. The facility had a driver section bore of 101.6 mm, and a driven section bore of 38.6 mm [143]. It was postulated that a free-piston driver would allow more test conditions to be created than had been possible in the Langley facility, and Paull et al. [143] found that additional operating conditions existed using an air test gas. However, test times were found to be shorter than what was predicted by theory. In 1992, Paull and Stalker [215] investigated expansion tube test flow disturbances by modelling disturbances which originated in the driver gas as first-order lateral acoustic waves. They found that in some situations these waves were transmitted into the test gas where they were able to prematurely end, or completely remove, the steady test time. These waves were transmitted to the test gas in the shock tube, from the driver/test gas interface, and then the waves were focussed to particular frequencies, which were so severe that they precluded useful steady flow, by the unsteady expansion process in the acceleration tube. Paull and Stalker [215] also found that this transmission could be attenuated by ensuring that there was a *“sufficient increase”* in sound speed from the unsteadily expanded driver gas to the shocked test gas at the driver/test

gas interface, preventing the disturbances from being able to pollute the test gas. The size of the increase required depended on the frequency of the waves to be inhibited at the driver gas sound speed. Paull and Stalker [215] established a criterion for ensuring clean flow which led to a revival in the use of expansion tubes. This finding and others led to what is now thirty years of sustained expansion tube research at UQ, which is discussed in detail in Gildfind et al. [146]. Since 2000, there has been increased interest in expansion tubes, and new facilities of different sizes and purposes have been commissioned by several groups, such as those discussed by Sasoh et al. [216], Ben-Yakar and Hanson [140], Dufrene et al. [217, 218], Abul-Huda and Gamba [219], Jiang et al. [220], and McGilvray et al. [221].

A representative schematic of a free piston driven expansion tube facility can be seen in Figure 4.3. Similar to a traditional free piston driven shock tube, the facility has a larger bore free piston driver section which produces the high pressure, high temperature (generally helium or a mixture of helium and argon) driver gas which powers the facility, an area change at the primary diaphragm location, and then a shock tube section with a smaller bore, where the test gas is located. Up until the ‘secondary diaphragm’ the facility is a shock tube. The ‘secondary diaphragm’ and the low pressure ‘acceleration tube’ are the extra components which make the facility an expansion tube. During an experiment, after the test gas reaches the end of the shock tube, it ruptures the secondary diaphragm, unsteadily expands to a much higher velocity and much lower pressure in the acceleration tube, and then enters the test section where it flows over the test model.

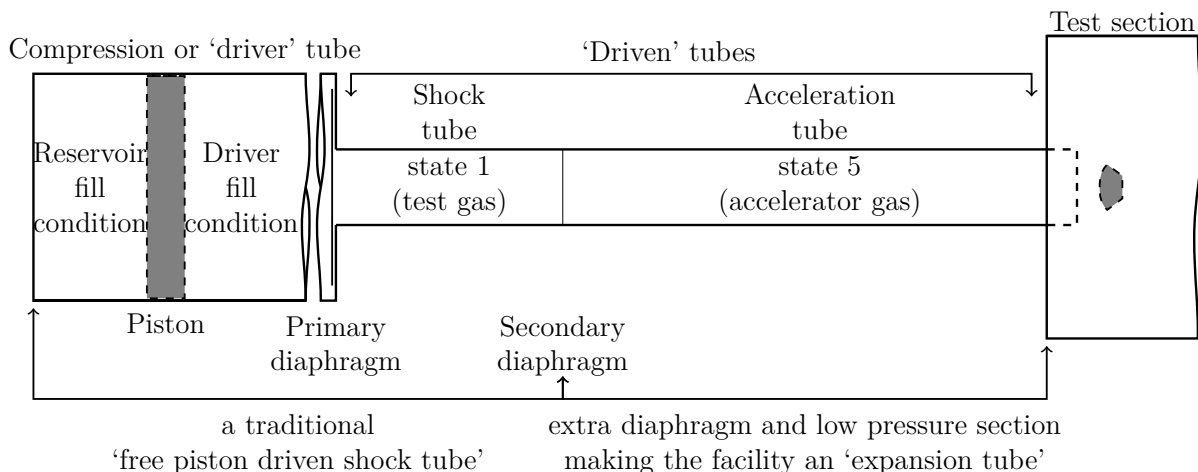


Figure 4.3: Representation of a basic free piston driven expansion tube.



### 4.3 The X2 Expansion Tube

The free piston driven X2 Expansion Tube at the University of Queensland is a 20 m long, medium sized experimental facility with a driven section bore of 85 mm and a nozzle exit diameter of 201.8 mm. Measured in terms of driver gas sound speed ( $a_4$ ), X2 has the highest performance driver of any operational expansion tube facility, which makes it capable of producing scaled test conditions for entry into most of the planets in our solar system. X2 is generally used to perform studies of blunt-body planetary entry radiation or to investigate new techniques for the improved simulation of planetary entry in ground testing facilities. X2 has been used extensively to simulate and measure radiating test flows for many planetary bodies in the solar system, including Earth, Mars, Titan, and Venus from 3 to 12 km/s [222, 1, 81, 127, 86, 78, 87, 79, 80], and it has also been used to develop and refine a new technique for the study of ablation phenomena in impulse facilities by using heated models [90, 91, 3, 7, 139].

X2 was originally commissioned in 1995 by Doolan and Morgan [223, 224, 225] as a two-stage free piston driven expansion tube, a representation of which can be seen in Figure 4.4. While a shock tube driver gives the most performance with an area change<sup>1</sup>, the original X2 configuration had more of a ‘small step’ than a defined area change, with a 91 mm diameter second stage of the compression tube and an 85 mm diameter driven section. While the two-stage free piston driver was not the highest performing option, X2 was originally built as a proof-of-concept facility for the much larger, 65 m long X3 expansion tube which was built in 2000 [226] with a driven section bore of 182.6 mm. The concept behind the outer sabot piston was that cost could be saved by performing the first part of the compression stroke with a light, cheap outer piston, and then performing the end of the compression stroke with a stronger but smaller inner piston. Today, both X2 and X3 use single-stage free piston drivers.

In 2004, a major facility modification was designed by Professor Richard Morgan and undertaken by Scott et al. [227, 228, 229] and X2’s original two-stage free piston driver was scrapped in favour of a new single-stage free piston driver using a 35 kg piston. Scott designed a new driver condition using the new single-stage driver, and as would have been expected, an increase in performance was seen with it [228]. To increase the model size which could be tested in the X2 facility, Scott also designed the current nozzle which is now used for most X2 experiments [229]. The nozzle is a full-capture, contoured, shock-free nozzle with a geometric

---

<sup>1</sup>This occurs because an unsteady expansion increases total temperature and total pressure in *supersonic* flow, but decreases it in *subsonic* flow. Therefore, the loss in total pressure and total temperature which would be incurred to unsteadily expand the stationary driver gas up to Mach 1 can be avoided by performing a steady expansion to a choked throat condition instead of an unsteady one into the driven tube while the driver gas is subsonic.

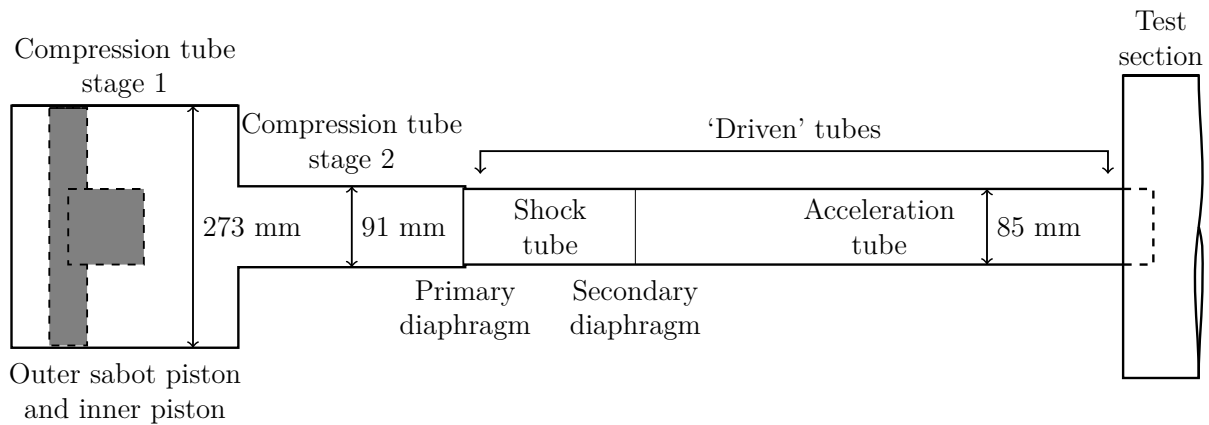


Figure 4.4: Representation of the original X2 configuration with a two-stage free piston driver.

exit-to-inlet area ratio of 5.64 which was built for an inflow Mach number of 7.3, and an outflow Mach number of 10. The bezier control points for the final nozzle design can be found in Table 5.4 of Scott’s PhD thesis, and the related engineering drawings can be found in Appendix E of the same document [229]. (The CFD geometry which Gildfind used to simulate the nozzle can be found in Figure 8.2 of Gildfind [230].)

In 2011, Gildfind et al. [231, 230] found that while Scott’s driver conditions had been suitable for high enthalpy experiments where the test gas reached the end of the driven tubes very quickly, the driver supply pressure ( $p_4$ ) of these conditions did not remain constant for long enough for the simulation of the slower but much higher total pressure scramjet test conditions which they were designing<sup>2</sup>. The driver pressure would drop too quickly, and the expansion wave processing the driver gas would reflect off the piston face in the driver section, and move down the tube and interfere with the test flow before it could reach the test model, effectively cancelling out any useful test time. To solve this problem, Gildfind et al. [231, 230] designed a new 10.5 kg piston, and a set of new ‘tuned’ driver conditions to be used with it.

An un-tuned free piston compression with a relatively heavy piston, like Scott’s [229], only gives the piston enough kinetic energy to compress the driver gas until it just ruptures the primary diaphragm ( $p_4$ ), after which the piston is effectively stopped, and for a very short period of time a high pressure burst of driver gas is achieved, which decays very quickly as the driver gas exits the driver tube. While a ‘tuned’ driver condition puts much more stress on the

<sup>2</sup>Using a high enthalpy condition with a 5,000 m/s shock tube shock speed ( $V_{s,1}$ ) and a 10,000 m/s acceleration tube shock speed ( $V_{s,2}$ ) as an example (basically the Hayabusa entry condition from Fahy et al. [81]). Theoretically, the acceleration tube shock would reach the end of the acceleration tube in 1.25 ms. For a much slower scramjet condition with  $V_{s,1} = 1,000$  m/s and  $V_{s,2} = 3,000$  m/s, similar to a condition from Gildfind et al. [232], the acceleration tube shock would take just over four times longer to reach the end of the acceleration tube.

piston itself and can be more challenging to design, requiring a correct combination of driver length, driver diameter, driven diameter, piston mass, and reservoir pressure limits, tuned operation can provide approximately constant driver pressures for a much longer duration of time. This is because it over-drives the piston and keeps it moving after diaphragm rupture so that the extra piston displacement after rupture compensates for the loss of driver gas exiting the driver tube. (The reader is referred to Stalker [233, 234], Itoh et al. [235], and Tanno et al. [236] for further discussion of tuned operation of free piston drivers.)

The tuned driver conditions designed by Gildfind et al. [231, 230] can be found in Table 4.1, and a simulation of the expected driver pressure for the three tuned 80%He/20%Ar (by volume) conditions using the one-dimensional facility simulation code L1d2 [237, 238] can be seen in Figure 4.5, where the region of approximately steady pressure after diaphragm rupture can be seen for each condition. As a comparison, a simulation of Scott’s original 35 kg piston, 100%He driver condition [229] has been time shifted to align it with the rupture pressure of the tuned new 1.2 mm diaphragm condition designed by Gildfind et al. [231, 230], showing the sharp pressure drop after rupture for Scott’s condition, and the millisecond of roughly steady driver supply pressure for Gildfind et al.’s.

Table 4.1: Current tuned X2 expansion tube lightweight piston driver conditions from Gildfind et al. [231, 230]. Designed using an 80%He/20%Ar (by volume) driver gas. (Updated values for X2-LWP-2.0 mm-0 can be found in Table 5.2.)

Driver case ID	Steel diaphragm thickness mm	Rupture pressure ( $p_4$ ) MPa	Rupture temp. ( $T_4$ ) K	Reservoir fill pressure MPa	Driver fill pressure kPa
X2-LWP-1.2 mm-0	1.2	15.5	1,993	4.94	110.3
X2-LWP-2.0 mm-0	2.0	27.9	2,700	6.85	92.8
X2-LWP-2.5 mm-0	2.5	35.7	3,077	6.08	77.2

Figure 4.6 shows the dimensions of the current X2 expansion tube when it is configured in various ways. Figure 4.6a shows the most commonly used X2 configuration, with the nozzle, but without a secondary driver section. Figure 4.6b shows another configuration with the nozzle, but also with a secondary driver section.<sup>3</sup> It can be seen that when the secondary driver section is used, the shock tube is moved downstream and the acceleration tube becomes shorter. Figure 4.6c, shows another configuration with a secondary driver section but this time *without* the nozzle. While an extra section is added to the end of the acceleration tube when

<sup>3</sup>The secondary driver is an extension of the primary driver which is used to increase driver performance or to act as an acoustic buffer to prevent noise generated from primary diaphragm rupture entering the test gas. The secondary driver is discussed further in Section 5.4.2, and the reader is directed to Morgan [196] and Gildfind et al. [1] for more information.

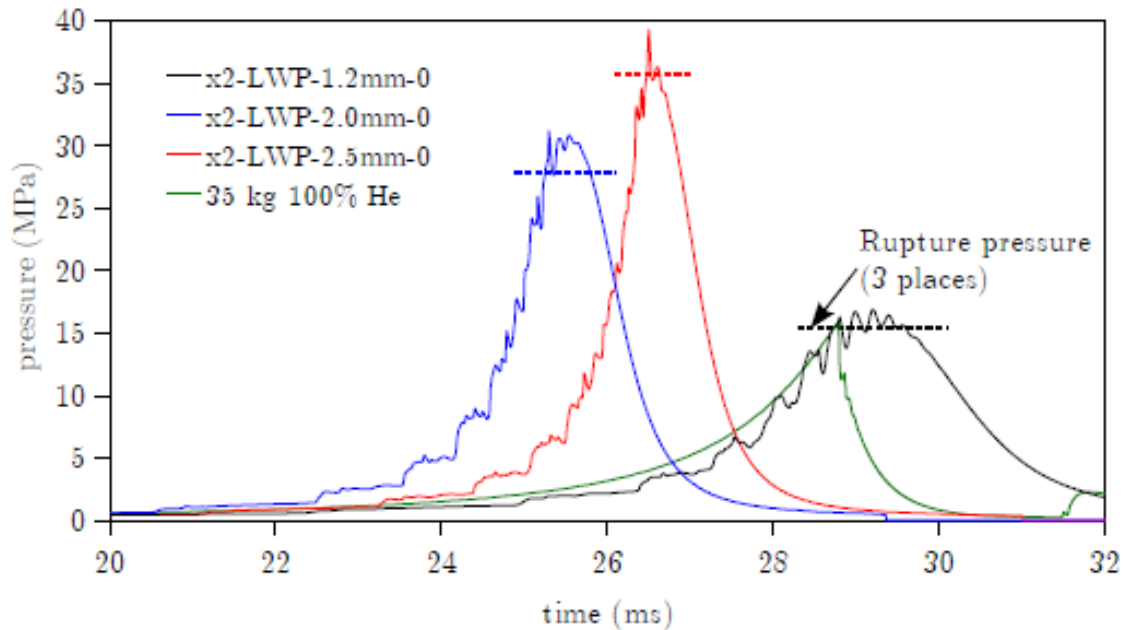


Figure 4.5: Driver pressure simulations from L1d2 [237, 238] for the three tuned driver conditions shown in Table 4.1 and the original 35 kg piston, 100%He driver condition designed by Scott [229], from Gildfind [231].

the nozzle is not used, the facility is still shorter overall without the nozzle. X2 could also be used without a secondary driver or nozzle, but this is not shown in Figure 4.6.

For many reasons, it is not simple to take experimental measurements of an X2 flow condition. Firstly, any physically intrusive measurement techniques performed along the facility length will change the flow condition itself, changing any measurements taken further downstream. Secondly, the experiments generally involve shock speeds of the order of 6 to 12 km/s, so any measurement device used must respond quickly enough to be able capture the arrival and passing of a shock wave at that order of magnitude. Thirdly, the measurement devices must be tough enough to survive not just the accelerator and test gases, but the hot, high pressure driver gas that flows down the tube behind it, and any diaphragm fragments which may be entrained in the flow.

Other physical instrumentation such as heat transfer gauges are sometimes mounted in the test section, and cameras and spectrometers are often used to optically probe the test flow of experiments, but general shot-to-shot instrumentation on the X2 expansion tube is performed by a series of twelve wall-mounted pressure transducers along the facility length. Wall-mounted pressure transducers are chosen because a passing shock provides a step increase in pressure, and if that can be captured in multiple locations, it can be used to measure the shock speed in

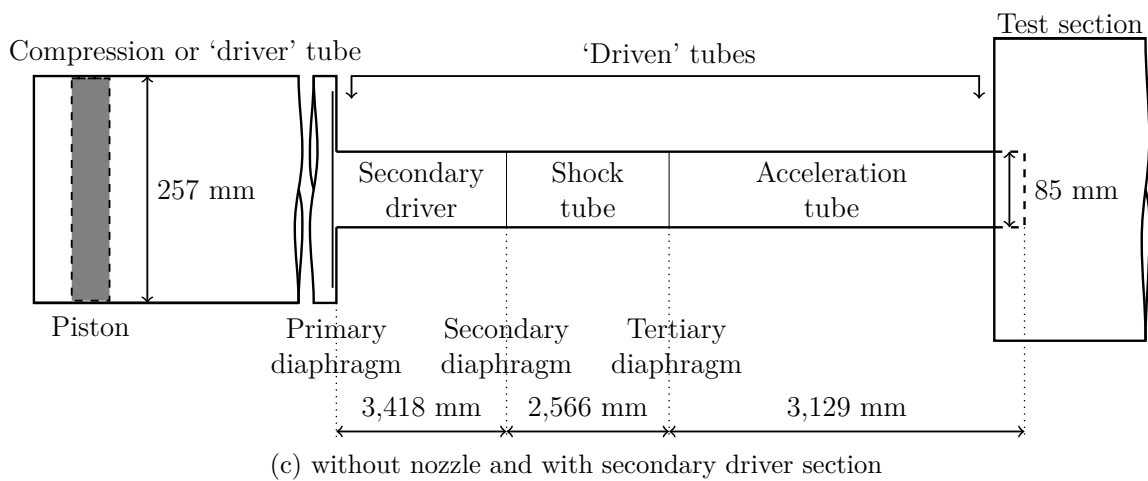
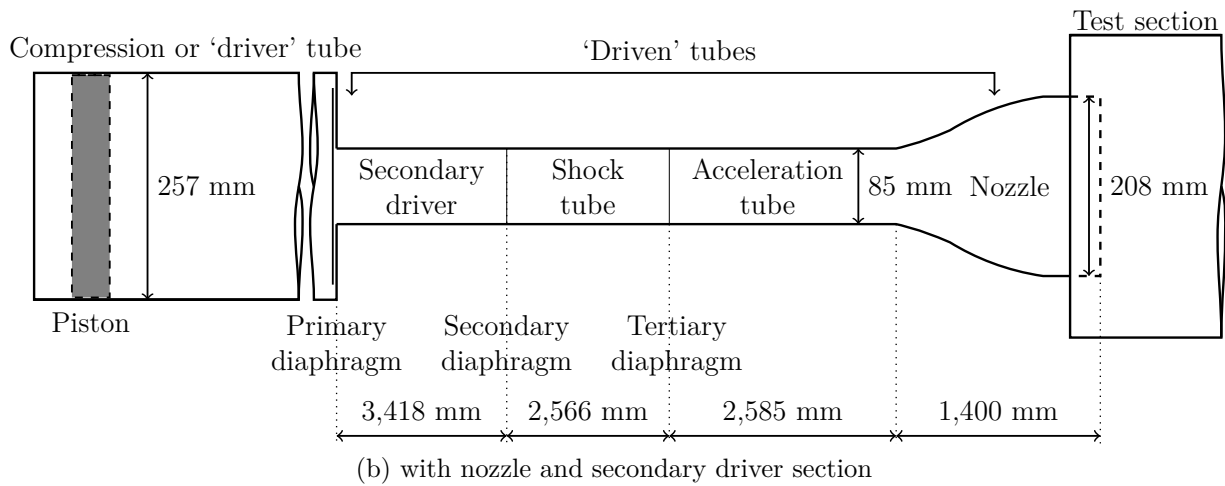
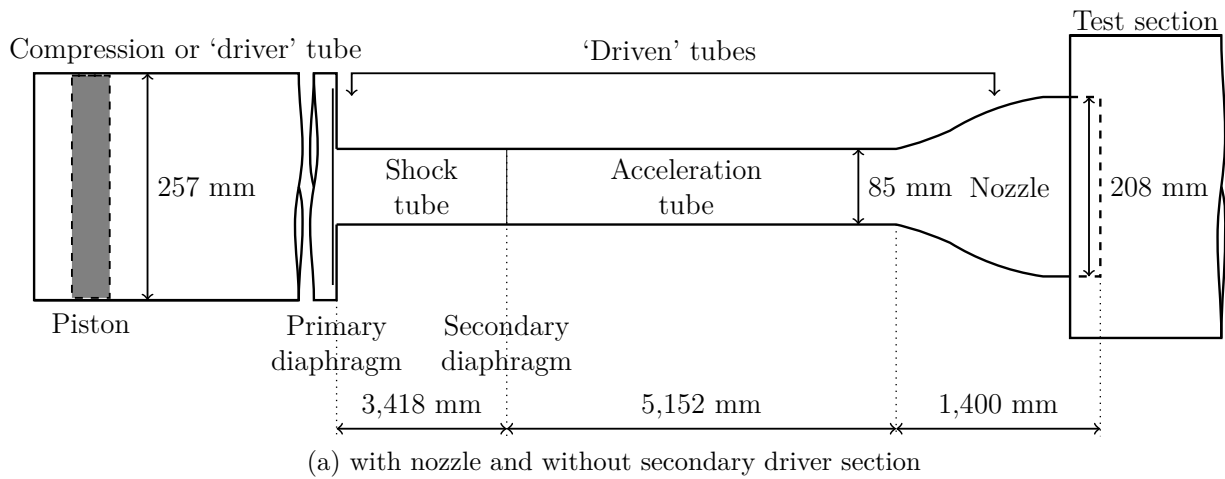


Figure 4.6: Schematics of the X2 expansion tube in various current configurations. (Roughly to scale.)

each section of the facility. These shock speed measurements can then be compared to theory or simulations to try and effectively 'fill in the gaps' of the flow condition with what cannot

be directly measured experimentally. Impact pressure probes mounted in a Pitot rake in the test section are used when new test conditions are being validated to measure the test flow pressure, test flow uniformity, and experimental test time. This can all be seen in Figure 4.7, where the pressure transducer configuration for each of the three facility configurations shown in Figure 4.6 are shown. When the secondary driver section is not used (see Figure 4.7a), the wall transducers ‘sd1’ to ‘sd3’ are used to measure the shock speed near the end of the shock tube, and wall transducers ‘st1’ to ‘st3’ are either not used or are used to measure the shock speed at the start of the acceleration tube. When the secondary driver section *is* used (see Figures 4.7b and 4.7c) the wall transducers ‘sd1’ to ‘sd3’ are used to measure the shock speed near the end of the secondary driver, and wall transducers ‘st1’ to ‘st3’ are used to measure the shock speed in the shock tube. In all configurations, the six acceleration tube wall transducers (‘at1’ to ‘at6’) are used to measure the shock speed in the acceleration tube, with an extra ‘at7’ transducer used when the facility is used without the nozzle. The actual locations of the wall pressure transducers from Gildfind et al. [239] can be found in Table 4.2.

Table 4.2: X2 wall transducer and diaphragm locations from Gildfind et al. [239]. Details of the locations of two new wall pressure transducer mounts at the end of the acceleration tube can be found in Section 4.5.1.

Description	x-location (mm)
Primary diaphragm downstream face	0
Transducer sd1	2,577
Transducer sd2	2,810
Transducer sd3	3,043
Secondary diaphragm downstream face	3,418
Transducer st1	4,231
Transducer st2	4,746
Transducer st3	5,260
Tertiary diaphragm downstream face	5,976
Transducer at1	6,437
Transducer at2	6,615
Transducer at3	6,796
Transducer at4	7,590
Transducer at5	7,846
Transducer at6	8,096
Transducer at7 (if used)	8,652

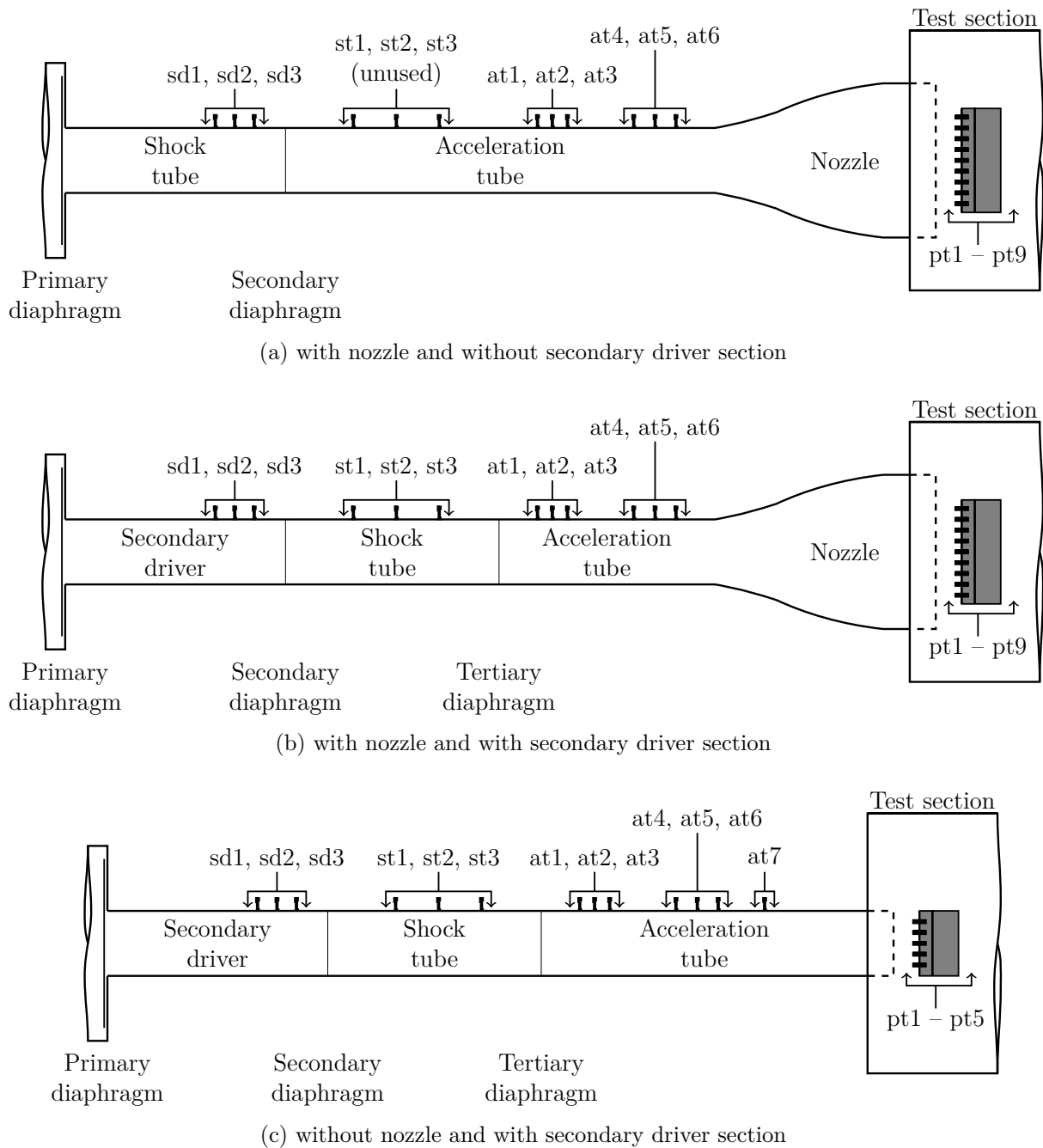


Figure 4.7: Current X2 wall pressure transducer locations. Both without (a) and with (b) a secondary driver section. (Not to scale.)

## 4.4 Proposed Test Models for the Project

Various different test models have been used in the X2 expansion tube. These include fundamental shapes such as spheres [240], circular cylinders [78, 79, 80] and wedges [86, 87], scaled blunt body aeroshell models of re-entry spacecraft such as Hayabusa and Stardust [82, 241, 242],

scaled scramjet models [137], heated cylinders [90, 91, 3, 7], and a Mach disk model for creating standing normal shocks [243, 88, 89]. This section will discuss the test models proposed for this project. They are the latest version of the Eichmann cylinder [244], the X2 Pitot rake model for validating new test conditions, a new ‘Pitot Rake Cylinder’ to be used for taking basic spectroscopic measurements when the Pitot Rake is in use, and two new smaller, standalone Pitot rake models which can be used under other test models for measuring test section Pitot pressure.

#### 4.4.1 The Eichmann Cylinder

The Eichmann cylinder is a 25 mm diameter, 75 mm long circular cylinder, giving an aspect ratio of 3:1. This was the cylinder geometry used by Eichmann for studying Mars entry radiation in X2 [78]. An earlier paper by Eichmann showed that the optimal aspect ratio, which maximised cylinder diameter (and also shock standoff) in X2 while producing a very close approximation of the expected shock standoff on a two-dimensional infinite length cylinder was 4:1 [244]. However, when Eichmann did experiments with an imaging spectroscopy system, and the 4:1 aspect ratio model, he found that the achievable spatial resolution was unsatisfactory [78]. Because he did not want to reduce the available shock standoff, by changing to a model with an aspect ratio of 3:1, he was able to achieve an acceptable spatial resolution. However, the trade off was an expected reduction in shock standoff of less than 5% compared to the 4:1 case. A 3:1 aspect ratio model has been used here too.

A Computer-aided design (CAD) representation of the Eichmann cylinder and the full X2 model mounting system can be seen in Figure 4.8. The system is designed to place the test model at the horizontal centre-line of the X2 facility. Adjustment can then be performed in several places to move the test model forward and backwards, up and down, or to place it at an angle of attack. The whole model mounting system is designed to be modular, with different test model designs making use of different parts of the model mounting system. In Figure 4.8 the test model is shown with its alignment plates in place, which are attached to the model using keys to ensure correct angular and horizontal alignment. A bolt is then used to secure them in the correct vertical location. Each plate has a 0.5 mm diameter hole in front of the test model at its vertical centre which a laser can be shone through for model angular and horizontal alignment.

The engineering drawings of the latest version of the Eichmann cylinder can be found in Appendix A. The drawing set also includes drawings of the full model mounting system which were made by the author from measurements of the existing model mounting components. This was done for posterity so that these drawings could be used by other experimenters in the



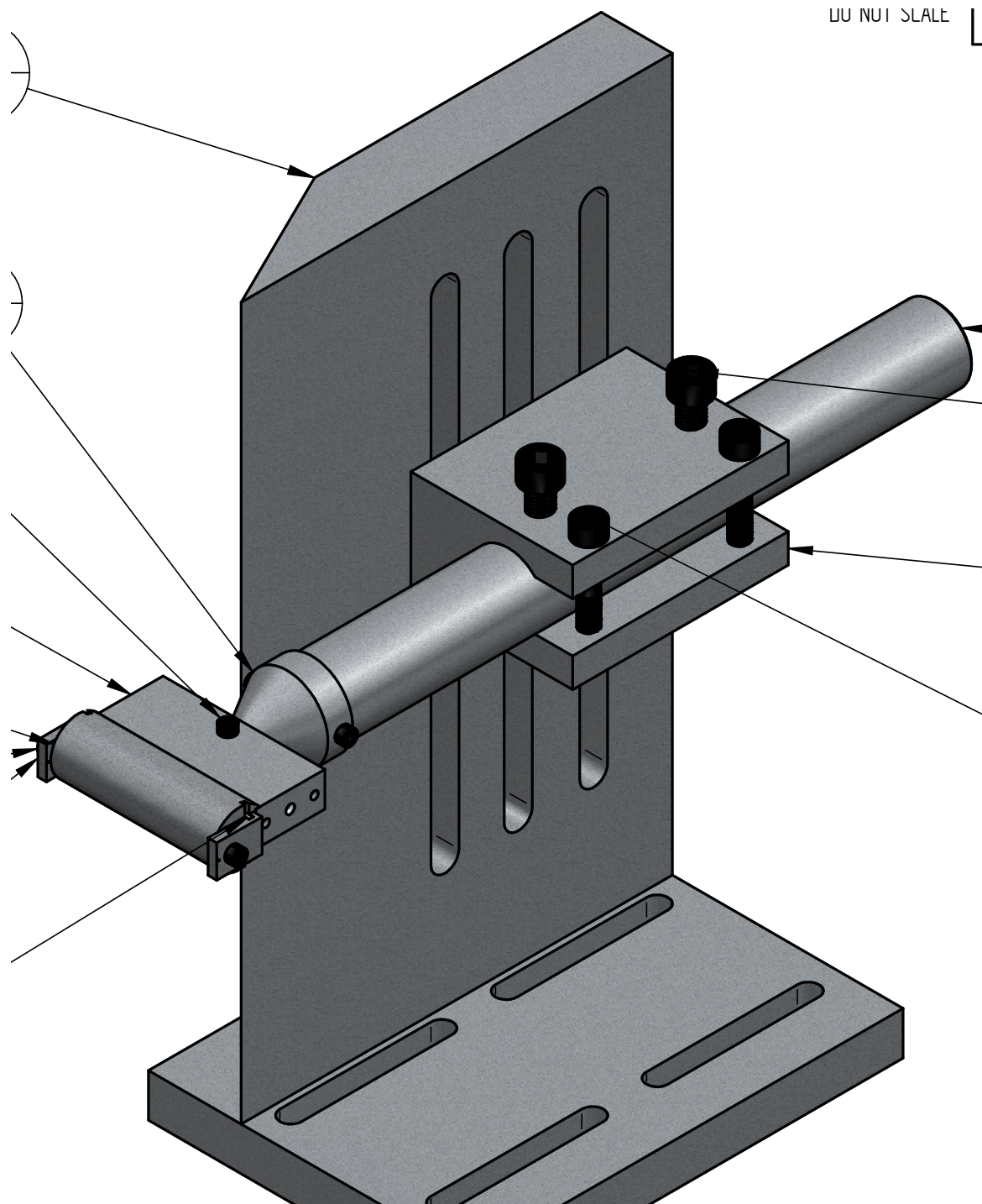


Figure 4.8: CAD representation of the Eichmann cylinder and full X2 model mounting system from Appendix A.

future to design models which work with the same mounting system. Since this has been done, various other experimenters have designed experimental systems using these drawings and all or some parts of the current model mounting system.

### 4.4.2 The Pitot rake

A Pitot rake is a test model used in a wind tunnel or impulse facility for the testing of new or established operating conditions. In a continuous flow facility, such as a wind tunnel, a Pitot rake would be used to measure core flow size and flow uniformity from Pitot pressure measurements. In an impulse facility, like X2, a Pitot rake is not only used to measure those two parameters, but also to measure the steady test time of the test condition being tested. Because most impulse facilities are generally made from circular tubes, the flow should be axisymmetric, and the simplest Pitot rake design therefore only requires a single row of sensors to be placed in the test section. X2's design is similar to this, and a photo of it from McLean [245], during experimental set up to measure pressures at the same axial location as the entrance to X2's nozzle, can be seen in Figure 4.9. More complex designs measure in two axes, or may have probes placed off axis. .



Figure 4.9: X2's Pitot rake during experimental set up to measure pressures at the same axial location as the entrance to X2's nozzle from McLean [245].

A representation of the X2 Pitot rake can be seen in the test section for all three facility configurations shown in Figure 4.7. X2's Pitot rake can be instrumented with nine pressure transducers mounted 17.5 mm apart vertically, covering a total centre-to-centre height of 140 mm. (Figure 4.7c only shows probes 'pt1' to 'pt5' to illustrate the smaller exit diameter of

the facility without the nozzle.) Generally, the middle probe is oriented with both the horizontal and vertical centre-lines of the facility, but it could be offset vertically if required. Different forebodies can be used to shield the pressure transducers. Either Pitot pressure probes designed by McGilvray et al. [246] or  $15^\circ$  cone pressure probes designed by Gildfind [230] are generally used. (The latest drawings for both forebody designs can be found in Appendices G and H of Gildfind [230], respectively.)

### 4.4.3 Pitot Rake Cylinders

It is proposed that this project will test many new operating conditions. For this reason, it was decided that it would be useful to build a test model which would allow basic spectroscopic measurements to be taken while also using the Pitot Rake, and for this reason, two Pitot Rake Cylinders and a mount for them were designed and built. Two different cylinders were made, an approximately half-size Eichmann cylinder (12 mm diameter, 36 mm long), and also an approximately  $2/3$  scale truncated Eichmann cylinder (17 mm diameter, 51 mm length). The truncated cylinder was designed to maximise the model radius, and with it, the shock standoff, by truncating the geometry beyond the sonic line which occurs at around  $45^\circ$  along the body.

A mount was then made to allow the cylinders to be mounted in one of the standard mounting holes of the X2 Pitot rake. An example high speed image showing the truncated cylinder in use when new argon test conditions were being tested on X2 can be seen in Figure 4.10. For this test condition, it can be seen that the truncated cylinder has a large wake flow, which was interfering with measurements from the probes on either side of it. However, the top and bottom 3 probes on the Pitot rake were undisturbed by it. The full set of engineering drawings for the cylinders and their mount can be found in Appendix D.

### 4.4.4 Standalone Pitot Probe Mount Models

In many early spectroscopic studies in the X2 expansion tube, no test section Pitot pressure measurements were taken. Test section pressures were measured in separate Pitot rake experiments and either these measurements, or high speed imagery captured using the actual experimental test model, were used to estimate when imaging spectroscopy systems should be triggered. In Sheikh [247], the test model was mounted on a very large mount which contained embedded vacuum ultraviolet optics. This mount provided space for the mounting of two Pitot pressure probes so that test section Pitot pressure could be obtained for each experiment.

Because they are designed conservatively, most test models used in X2 fit inside a maximum 100 mm core flow diameter, while Pitot rake measurements have indicated that some test conditions' core flow covers at least the 140 mm centre-to-centre height of the Pitot rake. Using

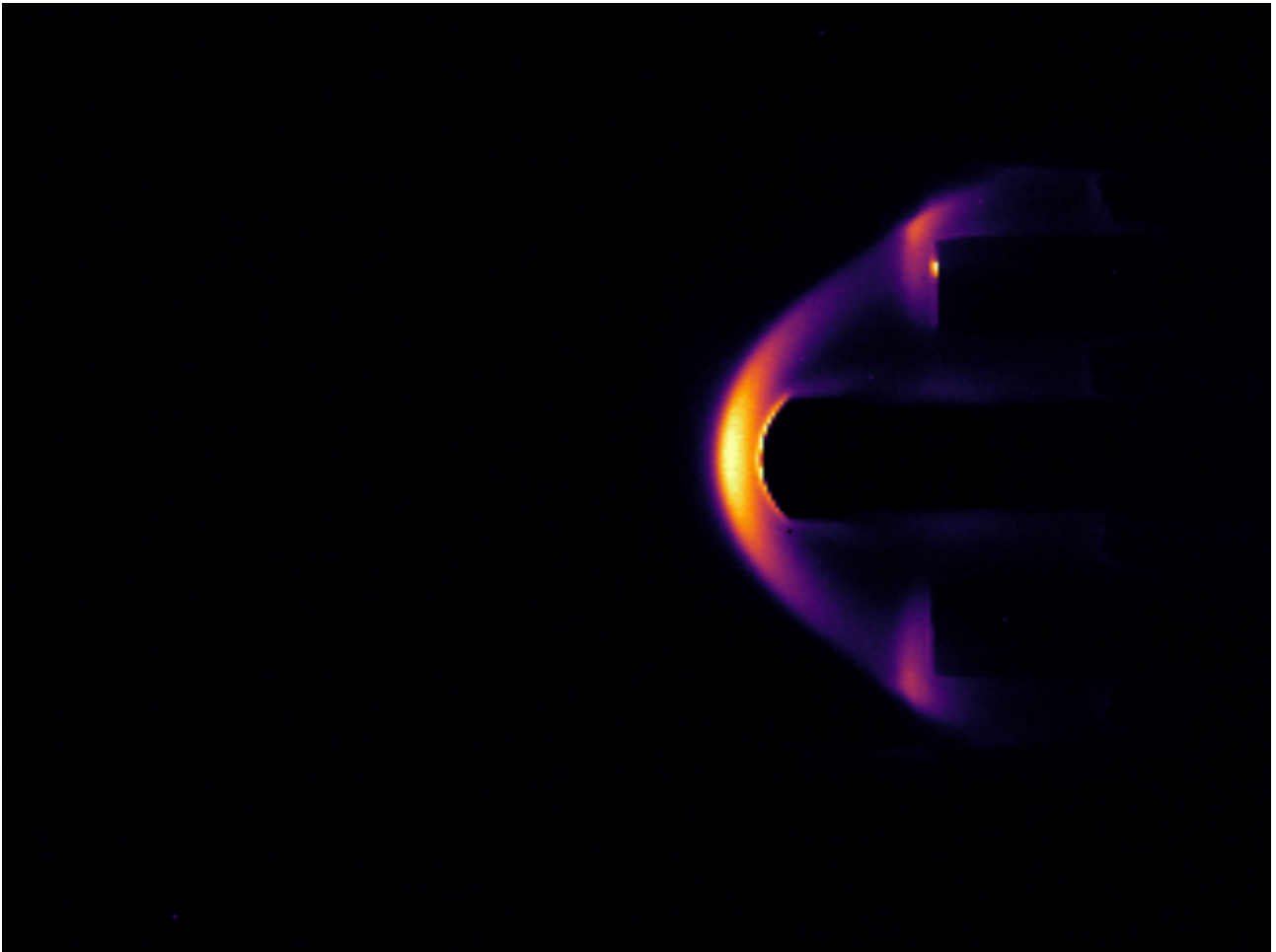


Figure 4.10: False colour sample high speed image from experiment x2s3119 testing argon test condition x2-mhd-lwp-02.

Sheikh's test section Pitot probe mounts [247] as an inspiration, two iterations of a standalone Pitot probe mount model were designed to interface with the current model mounting system. The goal of the mounts was to be compatible with the existing Pitot rake hardware, while also being as compact as possible so that they could be mounted as close to the main test model as possible. The first design was only able to mount a single probe, which was aligned with the horizontal centre-line of the facility. The second iteration, named 'the trident' in the laboratory, was able to use up to three separate probes, one aligned with the horizontal centre-line of the facility, and one probe either side using the same 17.5 mm probe spacing as the Pitot rake. The second iteration also provided more shielding behind the mount for the transducer cabling. A photo taken by the author of the second iteration model in place under a 3D printed version of the 1/5 scale Hayabusa test model from Fahy et al. [81] during experiments for Apirana et al. [248] can be seen in Figure 4.11. Engineering drawings for both iterations of the model can be found in Appendices B and C respectively.





Figure 4.11: Photo of the second iteration of the standalone Pitot probe mount model mounted underneath a 3D printed scaled Hayabusa test model.

These standalone probe mounts are now standard experimental hardware for most experimenters on the X2 expansion tube. As was discussed above, they are generally used for establishing the steady test time of the given test condition for setting the delays and exposure times for various optical hardware. Because most X2 test conditions strongly radiate, photodiodes are often used for triggering a central trigger box which triggers facility instrumentation. In some situations where test conditions are not as strongly radiating, the photodiodes become very sensitive to their exact placement, which can cause issues with the repeatability of the triggering or can cause hardware to trigger late after the experiment is over or not at all. In these situations, these Pitot probe mounts have been very useful for triggering facility instru-

mentation, and because they generally exhibit a sharp rise at test flow arrival, they provide a good, repeatable basis for setting up delays and exposure times for optical hardware. In the heated model experiments of Lewis et al. [7], a standalone Pitot probe mount was essential because when it had been attempted to use a photodiode for triggering, the luminosity of the heated model had been triggering the experimental hardware before test flow arrival. This problem was easily remedied by instead triggering using the test section Pitot probe.

## 4.5 Physical Upgrades to the X2 Expansion Tube

During this project, because of the need to perform experiments with acceleration tube fill pressures below 1 Pa and acceleration tube shock speeds around 20 km/s, several physical upgrades were made to the facility to better accommodate this. These mainly concerned improving the wall pressure transducer mounting to improve sealing on the facility, and to improve the wall pressure measurements and the shock speeds which are inferred from them.

### 4.5.1 New Wall Pressure Transducer Mounts

In 2015, new wall pressure transducer mounts were designed for the X2 expansion tube by Gildfind [249]. Instead of being bolted into the tube wall itself, to vibrationally isolate the probes from the facility, they were mounted through an 18 mm diameter hole in the tube wall, with o-rings mounted down the barrel of the probe and also on its face which was pressed against a flat section machined on the outside of the tube. The probes were held in place by a clamping piece bolted to the outside of the tube, with another o-ring used to vibrationally isolate the probe mount from the clamp. A CAD representation of one of the mounts can be seen in Figure 4.12.

Initially, three pilot mounts were made and used in sensor locations ‘at4’ to ‘at6’ near the end of X2’s acceleration tube. The probe locations are shown in Figure 4.7. Near the end of 2015, when the author started planning for a final set of experiments, the author made some modifications to the clamping piece (named ‘PCB tube holder’ in the engineering drawing set) to strengthen it for use in higher pressure sections of the facility, and organised the manufacture and installation of enough of these probes to replace every wall pressure transducer mount on the facility. Today, every mount except the ‘sd’ labelled mounts (‘sd1’ to ‘sd3’) have been replaced with these new mounts. Hardware has been built for these final locations, but due to the facility downtime which would be required to remove this final large section of the facility so that the new mounting holes could be machined, the job remains in the pipeline. A full modified drawing set which includes the author’s changes to the assembly and PCB tube

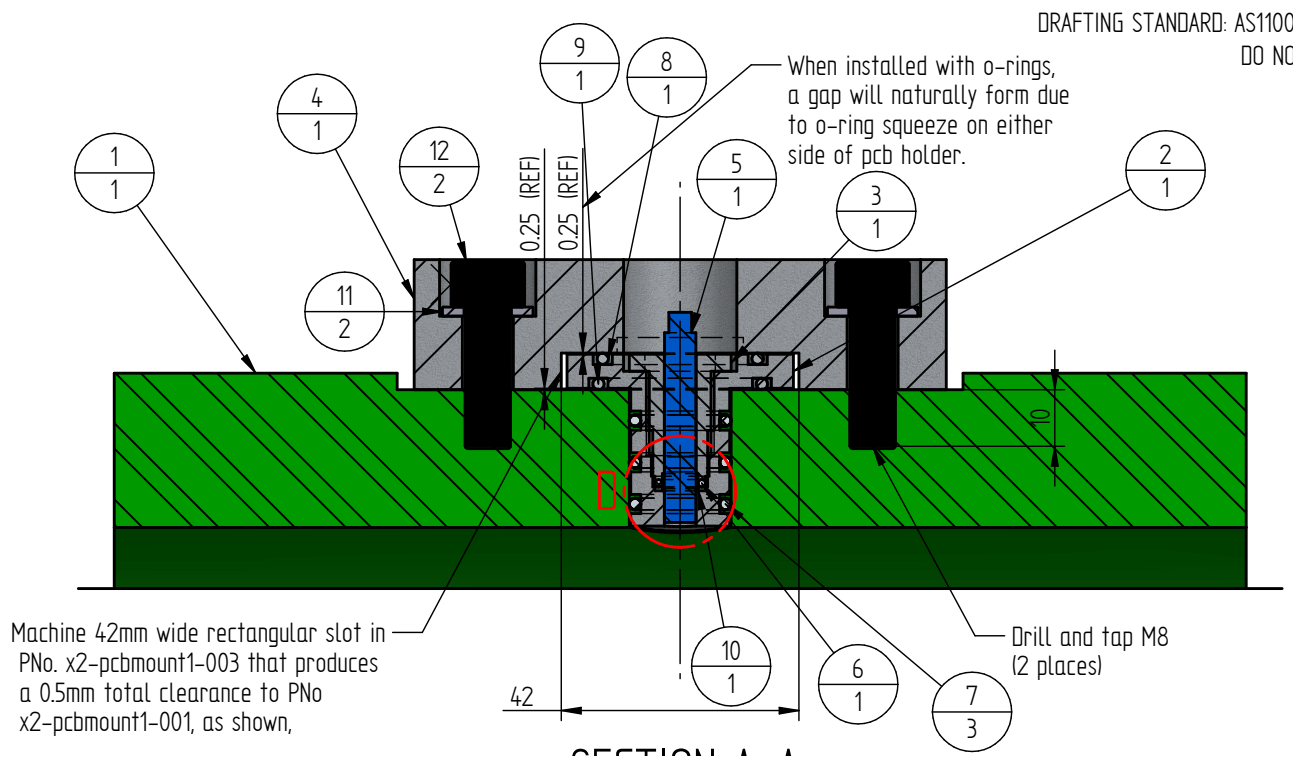


Figure 4.12: Section view of Gildfind's new wall transducer mount from Gildfind [249] and Appendix E.

holder drawings, as well as original drawings by Gildfind [249] for the other components, can be found in Appendix E.

While Gildfind's design was mainly concerned with vibrationally isolating the probe mounts, the interest in getting the mounts installed for this project was more about sealing issues and sensor reliability. The old probe mounts used on the X2 facility were very old, and the different mounting holes were not always consistent with each other. Their design was also somewhat opaque, and this meant that no one wanted to make changes to the installed probes and mounts, which created a situation where sensor reliability and facility sealing were at cross-purposes. A sensor may have needed replacing, but unless it was essential, no one would want to touch it for fear of causing issues with sealing or vice versa. For this reason as well, the new probe mounts are a large improvement. They are new and documented, with drawings which experimenters can access, and the mounts and the probes themselves can be removed and examined quite easily, which encourages experimenters to regularly examine the probes and replace them if required.

Another project carried out by the author was the creation of wall pressure transducer mounts in the place of four unused photodiode mounts just before the entrance to X2's nozzle. Sheikh [247] had four mounting holes drilled 20 mm apart in X2's acceleration tube just before

the nozzle entrance for mounting photodiodes for high speed shock detection. While this is a very good idea which should be investigated again in the future, the rise seen by Sheikh [247] using his mounts was not as defined as a pressure transducer, and the technique was not adopted by others and fell into disuse.

Because these mounting holes already existed, it was a simpler task to create and install probes for them, with the benefit that the same tightly spaced locations could be used just before the nozzle entrance. The author designed a wall transducer mount which was a more compact version of Gildfind's design for the other sensor locations [249]. A CAD representation showing one of the probes and a plug version for when sensors aren't used, can be seen in Figure 4.13. The related engineering drawings can be found in Appendix F.

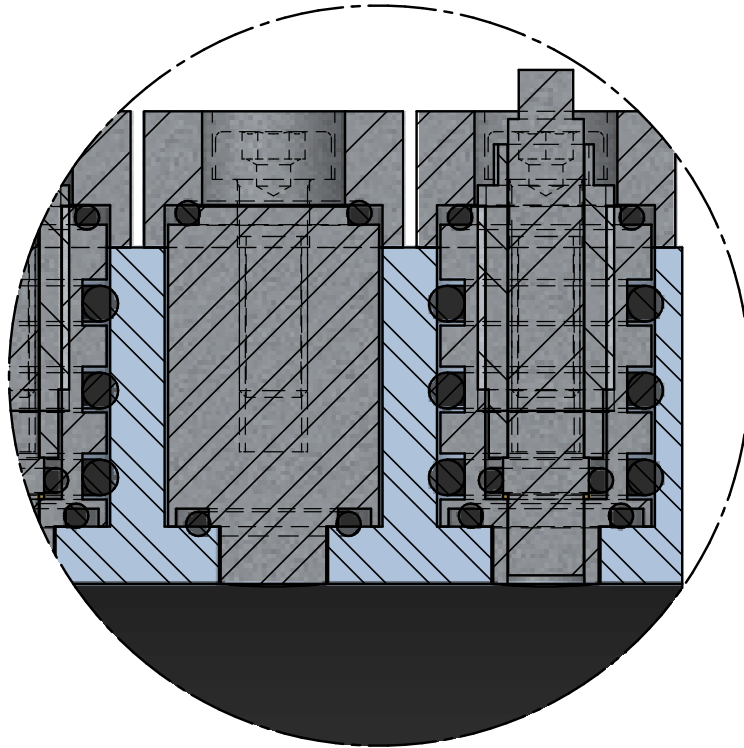


Figure 4.13: Section view of the photodiode mount pressure transducer mounts from Appendix F.

After the probes were manufactured, it was decided to install two probes in the second and fourth photodiode mounting holes away from sensor 'at6' as 'at7' and 'at8'. Their distances from the primary diaphragm (so that their locations are compatible with the values shown in Table 4.2 in Gildfind et al. [239]) are 8.157 m for 'at7' and 8.197 m for 'at8'. The distance for 'at7' was found by the author and one of the laboratory technicians using vernier callipers between the edge of its mounting hole and the edge of the 'at6' mounting hole as the original manufacturing drawings for the photodiode mounting holes only specified that they should be



placed as close as possible to the ‘at6’ mount, instead of an exact location. The location between ‘at7’ and ‘at8’ was taken to be 40 mm as the distances between the mounts were specified on the original manufacturing drawing. An updated X2 PCB diagram showing sensors ‘at7’ and ‘at8’ can be seen in Figure 4.14.

These new probes just before the nozzle entrance have been quite successful for pressure measurements, but taking tightly spaced pressure measurements and using them for shock speed calculations has some issues. Shock speeds are calculated between the sensor pairs using the time-of-flight method, i.e.  $V_s = \frac{\Delta x}{\Delta t}$ , which is explained further in Appendix G. As the time and distance uncertainties are generally fixed, as time-of-flight and distance get smaller, they both increase the uncertainty. Therefore, trying to measure a fast moving shock between two very tightly spaced mounts leads to very large uncertainties, compared to other sensor pairs on the facility which are between 200 and 500 mm apart. In the future, the probes may be able to be used with more complex curve fitting methods for calculating the shock speed down the length of the acceleration tube, but for now, they are generally used for calculating the wall pressure just before the nozzle entrance.

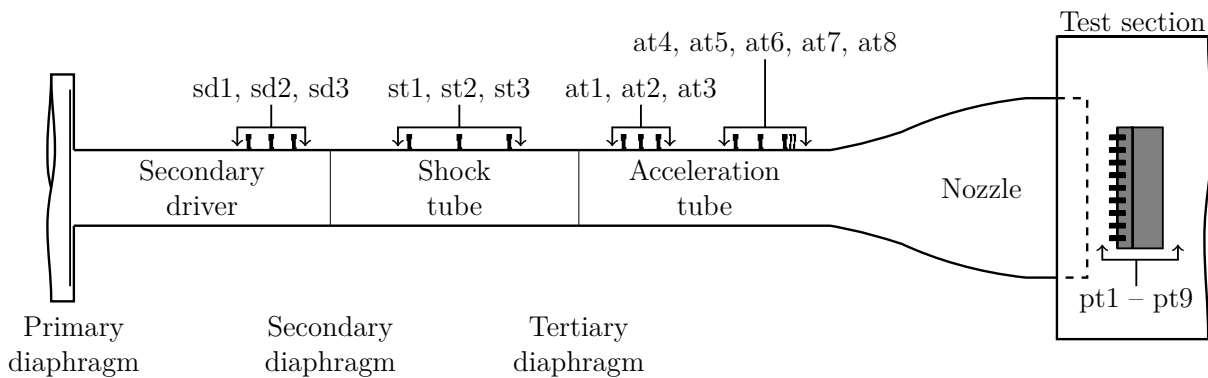


Figure 4.14: X2 PCB diagram with secondary driver section and ‘at7’ and ‘at8’

## 4.5.2 Improved Shock Speed Measurements

As is discussed further in Section 6.4.1, when the first experiments were performed for this project, the shock speed uncertainties were as high as  $\pm 1,000$  m/s. During investigation of the individual uncertainties which contribute to the overall shock speed uncertainties (see Appendix G), it was deduced that the sampling rate error caused by the 2.5 MHz maximum sampling rate of the facility’s data acquisition system (DAQ) was having a large effect on the uncertainty. For this reason, a 60 MHz National Instruments PXI-5105 high speed oscilloscope card was set up on the DAQ and all of the acceleration tube wall pressure traces except ‘at1’ (see Figure 4.7) were teed off into the high speed card.

However, when further experiments were performed for this project, it was found that in certain circumstances, as a result of the very low post-shock pressures, the high speed data acquisition did not lower the shock speed uncertainties because uncertainty in reliably ascertaining the shock arrival time became the limiting factor. The noise on the signal was also found to be too large for capturing the sub-microsecond response of the sensor to such a small step change. This is all discussed further in the experimental analysis presented in Section 6.4.1. In other situations, where the post-shock pressure in the acceleration tube is higher, such as the free piston driven air example presented in Section 5.5.4 with an acceleration tube shock speed of around 8,000 m/s, the 60 MHz card was much more successful at reducing shock speed uncertainties in X2's acceleration tube.

## 4.6 The Shot Class

When the author began this project they inherited a basic Python code called the 'Shot class' from Fabian Zander, a previous PhD student [250]. This code allowed experimental facility data to be loaded into a Python program which could then be used to calculate experimental shock speeds by selecting the shock arrival time at each wall pressure sensor location using a basic GUI system. From there, the Shot class has morphed into a much larger project.

The initial goal of the Shot class, for the author, was to make it simpler for experimenters to perform a rough analysis of their experimental facility data, as this was not a capability which fully existed in the laboratory when this project began. In terms of functionality, the goal was that within a couple of minutes of performing an experiment, an experimenter could know their experimental shock speeds, check wall and test section pressure data, and check the triggering times of optical components, so that this could be used to inform their next experiment on the facility. This was the original functionality provided by the author's first version of the code.

From there, the Shot class has morphed into a larger project for experiment analysis which is now somewhat of a 'one-stop shop' for analysing facility data. It is still used for performing the initial post-experiment analysis, but it can now also be used to do more in-depth analysis, such as the estimation of experimental diaphragm hold times, experimental test time from test section pressure measurements, and the calculation of experimental wall pressures with uncertainties included. It also calculates shock speed uncertainties using a procedure which is discussed in Appendix G, and in the latest version, is able to automatically calculate shock arrival times using several different methods.

A series of supporting tools were also written which can import the analysed Shot class objects and use them to make it simpler to compare different experiments, and also to collate and present data. These include tools for plotting experimental wall and test section pressures,

and shock speed data. These tools can also be configured to produce ‘journal quality’ outputs using  $\text{\LaTeX}$  based typesetting for simplifying the presentation of experimental facility data. All of the pressure and shock speed figures presented in the following chapters were made using these tools. Equivalent tools which allow experimental shock speed and pressure data with uncertainties to be exported in a format which can be pasted straight into  $\text{\LaTeX}$  as a table with or without automatic rounding to set significant figures were also made, and similarly, were used to produce most of the experimental tables presented in the following chapters. The last major tool created during this project was made to infer the test section conditions from experimental shock speed and pressure data. It uses experimental shock speeds and their uncertainties from the Shot class analysis to perform sensitivity analyses to infer facility uncertainties using PITOT, the facility simulation code discussed in Chapter 5. The exact procedure is discussed further in Section 5.5, and was used in that section and the experimental sections of the following chapters.

These supporting tools were all built to be user friendly, generic, and to run quickly. The goal of the Shot class project, in general, is to make the analysis and presentation of X2 facility data a simple task for experimenters, in the hope that this will result in better quality facility data being analysed and presented. All experimental analysis presented in the following chapters of this thesis were performed using the Shot class and various supporting tools. The Shot class does not have a user guide yet, but it is open source, well documented, and its progress is stored in an internal repository. Many examples are included in the repository, which mainly show users how to re-create the figures and tables presented by the author in this thesis and the related journal papers.

## 5

# Simulating the X2 Expansion Tube

*De qui et de quoi en effet puis-je dire : « Je connais cela ! » Ce cœur en moi, je puis l'éprouver et je juge qu'il existe. Ce monde, je puis le toucher et je juge encore qu'il existe. Là s'arrête toute ma science, le reste est construction. Car si j'essaie de saisir ce moi dont je m'assure, si j'essaie de le définir et de le résumer, il n'est plus qu'une eau qui coule entre mes doigts. Je puis dessiner un à un tous les visages qu'il sait prendre, tous ceux aussi qu'on lui a donnés, cette éducation, cette origine, cette ardeur ou ces silences, cette grandeur ou cette bassesse. Mais on n'additionne pas des visages. Ce cœur même qui est le mien me restera à jamais indéfinissable. Entre la certitude que j'ai de mon existence et le contenu que j'essaie de donner à cette assurance, le fossé ne sera jamais comblé.*

– Albert Camus, *Le Mythe de Sisyphe*, 1942 [251]

## 5.1 Chapter Overview

This chapter provides a description of how the X2 expansion tube can be simulated for quick condition design and characterisation using well known relations from isentropic and compressible flow theory. It is discussed in the context of explaining how the Centre for Hypersonics' equilibrium expansion tube and shock tunnel simulation code, PITOT, written by the author, works, but provides principles that could be applied to simulating an expansion tube without PITOT as well. Formulas are discussed where it is deemed necessary, however, the aim of this chapter is not to bog the reader down in the maths, but to give them an overview of how an expansion tube can be simulated quickly, and both the advantages and disadvantages of doing that. For a description of how an expansion tube works *with* all of the formulae included, the reader is directed to 'Chapter 3: Expansion Tube Theory and Operation' in the thesis of Gildfind [230]. The chapter begins by providing some context as to why quick expansion tube simulation is required, before giving a brief explanation of how to run a PITOT simulation and

then stepping the reader through how an expansion tube experiment is simulated from start to finish. The chapter ends with a couple of examples to illustrate how well this type of analysis is able to simulate the X2 expansion tube.

This chapter is made up of the final submitted version of the journal paper James et al. [25] with some of the introduction removed and instead discussed in Chapter 4.

## 5.2 Introduction

If expansion tubes are to be useful for the study of planetary entry and other situations, it is important to be able to characterise the test flows which they create, and this is not a simple task. Expansion tube test flows are fundamentally transient, and depending on the size of the facility and the individual test condition, useful test times will be of the order of tens to thousands of microseconds. This useful test time precedes the arrival of the hot, high pressure driver gas which is entrained with heavy particles from the diaphragms which were separating the different gas sections before the experiment was performed. It presents an extremely harsh flow environment, meaning that while expansion tubes require sensitive instrumentation which responds quickly to the transient flow, the instrumentation must also survive the harsh environment which follows it, limiting the types which can be used. Basic expansion tube instrumentation consists of pressure sensors mounted on the walls of the facility to measure shock speeds and wall static pressures, and test section mounted impact pressure probes to measure Pitot pressure. These diagnostics are used as input and validation data for analytical or numerical simulations which are used to infer extra information about the flow condition which cannot be measured directly. Shock speeds are often used to verify simulations of expansion tube flow conditions because they can be measured non-intrusively in the facility. If shock speeds match between experiment and simulation, it generally indicates that overall wave processes are being simulated with reasonable accuracy.

Different types of phenomena occur during an expansion tube experiment, such as diaphragm rupture, unsteady wave processes, viscous effects, and high temperature gas effects. This makes full numerical characterisation a costly computational process, and traditional techniques, such as the model presented in Neely and Morgan [252], used a semi-empirical approach, where measured shock speeds and wall and Pitot pressure measurements were used to calculate ‘mean’ or representative flow conditions. Current state-of-the-art requires compressible, high temperature, transient, two-dimensional axisymmetric computational fluid dynamics (CFD) calculations. These simulations generally cost tens or hundreds of thousands of hours of CPU time and are not suitable for the iterative design of new test conditions. Instead, two-dimensional CFD is used for accurate characterisation of established operating conditions.

UQ's one-dimensional CFD code, L1d3 [237, 238], can simulate phenomena such as free piston driver compression, equilibrium chemistry, various diaphragm rupture phenomena, and longitudinal wave processes. Depending on the fidelity of the simulation, L1d3 can perform a full facility simulation in the order of hours, making it more suitable for condition design. However, generally expansion tube acceleration tubes are affected by low density shock tube (or 'Mirels') effects [106, 107, 108], which cause over-expansion of the shocked test gas due to boundary layer growth in the acceleration tube. Due to its one-dimensional nature, L1d3 has no mechanism to simulate this phenomenon, making it unsuitable for the simulation of complete expansion tube test flows. Instead, L1d3 is generally used to provide the in-flow to higher fidelity simulations of the acceleration tube or to somewhat qualitatively verify overall wave processes.

By identifying important flow processes which occur during an expansion tube experiment and then modelling them from state to state using predominately analytical techniques, lower fidelity estimates can be made with orders of magnitude less computational expense. Coupling this with an understanding of where ideal processes may start to break down and what can be done to accommodate this analytically, reasonable predictions can still be made. This allows experimenters to perform preliminary design of new expansion tube test conditions in close to real-time. If a reasonable starting point can be found theoretically, the condition can then be further tuned, if necessary, after initial experiments have been carried out and any discrepancies between theory and experiment have been identified.

In this paper, a new code, PITOT, is described. PITOT was written in the Python programming language and makes use of the Python libraries written by Jacobs et al. [253] for use with the ESTCj program. An early version of the code was first presented by James et al. [10] in 2013. PITOT is UQ's in-house expansion tube and shock tunnel simulation code based on isentropic and compressible flow state-to-state gas processes. The code takes its name from a perfect gas expansion tube simulation code written by one of the authors in the early 90s. PITOT uses NASA's Chemical Equilibrium with Applications (CEA) equilibrium gas code [197, 198] to account for high-temperature gas effects, which are often important in the facility's acceleration tube, where shock speeds normally range from 6 to above 20 km/s. PITOT also incorporates a perfect gas solver. It is capable of performing an equilibrium expansion tube simulation on a single processor in several minutes and a perfect gas simulation in seconds.

PITOT was written to be a virtual impulse facility, and simulations are therefore configured like an experimenter would configure a real experiment. It uses facility fill condition as inputs and then the code runs through the flow processes in a state-to-state manner, analogous to how the different sections of the facility would operate in the real experiment. The code was written this way to create a simple and intuitive tool for trying to understand a facility and

how different parameters affect flow conditions. PITOT can also be easily scripted to perform parametric studies and sensitivity analyses, and tools are provided with the code to do this. PITOT is open source and forms part of the Compressible Flow Computational Fluid Dynamics (CFCFD) code collection at UQ's Centre for Hypersonics [254]. Instructions for obtaining the code can be found in Appendix H.

While this paper is based around the X2 expansion tube at UQ, the discussion is generally applicable to any such facility. The following section, Section 5.3, provides a brief introduction to the X2 facility and explains what occurs during an X2 experiment. Section 5.4 provides a summary of how each section of the facility is simulated in PITOT. The final section, Section 5.5, discusses how this analysis can then be calibrated to allow it to be used to quantify experimental data, similar to a traditional semi-empirical expansion tube model such as the one presented by Neely and Morgan [252].

### 5.3 The X2 Expansion Tube

The free piston driven X2 Expansion Tube at UQ is a 23 m long, medium sized facility with a driven tube bore of 85 mm and a nozzle exit diameter of 201.8 mm. Measured in terms of driver gas sound speed ( $a_4$ ), X2 has the highest performance driver of any operational expansion tube facility, and is capable of producing scaled test conditions for entry into most of the planets in our solar system. X2 is generally used to perform studies of blunt-body planetary entry radiation and it has been used extensively to generate and measure radiating test flows for many planetary bodies, including Earth, Mars, Titan, Venus, and Uranus from 3 to 20 km/s [222, 1, 81, 127, 86, 78, 87, 79, 80, 20]. X2 has also been used to develop and refine a new technique for the study of ablation phenomena in impulse facilities by using heated models [90, 91, 3, 7]. Fig. 5.1 shows the current dimensions of the X2 expansion tube when it is used in the most common configuration, with the nozzle, but without a secondary driver section. It also shows the notation employed for the different gas states, and the names and locations of the tube wall pressure sensors. A more detailed overview of X2 can be found in Gildfind et al. [146].

In its simplest configuration, an expansion tube has two driven sections: a shock tube, and a lower pressure downstream 'acceleration tube' which is used to accelerate the shocked test flow through an unsteady expansion (see Fig. 5.1). An expansion tube can also be configured with an extra driven section called a 'secondary driver', which is added between the primary diaphragm and the shock tube. This section is filled with a light gas (generally helium) and is used to increase the performance of the driver condition, allowing the facility to drive a more powerful shock through the test gas than it could have done otherwise [1].

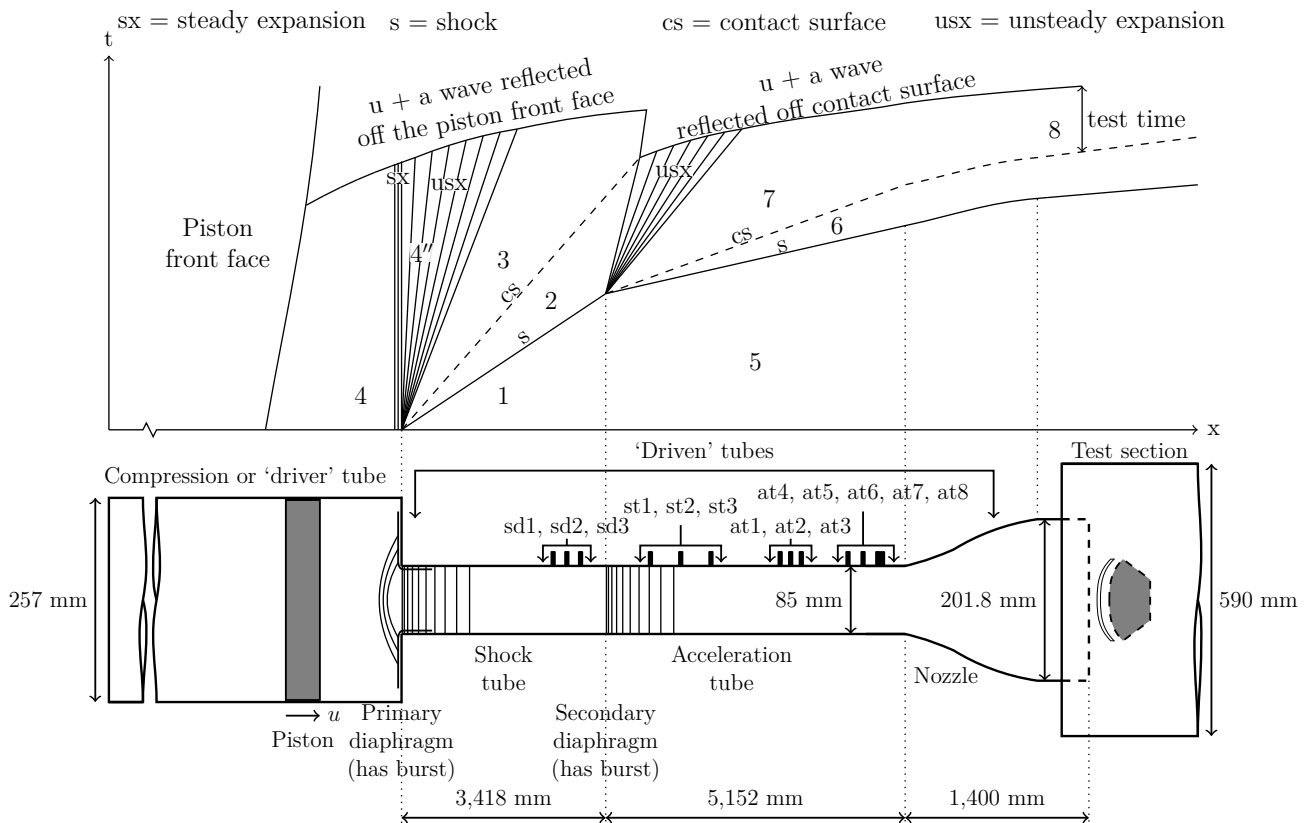


Figure 5.1: Schematic and position-time ( $x-t$ ) diagram of the X2 expansion tube. (Not to scale.) The exact locations of sensors at6, at7, and at8 are slightly obscured due to their tight spacing just before the nozzle entrance.



Before an experiment, all sections of the facility are evacuated and then filled with the required gases, at the required pressures. The experiment begins when the piston is released. The reservoir pressure (usually of the order of several MPa) causes the piston to rapidly accelerate, compressing the primary driver gas in front of it from its initial fill pressure to the primary diaphragm rupture pressure. At this rupture point, due to the compression of the driver gas, its pressure and temperature are both very high (tens of MPa, thousands of K). This hot, high pressure driver gas (state 4) is used to drive a shock wave through the driven sections of the facility, processing the test gas to the required condition before it flows into the test section.

Figure 5.1 includes a facility schematic and position-time ('x-t') diagram of the facility, showing the longitudinal wave processes which occur during an experiment. After primary diaphragm rupture, if the free piston driver is tuned [233, 234, 235, 236], the high speed piston maintains approximately constant gas properties in the driver ( $T_4 \approx \text{constant}$ ,  $p_4 \approx \text{constant}$ ) by matching mass loss from driver gas venting into the driven tube with further piston displacement. Due to the area change at the primary diaphragm, the driver rupture condition (state 4) undergoes a steady expansion to the throat Mach number ( $M_{throat}$ ) of 1 before it unsteadily expands into the shock tube (becoming state 3), driving a shock wave ( $V_{s,1}$ ) through the shock tube gas (state 1) and processing it to state 2. When this shock wave reaches the secondary diaphragm separating the shock and acceleration tubes, the diaphragm ruptures and the shocked test gas (state 2) starts to unsteadily expand into the acceleration tube (becoming state 7). The state 7 gas drives a shock wave ( $V_{s,2}$ ) through the accelerator gas (state 5) and processes it to state 6. Generally, X2 is operated with a contoured nozzle at the end of the acceleration tube which steadily expands the state 7 gas to the nozzle exit condition (state 8). The test time begins when the state 8 gas arrives at the test model, and it generally ends either with the arrival of the downstream edge of the test gas unsteady expansion or the leading u+a wave reflected off the driver/test gas contact surface [215].

## 5.4 Simulating an Expansion Tube with PITOT

This section details how PITOT simulates the complete operation of an expansion tube using state-to-state processes. Readers interested in a fully analytical solution procedure for expansion tube flow processes are directed to Appendix A of Gildfind et al. [1] where the equations are explained in detail.

The facility configuration for an example high enthalpy expansion tube condition from the work of Fahy et al. [81] is shown in Table 5.1. The condition is a binary scaled air condition designed to match the 13:52:20UTC trajectory point of the Hayabusa entry at 1/5 scale. This

flow condition is used in this section to illustrate how the selection of certain parameters in the code can affect the test flow estimates which it provides.

Table 5.1: Details of the 1/5 scale Hayabusa 13:52:20UTC trajectory point condition designed by Fahy et al. [81].

Driver condition	X2-LWP-2.0 mm-100He-0
Primary driver fill condition	92.8 kPa He
Primary diaphragm	1 x 2 mm cold rolled thick steel, scored diaphragm
Orifice plate diameter	65 mm
Shock tube fill condition	13.5 kPa lab air
Secondary diaphragm	1 x $\approx$ 14 $\mu$ m thick aluminium foil diaphragm
Acceleration tube fill condition	17.0 Pa lab air

### 5.4.1 Driver Simulation

Before an experiment is run, the primary driver section is filled to the required fill condition, consisting of a set driver pressure and gas composition, which is assumed to be at nominally atmospheric temperature. Next, the reservoir is filled to the required pressure with compressed air. The current X2 free piston driver conditions were designed by Gildfind et al. using a 10.5 kg piston and an 80%He/20%Ar (by volume) driver gas [231, 230]. Details of the conditions can be found in that work.

When the piston is released, it compresses the driver gas to the rupture condition of the primary diaphragm (state 4). This can be simulated in PITOT in two different ways. The first method assumes an isentropic compression of the driver gas from its initial fill condition to its rupture condition. If either the volumetric compression ratio of the driver condition ( $\lambda$ ) or the primary diaphragm rupture pressure ( $p_4$ ) are known, then the temperature at primary diaphragm rupture ( $T_4$ ), and with it, the gas state (state 4) can be found:

$$\left(\frac{T_4}{T_{fill}}\right) = \left(\frac{p_4}{p_{fill}}\right)^{1-\frac{1}{\gamma}} = \left(\frac{1}{\lambda}\right)^{\gamma-1} \quad (5.1)$$

This method does not take into account heat and total pressure losses in the compression process, and as such, tuned empirical estimates of the driver rupture condition can be used instead, which are hard coded into PITOT as reference driver conditions. As an example of this, ‘effective’ driver gas properties from Gildfind et al. [2] in 2015 were calculated for X2-LWP-2mm-0 from experimental shock speeds through a helium test gas and are summarised in Table 5.2.

Table 5.2: State 4 values for X2-LWP-2mm-0 from Gildfind et al. in 2015 [2].

Driver case ID	Driver gas composition (by volume)	Orifice plate diameter mm	Rupture pressure ( $p_4$ ) MPa	Rupture temp. ( $T_4$ ) K
X2-LWP-2.0 mm-0	80%He/20%Ar	None	23.9	2,747
X2-LWP-2.0 mm-100He-0	100%He	65	27.4	2,903

It is assumed that the driver rupture condition is approximately stagnated ( $M_4 \approx 0$ ), and after the diaphragm has ruptured (see Fig. 5.2a), due to the tube area change, state 4 undergoes a steady expansion to a choked throat condition ( $M_{throat} = 1$ ) at state 4'', before undergoing an unsteady expansion into the driven sections downstream.

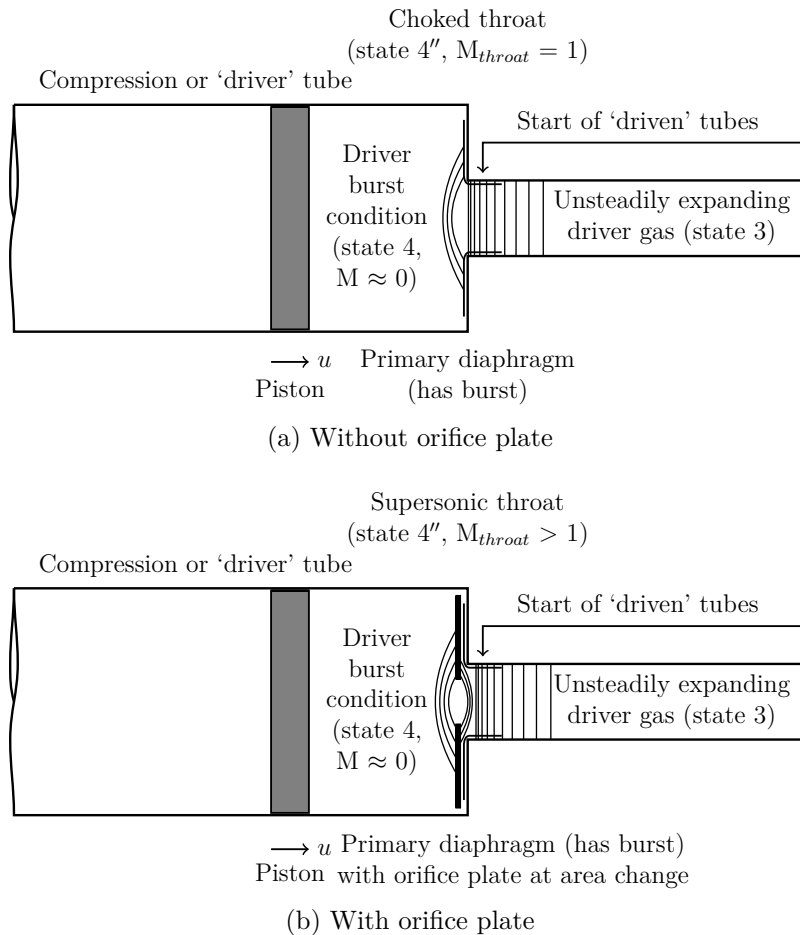


Figure 5.2: Driver after rupture representation. (Not to scale.)

Orifice plates are often used in X2 to introduce an additional contraction at the tunnel area change to allow existing driver conditions to be used with larger percentages of helium in the

driver gas than they were originally designed for. By sizing the orifice plate to maintain the choked volumetric flow rate out of the driver (i.e. preserving the  $u \cdot A$ , or in this case,  $a \cdot A^*$ , product) the piston dynamics can be preserved, while allowing the use of a higher sound speed driver gas. Generally, a choked throat is the most efficient driver configuration to use as the steady part of the expansion, which conserves total enthalpy and total pressure, is performed subsonically and the unsteady part of it, which reduces total enthalpy and total pressure in subsonic flow, but increases them in supersonic flow, is performed supersonically [196]. However, even though a higher sound speed driver gas used with an orifice plate undergoes a supersonic expansion into the driven tube, and therefore some of the available driver total pressure is lost, it will normally still drive a stronger shock than a choked throat condition with a lower sound speed. A further discussion of this, and a procedure for sizing the orifice plates, can be found in Gildfind et al. [2].

In PITOT, the orifice plate is simulated by performing a second steady expansion from the throat condition ( $M_{throat} = 1$ ) to a supersonic Mach number at state 4'' ( $M_{4''} > 1$ ), similar to how a de Laval nozzle would be modelled. (This is shown in Fig. 5.2b.)  $M_{4''}$  is found iteratively using the well-known Mach-area relation and the area ratio between the orifice plate ( $A^*$ ) and the driven tube ( $A_{driven}$ ):

$$\left(\frac{A_{driven}}{A^*}\right)^2 = \frac{1}{M_{4''}^2} \left[ \frac{2}{\gamma_D + 1} \left( 1 + \frac{\gamma_D - 1}{2} M_{4''}^2 \right) \right]^{\frac{\gamma_D + 1}{\gamma_D - 1}} \quad (5.2)$$

Starting from 2015, some X2 experiments have been performed without the free piston driver, instead using a small reservoir of room temperature helium as a ‘cold’ driver [87]. This can be simulated by manually setting state 4 ( $p_4$  and  $T_4$ ) to the cold driver rupture conditions. The authors used the methodology described in Gildfind et al. [2] to produce effective driver values for the cold driver, which are shown in Table 5.3. It should be noted that the sub-atmospheric rupture temperature ( $T_4$ ) values are not intended to be physical.

Table 5.3: Driver rupture conditions for two ‘cold driver’ conditions designed by Gu [87]. The rupture values ( $p_4$  and  $T_4$ ) were found by the authors.

Driver case ID	Driver gas composition (by volume)	Aluminium diaphragm thickness (mm)	Rupture pressure ( $p_4$ ) (MPa)	Rupture temp. ( $T_4$ ) (K)
Cold driver 1.8 MPa	100%He	0.5	1.8	169
Cold driver 2.2 MPa	100%He	0.6	2.2	169

While it is not relevant for X2, PITOT is also able to simulate a basic shock tube driver (i.e. no area change) by setting the throat Mach number to 0.

### 5.4.2 Secondary Driver Simulation

The unsteadily expanding driver gas (starting at state 4'' and unsteadily expanding to state sd3) drives a shock wave through the (typically) helium secondary driver gas (state sd1) processing it to state sd2. The speed of this shock ( $V_{s,sd}$ ) is dependent on both the fill condition in the secondary driver (state sd1) and the driver throat condition (state 4''), because it is the shock speed at which velocity and pressure are matched across the state sd3 / sd2 interface. This is shown in Fig. 5.3, where a partial facility schematic and position-time ('x-t') diagram centred around the secondary driver section can be seen.

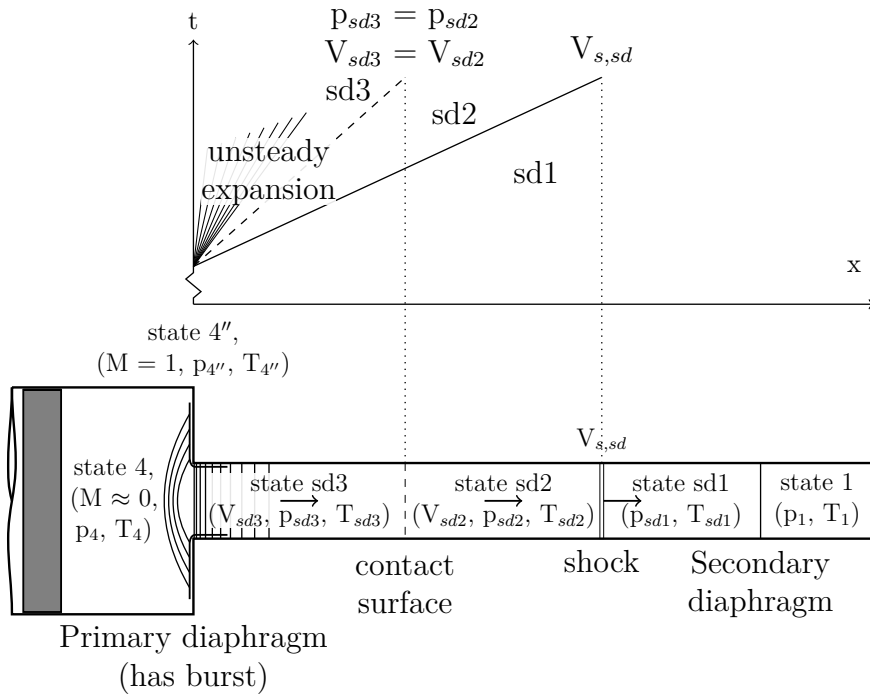


Figure 5.3: Secondary driver representation. (Not to scale.)

Generally, the secondary driver fill condition (state sd1) is set and PITOT uses an iterative secant solver to find the point at which  $V_{sd3} = V_{sd2}$  and  $p_{sd3} = p_{sd2}$ , and with it, the correct shock speed ( $V_{s,sd}$ ). This is done by guessing a  $V_{s,sd}$  value, finding the condition behind the shock wave (state sd2), and then expanding from the driver condition (state 4'') to the pressure behind the shock wave (i.e. making  $p_{sd3} = p_{sd2}$ ). If the correct shock speed has been guessed,  $V_{sd3}$  and  $V_{sd2}$  will be equal, and the secant solver set to find the zero of the function  $V_{sd3} - V_{sd2}$  will be satisfied, if not, a new guess for  $V_{s,sd}$  will be made, and the process is repeated until it converges.

A comprehensive study of expansion tube operation with a secondary driver can be found in Gildfind et al. [1].

### 5.4.3 Shock Tube Simulation

Either the unsteadily expanding driver gas (state 4'' unsteadily expanding to state 3) or the unsteadily expanding shock processed secondary driver gas (state sd2 unsteadily expanding to state 3) drive a shock wave through the test gas in the shock tube, processing it from state 1 to state 2. The speed of this shock ( $V_{s,1}$ ) is dependent on both the fill condition in the shock tube (state 1) and the condition of the driving gas (either state 4'' or state sd2). This is shown in Fig. 5.4, where two partial facility schematics (one with and one without a secondary driver section) and a position-time ('x-t') diagram centred around the shock tube can be seen.  $V_{s,1}$  is found in the same manner as  $V_{s,sd}$  was found in Section 5.3, except here the solution requires that  $V_3 = V_2$  and  $p_3 = p_2$ .

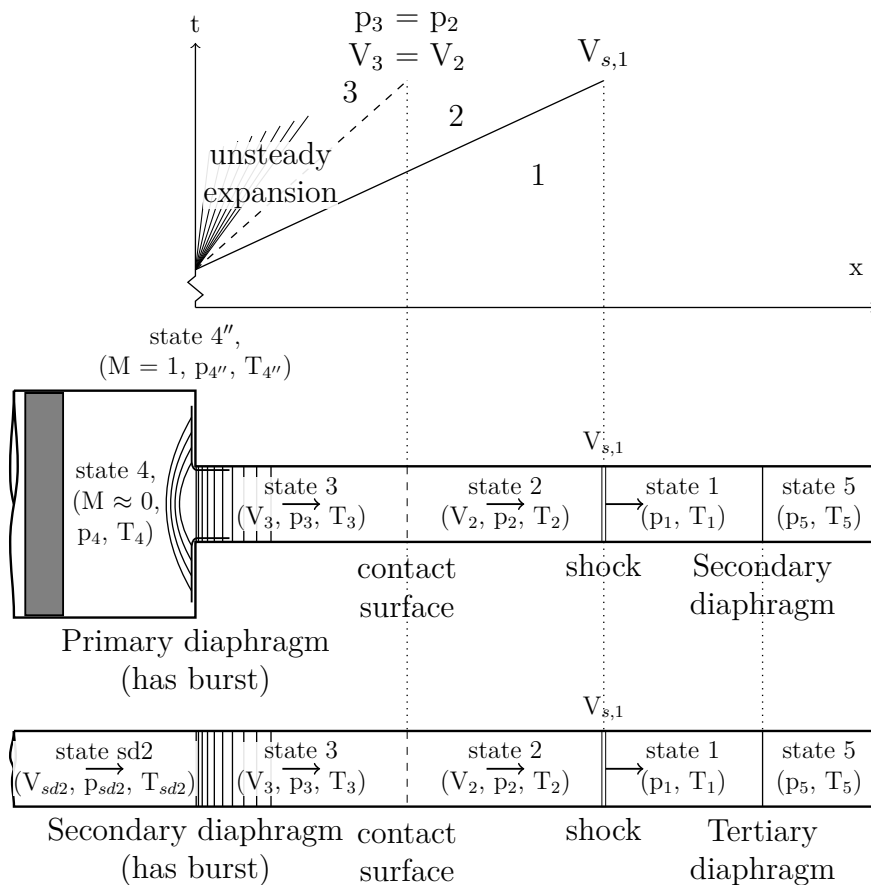


Figure 5.4: Shock tube representation. (Not to scale.)

As was discussed in the introduction, it should be noted that Paull and Stalker [215] found that if the sound speed of the shocked test gas ( $a_2$ ) was not sufficiently larger than the sound

speed of the expanded driver gas ( $a_3$ ), that flow disturbances originating in the driver were able to be transmitted into the test gas in the shock tube, potentially shortening or completely removing the steady test time. They did not provide a single recommendation for the increase required, instead stating that it grew with the frequency of the waves to be inhibited and decreased with increasing  $a_3$ . However, inspection of Figure 6 in their paper shows that an increase of at most 120% would be required to stop noise being transmitted in most situations. Users should keep this criterion in mind when designing test conditions. PITOT provides a summary of all gas states at the end of the calculation which can be used to check these values.

When very low density shock tube fill pressures are used, after the post-shock conditions have been found, a flag in the code can be used to artificially set the velocity of the shocked test gas ( $V_2$ ) to the shock speed in the shock tube ( $V_{s,1}$ ). This is done to help PITOT account for low density shock tube (or ‘Mirels’) effects [106, 107, 108] which are discussed further in Section 5.4.5.

#### 5.4.4 Secondary / Tertiary Diaphragm Modelling

Thin diaphragm modelling is an ever present problem for the simulation of expansion tubes. While a fully ideal expansion tube model assumes that the diaphragm effectively doesn’t exist, in certain cases the diaphragm’s inertia and its opening or ‘hold’ time have a non-trivial effect on the overall flow condition, and it cannot be ignored. Issues with diaphragm rupture and hold times are known contributors to situations where expansion tube flow conditions can differ from simple shock tube theory [255, 256, 257], and for this reason it is important to be able to simulate them.

The inertial diaphragm model [255, 258] shown in Fig. 5.5 treats the diaphragm as an obstacle that the shocked test gas (state 2) must accelerate, and it models the time dependent behaviour of the gas during this process. The inertial diaphragm model assumes that the diaphragm shears along its periphery as soon as the flow hits it and then it stays together as an obstacle in the flow-field. The model also assumes that the front of the gas slug which hits the diaphragm is fully stagnated by it, and that this twice shocked test gas (state 2r) then unsteadily expands from this state. The diaphragm then starts to accelerate into the tube in front of it, driving a shock in front of itself and acting as a ‘piston’ between the shocked gas in front of it (state 6) and the gas behind it which is unsteadily expanding after being processed by the reflected shock (state 7). As the diaphragm accelerates, the reflected shock behind the diaphragm gradually loses strength until it decays to a Mach wave ( $M_{2r} = 1$ ) and the effect of the diaphragm on the flow reaches a final steady state.

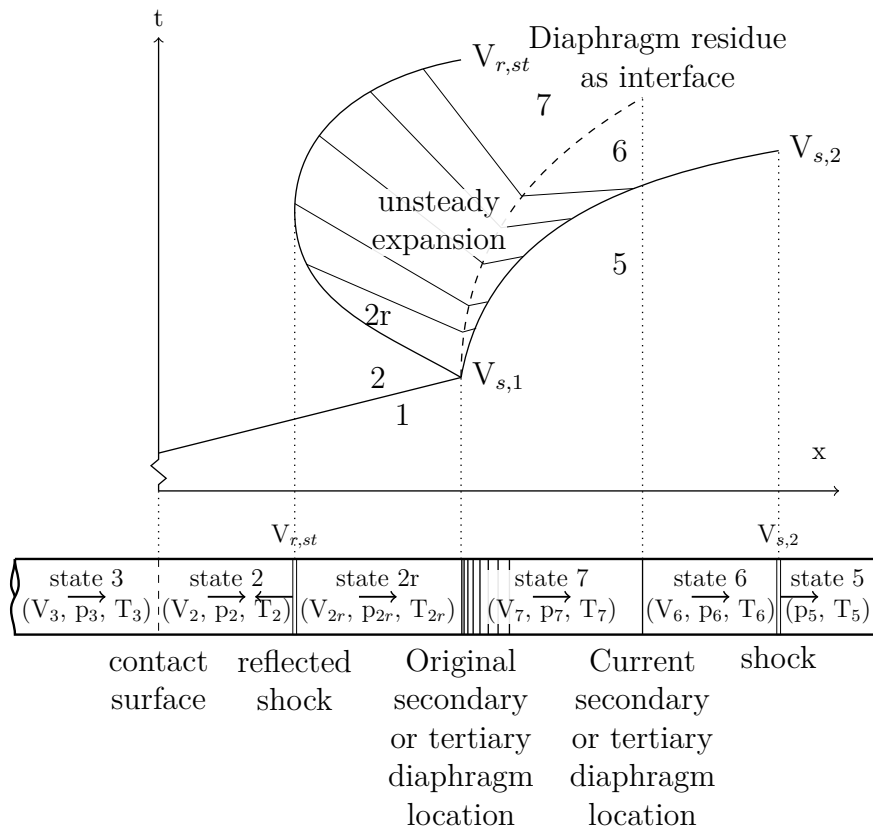


Figure 5.5: Partial shock and acceleration tube representation showing how an inertial diaphragm model simulates secondary or tertiary diaphragm rupture. (Not to scale.) Adapted from a theory and figure presented in Morgan and Stalker [255].

A study by Kendall et al. [256] in the X1 expansion tube compared experimental shock speed data around the secondary diaphragm to both Morgan and Stalker's [255] original inertial diaphragm model and a more sophisticated numerical inertial diaphragm model developed by Petrie-Repar [259]. Kendall et al. [256] found that Petrie-Repar's [259] model simulated the diaphragm rupture better than Morgan and Stalker's [255], but that good agreement between Petrie-Repar's [259] model and the experiment only lasted for 30  $\mu\text{s}$ . After this point, the two reflected shock trajectories started to diverge, and the experimental transmitted shock was faster than what was predicted by the inertial diaphragm model. Kendall et al. [256] stated that this meant that the inertial diaphragm model "*in its current form, is not complete*". It was suggested that the effect of the diaphragm on the test flow was lessened due to the diaphragm eventually vaporising. Petrie-Repar [259] investigated this numerically by simulating an initially curved diaphragm which then broke into a 7 or 14 pieces upon shock arrival at the diaphragm. Petrie-Repar's [259] 14 piece model gave "*good*" agreement with downstream experimentally measured pressure traces using what was called a "*heavy diaphragm*" (127  $\mu\text{m}$  thick), but shock arrival at that point occurred 65  $\mu\text{s}$  earlier than the experiment because the model did not



include viscous effects or a diaphragm hold time.

Wegener et al. [260] used holographic interferometry in X1 to optically investigate light diaphragm rupture. This was done by placing a light cellophane diaphragm at the end of the final driven section, turning X1 into a facility with a long shock tube, and then using the test section as an effective acceleration tube. It was found that upon rupture the initially curved diaphragm flattened, and after propagating a quarter of a tube diameter downstream, it began to fragment in the centre, gradually losing fragments as it travelled further downstream. Wegener et al. [260] found that the trajectory of the diaphragm and the gas interface were well approximated by the inertial diaphragm model for a short period of time after diaphragm rupture but that it gradually lost accuracy after the diaphragm had travelled half a tube diameter downstream from the rupture location. After this point, like Kendall et al. [256] had also observed, the interface began to accelerate more than the inertial diaphragm model predicted. Wegener et al. [260] stated that this was caused by the diaphragm losing mass as it fragmented. More recently, in 2007, Furakawa et al. [261] used the JX-1 expansion tube [216], which has a 50 mm driven section bore, to study thin secondary diaphragm rupture using both framing shadowgraph imaging of the diaphragm rupture process using a high speed camera and wall pressure measurements. The use of a section of acrylic tube which functioned as a set of aspherical lenses allowed the experiments to be performed in-situ in the facility. Three materials were tested: 23  $\mu\text{m}$  thick cellophane, and 3 and 25  $\mu\text{m}$  thick Mylar. Like what was found by Wegener et al. [260], the diaphragms could be seen travelling downstream after rupture and evidence of radiation from stagnated gas behind the diaphragm was seen for all but the 3  $\mu\text{m}$  thick Mylar. They concluded that the transmitted shock wave motion was influenced primarily by the diaphragm mass, and that only the 3  $\mu\text{m}$  thick Mylar diaphragm was shown to have almost negligible effect on the test flow.

Currently an inertial diaphragm model is not implemented in PITOT but some kind of inertial diaphragm model is planned as an upgrade to the code in the future to help model conditions which cannot be simulated well otherwise.

Another way to simulate thin diaphragm rupture is to use a hold time model, where it is assumed that when the shocked test gas (state 2) hits the diaphragm, the diaphragm remains closed for a set period of time, causing some of the gas to be processed by a reflected shock, before it opens fully and its effect is removed from the flow. While it was not called a ‘hold time’ model, this is the type of diaphragm model discussed by Haggard [262] in 1973, who stated that the effect of the mass of the secondary diaphragm could be modelled by a reflected shock at the diaphragm location. The hold time model has been used in several computational studies investigating the flow in an expansion tube [263, 258, 264] and comparing experimental results and the hold time model, Wilson [263] stated that *“Even with the very simple model*

for the opening time used in this work, the qualitative features of the disturbance compare well with the experiments”.

This type of diaphragm model (and the related hold time) can be easily implemented in the in-house one-dimensional facility simulation CFD code L1d3 [237, 238] with a simple flag in the input script. An example where different secondary diaphragm hold times (`dt_hold` in the code) have been used is shown in Fig. 5.6, using simulations of the scaled Hayabusa entry condition detailed in Table 5.1. The shock speeds in the shock and acceleration tubes are compared for hold times between 0 and 1,000  $\mu\text{s}$  to see the effect on the test flow. The nominal equilibrium solution from PITOT without a hold time model is also shown.

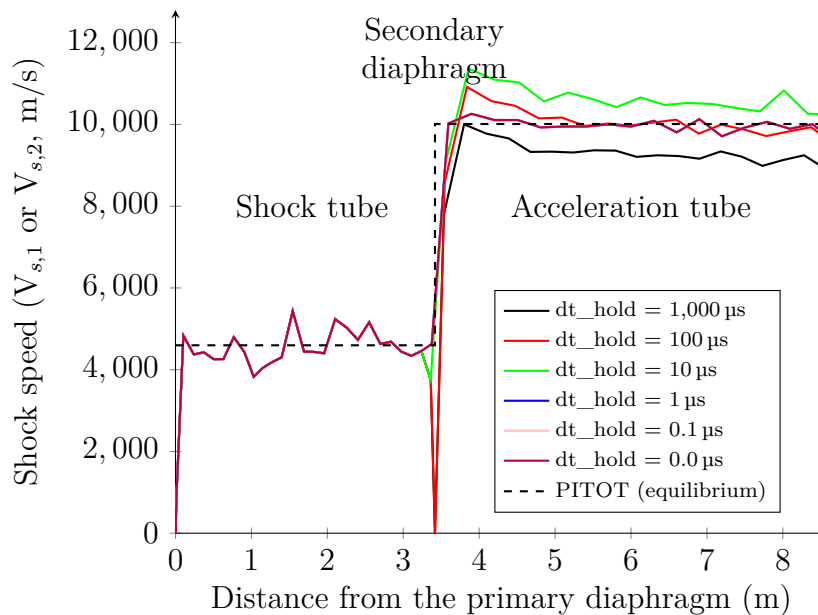


Figure 5.6: L1d3 [237, 238] one-dimensional CFD results showing how different diaphragm hold times (`dt_hold`) affect the shock speed of the test condition.

Firstly, looking at Fig. 5.6 it can be seen that without a hold time, PITOT simulates the expected shock speeds very well, both in the shock and acceleration tubes. It can also be seen that when the diaphragm hold time is below 1  $\mu\text{s}$ , no change in acceleration tube shock speed ( $V_{s,2}$ ) and no slow down of the shock speed at the secondary diaphragm is seen. With a hold time of 10  $\mu\text{s}$  a sustained increase in  $V_{s,2}$  is seen, as well as a small but noticeable slow down of the shock speed just before the secondary diaphragm. This increase in performance likely comes from the weak reflected shock off the diaphragm which was not able to fully stagnate the test gas and remove all of its kinetic energy. For the final two simulated hold times (100 and 1,000  $\mu\text{s}$ ) a fully reflected shock is seen at the secondary diaphragm, with the shock speed dropping to 0 m/s. With a hold time of 100  $\mu\text{s}$  a temporary increase in  $V_{s,2}$  is seen after diaphragm rupture, which decays to the nominal value by the time it reaches the end of the

tube. With a hold time of 1,000  $\mu\text{s}$ , directly after diaphragm rupture  $V_{s,2}$  is slower than the condition with no hold time, and it only continues slowing down.

For the simulation of conditions where it is believed that the diaphragm has a non-negligible effect on the flow, PITOT uses a time-independent hold time model where the effect of a diaphragm stopping the flow is modelled by a reflected shock. Like a normal hold time model, it cannot simulate the inertia of the diaphragm and it is only useful for simulating conditions where the diaphragm produces a measurable reflected shock in the test gas, but otherwise has a low inertial effect. What is shown in Fig. 5.8 below is similar to the condition with a hold time of 10  $\mu\text{s}$  in Fig. 5.6 where a sustained increase in acceleration tube shock speed ( $V_{s,2}$ ) is seen due to the shock reflection at the diaphragm. An experimental example discussed in Section 5.5.4 uses this diaphragm model to explain experimental results seen in the acceleration tube which would not otherwise be predicted.

This time-independent hold time model predicts and models the hold time as a reflected shock of specified strength. Using the shock tube as an example, state 2 is first found using the standard procedure outlined in Section 5.4.3 before it is processed by a reflected shock of specified Mach number ( $M_{r,st}$ ). The user can either choose to use the maximum Mach number, which will fully stagnate the state 2 gas, or a shock of user specified Mach number which will leave the gas with some residual velocity. This new reflected condition (labelled state 2r in the code), is then the gas which unsteadily expands downstream into the acceleration tube. This is shown in Fig. 5.7.

Fig. 5.8a shows the effect that  $M_{r,st}$  has on the shocked test gas (state 2), using the nominal equilibrium solution for the Hayabusa condition detailed in Table 5.1, and the 100% helium driver condition values shown in Table 5.2. All of the values in the figure have been normalised by the value of each variable when the reflected shock Mach number ( $M_{r,st}$ ) is equal to 1 (i.e. a reflected shock with no strength).

It can be seen in Fig. 5.8a that the flow variables most affected by the reflected shock are the pressure ( $p_{2r}$ ) and density ( $\rho_{2r}$ ), with maximum increases of around 1200% and 600% respectively, and the velocity ( $V_{2r}$ ) and Mach number ( $M_{2r}$ ), that both go to 0. The other flow variables show little variation. The stagnation enthalpy ( $H_{t,2r}$ ) shows an increase of 18% for a fully reflected shock, and the temperature ( $T_{2r}$ ) shows an increase of 61%.

The questions which arise from the discussion of this diaphragm model are: 1. what reflected shock Mach number should be chosen, and 2. how sensitive the resulting flow condition is to that choice. This is investigated in Fig. 5.8b by using the results from Fig. 5.8a as inputs to examine results further downstream. Test section conditions were found by expanding the shocked test gas (state 2r) results from Fig. 5.8a to the acceleration tube shock speed ( $V_{s,2}$ )

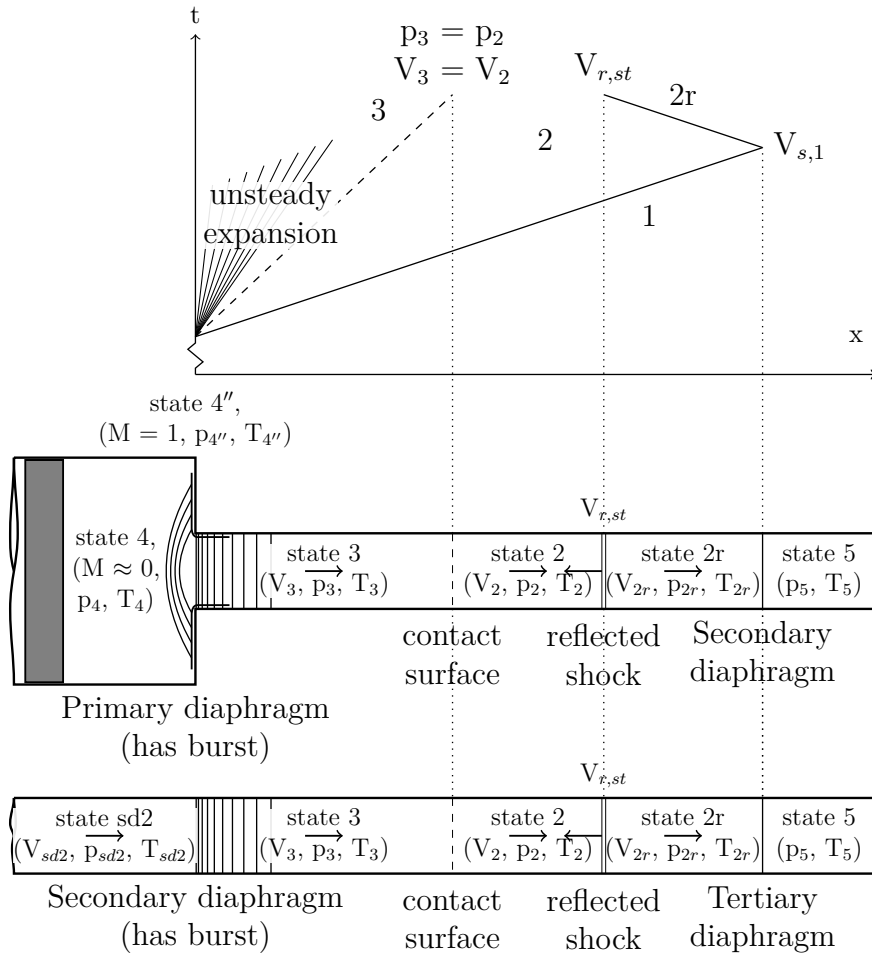


Figure 5.7: Shock tube representation with a reflected shock at the secondary or tertiary diaphragm. (Not to scale.)

and then steadily expanding them using the nozzle’s geometric area ratio of 5.64 [229]. Each variable has been normalised by the value when  $M_{r,st} = 1$ .

Examining Fig. 5.8b, the effect that the reflected shock Mach number has on various flow variables in the test section can be seen. The test section Mach number ( $M_8$ ), density ( $\rho_8$ ), and velocity ( $V_8$ ) are only affected slightly by the increasing reflected shock Mach number ( $M_{r,st}$ ) with maximum changes of -8%, -9%, and 5% respectively. The test section stagnation enthalpy ( $H_t$ ) is affected more with a maximum change of 14%, but the main changes are seen in the test section pressure ( $p_8$ ) and temperature ( $T_8$ ) with increases of 31% and 38% seen respectively.

To help predict if there is a hold time, PITOT is able to use facility length information and experimentally measured shock speeds to create ideal experimental x-t diagrams of facility test conditions. These ideal situations can then be compared to experimentally measured shock arrival times in the acceleration tube to roughly estimate experimental secondary diaphragm

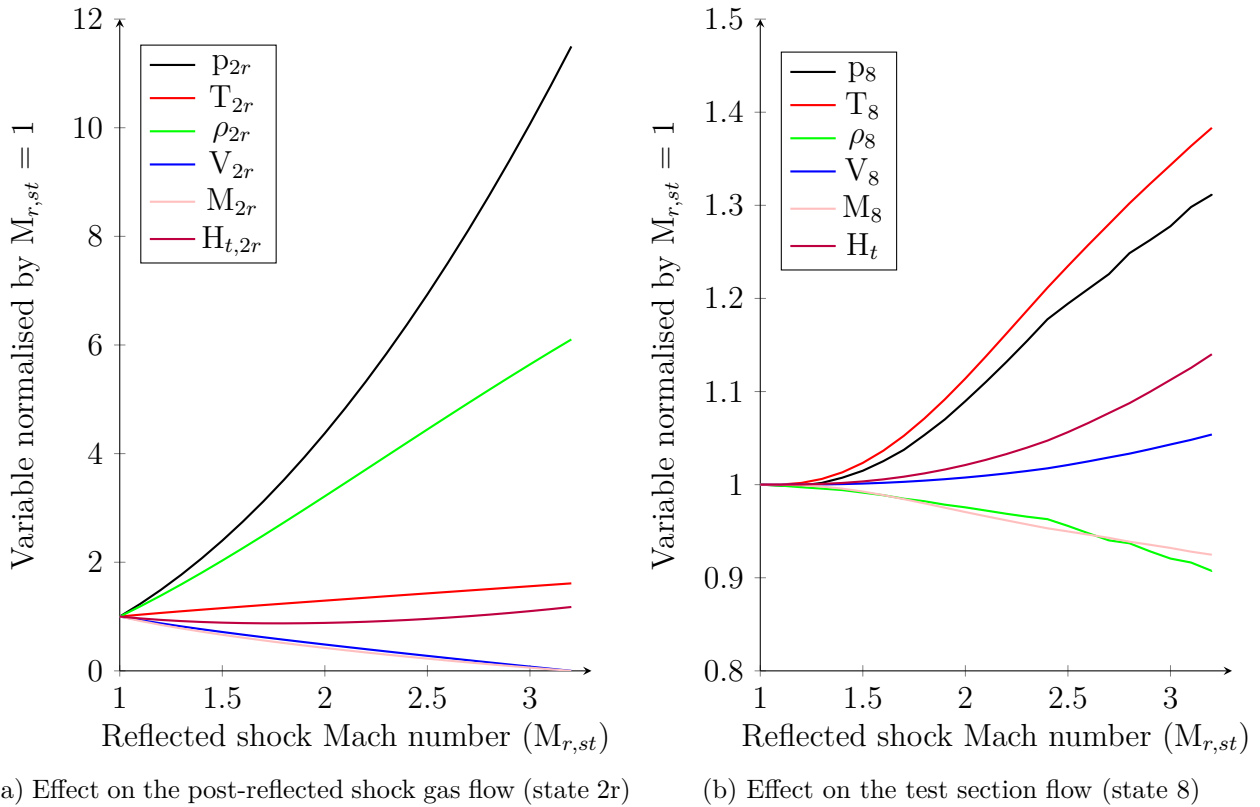


Figure 5.8: Effect of reflected shock Mach number ( $M_{r,st}$ ) on flow variables in the shock tube and test section for the nominal equilibrium solution for the Hayabusa condition detailed in Table 5.1. Values have been normalised by the value of each variable when  $M_{r,st} = 1$

hold times. For the two experimental examples presented in Section 5.5.4, both used the same aluminium secondary diaphragm, but they showed different behaviour in relation to the diaphragm. The first example, discussed in Section 5.5.4, was a low enthalpy test condition and was estimated to have an experimental hold time of around  $150 \mu\text{s}$ . It required a fully reflected shock to re-create the experimentally measured acceleration tube shock speeds. Whereas the second example, discussed in Section 5.5.4, was a much faster test condition which was found to have an experimental hold time of around  $30 \mu\text{s}$ . A reflected shock at the secondary diaphragm was not required for that condition.

### 5.4.5 Acceleration Tube Simulation

Initially, the acceleration tube conditions are found using the same process as the secondary driver and shock tube conditions discussed in Sections 5.4.2 and 5.4.3. The unsteadily expanding test gas (starting at state 2 and unsteadily expanding to state 7) drives a shock wave through the acceleration tube gas (state 5, generally lab air) processing it to state 6. The speed

of the shock ( $V_{s,2}$ ) is dependent on both the fill condition in the acceleration tube (state 5) and the condition of the shocked test gas (state 2), such that  $V_7 = V_6$ , and  $p_7 = p_6$ . This is shown in Fig. 5.9.  $V_{s,2}$  is found in the same manner as  $V_{s,sd}$  was found in Section 5.3, except here the solution requires that  $V_7 = V_6$  and  $p_7 = p_6$ .

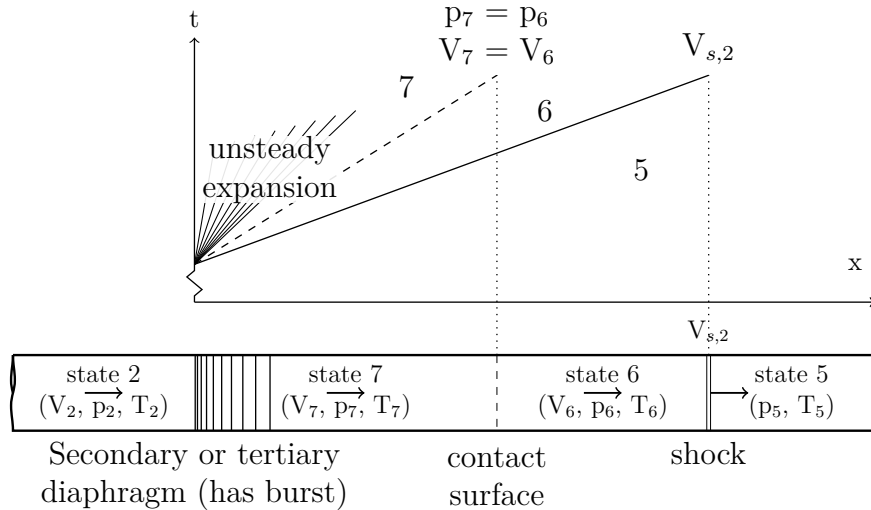


Figure 5.9: Acceleration tube representation without over-expansion. (Not to scale.)

However, due to the low density of the acceleration tube gas, generally low density shock tube boundary layer (or ‘Mirels’) effects [106, 107, 108] must be accounted for. Mirels proposed that these effects become significant below a 1 torr (133 Pa) fill pressure, and X2’s acceleration tube fill pressure ( $p_5$ ) is generally between 0.5 and 100 Pa. Mirels effects cause a further expansion of the test gas than would be expected from basic shock tube theory because as mass in the post-shock state (state 6) is lost to the boundary layer, the post-shock pressure ( $p_6$ ) drops, causing further expansion of the test gas (state 7) to re-equalise the pressure across the interface between the two gases. In the limiting case, the test gas expands to the shock speed ( $V_{s,2}$  in this case), and the interface between states 6 and 7 becomes stationary relative to the shock. This limiting case is shown in Fig. 5.10. It can be seen that Fig. 5.10 is very similar to the ideal case shown in Fig. 5.9, but that in Fig. 5.10 the contact surface is travelling at the same velocity as the shock wave. It should be noted that in both the ideal case (Fig. 5.9) and the limiting Mirels case (Fig. 5.10), pressure and velocity are both matched across the interface between state 7 and state 6, but each figure represents a *different* interface in terms of matched pressure and velocity, due to the over-expansion. In the limiting Mirels case shown in Fig. 5.10, the matched velocity would be faster than the ideal velocity shown in Fig. 5.9 and equal to the shock speed. Correspondingly, the matched pressure in Fig. 5.10 would be lower than the ideal matched pressure shown in Fig. 5.9.

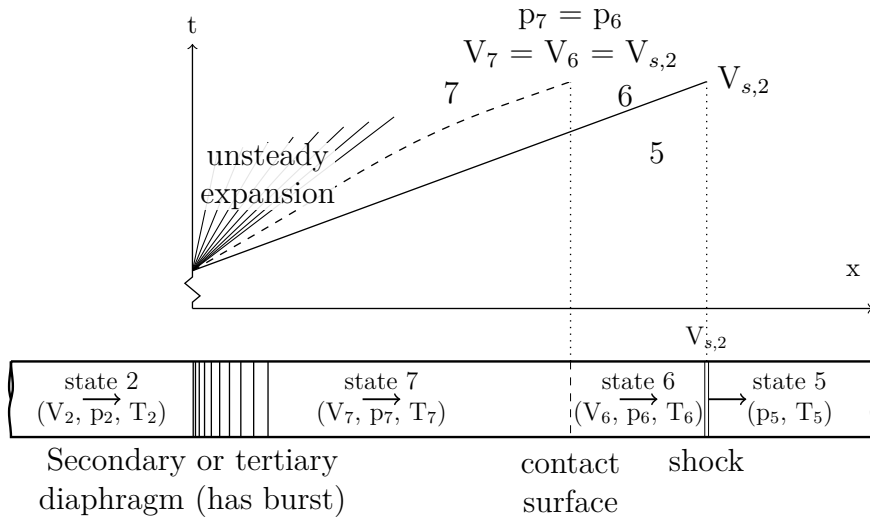


Figure 5.10: Acceleration tube representation with over-expansion. (Not to scale.)

PITOT currently does not directly apply the analytical methodology derived by Mirels [106, 107, 108] to account for this, but can instead practically account for the effect. It is common practice when estimating test gas conditions to assume Mirels’ limiting case, and to expand the test gas to  $V_{s,2}$  instead of  $V_6$ . The real solution should theoretically lie between these two limits, and can be tuned against experimental results. PITOT offers the choice between these two theoretical limits ( $V_7 = V_6$  and  $V_7 = V_{s,2}$ ) and when  $V_{s,2}$  is chosen, the ideal case is still solved using  $V_7 = V_6$  to find  $V_{s,2}$ , and then afterwards, the state 2 gas is unsteadily expanded to  $V_{s,2}$  instead of  $V_6$ .

It should be noted that these two limits can have a large effect on the related flow properties. Using the Hayabusa condition detailed in Table 5.1 the nominal theoretical solution predicts a shock tube shock speed ( $V_{s,1}$ ) of 4,597 m/s, and an acceleration tube shock speed ( $V_{s,2}$ ) of 10,011 m/s. Table 5.4 shows a comparison of the various flow properties at both the nozzle entrance (state 7) and exit (state 8, using the nozzle geometric area ratio of 5.64) when the shocked test gas (state 2) is expanded to  $V_6$  or  $V_{s,2}$ . The reference case was chosen to be the ideal condition (‘State 2 expanded to  $V_6$ ’).

It can be seen in Table 5.4 that there are large differences in variables between the two limits, and that in general, roughly the same level of percentage difference between the two conditions is carried from the nozzle inlet to the nozzle exit. Two very important quantities for performing scaled expansion tube experiments are the stagnation enthalpy ( $H_t$ ), a measure of the static and kinetic enthalpy of the test gas, and the density at the nozzle exit ( $\rho_8$ ). In Table 5.4 a +11.4% difference in stagnation enthalpy ( $H_t$ ) can be seen between the two limits, and a -47.4% change in nozzle exit density ( $\rho_8$ ). These are not trivial changes, and for the theoretical model’s results

Table 5.4: Comparison between expansion of the shocked test gas (state 2 which expands to state 7) to the gas velocity behind the shock ( $V_6$ ) or the acceleration tube shock speed ( $V_{s,2}$ ) for the nominal equilibrium solution for the Hayabusa condition detailed in Table 5.1. (While it is noted that the column selected as the reference for the percentage change calculations is arbitrary, it has been chosen to use ‘State 2 expanded to  $V_6$ ’ as the reference.)

	State 2 expanded to $V_6$ (9,384 m/s)	State 2 expanded to $V_{s,2}$ (10,010 m/s)	Percentage change (%)
State 7 (nozzle entry condition)			
Static pressure ( $p_7$ , Pa)	18,426	8,721	-52.7
Static temperature ( $T_7$ , K)	2,901	2,659	-8.34
Density ( $\rho_7$ , kg/m <sup>3</sup> )	$2.13 \times 10^{-2}$	$1.12 \times 10^{-2}$	-47.6
Velocity ( $V_7$ , m/s)	9,384	10,010	6.67
Mach number ( $M_7$ )	9.39	10.5	11.9
Stagnation enthalpy ( $H_t$ , MJ/kg)	47.9	53.4	11.4
State 8 (nozzle exit condition, using an area ratio of 5.64)			
Static pressure ( $p_8$ , Pa)	2,370	1,069	-54.9
Static temperature ( $T_8$ , K)	2,213	1,904	-13.9
Density ( $\rho_8$ , kg/m <sup>3</sup> )	$3.72 \times 10^{-3}$	$1.95 \times 10^{-3}$	-47.4
Velocity ( $V_8$ , m/s)	9,547	10,149	6.31
Mach number ( $M_8$ )	10.9	12.2	12.4
Stagnation enthalpy ( $H_t$ , MJ/kg)	47.9	53.4	11.4

to be most useful, it is important to calibrate PITOT against experimental measurements to ascertain how much the gas has expanded in the acceleration tube.

Sometimes chemical freezing is an issue in acceleration tubes due to how fast the gas expands and cools in the tube versus the time scales which may be required for the gas to chemically recombine [258]. For this reason, if necessary, PITOT also has the ability to freeze the chemistry of the shocked test gas (state 2) as it unsteadily expands to state 7 in the acceleration tube.

### 5.4.6 Nozzle Simulation

Generally, a contoured nozzle is used at the end of X2’s acceleration tube to increase the model sizes which can be tested in the facility, increase the flow Mach number, and increase the available test time. When a nozzle is used, it is simulated in PITOT by performing a steady expansion through a known area ratio to process the test gas from its state at the nozzle entrance (state 7, shown in Fig. 5.11a) to its state at the nozzle exit (state 8, shown in Fig. 5.11b). Generally, the geometric exit-to-inlet area ratio of 5.64 of X2’s contoured Mach 10



nozzle<sup>1</sup> [229] is used for PITOT calculations, but it does not always represent the true state of expansion of the core flow. Unlike a reflected shock tunnel where the test gas is stagnated before being expanded through a de Laval nozzle, an expansion tube nozzle is fully supersonic, and the gas flowing through the nozzle has an associated boundary layer which has developed through the acceleration tube, and which continues to grow through the nozzle. This is shown in Fig. 5.12. This boundary layer growth is something which is very hard to accurately measure in an operational expansion tube facility.

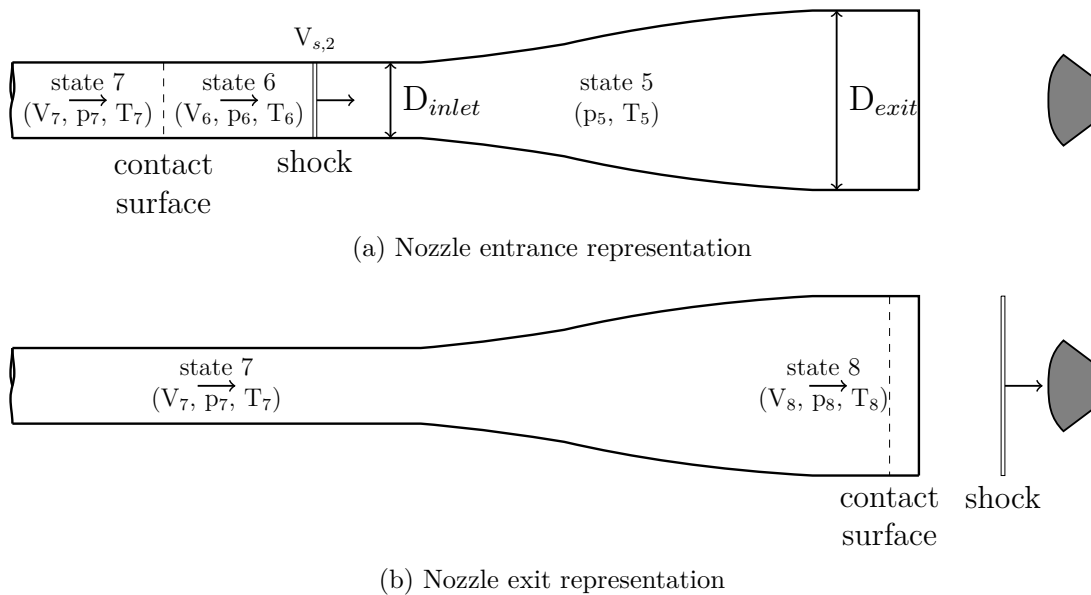


Figure 5.11: X2 nozzle representation, with the shock wave entering and exiting the nozzle. (Not to scale.)

As shown in Fig. 5.12, this changing boundary layer can be modelled with an ‘effective’ area ratio which accounts for the effect of the boundary layer profile on the steady expansion. Generally, a comparison between wall pressure traces before the nozzle entrance and impact pressure probe traces at the nozzle exit are used to establish the effective area ratio of the nozzle for a given operating condition. To aid this analysis, and to help understand the effect that changes in effective area ratio can have on the resultant flow in the test section, PITOT has an ‘area ratio check’ mode which lets the user specify a list of area ratios which are then analysed at the end of the analysis for a set nozzle inlet (state 7) condition.

In Fig. 5.13, a sample result using the Hayabusa condition from Table 5.1 for the nominal equilibrium condition can be seen. The test gas has been unsteadily expanded to the shock speed in the acceleration tube ( $V_{s,2} = 10,011$  m/s, see Section 5.4.5) and then steadily expanded

<sup>1</sup>The nozzle was designed by Scott [229] for an inlet Mach number of 7.2 and an exit Mach number of 10, but usage by the authors and their colleagues have shown it to work well for a wide range of different entry conditions.

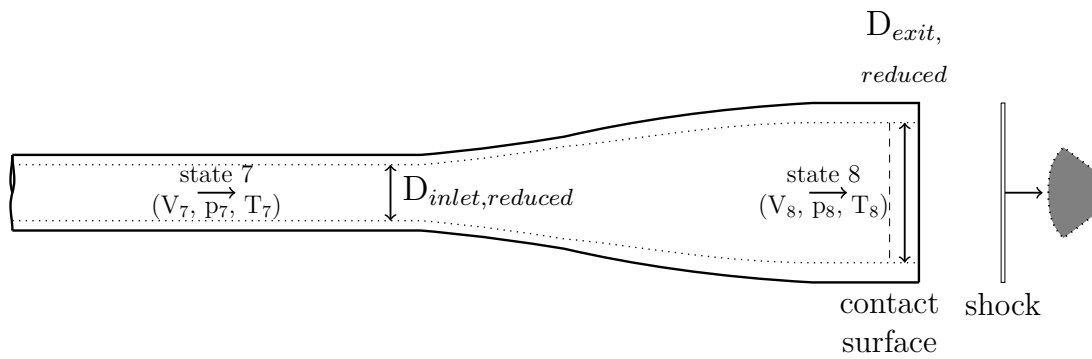


Figure 5.12: Nozzle exit representation showing an example of the boundary layer. (Not to scale.)

using area ratios from 2.0 to 9.0, in increments of 0.1, covering a range on either side of the nozzle's geometric area ratio of 5.64 [229]. The results have then been normalised by the results for the nozzle geometric area ratio of 5.64.

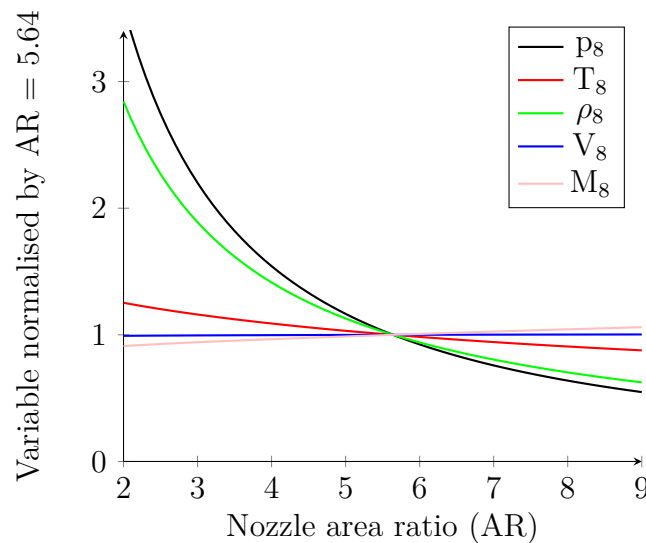


Figure 5.13: Effect of changing nozzle area ratio on flow variables at the nozzle exit (state 8) for the nominal solution for the Hayabusa condition detailed in Table 5.1.

Examining Fig. 5.13, and considering what occurs when the area ratio increases *above* the geometric area ratio, there are only small changes in nozzle exit velocity ( $V_8$ , a 0.4% maximum increase), nozzle exit Mach number ( $M_8$ , a 4% maximum increase), and nozzle exit temperature ( $T_8$ , a 10% maximum decrease) over the full range shown. However, the other two state variables, the nozzle exit density ( $\rho_8$ ) and pressure ( $p_8$ ) show much larger changes, with the variables decreasing by 38% and 44% respectively.

Now examining Fig. 5.13, and considering what occurs when the area ratio drops *below* the

geometric area ratio, there are only small changes in nozzle exit velocity ( $V_8$ , a maximum 1% decrease), nozzle exit Mach number ( $M_8$ , a maximum 8% decrease), and nozzle exit temperature ( $T_8$ , a 19% increase) over the full range shown. However, once again the other two state variables, the nozzle exit density ( $\rho_8$ ) and pressure ( $p_8$ ) show much larger changes, with increases of 284% and 345%.

Overall, Fig. 5.13 shows that the nozzle exit velocity ( $V_8$ ), Mach number ( $M_8$ ), and temperature ( $T_8$ ) are not sensitive to changes in the nozzle area ratio. However, the nozzle exit density ( $\rho_8$ ) and pressure ( $p_8$ ) are very sensitive to it for area ratios below the geometric one.

In addition to its effect in the acceleration tube (see Section 5.4.5), in some situations chemical freezing can also occur in expansion tube nozzles due to how fast the gas expands and cools in relation to the time scales required for chemical recombination. For this reason, if necessary, PITOT has the ability to freeze the chemistry of the steady expansion from state 7 to state 8.

### 5.4.7 Simulation of Various Basic Test Models

Many different types of test models are used in the X2 expansion tube, and PITOT has a series of modes which allow it to estimate the flow properties over these models. For the simulation of the stagnation streamline of blunt body models (see Fig. 5.14) or Pitot pressure probes in the test section, PITOT has the functionality to allow it to calculate conditions behind a normal shock in the test section for both frozen and equilibrium flow.

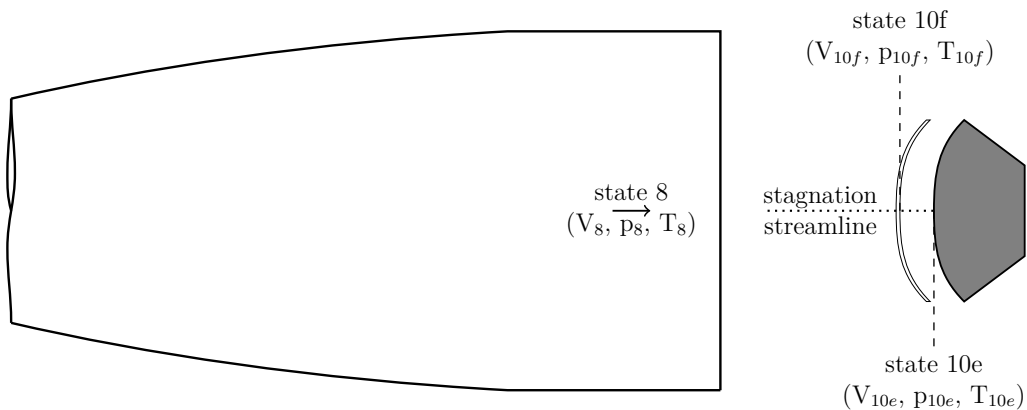


Figure 5.14: Representation of flow over a blunt body test model. (Not to scale.)

To protect the pressure transducers used in the test section from the high pressure driver gas and debris which follows the test gas down the tube, 15° half-angle conical pressure probes are often used instead of blunt Pitot pressure probes in UQ's expansion tubes, and PITOT has

the functionality to solve the Taylor-Maccoll conical flow equations [265, 266] to find the conical shock angle ( $\beta$ ) and surface gas state for a specified cone half-angle ( $\theta$ ) in the test section.

Both symmetric and asymmetric wedge models are common test models in UQ's expansion tubes, and PITOT has the functionality to find the shock angle ( $\beta$ ) and the post-shock gas state for a wedge model of specified wedge angle ( $\theta$ ) in the test section.

While Fig. 5.14 includes the contoured nozzle generally used at the end of the X2 expansion tube, PITOT can also simulate the same test models without a nozzle (state 8 in Fig. 5.14 would become state 7).

## 5.5 Quantifying Experimental Data using PITOT

For the purpose of analysing experimental data, PITOT has several experimental test modes which make use of experimentally measured shock speeds to perform parts of the analysis, effectively 'calibrating' the analysis by removing potential errors in the theoretical modelling of different sections of the facility. PITOT can be run in a fully experimental mode where all shock speeds are taken directly from experimental data, or a partially experimental mode where either the shock tube or acceleration tube shock speeds ( $V_{s,1}$  and  $V_{s,2}$ ) are taken from experimental data, and the remaining calculations are performed theoretically. How these modes function is discussed in this section.

### 5.5.1 Experimental Calibration of the Shock Tube

In Section 5.4.3, the shock tube shock speed ( $V_{s,1}$ ) was computed based on the shock tube fill condition (state 1) and the driver condition which is unsteadily expanding into the shock tube (either state 4'' or state sd2, both of which will unsteadily expand to state 3), by finding the point where  $p_3 = p_2$  and  $V_3 = V_2$ . While state 1 is experimentally well defined, the condition of the unsteadily expanding driver gas depends on the estimated driver rupture condition (state 4). While the state 4 estimate may be sufficient to perform reasonably accurate parametric studies of the facility, it may not be accurate enough for the rebuilding of an experiment. By shocking the state 1 gas with an experimentally measured  $V_{s,1}$  value instead of a value computed from state 4, driver modelling errors are largely removed from the flow calculation. Experimental uncertainty associated with the shock speed measurement and the shock tube fill condition are introduced to the calculation, but are usually much smaller and can be easily taken into account.

### 5.5.2 Experimental Calibration of the Acceleration Tube

In Section 5.4.5, the acceleration tube shock speed ( $V_{s,2}$ ) was computed based on the acceleration tube fill condition (state 5) and the condition of the shocked test gas which is unsteadily expanding into the acceleration tube (state 2 which will unsteadily expand to state 7), by finding the point where  $p_6 = p_7$  and  $V_6 = V_7$ . In most situations, after  $V_{s,2}$  has been found, the shocked test gas (state 2) is then ‘over-expanded’ to  $V_{s,2}$  to find state 7, simulating the limiting case of the Mirels effect for a low density shock tube [106, 107, 108]. Practically, there are some issues with this.

Firstly, by its nature the acceleration tube is a low density shock tube, and for some conditions with low acceleration fill pressures ( $p_5$ ),  $V_{s,2}$  can be very sensitive to small changes in  $p_5$ , and even small errors in state 5 can have a significant effect on the unsteadily expanded test gas (state 7). If  $V_{s,2}$  or the unsteadily expanded test gas pressure ( $p_7$ ) are known experimentally, state 2 can be expanded to either of these values, removing  $p_5$  from the calculation. Additional experimental uncertainty is added to the calculation, but by simulating the bounds of these inputs, the correct solution can be bounded, in a way which is independent of state 5. If the gas has in fact reached the limiting Mirels case where the unsteadily expanded test gas (state 7) has expanded to the shock speed, measurements of  $V_{s,2}$  and  $p_7$  can be used to verify this. If the pressure is greater than the limiting Mirels case, this can be used to ascertain the degree of expansion which has occurred.

Secondly, there is the issue of modelling the weak secondary or tertiary diaphragm separating the shock and acceleration tubes (see Section 5.4.4). While PITOT is able to simulate a reflected shock wave of user-specified strength at the end of the shock tube as a type of diaphragm hold time model, it is a limited model, and the effect of the diaphragm is generally assumed to be small. This may not be true, and must be kept in mind when assessing simulation results.

### 5.5.3 Experimental Calibration of the Nozzle

As was discussed in Section 5.4.6, due to the fact that an expansion tube flow is never stagnated, significant boundary layers can build up in the acceleration tube and nozzle. The boundary layer profile through the nozzle is a large source of experimental uncertainty, and it can cause the nozzle to behave as if it has a different area ratio than its geometric value (see Figs. 5.11 and 5.13). As was shown in Fig. 5.13, different nozzle area ratios can have a large effect on the nozzle exit density and pressure ( $\rho_8$  and  $p_8$ ).

During the testing of new flow conditions in X2, a pitot rake model is installed at the nozzle exit, where nine impact pressure probes (either Pitot or 15° half-angle conical probes) are

spaced 17.5 mm apart radially relative to the nozzle exit plane, covering a total centre-to-centre height of 140 mm. The middle probe ('pt5') is generally oriented with the centre-line of the nozzle. These pitot rake tests are used to measure the size of the core flow of test conditions, estimate steady test time, and to provide additional diagnostics to ascertain the gas state in the test section (state 8).

While it would be very useful to have measurements of the other state variables, by their nature, high enthalpy shock tunnel facilities are powered by driver gas which follows the test gas down the tube and whose high pressure and temperature can damage sensitive instrumentation. This makes it difficult to measure state variables other than pressure, and often other state variables must be inferred from changes in the flow pressure. If the condition of the unsteadily expanded test gas entering the nozzle (state 7) is known with a reasonable amount of accuracy from experimental measurements of  $V_{s,2}$  and the unsteadily expanded test gas pressure ( $p_7$ ), and if the impact pressure at the nozzle exit has been experimentally measured, PITOT's 'area ratio check' mode can be used to find the 'effective' nozzle area ratio which is consistent with both of these results. Once this effective area ratio is known, the related nozzle exit state (state 8) can then be found. Once again, this is affected by any uncertainties in the measured quantities, but the bounds of the real solution can be found.

#### 5.5.4 Examples

Now that experimental calibration has been discussed, two different examples will be presented.

The first example is a 'cold driver' air example from the work of Gu [87], using two experiments performed by the authors and Gu. The example was chosen since its low velocity nature should remove some of the high temperature effects normally present in an expansion tube facility, making it a condition which should be well suited to simulation using PITOT.

The second example is a regular X2 free piston driven air test condition that was originally designed by Zander et al. [90] and has since been used by Lewis et al. [91, 3, 7]. It was chosen because it is a condition which has been used for several years now, and because new pitot rake data was available for the condition from August 2016, which incorporated some upgraded diagnostics. Upgrades included replacing the static pressure mounts along the length of X2's acceleration tube with new vibrationally isolated ones. An extra two sensors ('at7' and 'at8') were also added to the end of the acceleration tube to give two pressure measurements just before the entrance to the nozzle. The majority of the 'at' labelled pressure sensors (all except 'at1') are now recorded both in the main data acquisition system at 2.5 MHz, and in a separate system at 60 MHz, lowering the sampling rate error on the shock speed calculations by an order of magnitude. The effect of the upgrades can be seen when comparing Table 5.6

in Section 5.5.4, with experimental data taken before the upgrades, to Tables 5.9 and 5.10 in Section 5.5.4, whose experimental data was taken after the upgrades. Pressures and shock speeds down the whole length of X2's acceleration tube are shown in Tables 5.9 and 5.10, whereas only values from the end of the acceleration tube are shown in Table 5.6.

The experimental shock speed naming convention for the two examples (i.e. 'sd1-sd3') is a reference to the two specific wall pressure sensor locations used to find that particular shock speed value, and where experimental shock speeds are shown in figures in this subsection (i.e. Figs. 5.15, 5.16, and 5.20), the values are shown at the midpoint between the two sensor locations. Where experimental pressure measurements are shown in Tables 5.6 and 5.10, the names either correspond to wall pressure sensor locations or the locations of pressure sensors in the X2 pitot rake. (Approximate X2 wall pressure sensor locations are shown in Fig. 5.1 and exact values can be found in Gildfind et al. [232].)

The experimental shock speed uncertainties shown in Tables 5.6 and 5.9 were found using the standard shock speed uncertainty calculation procedure described in Appendix G. The experimental pressure measurements shown in Tables 5.6 and 5.10 were found by filtering the data with a 6th order lowpass filter with a cutoff frequency of 100 kHz, taking the mean of the steady pressure time for the relevant signal, and then removing the mean of the noise taken just before shock arrival. The uncertainties on the pressure measurements were found using a 95% confidence interval on the standard deviation of the experimental data. This implies that 95% of the distribution of the experimental data sits within the uncertainty of the mean value. Mean uncertainties shown in the tables were calculated using the root sum squared method. Where experimentally measured pressure signals are shown in figures (i.e. Figs. 5.17, 5.18, 5.19, 5.21, and 5.22) they have been filtered using a 6th order lowpass filter with a cut off frequency of 100 kHz, with the unfiltered data shown behind it using a lower opacity.

### Example 1: Cold Driver Condition

The fill details of the 'cold driver' air example are shown in Table 5.5. The experimentally measured shock speeds, and wall transducer and pitot rake 15° half-angle cone pressure measurements for two experiments, x2s2902 and x2s2903, are shown in Table 5.6.

In Fig. 5.15 the experimental shock tube shock speed ( $V_{s,1}$ ) values shown in Table 5.6 for the two experiments are compared to the theoretical equilibrium shock speed value from PITOT when effective 'cold driver' values from Table 5.3 are used. It can be seen that the two experiments, x2s2902 and x2s2903, are statistically consistent with each other, with the first two shock speed measurements for each experiment having overlapping uncertainties, and the final measurement being almost the same. However, the theoretical result from PITOT

Table 5.5: Facility configuration details for the ‘cold driver’ air test condition used by the authors and Gu [267].

Driver condition	Cold helium driver
Primary driver fill condition	1.8 MPa He
Primary diaphragm	1 x 0.5 mm thick 5000 series aluminium sheet
Shock tube fill condition	900 Pa lab air
Secondary diaphragm	1 x $\approx$ 14 $\mu$ m thick aluminium foil diaphragm
Acceleration tube fill condition	40.0 Pa lab air

Table 5.6: Experimentally measured quantities from the two experiments performed by the authors and Gu [267]. Analysis was performed by the authors.

	x2s2902	x2s2903
Shock tube shock speeds ( $V_{s,1}$ )		
sd1-sd3 (m/s)	2,050 $\pm$ 10 (0.7%)	2,040 $\pm$ 10 (0.6%)
sd1-sd2 (m/s)	2,070 $\pm$ 30 (1.3%)	2,050 $\pm$ 30 (1.3%)
sd2-sd3 (m/s)	2,040 $\pm$ 30 (1.3%)	2,040 $\pm$ 30 (1.3%)
Mean value (m/s)	2,050 $\pm$ 10 (0.7%)	2,040 $\pm$ 10 (0.6%)
Acceleration tube shock speeds ( $V_{s,2}$ )		
at4-at6 (m/s)	3,660 $\pm$ 20 (0.7%)	3,690 $\pm$ 20 (0.7%)
at4-at5 (m/s)	3,700 $\pm$ 50 (1.3%)	3,720 $\pm$ 50 (1.3%)
at5-at6 (m/s)	3,610 $\pm$ 50 (1.3%)	3,650 $\pm$ 50 (1.3%)
Mean value (m/s)	3,660 $\pm$ 20 (0.7%)	3,690 $\pm$ 30 (0.7%)
Acceleration tube wall pressure traces ( $p_7$ )		
at4 (kPa)	3.5 $\pm$ 0.2 (5.2%)	3.3 $\pm$ 0.3 (8.1%)
at5 (kPa)	3.4 $\pm$ 0.3 (8.8%)	3.2 $\pm$ 0.3 (10%)
at6 (kPa)	3.1 $\pm$ 0.3 (9.7%)	3.1 $\pm$ 0.4 (13%)
Mean value (kPa)	3.3 $\pm$ 0.2 (4.6%)	3.2 $\pm$ 0.2 (6.0%)
Test section 15° half-angle cone pressure traces ( $p_{10c}$ )		
pt1 (kPa)	1.1 $\pm$ 0.3 (27%)	1.3 $\pm$ 0.5 (36%)
pt2 (kPa)	1.6 $\pm$ 0.5 (30%)	1.6 $\pm$ 0.4 (27%)
pt3 (kPa)	1.5 $\pm$ 1.6 (105%)	1.5 $\pm$ 1.9 (132%)
pt7 (kPa)	1.7 $\pm$ 0.4 (24%)	1.8 $\pm$ 0.5 (27%)
pt8 (kPa)	1.4 $\pm$ 0.3 (20%)	1.4 $\pm$ 0.3 (19%)
pt9 (kPa)	1.2 $\pm$ 1.1 (94%)	1.3 $\pm$ 0.9 (68%)
Mean value (kPa)	1.4 $\pm$ 0.4 (24%)	1.5 $\pm$ 0.4 (26%)

underestimates the experimental shock speeds by around 5%. As was discussed in Section 5.5.1, this error can be removed by not using the driver model in the calculation and instead specifying an experimentally measured  $V_{s,1}$  value. For the theoretical acceleration tube calculations shown in Figs. 5.16 and 5.17, an average  $V_{s,1}$  value of 2,050 m/s has been used instead of the driver model.



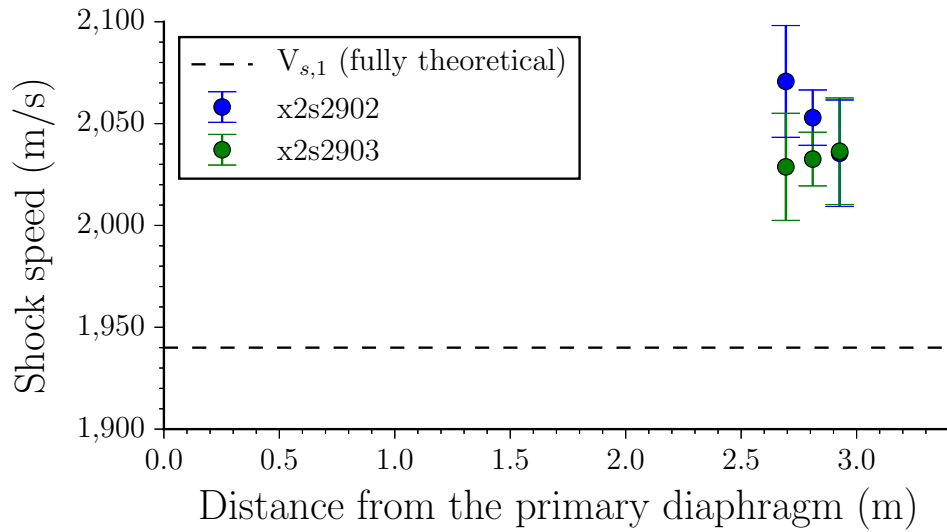


Figure 5.15: Experimentally measured shock tube shock speeds ( $V_{s,1}$ ) from Table 5.6 compared to the theoretical equilibrium result from PITOT.

In Fig. 5.16 the experimental acceleration tube shock speed ( $V_{s,2}$ ) values shown in Table 5.6 are compared to various theoretical equilibrium shock speed estimates from PITOT when the experimental shock tube fill condition (state 1) has been shocked by a specified average  $V_{s,1}$  value of 2,050 m/s. On the legend in Fig. 5.16 it can be seen that for some of the simulations, the velocity of the shocked test gas ( $V_2$ ) has been set to the shock tube shock speed ( $V_{s,1}$ ), and a reflected shock has been used at the end of the shock tube ( $M_{r,st} > 1$ ). These settings have been used to simulate the use of a low density shock tube and a secondary diaphragm which produces a measurable reflected shock in the already shocked test gas (state 2), but otherwise has a low inertial effect. These modes are discussed in Sections 5.4.3 and 5.4.4.

In Fig. 5.16, for the simulation where the shocked test gas velocity ( $V_2$ ) has not been changed and the reflected shock has not been used ( $M_{r,st} = 1$ ),  $V_{s,2}$  is underestimated by around 10%. This shows that it is not possible to simulate this condition closely with PITOT without using some kind of non-ideal model for either the low density shock tube or the secondary diaphragm (or both). By using the non-ideal shock tube model and making  $V_2 = V_{s,1}$  the discrepancy can be reduced to around 4%. By using only a full reflected shock at the end of the shock tube ( $M_{r,st} = \text{maximum} = 2.9$ ), the discrepancy can be reduced to around 7%. This shows that the discrepancy can only be reduced further by making  $V_2 = V_{s,1}$  and using a reflected shock at the end of the shock tube ( $M_{r,st} > 1$ ). The final three lines on the figure show the theoretical shock speeds with both non-ideal models and differing reflected shock Mach numbers ( $M_{r,st}$ ). It can be seen that each reflected shock Mach number value ( $M_{r,st} = 2.0, 2.4$ , and the maximum of 2.9) falls inside the range of some of the experimental measurements, but it is not obvious

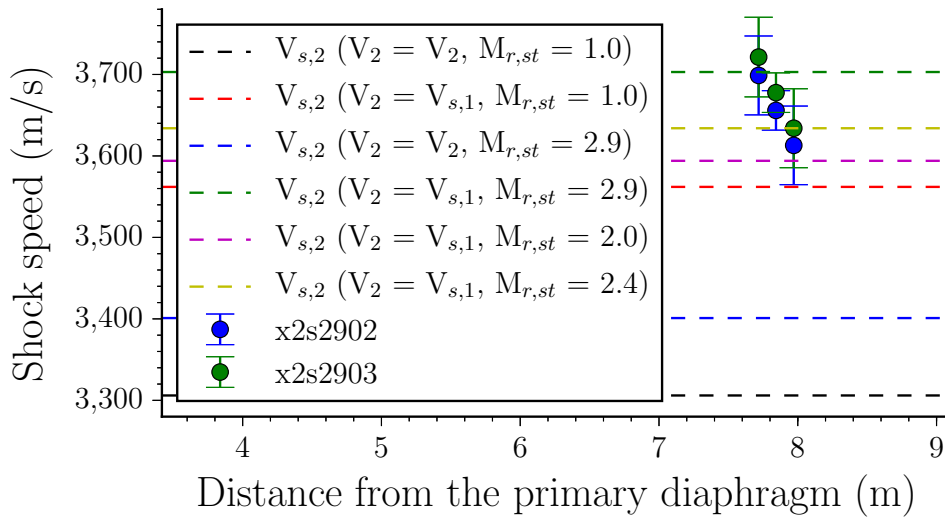


Figure 5.16: Experimentally measured acceleration tube shock speeds ( $V_{s,2}$ ) from Table 5.6 compared to various semi-experimental equilibrium PITOT simulations.

which value is the most correct. To resolve this, the pressure of the unsteadily expanded test gas (state 7) can be analysed. This is shown in Fig. 5.17.

Figure 5.17 shows the tube wall static pressure traces at the end of the acceleration tube for the two experiments compared to the expected theoretical unsteadily expanded test gas (state 7) pressures for the various simulations shown in Fig. 5.16. Fig. 5.17 shows theoretical data where the test gas has both been expanded to the acceleration tube shock speed ( $V_7 = V_{s,2}$ ) and the theoretical ideal gas velocity in the acceleration tube ( $V_7 = V_6$ ). Firstly, in general it can be seen that the theoretical  $p_7$  values where  $V_7 = V_6$  are all too large when compared to the experimental data. Therefore, the remaining discussion about Fig. 5.17 will focus on the theoretical data where  $V_7 = V_{s,2}$ .

Comparing the experimental and theoretical data shown in Fig. 5.17, it is difficult to ascertain exactly *where* to compare the experimental data to the theoretical equivalent. To estimate which part of each pressure trace is the accelerator gas and which is the test gas, a theoretical calculation of the accelerator gas slug length was performed from Mirels [106] using the measured  $V_{s,2}$  value. Equations 2 and 20 from Mirels [106] were used to find the slug length. It was assumed that the boundary layer was laminar and that the  $\beta$  value required for Equation 2 could be found from Equation 17 in the same paper. From this, the passage time of the accelerator gas slug was found to be around  $40 \mu\text{s}$  for each signal shown here, and this is shown in Fig. 5.17 for signal ‘at4’ as the ‘accelerator gas slug’. At the end of that gas slug, there is a section of steadily dropping pressure which is likely to be test gas, but without a stable pressure reading. This has been labelled the ‘start of test gas’. The next section is labelled ‘steady test

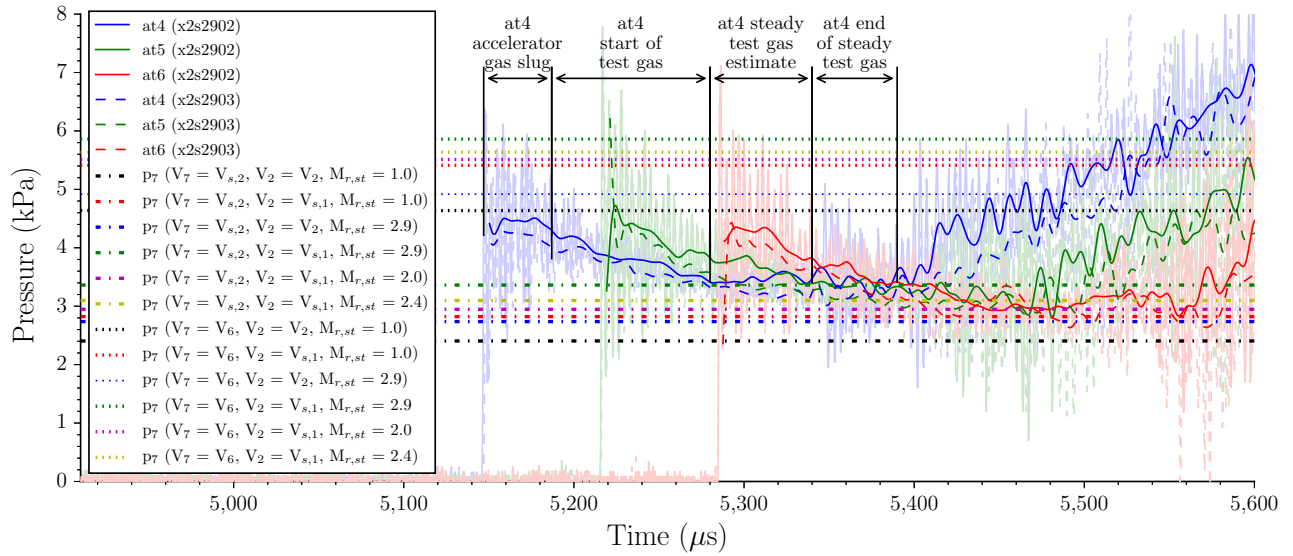


Figure 5.17: Measured acceleration tube wall pressure traces for two experiments performed using the test condition described in Table 5.5 compared to the unsteadily expanded test gas (state 7) pressures for the semi-experimental equilibrium PITOT simulations shown in Fig. 5.16.

gas estimate' and it has been used to calculate the experimental state 7 pressure values shown in Table 5.6 for signals 'at4', 'at5', and 'at6'. The section after this labelled 'end of steady test gas' appears to have a similar pressure to the 'steady' section before it, but with more noise. Potentially it is the section where the test and driver gases start to mix, and it has not been used to calculate the steady pressure values.

Considering the experimental  $p_7$  values shown in Table 5.6, the mean values for x2s2902 and x2s2903 are  $3.3 \pm 0.2$  kPa and  $3.2 \pm 0.2$  kPa respectively. In Fig. 5.16 it was shown that only the conditions with a shocked test gas velocity equal to the shock tube shock speed ( $V_2 = V_{s,1}$ ) and a reflected shock exiting the shock tube ( $M_{r,st} > 1$ ) were able to match the experimental shock speed data. Here it is similar, with only the simulations with reflected shock Mach number ( $M_{r,st}$ ) values of 2.4 and 2.9 falling within the uncertainties of the experimental data with theoretical unsteadily expanded test gas pressure ( $p_7$ ) values of 3.1 and 3.4 kPa respectively. For this reason it has been decided to use a shocked test gas velocity equal to the shock tube shock speed ( $V_2 = V_{s,1}$ ) and a fully reflected shock at the end of the shock tube ( $M_{r,st} = \text{maximum} = 2.9$ ) for all of the experimental data analysed in Figs. 5.18 and 5.19.

Figure 5.18 is similar to Fig. 5.17 above, however, in Fig. 5.18 the experimental wall pressure traces for the two experiments are compared to PITOT simulations based on experimental shock speeds only. While examining shock speed and wall pressure data in the acceleration tube in Figs. 5.16 and 5.17, it was found that setting the shocked test gas velocity in the shock tube to

the shock tube shock speed ( $V_2 = V_{s,1}$ ) and using a fully reflected shock at the end of the shock tube ( $M_{r,st} = \text{maximum} = 2.9$ ) gave the best comparison between PITOT and the experimental data. For this reason, this has again been done for the PITOT simulations shown in Figs. 5.18 and 5.19.

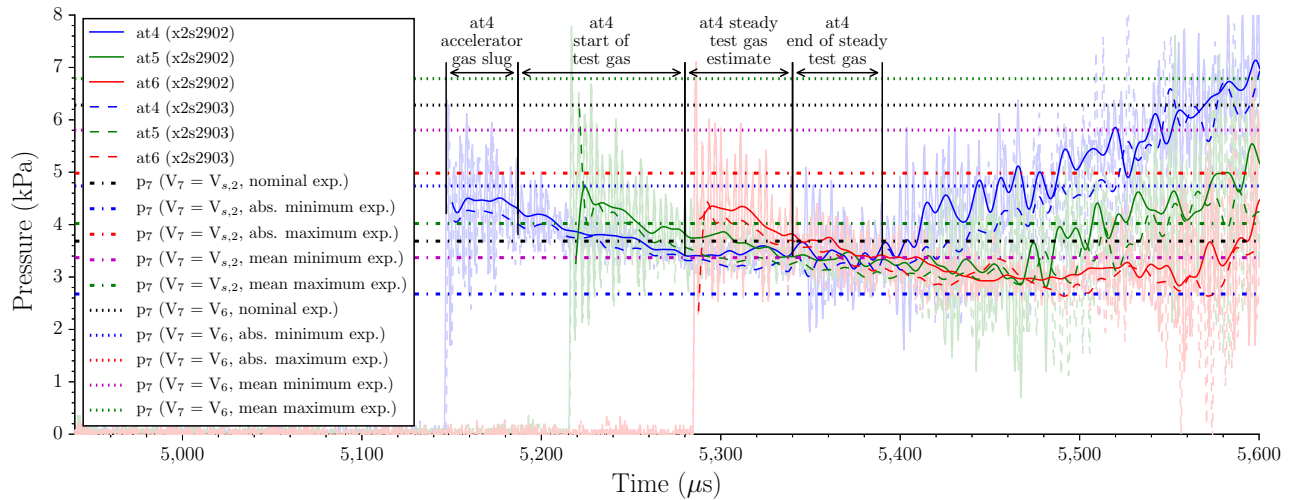


Figure 5.18: Measured acceleration tube wall pressure traces for two experiments performed using the test condition described in Table 5.5 compared to equilibrium PITOT simulations performed using experimentally measured shock speeds from experiment x2s2902.

The goal of Fig. 5.18 is to ascertain the effect that the uncertainty on the experimental shock speed data has on how well the overall flow condition can be known. If uncertainties on the shock tube and acceleration tube fill conditions (state 1 and state 5) are assumed to be sufficiently small, the main sources of uncertainty are the shock speed uncertainties in each section of the facility and the uncertainties about the effective nozzle area ratio (see Section 5.4.6). Using the extremities of the measured shock speed data, a sensitivity analysis can be performed to ascertain realistic bounds on the resulting flow condition parameters in the acceleration tube, and following that, the test section. This will be done here using the data from x2s2902 and a tool which the authors wrote to use PITOT to examine this. While the experimental data for both experiments are very similar, to simplify the discussion, it has been decided to focus on only x2s2902.

Considering the shock speed data for x2s2902 shown in Table 5.6, the absolute minimum shock tube shock speed ( $V_{s,1}$ ) possible is 2,010 m/s, and the absolute maximum is 2,100 m/s. If it is assumed that  $V_{s,1}$  is not changing across the locations where it is measured, the values can be averaged, giving a mean value of  $2,050 \pm 10$  m/s, and a much smaller shock speed range of 2,040 to 2,070 m/s. Similarly, for the acceleration tube shock speed ( $V_{s,2}$ ), the absolute maximum range possible is 3,570 to 3,750 m/s. Once again, if it is assumed that  $V_{s,2}$  is not

changing across the locations where it is measured, the values can be averaged, giving a mean value of  $3,660 \pm 20$  m/s, and a much smaller shock speed range of 3,630 to 3,680 m/s. Every possible combination of these shock speeds for both the ‘absolute minimum and maximum’ and ‘mean minimum and maximum’ cases were simulated in PITOT to find a realistic range of unsteadily expanded test gas pressure ( $p_7$ ) values, and these values are shown in Fig. 5.18 with the experimental acceleration tube wall pressure data.

Results where the test gas has both been expanded to the acceleration tube shock speed ( $V_7 = V_{s,2}$ ) and the theoretical ideal gas velocity in the acceleration tube ( $V_7 = V_6$ ) are shown in Fig. 5.18. Once again, the same as when Fig. 5.17 was discussed, the PITOT simulations shown in Fig. 5.18 where  $V_7 = V_6$  have an unrealistically high unsteadily expanded test gas pressure ( $p_7$ ) for every case. Therefore, the following analysis will only focus on the pressure values where  $V_7 = V_{s,2}$ .

From Table 5.6, it can be seen that the mean wall pressure trace ( $p_7$ ) values for x2s2902 and x2s2903 are  $3.3 \pm 0.2$  kPa and  $3.2 \pm 0.2$  kPa respectively. From the sensitivity analysis, the absolute maximum  $p_7$  range shown in Fig. 5.18 is 2.7 to 5.0 kPa. Using the less conservative mean uncertainty values, the  $p_7$  range is a more realistic 3.4 to 4.0 kPa, with a nominal value of 3.7 kPa. The simulated mean values from the sensitivity analysis and the experimental  $p_7$  measurements have overlapping uncertainties, indicating that the analysis so far has been adequate, with the pressure potentially around 3.4 kPa, where the two overlap.

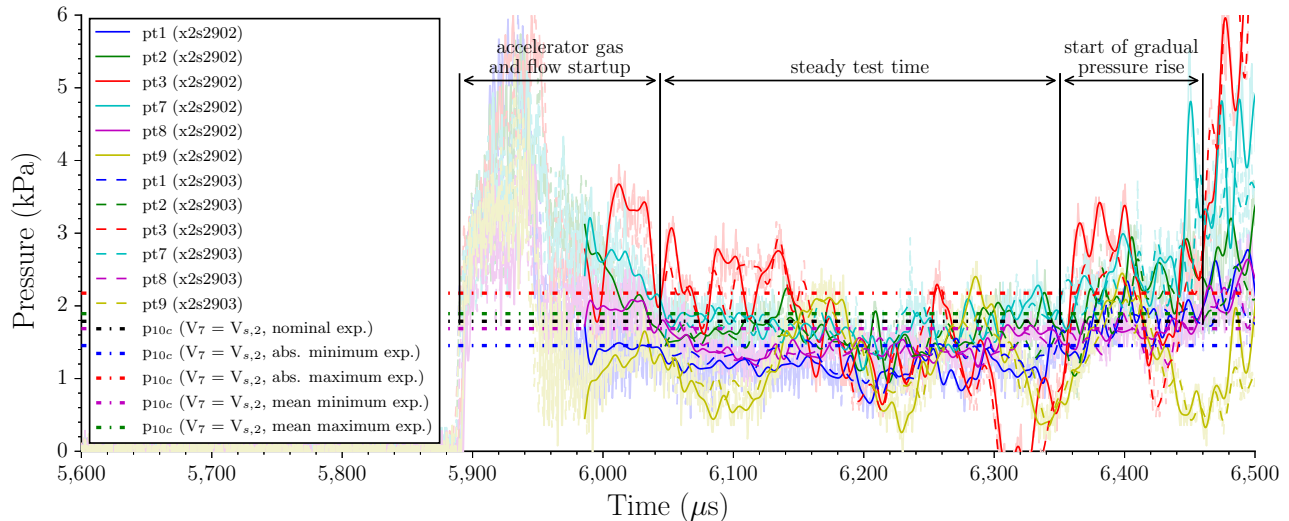


Figure 5.19: Measured  $15^\circ$  half-angle cone pressure traces in the test section ( $p_{10c}$ ) for two experiments performed using the test condition described in Table 5.5 compared to theoretical values from equilibrium PITOT simulations using the nozzle’s geometric area ratio of 5.64 and measured experimental shock speeds from experiment x2s2902.

Now that the bounds on the unsteadily expanded test gas (state 7) values have been considered, the last step is to find realistic bounds on the test section state (state 8). This is not necessarily a simple task. Firstly, there is uncertainty about the unsteadily expanded test gas state (state 7) entering the nozzle. Secondly, there is uncertainty about the effective area ratio of the nozzle, and finally, it is only possible to infer the nozzle exit state (state 8) from pressures measured over pressure probes in the test section (state 10), which in this case are 15° half-angle conical pressure probes. Fig. 5.19 shows the experimental cone pressure data for the two experiments from's X2 pitot rake. The pitot rake is generally instrumented with nine pressure probes mounted vertically along the nozzle exit plane, with the middle probe ('pt5') oriented with the centre-line of the nozzle. However, in this case, the centre-line probe was replaced with a small cylinder model to perform infrared radiation measurements, and the wake flow of this cylinder was interacting with probes 'pt4' and 'pt6' on either side of the model, so only data from probes 1 to 3 and 6 to 9 are shown in Fig. 5.19.

Flow arrival in the test section is generally seen as a spike in the measured impact pressure traces due to the different post nozzle expansion properties of the accelerator gas compared to the test gas. This is then followed by a short period of relatively steady test time, seen for around 300  $\mu\text{s}$  for this condition, where measurements would be taken for a more complicated experiment. In most cases, the steady test time is terminated by a gradual pressure rise as less expanded test gas starts to flow over the probes.

Due to fact that the PITOT results where the test gas was unsteadily expanded to the ideal gas velocity in the acceleration tube ( $V_7 = V_6$ ) shown in Figs. 5.17 and 5.18 were found to be too large to be a correct assumption, it was decided to only show PITOT results where the test gas has been unsteadily expanded to the acceleration tube shock speed ( $V_7 = V_{s,2}$ ) in Fig. 5.19. These unsteadily expanded test gas values (state 7) were then steadily expanded through the nozzle using the nozzle's geometric area ratio of 5.64 to find the values shown in Fig. 5.19.

The experimental 15° half-angle cone pressure ( $p_{10c}$ ) measurements shown in Table 5.6 were found using the 'steady test time' shown in Fig. 5.19. Looking at Table 5.6 it can be seen that the mean experimental  $p_{10c}$  values for x2s2902 and x2s2903 are  $1.4 \pm 0.4 \text{ kPa}$  and  $1.5 \pm 0.4 \text{ kPa}$  respectively. These results are imprecise as they have quite large percentage uncertainties (around 25%) and for some of the individual signals ('pt3' and 'pt9') the percentage uncertainties are quite large (around 100%). If the mean range from the sensitivity analysis is again considered, it can be seen in Fig. 5.19 that this mean data compares quite well to the experimental data, with a  $p_{10c}$  range of 1.7 to 1.9 kPa, with a nominal value of 1.8 kPa. This compares well with the experimental data. The range of the more conservative absolute minimum and maximum uncertainty simulations is 1.5 to 2.2 kPa, the bottom end of which also compares well with the experimental data.

Due to the large uncertainties on the cone pressure ( $p_{10c}$ ) data, it would be hard to perform an ‘area ratio check’ for different nozzle area ratios (see Section 5.4.6) and have confidence in the result. For this reason, the test section state (state 8) range found using the nozzle’s geometric area ratio of 5.64 and the mean uncertainties on the shock speed measurements have been used to estimate the flow condition parameters. This is shown in Table 5.7 where the final condition details at both nozzle entry (state 7) and nozzle exit (state 8) for experiment x2s2902 are shown. Both a nominal solution found using only the mean shock speeds and a solution bound for every variable found using the range of the uncertainties on those shock speeds are presented. This is already considered by the authors to be a conservative analysis, but it should be noted that more conservative estimates of the flow condition bounds could be found by using the absolute minimum and maximum shock speed ranges instead, or by performing an ‘area ratio check’ to ascertain what variation in area ratio would still fall inside the uncertainties on the experimentally measured  $p_{10c}$  data shown in Table 5.6.

Table 5.7: Final result of the condition analysis of the ‘cold driver’ air test condition from Table 5.5.

	Nominal	Solution bounds
State 7 (nozzle entry condition)		
Static pressure ( $p_7$ , kPa)	3.68	3.37 – 4.02
Static temperature ( $T_7$ , K)	1,690	1,640 – 1,740
Density ( $\rho_7$ , kg/m <sup>3</sup> )	$7.59 \times 10^{-3}$	$7.15 \times 10^{-3} - 8.04 \times 10^{-3}$
Velocity ( $V_7$ , m/s)	3,660	3,630 – 3,680
Mach number ( $M_7$ )	4.61	4.52 – 4.71
State 8 (nozzle exit condition, using an area ratio of 5.64)		
Static pressure ( $p_8$ , kPa)	0.349	0.318 – 0.381
Static temperature ( $T_8$ , K)	961	929 – 994
Density ( $\rho_8$ , kg/m <sup>3</sup> )	$1.26 \times 10^{-3}$	$1.19 \times 10^{-3} - 1.34 \times 10^{-3}$
Velocity ( $V_8$ , m/s)	3,890	3,860 – 3,910
Mach number ( $M_8$ )	6.40	6.27 – 6.53
Stagnation enthalpy ( $H_t$ , MJ/kg)	8.26	8.15 – 8.38

### Example 2: Free Piston Driven Condition

The fill details of the example free piston driven air condition can be found in Table 5.8. The experimentally measured shock speeds, and filtered wall transducer and pitot rake 15° half-angle cone pressure measurements for experiment x2s3232 are shown in Tables 5.9 and 5.10 respectively.

To simplify this second example, some lessons learnt while analysing the first example in Section 5.5.4 will be used. Considering Figs. 5.18 and 5.19 where the pressure values from

Table 5.8: Facility configuration details for the free piston driven air test condition designed by Zander et al. [90].

Driver condition	X2-LWP-2.0 mm-0
Primary driver fill condition	92.8 kPa 80%He/20%Ar (by volume)
Primary diaphragm	1 x 2 mm thick cold rolled steel, scored diaphragm
Orifice plate diameter	85 mm (i.e. no extra contraction)
Shock tube fill condition	3.0 kPa Coregas instrument air (79%N <sub>2</sub> /21%O <sub>2</sub> , by volume)
Secondary diaphragm	1 x ≈ 14 μm thick aluminium foil diaphragm
Acceleration tube fill condition	10.0 Pa lab air

Table 5.9: Experimentally measured shock speeds for the free piston driven air test condition detailed in Table 5.8 from experiment x2s3232.

Shock tube shock speeds ( $V_{s,1}$ )	
sd1-sd3 (m/s)	4,020 ± 30 (0.74%)
sd1-sd2 (m/s)	4,100 ± 60 (1.5%)
sd2-sd3 (m/s)	3,940 ± 60 (1.5%)
Mean value (m/s)	4,020 ± 30 (0.74%)
Acceleration tube shock speeds ( $V_{s,2}$ )	
st1-st3 (m/s)	7,840 ± 40 (0.46%)
st1-st2 (m/s)	7,660 ± 70 (0.91%)
st2-st3 (m/s)	8,030 ± 80 (0.94%)
at1-at3 (m/s)	7,910 ± 120 (1.5%)
at1-at2 (m/s)	7,610 ± 230 (3.0%)
at2-at3 (m/s)	8,270 ± 140 (1.6%)
at3-at4 (m/s)	7,890 ± 30 (0.37%)
at4-at6 (m/s)	7,990 ± 50 (0.58%)
at4-at5 (m/s)	8,000 ± 90 (1.2%)
at5-at6 (m/s)	7,990 ± 100 (1.2%)
Mean value (m/s)	7,920 ± 30 (0.44%)

the sensitivity analysis based on the shock speed uncertainties for experiment x2s2902 are compared to experimental data, it can be seen that the pressure values found from the bounds of the absolute minimum and maximum possible shock speeds (‘abs. minimum exp.’ and ‘abs. maximum exp.’) are much less representative of the real spread in the data than the pressure values found using the bounds of the mean uncertainties of the shock speeds (‘mean minimum exp.’ and ‘mean maximum exp.’), and in Table 5.7 the mean uncertainty values were used to find the expected range of the final flow condition data. For this reason, only the bounds of the mean uncertainties will be used for the sensitivity analysis for this example.

In Fig. 5.20a the experimental shock tube shock speed ( $V_{s,1}$ ) values shown in Table 5.9

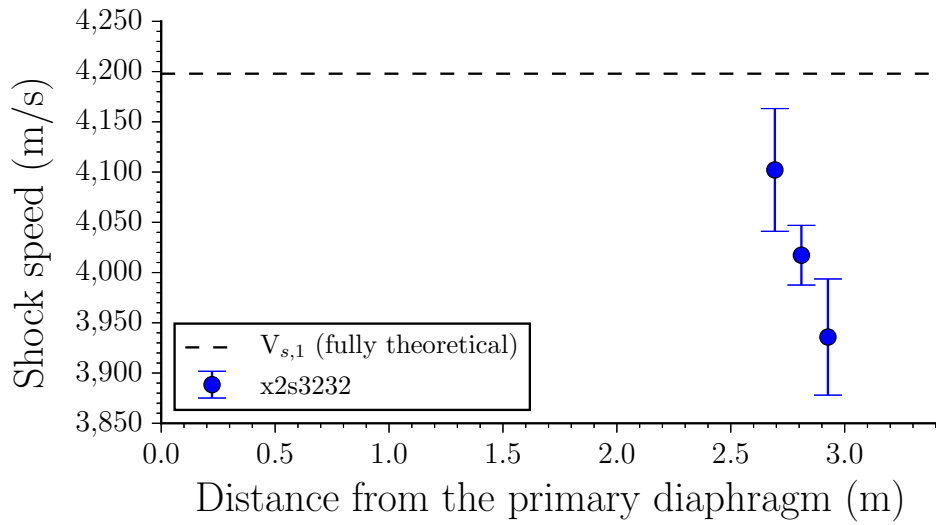


for experiment x2s3232 are compared to the theoretical equilibrium shock speed value from PITOT when the effective driver values from Table 5.2 are used. It can be seen that the theoretical result from PITOT overestimates the experimental shock speeds by around 5%. As was discussed in Section 5.5.1, this error can be removed by not using the driver model in the calculation and instead specifying an experimental  $V_{s,1}$  value. For the theoretical acceleration tube calculations shown in Fig. 5.20b, an average experimental  $V_{s,1}$  value of 4,020 m/s has been used instead of the driver model.

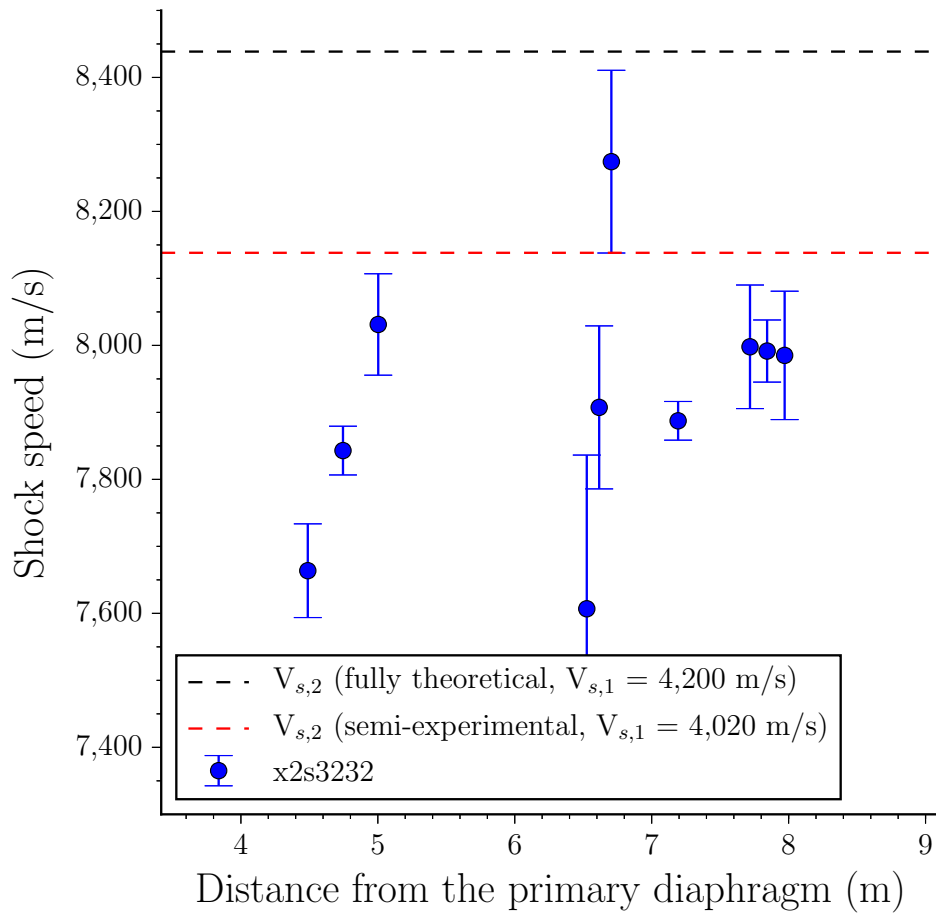
In Fig. 5.20b the experimental acceleration tube shock speed ( $V_{s,2}$ ) values shown in Table 5.9 for experiment x2s3232 are compared to both the fully theoretical equilibrium value from PITOT when the effective driver values from Table 5.2 were used, as well as a result from PITOT where the shock tube fill condition (state 1) was shocked by the specified experimental  $V_{s,1}$  value of 4,020 m/s. The driver model in PITOT overestimated  $V_{s,1}$  in Fig. 5.20a by around 5%, so it was expected that it would also overestimate  $V_{s,2}$  here, and that is what is seen, with the fully theoretical value being around 6% higher than the mean experimental  $V_{s,2}$  value from Table 5.9. Large variations are seen in the first seven experimental  $V_{s,2}$  measurement locations. However, the shock speed becomes fairly consistent for the last three downstream measurements. The authors believe that this could be caused by a few different phenomena, such as diaphragm effects, changing shock shape, or errors in the measured transducer locations for some of the sensors. It is also interesting to note in Fig. 5.20b that even using the experimentally measured mean  $V_{s,1}$  value of 4,020 m/s, PITOT still overestimates the acceleration tube shock speed by 2% compared to the measured ‘at4-at6’ value of  $7,990 \pm 50$  m/s, showing that either the shock has attenuated slightly and slowed down from the expected value, or that the acceleration tube fill pressure ( $p_5$ ) may have been slightly higher than expected.

If the uncertainties on the shock and acceleration tube fill conditions (state 1 and state 5) are assumed to be small, the main sources of uncertainty for the experiment are from the shock speed measurements in each section of the tube and the effective nozzle area ratio (see Section 5.4.6). By performing a sensitivity analysis using the uncertainties on the measured shock speed data, realistic bounds on the resulting flow condition parameters in the acceleration tube can be ascertained, and following that, the test section.

Considering the shock speed data for x2s3232 shown in Table 5.9, the mean shock tube shock speed ( $V_{s,1}$ ) is  $4,020 \pm 30$  m/s, giving a mean shock speed range of 3,990 to 4,050 m/s. The mean acceleration tube shock speed ( $V_{s,2}$ ) considering just the ‘at’ labelled shock speeds in Table 5.9 is  $7,950 \pm 50$  m/s, giving a mean shock speed range of 7,900 to 8,000 m/s. The sensitivity analysis simulated every possible combination of these mean shock speeds in PITOT to find the full potential range of unsteadily expanded test gas pressure ( $p_7$ ) values. These values are shown in Fig. 5.21 with the experimental acceleration tube wall pressure trace data from



(a) Shock tube shock speeds ( $V_{s,1}$ )



(b) Acceleration tube shock speeds ( $V_{s,2}$ )

Figure 5.20: Experimentally measured shock speeds from Table 5.9 compared to PITOT results.

Table 5.10: Filtered experimentally measured pressure data for the free piston driven air test condition detailed in Table 5.8 from experiment x2s3232.

Acceleration tube wall pressure traces ( $p_7$ )	
st1 (kPa)	$3.2 \pm 0.9$ (30%)
st2 (kPa)	$6.0 \pm 1.7$ (30%)
st3 (kPa)	$4.6 \pm 1.4$ (30%)
at1 (kPa)	$4.8 \pm 0.9$ (20%)
at2 (kPa)	$4.2 \pm 0.7$ (20%)
at3 (kPa)	$4.9 \pm 0.8$ (20%)
at4 (kPa)	$4.6 \pm 0.7$ (10%)
at5 (kPa)	$4.4 \pm 0.7$ (20%)
at6 (kPa)	$5.0 \pm 0.6$ (10%)
at7 (kPa)	$5.2 \pm 0.6$ (10%)
at8 (kPa)	$5.5 \pm 0.6$ (10%)
Mean value (all values) (kPa)	$4.8 \pm 0.3$ (6%)
Test section $15^\circ$ half-angle cone pressure traces ( $p_{10c}$ )	
pt1 (kPa)	$4.8 \pm 0.7$ (20%)
pt2 (kPa)	$5.8 \pm 0.8$ (10%)
pt3 (kPa)	$6.2 \pm 2.6$ (40%)
pt4 (kPa)	$6.4 \pm 1.5$ (20%)
pt5 (kPa)	$6.1 \pm 1.6$ (30%)
pt6 (kPa)	$6.7 \pm 2.0$ (30%)
pt7 (kPa)	$5.9 \pm 1.5$ (30%)
pt8 (kPa)	$6.0 \pm 0.7$ (10%)
pt9 (kPa)	$4.9 \pm 0.4$ (8%)
Mean value (without pt1 and pt9) (kPa)	$6.2 \pm 0.6$ (10%)

experiment x2s3232 for wall sensors ‘at1’ to ‘at8’. Fig. 5.21 shows data where the test gas has both been expanded to the acceleration tube shock speed ( $V_7 = V_{s,2}$ ) and the theoretical ideal gas velocity in the acceleration tube ( $V_7 = V_6$ ).

Firstly, it can be seen that for all of the PITOT results shown in Fig. 5.21 where  $V_7 = V_6$  the unsteadily expanded test gas pressure ( $p_7$ ) is too large for it to have been a correct assumption. Therefore, the following analysis will focus only on the pressure values where  $V_7 = V_{s,2}$ .

From Table 5.10, it can be seen that the mean wall pressure ( $p_7$ ) value for x2s3232 is  $4.8 \pm 0.3$  kPa. Where  $V_7 = V_{s,2}$ , the  $p_7$  range shown in Fig. 5.21 from the sensitivity analysis is 4.5 to 5.9 kPa, with a nominal value of 5.2 kPa. These values are consistent within the bounds of their associated uncertainties, and there is a -8.4% difference between the experimentally measured mean  $p_7$  value, and the nominal value from the sensitivity analysis using PITOT and the measured shock speeds.

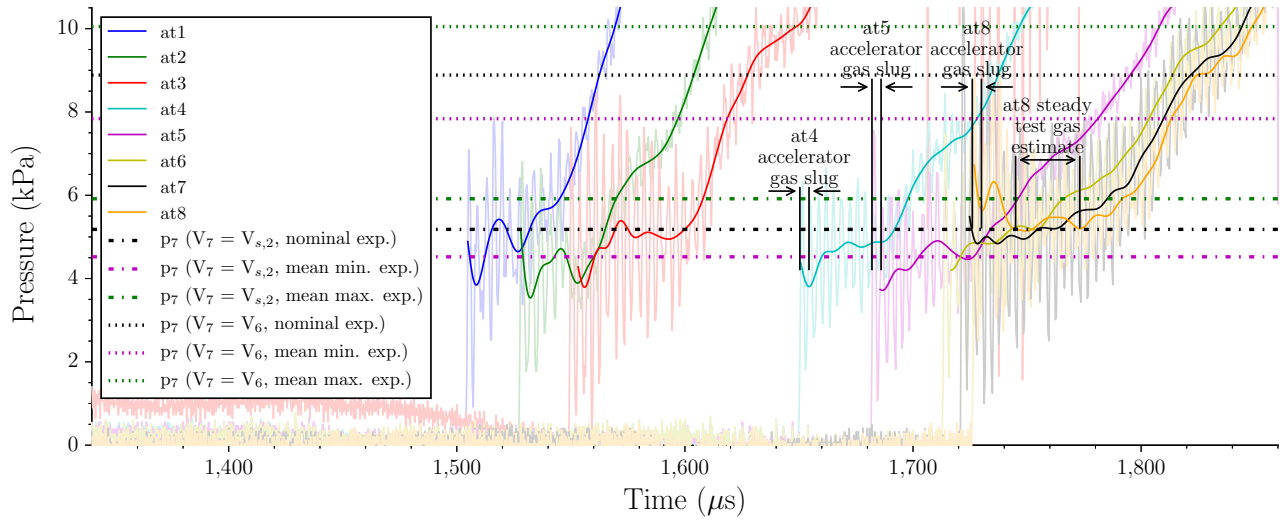


Figure 5.21: Measured acceleration tube wall pressure traces for the test condition described in Table 5.8 compared to equilibrium PITOT simulations performed using experimentally measured shock speeds from experiment x2s3232.

Now that the bounds on the unsteadily expanded test gas state (state 7) values have been considered, the final step is to assign realistic bounds to the nozzle exit state (state 8). This is not necessarily a simple task, because there are uncertainties about the gas state entering the nozzle (state 7) and about the effective area ratio of the nozzle, and it is only possible to infer the nozzle exit state (state 8) from measurements over pressure probes in the test section (state 10). Fig. 5.22 shows the experimental  $15^\circ$  half-angle cone pressure data for the experiment from the X2 pitot rake. To provide a starting point for the analysis, the state 7 values have been steadily expanded using the nozzle's geometric area ratio of 5.64 to find the values shown in Fig. 5.22. It can be seen in Fig. 5.22 that the condition appears to have a steady test time of around  $60 \mu\text{s}$ .

Once again, the same as when Fig. 5.21 was discussed, for all of the PITOT results shown in Fig. 5.22 where  $V_7 = V_6$  the  $15^\circ$  half-angle cone pressure ( $p_{10c}$ ) is too large for it to have been a correct assumption. Therefore, the following analysis will only focus on the pressure values where  $V_7 = V_{s,2}$ .

The experimental  $15^\circ$  half-angle cone pressure ( $p_{10c}$ ) measurements shown in Table 5.10 were found using the 'steady test time' shown on Fig. 5.22. Looking at Table 5.10, it can be seen that the pressures for sensors 'pt1' and 'pt9' have similar values ( $4.8 \pm 0.7 \text{ kPa}$  and  $4.9 \pm 0.4 \text{ kPa}$  respectively) which are lower than the other sensors by at least a kilopascal, indicating that they are probably out of the core flow of the test condition. Considering the geometry of the pitot rake, this gives a core flow of around 120 mm. For this reason, the mean

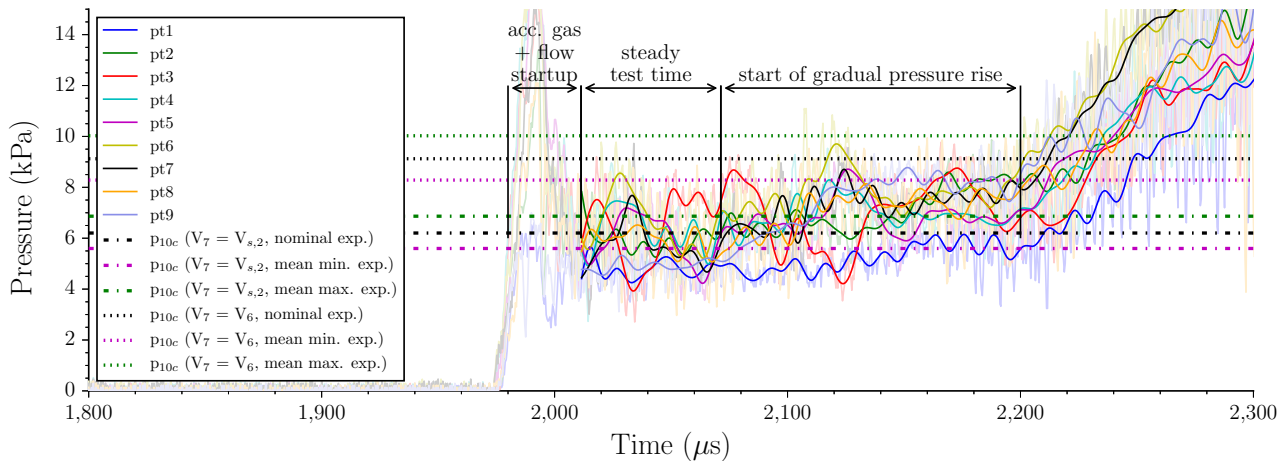


Figure 5.22: Measured  $15^\circ$  half-angle cone pressure traces in the test section ( $p_{10c}$ ) for the test condition described in Table 5.8 compared to equilibrium PITOT simulations performed using the nozzle's geometric area ratio of 5.64 and measured experimental shock speeds from experiment x2s3232.

$p_{10c}$  value for experiment x2s3232,  $6.2 \pm 0.6$  kPa, has been calculated without sensors 'pt1' and 'pt9'. With  $V_7 = V_{s,2}$ , the  $p_{10c}$  range found from the mean experimental shock speed values is 5.6 to 6.9 kPa, with a nominal value of 6.2 kPa, which is the same as the experimentally measured mean value. This difference of 0% between the experimentally measured mean  $p_{10c}$  value and the nominal value from the sensitivity analysis using PITOT and the measured shock speeds, indicates that the choice to use the geometric area ratio of 5.64 was reasonable.

Table 5.11 presents the final condition details at nozzle entry and exit (states 7 and 8) and also post-normal shock in the test section at equilibrium (state 10e) for experiment x2s3232 using the nozzle's geometric area ratio of 5.64. Both a nominal solution found using only the mean experimentally measured shock speeds and a solution bound for every variable found using the uncertainties on those mean values are presented. While the solution bounds show the potential variation which may exist for the flow condition, the analysis showed that the nozzle entry pressure ( $p_7$ ) from the sensitivity analysis was consistent with the experimentally measured values (with an 8.3% difference between the nominal theoretical value and the mean experimental one) and the nominal  $15^\circ$  half-angle cone pressure ( $p_{10c}$ ) was the same as the mean experimental value, showing that potentially it is reasonable to describe experiment x2s3232 in a less conservative manner using just the nominal solution.

### Concluding Remarks about the Examples

Overall, it has been shown that it is possible for both cold and free piston driven conditions to use an appropriately experimentally calibrated version of PITOT to re-create results obtained

Table 5.11: Final result of the condition analysis of the free piston driven air test condition from Table 5.8.

	Nominal	Solution bounds
State 7 (nozzle entry condition)		
Static pressure ( $p_7$ , kPa)	5.18	4.52 – 5.92
Static temperature ( $T_7$ , K)	2,580	2,520 – 2,640
Density ( $\rho_7$ , kg/m <sup>3</sup> )	$6.83 \times 10^{-3}$	$6.13 \times 10^{-3} - 7.59 \times 10^{-3}$
Velocity ( $V_7$ , m/s)	7,950	7,900 – 8,000
Mach number ( $M_7$ )	8.47	8.32 – 8.62
State 8 (nozzle exit condition, using an area ratio of 5.64)		
Static pressure ( $p_8$ , kPa)	0.625	0.534 – 0.728
Static temperature ( $T_8$ , K)	1,830	1,740 – 1,920
Density ( $\rho_8$ , kg/m <sup>3</sup> )	$1.19 \times 10^{-3}$	$1.07 \times 10^{-3} - 1.32 \times 10^{-3}$
Velocity ( $V_8$ , m/s)	8,120	8,070 – 8,170
Mach number ( $M_8$ )	9.92	9.69 – 10.2
Stagnation enthalpy ( $H_t$ , MJ/kg)	34.7	34.3 – 35.2
Flight equivalent velocity ( $U_e$ , m/s)	8,340	8,280 – 8,390
State 10e (eq post-normal shock condition in the test section)		
Static pressure ( $p_{10e}$ , kPa)	73.8	67.1 – 81.2
Static temperature ( $T_{10e}$ , K)	7,530	7,490 – 7,580
Density ( $\rho_{10e}$ , kg/m <sup>3</sup> )	$1.87 \times 10^{-2}$	$1.70 \times 10^{-2} - 2.06 \times 10^{-2}$
Velocity ( $V_{10e}$ , m/s)	7,600	7,560 – 7,650
Mach number ( $M_{10e}$ )	3.55	3.53 – 3.57

from experiments. It has also been shown that the experimentally measured shock speeds can be used to provide realistic solution bounds for the experimental data.

The main discrepancy was seen in the modelling of the driver, with driver rupture conditions ( $p_4$  and  $T_4$ ) inferred from experimental shock speeds through a helium test gas [2] under-predicting the shock tube shock speed ( $V_{s,1}$ ) by 5% for the first example, and over-predicting it by 5% for the other. Especially for the free piston driven example, there may be several reasons for this. Firstly, a free piston driver is complicated, and the variations may be real. The diaphragm scoring is performed by many different personnel and could have been performed slightly differently for each experiment; the wear rings on the piston may have had a different amount of wear for each experiment; the driver temperature could have been different for each experiment; or the back pressure of the high pressure bottle bank which is used to fill the reservoir could have been different, causing the temperature of the expanded reservoir gas to be different for each experiment. All of these small changes can affect the performance of the driver. Secondly, all of X2's shock tube wall pressure sensors are located in the last quarter of the tube's length (see Fig. 5.1) because the physical geometry of the facility leaves only a small straight section at the end where sensors can easily be placed. This is not ideal for monitoring

driver performance and complicates using measured shock speeds to try to understand the driver, because the shock may have slightly attenuated or even been sped up by compression waves sent down the tube from the driver before it reaches the sensors. While the inferred driver conditions used for the free piston driven condition were an average of ten different experiments performed at three different shock tube fill pressures, 50, 150, and 500 kPa [2], their ability to be universally applicable could still have been affected by the measurement locations. Colleagues of the authors have had success using initial experimental data to create more targeted effective driver rupture values that could then be used to accurately predict the shock speeds of new but similar conditions performed at a similar time, but existing data is not always available.

Before continuing, it is worth considering what effect that the inferred solution bounds would have on a real X2 experiment. As a simple way to simulate the relatively blunt models usually used on X2, conditions behind an equilibrium normal shock in the test section (state 10e) were added to the sensitivity analysis result shown in Table 5.11. Generally for expansion tube flow conditions, whether they are being used for scaled experiments or not, the stagnation enthalpy ( $H_t$ ) and the post-shock density are the most important flow variables. The first because it is a measure of the energy in the freestream gas which will be mainly converted to thermal energy behind the shock wave, and the second because it controls the chemical length scales behind the shock, which are important for scaling and more generally, for generating conditions focussed on studying either equilibrium or non-equilibrium behaviour. Looking at Table 5.11 and considering the nozzle exit (state 8)  $H_t$  value, the uncertainty on the nominal value caused by the solution bounds is  $\pm 1.3\%$ . The flight equivalent velocity ( $U_e$ ), which is a function of  $H_t$ , shows an even smaller uncertainty of  $\pm 0.7\%$ . If the post-shock (state 10e) values are now considered, it can be seen that the post-shock temperature ( $T_{10e}$ ), which is also a function of  $H_t$ , shows an uncertainty of  $\pm 0.6\%$ . This is a positive result for the accurate simulation of stagnation enthalpy, as its uncertainty was found to be of the same order as the shock speed uncertainties (around 1%, see Table 5.9). However, it also shows that even with shock speed uncertainties around 1%, the post-shock density is still very sensitive to that and has an uncertainty of around  $\pm 10\%$ . In a more general sense, this is something which would be expected for most test conditions, as it was discussed in Sections 5.4.5 and 5.4.6 that the pressure and density were the most sensitive variables to changes in how the gas expanded through the acceleration tube and nozzle. This is still a small uncertainty for an impulse facility, but it shows that blunt-body experiments which cannot tolerate post-shock density uncertainties of around  $\pm 10\%$  may not be suitable for expansion tube simulation, even with very small shock speed uncertainties.

## 5.6 Conclusions

This paper has presented a framework for the rapid simulation of an expansion tube facility by identifying central flow processes involved in facility operation, and simulating them from state to state through the facility by using isentropic and compressible flow relations, and equilibrium and frozen chemistry. Potential issues with modelling the light secondary and tertiary diaphragms, acceleration tube, and nozzle of an expansion tube facility were discussed, along with the solutions available in the model to deal with these issues. The theoretical effect of these solutions on the overall flow condition was also presented for an example expansion tube flow condition.

A method for using this framework to quantify experimental data using several different techniques was then presented. A technique for using the model with experimentally measured shock speeds in the shock tube to remove potential issues with driver modelling uncertainty was presented. A technique for using experimentally measured wall pressures and shock speeds in the acceleration tube to quantify the degree of over-expansion in the acceleration tube was also presented, as well as a technique to use experimentally measured pressures in the acceleration tube and test section to quantify the effective area ratio of a facility's nozzle.

Finally, two different experimental examples using data from the X2 expansion tube were presented to validate the model for quantifying experimental expansion tube flow conditions. One example was a 'cold driver' condition and the other was a free piston driven test condition regularly used in the laboratory. Both examples were able to be quantified using the model presented in this paper, by configuring the theoretical model to correctly re-create experimentally measured pressures and shock speeds. An inferred nominal solution for the test section state (state 8) of each example was presented, as well as a solution bound for each inferred quantity to take into account the uncertainty in the measured shock speed values used with the model. The authors believe that this is the current best practice to calculate an inferred expansion tube test section condition without using CFD simulation, as it provides an insight into the potential variation of the different test flow quantities.

Further work aims to improve the model where required by adding more complex models for different phenomena. This includes implementing an inertial diaphragm model [255, 258] to better model the thin secondary and tertiary diaphragm rupture, and directly implementing Mirels methodology for modelling the expected attenuation of the shock wave and over-expansion of the unsteadily expanding gas in a low density shock tube [106, 107, 108] to allow better prediction of acceleration tube behaviour. A larger goal is a more comprehensive validation of this model against both experimental and two-dimensional facility CFD simulation data, so that



the model can be compared to the full suite of data collected from these CFD simulations, instead of just the few experimental measurements which can be taken.

Another direction for further work is to implement an improved driver model into the code, because for both examples presented in Section 5.5.4 there was a 5% difference between the measured experimental shock tube shock speeds and the theoretical values predicted by the driver models used to simulate the experiments. This is not a large difference, and the driver model can be removed when simulating experimental data if necessary, but it limits the utility of fully theoretical simulations. This work could be taken in several different directions. The first direction would be to add estimated heat losses during the piston compression process and total pressure losses at the area change to the current fully theoretical driver model to make it more realistic. The second would be to perform a more comprehensive study of using shock speeds in the shock tube to infer effective driver rupture conditions than the one performed by Gildfind et al. [2]. Potentially taking data over a large range of shock tube fill pressures and test gases and providing a small database rather than a single value would provide results which are applicable to more situations. This could possibly also be done without performing any new experiments by mining old analysed experiments for this information. A more physical part of this proposed work would be to increase quality control for everything related to the driver, such as the diaphragm scoring depth, the accuracy of the driver and reservoir fill pressures, and estimating driver and reservoir gas temperatures at the time of firing to try to ensure that they remain inside specified limits.

## 6

# True Gas Composition Gas Giant Entry Simulation

*DP: “Exactly what do you mean by ‘guts’?”*

*EH: “I mean, grace under pressure.”*

– Ernest Hemingway, *being interviewed by Dorothy Parker for The New Yorker*, 30 November 1929

## 6.1 Chapter Overview

This chapter examines the possibility of simulating Uranus and Saturn entry in the X2 expansion tube. It begins by establishing the theoretical performance limits of X2 for the simulation of these entries, before experimental results are presented to verify the theoretical predictions. Issues with measuring shock speeds at such high velocities are also discussed. The chapter ends with a discussion of the possibilities available for more easily simulating gas giant entry in an X2 sized expansion tube facility by using a more powerful free piston driver.

## 6.2 Introduction

Previously, the majority of gas giant aerothermodynamic research has been focussed on the Galileo probe. Earlier research was performed in support of the design of the probe [59, 60, 61, 62], and subsequent analysis was conducted after it flew and the heat shield recession was found to be different from what had been expected [58, 64, 66]. This is discussed further in Section 3.3. Recently, there has been renewed interest in future gas giant entry probe missions. The US National Research Council ‘Vision and Voyages for Planetary Science in the Decade 2013-2022’ report identified future space missions to Uranus [68] and Saturn [69, 70]

as high priorities due to several significant scientific questions about the universe which these missions could help address, such as helping to improve models of solar system formation and evolution, or helping scientists understand extrasolar planetary systems, where gas giant planets are common. The proposed probe entry velocities are 22.3 km/s for Uranus [68] and 26.9 km/s for Saturn [69, 70]. The expected aeroheating uncertainties of these entries, and how different parameters contribute to these overall uncertainties, have been analysed by Palmer et al. [71]. Representative radiation was analysed experimentally by Cruden and Bogdanoff [72, 73]. Due to this renewed interest in gas giant entry probes, which may see the design of two new missions in the foreseeable future, it is worth considering how further ground testing can aid the development of this next generation of missions.

Planetary entry missions are extremely infrequent and expensive. For example, NASA's Galileo mission to Jupiter was estimated to have cost \$1.4 billion USD in 1988 dollars [268]. For this reason, various types of ground testing have proven to be essential to the design of planetary entry vehicles. Due to the stagnation enthalpy requirements of simulating planetary entry, it is not possible to simulate these flights in continuous flow wind tunnel type facilities. For example, the stagnation enthalpy of a 10 km/s Earth re-entry is 50 MJ/kg, and for the 22.3 km/s proposed Uranus entry [68] it is 250 MJ/kg. Arc jets [97, 98], plasma torches [99, 100], and plasma wind tunnels [101, 102] are high enthalpy test facilities which have test times long enough for the test model to reach temperatures at which hot-wall and ablation tests can be performed. However, while they can re-create flow stagnation enthalpy, they do not re-create the velocity or a real aerodynamic flow-field, and the tests are often subsonic. Impulse facilities, which are generally some variation of the shock tunnel concept, can often match the velocity and Reynolds number of the true flight condition, but experiments are performed on a 'cold' model because the test times are from tens to thousands of microseconds, depending on the size and type of facility. Considering the Galileo probe, none of the three sets of experiments performed were able to fully re-create the velocity of the Galileo probe's entry. However, in various ways, and at velocities ranging from 0 to 15 km/s, each experiment aimed to re-create the heating environment for a duration long enough to study the recession of an ablating model which could then be compared to Computational Fluid Dynamics (CFD) results [60, 61, 62]. This is discussed further in Section 3.3.

Most planetary entry test facilities are smaller than real flight vehicles. For this reason, it is common that blunt-body ground testing is performed using binary scaling, a technique originally suggested by Birkhoff [269]. Because the post-shock flow is often controlled by binary dissociation reactions, by matching the stagnation enthalpy and the  $\rho \cdot L$  product (where  $L$  is a characteristic length scale) between flight and scaled experiment, the ratio of the chemical relaxation distance to the body size remains unchanged and flow similarity is achieved [270].

Binary scaling is known to have its limitations, such as not correctly scaling post-shock radiation, three-body reactions such as recombination, and equilibrium compositions [271], but it is still an essential tool for laboratory simulation of planetary entry.

Due to the extreme stagnation enthalpy requirements of Jupiter entry (1,100 MJ/kg), Stalker and Edwards [67] proposed that the phenomena could be studied by only simulating the shock layer temperature of the condition. They proposed that higher levels of helium in the test gas or instead using neon, which is heavier, would result in hotter post-normal shock conditions during an experiment. This would allow gas giant entry shock layers to be simulated at lower flow velocities which are achievable in expansion tubes or non-reflected shock tunnels. This was investigated in the X2 expansion tube at the University of Queensland (UQ) in 2004 by Higgins [63], who studied the effect of atomic hydrogen ionisation on shock standoff. This is all discussed further in Section 3.4. The technique has not been used for radiation studies in the past. A preliminary theoretical analysis of how this could be examined again has been carried out by the author of this thesis [16, 17], with the final theoretical and experimental results found in Chapter 7 of this work. However, this is not the direction of this chapter.

Expansion tubes are well suited to simulating planetary entry because they process their test flow with a shock wave and then an unsteady expansion, instead of just a shock wave, allowing them to accelerate their test flow to superorbital conditions without causing it to be excessively dissociated and ionised [196]. This has allowed X2 to study entry into most planetary bodies in the solar system [222, 1, 81, 127, 78, 87, 79, 86, 80].

Due to the lower entry velocities of the proposed Uranus and Saturn entry missions [68, 69, 70], this paper examines whether an expansion tube with a high powered free piston driver (Stalker [234]) could be used to create relevant hypervelocity test conditions for the simulation of gas giant entry at true gas composition and true flight stagnation enthalpy. The X2 expansion tube will be used as a test case as it is an expansion tube facility currently principally used for the study of planetary entry phenomena. Further information about X2 can be found in Chapter 4, Gildfind et al. [146], or James et al. [25]. This chapter begins by examining the theoretical performance limits of X2 using the theoretical expansion tube and shock tunnel simulation code written by the author which is discussed in Chapter 5. Experiments are then presented to validate the theoretical results, and discrepancies between them are discussed. The final section of this chapter performs a second theoretical parametric study to investigate increasing the performance limits of an X2 sized facility by using a more powerful free piston driver.

## 6.3 Theoretical Condition Analysis

Expansion tubes are typically used for the simulation of planetary entry from 6 to 12 km/s [222, 1, 81, 127, 78, 87, 79, 86, 272, 134]. However, the simulation of gas giant entry involves velocities ranging from 20 to 50 km/s. Considering a simulated Uranus entry as an example, the molecular weight of the 85% $\text{H}_2$ /15% $\text{He}$  (by volume) [273] Uranus test gas mixture (2.31 g/mol) is 8% of the molecular weight of air (28.97 g/mol), which gives the possibility of generating higher shock speeds than usual air test conditions. Maximum performance requires an understanding of how the facility variables can be controlled to optimise the performance of each individual section of the facility, and then the facility as a whole. Therefore, in this section an equilibrium gas parametric study of the X2 expansion tube is performed with the condition building version of PITOT (see Chapter 5) using two different driver conditions (detailed in Table 6.1) and operation with and without a shock heated secondary driver section. To simulate the limiting Mirels case [106, 107, 108] for a low density shock tube, it has been chosen to over-expand the test gas in the acceleration tube to the shock speed for all test conditions. This is standard practice for high enthalpy expansion tube conditions and is discussed further in Section 5.4.5. All simulations have been performed with X2's contoured nozzle using its geometric area ratio of 5.64 [229]. The two driver conditions used in this paper have different compression ratios ( $\lambda$ ) and are both used here in a modified version where an orifice plate is used to restrict the mass flow through a choked throat, so that a lighter driver gas can be used to give higher performance [2].

Table 6.1: X2 driver conditions used for this study. Driver conditions are from [231, 230], except operated with a 100% $\text{He}$  driver gas and a 65 mm orifice plate [2].

Driver case ID	Diaphragm thickness	Rupture pressure, $p_4$	Rupture temp., $T_4$	Compression ratio, $\lambda$	Reservoir fill pressure	Driver fill pressure	Piston mass
-	mm	MPa	K		MPa	kPa	kg
X2-LWP-2.0 mm-0	2.0	27.9	2,700	30	6.85	92.8	10.5
X2-LWP-2.5 mm-0	2.5	35.7	3,077	40	6.08	77.2	10.5

All test conditions discussed in this chapter use a simulated Uranus entry test gas composition of 85% $\text{H}_2$ /15% $\text{He}$  (by volume) based on values from the work of Conrath et al. [273] which were found from Voyager fly-by measurements. They found a helium mole fraction in the upper troposphere of Uranus (where methane is insignificant) of  $0.152 \pm 0.033$ . For this work, the mole fraction has been assumed to be 0.15 based on this measurement. This same gas composition was also used by Palmer et al. [71] for their simulations and Cruden and Bogdanoff [72, 73] for their experiments in the EAST facility at NASA Ames. Separate Saturn

entry simulations have not been performed due to the fact that the percentage of helium in both atmospheres are very similar. Conrath and Gautier [274] gave a range for the possible helium percentage in Saturn's upper atmosphere of 9.9 to 13.8% (by volume) due to the large uncertainties in their approach, and Cruden and Bogdanoff performed Saturn entry experiments using an 89% $H_2$ /11% $He$  (by volume) test gas [72, 73]. Simulations by the authors of this paper found that Uranus and Saturn entry results were very similar, and the results in this chapter could therefore also be applied to Saturn entry.

Stagnation enthalpy ( $H_t$ ) is used to compare the performance of all test conditions in this chapter because it gives a measure of energy contained in a gas due to both its gas state *and* velocity. It is normally calculated for planetary entry using only the velocity component because the static enthalpy ( $h - h_0$ ) at true freestream temperatures ( $T_\infty \approx 200$  K) is insignificant compared to the kinetic enthalpy. For example, for the proposed 22.3 km/s Uranus entry, less than 1% of the stagnation enthalpy is due to static enthalpy. This is not true of expansion tube test flows, where the test gas freestream temperature can be several thousand kelvin, and the flow may be partially dissociated. The fact that expansion tube test flows can have significant energy stored as static enthalpy means that  $H_t$  for an expansion tube at a given velocity generally corresponds to a slightly higher true flight velocity, which is referred to as the 'flight equivalent velocity' ( $U_e$ ). This is shown in Equation 6.1.

$$H_t = (h - h_0) + \frac{U_\infty^2}{2} = \frac{U_e^2}{2} \quad (6.1)$$

While stagnation enthalpy can be theoretically maximised by minimising the acceleration tube fill pressure ( $p_5$ ), the following analysis limits  $p_5$  to 0.5 Pa or above of air for several reasons: Operationally, it can be difficult to maintain the pressure in the acceleration tube below 0.5 Pa for long enough to perform an experiment; the low fill pressure results in very low post shock pressures which make it difficult to obtain accurate shock speed measurements for the conditions; low density shock tube or 'Mirels' effects [106, 107, 108], which cause shock attenuation and over-expansion of the test gas, also become more pronounced when extremely low acceleration tube fill pressures are used.

Binary scaling is generally used to perform planetary entry experiments in X2 because it is a relatively small facility with a 201.8 mm nozzle exit diameter. Due to the boundary layer which builds up along the length of the tube, the useful core flow (and maximum model diameter used) is normally around 100 mm. Depending on the scale of the vehicle to be tested, this means that X2 must reproduce the flow condition at densities typically 5 to 10 times higher than in flight, and its driver has sufficient performance to allow it to perform binary scaled experiments for many useful mission profiles. For example, the 400 mm diameter Hayabusa re-entry capsule

was tested in X2 at 1/5 scale [81]. However, for gas giant entry conditions, where recreating the flow stagnation enthalpy becomes difficult, there may be insufficient performance to also binary scale the test conditions. This can be ameliorated by binary scaling the *post-shock*  $\rho \cdot L$  product over the test model between the two gas flows instead of the freestream one, because due to the elevated temperature of an expansion tube test flow, the freestream Mach number is lower [275]. For example, for the proposed 22.3 km/s Uranus entry test condition [68], using a freestream temperature of 200 K, the freestream Mach number is 22, whereas a representative X2 expansion tube condition with the same  $H_t$  would have a freestream Mach number around 10. This means that less total pressure is lost across the bow shock in an expansion tube, and as such, the same post-shock density can be generated from a lower density freestream [275]. For this reason post-shock density is compared in this paper.

### 6.3.1 Conditions Without a Secondary Driver

Without a secondary driver section, there are three main facility variables which control the resulting flow condition. The driver condition itself, which consists of the driver gas fill pressure, temperature, and composition, the air reservoir fill pressure, piston mass, and any orifice plates at the area change; the shock tube fill pressure ( $p_1$ ); and the acceleration tube air fill pressure ( $p_5$ ). This section analyses how changes in these variables affect the performance of the facility as a whole.

Fig. 6.1a shows how changes in driver condition, shock tube fill pressure ( $p_1$ ), and acceleration tube fill pressure ( $p_5$ ) influence the stagnation enthalpy ( $H_t$ ) of the test flow and Fig. 6.1b shows how the same changes affect the equilibrium post-normal shock density over the test model ( $\rho_{10e}$ ). Two driver conditions and four acceleration tube fill pressures are considered, and the shock tube fill pressure is varied.

In Fig. 6.1a, it can be seen that performance in terms of stagnation enthalpy is maximised and the equilibrium post-shock density ( $\rho_{10e}$ ) is minimised when  $p_5$  is set to the minimum value (0.5 Pa) and the more powerful driver is used (X2-LWP-2.5 mm-0). There is a single  $p_1$  value which gives maximum performance for each curve, but across the full range of  $p_1$  values shown in Fig. 6.1a, there is minimal variation in performance for each combination. However, looking at Fig. 6.1b it can be seen that  $\rho_{10e}$  rises monotonically with both  $p_1$  and  $p_5$ , showing that high  $H_t$  and  $\rho_{10e}$  are incompatible objectives.

This can be explained by examining the unsteady expansion equation from Cantwell [276] (Equation 6.2), where subscripts refer to gas states in Fig. 5.1.

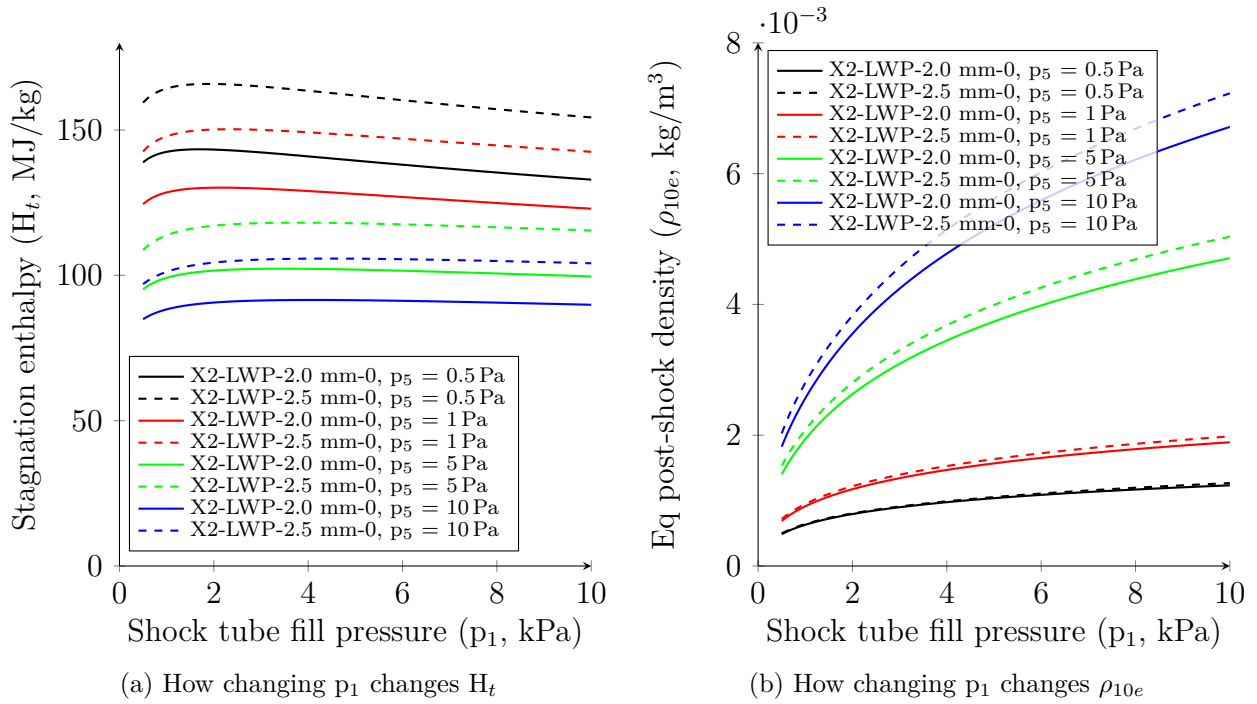


Figure 6.1: Effect of shock tube fill pressure ( $p_1$ ) on conditions without a secondary driver.

$$V_7 = V_2 + \frac{2a_2}{\gamma_2 - 1} \left[ 1 - \left( \frac{p_7}{p_2} \right)^{\frac{\gamma_2 - 1}{2\gamma_2}} \right] \quad (6.2)$$

Since the shocked test gas is initially supersonic, it gains velocity and total enthalpy through the unsteady expansion process by reducing pressure and temperature. This means that stagnation enthalpy can only be gained by reducing pressure, and with that, density. The reducing temperature also has an effect on the density, but its effect is much less pronounced because it reduces by at most an order of magnitude, whereas the pressure typically reduces by several orders of magnitude. This loss in density is then propagated through the facility's nozzle and through the normal shock calculation in the test section.

The analysis shows that to achieve maximum stagnation enthalpy for each driver condition, the minimum acceleration tube fill pressure of 0.5 Pa is required. The optimum shock tube fill pressure occurs around 2 kPa for both drivers when  $p_5 = 0.5$  Pa, and therefore  $p_1 = 2$  kPa was chosen for both drivers, giving theoretical stagnation enthalpies of 143 MJ/kg for X2-LWP-2.0 mm-0 and 166 MJ/kg for X2-LWP-2.5 mm-0.



### 6.3.2 Conditions With a Secondary Driver

The shock heated secondary driver is a section of typically helium gas placed between the primary driver and the shock tube to increase shock strength through the test gas [1]. The use of a secondary driver section adds another facility variable, the secondary driver fill pressure,  $p_{sd1}$ . This subsection examines how a secondary driver can be used to augment the performance of the facility for gas giant entry simulation.

Physically, considering the X2 schematic shown in Fig. 5.1, when the secondary driver is used, what is labelled as the shock tube on the figure becomes the secondary driver, and the first section of the acceleration tube becomes the shock tube. The behaviour and notation is similar to the shock tube part of the position-time diagram in Fig. 5.1, except, by notation, the states would be labelled sd1 (fill state), sd2 (post-shock state), and sd3 (unsteadily expanded driver gas), instead of 1, 2, 3. State sd2 then drives the shock tube gas instead of state 4". This is discussed further in Chapters 4 and 5.

If the shock through the secondary driver is over-tailored, then the shock heated secondary driver gas will be hotter than the unsteadily expanded driver gas, and as it travels at the same pressure and velocity as the original driver gas, it forms a more effective driver than the original unsteadily expanded driver gas. The shock speed in the secondary driver ( $V_{s,sd}$ ) required to give the maximum shock speed in the shock tube can be determined analytically for a perfect gas, and is shown by equilibrium gas numerical simulation here in Fig. 6.2. There is only an advantage in using a secondary driver if the required shock speed in the test gas is much greater than the undisturbed sound speed in the driver. This is discussed further in Morgan [196] and more discussion about secondary drivers can be found in Gildfind et al. [1].

Fig. 6.2 shows the performance of various conditions using both drivers and a secondary driver section. Stagnation enthalpy is shown on the left y-axis of the figure, while the related flight equivalent velocity is shown on the right (both from Equation 6.1). The acceleration tube fill pressure ( $p_5$ ) has been fixed at 0.5 Pa to maximise the unsteady expansion of the test gas for every simulation. Each curve represents a different shock tube fill pressure from 1 to 4 kPa, and the secondary driver fill pressure has been varied from 0.5 to 100 kPa.

In Fig. 6.2 it can be seen that as the shock tube fill pressure increases, a higher  $p_{sd1}$  is required to maximise performance. It can also be seen that maximum stagnation enthalpy increases with decreasing  $p_1$ , theoretically approaching an asymptotic limit with 0 kPa in the shock tube. This occurs because, theoretically, the maximum amount of over-tailoring occurs in the secondary driver with the highest  $V_{s,sd}$ , which occurs when the lowest  $p_{sd1}$  is used. However, if  $p_{sd1}$  is too low for the related shock fill condition (state 1), the post-shock pressure

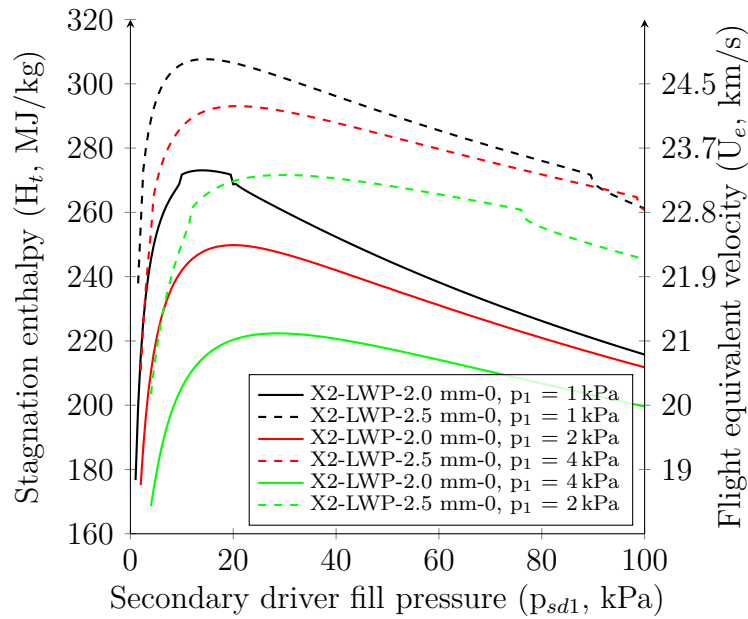


Figure 6.2: Effect of secondary driver fill pressure ( $p_{sd1}$ ) on performance for different test conditions with a set  $p_5$  value of 0.5 Pa.

in the secondary driver ( $p_{sd2}$ ), will not be large enough to adequately drive the shock in the shock tube, and the related  $V_{s,1}$  value will be lower. Conversely, if  $p_{sd1}$  is too high for the related shock tube fill condition, the performance will drop because the optimum  $p_{sd1}$  value has not been used. Using  $p_1$  values as close to zero as possible is impractical because if  $p_1$  is reduced too far, the condition will have insufficient test gas to produce a usable test flow, wall boundary layer effects become more significant, and the conditions become operationally more challenging. Also, residual air contamination prior to filling is particularly problematic with low  $p_1$  values for  $H_2/He$  experiments because the test gas is very light. An 85% $H_2$ /15% $He$  (by volume) Uranus test gas mixture contaminated with 1% air (by volume) is 14% more dense than a pure mixture, which would affect performance and the quality of the experiment itself.

For these reasons, 2 kPa was also chosen as the  $p_1$  value for both secondary driver conditions as a compromise between performance and test flow quality. This could be modified as required for future experiments, but it provides a reasonable starting point.

Now that a  $p_1$  value of 2 kPa has been selected for the conditions,  $p_{sd1}$  values need to be selected. In Fig. 6.2 it can be seen that for both conditions performance is approximately maximised (within 0.4% of the maximum) for  $p_{sd1} = 15$  to 25 kPa. A  $p_{sd1}$  value of 25 kPa was selected for X2-LWP-2.0 mm-0, and 21 kPa was selected for X2-LWP-2.5 mm-0, corresponding to stagnation enthalpies of 249 MJ/kg and 293 MJ/kg respectively. These correspond to flight equivalent velocities of 22.3 and 24.2 km/s respectively, meaning that the proposed 22.3 km/s

Uranus entry [68] could theoretically be simulated in X2 with a secondary driver.

Fig. 6.3 shows the related post-shock densities over the test model ( $\rho_{10e}$ ) for the conditions shown in Fig. 6.2 where  $p_1 = 2$  kPa. While X2's contoured nozzle allows larger models to be used, more density is lost through the steady expansion than is gained in the reduced scaling factor, so the nozzle actually reduces the achievable  $\rho \cdot L$  product. To show the effect of this, results are shown both with and without the nozzle expansion. In the maximum performance region where  $p_{sd1}$  ranges from around 20 to 25 kPa, the density remains fairly constant for both driver conditions with and without the nozzle. With the nozzle,  $\rho_{10e}$  is around  $4.4 \times 10^{-4}$  kg/m<sup>3</sup> for X2-LWP-2.0 mm-0 and  $3.3 \times 10^{-4}$  kg/m<sup>3</sup> for X2-LWP-2.5 mm-0, which are both the same order of magnitude as the equilibrium post-shock density for the first Uranus entry point analysed by Palmer et al. [71] ( $2.52 \times 10^{-4}$  kg/m<sup>3</sup> from a calculation performed by the authors in Section 6.5) showing that these flow conditions would not be suitable for binary scaled experiments in X2. Without the nozzle,  $\rho_{10e}$  is around  $2.4 \times 10^{-3}$  kg/m<sup>3</sup> for X2-LWP-2.0 mm-0 and  $1.8 \times 10^{-3}$  kg/m<sup>3</sup> for X2-LWP-2.5 mm-0, an order of magnitude higher than the results using the nozzle. A test model half the size would be required if the nozzle wasn't used. However, the  $\rho \cdot L$  product would still be higher, meaning it would be more likely that binary scaled experiments could be performed.

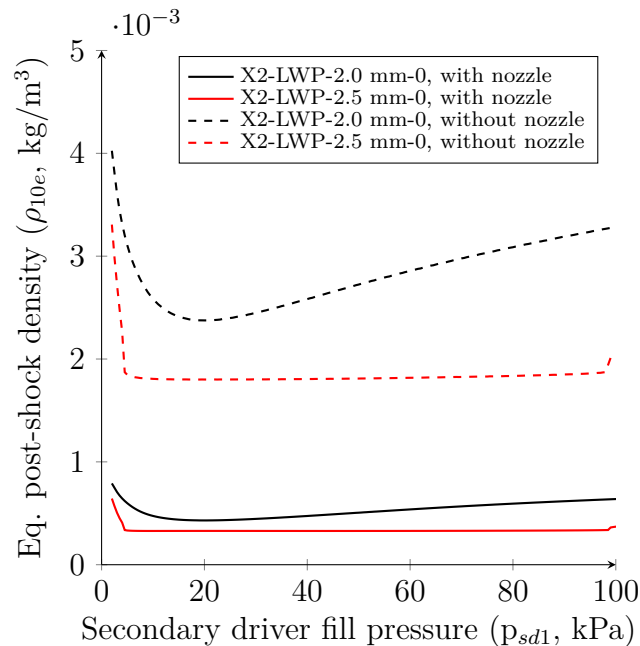


Figure 6.3: Effect of secondary driver fill pressure ( $p_{sd1}$ ) on  $\rho_{10e}$  for both drivers when  $p_1 = 2$  kPa. Results are shown both with and without X2's nozzle.

The flat density seen in Fig. 6.3 using X2-LWP-2.5 mm-0 appears to be non-physical, and is probably caused by an issue with the CEA backed equilibrium gas model [197, 198]. While

the temperature of the test gas never reaches the 20,000 K maximum temperature in CEA, the temperature of the shocked accelerator gas (state 6) may reach this temperature for high velocity conditions like this, causing the code to use a gas state which may not be physical. When the pressure and velocity are matched across the contact surface in the acceleration tube to find the acceleration tube shock speed ( $V_{s,2}$ ), this error would then be transmitted to the unsteadily expanded test gas. It is not expected that this would have a large effect on the test gas as it remains below 20,000 K, but it should still be noted.

### 6.3.3 Chosen Conditions

It was chosen to only examine conditions using the more powerful driver condition (X2-LWP-2.5 mm-0). Table 6.2 shows the details of the test conditions labelled with a naming convention which includes the name of the facility ('X2'), the entry simulated ('GG-UE' for gas giant and Uranus entry), the driver condition (2.5 mm), and a signifier for the secondary driver if it is used ('SD').

Table 6.2: Final details of the chosen test conditions.

Test condition ID	Driver condition	Secondary driver fill pressure (He, kPa)	Shock tube fill pressure (85%H <sub>2</sub> /15%He, by volume, kPa)	Acceleration tube fill pressure (Air, Pa)	Theoretical stagnation enthalpy (MJ/kg)
X2-GG-UE-2.5 mm	X2-LWP-2.5 mm-0	not used	2.0	0.5	166
X2-GG-UE-2.5 mm-SD	X2-LWP-2.5 mm-0	21.0	2.0	0.5	293

## 6.4 Experimental Results

This section presents experimental results for the test conditions shown in Table 6.2. An instrumented Pitot rake was used to measure the nozzle exit pressure, core flow size, and experimental test time of the conditions. The Pitot rake uses nine impact pressure probes, which are 15° half-angle conical probes for these experiments, spaced 17.5 mm apart radially relative to the nozzle exit plane, covering a total centre-to-centre height of 140 mm. The middle probe ('pt5') was oriented with the centre-line of the nozzle.

The naming conventions used here are the same as that which is used in Section 5.5. Each experimental shock speed, for example 'sd1-sd3', is a reference to the two specific tube wall pressure sensor locations used to find that particular shock speed value. Where experimental shock speeds are shown in figures, the values are shown at the midpoint between the two sensor locations. Where experimental pressure measurements are shown, the names either correspond to wall pressure sensor locations or locations within the X2 Pitot rake. (Approximate X2 wall

pressure sensor locations are shown in Fig. 5.1 and exact values from Gildfind et al. [232] can be found in Table 4.2.)

Experimental shock speed uncertainties were found using the uncertainty calculation procedure described in Appendix G. Experimental pressure measurements presented here were processed as follows: data was filtered with a 6th order lowpass filter with a cutoff frequency of 100 kHz; the mean of the steady pressure duration after shock arrival for the relevant signal was taken; the mean of the noise taken just before shock arrival was subtracted. The uncertainties on the pressure measurements were found using a 95% confidence interval (CI) on the standard deviation of the filtered experimental data.

In this section, shock speeds are used to compare the performance between theoretical predictions from PITOT and experimental data. Shock speeds can be measured non-intrusively, and if shock speeds match between experiment and simulation, it generally indicates that overall wave processes are being simulated accurately.

Due to the fact that hydrogen is a combustible gas, a special procedure for evacuating the gas from the tube during the filling of mix gas bottles and after each experiment was developed. The procedure and some notes about hydrogen safety can be found in Appendix J. A risk assessment for using the gas was also made and added to the university's risk assessment system.

### 6.4.1 Test Condition without Secondary Driver (X2-GG-UE-2.5 mm)

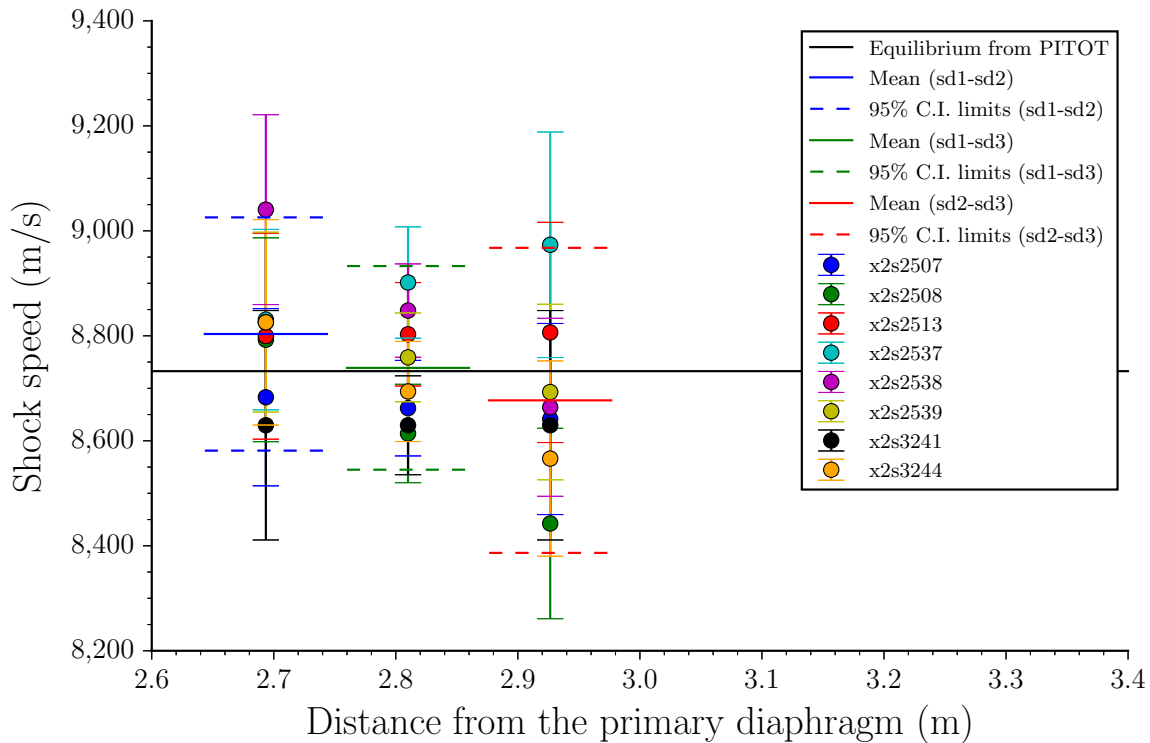
Two sets of experiments were performed to characterise test condition X2-GG-UE-2.5 mm. The first set of experiments were performed in July 2014 before various upgrades of the facility instrumentation were performed, and initial analysis of these experiments was partly the reason for the upgrades. The last two experiments for this condition (x2s3241 and x2s3244) were performed in August 2016 after the upgrades. Final condition characterisation has been carried out using one of the latter experiments. The facility configuration details of the test condition can be found in Table 6.3. The experimental shock and acceleration tube shock speed data from both experimental campaigns is presented in Figs. 6.4 and 6.5 respectively.

Fig. 6.4 shows the experimental shock tube shock speeds with the mean and 95% CI also shown for each calculated value. The predicted shock speed is 8,733 m/s using PITOT's equilibrium solver. It can be seen on the figure that all of the experimental data is inside the 95% CI for each value and contains no outliers. Therefore it can be concluded that the mean values are representative of the experimental data. It can be seen that the two experiments from the second experimental campaign, x2s3241 and x2s3244, are consistent with the first campaign.

Table 6.3: Facility configuration details of condition X2-GG-UE-2.5 mm.

Driver condition	X2-LWP-2.5 mm-0 [231, 230, 2]
Primary driver fill condition	77.2 kPa He
Primary diaphragm	1 x 2.5 mm thick cold rolled steel, scored diaphragm
Orifice plate diameter	65 mm
Shock tube fill condition	2.0 kPa 85% $H_2$ /15% $He$ (by volume) Uranus entry test gas
Secondary diaphragm	1 x $\approx 14 \mu m$ thick aluminium foil sheet
Acceleration tube fill condition	0.5 Pa laboratory air

It can also be seen that the experimental mean shock speeds are very similar to the equilibrium theoretical values, for example, there is a difference of 0.07% between the mean ‘sd1-sd3’ experimental value and the result from PITOT.

Figure 6.4: Experimental shock tube shock speeds ( $V_{s,1}$ ) for condition X2-GG-UE-2.5 mm.

While the mean values shown in Fig. 6.4 are statistically consistent, with no individual values which would be classed as outliers, some variation in shock speed can be seen both for the same experiments along the tube and between experiments at some transducer pairs. The mean value for every shock speed location shown in Fig. 6.4 is 8,740 m/s, and the minimum and maximum nominal values are 8,440 m/s and 9,040 m/s respectively. These three values are 0.08% above, 3% below, and 4% above the equilibrium value from PITOT respectively.

It is worth considering the effect of these variations on the flow condition downstream in the acceleration tube. If  $V_{s,1}$  is set to each of these shock speeds, a large change in performance is predicted using PITOT. The theoretical acceleration tube shock speed,  $V_{s,2}$ , varies from 17,100 to 18,600 m/s, and the subsequent stagnation enthalpy varies from 153 to 181 MJ/kg (a change in flight equivalent velocity from 17,500 to 19,000 m/s). These are non-trivial variations in the overall flow condition.

Fig. 6.5 shows the experimental acceleration tube shock speeds. The global mean and 95% CI are also shown for each shock speed. The predicted acceleration tube shock speed for this condition is 17,830 m/s. Focusing on the end of the acceleration tube, the global mean experimental shock speeds are  $19,300 \pm 400$  m/s for ‘at4-at5’,  $17,800 \pm 300$  m/s for ‘at5-at6’, and  $18,500 \pm 200$  m/s for ‘at4-at6’. It can be seen that the two experiments from the second experimental campaign, x2s3241 and x2s3244, are consistent with the first campaign. It can also be seen that PITOT’s equilibrium solver actually under-predicts the mean experimental ‘at4-at6’ value by around 4%. The mean shock speed appears to be falling at the end of the last set of sensors, and then again at the end of the second. However, it is hard to conclude trends with large individual uncertainties, large variation, and only three experimental shock arrival times in each set.

While the uncertainties for some of the mean  $V_{s,2}$  values discussed in the last paragraph are not large, in Fig. 6.5 it can be seen that the uncertainties on the individual measurements are relatively large. The mean, minimum, and maximum uncertainties for all of the data shown on the figure are  $\pm 800$  m/s,  $\pm 100$  m/s, and  $\pm 3,000$  m/s respectively, 5%, 0.8%, 17% of the nominal theoretical values. These large uncertainties make it difficult to decisively conclude the state of the gas in the acceleration tube for each experiment, and because of that, what later occurs in the nozzle and test section. When the shock tube variation was discussed above, it was found that it could cause a theoretical acceleration tube shock speed variation of 1,500 m/s, from 17,100 to 18,600 m/s, and considering the experimental data in Fig. 6.5, the various measurements and their associated uncertainties extend further than this range. This also makes it difficult to ascertain whether the source of the uncertainty is the shock tube or the acceleration tube.

It is worth considering what is causing the large uncertainties seen in Fig. 6.5. The uncertainty is calculated using the formula which is discussed fully in Appendix G, but in summary: A shock arrival range is selected manually by the experimenter. The midpoint is taken as the shock arrival time, and half of the full range is added as a time uncertainty. The total uncertainty includes the shock arrival uncertainty for each sensor, a distance uncertainty for each sensor location, and a conservative sampling rate uncertainty of the size of a full sample. The default sampling rate of X2’s data acquisition system (DAQ) is 2.5 MHz, which is the maximum

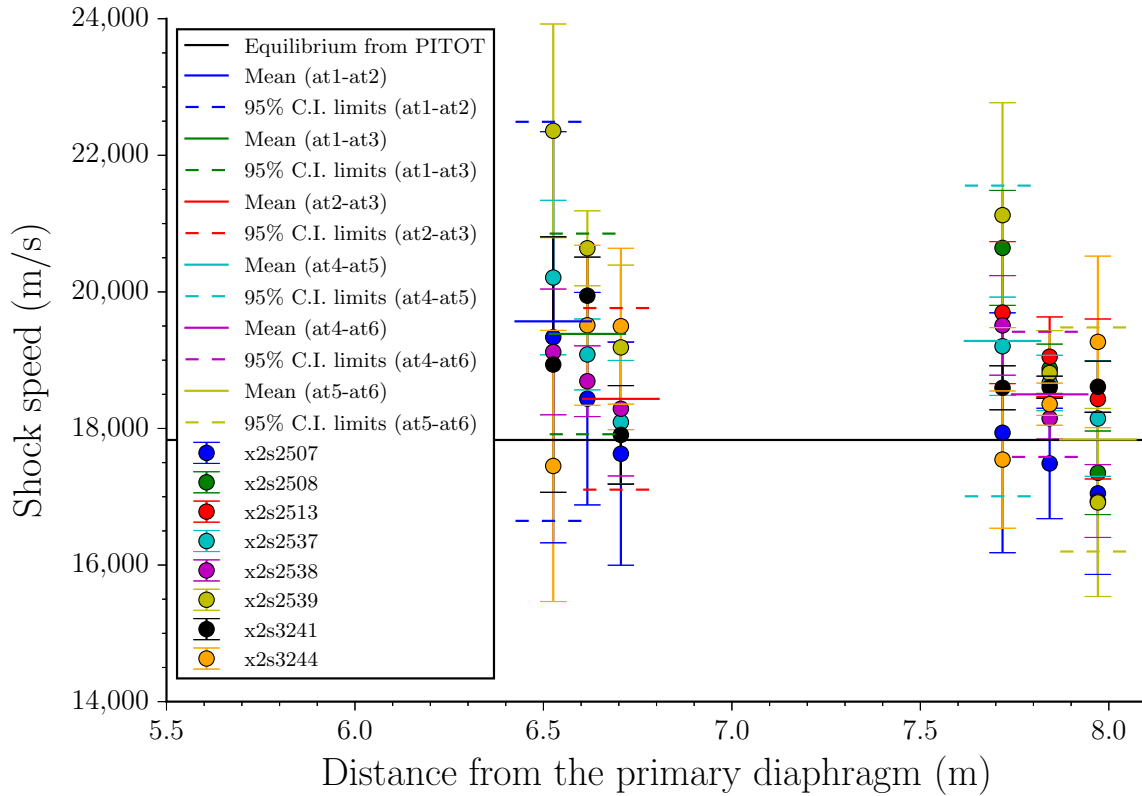


Figure 6.5: Experimental acceleration tube shock speeds ( $V_{s,2}$ ) for condition X2-GG-UE-2.5 mm from both the first and second experimental campaigns.

sampling rate of the DAQ hardware, corresponding to one sample every  $0.4 \mu\text{s}$ . The other issue is uncertainty in the shock arrival time at each sensor location due to the low post-shock static pressure for these conditions (of the order of a kilopascal), which is less than 1% of the range of the 50 psi ( $\approx 350 \text{ kPa}$ ) pressure transducers currently used on the wall in X2's acceleration tube [277]. It would be preferable to use more sensitive transducers, however, the high pressure unsteady expansion and driver gas which follows the test gas down the tube requires the use of relatively high range transducers.

The large uncertainties seen in Fig. 6.5 mainly show that this sampling rate is not fast enough for performing these experiments in a facility of this size. For example, considering shock speed 'at4-at6' calculated using the 2.5 MHz data for experiment x2s3244, the total uncertainty is 2.6%. If each of the components of the uncertainty are considered separately, the contributions from the shock arrival uncertainty (which is related to the sample size), the sampling rate, and the distance uncertainty are 2.1, 1.5 and 0.6% respectively. To reduce the sampling rate issue and aid in better selecting the shock arrival time for these experiments, a 60 MHz data acquisition card was installed for the second experimental campaign and used to



measure the acceleration tube wall pressure traces for experiments x2s3241 and x2s3244. When the example shock speed is re-calculated using the 60 MHz data, the total uncertainty is 1.8%, and the contributions from the shock arrival uncertainty, the sampling rate, and the distance uncertainty are 1.7, 0.06 and 0.6% respectively. Showing that the uncertainty for the 60 MHz data is instead dominated by uncertainty in determining the shock arrival time.

Referring to Fig. 6.5 and considering the experimental data from the second campaign, it can be seen that because of this uncertainty in determining the shock arrival time, recording the acceleration tube signals at 60 MHz did not consistently reduce the shock speed uncertainties. For example, the ‘at4-at5’ uncertainty for experiment x2s2513, which was sampled at 2.5 MHz, is  $\pm 1,000$  m/s; the same uncertainty for experiment x2s3241, with the 60 MHz sampling is  $\pm 300$  m/s. However, the ‘at4-at5’ uncertainty for experiment x2s3244 is also  $\pm 1,000$  m/s. These two wall sensors (‘at4’ and ‘at5’) are spaced 256 mm apart, whereas sensors ‘at4’ and ‘at6’ are spaced 506 mm apart. This shows that even with the 60 MHz card, uncertainty in determining the shock arrival time and the assigned distance uncertainty when sensors are closely spaced can still lead to large uncertainties.

All of these related uncertainties come from the compromises involved in measuring time-of-flight shock speeds. Larger sensor spacing gives lower uncertainties, and in an ideal case, it would be preferable. However, generally shock waves attenuate with distance, and the larger spacing gives an average value which can’t be used to measure attenuation. X2’s acceleration tube is also made up of a series of sections connected by collars and capstans, meaning that the exact length between sensors mounted on different physical sections can slightly change with time, making it hard to average over the whole acceleration tube with complete certainty.

The final issue is the sensor response time. The shock arrival times presented here were found manually using a range which indicated when the shock arrival occurred. Any uncertainty in the shock arrival time was added as a time uncertainty on the related shock speed calculations, which in some situations was what led to uncertainties not decreasing with the higher sampling rate. The quoted response time of the pressure transducers used is  $>2 \mu\text{s}$  [277], meaning that for a 1 kPa step change, they will reach 0.63 kPa (63% of the input) after  $2 \mu\text{s}$ , and faster response will be determined by the noise on the signal. The size of a single sample for the 60 MHz data is 16.66 ns. If the response is modelled as a first order system with a time constant of  $2 \mu\text{s}$  responding to a 1 kPa step change, its initial response will have a linear slope of  $1 \text{ kPa}/2 \mu\text{s}$  (due to the time constant of  $2 \mu\text{s}$ ). To respond in 16.66 ns, the system must be able to sense a change in pressure of 8.33 Pa, which is 0.0023% of the sensor range, or around 0.115 mV of raw signal. This would be impossible to sense with the current shock detection system.

The influence of shock speed uncertainties on the final test flow is considered in Section 5.5.

The technique calculates a nominal case and solution bounds by assuming that the uncertainty on the fill pressures are small and that the mean uncertainties on the mean experimental shock speeds in each section of the facility can be used to find the test section state using an experimental equilibrium version of PITOT. A sensitivity analysis is performed by perturbing the calculation using every permutation of the shock speeds with their mean uncertainties. The nominal case is the result using the mean shock speeds, and the solution bounds are the minimum and maximum of each quantity from all of the permutations of the shock speeds.

The sensitivity analysis is calibrated to scale the experimental tube wall static pressure at the entrance to the nozzle and the nozzle exit impact pressure within the uncertainty of the overall solution. This is achieved by running the sensitivity analysis with several different settings to find the best match for both the experimental shock speeds, and tube wall and test section pressure data. The major settings used to change the results of the sensitivity analysis are discussed in detail in Section 5.5, but a short summary of them is provided here. Firstly, the nozzle entrance state (state 7) is influenced by two factors: the first is whether a reflected shock of non-negligible effect is deemed to have occurred at the secondary diaphragm or not, and if so, the strength of that reflected shock; the second is to determine what state the shocked test gas unsteadily expands to in the acceleration tube. Generally, due to Mirels effects [106, 107, 108] the test gas over-expands in the acceleration tube, reaching a lower pressure and higher velocity than would be expected from ideal shock tube theory. The limiting case is when the shocked test gas unsteadily expands to the shock speed in the acceleration tube (i.e.  $V_7 = V_{s,2}$ ). Then moving into the test section, a decision must be made about what area ratio to use for the steady expansion through the facility's nozzle. Due to boundary layer build up along the acceleration tube, and further boundary layer growth through the nozzle, often an 'effective' area ratio is required instead of the actual geometric one.

It was decided to use this method to quantify the test section state of experiment x2s3244 from the second experimental campaign. While this experiment has higher calculated shock speed uncertainties than experiment x2s3241 it was chosen to show how this method can be successfully applied for conditions with higher acceleration tube shock speed uncertainties. The mean  $V_{s,1}$  and  $V_{s,2}$  values for x2s3244 are  $8,700 \pm 100$  m/s and  $18,700 \pm 400$  m/s respectively.

For experiment x2s3244, the mean experimental unsteadily expanded test gas pressure ( $p_7$ ) is  $1.2 \pm 0.1$  kPa. The  $p_7$  range from the sensitivity analysis *without* a reflected shock at the secondary diaphragm, and with the shocked test gas (state 2) unsteadily expanded to  $V_{s,2}$ , is 0.28 to 0.76 kPa, which is too low. If instead the shocked test gas is expanded to the ideal gas velocity in the acceleration tube (i.e.  $V_7 = V_6$ ), the pressure range is 0.68 to 1.4 kPa, which is consistent with the experimental data. However, due to the low acceleration tube fill pressure ( $p_5 = 0.5$  Pa), it is expected that  $V_6$  would be closer to  $V_{s,2}$ . It is therefore likely

that the reflected shock has non-negligible effect. Comparing the theoretical minimum time for the mean experimental  $V_{s,1}$  and  $V_{s,2}$  values to reach the wall sensors in the acceleration tube against the experimentally measured shock arrival times gives an estimated delay of around  $60\ \mu\text{s}$ , some of which would be a hold time at the secondary diaphragm, meaning that a non-negligible reflected shock would be expected. With a fully reflected shock at the secondary diaphragm, and with the shocked test gas unsteadily expanded to  $V_{s,2}$ , the  $p_7$  range is 0.78 to 1.6 kPa. This range is consistent with the experimental data so it was decided to use these settings to find the test section state.

Fig. 6.6 shows the experimental test section  $15^\circ$  half-angle cone pressure ( $p_{10c}$ ) data for experiment x2s3244. The data has been filtered using a 6th order lowpass filter with a cut off frequency of 100 kHz, with the unfiltered data shown behind it using a lower opacity. Sensor ‘pt5’ is not shown because another type of probe was mounted in that location for another experiment. There is a region of quasi-steady pressure for around  $73\ \mu\text{s}$  after flow startup and this is identified on the figure. Sensor ‘pt8’ appears to not be working properly as its pressure signal rises when the flow arrives but then quickly falls. Sensors ‘pt1’ and ‘pt9’ record lower pressures, indicating that they are outside the core flow of the test condition; giving a core flow of around 122.5 mm considering the geometry of the Pitot rake. For these reasons, sensors ‘pt1’, ‘pt5’, ‘pt8’, and ‘pt9’ have not been used to calculate the mean  $15^\circ$  half-angle cone pressure. The mean  $p_{10c}$  value during the test time using the remaining sensors is  $2.1 \pm 0.2$  kPa. Using a fully reflected shock at the secondary diaphragm and with the shocked test gas unsteadily expanded to  $V_{s,2}$ , choosing an effective nozzle area ratio of 3.5 gave the best match with the experiment data, with a nominal  $p_{10c}$  value of 2.0 kPa which is consistent with the experimental data. There appears to be pressure variation in space during the test time, with the minimum value being ‘pt4’ with a  $p_{10c}$  value of  $1.6 \pm 0.3$  kPa and the maximum being ‘pt2’ with a value of  $2.5 \pm 0.5$  kPa. However, as can be seen in Fig. 6.6 where the theoretical values from the sensitivity analysis with an effective area ratio of 3.5 are shown alongside the experimental data, this experimental range is covered by the theoretical  $p_{10c}$  range of 1.6 to 2.5 kPa.

Table 6.4 presents the final condition details in the test section at the nozzle exit (state 8) and post-normal shock at equilibrium (state  $10_e$ ) for experiment x2s3244 using a fully reflected shock at the secondary diaphragm, before unsteadily expanding the shocked test gas to the acceleration tube shock speed, and then steadily expanding the gas through the nozzle using an effective area ratio of 3.5. Both a nominal solution and solution bounds are presented. It can be seen that the state variables,  $p_8$ ,  $T_8$ , and  $\rho_8$ , show the largest variation, with the pressure uncertainty being  $-32\% / +43\%$  and the density uncertainty being  $-22\% / +26\%$ . This shows that the large shock speed uncertainties would potentially prevent scaled testing being performed because the density uncertainties may be too large to get an exact scaled

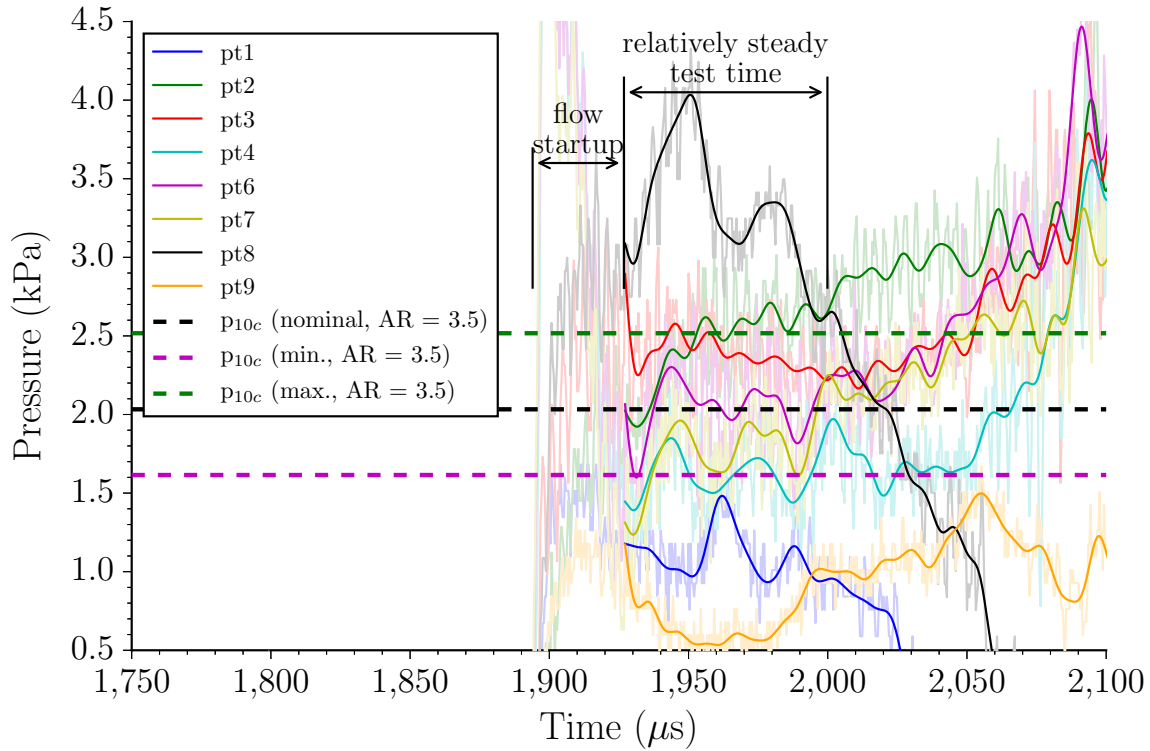


Figure 6.6: Experimental test section  $15^\circ$  half-angle cone pressures ( $p_{10c}$ ) from experiment x2s3244.

value. However, if only stagnation enthalpy and flight equivalent velocity are important, the uncertainties are much smaller, with uncertainties of  $-4.0\%$  /  $+4.1\%$  and  $-2.0\%$  /  $+2.0\%$  respectively.

Table 6.4: Computed test section freestream and post-shock state ranges for experiment x2s3244.

	Nominal	Solution bounds	Uncertainties
State 8 (nozzle exit condition, using an effective area ratio of 3.5)			
Static pressure ( $p_8$ , Pa)	193	130 – 276	$-32\%$ / $+43\%$
Static temperature ( $T_8$ , K)	775	673 – 885	$-13\%$ / $+14\%$
Density ( $\rho_8$ , $\text{kg}/\text{m}^3$ )	$6.92 \times 10^{-5}$	$5.40 \times 10^{-5} - 8.70 \times 10^{-5}$	$-22\%$ / $+26\%$
Velocity ( $V_8$ , m/s)	19,100	18,700 – 19,500	$-2.1\%$ / $+2.1\%$
Mach number ( $M_8$ )	9.61	8.84 – 10.5	$-8.0\%$ / $+9.2\%$
Stagnation enthalpy ( $H_t$ , MJ/kg)	188	180 – 195	$-4.0\%$ / $+4.1\%$
Flight equivalent velocity ( $U_e$ , m/s)	19,400	19,000 – 19,800	$-2.0\%$ / $+2.0\%$
State 10e (equilibrium post normal shock pressure in the test section)			
Static pressure ( $p_{10e}$ , kPa)	23.7	19.1 – 28.7	$-19\%$ / $+21\%$
Static temperature ( $T_{10e}$ , K)	3,870	3,810 – 3,940	$-1.5\%$ / $+1.8\%$
Density ( $\rho_{10e}$ , $\text{kg}/\text{m}^3$ )	$1.01 \times 10^{-3}$	$8.01 \times 10^{-4} - 1.24 \times 10^{-3}$	$-21\%$ / $+23\%$
Velocity ( $V_{10e}$ , m/s)	17,800	17,400 – 18,100	$-2.1\%$ / $+2.1\%$
Mach number ( $M_{10e}$ )	3.35	3.32 – 3.38	$-0.92\%$ / $+0.73\%$

### 6.4.2 Test Condition with Secondary Driver (X2-GG-UE-2.5 mm-SD)

The facility configuration details for test condition X2-GG-UE-2.5 mm-SD can be found in Table 6.5. Similar to test condition X2-GG-UE-2.5 mm (Section 6.4.1), experiments were performed in both experimental campaigns. The experimental shock speed data for the condition from both experimental campaigns are presented in Figs. 6.7, 6.8, and 6.9. Fig. 6.7 presents the secondary driver data, Fig. 6.8 presents the shock tube data, and Fig. 6.9 presents the acceleration tube data.

Table 6.5: Facility configuration details of condition X2-GG-UE-2.5 mm-SD.

Driver condition	X2-LWP-2.5 mm-0 [231, 230, 2]
Primary driver fill condition	77.2 kPa He
Primary diaphragm	1 x 2.5 mm thick cold rolled steel, scored diaphragm
Orifice plate diameter	65 mm
Secondary driver fill condition	21 kPa He
Secondary diaphragm	Initial experiments: 2 x $\approx 14 \mu\text{m}$ thick aluminium foil sheet Later experiments: 1 x 12.5 or 25 $\mu\text{m}$ thick Mylar sheet
Shock tube fill condition	2.0 kPa 85% $\text{H}_2$ /15%He (by volume) Uranus entry test gas
Tertiary diaphragm	1 x $\approx 14 \mu\text{m}$ thick aluminium foil sheet
Acceleration tube fill condition	0.5 Pa laboratory air

Fig. 6.7 shows the experimental secondary driver shock speeds with the global mean and 95% CI bounds also shown for each calculated value. The predicted secondary driver shock speed is 7,386 m/s. Similar to the shock tube shock speeds shown in Section 6.4.1, all data was statistically consistent and very similar to the result from PITOT, for example, with a difference of 0.8% between the global mean ‘sd1-sd3’ experimental value and PITOT.

When the first experimental campaign was performed in July 2014, the shock and acceleration tube performance for this condition was much lower than had been expected. In Section V of James et al. [16] it was proposed that the issues were caused by air contamination in the test gas either from residual air left in the shock tube before filling, leaking during filling, or further leaking before the experiment was conducted. Before the second experimental campaign was performed in August 2016, a helium leak detection system was purchased, and many leaks on the facility were found and fixed. As such, when the second experimental campaign began, it was thought that every section of the facility sealed well.

However, the first three experiments from the second experimental campaign were actually slower than the fastest experiments from the first one. The problem was found to be an issue

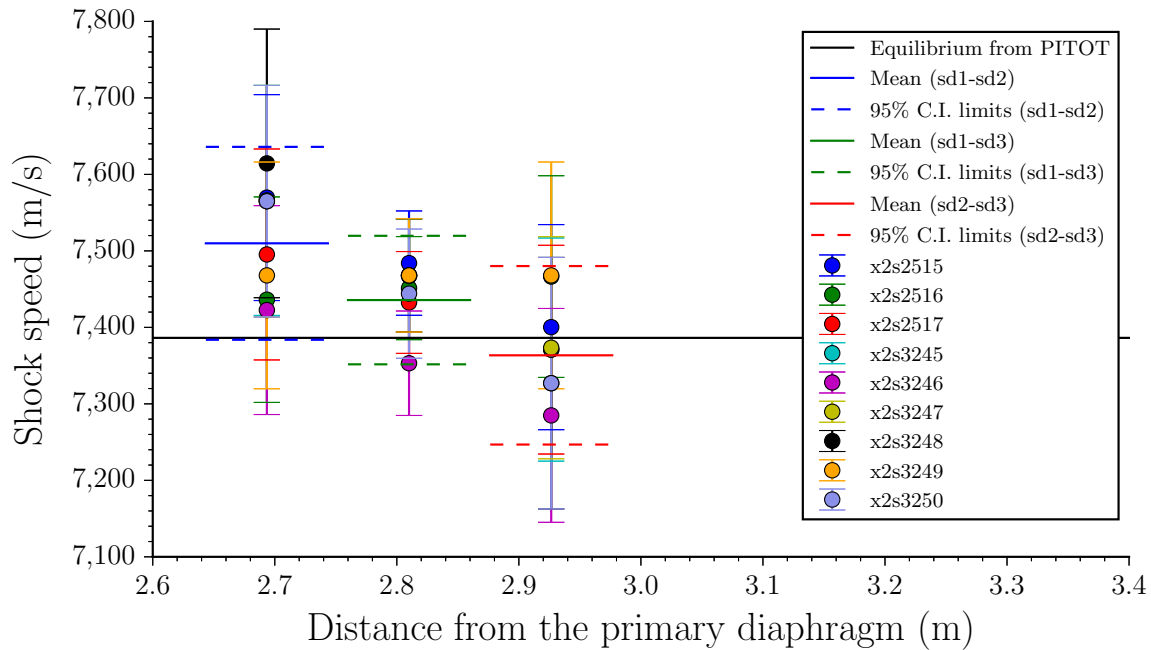


Figure 6.7: Experimental secondary driver shock speeds ( $V_{s, sd}$ ) for condition X2-GG-UE-2.5 mm-SD from the first and second experimental campaigns.

with the two sheets of aluminium foil which were being used as the secondary diaphragm separating the secondary driver and shock tubes. In the experimental procedure, the secondary driver was filled first, causing a leak in the shock tube which would then subsequently jeopardise the experiment. Some static diaphragm testing was performed in situ, and it was found that the single aluminium sheets would rupture statically at around 14 kPa, and that even near the burst pressure, no leak was caused by diaphragm deformation under pressure. However, it was also found that when a double aluminium sheet diaphragm was used with any pressure difference above the static rupture pressure of a *single* diaphragm, the double diaphragm would not burst, but would leak through itself into the adjacent tube. This was seen with both helium and air placed in the secondary driver. After discovering this, the final three experiments for this condition, x2s3248, x2s3249, and x2s3250, were performed with a Mylar secondary diaphragm. Testing showed that Mylar did not leak through itself when filled to the required pressure difference to perform the experiment. x2s3248 and x2s3249 were performed with 12.5  $\mu\text{m}$  thick Mylar diaphragms, and x2s3250 was performed with a 25  $\mu\text{m}$  thick Mylar diaphragm.

Fig. 6.8 presents experimental  $V_{s, 1}$  values for these three final experiments, and much better performance is seen. The predicted shock tube shock speed from PITOT is 10,860 m/s. x2s3248 and x2s3249, using the thinner 12.5  $\mu\text{m}$  thick Mylar diaphragms, show a reduction from the equilibrium theoretical value of around 7%, with both experiments having ‘st1-st3’ shock speeds of  $10,000 \pm 60$  m/s. The condition with the 25  $\mu\text{m}$  thick Mylar diaphragm, x2s3250, is as slow

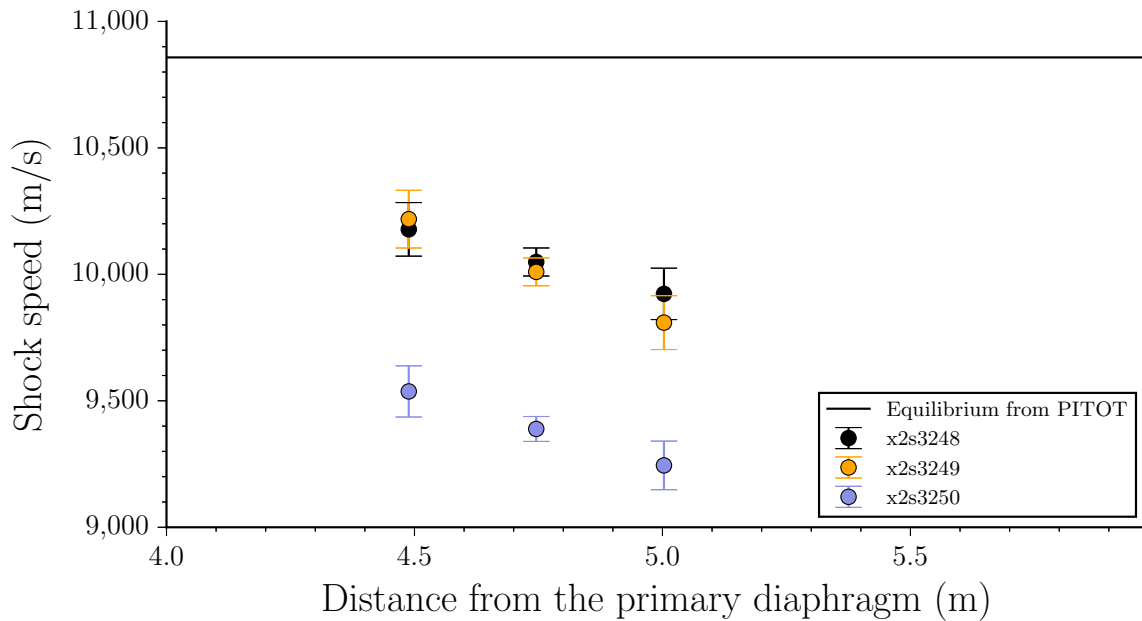


Figure 6.8: Experimental shock tube shock speeds ( $V_{s,1}$ ) for condition X2-GG-UE-2.5 mm-SD from the first and second experimental campaigns.

as the fastest conditions from the earlier experiments, with a percentage reduction from the equilibrium theoretical value of around 10% using its ‘st1-st3’ shock speed of  $9,390 \pm 50$  m/s, showing that losses caused by the mass of the secondary diaphragm may explain the performance loss compared to the theoretical result. At the time that these experiments were performed, the thinnest Mylar material used in the laboratory was the  $12.5 \mu\text{m}$  thick Mylar. Later testing by one of the authors with colleagues from Oxford University for another project [278] found that Mylar diaphragms down to a thickness of  $5 \mu\text{m}$  could be used reliably on X2, with a static burst pressure of around 35 kPa. These diaphragms are recommended for future testing at these conditions.

Fig. 6.9 shows the experimental acceleration tube shock speeds. All shock speeds shown on the figure except the first shock speed near 6.5 m were calculated using data from the high speed 60 MHz oscilloscope card. The predicted acceleration tube shock speed from PITOT is 23,720 m/s, which is also shown on the figure. Due to the fact that the shock tube shock speeds were slower than predicted, the acceleration tube shock speeds would be expected to be slower also, so the predicted equilibrium  $V_{s,2}$  values from semi-theoretical PITOT runs using the nominal ‘st1-st3’ values of 10,000 m/s for experiments x2s3248 and x2s3249, and 9,390 m/s for experiment x2s3250 are also shown. Looking at the values near the end of the acceleration tube, it can be seen that the majority of the values from experiments x2s3248, x2s3249, and x2s3250 are clustered around the semi-theoretical  $V_{s,2}$  value from PITOT using

$V_{s,1} = 9,390$  m/s, and that experiments x2s3248 and x2s3249 have not reached their expected theoretical value, whereas x2s3250 has actually exceeded it by 2% using the ‘at4-at6’ value from the 60 MHz card.

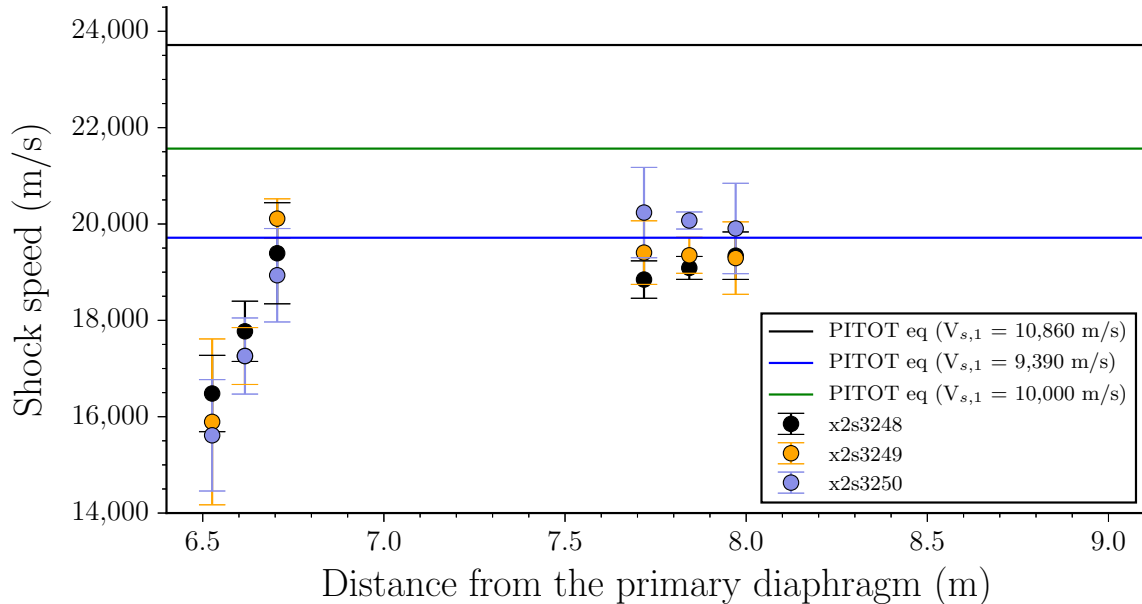


Figure 6.9: Experimental acceleration tube shock speeds ( $V_{s,2}$ ) for condition X2-GG-UE-2.5 mm-SD from the first and second experimental campaigns.

In Section 6.4.1 when the acceleration tube shock speeds were discussed for condition X2-GG-UE-2.5 mm, it was mentioned that the shock speed uncertainties in the acceleration tube for conditions this fast can be quite large, and this is also seen here when individual shock speeds are considered. Using the 60 MHz data, the ‘at4-at5’ and ‘at4-at6’ shock speeds for experiment x2s3248 are  $18,800 \pm 400$  m/s and  $19,100 \pm 200$  m/s respectively. These are relatively small uncertainties. However, when the original DAQ data recording at 2.5 MHz is considered the same shock speeds become  $19,400 \pm 1,000$  m/s and  $19,300 \pm 700$  m/s respectively. The results are quite similar for x2s3249. Its shock speeds are slightly faster and have slightly larger uncertainties, its ‘at4-at6’ shock speed using the 60 MHz data is  $19,300 \pm 400$  m/s, but they are all statistically consistent with the results for x2s3248. The acceleration tube wall pressures for both experiments are also consistent with each other with a pressure of  $2.2 \pm 0.5$  kPa for experiment x2s3248 and  $2.3 \pm 0.3$  kPa for experiment x2s3249 using only the ‘at5’ to ‘at8’ values due to the very short period of steady pressure behind the moving shock wave before that.

Considering experiment x2s3250, due to the large uncertainties using the 2.5 MHz data, it is statistically consistent with x2s3248 and x2s3249, but only for shock speed ‘at5-at6’ using the 60 MHz data, as can be seen in Fig. 6.9. It can also be seen that x2s3250 is faster than the



other two experiments. This is not what would be expected as it had a slower shock tube shock speed by around 5% (see Fig. 6.8). At such low acceleration tube fill pressures ( $p_5 = 0.5$  Pa), the conditions become very sensitive to small changes, because, for example, a change of 0.1 Pa becomes a 20% change in density in front of the acceleration tube shock. Potentially either the fill pressure was lower for x2s3250 or higher for the other two experiments. This is backed up by the fact that x2s3250 has an acceleration tube wall pressure of  $1.6 \pm 0.2$  kPa which is lower than the other two experiments, potentially indicating a lower fill pressure. This is something which can be investigated further in the future when more experiments are carried out.

It was decided to use the same sensitivity analysis technique from Section 5.5 which was used in Section 6.4.1 for X2-GG-UE-2.5 mm to quantify the test section state of this condition using experiment x2s3249. It is not necessary to use the secondary driver shock speed to perform the sensitivity analysis, as the secondary driver functions as an extension of the driver, so it will not be discussed here. The mean  $V_{s,1}$  for experiment x2s3249 is  $10,000 \pm 60$  m/s and the mean  $V_{s,2}$  using wall sensors ‘at4’, ‘at5’, and ‘at6’ is  $19,300 \pm 400$  m/s.

As this condition is similar to condition X2-GG-UE-2.5 mm from Section 6.4.1 it was decided to start the calculation with settings similar to that condition. As such, the first calculations were also performed with a fully reflected shock at the tertiary diaphragm, before unsteadily expanding the shocked test gas to the acceleration tube shock speed (i.e.  $V_7 = V_{s,2}$ ). This gave an unsteadily expanded test gas ( $p_7$ ) pressure range of 3.3 to 4.8 kPa which is higher than the experimental value of  $2.3 \pm 0.3$  kPa. If the reflected shock at the tertiary diaphragm is removed, the  $p_7$  range becomes 2.1 to 3.5 kPa which is consistent with the experimental data. However, this is not likely to be a correct assumption due to the estimated roughly 50  $\mu$ s hold time at the tertiary diaphragm, which was found using the same method discussed in Section 6.4.1 for experiment x2s3244 and is of similar magnitude to the hold time estimated there, where a fully reflected shock was used. There are two other possible solutions, either there is a total pressure loss at the tertiary diaphragm which is causing the gas to expand either from a lower velocity ( $V_2$ ) or lower pressure ( $p_2$ ) (or a combination of the two), or the mean  $V_{s,2}$  being used is too low and the gas is actually unsteadily expanding further than this. Due to the fact that no such total pressure loss was seen for experiment x2s3244 in Section 6.4.1 and that the acceleration tube shock speed uncertainties for this condition are quite large (up to  $\pm 2,000$  m/s using the 2.5 MHz DAQ data), it was decided to consider unsteadily expanding the shocked test gas further. By unsteadily expanding the test gas using an over-expansion factor of 1.08, the effective nominal  $V_{s,2}$  value is 20,900 m/s. The related  $p_7$  range is 1.7 to 2.7 kPa, which is consistent with the experimental data. If this is correct, it would show that potentially the piezoelectric pressure transducers cannot respond quickly enough to the passing shock wave to correctly capture the shock speed. To capture this uncertainty about the state of the test

gas entering the nozzle, the sensitivity analysis was performed again using the permutations of the absolute minimum and maximum experimental shock speeds measured, giving a larger  $p_7$  range of 1.1 to 4.0 kPa

Fig. 6.10 shows the experimental test section  $15^\circ$  half-angle cone pressure ( $p_{10c}$ ) data for experiment x2s3249. The data has been filtered using a 6th order lowpass filter with a cut off frequency of 100 kHz, with the unfiltered data shown behind it using a lower opacity. Once again sensor ‘pt5’ is not shown as a probe was mounted in that location for another experiment. There appears to be a relatively steady test time of 60  $\mu$ s and this is marked on the figure. While the mean  $p_{10c}$  value for all of the sensors except ‘pt5’ and ‘pt8’ is  $2.5 \pm 0.2$  kPa, if individual sensors are considered, there appears to be a large asymmetrical pressure variation during the test time. The minimum value during the test time is ‘pt4’ with a  $p_{10c}$  of  $1.8 \pm 0.6$  kPa and the maximum value is ‘pt2’ with a  $p_{10c}$  of  $3.7 \pm 0.3$  kPa. Interestingly, these are the same two sensors which gave the minimum and maximum individual pressures for experiment x2s3244 in Fig. 6.6, meaning that the asymmetrical pressure variation may be caused by the pressure transducers not responding linearly to the small input pressure. The manufacturer specifications for the transducers state that they should be linear to 1% of full scale [277], which would be 3.45 kPa, meaning that they could have a non-linear response which is causing the behaviour. At this time, it is not possible to conclude if this is the case or not, but further experiments with Pitot pressure probes could be carried out to examine whether or not the pressure variations in space are real.

Using the sensitivity analysis with the more conservative option which was used to find the nozzle inlet conditions, the  $p_{10c}$  range using an effective area ratio of 3.5 (the same as was used in Section 6.4.1) is 2.0 to 4.9 kPa, which is consistent with the variation of the experimental data. This result is also shown in Fig. 6.6.

Table 6.6 presents the final condition details in the test section at the nozzle exit (state 8) and post-normal shock at equilibrium (state  $10_e$ ) for experiment x2s3249 using a fully reflected shock at the secondary diaphragm, before unsteadily expanding the shocked test gas to the acceleration tube shock speed, and then steadily expanding the gas through the nozzle using an effective area ratio of 3.5. Both a nominal solution and solution bounds found using the absolute minimum and maximum experimental shock speeds are presented. Similar to Table 6.4 in Section 6.4.1, in Table 6.6 the state variables show the largest variation (up to 110%), and the stagnation enthalpy and flight equivalent velocity show much less variation (up to 8.2%). However, in Table 6.6 the percentage uncertainties are generally around double the uncertainties which were seen in Table 6.4 for the slower test condition.

Overall, it has been shown that a 20 km/s experiment can be performed in X2, and also

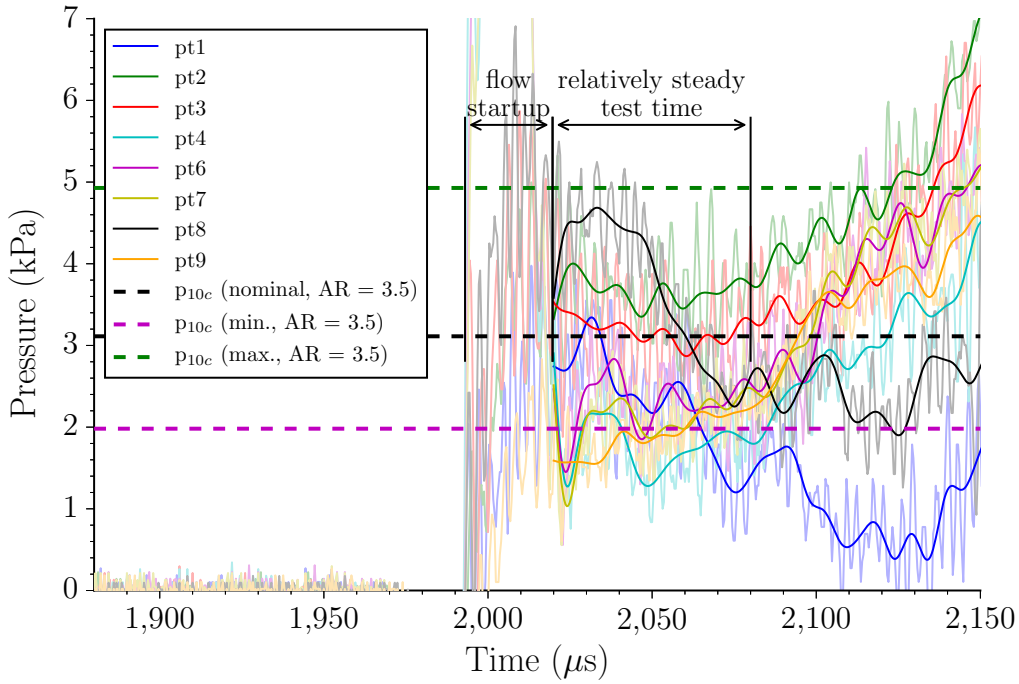


Figure 6.10: Experimental test section  $15^\circ$  half-angle cone pressures ( $p_{10c}$ ) from experiment x2s3249.

Table 6.6: Computed test section freestream and post-shock state ranges for experiment x2s3249.

	Nominal	Solution bounds	Uncertainties
State 8 (nozzle exit condition, using an effective area ratio of 3.5)			
Static pressure ( $p_8$ , kPa)	0.407	0.187 – 0.860	–54% / +110%
Static temperature ( $T_8$ , K)	1,390	1,020 – 1,830	–26% / +31%
Density ( $\rho_8$ , kg/m <sup>3</sup> )	$8.13 \times 10^{-5}$	$5.09 \times 10^{-5} - 1.31 \times 10^{-4}$	–37% / +61%
Velocity ( $V_8$ , m/s)	21,400	20,500 – 22,200	–4.1% / +3.6%
Mach number ( $M_8$ )	8.14	7.09 – 9.70	–13% / +19%
Stagnation enthalpy ( $H_t$ , MJ/kg)	242	222 – 261	–8.2% / +7.8%
Flight equivalent velocity ( $U_e$ , m/s)	22,000	21,100 – 22,900	–4.2% / +3.8%
Pitot pressure ( $p_{pitot}$ , kPa)	34.5	22.8 – 52.5	–34% / +52%
Stagnation pressure ( $p_t$ , MPa)	151	98.4 – 225	–35% / +48%
State 10e (equilibrium post normal shock pressure in the test section)			
Static pressure ( $p_{10e}$ , kPa)	34.6	22.8 – 51.9	–34% / +50%
Static temperature ( $T_{10e}$ , K)	5,240	4,500 – 6,260	–14% / +19%
Density ( $\rho_{10e}$ , kg/m <sup>3</sup> )	$9.96 \times 10^{-4}$	$5.99 \times 10^{-4} - 1.63 \times 10^{-3}$	–40% / +64%
Velocity ( $V_{10e}$ , m/s)	19,600	19,000 – 20,200	–3.5% / +2.7%
Mach number ( $M_{10e}$ )	2.67	2.44 – 3.04	–8.3% / +14%

that the condition may have actually had an acceleration tube shock speed closer to 21 km/s. The condition's nominal flight equivalent velocity is 22 km/s, so it would be almost able to simulate the 22.3 km/s proposed Uranus entry [68], however, due its large uncertainties, its

flight equivalent velocity may actually be anywhere between 21.1 and 22.9 km/s, so it is difficult to conclude its suitability at this time. The post-shock density range is large also, from  $5.99 \times 10^{-4} - 1.63 \times 10^{-3} \text{ kg/m}^3$ , however, the fact that the nominal value ( $9.96 \times 10^{-4} \text{ kg/m}^3$ ) is four times greater than the equilibrium post-shock density for the first Uranus entry point analysed by Palmer et al. [71] ( $2.52 \times 10^{-4} \text{ kg/m}^3$  from a calculation performed by the authors in Section 6.5) shows that without X2's nozzle a modified version of this condition could easily simulate the proposed Uranus entry using binary scaling.

In the future, to help better quantify this condition, a new shock detection system would be required which could respond quickly enough to the passing shock to allow the shock speeds to be found more accurately and with more certainty. Some form of focused optical technique utilising either lasers or photomultiplier tubes which could respond faster than a physical object placed under load would be required. This is also a test condition which should first be tested without the nozzle so that Pitot pressure probes can be used to measure the state of the gas before it enters the nozzle, removing uncertainty associated with the nozzle inlet condition.

## 6.5 Theoretical Expansion Tube Compression Ratio Analysis

X2 is driven in the same manner as a free piston driven shock tunnel [234]. A free piston driven shock tunnel applies an isentropic compression to a lightweight gas (usually helium or a mixture of helium and argon) to greatly improve the performance of the facility's driver section [234]. A diaphragm which ruptures at a set pressure is used to control the compression ratio ( $\lambda$ ) from a set driver fill condition.

Considering as a simplified example the unsteady expansion equation for a shock tube driver without an area change [276] (see Equation 6.3), it can be seen why the free piston compression is advantageous. The degree to which velocity can be added to the unsteadily expanding driver gas (state 3) is dependent on the sound speed of the stagnated driver condition (state 4,  $V_4 \approx 0 \text{ m/s}$ ). The driver gas sound speed ( $a_4 = \sqrt{\gamma_4 R_4 T_4}$ ) is a function of temperature, which for an isentropic compression, is a function of the compression ratio. In general, driver performance corresponds far more to driver rupture temperature ( $T_4$ ), which is controlled by the compression ratio, than it does to driver rupture pressure ( $p_4$ ) which is controlled by the chosen diaphragm thickness.

$$V_3 = V_4 + \frac{2a_4}{\gamma_4 - 1} \left[ 1 - \left( \frac{p_3}{p_4} \right)^{\frac{\gamma_4 - 1}{2\gamma_4}} \right] \quad (6.3)$$

Currently, the two most common X2 driver conditions (summarised in Table 6.1) have compression ratios of 30 and 40 respectively and estimated primary diaphragm rupture pressures of 27.4 and 35.7 MPa [231]. While X2's current driver conditions give it the ability to simulate entry to many planetary bodies in our solar system [222, 1, 81, 127, 78, 87, 79, 86], as Section 6.3 has shown, more powerful driver conditions would be required to easily simulate gas giant entry.

Considering other facilities around the world, higher compression ratios and rupture pressures are common for free piston driven facilities. The T4 reflected shock tunnel at UQ uses compression ratios up to 60, and rupture pressures up to 75 MPa [279]. The High Enthalpy shock tunnel Göttingen (HEG) facility at DLR in Göttingen, Germany uses rupture pressures above 100 MPa, and compression ratios around 55 [280]. It has also been fired at rupture pressures up to 200 MPa [281]. The T5 Shock Tunnel at the California Institute of Technology uses rupture pressures up to 130 MPa [282] and when first commissioned was using a compression ratio of 47 [283]. The High Enthalpy Laboratory Munich (HELM) shock tunnel at the Bundeswehr University Munich in Munich, Germany has a driver section rated to 185 MPa, has been fired with rupture pressures up to around 80 MPa, and has a compression ratio range from 64 to 124 [284].

To examine the possibilities available with higher compression ratios and rupture pressures, a new mode was added to PITOT allowing it to perform parametric studies of different compression ratios by specifying either the driver fill or rupture pressure. Based on what was seen in the literature, it was chosen to theoretically examine four set driver rupture pressures up to 200 MPa, in increments of 50 MPa, and compression ratios up to 100. The analysis will focus on the potential for using an expansion tube with a more powerful primary driver condition to study the aforementioned proposed Uranus and Saturn entries at 22.3 and 26.9 km/s [68, 69, 70] analysed by Palmer et al. [71] and Cruden and Bogdanoff [72, 73], as well as another proposed Saturn entry at 28.2 km/s also analysed by Palmer et al. [71] and Cruden and Bogdanoff [72, 73], and the 29 km/s Neptune entry proposed by Jits et al. [189], of which the entry radiation was analysed by Park [187]. Park analysed the whole entry but focused on the 174 second point at 30.1 km/s, where the maximum radiative heat flux was seen [187]. That point will be the focus of any discussion of that proposed entry in this analysis also. The details of these entry points can be seen in Table 6.7. The first Saturn entry value, Saturn point 1 from Table 8 in Palmer et al. [71], is from the proposed Saturn entry at 26.9 km/s [69, 70]. The other Saturn entry value, Saturn point 3 from the same table, is from the faster proposed 28.2 km/s Saturn entry. Equilibrium post-normal shock densities and temperatures calculated by the authors using CEA [197, 198] are also shown in Table 6.7 for all four entries. The Saturn entry post-shock values were calculated using an 89%He/11%H<sub>2</sub> (by volume) gas composition from Conrath and Gautier [274], and the Neptune entry post-shock value was cal-

Table 6.7: Gas giant entry points from the literature used for comparison in this paper. Significant figures from the sources have been maintained.

Entry and source	Entry point (s)	Freestream density ( $\rho_\infty$ , kg/m <sup>3</sup> )	Freestream temperature ( $T_\infty$ , K)	Freestream velocity ( $U_\infty$ , km/s)	Eq post-shock density (kg/m <sup>3</sup> )	Eq post-shock temperature (K)
Uranus point 1 from Table 4 in Palmer et al. [71]	34.5	$2.04 \times 10^{-5}$	128.2	22.504	$2.52 \times 10^{-4}$	5,680
Saturn point 1 from Table 8 in Palmer et al. [71]	206	$1.80 \times 10^{-5}$	141.0	26.316	$1.81 \times 10^{-4}$	8,670
Saturn point 3 from Table 8 in Palmer et al. [71]	91.5	$5.77 \times 10^{-5}$	141.2	27.706	$5.59 \times 10^{-4}$	9,830
Neptune entry point from Jits et al. [189] examined by Park [187]	174	$1.11 \times 10^{-4}$	not provided	30.090	$1.09 \times 10^{-3}$	12,000

culated using an 81%He/19%H<sub>2</sub> (by volume) gas composition from Gautier et al. [190] and a 140 K freestream temperature (as the freestream temperature was not specified in either Jits et al. [189] or Park [187]).

It was decided to base the test conditions to be analysed in this section on the conditions discussed in Sections 6.3 and 6.4. The specific details of these conditions can be found in Table 6.2: simulated Uranus entry test gas composition of 85%H<sub>2</sub>/15%He (by volume),  $p_1 = 2$  kPa,  $p_5 = 0.5$  Pa, X2's contoured nozzle with an area ratio of 5.64 [229] and if used, a secondary driver fill pressure ( $p_{sd1}$ ) of 21 kPa. It is not known whether these values would be nominal for other compression ratios and driver rupture pressures, but they form a reasonable basis for a theoretical parametric study like this.

The model employed to simulate these theoretical conditions is the normal theoretical equilibrium solver in PITOT and it should be noted that it is a state-to-state solver with no loss mechanisms modelled. This means that the calculations performed and discussed in this section provide a theoretical maximum of what would be possible for expansion tubes with these driver conditions. It is expected that because of increased driver losses due to high temperatures, diaphragm losses, and low density shock tube effects in the acceleration tube [106, 107, 108], that performance in practice would probably be lower than what is seen here.

Similar to what was seen in Fig. 6.3 in Section 6.3, there are 'kinks' on some of the plots in this section which may be non-physical and caused by interpolating beyond the CEA [197, 198] temperature limits to find the state of the shocked accelerator gas condition (state 6). Also, where curves are truncated it is because PITOT was not able to find a solution for the input conditions.

### 6.5.1 Maximum Stagnation Enthalpy

As has been discussed earlier, an expansion tube accelerates the post-shock shock tube condition (state 2) to superorbital conditions in the acceleration tube by processing the gas through an unsteady expansion. Stagnation enthalpy ( $H_t$ ) will generally be maximised by using the lowest acceleration tube fill pressure ( $p_5$ ) possible. Fig. 6.11 shows what would be considered ‘maximum performance’ for the eight different driver conditions shown on the plot by showing their stagnation enthalpies (and the related flight equivalent velocities, see Equation 6.1) when  $p_5$  is set to 0.5 Pa, the general operational limit of the X2 expansion tube.

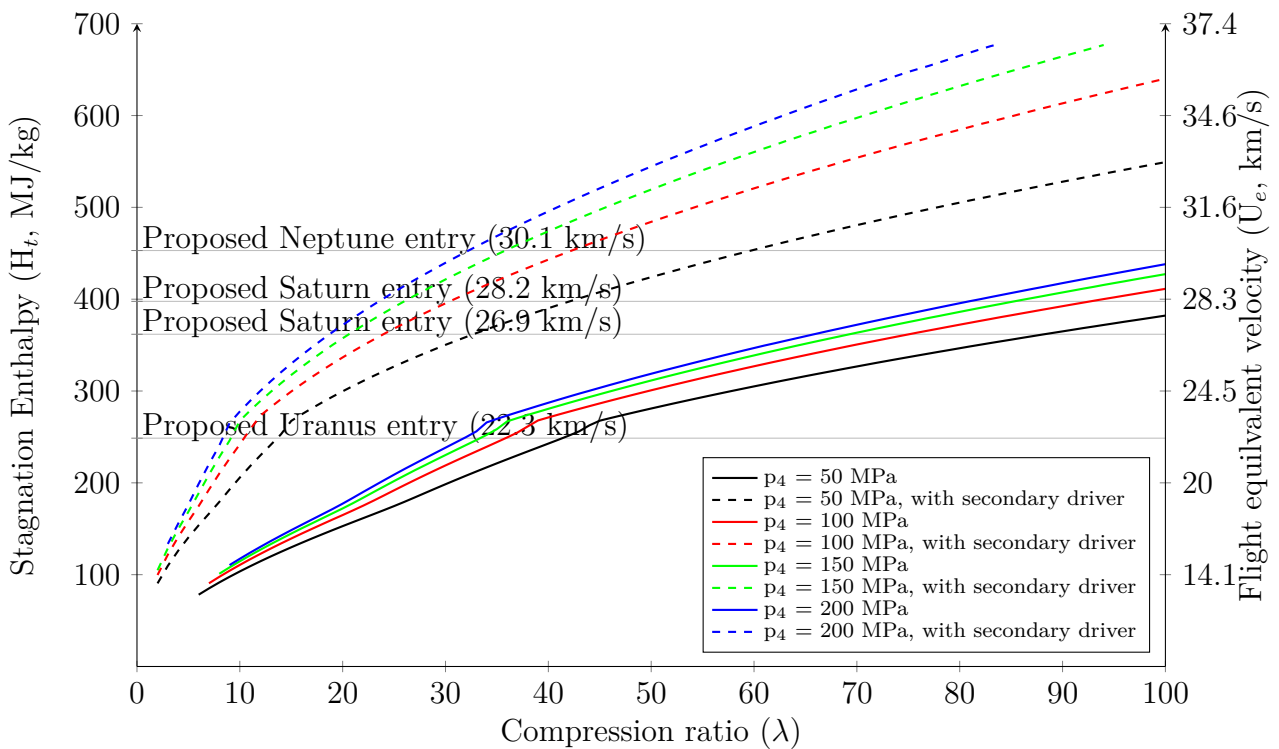


Figure 6.11: Performance of different conditions with set driver rupture pressures ( $p_4$ ), when the driver compression ratio ( $\lambda$ ) is varied from 0 to 100, and  $p_5 = 0.5$  Pa.

Examining Fig. 6.11, firstly, it shows that without a secondary driver section the performance appears to be rather insensitive to increases in driver rupture pressure above 100 MPa. A similar trend can be seen for the secondary driver conditions, with a large gap in performance between the conditions with 50 and 100 MPa rupture pressures, and a smaller gap beyond that. Beyond 100 MPa, the performance still increases with increasing rupture pressure, but it is less pronounced, and concentrated towards the higher compression ratios. It can also be seen that without a secondary driver, both of the proposed Saturn entries could be potentially simulated by an expansion tube driver with a compression ratio of 100, but that a secondary driver is

required to simulate the 30.1 km/s Neptune trajectory point analysed by Park [187]. With a compression ratio above 50, a secondary driver section, and a driver rupture pressure around 100 MPa, all of the entry velocities could be simulated.

### 6.5.2 Density Requirements

If this analysis is considered for an X2 sized expansion tube, scaling must be considered. As was discussed in the introduction to Section 6.3, X2 has a relatively small driven section diameter (85 mm with a nozzle exit diameter of 201.8 mm) and aerothermodynamic testing is generally performed using binary scaled test conditions. This requirement adds another limit to the  $H_t$  values for gas giant entry conditions where the driver is only just powerful enough to simulate the conditions. This would be less of a problem for facilities with larger driven section or nozzle exit diameters. In figures throughout this section, equilibrium post-normal shock densities over the test model ( $\rho_{10e}$ ) are compared to the related values from Palmer et al. [71] and Park [187] shown in Table 6.7. Scaled entry densities for simulation in X2 are also shown in figures where appropriate. The proposed aeroshell diameters for the Saturn and Uranus entries proposed by the US National Research Council [68, 69, 70] are 1,000 mm for Saturn and 760 mm for Uranus. Therefore, Fig. 6.12 shows density values for Saturn entry based on a 100 mm diameter scaled model (1/10 scale) and a 108.6 mm diameter scaled model (1/7 scale) for Uranus entry. The Saturn entry point 3 value from Palmer et al. [71] which is shown in Table 6.7 is actually from another proposed entry, but Palmer et al. [71] simulated it as a 1,000 mm diameter aeroshell as well, so the same has been done here. Two separate scale values are provided for the Neptune entry point, because the vehicle proposed by Jits et al. [189] is a more complex biconic vehicle design. The radius of the nose cone is 0.33 m, but the radius on the back face of the whole vehicle is 0.5 m. Therefore, a 1/6 scale model could simulate just the nose cone with a 110 mm diameter model, and a 1/10 scale model could simulate the whole vehicle with a 100 mm model.

In Fig. 6.12,  $\rho_{10e}$  values for the conditions in Fig. 6.11 are shown compared to the unscaled post-normal shock densities for the entry points shown in Table 6.7, as well as the densities required for post-shock binary scaling for two of the entry points. Binary scaled results are not shown for Saturn entry point 3 from Palmer et al. [71] or the Neptune entry point examined by Park [187] because they would be an order of magnitude larger than the other points shown. It can be seen that the overall  $\rho_{10e}$  range for all of the test conditions ( $3.282 \times 10^{-4}$  to  $8.070 \times 10^{-4}$  kg/m<sup>3</sup>) is of the same order of magnitude as the three trajectory points from Palmer et al. [71] shown on the figure, with only Saturn point 3 passing through the expansion tube values. It is believed that with slight modifications to the tunnel fill pressures Uranus point 1 and Saturn point 1 could also be covered by the tunnel conditions. However, overall Fig. 6.12 shows that these conditions would not be appropriate for binary scaled experiments.



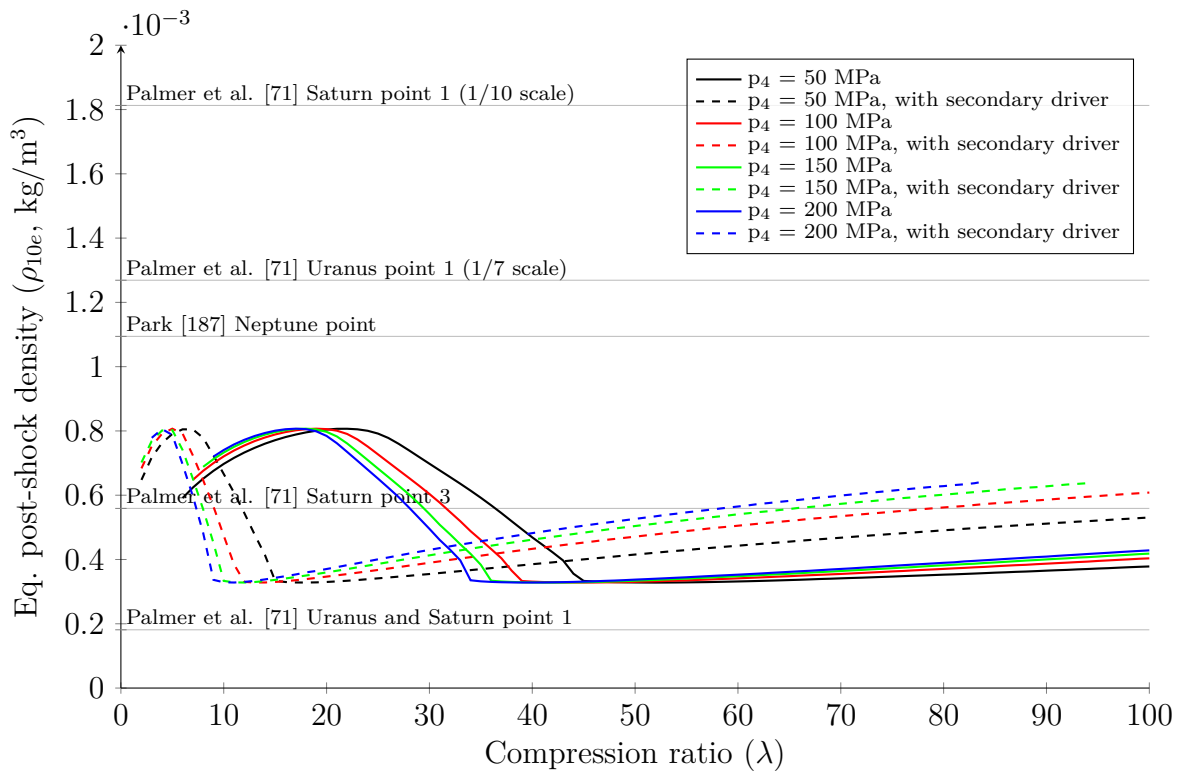


Figure 6.12:  $\rho_{10e}$  for the conditions shown in Fig. 6.11 *with* a nozzle expansion performed at the end of the acceleration tube.

As was discussed in Section 6.3,  $\rho \cdot L$  reduces through a steady expansion nozzle, therefore in Fig. 6.13 the same result as Fig. 6.12 is shown *without* a steady expansion at the end of the acceleration tube to simulate a nozzle. Because the nozzle expansion is nominally an isentropic process, the stagnation enthalpy of the test gas remains constant through the nozzle, and the values shown in Fig. 6.11 are still able to be compared to the results shown in Fig. 6.13. It has been assumed that without the nozzle the maximum model diameter would be 50 mm, so the scaling factors have been doubled compared to Fig. 6.12.

Considering Fig. 6.13, where the  $\rho_{10e}$  values calculated for the conditions *without* the nozzle expansion can be seen, the test conditions now overlap with the densities required to simulate the post-shock condition for Uranus entry point 1 and Saturn entry point 1 from Palmer et al. [71], even if the scaling factor is now higher. However, to be able to simulate post-shock binary scaled versions of Saturn entry point 3 from Palmer et al. [71] or the Neptune entry point analysed by Park [187], more density is required, which would require higher acceleration tube fill pressures.

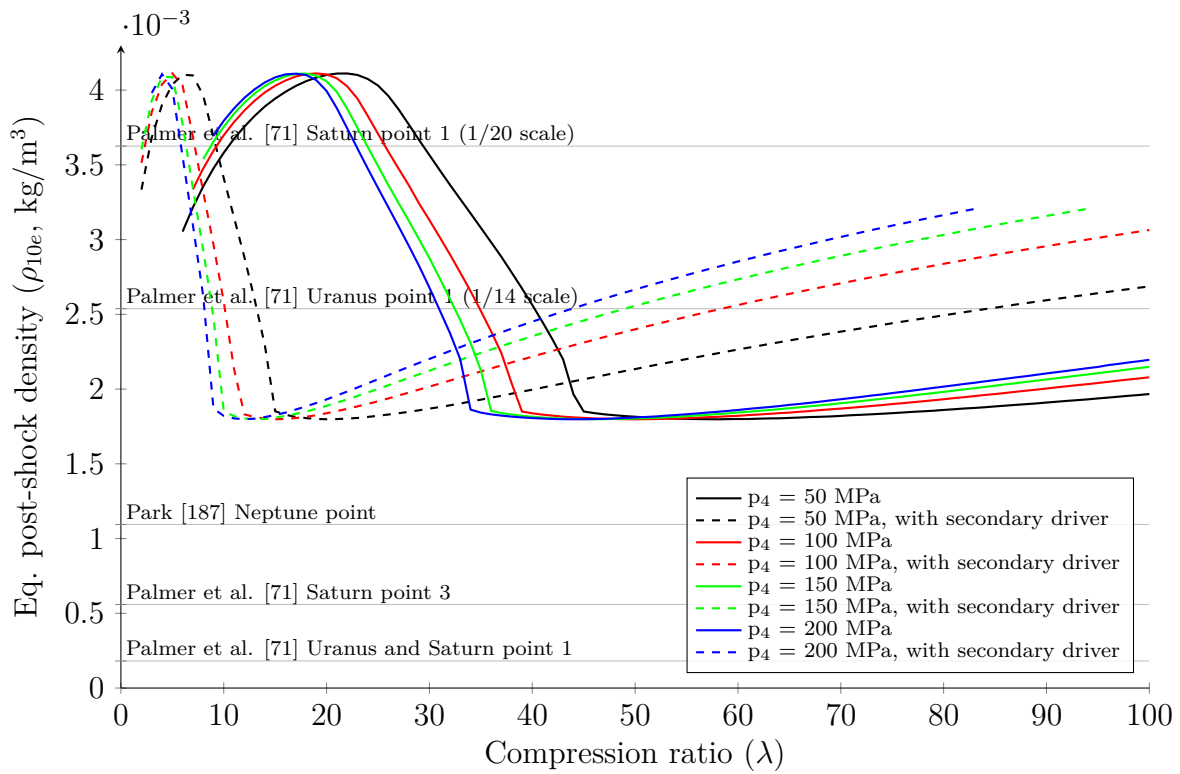


Figure 6.13:  $\rho_{10e}$  for the conditions shown in Fig. 6.11 *without* a steady expansion through a nozzle performed at the end of the acceleration tube.

### 6.5.3 Higher Acceleration Tube Fill Pressures

Fig. 6.14 explores the density potential of different acceleration tube fill pressure ( $p_5$ ) values by taking the same conditions analysed in Figs. 6.11 and 6.12, but instead fixing the compression ratio at the maximum value of 100 and varying  $p_5$  from 0.1 to 10 Pa. The equilibrium post-normal shock density values from Palmer et al. [71] and Park [187] shown in Table 6.7 are also shown along with scaled entry densities appropriate for an X2 sized facility.

Considering Fig. 6.14, it can be seen that there are combinations of driver condition and acceleration tube fill pressure ( $p_5$ ) which would be able to simulate the equilibrium post-normal shock densities of all three Palmer et al. [71] entry points and the Neptune entry point analysed by Park [187] at true flight density, and Uranus entry point 1 and Saturn entry point 1 from Palmer et al. [71] at scaled post-normal shock densities appropriate for an X2 sized facility using X2’s nozzle. All of this can be done with a maximum acceleration tube fill pressure of around 4.5 Pa, showing that a large increase in acceleration tube fill pressure is not required to increase the density. It can be also be done both with and without the use of a secondary driver section, giving many options in terms of generating the stagnation enthalpy required to simulate the conditions. It can also be seen that it would not be possible to simulate the binary

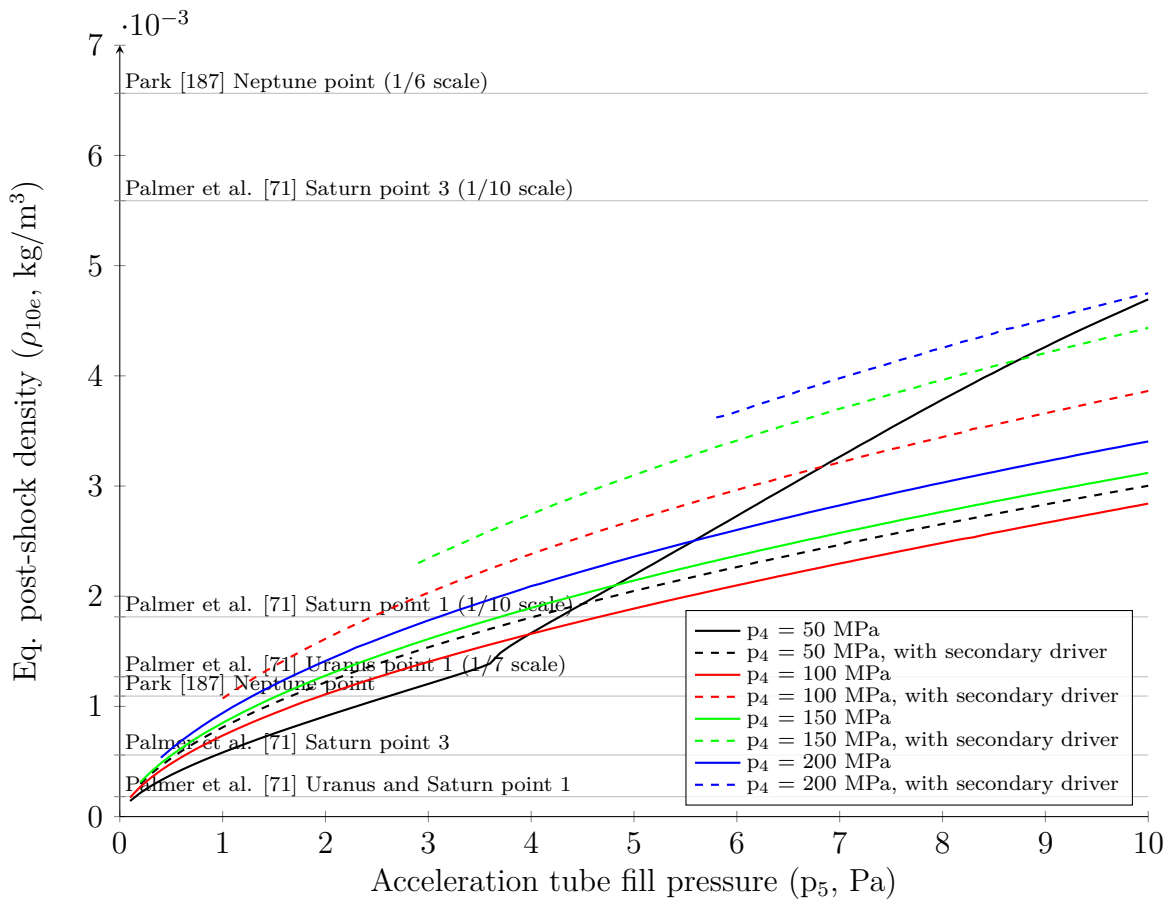


Figure 6.14:  $\rho_{10e}$  of different conditions with set driver rupture pressures ( $p_4$ ),  $\lambda = 100$ , with a nozzle expansion, when  $p_5$  is varied from 0.1 to 10 Pa.

scaled post-shock density of either Saturn entry point 3 from Palmer et al. [71] or the Neptune entry point analysed by Park [187] with these conditions. To examine how these higher density conditions could be simulated, Fig. 6.15 shows the same results shown in Fig. 6.14 except *without* using a steady expansion through a nozzle at the end of the acceleration tube.

In Fig. 6.15, where the nozzle is not used, much lower acceleration tube fill pressures are required than in Fig. 6.14. It can be seen in Fig. 6.15 that now a  $p_5$  value between 0.5 and 1 Pa would be required to simulate Uranus entry point 1 and Saturn entry point 1 from Palmer et al. [71] at scaled post-normal shock densities appropriate for an X2 sized facility. Depending on the driver condition and whether or not the secondary driver is used, the binary scaled post-shock density of Saturn entry point 3 from Palmer et al. [71] could be simulated with a  $p_5$  value between 2.8 and 5.6 Pa. For the Neptune entry point analysed by Park [187]  $p_5$  value between 3.6 and 7.4 Pa would be required.

Overall, this subsection and Section 6.5.2 have shown that there are different approaches to

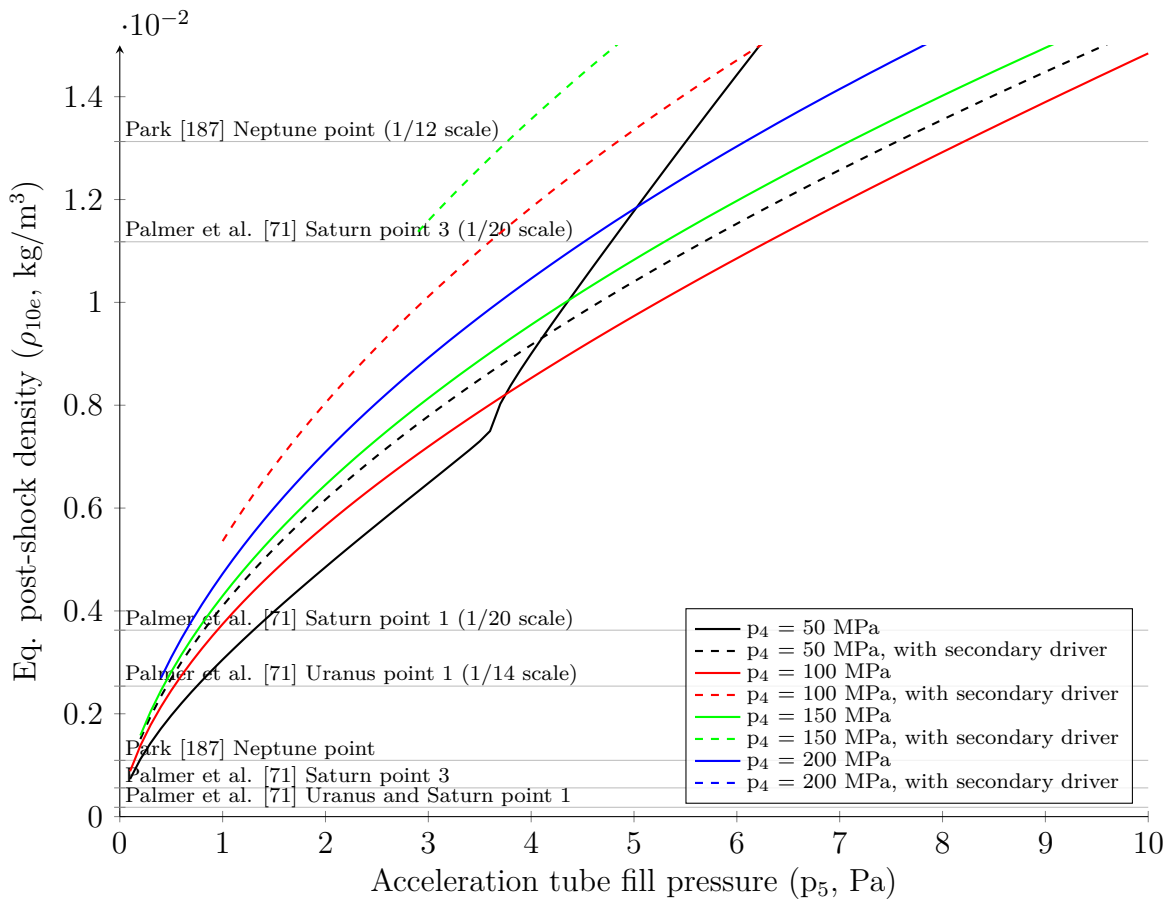


Figure 6.15:  $\rho_{10e}$  of different conditions with set driver rupture pressures ( $p_4$ ),  $\lambda = 100$ , *without* a nozzle expansion, when  $p_5$  is varied from 0.1 to 10 Pa.

simulate the density requirements of post-normal shock binary scaled gas giant entry conditions. These subsections have not identified the exact combinations required to do this, but it has been shown that simulating the post-normal shock binary scaled conditions for Uranus entry point 1 and Saturn entry point 1 from Palmer et al. [71] should be possible for an X2 sized facility both with and without a nozzle. A more powerful driver would be required if the nozzle was used. Without a nozzle, it should be possible to simulate the post-normal shock binary scaled conditions for both Saturn entry point 3 from Palmer et al. [71] and the Neptune entry point analysed by Park [187].

## 6.6 Conclusions

This chapter has investigated the possibility of simulating the proposed 22.3 km/s Uranus entry [68] and 26.9 km/s Saturn entry [69, 70] in the X2 expansion tube. It was first examined theoretically by investigating how to maximise the performance of the facility both with and

without a secondary driver section. Theoretically, it was shown that it should be possible to experimentally simulate the proposed 22.3 km/s Uranus entry [68] in X2 using a secondary driver section to augment the performance of X2's current most powerful driver condition. It was also shown it would not be possible at this time to simulate the proposed 26.9 km/s Saturn entry [69, 70] in X2. While the theoretical investigation principally focused on conditions using X2's contoured nozzle, it was seen that it would likely be necessary to remove X2's nozzle to simulate the proposed Uranus entry with a binary scaled test condition, as a higher  $\rho \cdot L$  product is achievable without the nozzle.

Experimentally, both a condition with and without a secondary driver were investigated. The condition without a secondary driver, X2-GG-UE-2.5 mm, had a flight equivalent velocity range of 19 to 19.8 km/s, too slow to simulate the proposed Uranus entry. Its individual shock speed uncertainties were large due to its high shock speeds, however, it was also seen that the expected uncertainties on the stagnation enthalpy and flight equivalent velocity values were still small considering this, being only  $-4.0\%$  /  $+4.1\%$  and  $-2.0\%$  /  $+2.0\%$  respectively. However, the uncertainties on the state variables were larger, with the worst case being a freestream density variation of  $-22\%$  /  $+26\%$ , indicating that these test conditions may not be suitable for simulating situations which are very sensitive to changes in the state variables of the test gas.

The condition with a secondary driver, X2-GG-UE-2.5 mm-SD, showed performance losses in the shock tube of at least 7%, which was attributed to diaphragm losses between the secondary driver and shock tube. The thinnest Mylar diaphragm separating the tubes was 12.5  $\mu\text{m}$  thick, and it was proposed to use 5  $\mu\text{m}$  thick diaphragms in the future to recover some of the lost performance. Due to the large shock speed uncertainties and uncertainty about how far the test gas unsteadily expanded in the acceleration tube, the test section uncertainties were generally double what was found for condition X2-GG-UE-2.5 mm. The inferred flight equivalent velocity range for this condition was 21.1 to 22.9 km/s. Even though the range is large, it does include the proposed 22.3 km/s Uranus entry and shows that if the uncertainties could be reduced, X2 could be used to simulate Uranus entry flight conditions. The post-shock density over the test model for the condition was of the same order of magnitude as the post-shock density of some of the Uranus entry points analysed by Palmer et al. [71], but binary scaled experiments could be performed by removing X2's nozzle.

To investigate what could be done beyond the limitations of X2's current driver configurations, a theoretical parametric study of free piston driven expansion tubes with more powerful drivers was performed. Primary diaphragm rupture pressures up to 200 MPa and compression ratios up to 100 were used as these values were found to have been used by other facilities. It was found that using various combinations of driver rupture pressure, compression ratio,

whether to use a secondary driver or not, acceleration tube fill pressure, and whether to use a nozzle or not, an X2 sized facility could simulate the proposed Uranus and Saturn entries [68, 69, 70], another proposed Saturn entry at 28.2 km/s analysed by Palmer et al. [71], and a 30.1 km/s Neptune entry proposed by Jits et al. [189] both with and without binary scaling. More powerful driver conditions would be required to simulate the faster entries, and to produce binary scaled test conditions. The possibility of designing more powerful driver conditions within the physical constraints of X2's current driver is being investigated.

Further work should be aimed at reducing the large uncertainties seen in this work. This means removing potential losses by ensuring that absolute minimum thickness diaphragms are used for future experiments; developing a shock detection system which is fit for purpose for detecting 20 km/s shocks; performing experiments without X2's contoured nozzle to reduce uncertainty about the flow entering the nozzle; using only Pitot pressure probes in the test section to ensure that measured test section pressures are high enough to be out of the non-linear range of the sensors; and writing more complex expansion tube analysis programs to give a more complete picture of the real uncertainty which exists for expansion tube flow conditions.

In the meantime, while these issues are being worked through, as was discussed in the introduction to this chapter, another direction would be to continue on from the work of Stalker and Edwards [67] and simulate only the shock layer temperature, without reproducing the stagnation enthalpy, by using either more helium or neon in the test gas. Without the requirement to reproduce the stagnation enthalpy, lower velocity conditions could be used, reducing shock speed uncertainties, and with them, the inferred uncertainties in the test section. This would also increase the available  $\rho \cdot L$  range for producing binary scaled test conditions as excess driver performance could be used to produce slower conditions with higher density. The need to remove X2's nozzle to maintain more density could also be relaxed, allowing larger models to be used, with less scaling. Considering all of the issues with directly simulating gas giant entry in an expansion tube facility which this paper has discussed, at this time it appears that this may be the most promising direction to take this work in. This is examined further in the following chapter.

# 7

## Using Higher Amounts of Diluent for Gas Giant Entry Simulation

*Tiger got to hunt, bird got to fly; Man got to sit and wonder, 'Why, why, why?' Tiger got to sleep, bird got to land; Man got to tell himself he understand.*

– Kurt Vonnegut, *Cat's Cradle*, 1963 [285]

### 7.1 Chapter Overview

Due to the fact that Chapter 6 showed that the X2 expansion tube cannot currently re-create the 26.9 km/s entry velocity required to simulate Saturn entry, and that conditions which could re-create the velocity of a 22.3 km/s Uranus entry have not yet been experimentally validated, it is important that other avenues be explored to potentially allow the simulation of these conditions in the facility in the future. This section examines how utilising a higher amount of helium diluent than the actual entries (or the change to a heavier neon diluent) would allow hotter shock layers to be simulated at shock speeds currently achievable in the X2 expansion tube.

This chapter is made up of the final submitted version of the journal paper James et al. [26] with some repetition removed from the document and links to previous chapters added.

### 7.2 Introduction

The four outermost planets in our solar system (Jupiter, Saturn, Uranus, and Neptune) are collectively known as 'the gas giants' or 'the Jovian planets'. They are large gaseous planets, with densities close to that of the sun, which together comprise 99.56% of the planetary mass in our solar system [37]. All four gas giants are made up of primarily molecular hydrogen and

ten to twenty percent helium (by volume), with small amounts of other trace elements such as methane [39]. The Galileo probe's 47.4 km/s entry into Jupiter on the 7th of December 1995 is the only entry into a gas giant planet ever performed by humankind [58]. The majority of previous gas giant entry research was either performed to support the design of the Galileo probe [59, 60, 61, 62], or to analyse the results from the mission [58, 64, 66].<sup>1</sup> However, there is now an interest in new missions to the gas giants, especially Saturn and Uranus.

In the US National Research Council's 'Vision and Voyages for Planetary Science in the Decade 2013-2022' report, scientific missions involving atmospheric entry to Uranus and Saturn [68, 69, 70] were identified as high priorities for future space research due to several important unanswered scientific questions. Firstly, gas giants are old planets, containing matter produced early in the existence of the solar system which could be used to help calibrate and improve models of solar system evolution. Secondly, gas giant planets are relatively common in extra-solar planetary systems, providing a valuable link between our own solar system and the greater universe. The last question relates to the fact that two types of gas giant planets exist in our solar system. Jupiter and Saturn are 'gas giants', whereas, Neptune and Uranus are technically 'ice giants' due to the heavy elements trapped in their atmospheres in an ice-like state. It is hoped that if missions are performed into both gas and ice giant planets, humankind will gain a better understanding of these types of planets.

The two scientific missions proposed in the report were a 22.3 km/s entry into Uranus [68] and a 26.9 km/s entry into Saturn [69, 70]. The expected aeroheating uncertainties of these entries, as well as a third steeper descent angle Saturn entry at 28.2 km/s, were analysed by Palmer et al. [71] in 2014 by performing a Monte Carlo study on the input parameters to their data parallel line relaxation computational fluid dynamics (CFD) code. They found that radiative heating for Uranus entry was negligible but at the highest velocity examined for Saturn entry, radiative heating contributed up to 20% of the heat load. In general, they found that the uncertainty in convective heating for Uranus and Saturn entry was only a few percent, but that for Saturn entry, where the post-shock temperatures are higher, the radiative heating uncertainty was substantial. The strongest contributor to the radiative heating variation was found to be the H<sub>2</sub> dissociation reaction rates, because the radiative heating seen at the wall is strongly influenced by the chemistry which occurs just behind the bow shock.

More recently, Cruden and Bogdanoff [72, 73] experimentally examined the expected post-shock radiation for parts of these three entry trajectories in the Electric Arc Shock Tube (EAST) facility at NASA Ames Research Center [76]. This constitutes the first significant gas giant entry experimental research study since the design of the Galileo probe [60, 61, 62], and the first

---

<sup>1</sup>This is discussed further in Section 3 where a larger literature review about gas giant entry can be found.



attempt to spectrally quantify the shock layer radiation for these missions. Previous gas giant experiments in EAST were believed to have been compromised by radiation from the driver gas (see Bogdanoff and Park [194]). EAST is a non-reflected shock tube (NRST) capable of re-creating planetary entry shock layers at the true flight velocity and pressure. A suite of spectrometers examine the relaxation behind the moving shock wave as it moves past a specific axial location in the test section. Cruden and Bogdanoff used an 89% $\text{H}_2$ /11%He (by volume) simulated Saturn entry test gas, based on the work of Conrath et al. [274], and examined freestream pressures from 13 Pa to 66 Pa and velocities from 20 km/s to 30 km/s. Consistent with Palmer et al.'s [71] conclusion that radiative heating for Uranus entry was negligible, Cruden and Bogdanoff found that, within their measurement limits, no shock layer radiation was detectable below 25 km/s. Above 25 km/s, radiation was observed, and they found that the post-shock non-equilibrium region was very large, with the shocks not reaching equilibrium over several centimetres. They also found that in many cases, the state distributions were non-Boltzmann. Due to the fact that NEQAIR [77], NASA's in-house radiation code, is only able to simulate  $\text{H}_2$ /He flows in Boltzmann states, they found that NEQAIR currently over-predicts the radiation by up to a factor of 10.

This chapter examines the possibility of simulating gas giant entry in an expansion tube, a different type of ground testing facility. An expansion tube is a modified shock tunnel facility which is often used for the study of planetary entry aerothermodynamics. The expansion tube circumvents a fundamental limitation of shock tubes and tunnels by processing the test gas through an unsteady expansion after it has been shock processed [196]. If a basic shock tube is driven too quickly, it creates a dissociated and ionised test flow which is generally only suitable for the study of post-shock radiation phenomena, like what is studied in EAST [76]. If the more common reflected shock tunnel is driven too quickly, the flow chemistry created in the stagnation region when the already shocked test gas is shocked again as it reflects off the shock tube end wall can chemically freeze in the facility's nozzle causing the generated freestream flow to be chemically excited [112, 113]. Processing the shock-processed test gas with an unsteady expansion means that the shock processing can be weaker as additional total enthalpy can be added to the flow while the gas is actually cooling down [196]. Expansion tubes can still suffer from chemical freezing if the shock tube is driven too quickly, but the use of these two modes of enthalpy addition means that generally these effects can be minimised. The specific facility examined in this chapter is the X2 expansion tube at the University of Queensland (UQ). Prior to this study, X2 has been used to study planetary entry into Earth, Mars, Titan, and Venus [104, 222, 81, 127, 286, 82, 78, 79, 80, 86, 87] from around 3 km/s to 12 km/s. More information about X2 can be found in Chapter 4.

While an NRST facility like EAST has the ability to simulate and capture the relaxation

behind a shock wave at the true flight condition, test times are very short in NRSTs, making it hard to perform experiments using test models. An expansion tube is a more versatile facility for several reasons. For a very short period of time (typically around a hundred microseconds for X2) an expansion tube is able to create a representative aerothermodynamic test flow, which means that it can be used to test scaled models. This has allowed X2 to examine flows using many different types of models, including quasi two-dimensional cylinders [78, 79, 80, 4], scaled aeroshells [81, 82], instrumented models [83, 84, 85], wedge models to study expanding post-shock flows [86, 87], Mach disk models which produce standing normal shocks to study radiation over long relaxation distances [88, 89], and resistively heated models to re-create the surface temperature of planetary entry vehicles [90, 91, 3, 7]. This versatility means that it would be advantageous to be able to re-create gas giant entry flows in the X2 expansion tube so that experiments with test models could be performed for the study of post-shock radiation and other phenomena such as heat transfer and shock standoff.

In Chapter 6, the author performed a theoretical parametric study of the X2 expansion tube operating with and without a shock heated secondary driver section to increase facility performance (refer to Gildfind et al. [1] for more information about secondary drivers) using the in-house expansion tube analysis code PITOT (see Chapter 5), and attempted to quantify the performance envelope of X2 for the simulation of true gas composition gas giant entry flow conditions. Theoretical stagnation enthalpy ( $H_t$ ), a measure of the energy contained in a gas due to both its gas state ( $h - h_0$ ) and its velocity ( $\frac{U_\infty^2}{2}$ ), was used to assess the performance of the test conditions. A related quantity called the ‘flight equivalent velocity’ ( $U_e$ ) was also discussed. It is a measure of the true flight stagnation enthalpy simulated by a ground test facility where the experimental freestream may have an elevated temperature compared to flight. This is shown in Equation 6.1.

In that previous chapter it was found that it should theoretically be possible to simulate the proposed 22.3 km/s Uranus entry [68] in X2, but that it would not be possible to directly simulate the 26.9 km/s proposed Saturn entry [69, 70]. However, experiments conducted found that only the condition without a secondary driver section, with an estimated  $U_e$  of 19,400 m/s was able to be experimentally reproduced without very large uncertainties. The fastest and potentially most useful condition, which made use of the secondary driver, suffered from diaphragm losses and uncertainty about the quality and state of the test flow. Since this earlier chapter showed that X2 cannot currently re-create either proposed gas giant entries, other avenues have been explored here to perform meaningful aerothermodynamic simulation of these conditions. This problem was previously considered by Stalker and Edwards [67] who proposed that for blunt-body simulation of gas giant entry, increasing the molar percentage of helium above the true atmospheric composition, or substituting it with neon, which is heavier, could

be used to create hotter shock layer conditions at slower speeds. This chapter examines the potential of using this technique in X2 to overcome the aforementioned limitations in directly simulating the entries. Section 7.3 presents an overview of the aforementioned ‘Stalker substitution’; Section 7.4 presents a theoretical parametric study of X2 using different percentages of helium or neon diluent; and Section 7.5 presents experimental validation for the helium case.

### 7.3 The Stalker Substitution

As gas giant entry velocities are generally too fast to be directly simulated in impulse facilities designed for use with test models, in 1998 Stalker and Edwards [67] proposed a test gas substitution for the study of gas giant entry conditions in ground testing facilities. Their theoretical analysis for inviscid gas giant entry flows showed that, due to its large ionisation energy, the helium in the H<sub>2</sub>/He flow-field acted as an ‘inert diluent’ and collision partner for the hydrogen molecules and atoms. They started their analysis with a completely dissociated shock layer flow, which would be justified by the short dissociation distance associated with very fast gas giant entries, such as Jupiter entry. However, it would not be true for the aforementioned Uranus and Saturn entries, where both simulation [71] and experiment [72, 73] showed that the post-shock flow relaxation for these entries principally consisted of large dissociation regions which occurred over centimetres.

In their basic shock relaxation analysis, Stalker and Edwards [67] found that the amount of inert diluent in the flow-field, and even the *type* of inert diluent, did not affect the ionising relaxation of the test flow. They examined both H<sub>2</sub>/He test flows, and test flows with a heavier diluent, neon, because of its similar excitation energy compared to helium (17 eV, compared to helium’s 21 eV). They examined diluent fractions from 1 – 99% (by volume) and different constant post-shock temperatures and pressures to simulate different post-shock streamlines with different enthalpies. They found that with a constant post-shock temperature of 60,000 K, the neon itself began to ionise near equilibrium in situations where helium would not. At temperatures of 40,000 K and below, they found that the substitution held and the ionising relaxation of H<sub>2</sub>/Ne test flows were similar to H<sub>2</sub>/He ones for the situations which they analysed. Both 40,000 K to 60,000 K are very high temperatures to be using reaction rate and thermodynamic data at, so these values should obviously be considered approximate.

Stalker and Edwards [67] also adapted the results of a previous blunt-body flow similarity study [175] to the simulation of gas giant entry. The original study had investigated how, for a generalised shape at an angle of incidence, different freestream and model parameters could be varied to produce similar shock layer flows. It was found that if appropriate freestream and model parameters were chosen, the distribution of flow variables in one shock layer could be

obtained from another shock layer, allowing conditions which cannot be simulated directly to be simulated indirectly with more achievable flow conditions.

Four requirements needed to be satisfied for the similarity to be valid. These are discussed in depth in their original paper [67], and therefore only a small summary is provided here. Requirements 1, 2, and 3 related mainly to the flow geometry; principally the angle of incidence between the model and the freestream flow, and the slope of the body surface. Both the angle of incidence with the flow and the slope of the body surface must be small, and the angle of incidence must be adjusted to take into account the change in normal shock density ratio between the two flows. This is shown in Fig. 2 in Stalker and Edwards [67]. This thesis only considers stagnation streamline flows at zero angle of attack (i.e. angle of incidence =  $90^\circ$ ), so these first three requirements do not need to be considered presently.

Requirement 4 is more difficult to satisfy: Variation of density along post-shock flow streamlines must be the same for the two flows. For frozen or equilibrium flow-fields this requirement is easily satisfied because the post-shock density effectively remains constant, but for non-equilibrium flow, where the gas composition is changing along the streamline, it is more complicated. Stalker and Edwards [67] found that if the reactions were binary (i.e. no recombination) it could hold, and then it was shown that for a given post-shock temperature, the non-equilibrium variation of the density ratio with normalised distance was independent of whether helium or neon was used as a diluent, and was roughly independent of the diluent fraction used. From this conclusion, they stated that Requirement 4 would be satisfied by a modified binary scaling parameter term which takes into account the molecular hydrogen partial pressure and must be comparable for both shock layers. This modified binary scaling parameter scales the binary chemical reactions with distance like a normal binary scaling parameter does, while allowing the variation caused by the use of different diluent fractions to be taken into account. The modified binary scaling parameter is:

$$\Omega = \frac{rp_n L [\varepsilon_n (1 - \varepsilon_n)]^{-0.5}}{U_\infty} \quad (7.1)$$

where  $r$  is the fraction of molecular hydrogen (by volume) in the gas mixture before dissociation and ionisation. For an experiment, this is the hydrogen fraction in the test gas in its fill condition, and for an actual entry, this is the hydrogen fraction in the undisturbed atmosphere.  $p_n$  is the post-shock pressure for each flow,  $L$  is an appropriate length scale,  $\varepsilon_n$  is the inverse shock density ratio ( $\rho/\rho_s$ ) for each flow, and  $U_\infty$  is the freestream velocity of the flow.

This means in practice that with appropriate selection of experimental parameters, the limits of a ground testing facility can be circumvented for gas giant blunt-body flow simulation because the shock layers of unobtainable true flight speeds can be simulated at slower speeds

using either an increased amount of helium diluent or a heavier neon diluent. Both of these substitutions produce stronger shock waves over the test model in the test section, resulting in a hotter post-shock flow for a given freestream velocity.

It is interesting to note that in 1969 one of the first ever journal articles about Jupiter entry, Tauber [149], actually included calculations for Jupiter entry with differing percentages of helium in the atmosphere due to uncertainty about the exact percentages of hydrogen and helium in Jupiter's atmosphere at the time. It was predicted that the shock layer temperature and also the radiative heat transfer would increase as the helium percentage in the atmosphere increased.

Stalker and Edwards [67] performed experiments on a hemispherically blunted cone model in the T3 shock tunnel at the Australian National University (ANU) in non-reflected shock tunnel mode with a 60% $\text{H}_2$ /40%Ne (by volume) test gas, producing flows which re-created the frozen post-shock temperatures of gas giant entries between 24 km/s and 28 km/s. They noted that, because their experiments were performed using a non-reflected shock tunnel driven very quickly (from 8.3 km/s to 11.1 km/s), a large source of error was added to their results because the freestream flow was fully dissociated. They estimated that up to 30% of the freestream stagnation enthalpy was chemical (the  $h - h_0$  in Equation 6.1), compared to true flight, where the freestream chemical enthalpy is negligible. They stated that expansion tubes, where only part of the final test flow enthalpy is added through a shock wave, generally resulting in less freestream chemistry compared to a non-reflected shock tunnel, would potentially allow these errors to be minimised.

In 2004, Higgins [63] expanded Stalker and Edward's [67] work using the X2 expansion tube. Experiments were performed with a 15% $\text{H}_2$ /85%Ne (by volume) test condition designed by Herbrig [92] to maximise the strength of the test model bow shock and create an ionising post-shock flow over the model. All of Higgins' experiments were nominally performed with this test condition, with variation discussed later in this section caused by variation in facility performance between experiments. Higgins took measurements of shock standoff and electron number density for sphere and cylinder test models and compared this to a theoretical model, observing good agreement. However, the work was potentially at the edge of the validity of the substitution due to ionising neon in the post-shock flow over the test model. Higgins stated that the neon was a partially ionised diluent in the post-shock flow over the test model for the experiments [63]. Using PITOT<sup>2</sup> and Higgins' experimental shock speeds (from Table 5.1 of Higgins [63]), the present author confirmed this, finding that for one experiment (shot 674) PITOT predicted that almost half of the ions in the post-shock stagnation streamline flow at

---

<sup>2</sup>See Chapter 5 for more information about PITOT.

equilibrium were produced by ionising neon, and over a third were produced by ionising neon for another (shot 752). This goes against the conclusions of Stalker and Edwards [67] who had found that differences in post-shock relaxation between helium and neon diluents were only found near equilibrium at the highest temperatures, where the neon would start to ionise. This shows that the substitution was potentially used beyond its useful limits.

Higgins' [63] analysis also showed (and the present author predicted using PITOT that depending on the condition, the hydrogen in the experimental freestream flow (state 7, by convention, as X2 was not being used with a nozzle then) was either almost fully dissociated or partially ionised at equilibrium, with a large percentage of the stagnation enthalpy being chemical. From the same equilibrium PITOT simulations performed for two of Higgins' experiments above, one of the experiments (shot 674) was predicted to have a stagnation enthalpy that was 8% chemical, a common percentage for X2 flow conditions. However, the other experiment (shot 752) had a  $H_t$  which was 21% chemical, a value approaching the amount of stagnation enthalpy error predicted for the original non-reflected shock tunnel experiments performed by Stalker and Edwards [67], and effectively negating the benefits they believed expansion tubes would bring to experiments using the substitution.

It should be noted that the original substitution was proposed for primarily ionising flows where the post-shock dissociation distance is small, thereby allowing the flow to be assumed to be fully dissociated. For the proposed Uranus and Saturn entry conditions, this is not the case. Simulations in Palmer et al. [71] showed dissociation distances of 17 mm for Uranus entry (where recombination begins) and 10 mm for Saturn entry (where ionisation begins). These flows are therefore primarily dissociating flows, *not* ionising ones. Currently the author has not established what effect this will have on the validity of the substitution, but because the reactions remain binary, it is considered reasonable to use the substitution for dissociating flows. Stalker and Edwards drew a similar conclusion for their ionising conditions. They noted that for some of their simulated post-shock conditions, the hydrogen atoms may not be fully dissociated when ionisation begins, which would slightly modify their relaxation curves, but due to the processes being binary in nature, the trends should remain the same. How the substitution affects the relaxation in dissociating flows will require further investigation in the future using finite rate chemistry models. This will be simple for  $H_2/He$  conditions, as reaction schemes are readily available due to it being the real composition of gas giant planets, but may be more complicated for  $H_2/Ne$  ones. However, reaction schemes were used by Higgins [63] and Stalker and Edwards [67] for  $H_2/Ne$  relaxation. Higgins [63] used an approximate hydrogen dissociation rate for collisions with neon based on a rate for collisions with argon. Stalker and Edwards [67] used a hydrogen ionisation reaction rate with a generic collision partner of either a hydrogen, neon, or helium atom, which was actually derived by Stalker [159] from shock tunnel

measurements using a H<sub>2</sub>/Ne test gas.

## 7.4 Theoretical Analysis for Helium and Neon Diluents

This section examines theoretically how a changing helium or neon diluent fraction in the test gas fill state (by volume) affects a specified flow condition in various ways. The figures presented in this section present results calculated using the equilibrium gas expansion tube simulation code PITOT. With the exception of Figs. 7.7 and 7.8, all of the results shown are based purely on test condition X2-GG-UE-2.5 mm from Table 6.2 in Chapter 6. This condition uses the X2-LWP-2.5 mm-0 driver condition [231, 230] with a pure helium driver gas and its associated orifice plate [2], no secondary driver, a 2 kPa shock tube fill pressure ( $p_1$ ), a 0.5 Pa acceleration tube fill pressure ( $p_5$ ), and X2's contoured nozzle with a geometric area ratio of 5.64 [229].  $p_1$  and  $p_5$  are kept constant for all simulations. Calculations were performed from 10 to 90% diluent (by volume), as the helium fraction used in Cruden and Bogdanoff to simulate Saturn entry was 11% [72, 73], based on the work of Conrath et al. [274]. 90% diluent (by volume) was deemed to be a reasonable maximum value. Where normalised values are shown, they are normalised by the results with the minimum 10% diluent fraction (by volume).

### 7.4.1 Effect on the Test Conditions in the Driven Tubes

Fig. 7.1 shows how a changing diluent fraction in the test gas fill state changes the performance of the test conditions in terms of stagnation enthalpy ( $H_t$ , Equation 6.1), and also the related shock and acceleration tube shock speeds ( $V_{s,1}$  and  $V_{s,2}$  respectively).

Considering the helium diluent results shown in Fig. 7.1a first, it can be seen that over the full range from 10 to 90% diluent,  $H_t$  is almost constant, with a maximum deviation of less than 0.2%.  $V_{s,1}$  decreases by around 4% before rising again, and  $V_{s,2}$  increases over the whole range shown on the figure, but only by 0.8%. Now considering the neon diluent results shown in Fig. 7.1b, much larger changes are seen.  $H_t$ ,  $V_{s,1}$ , and  $V_{s,2}$  all decrease approximately linearly from 10 to 60% diluent before all showing a slight rise or remaining constant for higher neon fractions. This is very different to Fig. 7.1a, where  $H_t$  and  $V_{s,2}$  stayed almost constant across the full range of helium diluent fractions shown. These differences are explained by examining Figs. 7.2 and 7.3 where the test gas fill and post-shock conditions (states 1 and 2) are shown.

The effect of the changing diluent fraction on the test gas fill condition (state 1) is shown in Fig. 7.2a for the helium diluent. Over the full range of helium diluent fractions shown, the specific heat ratio ( $\gamma_1$ ) increases by at most around 13%, the specific gas constant ( $R_1$ ) decreases by at most around 40%, and the molecular weight and density ( $MW_1$  and  $\rho_1$ ) increase by at most

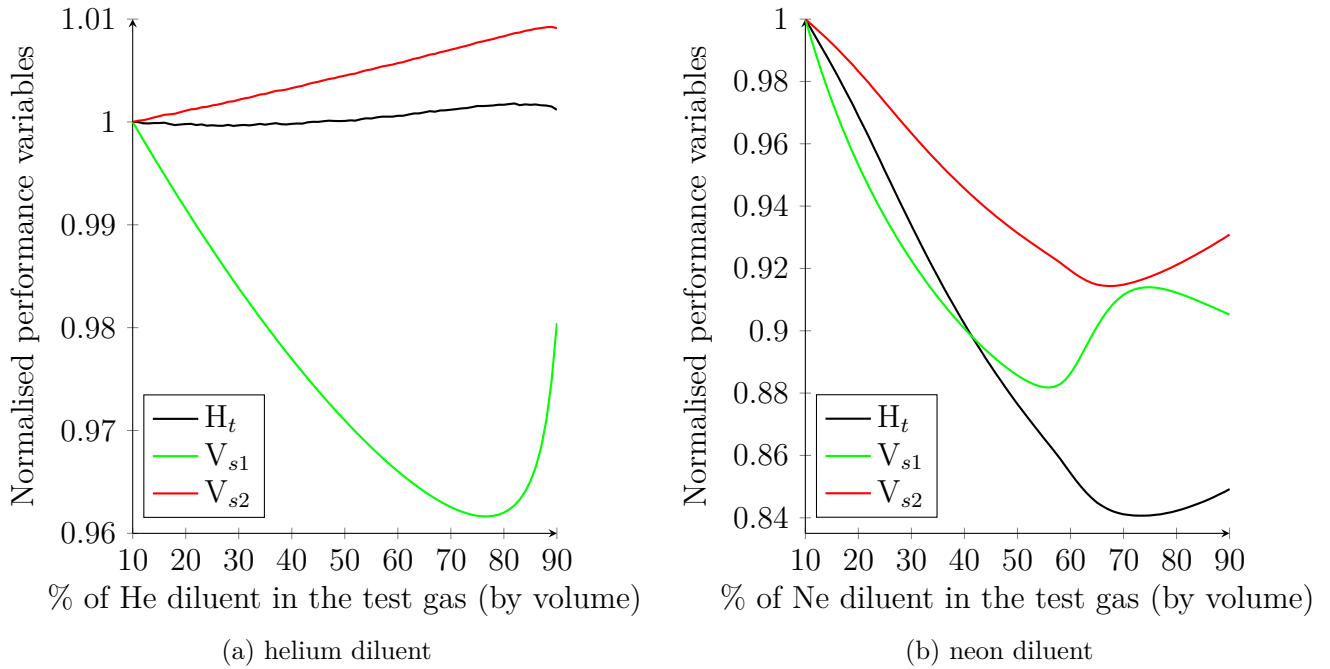


Figure 7.1: Effect of diluent fraction on the performance of the condition. Normalised by 10% diluent.

around 72%. When compared to other gases, these changes are very small. Using the molecular weight as an example, which along with density showed the largest variation, mixtures with helium diluent fractions of 10 and 90% have molecular weights of 2.2 and 3.8 g/mol respectively. In comparison, air has a molecular weight of 28.97 g/mol, which is an order of magnitude higher. The equivalent neon diluent fill conditions shown in Fig. 7.2b have a molecular weight range of 3.8 g/mol to 18.4 g/mol. The lightest  $H_2/Ne$  fill condition shown in Fig. 7.2b is as heavy as the heaviest  $H_2/He$  fill condition shown in Fig. 7.2a. Because of this, much larger changes are seen in Fig. 7.2b over the neon diluent fraction range. The molecular weight ( $MW_1$ ), density ( $\rho_1$ ), and specific gas constant ( $R_1$ ) of the fill condition each change by almost 500% over the neon diluent fraction range shown.

Similar behaviour is seen in Fig. 7.3, where the effect that the changing diluent fraction has on various post-shock variables in the shock tube (state 2) is shown. Examining a form of the unsteady expansion equation from Cantwell [276] of the shocked test gas (state 2) to state 7 in the acceleration tube (Equation 7.2), it can be seen that the unsteady expansion is a function of the change in test gas velocity ( $V_2$  and  $V_7$ ), the initial post-shock sound speed ( $a_2$ ), the change in pressure ( $p_2$  and  $p_7$ ), and the post-shock specific heat ratio ( $\gamma_2$ ). When the helium diluent is considered, none of the state 2 variables shown in Fig. 7.3a show a large variation over the diluent fraction range shown. The maximum variation of any post-shock variable over



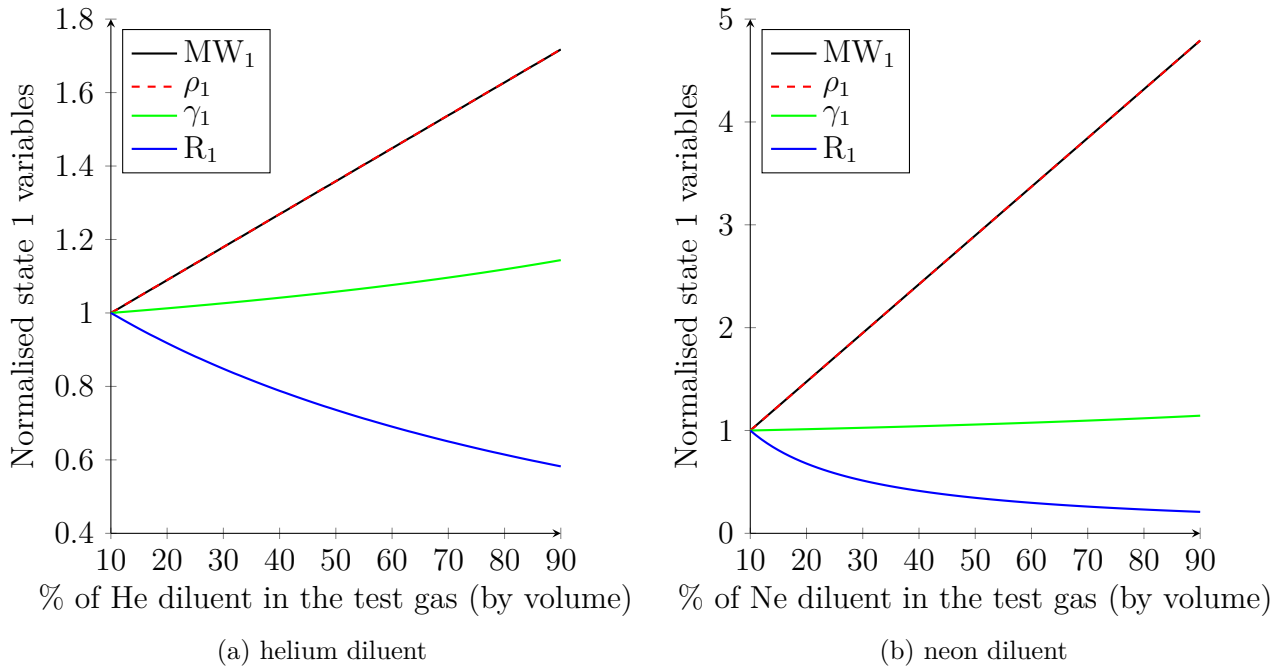


Figure 7.2: Effect of diluent fraction on the test gas fill condition (state 1). Normalised by 10% diluent.

the whole range is the density ( $\rho_2$ ), with an increase of 65%.

$$V_7 = V_2 + \frac{2a_2}{\gamma_2 - 1} \left[ 1 - \left( \frac{p_7}{p_2} \right)^{\frac{\gamma_2 - 1}{2\gamma_2}} \right] \quad (7.2)$$

The results shown in Fig. 7.3a explain what was seen earlier in Fig. 7.1a: As the helium diluent fraction changes, small variations in state 2 variables cancel each other out, causing  $H_t$  and  $V_{s,2}$  to remain almost constant over the whole diluent fraction range. For example, as was shown in Fig. 7.1a, the shock tube shock speed ( $V_{s,1}$ ) decreases with increasing diluent fraction over most of the range shown. However, the shock tube post-shock density ( $\rho_2$ ) also decreases with increasing diluent fraction over most of the range. This causes  $V_{s,1} - V_2$  to decrease, which makes the post-shock velocity ( $V_2$ ) remain almost constant. Another example is the post-shock sound speed ( $a_2$ ), which decreases slightly over most of the diluent fraction range, but is offset by the increase in post-shock pressure ( $p_2$ ).

Considering the neon diluent results shown in Fig. 7.3b, much larger changes in the state 2 variables are seen, with, for example, maximum changes in the post-shock density and pressure ( $\rho_2$  and  $p_2$ ) of almost 400%. The large changes seen in Figs. 7.2b and 7.3b over the whole

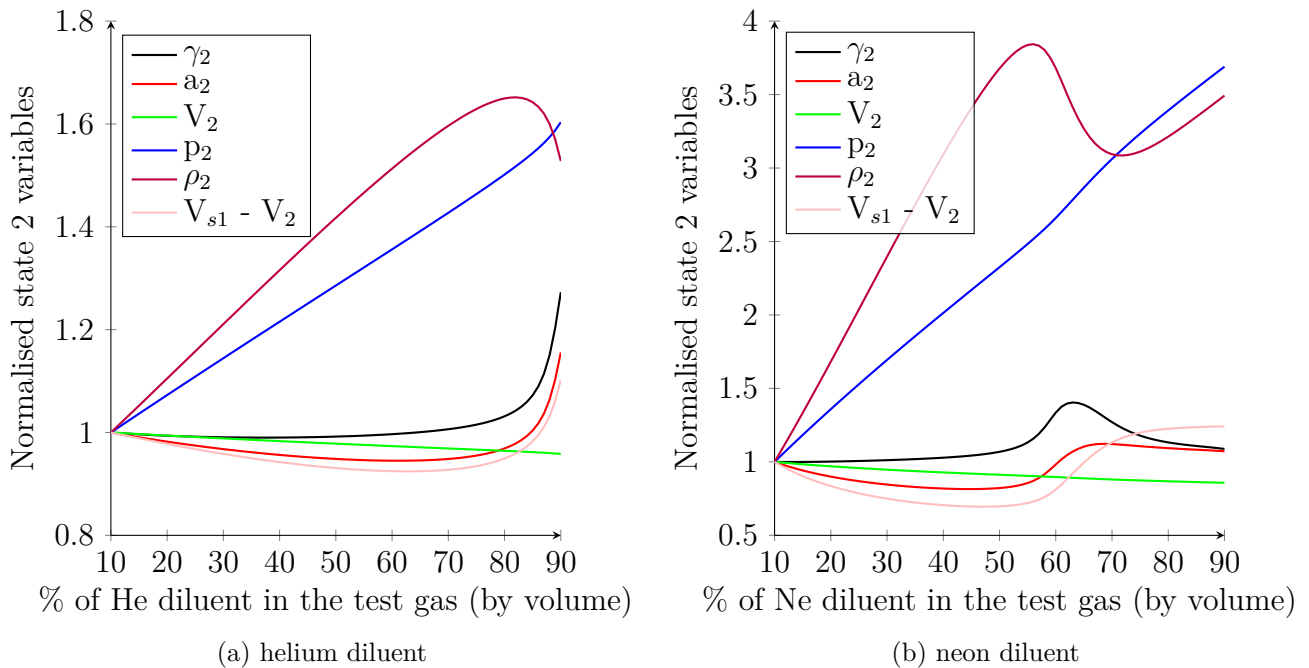


Figure 7.3: Effect of diluent fraction on the post-shock test gas condition (state 2). Normalised by 10% diluent.

neon diluent fraction range explain why larger changes are seen in Fig. 7.1b than was seen in Fig. 7.1a using the helium diluent.

#### 7.4.2 Effect on the Final Test Flow (states 8 and 10)

The figures in this subsection show how the initial test gas diluent fraction affects the fully processed test flow (state 8) and its post-normal shock state (state 10). Figs. 7.4, 7.5, 7.6, and 7.7, show its effect on the temperature in the stagnation region behind the bow shock over the test model for both frozen and equilibrium flow, the equilibrium composition in the stagnation region, various test section variables, and the modified binary scaling parameter (Equation 7.1). Frozen results are presented to illustrate the effect directly behind the shock wave, before reactions have occurred, and equilibrium results are presented to compare the effect on the final equilibrium state.

Considering the helium diluent (Fig. 7.4a) it can be seen that the temperature behind both the frozen and equilibrium normal shock waves increases approximately linearly with increasing helium diluent fraction. The frozen temperature varies from 12,800 K to 27,800 K over the 10 to 90% helium diluent range, and the equilibrium temperature increases from 3,500 K to 14,000 K over the same range.

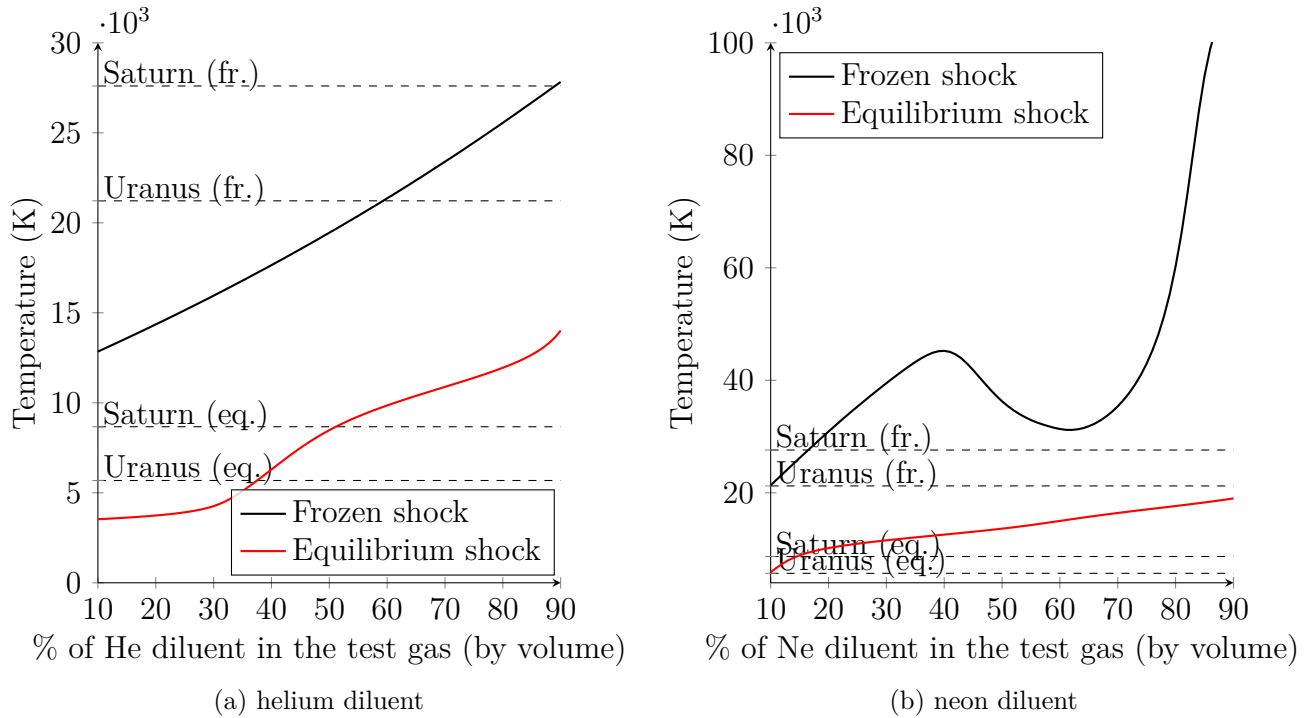


Figure 7.4: Effect of diluent fraction on the frozen and equilibrium post-normal shock temperatures in the stagnation region over the test model (state 10)

To understand the practical implications of Fig. 7.4, it is useful to compare these temperatures to the aforementioned proposed Uranus and Saturn missions. For this reason, related temperatures from trajectory points analysed by Palmer et al. [71] were calculated and are also shown in Fig. 7.4. Considering the 34.5s Uranus entry point from Table 4 in that paper [71] (shown here in Table 7.1), calculations performed by the author with NASA's Chemical Equilibrium with Applications (CEA) code [197, 198], gave post-normal shock frozen and equilibrium temperatures of 21,200 K and 5,700 K, respectively. Fig. 7.4a shows that the frozen and equilibrium temperatures could be re-created with 54 and 36% helium fractions respectively. Both the CEA equilibrium calculation for the Uranus entry point and the related test condition utilising a 36% helium diluent fraction have 99.8%  $H_2$  dissociation in the shock layer at equilibrium. A difference between the real flight conditions and the simulated conditions is seen when considering shock relaxation. Whilst the condition with 36% helium diluent is able to re-create both the post-shock equilibrium temperature and  $H_2$  dissociation percentage, due to the increased helium diluent fraction in the experimental conditions (and potentially different post-shock densities to true flight), the experimental conditions do not relax from the same frozen condition to the same equilibrium one. This is still a useful conclusion, but it means that different amounts of diluent would need to be used to study non-equilibrium behaviour

Table 7.1: Uranus and Saturn entry points from Tables 4 and 8 in Palmer et al. [71] used for comparison in this chapter. Significant figures from Palmer et al. [71] have been maintained.

Planet	Entry point (s)	Freestream density ( $\rho_\infty$ , kg/m <sup>3</sup> )	Freestream temperature ( $T_\infty$ , K)	Freestream velocity ( $U_\infty$ , m/s)	Composition of outer atmosphere (by volume)
Uranus	34.5	$2.04 \times 10^{-5}$	128.2	22,504	85% $H_2$ /15%He [274]
Saturn	206	$1.80 \times 10^{-5}$	141.0	26,316	89% $H_2$ /11%He [273]

directly behind the shock wave and equilibrium behaviour further away from the shock. It should be noted that in reality shock waves rarely reach the frozen limit due to the finite width of the shock itself. This means that even a test condition which does not match the frozen condition exactly, such as one with a lower helium diluent fraction, may still produce sufficient non-equilibrium behaviour.

Now considering Palmer et al.'s [71] 206 s Saturn entry point from Table 8 in that paper (shown here in Table 7.1) the same calculation as above gave a frozen temperature directly behind the shock of 27,600 K and an equilibrium temperature of 8,700 K. The frozen and equilibrium temperatures could be re-created with helium diluent fractions of 84 and 50% respectively. A CEA [197, 198] calculation for the Saturn entry point indicates full  $H_2$  dissociation and 1.6% H ionisation in the shock layer at equilibrium. The theoretical test condition with 50% helium diluent is fully dissociated at equilibrium also, with 1.98% of the H ionised. Once again, different helium diluent fractions would be needed to study non-equilibrium and equilibrium behaviour for this entry point.

Fig. 7.4b shows the equivalent post-shock temperatures for the neon diluent. The frozen result shows a linear increase in temperature from 10 to 40% diluent, before then showing a parabolic decrease to 60% diluent and then a parabolic increase after that. The equilibrium result increases linearly from 20 to 90% diluent. Over the diluent fraction range shown, the frozen temperature increases from 21,300 K to 109,000 K and the equilibrium temperature increases from 5,890 K to 19,000 K. Comparing this to the helium results shown in Fig. 7.4a, there is a theoretical 33% increase to the maximum equilibrium temperature achievable by using a neon diluent. However, the study by Stalker and Edwards [67] stated that their substitution stopped being valid when the neon started to ionise, because at this point the  $H_2/He$  and  $H_2/Ne$  results began to diverge. Examining Fig. 7.5, which shows the equilibrium composition behind the bow shock for both diluents, the neon begins to ionise with 49% diluent. This invalidates any conditions with neon diluent beyond this for equilibrium studies if their rules are followed [67]. This reduces the maximum achievable equilibrium temperature with  $H_2/Ne$  to 14,700 K for this condition, a 2% increase from the maximum  $H_2/He$  value.

A difference which can be seen in Fig. 7.4 is the diluent fraction which is required to simulate the planetary entry trajectory points. In Fig. 7.4b, it can be seen that the Uranus entry trajectory point is actually too cold for the  $H_2/Ne$  results shown, but it could be simulated with a different, slower test condition. For the Saturn entry point, a 15% diluent fraction (by volume) is required to simulate the frozen post-shock temperature, and 14% is required to simulate the equilibrium post-shock temperature. This means that the same condition could be used to simulate both non-equilibrium phenomena directly behind the shock and equilibrium phenomena further away from it when a neon diluent is used. This diluent fraction is also much closer to the helium fractions of the real entries, which are 11% for Saturn [274] and 15% for Uranus [273]. It also means that if only around 15% diluent (by volume) is needed to simulate Saturn entry, there is a lot of extra performance there to be exploited in the future for the simulation of faster entries.

Fig. 7.5 shows how the equilibrium composition of the shocked test gas in the stagnation region over the test model varies with changing diluent fraction. For the helium diluent (Fig. 7.5a), it can be seen that the mole fraction of atomic hydrogen initially rises to a peak at 30% diluent, at which point the  $H_2$  is fully dissociated. H ionisation begins when the helium diluent fraction is 35%, and with a diluent fraction of 90% the calculations predict almost complete ionisation of the hydrogen atoms.

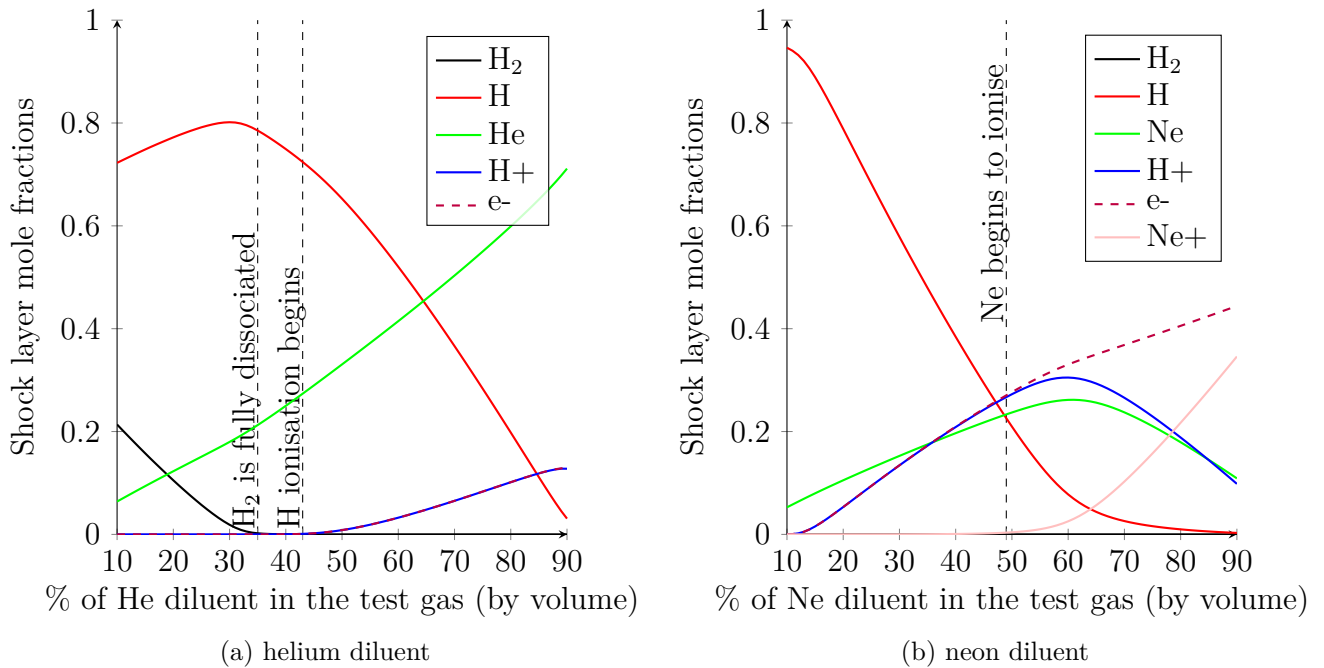


Figure 7.5: Effect of diluent fraction on the equilibrium composition of the test gas in the stagnation region over the test model (state 10).

In Fig. 7.5b, larger changes are seen with the neon diluent. Firstly, the hydrogen is already completely dissociated with a 10% diluent fraction, and above 49% diluent, the neon itself starts to ionise, which is the point at which Stalker and Edwards said their substitution was no longer valid [67] because the  $H_2/He$  and  $H_2/Ne$  results began to diverge.

Comparing Fig. 7.5 to the equilibrium calculations performed for the trajectory points from Palmer et al. [71] shown in Table 7.1, the Uranus entry point is predicted to be fully dissociated but with only negligible ionisation (an ion/electron mole fraction of  $8.0 \times 10^{-5}$ ), which could be simulated with a helium diluent fraction of around 35%. The Saturn point is predicted to be fully dissociated, and slightly ionised (an ion/electron mole fraction of 0.02), which could be simulated with a helium diluent fraction of around 50% or a neon diluent fraction of around 15%. As was found when the post-shock temperature results shown in Fig. 7.4 were discussed, higher neon diluent fractions would only be able to be used to simulate faster entries for these facility fill conditions.

To examine the flow properties immediately before and after the bow shock over the test model, Fig. 7.6 shows how temperature, density, pressure, and velocity in the nozzle exit / test section freestream flow (state 8) and the frozen post-shock flow in the stagnation region (state 10fr) change with differing diluent fraction. Considering the helium diluent results shown in Fig. 7.6a, most variables change by less than 20% over the full range of diluent fractions shown, with the exception of the freestream pressure ( $p_8$ ) which drops by around 50%, and the frozen post-shock temperature ( $T_{10,fr}$ ), which more than doubles over the full range. This shows that the main change made to the flow by adding more helium diluent is to increase the immediate post-shock temperature, simulating a faster and hotter entry.

Consistent with earlier results, much larger changes are seen with the neon diluent (Fig. 7.6b). The largest change seen is still the frozen post-shock temperature ( $T_{10,fr}$ ) with a maximum increase of 500% with 90% diluent. There is also a very large increase in freestream temperature ( $T_8$ ) which was not seen for the helium diluent in Fig. 7.6a. Similar to Fig. 7.6a, the changes in velocity, pressure, and freestream density ( $\rho_8$ ) are not large compared to the changes in temperature, however, there is a large increase in the frozen post-shock density ( $\rho_{10,fr}$ ) for neon diluent fractions between 40 and 80% which was not seen for the helium diluent (Fig. 7.6a).

Fig. 7.7 shows how the modified binary scaling parameter proposed by Stalker and Edwards ( $\Omega$ , see Equation 7.1) varies with changing diluent fraction at the immediate post-bow shock condition (i.e. the frozen condition).  $\Omega$  aims to scale the reaction lengths in space like a normal binary scaling parameter, but while also taking into account the changing diluent fraction in the test gas. This is explained further in Section 7.3. The modified binary scaling parameter is compared to the aforementioned trajectory points from Palmer et al. [71] which are shown in

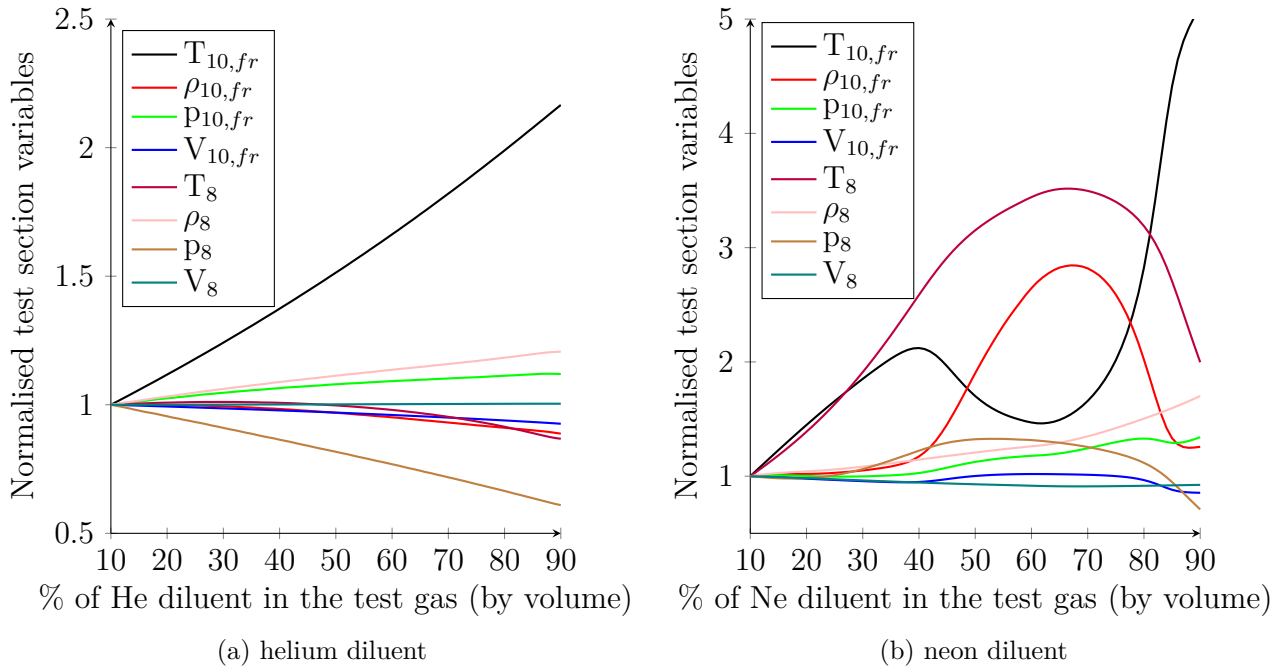


Figure 7.6: Effect of diluent fraction on the test gas in the test section both before (state 8) and immediately after (state 10fr) the normal shock over the test model. Normalised by 10% diluent.

Table 7.1 at both the full size, and the maximum feasible test model diameter for simulation in X2 ( $\approx 100$  mm). The full scale  $\Omega$  values for the trajectory points are 0.896 and 0.821 for the Saturn and Uranus entry points respectively. The scaled Saturn entry value of 8.96 is based on a 1,000 mm diameter aeroshell scaled down to 100 mm (1/10 scale), and the scaled Uranus entry value of 5.75 is based on a 760 mm diameter aeroshell scaled down to 108.6 mm (1/7 scale). The full scale aeroshell sizes are the values which were used by Palmer et al. [71] for their analysis. The results of six different simulations are shown on the figures to illustrate which facility parameters can be modified to change the  $\Omega$  of the resulting X2 test condition. The test conditions are based on conditions X2-GG-UE-2.5 mm and X2-GG-UE-2.5 mm-SD from Table 2 in James et al. [20], but instead of leaving the acceleration tube fill pressure ( $p_5$ ) constant at 0.5 Pa, simulations were performed using  $p_5$  values of 0.5, 5.0, and 10 Pa. The curves labelled ‘No S.D.’ are simulations without a secondary driver section, whereas the dashed curves labelled ‘With S.D.’ are simulations *with* a secondary driver. It should be noted that the curves labelled ‘No S.D.,  $p_5 = 0.5$  Pa,  $H_t \approx 166$  MJ/kg’ for the helium diluent and ‘No S.D.,  $p_5 = 0.5$  Pa,  $H_t \approx 136 - 166$  MJ/kg’ for the neon diluent are for the test condition analysed in the other parts of this section. Where  $H_t$  ranges are shown on the labels, this is because  $H_t$  is changing over the diluent fraction range shown.

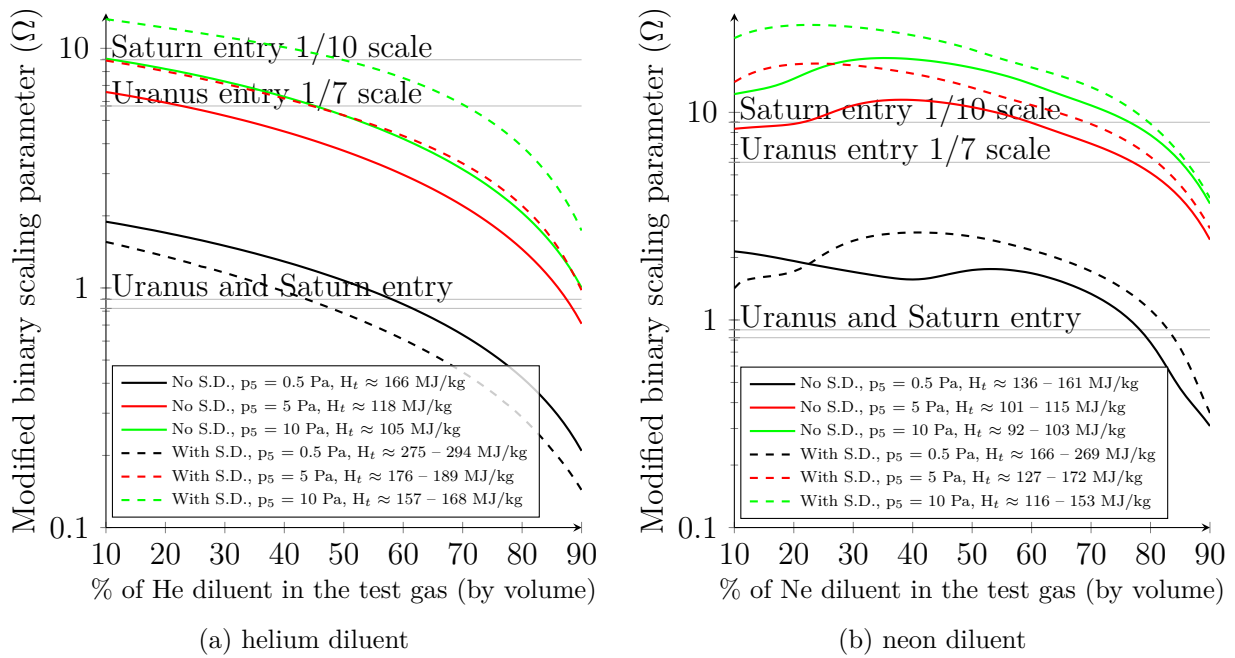


Figure 7.7: Effect of diluent fraction on the immediate post-shock modified binary scaling parameter ( $\Omega$ ) for different test conditions.

In Fig. 7.7a where the helium diluent results are shown, there is generally around an order of magnitude difference in modified binary scaling parameter for each condition over the full range of diluent fractions, with a higher value seen with lower diluent fractions because Equation 7.1 scales linearly with the amount of molecular hydrogen in the shock tube fill condition. It can also be seen that higher  $\Omega$  values are seen with higher  $p_5$  values because these conditions are expanded less in the acceleration tube. However, they are also slower, and would have a lower  $H_t$ . For the condition without a secondary driver and  $p_5 = 10$  Pa,  $\Omega$  varies from 9.05 to 1.00 and this condition could potentially be used to simulate Uranus entry at 1/7 scale. However, a 39% reduction in  $H_t$  to around 105 MJ/kg compared to the condition with  $p_5 = 0.5$  Pa means that the condition may no longer have enough flow stagnation enthalpy to generate the post-shock temperatures required. The effect of using higher  $p_5$  values with the helium diluent is examined further in Section 7.4.3.

There are several solutions shown in Fig. 7.7 which would allow post-shock temperature and  $\Omega$  to be more easily matched. One would be the use of a secondary driver section, which would allow the freestream density to be modified while still maintaining the same flow stagnation enthalpy [1]. While in Chapter 6 a secondary driver was used to increase the achievable stagnation enthalpy beyond the ability of a basic expansion tube, it can also be used to allow flow density to be increased while maintaining flow stagnation enthalpy by allowing higher fill



pressures to be used. Here, higher  $p_5$  values have been used, and in Fig. 7.7a the results with the secondary driver have much higher  $H_t$  values for similar  $\Omega$  values.

Another solution is using the neon diluent, which is shown in Fig. 7.7b. In previous figures it was shown that very small neon diluent fractions (13 to 15%) were required to simulate the proposed Saturn entry, therefore, it would be much more likely that scaled neon conditions could be used with either higher fill pressures or low diluent fractions to reach the required  $\Omega$  values. As a much lower  $H_t$  is needed to simulate the required shock layer conditions using neon, a secondary driver would also probably not be required. This is an advantage of using a neon diluent and something which can be investigated further in the future.

While it will not be discussed further here, another solution for achieving the required binary scaled conditions is to use the facility without its contoured nozzle, because generally the order of magnitude of the density loss through the nozzle expansion is greater than the decrease in scaling factor gained in increased model size. In James et al. [20] conditions without a nozzle were able to simulate binary scaled conditions which could not be simulated with the nozzle.

### 7.4.3 Using a Higher $p_5$ Value with the Helium Diluent

In Section 7.4.2 it was discussed that higher acceleration tube fill pressures ( $p_5$ ) may be required to allow scaled test conditions to be re-created with a helium diluent. For this reason, Fig. 7.8 here examines the effect of using a higher  $p_5$  value by re-creating Fig. 7.4a with the related temperatures for acceleration tube fill pressures of 5 and 10 Pa added to the figure. The original result from Fig. 7.4a is shown as ' $p_5 = 0.5$  Pa'.

Examining Fig. 7.8 it can be seen that it is only possible to simulate the frozen conditions directly behind the shock for the two entries using a  $p_5$  value of 0.5 Pa. This shows that  $p_5 = 0.5$  Pa is definitely required for the study of non-equilibrium phenomena near the shock for these test conditions. However, looking at the equilibrium results shown on the figure, it can be seen that a low  $p_5$  value is not as important. Between 10 and 20% helium diluent fraction, all three acceleration tube fill pressures shown on the figure ( $p_5 = 0.5$ , 5, and 10 Pa) equilibrate to the same temperature around 4,000 K. After this, there is a period from 20 to around 48% diluent fraction where the  $p_5 = 0.5$  Pa result begins increasing and the  $p_5 = 5$  and 10 Pa results remain fairly flat. After this point, the  $p_5 = 5$  and 10 Pa curves start to increase, and above around 70% diluent fraction, their temperatures are around 90% of the  $p_5 = 0.5$  Pa temperature. This is another interesting result, showing that equilibrium phenomena away from the shock could potentially be simulated with much slower conditions if it is necessary. It is also useful because the post-shock flow is more likely to actually equilibrate at higher pressures as well.

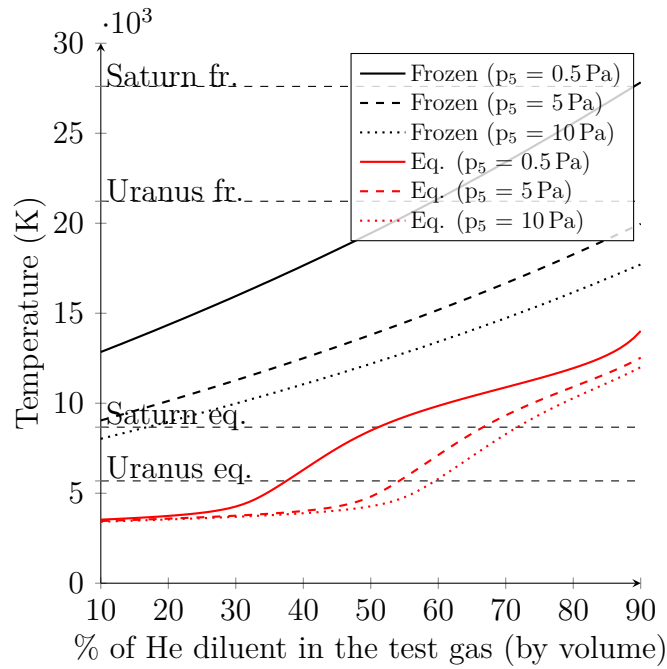


Figure 7.8: Effect of diluent fraction and  $p_5$  on the frozen and equilibrium post-normal shock temperatures in the stagnation region over the test model (state 10)

#### 7.4.4 Effect on the Post-shock Radiation

As part of this thesis, the author added atomic hydrogen, helium, and neon line radiation to the SPECAIR radiation analysis code [287, 288]. To examine the effect that the diluent fraction would have on the radiation of the post-normal shock test flow in the test section, equilibrium gas spectral calculations were performed using SPECAIR for a 1 cm tangent slab for each simulated diluent concentration with self absorption turned on. No slit function was used for the calculations. Calculations were performed both using atomic hydrogen as the only radiating species and using radiating atomic hydrogen and the relevant diluent (helium or neon). The total power density from line radiation in both the Lyman series in the vacuum ultraviolet (VUV) from 91.9 nm to 121.6 nm and the Balmer series in the ultraviolet (UV) and visible range from 364.6 nm to 656.3 nm was integrated for each diluent fraction. The results were separated this way to show how much of the radiation comes from the VUV region which is operationally difficult to measure as it is absorbed by the oxygen in the air. How VUV radiation can be measured in X2 is discussed in Sheikh et al. [127, 286] and Wei et al. [86]. The results are shown in Fig. 7.9. To provide an approximate comparison, similar equilibrium radiation calculations were also performed for the trajectory points from Palmer et al. [71] which are shown in Table 7.1. A single line was provided for each trajectory point as the Lyman and Balmer series radiation was found to be very similar for both trajectory points. Uranus entry

results are not provided for the neon diluent as they were too small to be shown on the figure.

In Fig. 7.9a, for the helium diluent, the final calculations were performed without helium as a radiating species, because no difference was seen in the results with and without helium radiation. In Fig. 7.9b, for the neon diluent, no difference in radiation was seen for the Lyman radiation results with and without neon as a radiating species, so only the result without neon radiation is shown. For the Balmer series radiation shown in Fig. 7.9b, results are shown with radiating neon.

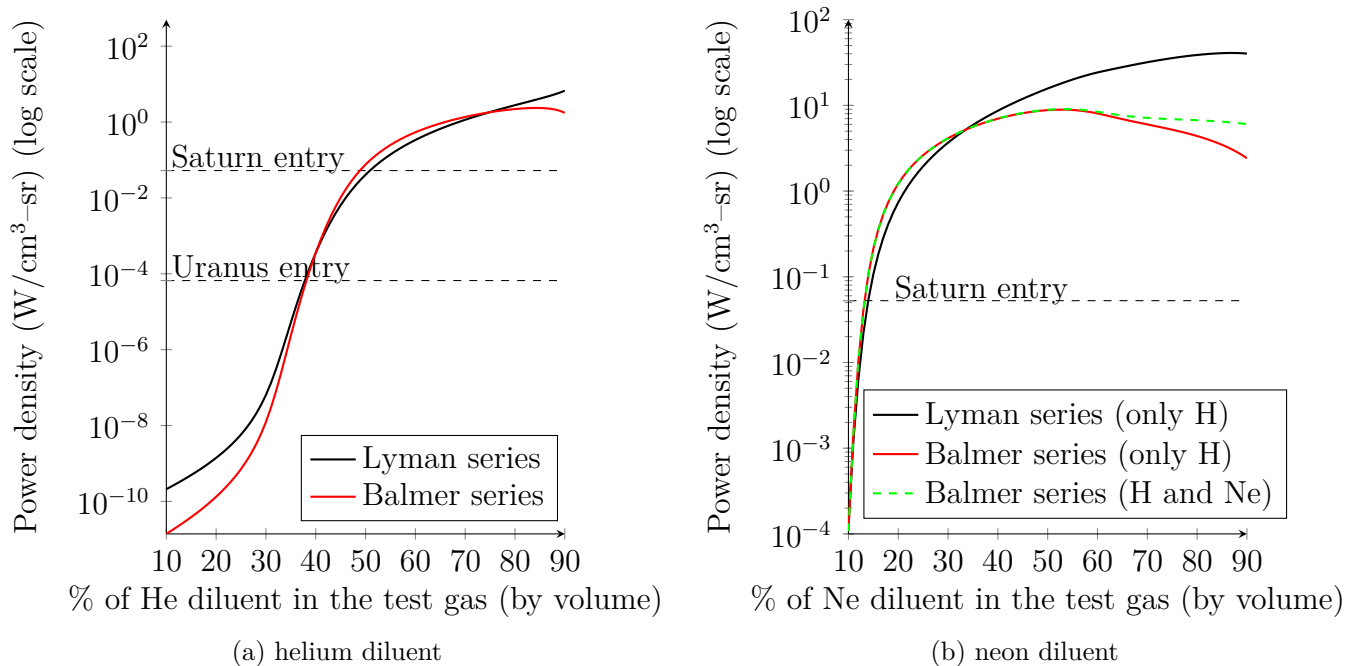


Figure 7.9: Effect of diluent fraction on the theoretical total power density in the Balmer and Lyman series from a 1 cm tangent slab in thermochemical equilibrium.

In Fig. 7.9a, it can be seen that for every case shown on the figure, there is around an eleven order of magnitude increase in power density over the full range of helium diluent fractions shown in the figure. It can also be seen that the steepest increase occurs between 30 and 40% helium diluent, and that the power density is increasing linearly above around 70%. It can also be seen that diluent fractions of around 40 and 50% are required to re-create the equilibrium radiation of the Uranus and Saturn entry trajectory points. It should also be noted that what is shown for each case is the *total* power density in that wavelength region; it is not scaled by the  $H_2$  fraction in the fill condition (state 1). This means that even though the diluent fraction is increasing, and therefore the amount of molecular hydrogen in the fill state is decreasing, the power density is still increasing due to the increased shock layer temperature. Considering the

individual curves, it can be seen that the power density in both the Lyman and Balmer series are both very similar for most of the range.

In Fig. 7.9b, for the neon diluent, it can be seen that in general there is an increase in power density of around five orders of magnitude over the full neon diluent fraction range. The Lyman radiation initially shows a steep increase from 10 to 15% diluent followed by a slower increase over the rest of the diluent range which appears to be reaching a plateau at 90% diluent. Considering the Balmer series radiation *with* radiating neon, the same steep increase is seen for diluent fractions from 10 to 15% as was seen for the Lyman radiation but it then plateaus beyond a diluent fraction of 50%. For the conditions simulated *without* neon radiation, after this plateau the power density continues to drop. For the conditions simulated *with* neon radiation, the power density drops from around 50 to 60% diluent fraction before the gradient flattens out presumably due to neon line radiation appearing in the integration region between 364.6 and 656.3 nm. While it is not anticipated that the neon line radiation would interfere with the hydrogen line radiation, this is interesting to note because it means that the neon is definitely no longer acting as an inert diluent. It is electronically excited and it is affecting the radiating flow-field which it has created. It can also be seen that a diluent fraction of only around 15% is required to simulate the Saturn entry trajectory point.

Similar to Fig. 7.9a, the results in Fig. 7.9b are not scaled by the H<sub>2</sub> fraction in the test gas fill state. This means that the total power density is increasing with increasing diluent fraction, even as the amount of H<sub>2</sub> in the test gas fill state is decreasing, showing once again that the increased temperature is having a large effect on the radiation.

#### 7.4.5 Effect on the Stagnation Point Heat Flux

An important consideration for planetary entry is the stagnation point heat flux, which is generally either quoted at different points of a trajectory as a rate or as an integrated heat load for whole entry trajectories. Many simple correlations exist for calculating the stagnation point heat flux to simple axisymmetric entry bodies entering atmospheres in the solar system. To examine the effect that the substitution will have on the stagnation point heat flux generated by the test conditions, convective and radiative heat flux correlations have been utilised with the results presented in Fig. 7.10. The convective stagnation point heat flux correlation from Sutton and Graves [289] was used to calculate the convective heat flux, with a more generic equation and the results from Section 7.4.4 used to find the radiative heat flux. Further information about how the correlations were used to produce the plot can be found in Appendix K. Calculations were performed for an axisymmetric body with a nose radius of 70 mm, which was the nose radius of the test model used in a recent preliminary gas giant entry radiation study performed

in X2 by Liu et al. [22]. Calculations performed using the correlations for the Uranus and Saturn trajectory points from Palmer et al. [71] (which are shown here in Table 7.1) also used the same model size to facilitate easy comparison. Due to the minute radiative heat flux seen for the conditions, comparisons with the trajectory points were performed using only convective heat flux calculations.

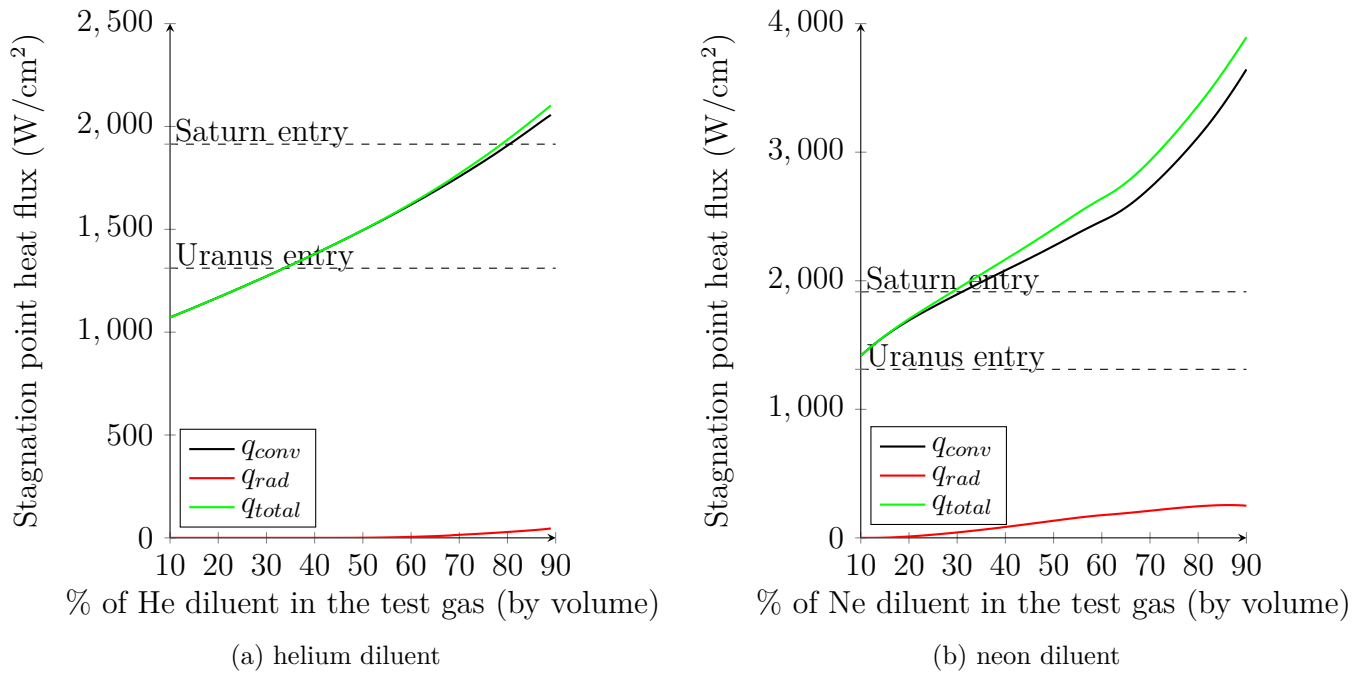


Figure 7.10: Effect of diluent fraction on the stagnation point heat flux to a spherical test model.

Examining Fig. 7.10, it can be seen that an increased diluent fraction results in increased stagnation point heat flux, with an increase of around 100% seen over the range shown for the helium diluent (Fig. 7.10a) and an increase of around 200% seen for the neon diluent (Fig. 7.10b). It can be seen in Fig. 7.10a that a helium diluent fraction of around 35% would be required to re-create the stagnation point heat flux of the Uranus trajectory point and a helium fraction of around 80% would be required to re-create the heat flux for the Saturn trajectory point. For the neon diluent, the Uranus trajectory point is actually off the scale of the plot, and a neon diluent fraction of around 30% would be required to recreate the stagnation point heat flux of the Saturn trajectory point. It can be seen that overall the contribution of the radiative heat flux is quite small, especially for the helium diluent (Fig. 7.10a). This could be an issue with the basic formula which was used to calculate the radiative heat flux (see Appendix K) but it is more likely that these are just not strongly radiating conditions. For the aforementioned Uranus and Saturn entry trajectory points (see Table 7.1, considering their

CFD stagnation point heat flux values from Tables 4 and 8 in Palmer et al. [71], the radiative heat fluxes are 0.85% and 5% of the convective heat fluxes respectively. Also, as is discussed in Section VI.A. of Capra and Morgan [290], convective heat flux to scaled test models increases with decreasing model size while radiative heat flux remains similar to the full scale case. This generally causes convective heating to dominate in scaled experiments.

## 7.5 Experimental Results

Experiments were performed for three different helium diluent fractions to confirm the results of the theoretical analysis presented in Section 7.4. Due to experimental time constraints, no experiments were performed using a neon diluent. The experimental test condition analysis is presented in Section 7.5.1 and an experimental analysis of the time-resolved test flow radiative emission from a high speed camera is presented in Section 7.5.2.

X2's Pitot rake was used as the test model for all of the experiments presented here to ascertain the nozzle exit pressure, core flow size, and test times for the test conditions. The Pitot rake uses nine impact pressure probes, which are 15° half-angle conical probes for these experiments, spaced 17.5 mm apart radially along the nozzle exit plane, covering a total centre-to-centre height of 140 mm. The middle probe ('pt5' by convention) was oriented with the centre-line of the nozzle. The majority of the experiments (all except x2s3241 and x2s3242) made use of a Pitot pressure probe in the centre location of the Pitot rake ('pt5') as a separate experiment to examine the time resolved total post-normal shock radiative emission of the test conditions using a high speed camera. These results are presented in Section 7.5.2.

### 7.5.1 Test Condition Analysis

The condition tested here is the one discussed in Section 7.4, which is based on condition X2-GG-UE-2.5 mm from Table 6.2 in Chapter 6. The facility configuration details of the test condition can be seen in Table 7.2. The three different test gas compositions cover most of the range discussed in Section 7.4 using a helium diluent. 85% $\text{H}_2$ /15%He (by volume) is the composition of the outer atmosphere of Uranus [273], 60% $\text{H}_2$ /40%He (by volume) is at the end of the steep rise in expected radiative power density seen in Fig. 7.9a, and 30% $\text{H}_2$ /70%He (by volume) is the composition on the same figure where the power density plateaus.

Two experiments were performed with an 85% $\text{H}_2$ /15%He (by volume) test gas (x2s3241 and x2s3244), which are also presented in Chapter 6 as condition X2-GG-UE-2.5 mm. Two experiments were performed with a 60% $\text{H}_2$ /40%He (by volume) test gas (x2s3242 and x2s3243) and because the authors only had access to two gas bottles to fill and store the required mixtures

Table 7.2: Facility configuration details of the test condition used.

Driver condition	X2-LWP-2.5 mm-0 [231, 230] using modification for orifice plate [2]
Primary driver fill condition	77.2 kPa 100%He (by volume)
Primary diaphragm	1 x 2.5 mm thick cold rolled steel, scored diaphragm
Orifice plate diameter	65 mm
Shock tube fill condition	2.0 kPa either 85%H <sub>2</sub> /15%He, 60%H <sub>2</sub> /40%He, or 30%H <sub>2</sub> /70%He, (by volume)
Secondary diaphragm	1 x 14 $\mu$ m thick aluminium foil diaphragm
Acceleration tube fill condition	0.5 Pa laboratory air

in, four 30%H<sub>2</sub>/70%He (by volume) experiments were performed to test how the filling process affected the test conditions. The first two experiments (x2s3253 and x2s3254) were filled to 1 kPa using the 60%H<sub>2</sub>/40%He (by volume) mixture used for those experiments, and then with another 1 kPa from a helium bottle. The final two experiments (x2s3255 and x2s3256) were filled directly into the shock tube from a helium bottle and then a hydrogen bottle.

The naming conventions used here are the same as that which is used in other parts of this thesis. The experimental shock speed naming convention, for example ‘sd1-sd3’, is a reference to the two specific wall pressure sensor locations used to find that particular shock speed value. Where experimental shock speeds are shown in figures, the values are shown at the midpoint between the two sensor locations. When experimental pressure measurements are discussed, their names either correspond to wall pressure sensor locations or the locations of the sensors in the X2 Pitot rake. (Approximate X2 wall pressure sensor locations are shown in Fig. 5.1 and exact values from Gildfind et al. [232] can be found in Table 4.2.)

Experimental shock speed uncertainties were found using a shock speed uncertainty calculation procedure described in Appendix G. The experimental pressure measurements presented here were also found using the same methodology used in that work. To take into account the uncertainty which exists when modelling an expansion tube experiment, principally due to the shock speed uncertainties, a technique for calculating both a nominal case as well as a set of solution bounds for important gas states from Chapter 5 was used to find the flow properties discussed in this section. The technique calculates the nominal case and the overall solution bounds of each facility gas state by assuming that the uncertainties on the fill pressures have a small effect compared to the shock speed uncertainties and can be ignored. The mean uncertainties on the mean experimental shock speeds (i.e. the root sum squared [RSS] uncertainties) in each section of the facility can then be used to find the test section state using an experimental equilibrium version of PITOT which performs an experimentally inferred uncertainty analysis on the nozzle entrance and final test section state by perturbing the calculation using

every permutation of the shock speeds and their mean uncertainties. The nominal case is the result using the mean shock speeds, and the solution bounds are the minimum and maximum of each quantity from all of the shock speed permutations. The analysis is then calibrated so that the experimental wall pressure measured in the acceleration tube and the pressure on the probes in X2's Pitot rake fall inside the bounds of the overall solution by running the analysis with several different assumptions for the different situations where expansion tubes often diverge from ideal theory. These situations are discussed further in Section 5.5.

In Chapter 6, where the simulation of true flight velocity gas giant entry in X2 was considered, this experimentally inferred analysis was also used to quantify two different experiments, one of which was experiment x2s3244, which is also part of this analysis here. For this reason, it was chosen to start the analysis here using the specific assumptions which were found most suitable for experiment x2s3244 in that chapter. This was a fully reflected shock at the secondary diaphragm to simulate the effect of the secondary diaphragm on the test flow, expanding the shocked test gas to the shock speed in the acceleration tube to simulate low density shock tube (or 'Mirels') effects [106, 107, 108], and an effective nozzle area ratio of 3.5 to simulate the effect of the boundary layer in the acceleration tube and nozzle on the nozzle's performance. Different effective area ratios have also been tested in this chapter, but 3.5 was used as a starting point.

The experimental shock speed data for all of the experiments are presented in Figs. 7.11 and 7.12. Even though the conditions have different test gas compositions, because the shock speeds were expected to stay almost the same in both tubes in Section 7.4 (see Fig. 7.1a), theoretical equilibrium data from PITOT is also shown based on the mean shock speed value for all of the compositions analysed in Section 7.4. Global mean and 95% CI values are also shown for each measured shock speed.

Fig. 7.11 shows the experimental shock tube shock speeds measured at three locations near the end of X2's shock tube. The mean equilibrium theoretical  $V_{s,1}$  value from the analysis presented in Section 7.4 is 8,552 m/s, where the maximum reduction from the initial 10% diluent value was less than 4% (see Fig. 7.1a). It can be seen that all of the experimental data is inside the 95% CI for each value and contains no outliers, even if two experiments (x2s3244 and x2s3256) are just inside the bounds for some measurements. It can also be seen that the experimental data is very similar to the mean equilibrium theoretical value with, for example, a 0.5% reduction between the global mean 'sd1-sd3' experimental value and the theoretical result. All of the experiments being statistically the same and close to the theoretical model is a very positive result, as it shows that inside the uncertainty of the experiments, the results of the theoretical analysis are valid.

Fig. 7.12 shows experimental acceleration tube shock speeds measured near the end of X2's



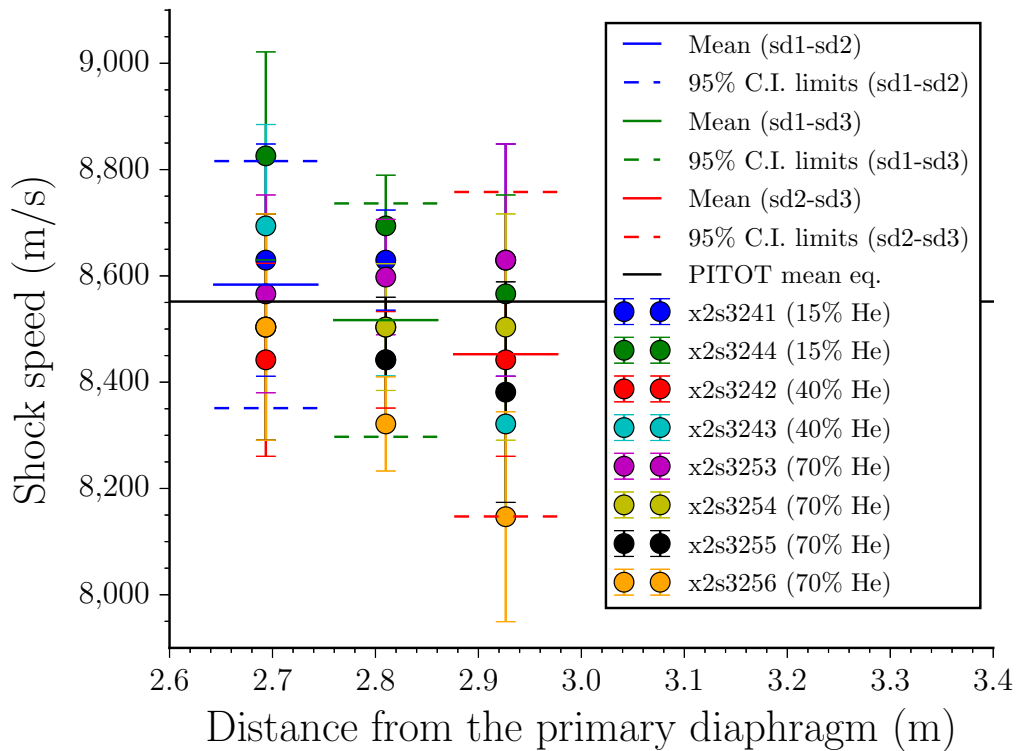


Figure 7.11: Experimental shock tube shock speeds ( $V_{s,1}$ ).

acceleration tube. The mean equilibrium theoretical  $V_{s,2}$  value from the analysis presented in Section 7.4 is 17,900 m/s, where the maximum increase from the initial 10% diluent value was around 1% (see Fig. 7.1a). When a fully reflected shock at the secondary diaphragm is added to the theoretical model, the mean  $V_{s,2}$  value over the full range examined in Section 7.4 becomes 19,140 m/s. Both of these values are also shown in Fig. 7.12. Similar to the shock tube results shown in Fig. 7.11, all of the global means are representative of all of the experimental data shown, which is once again a positive result, as it further confirms the theoretical results from Section 7.4 about the effect of the helium diluent fraction on the test conditions.

In Fig. 7.12 it can be seen that when the reflected shock at the secondary diaphragm is *not* used, the theoretical  $V_{s,2}$  is 5% less than the global mean values, and only the 95% CI range for value ‘at4-at5’ (probably due to the large uncertainty for experiment x2s3244) overlaps with the theoretical result. With the reflected shock used at the secondary diaphragm, the theoretical result is 2% greater than the the global mean ‘at4-at6’ experimental value, and all three 95% CI ranges include the theoretical result, showing that it is the better assumption to model the experimental data.

The unsteadily expanded test gas ( $p_7$ ) results both from the experiments and the experimentally inferred theoretical analysis can be seen in Table 7.3. The experimental results are

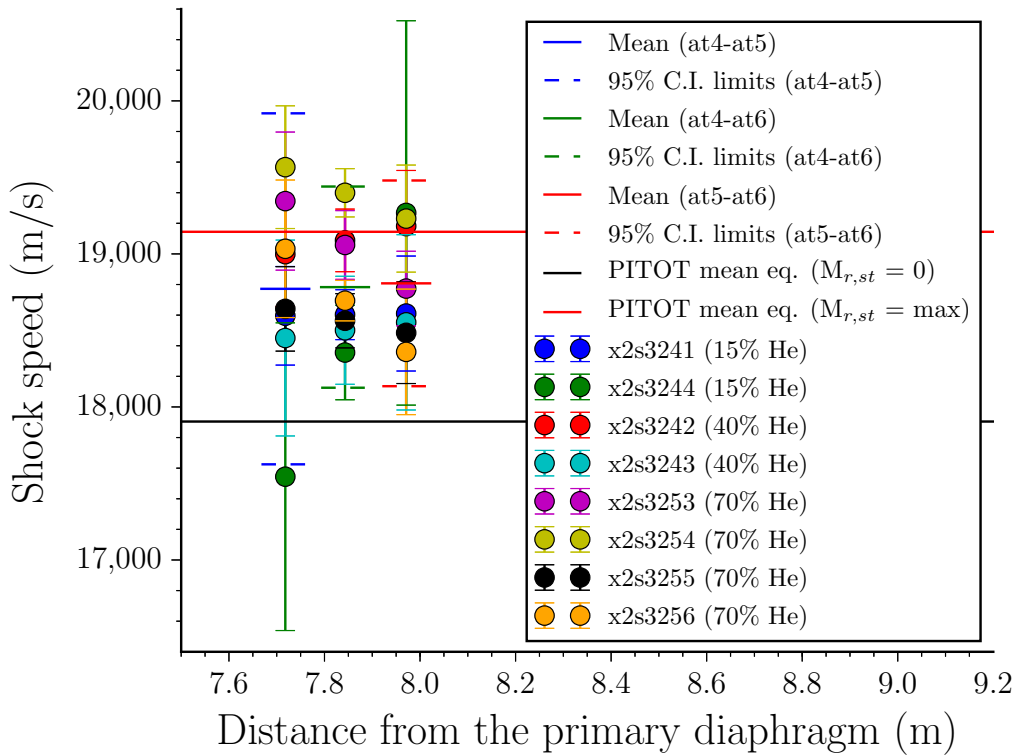


Figure 7.12: Experimental acceleration tube shock speeds ( $V_{s,2}$ ).

the mean of the filtered experimentally measured pressures from all eight ‘at’ labelled sensor locations in X2’s acceleration tube (‘at1’ to ‘at8’). The theoretical values shown from the analysis (both the nominal case and the solution bounds) were found using a fully reflected shock at the secondary diaphragm, and with the shocked test gas (state 2) unsteadily expanded to the acceleration tube shock speed ( $V_{s,2}$ ) in the acceleration tube. For every experiment, the uncertainties on the experimentally measured values overlap with the solution bounds from the experimentally inferred analysis, making the experiments and the theoretical results statistically consistent. From this it can be concluded that the aforementioned assumptions used with the theoretical model are valid. For this reason, these assumptions have been used for the following theoretical calculations presented in Table 7.4 and Figs. 7.13 and 7.14.

The test section  $15^\circ$  half-angle cone pressure ( $p_{10c}$ ) results both from the experiments and the experimentally inferred theoretical analysis can be seen in Table 7.4. Sensors ‘pt1’ and ‘pt9’ were deemed to be out of the core flow for all experiments, giving a core flow size of at least 120 mm based on the geometry of X2’s Pitot rake. A Pitot pressure probe was used in location ‘pt5’ for most experiments and sensor ‘pt8’ was deemed to be malfunctioning, so mean values were calculated using all remaining sensors. The experimentally inferred theoretical values shown were found by using the same assumptions which were used to find the results shown

Table 7.3: Experimental and theoretical unsteadily expanded test gas pressure ( $p_7$ ) results for all of the experiments.

Experiment	Experimental $p_7$ (kPa)	Theoretical nominal $p_7$ (kPa)	Theoretical $p_7$ solution bounds (kPa)
x2s3241	$1.61 \pm 0.14$ (8.7%)	1.12	0.85 – 1.44
x2s3244	$1.16 \pm 0.13$ (11%)	1.39	0.88 – 2.10
x2s3242	$0.94 \pm 0.12$ (13%)	0.83	0.62 – 1.07
x2s3243	$1.05 \pm 0.14$ (13%)	1.29	0.93 – 1.75
x2s3253	$1.18 \pm 0.18$ (15%)	1.38	1.07 – 1.74
x2s3254	$1.26 \pm 0.16$ (13%)	0.99	0.73 – 1.30
x2s3255	$1.04 \pm 0.14$ (13%)	1.44	1.11 – 1.81
x2s3256	$1.17 \pm 0.18$ (15%)	1.10	0.81 – 1.46

in Table 7.3 above and then calculating results with different effective area ratios in intervals of 0.5 to find the best match for the experimental data. The results are shown in Table 7.4. While it is not shown here, for the experiments where the Pitot pressure probe was used in location ‘pt5’, the Pitot pressure was also compared as a check of the effective ratio results. Except for experiments x2s3244 and x2s3243 where the Pitot pressure probe gave unrealistically low values, which can occur when the front of the probe mount is not tight enough, the same effective area ratio was able to be used for the Pitot pressure as well. In Table 7.4 it is interesting to note how often different effective area ratios are required for conditions with the same test gas composition, showing how sensitive this parameter is. The freestream conditions found using these effective area ratios are used to find the post-normal shock data shown in Figs. 7.13 and 7.14.

Another conclusion presented in Section 7.4 was that the stagnation enthalpy ( $H_t$ ) of the test conditions should remain virtually constant for all helium diluent fractions. Fig. 7.13 examines this by comparing the expected stagnation enthalpy values from the fully theoretical analysis from Section 7.4 with the reflected shock added at the secondary diaphragm to the experimentally inferred values for the individual experiments. Each experimental point shown on the figure is a different experiment. Considering the experimental data shown on the figure, it can be seen that more than half of the experiments, which includes the two experiments with a 15% helium diluent fraction (x2s3241 and x2s3242), one of the experiments with a 40% diluent fraction (x2s3243), and two experiments with 70% (x2s3255 and x2s3256, the two experiments filled directly into the shock tube), show a nominal reduction from what was expected theoretically of around 5 to 6%. The authors are not sure what this is caused by. It could be a small loss of total pressure at the secondary diaphragm or something caused by the shock speed uncertainties. One experiment with a 40% diluent fraction (x2s3242) is statistically consistent with the theoretical result, and so is one experiment with 70% (x2s3253). The remaining 70% diluent fraction experiment (x2s3254) is nominally around 2% faster than

Table 7.4: Experimental and theoretical test section  $15^\circ$  half-angle cone pressure ( $p_{10c}$ ) results for all of the experiments.

Experiment	Effective area ratio	Experimental $p_{10c}$ (kPa)	Theoretical nominal $p_{10c}$ (kPa)	Theoretical $p_{10c}$ solution bounds (kPa)
x2s3241	3.0	$2.22 \pm 0.19$ (8.7%)	2.34	1.98 – 2.74
x2s3244	4.0	$2.05 \pm 0.15$ (7.4%)	1.98	1.51 – 2.53
x2s3242	3.0	$2.13 \pm 0.26$ (12%)	2.02	1.72 – 2.35
x2s3243	3.5	$2.05 \pm 0.32$ (15%)	2.23	1.84 – 2.66
x2s3253	3.5	$2.48 \pm 0.36$ (14%)	2.38	2.04 – 2.77
x2s3254	3.5	$1.96 \pm 0.25$ (13%)	1.95	1.65 – 2.29
x2s3255	4.0	$2.10 \pm 0.30$ (15%)	2.11	1.82 – 2.44
x2s3256	4.0	$1.84 \pm 0.23$ (12%)	1.82	1.54 – 2.13

the theoretical result.

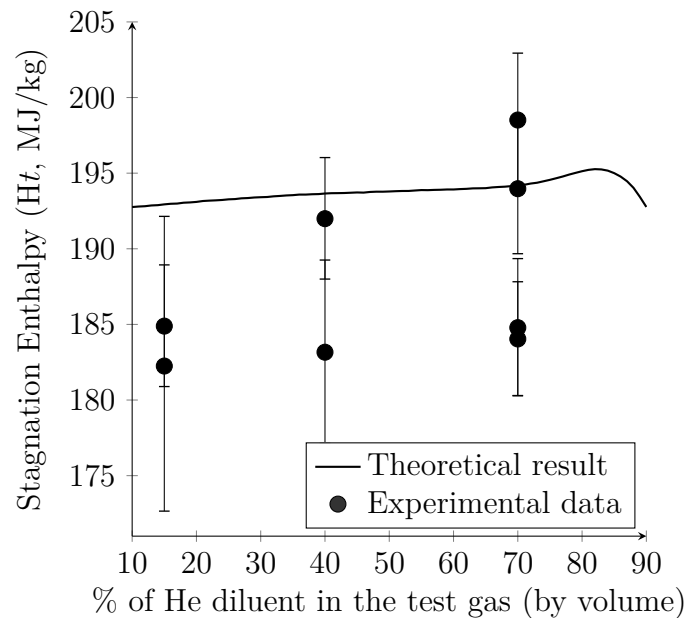


Figure 7.13: Comparing theoretical and experimental results for how changing helium diluent affects the stagnation enthalpy of the test condition.

As more than a half of the experiments showed a slight reduction from the expected theoretical stagnation enthalpy in Fig. 7.13, it is interesting to examine what effect that has on the expected post-normal shock temperatures in the test section. This is shown in Fig. 7.14. Once again, a fully reflected shock has been added to the fully theoretical calculation at the secondary diaphragm (which makes the theoretical results shown here different to Fig. 7.4a), and the theoretical results are compared to the experimentally inferred values for each individual experiment. Considering the frozen experimental data, the five experiments with a roughly 5 to 6% reduction in stagnation enthalpy show a nominal reduction in frozen post-shock temper-

ature of also around 5 to 6%, which would be expected for the frozen case due to its post-shock temperature only being a function of the stagnation enthalpy. Considering the equilibrium experimental data, it is interesting to note that the majority of the experiments which showed the 5 to 6% nominal reduction in stagnation enthalpy do not show a reduction in equilibrium post-shock temperature. For the 15% helium diluent fraction results, a small increase (0.2% for x2s3241 and 2% for experiment x2s3244) in equilibrium post-shock temperature is actually seen. This is also seen for the 70% diluent fraction data where a nominal 0.7% increase above the expected theoretical value is seen for experiment x2s3255 and 0.2% increase is seen for experiment x2s3256. It is only the 40% diluent fraction experiment (x2s3243) which shows a reduction more in line with its reduction in stagnation enthalpy, with a 7% nominal reduction in equilibrium post-shock temperature compared to the theoretical value. As most of the stagnation enthalpy goes into thermal modes behind the shock wave, this can be explained using CEA [197, 198] to examine how the equilibrium state of these different mixtures change as the static enthalpy ( $h - h_0$ ) changes around 180 MJ/kg. For the 15% and 70% helium diluent conditions, the gradient of temperature with changing enthalpy is very shallow around 180 MJ/kg, with most of the enthalpy change going into dissociation or ionisation, respectively. For the 40% helium diluent, the opposite is true, and the temperature is rising very steeply around 180 MJ/kg as the H is fully dissociated but has not yet started to ionise. Overall, these results are similar to what was seen in Fig. 7.8 in Section 7.4.3 where the temperatures of higher acceleration tube fill pressure, and therefore lower stagnation enthalpy, conditions were shown. It was seen that the lower stagnation enthalpy conditions showed similar equilibrium post-shock temperatures for helium diluent fractions either below around 20% or above around 70%, with a reduction seen in between these limits.

### 7.5.2 High Speed Imagery Analysis

High speed imagery was taken for all experiments discussed in this section using a Shimadzu HPV-1 high speed camera which can record 100 greyscale images at a recording speed of up to 1 MHz. As was discussed in Section 7.5.1, after the first two experiments (x2s3241 and x2s3242) were performed, a Pitot pressure probe was added to the middle sensor in the Pitot rake ('pt5') to create a small stagnation region which could be used to compare the time-resolved radiative emission in the stagnation region between experiments. Camera settings were kept constant for all experiments, with a recording frequency of 250 kHz (giving a total recording time of 400  $\mu$ s), an exposure time of 1/2, a gain of 1, and an f-number of 5.6. The lens used was a Nikon Zoom-nikkor 100-300mm which was set up to cover and focus on all nine probes in X2's Pitot rake.

The spectral response curve of the Shimadzu HPV-1 camera (found in Appendix F of

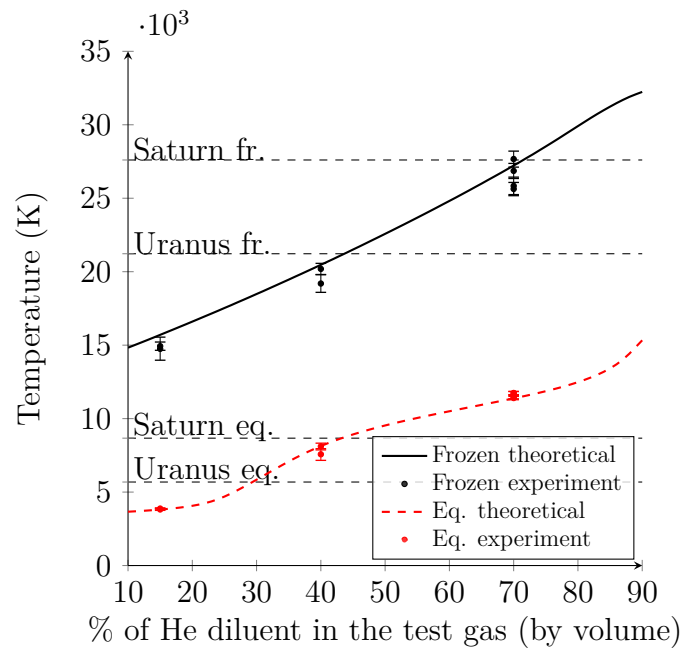


Figure 7.14: Comparing theoretical and experimental results for how helium diluent fraction affects the post-shock temperature of the test gas along the stagnation streamline over the test model.

Eichmann [78] from Eichmann's personal communication with Shimadzu) is from around 320 nm to 950 nm. It has a maximum response at 500 nm with the sensitivity dropping off gradually on either side. The camera is essentially capturing spectrally integrated radiative emission in time before, during, and after the experimental test time. It should be noted that, while this spectral range includes the whole Balmer series of atomic hydrogen from 364.6 nm to 656.3 nm, it also includes two bright contaminant lines from the aluminium foil secondary diaphragm at 394 and 396 nm, and a lot of weak iron contamination lines from the tube walls. The next step after this work would be to use a larger test model and a spectrometer to spectrally resolve the radiation seen, but the current study sought to establish if the post-shock radiative emission increased with increasing helium diluent as had been predicted in Section 7.4.4.

To perform the analysis, the raw images were analysed using a code described in James et al. [4]. A selected region in space which corresponded to the stagnation region on the Pitot pressure probe was spatially integrated in each image to find a time-resolved camera intensity which could be used to examine the flow radiative emission between experiments. The results can be seen in Fig. 7.15. The x-axis on the figure has been zeroed at flow arrival in the test section.

Based on the cone pressure measurements discussed in Section 7.5.1 (even though the time-resolved pressures were not shown) and the radiative emission measurements shown in Fig. 7.15,

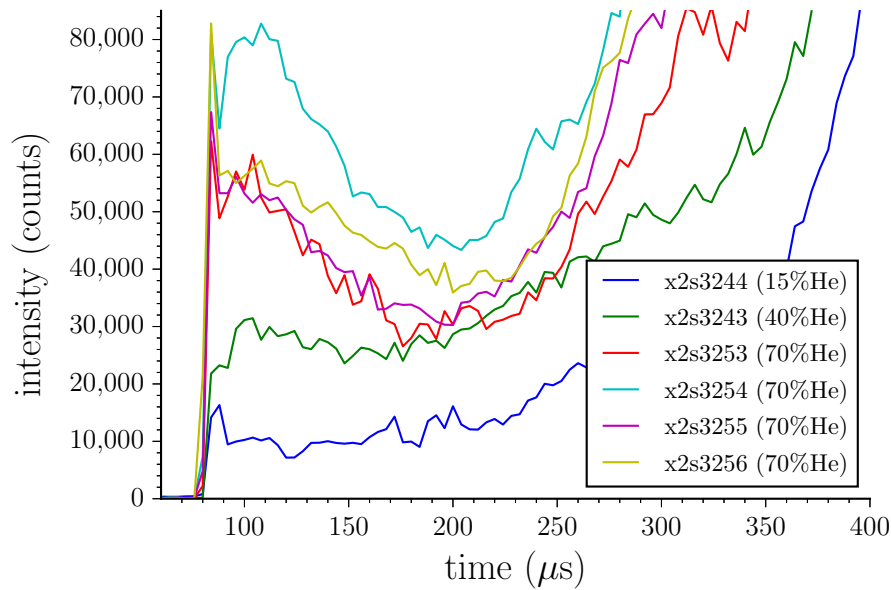


Figure 7.15: Time-resolved integrated high speed camera intensity over a Pitot pressure probe for different percentages of helium diluent (by volume).

the test time for all of the conditions appears to be around  $100 \mu\text{s}$ . It starts around  $20 \mu\text{s}$  after flow arrival and ends around  $120 \mu\text{s}$  after flow arrival when the increase in emission seen in Fig. 7.15 indicates the arrival of the unsteady expansion which processed the test gas to its final state. (See Paull and Stalker [215] or James et al. [4] for more discussion of how expansion tube test time begins and ends.)

In Fig. 7.15, it can be seen that a higher amount of helium diluent does indeed result in more radiative emission. For experiment x2s3244, the 15% helium diluent fraction condition, a spike in emission is seen at shock arrival when the hot accelerator gas passes the model and the flow starts up before the colder test gas brings with it a reduction in emission. This is generally normal for X2 conditions, and is something which is not as pronounced for the 40 and 70% helium diluent fraction conditions, which show the initial shock arrival and then almost constant emission after it. While the 15% diluent fraction condition has less counts during the test time, its emission remains almost constant until around  $120 \mu\text{s}$  after flow arrival when the test time ends and the flow emission increases. The 40% diluent fraction experiment (x2s3243) shows a gradual reduction from shock arrival to a steady period of radiative emission at around 28,000 counts for around  $50 \mu\text{s}$ . The 70% helium diluent fraction conditions show an even longer reduction, and an even shorter steady emission period, with two of the experiments (x2s3253 and x2s3255) showing a steady period at around 30,000 counts for around  $20 \mu\text{s}$ . The other two experiments (x2s3254 and x2s3256) show a similar length period but with more counts. This reduction in emission seen during the test time for the 70% helium diluent fraction conditions

is interesting and is something which should be investigated further in the future. It is also interesting to compare the emission of the 70% helium diluent fraction experiments to their inferred stagnation enthalpies from the results presented in Section 7.5.1. Experiment x2s3254 had an inferred stagnation enthalpy which was 2% higher than the nominal result, and as such, it is to be expected that it would be the condition with the highest emission during the test time in Fig. 7.15. Experiments x2s3255 and x2s3256 both had their test gas filled directly into the shock tube and had an inferred stagnation enthalpy reduction of 5 to 6% compared to the nominal result, however, in Fig. 7.15, x2s3256 has the second highest emission. Experiment x2s3255 has almost exactly the same time-resolved emission profile as experiment x2s3253, which did not have the inferred stagnation enthalpy reduction. These results show that there does not appear to be a conclusive relationship between how the test gas is filled, the inferred stagnation enthalpy, and the flow radiative emission.

Fig. 7.16 shows sample false colour images near the end of the test time (around 100  $\mu\text{s}$  after flow arrival) from both x2s3244, a 15% diluent fraction test condition, and x2s3254, one of the 70% diluent fraction test conditions. The images have been zoomed in to the region near the Pitot pressure probe and the intensity scale has been set to the same maximum value for both images so that they can easily be compared. Comparing the 70% helium diluent image (Fig. 7.16b) to the 15% one (Fig. 7.16a), it can be seen that there is not only more emission over the Pitot pressure probe, but there are also other radiating features in the flow-field, such as a bright wake flow behind the probe.

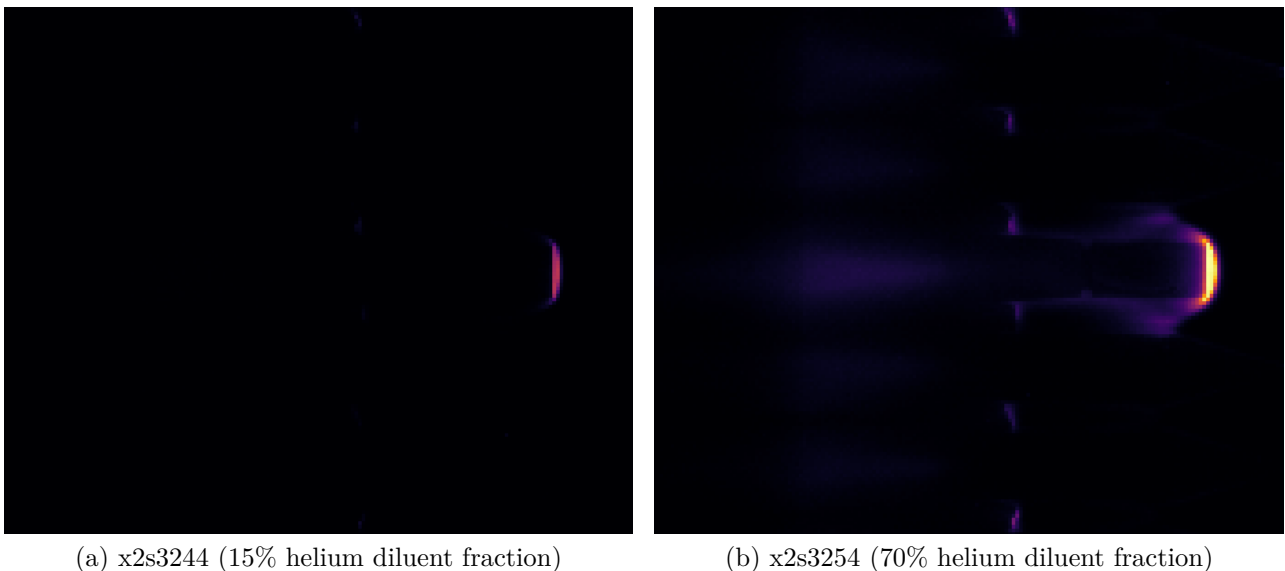


Figure 7.16: False colour high speed camera images around 100  $\mu\text{s}$  after flow arrival for experiments with helium diluent fractions of 15 and 70% (by volume).



Considering the theoretical Balmer series radiation shown in Fig. 7.9a, a seven order of magnitude increase in radiative emission would be expected between diluent fractions of 15 and 40%, and then another four orders of magnitude would be expected from 40 to 70%. This is not what is seen in Fig. 7.15, where at most an order of magnitude increase is seen between diluent fractions of 15 and 70%. This is probably caused by a combination of non-equilibrium chemistry and flow contamination. The results shown in Fig. 7.9a are for a gas in thermochemical equilibrium, and Cruden and Bogdanoff found that a lot of their experimental shock relaxation data was non-equilibrium and radiating at lower levels than the expected equilibrium values [72, 73]. Considering that the radiative emission measurements shown in Fig. 7.15 were taken over a Pitot pressure probe with a small shock standoff, this could have a significant affect. The effect of the contamination lines from the aluminium foil secondary diaphragm are shown in Fig. 7.17, where the Balmer series radiative power density (which is fully captured by the sensitivity of the HPV-1 high speed camera) from Fig. 7.9a has been re-plotted along with similar calculations performed with the post-shock equilibrium flow contaminated by 1, 0.1, and 0.01 percent aluminium (by volume). Examining Fig. 7.17 it can be seen that the contamination dramatically reduces the change in power density between conditions with low and high percentages of the helium diluent, with only a small dependence on the contamination percentage at diluent fractions of less than 30%. At higher diluent fractions, a combination of the aluminium ionising and the flow radiating much more strongly means that there is a point for each contamination percentage where the contamination no longer has an effect on the power density at all. Depending on the percentage of aluminium contamination, Fig. 7.17 still predicts a difference of three or four orders of magnitude between diluent fractions of 15 and 70%, but this is a very large reduction compared to eleven orders of magnitude, and is able to explain a large amount of the discrepancies seen between theory and experiment. In future work, high speed imagery should be performed with optical filters to better isolate the Balmer series radiation from the contaminants.

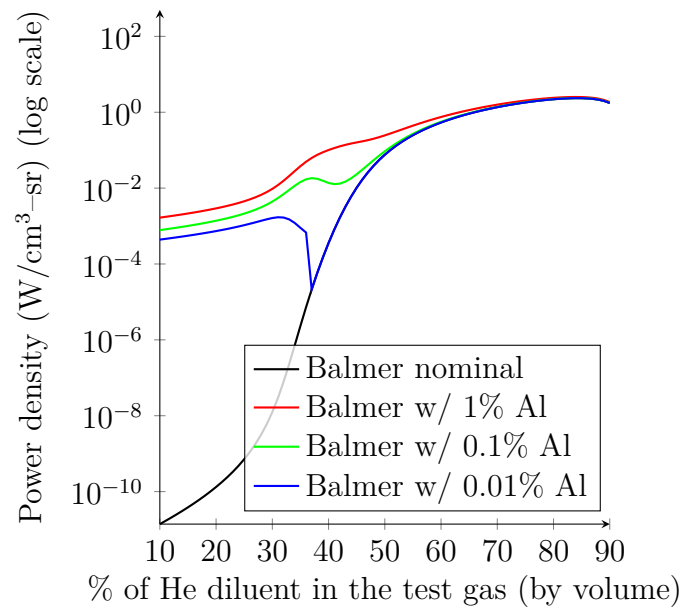


Figure 7.17: Effect of aluminium secondary diaphragm contamination on the theoretical total power density in the same wavelength region as the Balmer series from a 1 cm tangent slab in thermochemical equilibrium.

## 7.6 Conclusions

Due to large uncertainties when the author attempted to simulate Uranus entry directly in X2 in Chapter 6, it was proposed to investigate a test gas substitution from the literature which allows for the simulation of only the shock layers of blunt-body gas giant entry conditions by using either an increased amount of helium diluent in the test gas, or by replacing the helium with a heavier diluent, neon. This was examined theoretically for a test condition from Chapter 6 using both helium and neon diluent fractions from 10 to 90% (by volume).

Using the helium diluent, it was found that increasing the diluent fraction did not affect the test condition gas dynamically in the expansion tube as the stagnation enthalpy of the test condition remained constant over the whole range. In general, the only large increase seen over the whole diluent fraction range was in the post-shock temperature over the test model in the test section. Theoretically, it was shown that the analysed condition should be able to simulate both frozen and equilibrium shock layers of proposed Uranus and Saturn entries using different amounts of helium diluent, and that a secondary driver section could potentially be used to simulate these conditions with modified binary scaling parameters which took into account the changing amount of  $H_2$  in the test gas fill condition. It was also found that with large helium diluent fractions (70% and above, by volume) the conditions became less sensitive to the acceleration tube fill pressure for simulating the equilibrium temperature, meaning slower

conditions than the one investigated here could be used to generate these conditions. Basic theoretical predictions of post-shock radiation showed that atomic hydrogen radiation from the Lyman and Balmer series should increase over the helium diluent range investigated, allowing the radiation from proposed Uranus and Saturn entries to be simulated.

With the neon diluent, larger changes were seen. The conditions became slower with increasing neon diluent fraction due to the larger change in the test gas molecular weight from the use of the heavy neon diluent. It was shown that the neon diluent could easily generate the post-shock temperatures required to simulate the proposed Uranus and Saturn entries, meaning that it would be able to simulate faster entries or binary scaled conditions more easily. However, it was also seen that the neon ionised for some of the very high temperature conditions, a situation which Stalker and Edwards [67], said rendered their substitution invalid, because the neon was no longer acting as an inert diluent. Basic theoretical predictions of post-shock radiation showed that atomic hydrogen radiation from the Lyman and Balmer series should increase over the full neon diluent range investigated.

Finally,  $\text{H}_2/\text{He}$  Pitot rake experiments were performed, using diluent fractions of 15, 40, and 70% (by volume). The analysis confirmed the theoretical prediction that the performance of the test conditions would not be affected by the changing diluent fraction, with the experimentally measured shock speeds for each experiment being represented by the same global means, making them statistically the same. While some of the experiments were shown to have stagnation enthalpies 5 to 6% lower than would have been expected theoretically, their temperature predictions were still very close to the theoretical predictions both at the frozen and equilibrium limits. This is a very positive result as in Chapter 6, the shock speed uncertainties were large, and the conditions were very sensitive to that. Because these conditions appear to be insensitive to minute differences in the flow conditions, they are more likely to be able to be used successfully. The intensity of a high speed camera was also used to show that there was in fact more radiative emission seen with higher amounts of helium diluent.

Further work should aim to spectrally quantify the shock layers generated by these flows. Due to how dark these conditions are when compared to planetary entries which are normally studied in expansion tubes, such as Earth, Mars, or Titan, this should be done with a blunt quasi two-dimensional model to start with to ensure that a large stagnation region exists to be imaged. Following this, the technique can be progressed to more representative aeroshell models after experimenters have an idea of the intensity of the radiation seen versus the sensitivity of their equipment. Further experiments should also experimentally examine the performance of the neon diluent against the theoretical results presented here, as due to experimental time constraints, the authors were not able to take experimental data for the  $\text{H}_2/\text{Ne}$  test conditions. In a more general sense, further work should aim to leverage the ability of expansion tubes

to simulate gas giant entry test conditions using test models as this is a niche which cannot currently be filled by other types of test facilities. This means focusing on phenomena which is currently studied in expansion tubes, such as heat transfer, the flow around scaled aeroshells, and the use of resistively heated test models to study the interaction of the test flow with an ablating model. This process of further experimentation has already started, with preliminary gas giant entry radiation experiments having been performed by Liu et al. [22] this year using the test conditions described in this chapter.

# 8

## Conclusions and Recommendations

*An earthquake is such fun when it is over.*

– George Orwell, *Burmese Days*, 1934 [291]

### 8.1 Chapter Overview

This chapter presents the final conclusions and recommendations of this thesis.

### 8.2 Conclusions

The goal of this thesis was to examine the possibility of simulating radiating Uranus and Saturn entry in the X2 expansion tube at UQ. Examining this was a multi-faceted process, which required a lot of scaffolding to be built before the project could progress. This allowed the operational procedures of UQ's whole expansion tube laboratory to be improved. Consequently, some of the deliverables of this thesis changed from something very specific, related to planetary exploration missions, and into more general ground testing aims. At the end of Chapter 4, there is a brief discussion of the upgrades performed to X2 both physically and procedurally, which were either fully designed by the author, or in the case of the wall transducer mounts, designed by one of the author's supervisors, and modified and further implemented by the author. The Shot Class code written specifically for analysing the facility data for this thesis, is now used by every experimenter on the X2 facility. The miniature Pitot rake test models, which can be mounted below another test model, were never used by the author for this project due to changes in its scope. However, they are now part of the standard experimental hardware used by the majority of X2 experimenters for understanding their equipment trigger times in relation to experimental test times.

PITOT, the equilibrium gas state-to-state expansion tube analysis code presented in Chapter 5 is also one of the generic deliverables of this thesis, and has proven to be a very useful tool for the author and other X2 experimenters. PITOT was written to allow ‘virtual experiments’ to be performed quickly and easily, in a way which is analogous to how the facility is configured during a real experiment. In a more fundamental sense, PITOT was shown to not just be useful for approximately designing new test conditions or for qualitatively assessing trends in the facility’s performance. The air test gas examples presented in Chapter 5 demonstrated how facility shock speed and pressure data could be used with PITOT to model experiments and estimate experimental freestream properties in a semi-empirical manner. This was also shown to generally be true when PITOT was used for the simulation of gas giant entry test conditions in the later chapters of the thesis.

Initial theoretical performance predictions showed that attempting to simulate true gas composition and true flight velocity Uranus and Saturn entry in X2 was not going to be straightforward, and that trends in facility performance would need to be maximised to achieve the required stagnation enthalpies. However, other difficulties were not foreseen. During the first experimental campaign, it was difficult to get the facility to seal as well as was necessary to operate with an uncontaminated test gas and to reach the required acceleration tube fill pressures. When operating conditions were adequate, the shock speed uncertainties were large due to the very fast shock speeds, which were at least 50% higher than X2’s more typical maximum shock speeds of around 12 km/s.

To help address these issues on X2 in general, a helium leak detector was purchased and used to remove leaks on the facility. However, during the second experimental campaign, other issues were then found. These issues included leaking through the double aluminium foil secondary diaphragm, which compromised experiments using a secondary driver section. The stronger Mylar diaphragms used in their place then caused performance losses between the secondary driver and shock tubes. The main issues were still caused by the very large shock speed uncertainties from the 20 km/s low pressure, acceleration tube shock speeds. Even with the wall transducer pressure signals recorded at 60 MHz to reduce the sampling rate error, uncertainty in finding the shock arrival time in the signals resulted in very large shock speed uncertainties, which, in turn, resulted in very large uncertainties on the test conditions themselves. The fastest condition tested had a flight equivalent velocity range of 21.1 to 22.9 km/s, showing that potentially the required 22.3 km/s velocity to simulate Uranus entry was achieved. However, the results are not conclusive. It was also shown theoretically that with a more powerful free piston driver, an X2 sized facility could be used to simulate the proposed Uranus and Saturn entry conditions. Either way, a faster response shock detection system, which would be fit for purpose for measuring shock speeds above 20 km/s, would be required before true gas

composition and true flight velocity Uranus and Saturn entry simulation is again considered in X2. These requirements are expanded on further in the recommendations section below.

However, the simulation of Uranus and Saturn entry using the Stalker substitution, where either an increased molar percentage of helium, or a substitution to neon instead of the helium, is used in the test gas, was shown to be much more promising. A modified version of a 19 km/s condition tested in the true gas composition study was theoretically shown to be able to easily simulate the required shock layer temperatures for the simulation of both Uranus and Saturn entry in X2. This could either be achieved by using a large molar percentage of helium or a molar percentage of neon which was similar to the ten to twenty percent helium percentage in the real atmospheres. Interestingly, it was also shown that the helium substitution did not affect the stagnation enthalpy of the test condition as it travelled through the expansion tube, with the only large change shown to be the post-shock temperature over the test model. Experimental validation using the helium substitution confirmed that the test conditions would behave in the driven sections of X2 as had been predicted, and also clearly showed that more radiation was seen in the post-shock flow in the test section. This is a very promising result, because it shows that using this substitution, the shock layers of the proposed Uranus and Saturn entries can be simulated in X2 at conditions which are more easily achievable. The conditions being slower also means that the shock speed uncertainties, and the related test condition uncertainties, are smaller than when it was attempted to simulate the conditions at true flight velocity.

This will be expanded upon further in the recommendations section below, but it should not be forgotten how difficult it is to simulate gas giant entry. When the Galileo probe was designed in the 1980's, the heat loads were able to be re-created, but the fastest experiments were performed at 15.5 km/s. The shock layers of entry conditions for Uranus and Saturn were recently simulated in the EAST facility at NASA Ames, but those conditions could never be used for the generation of true aerothermodynamic flow-fields like those which can be generated in an expansion tube. The final results are promising because they open up X2 for the experimental simulation of other phenomena related to these entries, such as heat transfer rates, studies of the boundary layer around the test model, or the effect of a heated wall on the post-shock flow-field.

## 8.3 Recommendations

In terms of the theoretical simulation of expansion tubes in general, and the experimental simulation of gas giant entry in them, much work remains to be done. The following further work is recommended:

- *Addition of more complex time and distance dependent models to PITOT.* Currently, PITOT simulates an expansion tube experiment using state-to-state processes, which are independent of time and distance. It can take into account time and distance dependent phenomena, such as a secondary diaphragm hold time, or the over-expansion of the shocked test gas in the acceleration tube due to low density shock tube ('Mirels') effects using various settings, but it cannot simulate them directly. One upgrade to the code would be the addition of models such as an inertial diaphragm model and a Mirels solver to allow it to simulate expansion tube phenomena which need time and/or distance based calculations to be modelled correctly.
- *Validate PITOT against higher fidelity numerical simulation models.* The main benefit of PITOT is that it is able to complete a simulation of an expansion tube facility in a couple of minutes, whereas quasi one-dimensional facility simulations such as the in-house L1d3 facility simulation code can take hours, and higher fidelity two-dimensional simulations can take weeks. While so far PITOT simulations have only been compared to experimental data, it would be interesting and useful to compare results found from PITOT to higher fidelity simulations to see where the different techniques agree, and where they don't. Whereas real experimental data is effectively 'the gold standard' of validation data, what can be measured during an experiment is very limited, and if PITOT is compared to higher fidelity simulations, there will be a lot more data available for comparison.
- *Improved driver modelling for use with PITOT.* During the experimental validation of PITOT, it was found for the experimental test conditions that the empirically evaluated driver condition estimates used in the code generally either over or under-estimated the shock tube shock speed by 5%, compared to experimental results. While PITOT can be run in various experimental modes which remove the driver model from the simulation, the accuracy of PITOT's purely theoretical results, which are used for initial condition characterisation, are based on the accuracy of the driver estimates. For this reason it is suggested that additional time should be spent on improving the current driver estimates used in PITOT. This model could be improved in two ways. The first would be purely theoretical, by allowing PITOT to simulate heat losses during the piston compression and total pressure losses through the area change into the shock tube to improve theoretical driver estimates. The second would be experimental, by performing a comprehensive study of driver performance for different test conditions and aiming to provide a look up table for driver performance instead of a single set of rupture pressure and temperature values for each driver condition.
- *Investigation of new and thinner secondary or tertiary diaphragm materials.* When ex-



periments were performed to validate the theoretical performance predictions for true gas composition gas giant entry simulation, it was found that the dual aluminium foil diaphragms which were being used as the secondary diaphragm for the conditions with a secondary driver had been leaking before the experiment and compromising the results. As such, experiments were instead performed using either 12.5 or 25  $\mu\text{m}$  mylar diaphragms. However, these diaphragms were found to lower the performance seen after the secondary driver section when compared to theory. This became more severe when the 25  $\mu\text{m}$  material was used. At the time when the experiments were performed, these were the thinnest mylar diaphragms in use in the laboratory. Since then, the author and colleagues have performed limited testing using mylar diaphragms down to 1  $\mu\text{m}$  for other projects. The diaphragms are very weak, and sometimes unreliable, but a 5  $\mu\text{m}$  mylar diaphragm was found to have a static rupture pressure of 35 kPa, which would make it appropriate for simulating the conditions discussed in this work, as the secondary driver fill pressure used here was between 21 and 25 kPa. In a more general sense, the investigation of new and thinner secondary diaphragm materials is always necessary, because the secondary and tertiary diaphragms used in an expansion tube often have a significant and negative effect on the flow. Just after diaphragm rupture, it has an effect on the shocked test gas, which can cause flow conditions to depart from what would be expected from ideal theory, where the diaphragm is not modelled. This causes some conditions to be slower than theory, and others to be faster. The diaphragm also adds contamination to the test flow, as particles from the final diaphragm become entrained in the test gas. The mylar diaphragms once used on X2 were replaced with aluminium foil for radiation studies because it removed hydrocarbon contamination from the flow. However, it does add aluminium and potentially iron contamination, as many common aluminium alloys used for making foil contain iron. Potentially thinner mylar diaphragms would be more appropriate, as mylar is a stronger material, so less diaphragm mass is required for a given rupture pressure, or another material could be found. A study should be carried out, focusing both on facility performance from different diaphragms, and the contamination seen in the spectra when different diaphragms are used.

- *Designing a faster response shock detection system for when true gas composition Uranus and Saturn entry is simulated in X2.* When experiments were performed to validate the theoretical performance predictions for simulating true gas composition gas giant entry, one of the biggest issues found were how large the shock speed uncertainties were. The large uncertainties were not surprising, as the shock speed uncertainties generally increase with increasing shock speed, but uncertainty about the shock arrival times meant that even wall pressure data recorded at 60 MHz to try to reduce the sampling rate error

still had large uncertainties. For the fastest conditions tested, the freestream pressure uncertainties were up to 100% and even the stagnation enthalpy uncertainty was almost 10%. If at some point in the future these entries were to be simulated in X2 using a more powerful driver, a shock detection system which was fit for purpose for these very fast shock speeds would be required, as the pressure transducers currently used do not seem to be able to respond quickly enough to the passing shock wave. This is something which would have to be investigated in the future, but potentially a focused optical system would be required as it should be able to respond quicker than force on a physical pressure transducer.

- *Design of new driver conditions for X2 to allow for true gas composition simulation of Uranus and Saturn entry.* The theoretical study performed at the end of the investigation into simulating true gas composition gas giant entry found that with a more powerful driver condition, an X2 sized facility could be used to simulate entry into Uranus and Saturn, or potentially even Neptune. While X2's driver has many limitations, such as its short length, and its low driver pressure rating of 40 MPa (compared to other facilities which are often above 100 MPa), like many other facilities in the world, it does have the benefit that its current free piston driver conditions were designed to be tuned and to produce long hold times. This tuning means that the driver conditions are overdriven to keep the piston moving after diaphragm rupture to ensure that the driver supply pressure does not drop too quickly. While tuning is very important for the slow, scramjet test conditions which the driver conditions were designed for, for the simulation of very fast test conditions, not as much tuning would be required, and instead, slower piston speeds could be used to increase the driver compression ratio inside the physical limitations of X2's geometry. Recently, this has been comprehensively examined by an undergraduate thesis student of the author [292], with plans to test a diaphragm rupture condition with a compression ratio of 70 in X2 in the coming year. This is a large increase from the current maximum compression ratio of 40, and current simulations predict that the new driver condition will be as powerful as the current compression ratio of 40 condition with a secondary driver. If this is the case, this new driver would allow for true gas composition simulation of Uranus entry in X2, and potentially even Saturn entry.
- *Further investigation of using either a larger molar percentage of helium or neon for the simulation of radiating gas giant entry test conditions.* For various reasons, the tasks completed in this thesis became larger than was expected, and because of this, it was not possible to comprehensively study the effect which using either an increased molar percentages of helium or neon has on the shock layer radiation. For this reason, it is important that further work aims to spectrally quantify the shock layers generated using

either helium or neon substitutions. Because the expected radiative emission is much lower for these conditions compared to planetary entries which are normally studied in X2, such as Earth, Mars or Titan, initial experiments should either be performed using either a blunt quasi two-dimensional model or a very large model to ensure that a large stagnation region exists to be imaged. Thermochemical non-equilibrium CFD simulations could also be used to examine the effect of the substitution on the chemistry of the whole flow-field for various fundamental geometries which could be tested in X2.

- *Using the substituted test gas conditions to capitalise on the benefits of expansion tubes for the simulation of gas giant entry.* Because an expansion tube effectively relies on two separate shock tubes separated by a diaphragm to generate its test flows, expansion tubes will always have higher uncertainties than facilities like NASA's EAST where radiation directly behind a well quantified moving shock can be imaged. However, generally an expansion tube can generate a much larger test gas slug than a non-reflected shock tube, allowing experiments with scaled test models to be easily performed. This means that to be useful, an expansion tube must capitalise on these benefits. In support of Uranus and Saturn entry, many different types of experiments could be performed in X2 using the test gas substitution. Experiments could be performed over scaled aeroshell models with surface mounted instrumentation to study heat transfer rates, as for gas giant entry, even when the radiative heat transfer rates are low, the convective heat transfer rates are as high as hyperbolic Earth entries. The discrepancies seen between the expected and measured heat shield ablation of the Galileo probe are now thought to be caused by ablation products absorbing heat in the stagnation region, and then travelling downstream and increasing the heat transfer rates on the flank of the vehicle. Similar behaviour to this for Uranus and Saturn entry could be explored in X2 using the resistively heated test model techniques which are currently employed in the laboratory. A continuation of this work using test models has already started, with preliminary gas giant entry radiation experiments having been performed by Liu et al. [22] this year using a scaled aeroshell model and the test conditions described in this thesis.

# Bibliography

- [1] Gildfind, D., James, C., Toniato, P., and Morgan, R., “Performance considerations for expansion tube operation with a shock-heated secondary driver,” *Journal of Fluid Mechanics*, Vol. 777, 2015, pp. 364–407. doi:10.1017/jfm.2015.349
- [2] Gildfind, D., James, C., and Morgan, R., “Free-piston driver performance characterisation using experimental shock speeds through helium,” *Shock Waves*, Vol. 25, No. 2, 2015, pp. 169–176. doi:10.1007/s00193-015-0553-8
- [3] Lewis, S. W., James, C., Morgan, R. G., McIntyre, T. J., Alba, C. R., and Greendyke, R. G., “Carbon Ablative Shock-Layer Radiation with High Surface Temperatures,” *Journal of Thermophysics and Heat Transfer*, Vol. 31, No. 1, 2017, pp. 193–204. doi:10.2514/1.T4902
- [4] James, C., Cullen, T., Wei, H., Lewis, S., Gu, S., Morgan, R., and McIntyre, T., “Improved test time evaluation in an expansion tube,” *Experiments in Fluids*, Vol. 59, No. 5, 2018, pp. 59–87. doi:10.1007/s00348-018-2540-1
- [5] Parekh, V., Gildfind, D., Lewis, S., and James, C., “X3 Expansion Tube Driver Gas Spectroscopy and Temperature Measurements,” *Shock Waves*, Vol. 28, No. 4, 2018, pp. 851–862. doi:10.1007/s00193-017-0754-4
- [6] Sheikh, U., Wei, H., Lewis, S., James, C., Leyland, P., Morgan, R., and McIntyre, T., “Spectrally Filtered Imaging and VUV Spectroscopy of Preheated Models in X2,” *AIAA Journal*, Vol. 55, No. 12, 2017, pp. 4167–4180. doi:10.2514/1.J056021
- [7] Lewis, S. W., James, C., Ravichandran, R., Morgan, R. G., and McIntyre, T. J., “Carbon Ablation in Hypervelocity Air and Nitrogen Shock Layers,” *Journal of Thermophysics and Heat Transfer*, Vol. 32, No. 2, 2018, pp. 449–468. doi:10.2514/1.T5270
- [8] James, C., Bourke, E., and Gildfind, D., “Calculating shock arrival in expansion tubes and shock tunnels using Bayesian changepoint analysis,” *Experiments in Fluids*, Vol. 59, No. 6, 2018, pp. 59–92. doi:10.1007/s00348-018-2546-8

- [9] James, C. and Morgan, R., "Radiation from simulated atmospheric entry into the gas giants," *18th Australasian Fluid Mechanics Conference*, Launceston, Tasmania, Australia, December 3-7, 2012
- [10] James, C., Gildfind, D., Morgan, R., Jacobs, P., and Zander, F., "Designing and Simulating High Enthalpy Expansion Tube Conditions," *5th Asia-Pacific International Symposium on Aerospace Technology*, Takamatsu, Japan, November 20-22, 2013
- [11] James, C., Gildfind, D., Morgan, R., and McIntyre, T., "Working Towards Simulating Gas Giant Entry Radiation in an Expansion Tube," *Proceedings of the 29th International Symposium on Shock Waves*, Madison, WI, U.S.A., July 14-19, 2013. doi:10.1007/978-3-319-16835-7\_89
- [12] James, C., Gildfind, D., Morgan, R., and McIntyre, T., "Theoretical Validation of a Test Gas Substitution for Expansion Tube Simulation of Gas Giant Entry," *44th AIAA Thermophysics Conference*, San Diego, California, U.S.A., 2013. doi:10.2514/6.2013-2506
- [13] James, C., Gildfind, D., Morgan, R., Lewis, S., Fahy, E., and McIntyre, T., "On the limits of simulating gas giant entry at true gas composition and true flight velocities in an expansion tube," *6th International Workshop on Radiation of High Temperature Gases in Atmospheric Entry*, St Andrews, Scotland, United Kingdom, November 24-28, 2014
- [14] James, C., Gildfind, D., Morgan, R., and McIntyre, T., "The limits of simulating gas giant entry at true gas composition and true flight velocities in an expansion tube," *19th Australasian Fluid Mechanics Conference*, Melbourne, VIC, Australia, 2014
- [15] James, C., Gildfind, D., Morgan, R., Lewis, S., Fahy, E., and McIntyre, T., "Limits of Simulating Gas Giant Entry at True Gas Composition and True Flight Velocities in an Expansion Tube," *8th European Symposium on Aerothermodynamics for Space Vehicles*, Lisbon, Portugal, March 2-6, 2015
- [16] James, C., Gildfind, D., Morgan, R., Lewis, S., Fahy, E., and McIntyre, T., "On the Current Limits of Simulating Gas Giant Entry Flows in an Expansion Tube," *20th AIAA International Space Planes and Hypersonic Systems and Technologies Conference*, Glasgow, Scotland, July 6-9, 2015. doi:10.2514/6.2015-3501
- [17] James, C., Gildfind, D., Morgan, R., Lewis, S., and McIntyre, T., "Simulating Gas Giant Entry with Increased Helium Diluent in an Expansion Tube," *30th International Symposium on Shock Waves*, Tel Aviv, Israel, 2015. doi:10.1007/978-3-319-44866-4\_104

- [18] James, C., Gildfind, D., Morgan, R., Lewis, S., Fahy, E., and McIntyre, T., “Simulating gas giant entry in an expansion tube,” *7th Asia-Pacific International Symposium on Aerospace Technology*, Cairns, Australia, November 25-27, 2015
- [19] Morgan, R., Rees, B., Rutherford, J., Jefferey, M., Sollart, M., Morris, N., Basore, K., James, C., Wei, H., Gu, S., Lewis, S., and Landsberg, W., “Advanced hypersonic vehicle component testing using pre-heated models and infrared scanning,” *7th Asia-Pacific International Symposium on Aerospace Technology*, Cairns, Australia, November 25-27, 2015
- [20] James, C., Gildfind, D., Morgan, R., Lewis, S., and McIntyre, T., “Experimentally Simulating Gas Giant Entry in an Expansion Tube,” *21th AIAA International Space Planes and Hypersonic Systems and Technologies Conference*, Xiamen, China, March 6-9, 2017. doi:10.2514/6.2017-2152
- [21] James, C., Smith, D., McLean, C., Morgan, R., Lewis, S., and Toniato, P., “Improving High Enthalpy Expansion Tube Condition Characterisation Using High Speed Imagery,” *2018 AIAA Aviation and Aeronautics Forum and Exposition*, Atlanta, GA, U.S.A., June 25-29, 2018. doi:10.2514/6.2018-3805
- [22] Liu, Y., James, C., Morgan, R., and McIntyre, T., “Experimental Study of Saturn Entry Radiation with Higher Amount of Diluent in an Expansion Tube,” *2018 AIAA Aviation and Aeronautics Forum and Exposition*, Atlanta, GA, U.S.A., June 25-29, 2018. doi:10.2514/6.2018-4070
- [23] Gildfind, D., Smith, D., Lewis, S., Kelly, R., James, C., Wei, H., and McIntyre, T., “Expansion Tube Magneto-hydrodynamic Experiments with Argon Test Gas,” *2018 AIAA Aviation and Aeronautics Forum and Exposition*, Atlanta, GA, U.S.A., June 25-29, 2018. doi: 10.2514/6.2018-3754
- [24] Smith, D., Gildfind, D., James, C., McIntyre, T., and Wheatley, V., “Magneto-hydrodynamic Drag Force Measurements in an Expansion Tube,” *2018 AIAA Aviation and Aeronautics Forum and Exposition*, Atlanta, GA, U.S.A., June 25-29, 2018. doi:10.2514/6.2018-3755
- [25] James, C., Gildfind, D., Lewis, S., Morgan, R., and Zander, F., “Implementation of a state-to-state analytical framework for the calculation of expansion tube flow properties,” *Shock Waves*, Vol. 28, No. 2, 2018, pp. 349–377. doi:10.1007/s00193-017-0763-3

- [26] James, C., Gildfind, D., Morgan, R., Lewis, S., and McIntyre, T., “Simulating Gas Giant Atmospheric Entry Using Helium and Neon Test Gas Substitutions,” *accepted for publication in Journal of Spacecraft and Rockets*, 2018.
- [27] “1962-09-12 Rice University - John F. Kennedy Presidential Library & Museum,” <http://www.jfklibrary.org/Asset-Viewer/MkATd0cdU06X5uNHbmqm1Q.aspx>, Jan. 2016, Accessed January 2, 2016.
- [28] Sanz Fernández de Córdoba, S., “The 100 km Boundary for Astronautics,” <http://www.fai.org/icare-records/100km-altitude-boundary-for-astronautics>, Jan. 2016, Accessed January 2, 2016.
- [29] National Aeronautics and Space Administration, “The Apollo Missions | NASA,” [https://www.nasa.gov/mission\\_pages/apollo/missions/index.html](https://www.nasa.gov/mission_pages/apollo/missions/index.html), Nov. 2017, Accessed November 9, 2017.
- [30] Japan Aerospace Exploration Agency, “JAXA | Asteroid Explorer “HAYABUSA” (MUSES-C),” [http://global.jaxa.jp/projects/sat/muses\\_c/](http://global.jaxa.jp/projects/sat/muses_c/), Nov. 2017, Accessed November 9, 2017.
- [31] European Space Agency, “Europe’s Comet Chaser,” [http://www.esa.int/Our\\_Activities/Space\\_Science/Rosetta/Europe\\_s\\_comet\\_chaser](http://www.esa.int/Our_Activities/Space_Science/Rosetta/Europe_s_comet_chaser), Oct. 2018, Accessed October 17, 2018.
- [32] National Aeronautics and Space Administration, “Voyager 1 | Missions - NASA Solar System Exploration,” <https://solarsystem.nasa.gov/missions/voyager1>, Nov. 2017, Accessed November 9, 2017.
- [33] National Aeronautics and Space Administration, “Voyager 2 | Missions - NASA Solar System Exploration,” <https://solarsystem.nasa.gov/missions/voyager2>, Nov. 2017, Accessed November 9, 2017.
- [34] National Aeronautics and Space Administration, “About the Hubble Space Telescope | NASA,” [https://www.nasa.gov/mission\\_pages/hubble/story/index.html](https://www.nasa.gov/mission_pages/hubble/story/index.html), Nov. 2017, Accessed November 9, 2017.
- [35] Hubblesite, “Hubblesite News Release Archive: Space Phenomenon Imitates Art in Universe’s Version of van Gogh Painting,” <http://hubblesite.org/newscenter/archive/releases/2004/10/image/a/>, March 2004, Accessed November 15, 2012.
- [36] Swinburne Astronomy Online, “Jovian Planet | COSMOS,” <http://astronomy.swin.edu.au/cosmos/J/Jovian+Planet>, Nov. 2017, Accessed Nov 9, 2017.

- [37] Irwin, P., *Giant Planets of Our Solar Systems: Atmospheres, Composition, and Structure*, Springer, New York, 2003.
- [38] National Aeronautics and Space Administration, “Solar System Exploration: Gas Planet Sizes,” [http://solarsystem.nasa.gov/multimedia/display.cfm?IM\\_ID=180](http://solarsystem.nasa.gov/multimedia/display.cfm?IM_ID=180), Jan. 2011, Accessed November 15, 2012.
- [39] Williams, D., “NASA Planetary Fact Sheets,” <http://nssdc.gsfc.nasa.gov/planetary/planetfact.html>, Jan. 2005, Accessed November 12, 2012.
- [40] “Cosmos: A Personal Voyage, Season 1, Episode 6: Travellers’ Tales,” 1980, Premiered on PBS.
- [41] Sachs, A., “Babylonian Observational Astronomy,” *Philosophical Transactions of the Royal Society of London. Series A, Mathematical and Physical Sciences*, Vol. 276, No. 1257, 1974, pp. 43–50.
- [42] National Aeronautics and Space Administration, “Solar System Exploration: Jupiter: Read More,” <http://solarsystem.nasa.gov/planets/profile.cfm?Object=Jupiter&Display=OverviewLong>, Nov. 2017, Accessed November 9, 2017.
- [43] Murdin, P., *Encyclopedia of Astronomy and Astrophysics*, Bristol: Institute of Physics Publishing, Bristol, 2000.
- [44] National Aeronautics and Space Administration, “Solar System Exploration: Gas Planet Sizes,” [http://solarsystem.nasa.gov/multimedia/display.cfm?Category=Planets&IM\\_ID=2052](http://solarsystem.nasa.gov/multimedia/display.cfm?Category=Planets&IM_ID=2052), Feb. 2012, Accessed Nov 15, 2012.
- [45] National Aeronautics and Space Administration, “Missions - Solar System Exploration - Jupiter,” <https://solarsystem.nasa.gov/missions/target/jupiter>, Nov. 2017, Accessed November 9, 2017.
- [46] National Aeronautics and Space Administration, “Solar System Exploration: Huygens Probe,” <http://solarsystem.nasa.gov/missions/profile.cfm?Sort=Alpha&Letter=H&Alias=Huygens%20Probe>, Nov. 2010, Accessed May 30, 2013.
- [47] National Aeronautics and Space Administration, “Where is Juno?” [http://www.nasa.gov/mission\\_pages/juno/where](http://www.nasa.gov/mission_pages/juno/where), Oct. 2017, Accessed October 22, 2017.
- [48] National Aeronautics and Space Administration, “Mission Juno,” <http://missionjuno.swri.edu/#/jupiter/origin>, Oct. 2017, Accessed October 22, 2017.



- [49] Spaceflight101.com, “Juno Mission & Trajectory Design,” <http://spaceflight101.com/juno/juno-mission-trajectory-design/>, Nov. 2017, Accessed November 9, 2017.
- [50] Mike Wall, Space.com, “NASA Extends Juno Jupiter Mission Until July 2021,” <https://www.space.com/40830-nasa-extends-juno-jupiter-mission-2021.html>, Oct. 2018, Accessed October 17, 2018.
- [51] National Aeronautics and Space Administration, “Jupiter’s Great Red Spot in True Color,” <https://www.missionjuno.swri.edu/news/great-red-spot-in-true-color>, Oct. 2017, Accessed October 22, 2017.
- [52] NASA Jet Propulsion Laboratory, “Nasa Jet Propulsion Laboratory Photojournal: PIA01299: The Galilean Satellites,” <http://photojournal.jpl.nasa.gov/catalog/PIA01299>, May 1998, Accessed November 18, 2012.
- [53] D’Amario, L., Bright, L., and Wolf, A., “Galileo Trajectory Design,” *Space Science Reviews*, Vol. 60, 1992, pp. 23–78. doi:10.1007/BF00216849
- [54] Gnoffo, P., “Planetary-Entry Gas Dynamics,” *Annual Review of Fluid Mechanics*, Vol. 31, 1999, pp. 459–494. doi:10.1146/annurev.fluid.31.1.459
- [55] Incropera, F., *Fundamentals of Heat and Mass Transfer*, John Wiley & Sons, Inc., Hoboken, NJ, U.S.A., 6th ed., 2006.
- [56] Curry, D., Rochelle, W., Chao, D., and Ting, P., “Space Shuttle Orbiter nose cap thermal analysis,” *24th AIAA Aerospace Sciences Meeting*, Reno, NV, U.S.A., 1986. doi:10.2514/6.1986-388
- [57] Davies, C., *Planetary Mission Entry Vehicles Quick Reference Guide, Version 3.0*, NASA SP-2006-3401, 2006.
- [58] Milos, F., “Galileo Probe Heat Shield Ablation Experiment,” *Journal of Spacecraft and Rockets*, Vol. 34, No. 6, 1997, pp. 705–713. doi:10.2514/2.3293
- [59] Talley, R., *Galileo Probe Deceleration Module Final Report*, Re-Entry Systems Operations, General Electric Co., Rept. 84SDS2020, Jan. 1984.
- [60] Lundell, J., “Spallation of the Galileo probe Heat Shield,” *3rd Joint Thermophysics, Fluids, Plasma and Heat Transfer Conference*, St. Louis, MO ,U.S.A., June 7-11, 1982. doi:10.2514/6.1982-852
- [61] Park, C. and Balakrishnan, A., “Ablation of Galileo Probe Heat-Shield Models in a Ballistic Range,” *AIAA Journal*, Vol. 23, No. 2, 1985, pp. 301–308. doi:10.2514/3.8910

- [62] Park, C., Lundell, J., Green, M., Winovich, W., and Covington, M., “Ablation of Carbonaceous Materials in a Hydrogen-Helium Arcjet Flow,” *AIAA Journal*, Vol. 22, No. 10, 1984, pp. 1491–1498. doi:10.2514/3.48589
- [63] Higgins, C., *Aerothermodynamics of the Gas Giants*, Ph.D. thesis, the University of Queensland, St. Lucia, Australia, 2004.
- [64] Matsuyama, S., Ohnishi, N., Sasoh, A., and Sawada, K., “Numerical Simulation of Galileo Probe Entry Flowfield with Radiation and Ablation,” *Journal of Thermophysics and Heat Transfer*, Vol. 19, No. 1, 2005, pp. 28–35. doi:10.2514/1.10264
- [65] Park, C., “Injection-Induced Turbulence in Stagnation Point Boundary Layers,” *AIAA Journal*, Vol. 22, No. 2, 1984, pp. 219–255. doi:10.2514/3.8371
- [66] Park, C., “Stagnation-Region Heating Environment of the Galileo Probe,” *Journal of Thermophysics and Heat Transfer*, Vol. 23, No. 3, 2009, pp. 417–424. doi:10.2514/1.38712
- [67] Stalker, R. and Edwards, B., “Hypersonic Blunt-body Flows in Hydrogen-Neon Mixtures,” *Journal of Spacecraft and Rockets*, Vol. 35, No. 6, 1998, pp. 729–735. doi:10.2514/2.3399
- [68] Hubbard, W., “Ice Giants Decadal Study,” *Vision and Voyages for Planetary Science in the Decade 2013 – 2022*, National Academy Press, Washington, D.C., 2010, pp. 1–40.
- [69] Spilker, T. R., “Saturn Atmospheric Entry Probe Trade Study,” *Vision and Voyages for Planetary Science in the Decade 2013 – 2022*, National Academy Press, Washington, D.C., 2010, pp. 1–13.
- [70] Spilker, T. R., “Saturn Atmospheric Entry Probe Mission Study,” *Vision and Voyages for Planetary Science in the Decade 2013 – 2022*, National Academy Press, Washington, D.C., 2010, pp. 1–19.
- [71] Palmer, G., Prabhu, D., and Cruden, B., “Aeroheating Uncertainties in Uranus and Saturn Entries by the Monte Carlo Method,” *Journal of Spacecraft and Rockets*, Vol. 51, No. 3, 2014, pp. 801–814. doi:10.2514/1.A32768
- [72] Cruden, B. and Bogdanoff, D., “Shock Radiation Tests for Saturn and Uranus Entry Probes,” *45th AIAA Thermophysics Conference*, Dallas, Texas, U.S.A., 2015. doi:10.2514/6.2015-2965
- [73] Cruden, B. and Bogdanoff, D., “Shock Radiation Tests for Saturn and Uranus Entry Probes,” *Journal of Spacecraft and Rockets*, Vol. 54, No. 6, 2017, pp. 1246–1257. doi:10.2514/1.A33891

- [74] Sharma, S. P. and Park, C., “Operating characteristics of a 60- and 10-cm electric arc-driven shock tube. Part I. The driver,” *Journal of Thermophysics and Heat Transfer*, Vol. 4, No. 3, 1990, pp. 259–265. doi:10.2514/3.175
- [75] Sharma, S. P. and Park, C., “Operating characteristics of a 60- and 10-cm electric arc-driven shock tube. Part II. The driven section,” *Journal of Thermophysics and Heat Transfer*, Vol. 4, No. 3, 1990, pp. 266–272. doi:10.2514/3.56243
- [76] Cruden, B., *Absolute Radiation Measurements in Earth and Mars Entry Conditions*, Technical Report RTO-EN-AVT-218, NATO.
- [77] Cruden, B. A. and Brandis, A. M., “Updates to the NEQAIR Radiation Solver,” *6th International Workshop on Radiation of High Temperature Gases in Atmospheric Entry*, St Andrews, Scotland, United Kingdom, 2014
- [78] Eichmann, T., *Radiation Measurements in a Simulated Mars Atmosphere*, Ph.D. thesis, the University of Queensland, St. Lucia, Australia, 2012.
- [79] Porat, H., *Measurement of radiative heat transfer in simulated Titan and Mars atmospheres in expansion tubes*, Ph.D. thesis, the University of Queensland, St. Lucia, Australia, 2016.
- [80] de Crombrughe de Looringhe, G., *On binary scaling and ground-to-flight extrapolation in high-enthalpy facilities*, Ph.D. thesis, the University of Queensland, St. Lucia, Australia, 2017.
- [81] Fahy, E., Gollan, R., Buttsworth, D., Jacobs, P., and Morgan, R., “Experimental and Computational Fluid Dynamics Studies of Superorbital Earth Re-entry,” *46th AIAA Thermophysics Conference*, Washington, D.C., U.S.A., June 13-17, 2016. doi:10.2514/6.2016-3532
- [82] D’Souza, M., Eichmann, T., Potter, D., Morgan, R., McIntyre, T., Jacobs, P., and Mudford, N., “Observation of an Ablating Surface in Expansion Tunnel Flow,” *AIAA Journal*, Vol. 48, No. 7, 2010, pp. 1557–1560. doi:10.2514/1.J050207
- [83] Porat, H., Morgan, R., and McIntyre, T., “Radiative Heatflux Measurements for Titan Atmospheric Entry Condition in Superorbital Expansion Tunnel,” *30th International Symposium on Shock Waves*, Tel Aviv, Israel, 2015. doi:10.1007/978-3-319-46213-4\_22
- [84] Vella, S., *Expansion Tunnel Heat Transfer Measurements of the ESA-IXV Re-entry Vehicle*, Bachelor of engineering thesis, the University of Queensland, St. Lucia, Australia, 2016.

- [85] Penty Geraets, R., McGilvray, M., Doherty, L., Morgan, R., James, C., Vanyai, T., and Buttsworth, D., "Development of a Fast-Response Calorimeter Gauge for Hypersonic Ground Testing," *47th AIAA Thermophysics Conference*, Denver, CO, U.S.A., June 5-9, 2017. doi:10.2514/6.2017-3238
- [86] Wei, H., Morgan, R., McIntyre, T., Brandis, A., and Johnston, C., "Experimental and Numerical Investigation of Air Radiation in Superorbital Expanding Flow," *47th AIAA Thermophysics Conference*, Denver, CO, U.S.A., June 5-9, 2017. doi:10.2514/6.2017-4531
- [87] Gu, S., Morgan, R., and McIntyre, T., "Study of Afterbody Radiation during Mars Entry in an Expansion Tube," *55th AIAA Aerospace Sciences Meeting, AIAA SciTech Forum*, Grapevine, TX, U.S.A, January 9-13, 2017. doi:10.2514/6.2017-0212
- [88] Zander, F., Morgan, R., Molder, S., Jacobs, P., Gollan, R., Porat, H., and McIntyre, T., "Mach disk platform for studying radiating flows," *5th International Workshop on Radiation of High Temperature Gases in Atmospheric Entry*, Barcelona, Spain, October 16-19, 2012
- [89] Porat, H., Zander, F., Morgan, R., and McIntyre, T., "Emission spectroscopy of a mach disk at Titan atmospheric entry conditions," *Proceedings of the 29th International Symposium on Shock Waves*, Madison, WI, U.S.A., July 14-19, 2013. doi:10.1007/978-3-319-16835-7\_94
- [90] Zander, F., Morgan, R., Sheikh, U., Buttsworth, D., and Teakle, P., "Hot-Wall Reentry Testing in Hypersonic Impulse Facilities," *AIAA Journal*, Vol. 51, No. 2, 2013, pp. 476–484. doi:10.2514/1.J051867
- [91] Lewis, S. W., Morgan, R. G., McIntyre, T. J., Alba, C. R., and Greendyke, R. G., "Expansion Tunnel Experiments of Earth Reentry Flow with Surface Ablation," *Journal of Spacecraft and Rockets*, Vol. 53, No. 5, 2016, pp. 887–899. doi:10.2514/1.A33267
- [92] Herbrig, H., *Investigation of Hypervelocity Flows with Large Amounts of Ionisation and Dissociation in a H<sub>2</sub>/Ne Test Gas*, Diploma of engineering thesis (the university of stuttgart, germany), the University of Queensland, St. Lucia, Australia, 1999.
- [93] Anderson, J. D., *Hypersonic and high-temperature gas dynamics*, American Institute of Aeronautics and Astronautics, Reston, Va, 2nd ed., 2006.
- [94] Stalker, R., "Hypervelocity Aerodynamics With Chemical Equilibrium," *Annual Review of Fluid Mechanics*, Vol. 21, 1989, pp. 37–60.

- [95] Baals, D. and Corliss, W., *Wind Tunnels of NASA (NASA SP 440)*, Scientific and Technical Information Branch, National Aeronautics and Space Administration (NASA), 1981, Now available online at: <http://history.nasa.gov/SP-440/cover.htm>.
- [96] Smelt, R., *Test Facilities for Ultra-high-speed Aerodynamics, AEDC-TR-55-6*, Arnold Engineering Development Center, Air Research and Development Command, USAF, 1955.
- [97] Scott, C. D., “Survey of measurements of flow properties in arcjets,” *Journal of Thermophysics and Heat Transfer*, Vol. 7, No. 1, 1993, pp. 9–24. doi:10.2514/3.11563
- [98] Park, C., “Evaluation of real-gas phenomena in high-enthalpy aerothermal test facilities: A review,” *Journal of Thermophysics and Heat Transfer*, Vol. 11, No. 3, 1997, pp. 330–338. doi:10.2514/2.6263
- [99] Laux, C., *Optical Diagnostics and Radiative Emission of Air Plasmas*, Ph.D. thesis, Stanford University, Stanford, California, U.S.A., 1993.
- [100] MacDonald, M. E., Jacobs, C. M., Laux, C. O., Zander, F., and Morgan, R. G., “Measurements of Air Plasma/Ablator Interactions in an Inductively Coupled Plasma Torch,” *Journal of Thermophysics and Heat Transfer*, Vol. 29, No. 1, 2015, pp. 12–23. doi:10.2514/1.T4402
- [101] Auweter-Kurtz, M., Kurtz, H. L., and Laure, S., “Plasma generators for re-entry simulation,” *Journal of Propulsion and Power*, Vol. 12, No. 6, 1996, pp. 1053–1061. doi:10.2514/3.24143
- [102] Herdrich, G., Auweter-Kurtz, M., Kurtz, H., Laux, T., and Winter, M., “Operational behavior of inductively heated plasma source IPG3 for entry simulations,” *Journal of Thermophysics and Heat Transfer*, Vol. 16, No. 3, 2002, pp. 440–449. doi:10.2514/2.6698
- [103] Hermann, T., Löhle, S., Fasoulas, S., Leyland, P., Marraffa, L., and Bouilly, J.-M., “Influence of Ablation on Vacuum-Ultraviolet Radiation in a Plasma Wind Tunnel Flow,” *Journal of Thermophysics and Heat Transfer*, Vol. 31, No. 3, 2017, pp. 575–585. doi:10.2514/1.T4936
- [104] Morgan, R., “A Review of the Use of Expansion Tubes for Creating Superorbital Flows,” *AIAA 35th Aerospace Sciences Meeting and Exhibit*, Reno, NV, U.S.A., Jan 6-10, 1997. doi:10.2514/6.1997-279
- [105] Lino Da Silva, M., Brotas de Carvalho, B., and Smith, A., “High-Pressure H<sub>2</sub>/He/O<sub>2</sub> Combustion Experiments for the Design of the ESTHER Shock-Tube Driver,” *46th*

- AIAA Thermophysics Conference*, Washington, D.C., U.S.A., June 13-17, 2016. doi:<https://doi.org/10.2514/6.2016-4156>
- [106] Mirels, H., “Test Time in Low-Pressure Shock Tubes,” *The Physics of Fluids*, Vol. 6, No. 9, 1963, pp. 1201–1214. doi:10.1063/1.1706887
- [107] Mirels, H., “Shock Tube Test Time Limitation Due to Turbulent-Wall Boundary Layer,” *AIAA Journal*, Vol. 2, No. 1, 1964, pp. 84–93. doi:10.2514/3.2218
- [108] Mirels, H. and Mullen, J. F., “Small Perturbation Theory for Shock-Tube Attenuation and Nonuniformity,” *Physics of Fluids*, Vol. 7, No. 8, 1964, pp. 1208–1218. doi:10.1063/1.1711363
- [109] Mudford, N. and Stalker, R., “The production of pulsed nozzle flows in a shock tube,” *9th Fluid and Plasma Dynamics Conference*, San Diego, C.A., U.S.A., 1976. doi:10.2514/6.1976-357
- [110] Mudford, N., Stalker, R., and Shields, I., “Hypersonic nozzles for high enthalpy non equilibrium flow,” *The Aeronautical Quarterly*, Vol. 31, No. 2, 1980, pp. 113–131. doi:10.1017/S0001925900010945
- [111] Stalker, R. and Mudford, N., “Unsteady shock propagation in a steady flow nozzle expansion,” *Journal of Fluid Mechanics*, Vol. 241, 1992, pp. 525–548. doi:10.1017/S0022112092002143
- [112] Bray, K. N. C., “Atomic recombination in a hypersonic wind-tunnel nozzle,” *Journal of Fluid Mechanics*, Vol. 6, No. 1, 1959, pp. 1–32. doi:10.1017/S0022112059000477
- [113] Park, C., “Thermochemical relaxation in shock tunnels,” *Journal of Thermophysics and Heat Transfer*, Vol. 20, No. 4, 2006, pp. 689–698. doi:10.2514/1.22719
- [114] Hollis, B. R. and Prabhu, D. K., “Assessment of Laminar, Convective Aeroheating Prediction Uncertainties for Mars-Entry Vehicles,” *Journal of Spacecraft and Rockets*, Vol. 50, No. 1, 2013, pp. 56–68. doi:10.2514/1.A32257
- [115] Peter Noeding, H. and Martinez Schramm, J., “Numerical Rebuilding of Shock Tube Experiments in CO<sub>2</sub> Flow under Conditions Relevant for Mars Entry Probes,” *11th AIAA/ASME Joint Thermophysics and Heat Transfer Conference*, Atlanta, GA, U.S.A., June 16-20, 2014. doi:10.2514/6.2014-2549
- [116] Tanno, H., Komuro, T., Sato, K., and Itoh, K., “Free-flight tests of reentry capsule models in free-piston shock tunnel,” *43rd Fluid Dynamics Conference*, San Diego, CA, U.S.A., June 24-27, 2013. doi:10.2514/6.2013-2979

- [117] Tanno, H., Komuro, T., Sato, K., Itoh, K., Lillard, R., and Olejniczak, J., “Aeroheating measurement of Apollo shaped capsule with boundary layer trip in the free-piston shock tunnel HIEST,” *52nd AIAA Aerospace Sciences Meeting*, National Harbor, Maryland, U.S.A., January 13-17, 2014. doi:10.2514/6.2014-0434
- [118] Tanno, H., Komuro, T., Sato, K., and Itoh, K., “Free-flight aerodynamic tests of reentry vehicles in high-temperature real-gas flow,” *52nd Aerospace Sciences Meeting*, National Harbor, Maryland, U.S.A., January 13-17, 2014. doi:10.2514/6.2014-3109
- [119] Tanno, H., Komuro, T., Sato, K., and Itoh, K., “Free-flight aerodynamic test of elliptic cone in Shock Tunnel,” *20th AIAA International Space Planes and Hypersonic Systems and Technologies Conference*, Glasgow, Scotland, 2015. doi:10.2514/6.2015-3655
- [120] Stalker, R. J., Paull, A., Mee, D. J., Morgan, R. G., and Jacobs, P. A., “Scramjets and shock tunnels - The Queensland experience,” *Progress in Aerospace Sciences*, Vol. 41, No. 6, 2005, pp. 471–513. doi:10.1016/j.paerosci.2005.08.002
- [121] Itoh, K., Ueda, S., Tanno, H., Komuro, T., and Sato, K., “Hypersonic aerothermodynamic and scramjet research using high enthalpy shock tunnel,” *Shock Waves*, Vol. 12, No. 2, 2002, pp. 93–98. doi:10.1007/s00193-002-0147-0
- [122] Hannemann, K., Martinez Schramm, J., Karl, S., and Laurence, S., “Free Flight Testing of a Scramjet Engine in a Large Scale Shock Tunnel,” *20th AIAA International Space Planes and Hypersonic Systems and Technologies Conference*, Glasgow, Scotland, July 6-9, 2015. doi:10.2514/6.2015-3608
- [123] Laurence, S. J. and Hornung, H. G., “Image-based force and moment measurement in hypersonic facilities,” *Experiments in Fluids*, Vol. 46, No. 2, 2009, pp. 343–353. doi:10.1007/s00348-008-0565-6
- [124] Laurence, S. J. and Karl, S., “An improved visualization-based force-measurement technique for short-duration hypersonic facilities,” *Experiments in Fluids*, Vol. 48, No. 6, 2010, pp. 949–965. doi:10.1007/s00348-009-0780-9
- [125] Resler, E. and Bloxsom, D., *Very high Mach number principles by unsteady flow principle*, Cornell University Graduate School of Aerodynamic Engineering, 1952.
- [126] Morgan, R., “Free Piston-Driven Reflected Shock Tunnels,” *A Handbook of Shock Waves Vol. 1.*, edited by G. Ben-Dor, chap. 4.2, Academic Press, 2001, pp. 587–601.

- [127] Sheikh, U., Morgan, R., and McIntyre, T., “Vacuum Ultraviolet Spectral Measurements for Superorbital Earth Entry in X2 Expansion Tube,” *AIAA Journal*, Vol. 53, No. 12, 2015, pp. 3589–3602. doi:10.2514/1.J054027
- [128] Banerji, N., Leyland, P., Fahy, E., and Morgan, R., “Earth Reentry Flow Over a Phenolic Aeroshell in the X2 Expansion Tube,” *Journal of Thermophysics and Heat Transfer*, Vol. 32, No. 2, 2018, pp. 414–428. doi:10.2514/1.T5255
- [129] Palmer, R., *Measurement of Heat Transfer in Superorbital Flows*, Ph.D. thesis, the University of Queensland, St. Lucia, Australia, 1999.
- [130] Banerji, N., Leyland, P., Fahy, E., and Morgan, R., “Venus Entry Flow Over a Decomposing Aeroshell in the X2 Expansion Tube,” *Journal of Thermophysics and Heat Transfer*, Vol. 32, No. 2, 2018, pp. 292–302. doi:10.2514/1.T5172
- [131] MacLean, M., Dufrene, A., and Holden, M., “Spherical Capsule Heating in High Enthalpy Carbon Dioxide in LENS-XX Expansion Tunnel,” *51st AIAA Aerospace Sciences Meeting including the New Horizons Forum and Aerospace Exposition*, Grapevine, TX, U.S.A., January 7-10, 2013. doi:10.2514/6.2013-906
- [132] Kirk, L., Lillard, R., Olejniczak, J., and Tanno, H., “Measurements and Analysis of Mars Entry, Descent, and Landing Aerothermodynamics at Flight-Duplicated Enthalpies in LENS-XX Expansion Tunnel,” *53rd AIAA Aerospace Sciences Meeting*, Kissimmee, Florida, U.S.A., January 5-9, 2015. doi:10.2514/6.2015-1897
- [133] Weisberger, J., DesJardin, P., MacLean, M., Parker, R., and Carr, Z., “Near-Surface CO<sub>2</sub> Tunable Diode Laser Absorption Spectroscopy Concentration Measurement in the LENS-XX Expansion Tunnel Facility,” *54th AIAA Aerospace Sciences Meeting*, San Diego, C.A., U.S.A., January 4-8, 2016. doi:10.2514/6.2016-0246
- [134] Hollis, B. R., Prabhu, D. K., Maclean, M., and Dufrene, A., “Blunt-Body Aerothermodynamic Database from High-Enthalpy Carbon-Dioxide Testing in an Expansion Tunnel,” *Journal of Thermophysics and Heat Transfer*, Vol. 31, No. 3, 2017, pp. 712–731. doi:10.2514/1.T5019
- [135] Hollis, B., Wright, M., Olejniczak, J., Takashima, N., Sutton, K., and Prabhu, D., “Turbulent Aeroheating Measurements on a 7-deg Half-Angle Cone in a High-Enthalpy CO<sub>2</sub> Expansion Tunnel,” *2018 AIAA Aerospace Sciences Meeting*, 2018. doi:10.2514/6.2018-0377



- [136] Hass, N., Shih, A., and Rogers, R., “Mach 12 & 15 Scramjet Test Capabilities of the HY-PULSE Shock-Expansion Tunnel,” *43rd AIAA Aerospace Sciences Meeting and Exhibit*, Reno, NV, U.S.A., January 10-13, 2005
- [137] McGilvray, M., Morgan, R. G., and Jacobs, P. A., “Scramjet Experiments in an Expansion Tunnel: Evaluated Using a Quasi-Steady Analysis Technique,” *AIAA Journal*, Vol. 48, No. 8, 2010, pp. 1635–1646. doi:10.2514/1.J050024
- [138] McGilvray, M., Kirchhartz, R., and Jazra, T., “Comparison of Mach 10 Scramjet Measurements from Different Impulse Facilities,” *AIAA Journal*, Vol. 48, No. 8, 2010, pp. 1647–1651.
- [139] Ravichandran, R., Lewis, S., James, C., Morgan, R., and McIntyre, T., “Interaction of Ablating Carbon with Expanding Earth Entry Flows in the X2 Expansion Tube,” *9th Ablation Workshop*, Montana State University, Bozeman, MT, U.S.A., August 30-31, 2017, pp. 38–39
- [140] Ben-Yakar, A. and Hanson, R. K., “Characterization of Expansion Tube Flows for Hypervelocity Combustion Studies,” *Journal of Propulsion and Power*, Vol. 18, No. 4, 2002, pp. 943–952. doi:10.2514/2.6021
- [141] Abul-Huda, Y. and Gamba, M., “Combustion Effects of a Staged Transverse Jet and Pulsed Detonation in Supersonic Crossflow,” *54th AIAA Aerospace Sciences Meeting*, San Diego, CA, U.S.A., January 4-8, 2016
- [142] Abul-Huda, Y. M. and Gamba, M., “Flow Characterization of a Hypersonic Expansion Tube Facility for Supersonic Combustion Studies,” *Journal of Propulsion and Power*, Vol. 33, No. 6, 2017, pp. 1504–1519. doi:https://doi.org/10.2514/1.B36543
- [143] Paull, A., Stalker, R. J., and Stringer, I., “Experiments on an expansion tube with a free piston driver,” *15th AIAA Aerodynamic Testing Conference*, San Diego, CA, U.S.A., May 18-20, 1988
- [144] Paull, A., *Theoretical Analysis of Test Conditions in an Expansion Tube*, Departmental Report 10/89, Department of Mechanical Engineering, University of Queensland, Australia, 1989.
- [145] Stringer, I., “*TQ* Free Piston Expansion Tube – Design and Operation, Report 4/1989”, Department of Mechanical Engineering, The University of Queensland, Brisbane, Australia, 1989.

- [146] Gildfind, D., Morgan, R. G., and Jacobs, P., “Expansion Tubes in Australia,” *Experimental Methods of Shock Wave Research*, edited by O. Igra and F. Seiler, Springer, 2016, pp. 399–431.
- [147] Thompson, H. S., *Gonzo Papers, Vol. 3: Songs of the Doomed*, Simon and Schuster, 1990.
- [148] Eggers, A. and Cohen, N., “Progress and Problems in Atmosphere Entry,” *XVIIth IAF International Congress*, Athens, Greece, September 13-18, 1965
- [149] Tauber, M., “Atmospheric entry into Jupiter,” *Journal of Spacecraft and Rockets*, Vol. 6, No. 10, 1969, pp. 1103–1109. doi:10.2514/3.29771
- [150] Stickford, G. and Menard, W., “Bow Shock Composition and Radiation Intensity Calculations for a Ballistic Entry Into the Jovian Atmosphere,” *AIAA Paper 68-787*, Los Angeles, California, 1968
- [151] Tauber, M. and Wakefield, R., “Heating Environment and Protection During Jupiter Entry,” *AIAA Paper 70-1324*, Houston, TX, 1970
- [152] Tauber, M., “Heat Protection for Atmospheric Entry into Saturn, Uranus and Neptune,” *Advances in the Astronautical Sciences*, Vol. 29, No. 2, 1971, pp. 215–228.
- [153] Page, W., “Aerodynamic Heating for Probe Vehicles Entering the Outer Planets,” *Advances in the Astronautical Sciences*, Vol. 29, No. 2, 1971, pp. 191–214.
- [154] Leibowitz, L., “Measurement of the Structure of an Ionizing Shock Wave in a Hydrogen-Helium Mixture,” *The Physics of Fluids*, Vol. 16, No. 1, 1973, pp. 59–68. doi:10.1063/1.1694174
- [155] Menard, W. A., “A higher performance electric-arc-driven shock tube,” *AIAA Journal*, Vol. 9, No. 10, 1971, pp. 2096–2098. doi:10.2514/3.6481
- [156] Howe, J., “Hydrogen Ionization in the Shock Layer for Entry into the Outer Planets,” *AIAA Journal*, Vol. 12, No. 6, 1974, pp. 875–876. doi:10.2514/3.49371
- [157] Leibowitz, L. and Kuo, T., “Ionizational Nonequilibrium Heating During Outer Planetary Entries,” *AIAA Journal*, Vol. 14, No. 9, 1976, pp. 1324–1329. doi:10.2514/3.61465
- [158] Belozarov, A. and Measures, R., “The Initial Ionization of Hydrogen in a Strong Shock Wave,” *Journal of Fluid Mechanics*, Vol. 36, 1969, pp. 695–720. doi:10.1017/S0022112069001947

- [159] Stalker, R., "Shock Tunnel Measurement of Ionization Rates in Hydrogen," *AIAA Journal*, Vol. 18, No. 4, 1980, pp. 478–480. doi:10.2514/3.7652
- [160] Dannenberg, R., "A conical arc driver for high-energy test facilities," *AIAA Journal*, Vol. 10, No. 12, 1972, pp. 1692–1694. doi:10.2514/3.6707
- [161] Leibowitz, L., "Attainment of Jupiter Entry Shock Velocities," *AIAA Journal*, Vol. 13, No. 3, 1975, pp. 403–405. doi:10.2514/3.49715
- [162] Livingston, F. and Menard, W., "Toward understanding the conical arc-chamber driver," *9th International Symposium on Recent Developments in Shock Tube Research*, Stanford, CA, U.S.A., July 16-19, 1973
- [163] Kumar, A. and Graves, R., *User's Guide for the Computer Code 'COLTS' for Calculating the Coupled Laminar and Turbulent Flows Over a Jovian Probe*, Nasa Langley Research Center, Virginia, U.S.A., 1980.
- [164] Brewer, R., Brant, D., and Fogaroli, R., "Development of a Steady-State Shape Change Ablation Code for the Design of Outer Planet Probes," *AIAA Paper 77-95*, Jan. 1977
- [165] Balakrishnan, A. and Nicolet, W., *Galileo Probe Forebody Thermal Protection Benchmark Heating Environment Calculations. TSI Final Report FR-80/1*, Thermal Sciences, Inc., Sunnyvale, CA, U.S.A., 2008.
- [166] Green, M. and Davy, W., "Galileo Probe Forebody Thermal Protection," *AIAA Paper 81-1073*, June 1981
- [167] Moss, J. and Simmonds, A., "Galileo Probe Forebody Flowfield Predictions During Jupiter Entry," *AIAA Paper 82-0874*, June 1982
- [168] Park, C., "Calculation of radiation from argon shock layers," *Journal of Quantitative Spectroscopy and Radiative Transfer*, Vol. 28, No. 1, 1982, pp. 29–40. doi:10.1016/0022-4073(82)90094-2
- [169] Park, C., "Stagnation-point ablation of carbonaceous flat disks. I Theory," *AIAA Journal*, Vol. 21, No. 11, 1983, pp. 1588–1594. doi:10.2514/3.8293
- [170] Park, C., "Stagnation-point ablation of carbonaceous flat disks. II Experiment," *AIAA Journal*, Vol. 21, No. 12, 1983, pp. 1748–1754. doi:10.2514/3.8319
- [171] Norfleet, G. D., Hendrix, R. E., Raper, R. M., and Jr, E. C., "Development of an Aeroballistic Range Capability for Testing Re-Entry Materials," *Journal of Spacecraft and Rockets*, Vol. 12, No. 5, 1975, pp. 302–307. doi:10.2514/3.56976

- [172] Milos, F., Chen, Y.-K., Squire, T., and Brewer, R., “Analysis of Galileo Probe Heatshield Ablation and Temperature Data,” *Journal of Spacecraft and Rockets*, Vol. 36, No. 3, 1999, pp. 298–306. doi:10.2514/2.3465
- [173] Niemann, H. B., Atreya, S. K., Carignan, G. R., Donahue, T. M., Haberman, J. A., Harpold, D. N., Hartle, R. E., Hunten, D. M., Kasprzak, W. T., Mahaffy, P. R., Owen, T. C., Spencer, N. W., and Way, S. H., “The Galileo Probe Mass Spectrometer: Composition of Jupiter’s Atmosphere,” *Science*, Vol. 272, No. 5263, 1996, pp. 846–849. doi:10.1126/science.272.5263.846
- [174] Zahn, U. v. and Hunten, D. M., “The Helium Mass Fraction in Jupiter’s Atmosphere,” *Science*, Vol. 272, No. 5263, 1996, pp. 849–851.
- [175] Stalker, R., “A similarity Transformation for Blunt Body Flows,” *AIAA 24th Aerospace Sciences Meeting, AIAA Paper 86-0125*, Reno, Nevada, USA, Jan. 1986
- [176] Furudate, M., “Nonequilibrium Calculation of High-Temperature Radiating H<sub>2</sub>-He Flow-field,” *Journal of Thermophysics and Heat Transfer*, Vol. 23, No. 4, 2009, pp. 651–659. doi:10.2514/1.43961
- [177] Park, C., “Effect of Lyman Radiation on Nonequilibrium Ionization of Atomic Hydrogen,” *AIAA Paper 2004-2277*, June 2004
- [178] Kim, J., Kwon, O., and Park, C., “Master Equation Study and Nonequilibrium Chemical Reactions for H + H<sub>2</sub> and He + H<sub>2</sub>,” *Journal of Thermophysics and Heat Transfer*, Vol. 23, No. 3, 2009, pp. 443–453. doi:10.2514/1.41741
- [179] Kim, J., Kwon, O., and Park, C., “Master Equation Study and Nonequilibrium Chemical Reactions for Hydrogen Molecule,” *Journal of Thermophysics and Heat Transfer*, Vol. 24, No. 2, 2010, pp. 281–290. doi:10.2514/1.45283
- [180] Cohen, N. and Westberg, K., “Chemical Kinetic Data Sheets for High-Temperature Chemical Reactions,” *Journal of Physical and Chemical Reference Data*, Vol. 12, No. 3, 1983, pp. 531–590. doi:10.1063/1.555692
- [181] Hurle, I., *Measurements of Hydrogen-Atom Recombination Rates Behind Shock Waves*, Combustion Inst., Pittsburgh, PA, U.S.A., 1967.
- [182] Jacobs, T., Giedt, R., and Cohen, N., “Kinetics of Hydrogen Halides in Shock Waves. II. New Measurement of Hydrogen Dissociation Rate,” *Journal of Chemical Physics*, Vol. 47, No. 1, 1967, pp. 54–57. doi:10.1063/1.1711890

- [183] Rink, J., “Shock Tube Determination of Dissociation Rates of Hydrogen,” *Journal of Chemical Physics*, Vol. 36, No. 1, 1962, pp. 262–265. doi:10.1063/1.1732309
- [184] Sutton, E., “Measurement of the Dissociation Rates of Hydrogen and Deuterium,” *Journal of Chemical Physics*, Vol. 36, No. 11, 1962, pp. 2923–2931. doi:10.1063/1.1732403
- [185] Schwenke, D., “Calculations of Rate Constants for the Three-Body Recombination of H<sub>2</sub> in the Presence of H<sub>2</sub>,” *Journal of Chemical Physics*, Vol. 89, No. 4, 1988, pp. 2076–2091. doi:10.1063/1.455104
- [186] Furudate, M., Fujita, K., and Abe, T., “Coupled Rotational-Vibrational Relaxation of Molecular Hydrogen at High Temperatures,” *Journal of Thermophysics and Heat Transfer*, Vol. 20, No. 3, 2006, pp. 457–464. doi:10.2514/1.16323
- [187] Park, C., “Nonequilibrium Ionization and Radiation in Hydrogen-Helium Mixtures,” *Journal of Thermophysics and Heat Transfer*, Vol. 26, No. 2, 2012, pp. 231–243. doi:10.2514/1.T3689
- [188] Livingston, F. and Poon, P., “Relaxation Distance and Equilibrium Electron Density Measurements in Hydrogen-Helium Plasmas,” *AIAA Journal*, Vol. 14, No. 9, 1976, pp. 1335–1337. doi:10.2514/3.61466
- [189] Jits, R., Wright, M., and Chen, Y.-K., “Closed-Loop Trajectory Simulation for Thermal Protection System Design for Neptune Aerocapture,” *Journal of Spacecraft and Rockets*, Vol. 42, No. 6, 2005, pp. 1025–1034. doi:10.2514/1.13428
- [190] Gautier, D., Conrath, B., Owen, T., de Pater, I., and Atreya, S., *The troposphere of Neptune*, University of Arizona Press, 1995, pp. 547–612.
- [191] Park, C., “Nonequilibrium Chemistry and Radiation for Neptune Entry,” *Journal of Spacecraft and Rockets*, Vol. 48, No. 6, 2011, pp. 897–903. doi:10.2514/1.51810
- [192] Park, C., “Viscous Shock-Layer Calculation of Stagnation-Region Heating Environment in Neptune Aerocapture,” *Journal of Spacecraft and Rockets*, Vol. 51, No. 2, 2014, pp. 635–640. doi:10.2514/1.A32591
- [193] Hollis, B., Wright, M., Olejniczak, J., Takashima, N., Sutton, K., and Prabhu, D., “Preliminary Convective-Radiative Heating Environments for a Neptune Aerocapture Mission,” *AIAA Atmospheric Flight Mechanics Conference and Exhibit*, 2004
- [194] Bogdanoff, D. and Park, C., “Radiative Interaction Between Driver and Driven Gases in an Arc-Driven Shock Tube,” *Shock Waves*, Vol. 12, 2002, pp. 205–214. doi:10.1007/s00193-002-0157-y

- [195] Luis Borges, J., *The Book of Sand*, Dutton, 1977.
- [196] Morgan, R., "Free piston driven expansion tubes," *A Handbook of Shock Waves Vol. 1.*, edited by G. Ben-Dor, chap. 4.3, Academic Press, 2001, pp. 603–622.
- [197] Gordon, G. and McBride, B., *Computer Program for Calculation of Complex Chemical Equilibrium Compositions and Applications I. Analysis*, NASA Lewis Research Center, Cleveland, OH, U.S.A., 1994.
- [198] McBride, B. and Gordon, G., *Computer Program for Calculation of Complex Chemical Equilibrium Compositions and Applications II. Users Manual and Program Description*, NASA Lewis Research Center, Cleveland, OH, U.S.A., 1996.
- [199] Trimpi, R., *A Preliminary Theoretical Study of the Expansion Tube, a New Device for Producing High-Enthalpy Short-Duration Hypersonic Gas Flows*, NASA TR R-133, NASA Langley Research Center, Langley Station, Hampton, VA, U.S.A., 1962.
- [200] Trimpi, R. and Callis, L., *A Perfect-Gas Analysis of the Expansion Tunnel, a Modification to the Expansion Tube*, NASA TR R-223, NASA Langley Research Center, Langley Station, Hampton, VA, U.S.A., 1965.
- [201] Trimpi, R., *A Theoretical Investigation of Simulation in Expansion Tubes and Tunnels*, NASA TR R-243, NASA Langley Research Center, Langley Station, Hampton, VA, U.S.A., 1966.
- [202] Norfleet, G. and Loper, F., *A theoretical real-gas analysis of the expansion tunnel*, Technical Report 66-71, Arnold Engineering Development Center, Arnold Air Force Station, Tullahoma, TN, U.S.A., 1966.
- [203] Jones, J., "Some Performance Characteristics of the LRC 3 and 3/4 inch Pilot Expansion Tube Using an Unheated Hydrogen Driver," *Proceedings of the Fourth Hypervelocity Techniques Symposium: Advanced Experimental Techniques for Study of Hypervelocity Flight*, Arnold Engineering Development Center, Arnold Air Force Station, Tullahoma, TN, U.S.A., November 15-16, 1965, pp. 7–26
- [204] Givens, J., Page, W., and Reynolds, R., "Evaluation of Flow Properties in a Combustion-Driven Expansion Tube Operating at 7.5 km/sec," *Proceedings of the Fourth Hypervelocity Techniques Symposium: Advanced Experimental Techniques for Study of Hypervelocity Flight*, Arnold Engineering Development Center, Arnold Air Force Station, Tullahoma, TN, U.S.A., November 15-16, 1965, pp. 27–48

- [205] Norfleet, G., Lacey Jr, J., and Whitfield, J., “Results of an Experimental Investigation of the Performance of an Expansion Tube,” *Proceedings of the Fourth Hypervelocity Techniques Symposium: Advanced Experimental Techniques for Study of Hypervelocity Flight*, Arnold Engineering Development Center, Arnold Air Force Station, Tullahoma, TN, U.S.A., November 15-16, 1965, pp. 49–110
- [206] Spurk, J., “Design, Operation, and Preliminary Results of the BRL Expansion Tube,” *Proceedings of the Fourth Hypervelocity Techniques Symposium: Advanced Experimental Techniques for Study of Hypervelocity Flight*, Arnold Engineering Development Center, Arnold Air Force Station, Tullahoma, TN, U.S.A., November 15-16, 1965, pp. 111–144
- [207] Jones, J. and Moore, J., *Exploratory study of performance of the Langley pilot model expansion tube with a hydrogen driver*, Technical Note D-3421, NASA Langley Research Center, Langley Station, Hampton, VA, U.S.A., 1966.
- [208] Miller, C. G. and Jones, J., “Development and Performance of the NASA Langley Research Center Expansion Tube/Tunnel, a Hypersonic-Hypervelocity Real-Gas Facility,” *The 14th International Symposium on Shock Waves*, Sydney, NSW, Australia, 1983
- [209] Moore, J., *Description and Operating Performance of a Parallel-Rail Electric-Arc System with Helium Driver Gas for the Langley 6-inch Expansion Tube*, NASA TM X-3448, NASA Langley Research Center, Langley Station, Hampton, VA, U.S.A., 1976.
- [210] Creel, T., *Experimental Performance of an Internal Resistance Heater for Langley 6-inch Expansion Tube Driver*, NASA TN D-7070, NASA Langley Research Center, Langley Station, Hampton, VA, U.S.A., 1972.
- [211] Miller, C. G. and Jones, J., *Incident Shock-Wave Characteristics in Air, Argon, Carbon Dioxide, and Helium in a Shock Tube with Unheated Helium Driver*, NASA TN-8099, Nasa Langley Research Center, Langley, VA, U.S.A., 1975.
- [212] Miller, C. and Moore, J., “Flow-establishment times for blunt bodies in an expansion tube,” *AIAA Journal*, Vol. 13, No. 12, 1975, pp. 1676–1678. doi:10.2514/3.7048
- [213] Shinn, J., *Comparison of predicted and experimental real-gas pressure distributions on space shuttle orbiter nose for shuttle entry air data system*, NASA-TP-1627, Nasa Langley Research Center, Langley, VA, U.S.A., 1980.
- [214] Tamagno, J., Bakos, R., Pulsonetti, M., and Erdos, J., “Hypervelocity Real Gas Capabilities of GASL’s Expansion Tube (HYPULSE) Facility,” *16th AIAA Aerodynamic Ground Testing Conference*, Seattle, WA, U.S.A., June 18-20, 1990

- [215] Paull, A. and Stalker, R. J., “Test flow disturbances in an expansion tube,” *Journal of Fluid Mechanics*, Vol. 245, No. 1, 1992, pp. 493–521. doi:10.1017/S0022112092000569
- [216] Sasoh, A., Ohnishi, Y., Ramjaun, D., Takayama, K., Otsu, H., and Abe, T., “Effective Test Time Evaluation in High-Enthalpy Expansion Tube,” *AIAA Journal*, Vol. 39, No. 11, 2001, pp. 2141–2147. doi:10.2514/2.1210
- [217] Dufrene, A., Sharma, M., and Austin, J. M., “Design and Characterization of a Hypervelocity Expansion Tube Facility,” *Journal of Propulsion and Power*, Vol. 23, No. 6, 2007, pp. 1185–1193. doi:10.2514/1.30349
- [218] Dufrene, A., MacLean, M., Parker, R., Wadhams, T., and Holden, M., “Characterization of the New LENS Expansion Tunnel Facility,” *48th AIAA Aerospace Sciences Meeting Including the New Horizons Forum and Aerospace Exposition*, Orlando, FL, U.S.A., January 4-7, 2010
- [219] Abul-Huda, Y. and Gamba, M., “Design and Characterization of the Michigan Hypersonic Expansion Tube Facility (MHEXT),” *53rd AIAA Aerospace Sciences Meeting*, Kissimmee, Florida, U.S.A., January 5-9, 2015
- [220] Jiang, Z., Wu, B., Gao, Y., Zhao, W., and Hu, Z., “Development of the detonation-driven expansion tube for orbital speed experiments,” *Science China Technological Sciences*, Vol. 58, No. 4, 2015, pp. 695–700. doi:10.1007/s11431-014-5756-1
- [221] McGilvray, M., Doherty, L., Morgan, R., and Gildfind, D., “T6: The Oxford University Stalker Tunnel,” *20th AIAA International Space Planes and Hypersonic Systems and Technologies Conference*, Glasgow, Scotland, 2015. doi:10.2514/6.2015-3545
- [222] Morgan, R., McIntyre, T., Buttsworth, D., Jacobs, P., Potter, D., Brandis, A., Gollan, R., Jacobs, C., Capra, B., McGilvray, M., and Eichmann, T., “Impulse facilities for the simulation of hypersonic radiating flows,” *AIAA 38th Fluid Dynamics Conference and Exhibit*, Seattle, WA, U.S.A., June 23-26, 2008
- [223] Doolan, C., *Design and Construction of the X-2 Two-Stage Free Piston Driven Expansion Tube*, Department of Mechanical Engineering, The University of Queensland, Brisbane, Australia, 1995.
- [224] Doolan, C. and Morgan, R., “A two-stage free piston driver for expansion tubes,” *34th AIAA Aerospace Sciences Meeting and Exhibit*, Reno, NV, U.S.A., January 15-18, 1996
- [225] Doolan, C. and Morgan, R., “A two-stage free piston driver,” *Shock Waves*, Vol. 9, 1999, pp. 239–248. doi:10.1007/s001930050161



- [226] Morgan, R., “Development of X3, a Superorbital Expansion Tube,” *AIAA 38th Aerospace Sciences Meeting and Exhibit*, Reno, NV, Jan 10-13, 2000
- [227] Scott, M., Jacobs, P., and Morgan, R., “Nozzle development for an expansion tunnel,” *The 24th International Symposium on Shock Waves*, Beijing, China, July 11-16, 2004
- [228] Scott, M., Morgan, R., and Jacobs, P., “A new single stage driver for the X2 expansion tube, AIAA paper No. 2005-0694,” *43rd AIAA Aerospace Sciences Meeting and Exhibit*, Reno, NV, U.S.A., January 10-13, 2005
- [229] Scott, M., *Development and Modelling of Expansion Tubes*, Ph.D. thesis, the University of Queensland, St. Lucia, Australia, 2006.
- [230] Gildfind, D., *Development of High Total Pressure Scramjet Flows Conditions Using the X2 Expansion Tube*, Ph.D. thesis, the University of Queensland, St. Lucia, Australia, 2012.
- [231] Gildfind, D., Morgan, R., McGilvray, M., Jacobs, P., Stalker, R., and Eichmann, T., “Free-piston driver optimisation for simulation of high Mach number scramjet flow conditions,” *Shock Waves*, Vol. 21, No. 6, 2011, pp. 559–572. doi:10.2514/6.2012-5954
- [232] Gildfind, D. E., Morgan, R. G., Jacobs, P. A., and McGilvray, M., “Production of High-Mach-Number Scramjet Flow Conditions in an Expansion Tube,” *AIAA Journal*, Vol. 52, No. 1, 2014, pp. 162–177. doi:10.2514/1.J052383
- [233] Stalker, R., “Use of Argon in a Free Piston Shock Tunnel,” *AIAA Plasmadynamics Conference*, Monterey, CA, U.S.A., March 2-4, March 1966
- [234] Stalker, R., “A study of the free-piston shock tunnel,” *AIAA Journal*, Vol. 5, No. 12, 1967, pp. 2160–2165. doi:10.2514/3.4402
- [235] Itoh, K., Ueda, S., Komuro, T., Sato, K., Takahashi, M., Miyajima, H., Tanno, H., and Muramoto, H., “Improvement of a free piston driver for a high-enthalpy shock tunnel,” *Shock Waves*, Vol. 8, No. 4, 1998, pp. 215–233. doi:10.1007/s001930050115
- [236] Tanno, H., Itoh, K., Komuro, T., and Sato, K., “Experimental study on the tuned operation of a free piston driver,” *Shock Waves*, Vol. 10, No. 1, 2000, pp. 1–7. doi:10.1007/s001930050174
- [237] Jacobs, P., *L1d: A computer program for the simulation of transient-flow facilities. Report 1/99*, Department of Mechanical Engineering, University of Queensland, Australia, 1999.

- [238] Jacobs, P., “Quasi-One-Dimensional Modeling of a Free-Piston Shock Tunnel,” *AIAA Journal*, Vol. 32, No. 1, 1994, pp. 137–145. doi:10.2514/3.11961
- [239] Gildfind, D. E., Jacobs, P. A., and Morgan, R. G., “Vibration isolation in a free-piston driven expansion tube facility,” *Shock Waves*, Vol. 23, No. 5, 2013, pp. 431–438. doi:10.1007/s00193-013-0433-z
- [240] Zander, F., Gollan, R., Jacobs, P., and Morgan, R., “Hypervelocity shock standoff on spheres in air,” *Shock Waves*, Vol. 24, No. 2, 2014, pp. 171–178. doi:10.1007/s00193-013-0488-x
- [241] Park, G., Gai, S. L., and Neely, A. J., “Aerothermodynamics behind a blunt body at superorbital speeds,” *AIAA journal*, Vol. 48, No. 8, 2010, pp. 1804–1816.
- [242] Fahy, E., *Superorbital Re-entry Shock Layers: Flight and Laboratory Comparisons*, Ph.D. thesis, the University of Queensland, St. Lucia, Australia, 2017.
- [243] Zander, F., Molder, S., Morgan, R., Jacobs, P., and Gollan, R., “High Temperature gas effects for Converging Conical Shocks,” *18th AIAA/3AF International Space Planes and Hypersonic Systems and Technologies Conference*, Tours, France, September 24-28, 2012. doi:10.2514/6.2012-5939
- [244] Eichmann, T. N., McIntyre, T. J., Bishop, A. I., Vakata, S., and Rubinsztein-Dunlop, H., “Three-dimensional effects on line-of-sight visualization measurements of supersonic and hypersonic flow over cylinders,” *Shock Waves*, Vol. 16, No. 4, 2007, pp. 299–307. doi:10.1007/s00193-007-0075-0
- [245] McLean, C., *Pressure Measurements at the Entrance and Exit of the Nozzle on X2*, Bachelor of engineering thesis, the University of Queensland, St. Lucia, Australia, 2017.
- [246] McGilvray, M., Jacobs, P. A., Morgan, R. G., Gollan, R. J., and Jacobs, C. M., “Helmholtz Resonance of Pitot Pressure Measurements in Impulsive Hypersonic Test Facilities,” *AIAA Journal*, Vol. 47, No. 10, 2009, pp. 2430–2439. doi:10.2514/1.42543
- [247] Sheikh, U., *Re-Entry Radiation Aerothermodynamics in the Vacuum Ultraviolet*, Ph.D. thesis, the University of Queensland, St. Lucia, Australia, 2014.
- [248] Apirana, S., James, C., Eldridge, R., Lewis, S., and Morgan, R., “Manufacturing Hypervelocity Expansion Tube Test Models Using Rapid Prototyping,” *to be submitted to Aerospace Science and Technology*, 2018.

- [249] Gildfind, D., “X2 PCB Mount Assembly Drawing Set, Drawing Number x2-pcbmount1-000,” can be accessed online at <https://espace.library.uq.edu.au/view/UQ:372806>, 2015, Accessed November 12, 2017.
- [250] Zander, F., personal communication, 2012.
- [251] Camus, A., *Le Mythe de Sisyphe*, Gallimard, 1942.
- [252] Neely, A. and Morgan, R., “The Superorbital Expansion Tube concept, experiment and analysis,” *The Aeronautical Journal*, Vol. 98, 1994, pp. 97–105. doi:10.1017/S0001924000050107
- [253] Jacobs, P., Gollan, R., Potter, D., Zander, F., Gildfind, D., Blyton, P., Chan, W., and Doherty, L., *Estimation of high-enthalpy flow conditions for simple shock and expansion processes using the ESTCj program and library. Mechanical Engineering Report 2011/02*, Department of Mechanical Engineering, University of Queensland, Australia, 2011.
- [254] Jacobs, P. and Gollan, R., “The Compressible-Flow CFD Project,” <http://www.mech.uq.edu.au/cfcfd/>, Dec. 2012, Accessed December 21, 2012.
- [255] Morgan, R. and Stalker, R., “Double Diaphragm Driven Free Piston Expansion Tube,” *The 18th International Symposium on Shock Waves*, Sendai, Japan, July 21-26, 1991
- [256] Kendall, M., Morgan, R., and Petrie-Repar, P., “A study of free piston double diaphragm drivers for expansion tubes,” *AIAA 35th Aerospace Sciences Meeting and Exhibit*, Reno, NV, U.S.A., Jan 6-10, 1997
- [257] Roberts, G., Kendall, M., and Morgan, R., “Shock diaphragm interaction in expansion tubes,” *Proceedings of the 21st International Symposium on Shock Waves*, Great Keppel Island, QLD, Australia, July 20-25, 1997
- [258] Bakos, R. J. and Morgan, R. G., “Chemical recombination in an expansion tube,” *AIAA Journal*, Vol. 32, No. 6, 1994, pp. 1316–1319. doi:10.2514/3.12135
- [259] Petrie-Repar, P., *Numerical Simulation of Diaphragm Rupture*, Ph.D. thesis, the University of Queensland, St. Lucia, Australia, 1997.
- [260] Wegener, M., Sutcliffe, M., and Morgan, R., “Optical study of a light diaphragm rupture process in an expansion tube,” *Shock Waves*, Vol. 10, No. 3, 2000, pp. 167–178. doi:10.1007/s001930050003
- [261] Furukawa, T., Aochi, T., and Sasoh, A., “Expansion Tube Operation with Thin Secondary Diaphragm,” *AIAA Journal*, Vol. 45, No. 1, 2007, pp. 214–217. doi:10.2514/1.23846

- [262] Haggard, K., *Free-stream temperature, density, and pressure measurements in an expansion tube flows*, NASA-TN-D-7273, Nasa Langley Research Center, Langley, VA, U.S.A., 1973.
- [263] Wilson, G., “Time-dependent quasi-one-dimensional simulations of high enthalpy pulse facilities, AIAA Paper No. 92-5096,” *AIAA Fourth International Aerospace Planes Conference*, Orlando, FL, U.S.A., December 1-4, 1992
- [264] Roberts, G., Morgan, R., and Stalker, R., “The effect of diaphragm inertia on expansion tubes,” *The 13th International Symposium on Shock Waves*, Marseille, France, July 26-30, 1993
- [265] Taylor, G. I. and Maccoll, J. W., “The Air Pressure on a Cone Moving at High Speeds. I,” *Proceedings of the Royal Society of London. Series A*, Vol. 139, No. 838, 1933, pp. 278–297. doi:10.1098/rspa.1933.0017
- [266] Taylor, G. I. and Maccoll, J. W., “The Air Pressure on a Cone Moving at High Speeds. II,” *Proceedings of the Royal Society of London. Series A*, Vol. 139, No. 838, 1933, pp. 298–311. doi:10.1098/rspa.1933.0018
- [267] Gu, S., personal communication, 2015.
- [268] “Space Exploration: Cost, Schedule, and Performance of NASA’s Galileo Mission to Jupiter,” Tech. Rep. NSIAD-88-138FS, United States Government Accountability Office, Washington DC, U.S.A., May 1988.
- [269] Birkhoff, G., *Hydrodynamics; a study in logic, fact, and similitude*, Dover Publications, New York, N.Y., U.S.A., 1955.
- [270] Ellington, D., “Binary scaling limits for hypersonic flight,” *AIAA Journal*, Vol. 5, No. 9, 1967, pp. 1705–1706. doi:10.2514/3.4284
- [271] Morgan, R., McIntyre, T., Gollan, R., Jacobs, P., Brandis, A., McGilvray, M., van Diem, D., Gnoffo, P., Pulsonetti, M., and Wright, M., “Radiation Measurements in Nonreflected Shock Tunnels,” *25th AIAA Aerodynamic Measurement Technology and Ground Testing Conference*, San Francisco, CA, U.S.A., June 5-8, 2006
- [272] Capra, B. and Morgan, R., “Radiative and Total Heat Transfer Measurements to a Titan Explorer Model,” *Journal of Spacecraft and Rockets*, Vol. 49, No. 1, 2012, pp. 12–23. doi:10.2514/1.52961

- [273] Conrath, B., Gautier, D., Hanel, R., Lindal, G., and Marten, A., “The Helium Abundance of Uranus from Voyager Measurements,” *Journal of Geophysical Research*, Vol. 92, No. A13, 1987, pp. 15003–15010. doi:10.1029/JA092iA13p15003
- [274] Conrath, B. and Gautier, D., “Saturn Helium Abundance: A Reanalysis of Voyager Measurements,” *Icarus*, Vol. 144, No. 1, 2000, pp. 124 – 134. doi:10.1006/icar.1999.6265
- [275] Morgan, R., “Transitional and Turbulent Heating in Re-Entry flows,” Presentation to the meeting of the NATO STO AVT-240 & RTG-082 working group on Hypersonic Transition, Tuscon, AZ, U.S.A., March 26-27, 2015.
- [276] Cantwell, B., “Chapter 13: Unsteady waves in compressible flow,” Course Notes for AA210 Fundamentals of Compressible Flow at Stanford University, 2015.
- [277] *Model 112A22 High resolution ICP pressure probe, 50 psi, 100 mV/psi, 0.218" dia. Installation and Operating Manual*, PCB Piezotronics, Inc., Depew, N.Y., U.S.A.
- [278] McGilvray, M., Pearce, W., and James, C., “Non-Helium Secondary Driver,” *7th International Workshop on Radiation of High Temperature Gases in Atmospheric Entry*, Stuttgart, Germany, November 21-26, 2016
- [279] Robinson, M., Rowan, S., and Odam, J., *T4 Free Piston Shock Tunnel Operator’s Manual. Research Report Number 2003-1*, Department of Mechanical Engineering, University of Queensland, Australia, 2003.
- [280] Jacobs, P., Gardner, A., Buttsworth, D., Martinez Schramm, J., Karl, S., and Hanne-  
mann, K., “End-to-End Modelling of the HEG Shock Tunnel,” *The 24th International Symposium on Shock Waves*, Beijing, China, 2004
- [281] McIntyre, T., Maus, J., Laster, M., and Eitelberg, G., “Comparison of the Flow in the High-Enthalpy Shock Tunnel in Gottingen with Numerical Simulations,” *The 13th International Symposium on Shock Waves*, Marseille, France, July 26-30, 1993
- [282] Hannemann, K., Itoh, K., Mee, D., and Hornung, H., “Free Piston Shock Tunnels HEG, HIEST, T4 and T5,” *Experimental Methods of Shock Wave Research*, edited by O. Igra and F. Seiler, Springer, 2016, pp. 181–264.
- [283] Hornung, H., Sturtevant, B., Bélanger, J., Sanderson, S., Brouillette, M., and Jenkins, M., *Performance data of the new free-piston shock tunnel T5 at GALCIT*, Springer Berlin Heidelberg, 1992, pp. 603–610.

- [284] Mundt, C., “Development of the New Piston-Driven Shock-Tunnel HELM,” *Experimental Methods of Shock Wave Research*, edited by O. Igra and F. Seiler, Springer, 2016, pp. 265–283.
- [285] Vonnegut Jr., K., *Cat’s Cradle*, Holt, Rinehart and Winston, 1963.
- [286] Sheikh, U., Morgan, R., and McIntyre, T., “Optical Thickness Measurements of Vacuum Ultraviolet Radiation in the X2 Expansion Tube,” *AIAA Journal*, Vol. 54, No. 8, 2016, pp. 2407–2417. doi:10.2514/1.J054659
- [287] Laux, C., “Radiation and Nonequilibrium Collisional-Radiative Models,” *Von Karman Institute Lecture Series 2002-07, Physico-Chemical Modeling of High Enthalpy and Plasma Flows*, edited by D. Fletcher, J.-M. Charbonnier, G. Sarma, and T. Magin, Rhode-Saint-Genèse, Belgium, 2002.
- [288] Laux, C., Spence, T., Kruger, C., and Zare, R., “Optical diagnostics of atmospheric pressure air plasmas,” *Plasma Sources Science and Technology*, Vol. 12, No. 2, 2003, pp. 125–138. doi:10.1088/0963-0252/12/2/301
- [289] Sutton, K. and Graves Jr, R. A., *A general stagnation-point convective heating equation for arbitrary gas mixtures, NASA-TR- R-376*, Nasa Langley Research Center, Langley, VA, U.S.A., 1971.
- [290] Capra, B. R. and Morgan, R. G., “Total Heat Transfer Measurements on a Flight Investigation of Reentry Environment Model,” *Journal of Spacecraft and Rockets*, Vol. 50, No. 3, 2013, pp. 494–503. doi:10.2514/1.A32333
- [291] Orwell, G., *Burmese Days*, Harper & Brothers, 1934.
- [292] Thompson, M., *Development of High Enthalpy Driver Conditions for X2 Expansion Tube*, Bachelor of engineering thesis, the University of Queensland, St. Lucia, Australia, 2017.
- [293] Jacobs, P. and Gollan, R., “PITOT,” <http://cfcfd.mechmining.uq.edu.au/pitot.html>, May 2017, Accessed May 12, 2017.
- [294] Yaws, C., *Matheson Gas Data Book*, McGraw-Hill, NY, U.S.A., 7th ed., 2001.
- [295] Gas, M. T., “Lower and Upper Explosive Limits for Flammable Gases and Vapors (LEL/UEL),” [http://www.mathesongas.com/pdfs/products/Lower-\(LEL\)-&-Upper-\(UEL\)-Explosive-Limits-.pdf](http://www.mathesongas.com/pdfs/products/Lower-(LEL)-&-Upper-(UEL)-Explosive-Limits-.pdf), Accessed April 17, 2013.
- [296] Sutton, K., “Radiative heating about outer planet entry probes,” *Journal of Spacecraft and Rockets*, Vol. 13, No. 5, 1976, pp. 294–300. doi:10.2514/3.57091

- [297] Brandis, A. and Johnston, C., “Characterization of stagnation-point heat flux for earth entry,” *45th AIAA Plasmadynamics and Lasers Conference*, Atlanta, GA, U.S.A., June 16-20, 2014. doi:10.2514/6.2014-2374
- [298] Park, C., “Stagnation-Point Radiation for Apollo 4,” *Journal of Thermophysics and Heat Transfer*, Vol. 18, No. 3, 2004, pp. 349–357. doi:10.2514/1.6527
- [299] Ried Jr, R., Rochelle, W., and Milhoan, J., *Radiative heating to the Apollo command module: Engineering prediction and flight measurement*, NASA TM X -58091, NASA Manned Spacecraft Center, Houston, TX, U.S.A., 1972.

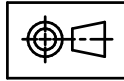
## Appendix A

# Eichmann Cylinder Drawings

This appendix collects the drawing set for the latest iteration of the 75 mm long, 25 mm diameter Eichmann cylinder that was used for some experiments during this project. The drawing of the cylinder is included, as well as drawings of an aligning tool, and a key to mount the aligning tool to the model. Drawings of the rest of the X2 model mounting system are also included, including the model mount, sting adapter, sting, sting clamps, and the model mount that bolts to the rail at the bottom of the X2 test section.

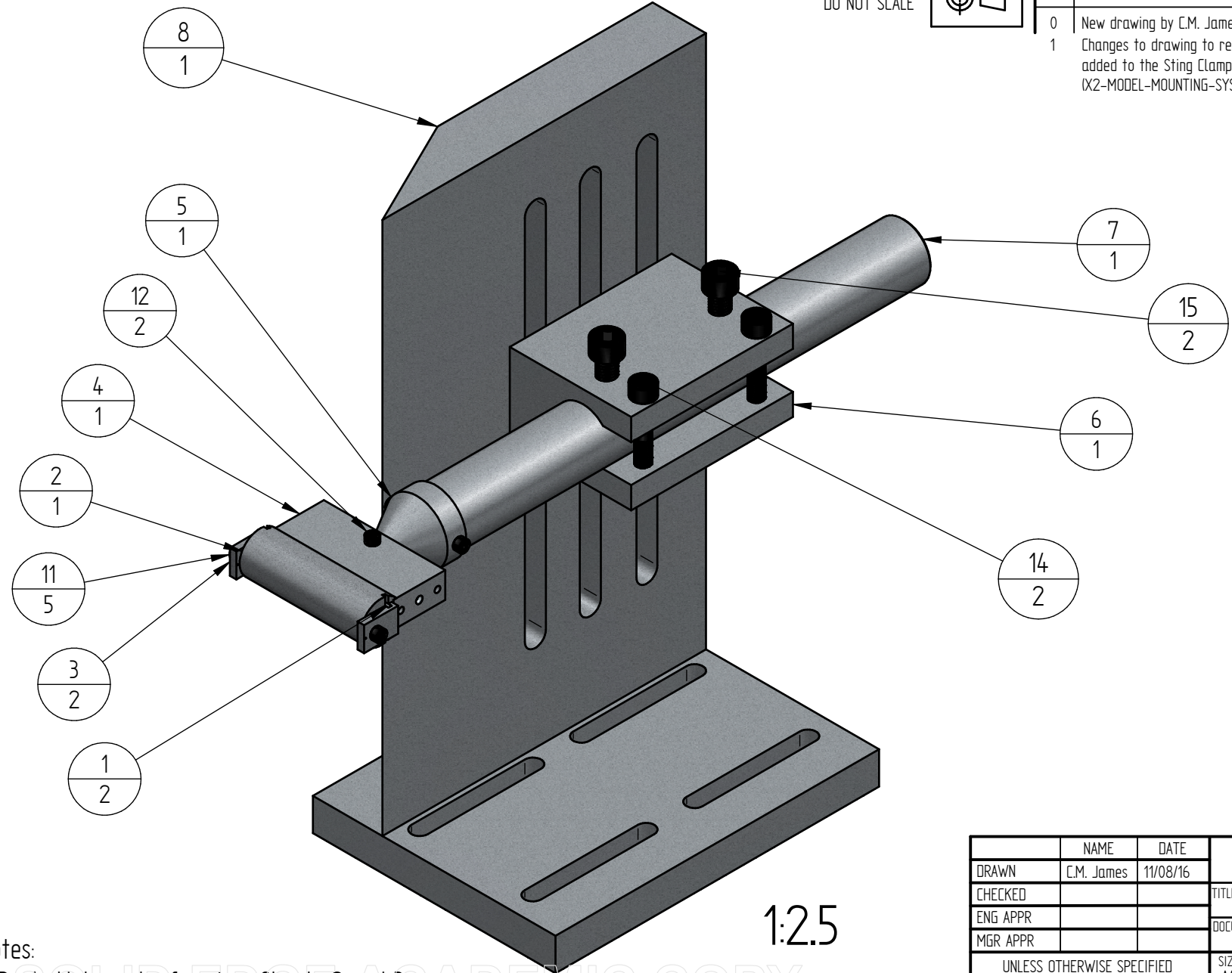


DRAFTING STANDARD: AS1100 - 1992  
DO NOT SCALE



REVISION HISTORY

REV	DESCRIPTION	DATE	APPROVED
0	New drawing by C.M. James	05/04/16	
1	Changes to drawing to reflect extra detail added to the Sting Clamp (X2-MODEL-MOUNTING-SYSTEM-007)	11/08/16	

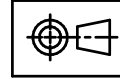


1:2.5

Notes:  
- Parts List can be found on Sheets 2 and 3.

	NAME	DATE		
DRAWN	C.M. James	11/08/16	TITLE Assembly	
CHECKED			DOCUMENT NO. X2-MODEL-MOUNTING-SYSTEM-000	
ENG APPR			PROJECT Chris James PhD model	
MGR APPR			FILE NAME: x2-m-m-system-000-1-model-assembly.dft	REV 1
UNLESS OTHERWISE SPECIFIED DIMENSIONS ARE IN MILLIMETERS ANGULAR TOLERANCE ±0.1° DIMENSIONAL TOLERANCE ±0.1mm			SCALE: AS SHOWN	WEIGHT: SHEET 1 OF 3

DRAFTING STANDARD: AS1100 - 1992  
DO NOT SCALE



REVISION HISTORY

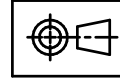
REV	DESCRIPTION	DATE	APPROVED
0	New drawing by C.M. James	05/04/16	
1	Changes to drawing to reflect extra detail added to the Sting Clamp (X2-MODEL-MOUNTING-SYSTEM-007)	11/08/16	

Item Number	Document Number	Revision number	Title	Material	Author	Quantity	File Name (no extension)
1	X2-MODEL-MOUNTING-SYSTEM-003	1	Key	Steel	C.M. James	2	key
2	X2-MODEL-MOUNTING-SYSTEM-001	1	New Eichmann Cylinder	Steel	C.M. James	1	eichmann cylinder
3	X2-MODEL-MOUNTING-SYSTEM-002	1	Aligning Tool	Stainless steel	C.M. James	2	aligning tool
4	X2-MODEL-MOUNTING-SYSTEM-004	0	Mounting Block	Steel	C.M. James	1	old_mounting_block
5	X2-MODEL-MOUNTING-SYSTEM-005	0	Sting Adapter	Steel	C.M. James	1	adapter
6	X2-MODEL-MOUNTING-SYSTEM-007	0	Sting Clamp	Steel	C.M. James	1	sting_clamp
7	X2-MODEL-MOUNTING-SYSTEM-006	0	Solid Sting	Steel	C.M. James	1	solid_sting
8	X2-MODEL-MOUNTING-SYSTEM-008	0	Model Mount	Steel	C.M. James	1	model_mount

	NAME	DATE		
DRAWN	C.M. James	11/08/16		
CHECKED			TITLE Assembly	
ENG APPR			DOCUMENT NO. X2-MODEL-MOUNTING-SYSTEM-000	
MGR APPR				
UNLESS OTHERWISE SPECIFIED DIMENSIONS ARE IN MILLIMETERS ANGULAR TOLERANCE ±0.1° DIMENSIONAL TOLERANCE ±0.1mm			SIZE A4	PROJECT Chris James PhD model
			FILE NAME: x2-m-m-system-000-1-model-assembly.dft	
			SCALE: AS SHOWN	WEIGHT: SHEET 2 OF 3

SOLID EDGE ACADEMIC COPY

DRAFTING STANDARD: AS1100 - 1992  
DO NOT SCALE



REVISION HISTORY

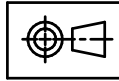
REV	DESCRIPTION	DATE	APPROVED
0	New drawing by C.M. James	05/04/16	
1	Changes to drawing to reflect extra detail added to the Sting Clamp (X2-MODEL-MOUNTING-SYSTEM-007)	11/08/16	

Item Number	Document Number	Revision number	Title	Material	Author	Quantity	File Name (no extension)
9*	N/A	N/A	M10 High Tensile Washer	Steel	C.M. James	2	M10_high_tensile_washer
10*	N/A	N/A	M10 x 50 mm Cap Screw	Steel	C.M. James	2	M10-50mm
11	N/A	N/A	M4 x 10 mm Cap Screw	Steel	C.M. James	5	M4 x 10mm
12	N/A	N/A	M4 x 5 mm Cap Screw	Steel	C.M. James	2	M4 x 5mm
13*	N/A	N/A	M6 x 25 mm Cap Screw	Steel	C.M. James	2	M6 x 25mm
14	N/A	N/A	M8 x 50 mm Cap Screw	Steel	C.M. James	2	M8 x 50mm
15	N/A	N/A	M10 x 20 mm Cap Screw	Steel	C.M. James	2	M10 x 20mm

	NAME	DATE			
DRAWN	C.M. James	11/08/16			
CHECKED			TITLE Assembly		
ENG APPR			DOCUMENT NO. X2-MODEL-MOUNTING-SYSTEM-000		
MGR APPR					
UNLESS OTHERWISE SPECIFIED DIMENSIONS ARE IN MILLIMETERS ANGULAR TOLERANCE ±0.1° DIMENSIONAL TOLERANCE ±0.1mm			SIZE A4	PROJECT Chris James PhD model	REV 1
			FILE NAME: x2-m-m-system-000-1-model-assembly.dft		
			SCALE: AS SHOWN	WEIGHT:	SHEET 3 OF 3

SOLID EDGE ACADEMIC COPY

DRAFTING STANDARD: AS1100 - 1992  
DO NOT SCALE



REVISION HISTORY

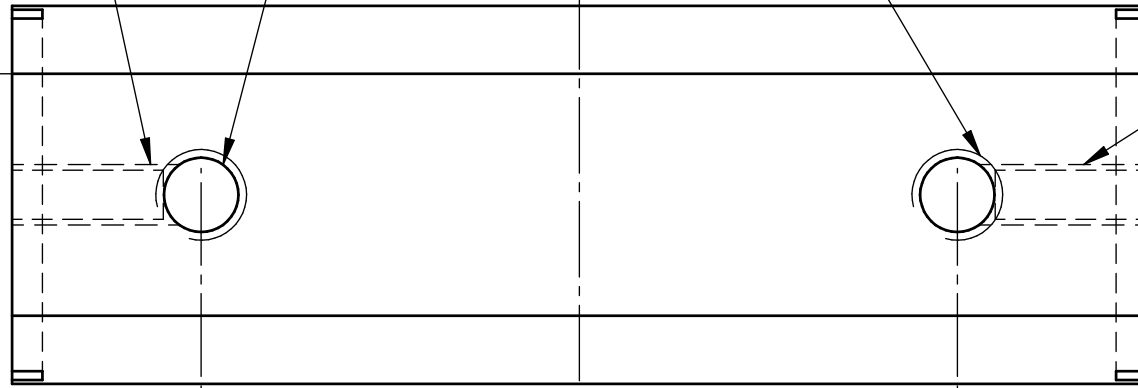
REV	DESCRIPTION	DATE	APPROVED
0	New drawing by C.M. James.	25/03/14	
1	Updates to drawing to make it part of X2-MODEL-MOUNTING-SYSTEM drawing set.	03/04/16	

M4 - 10 DEEP

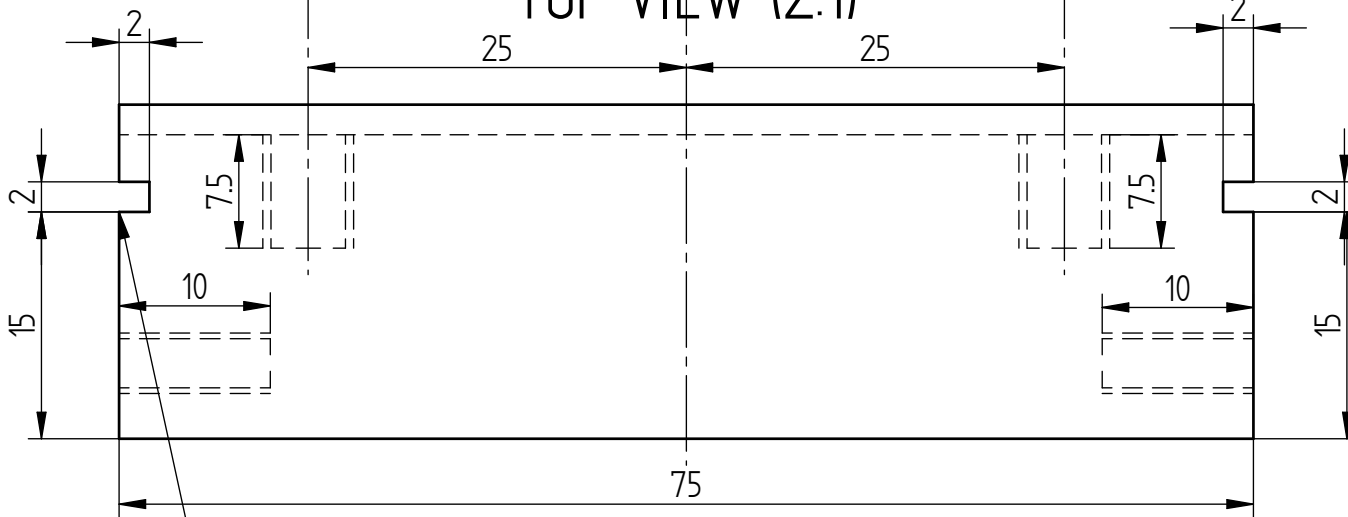
M6 - 7.5 DEEP

M6 - 7.5 DEEP

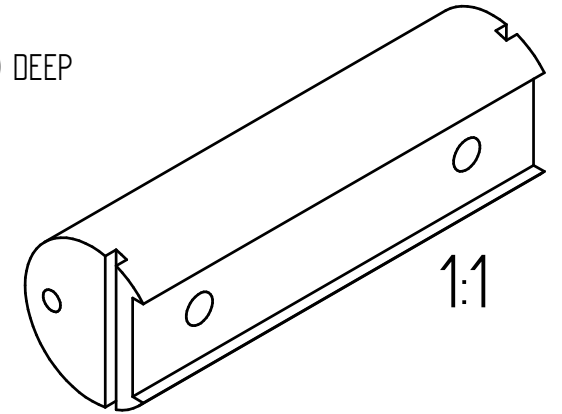
M4 - 10 DEEP



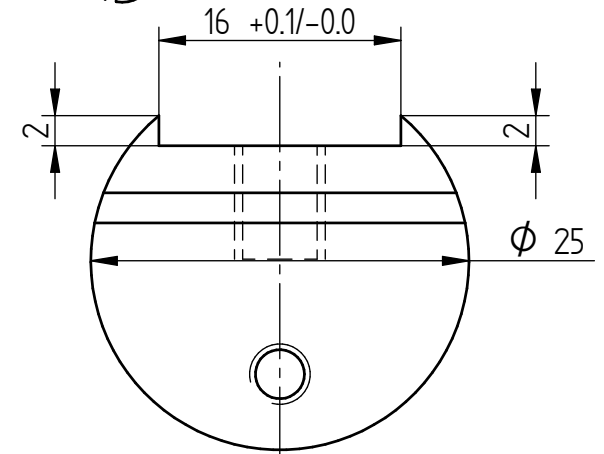
TOP VIEW (2:1)



FRONT VIEW (2:1)



1:1



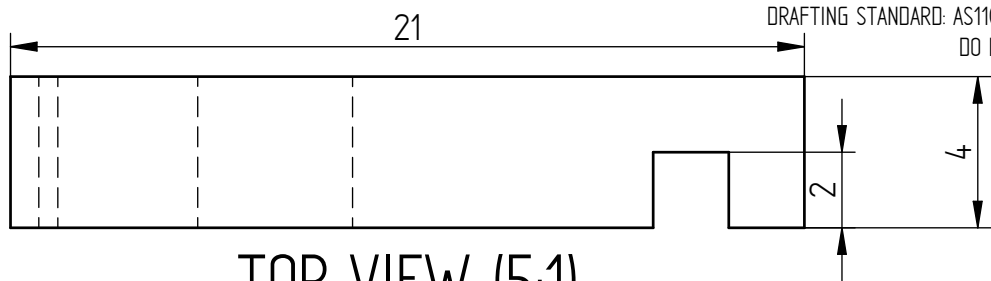
SIDE VIEW (2:1)

NEED TIGHT TOLERANCE ON CUTOUTS ON END TO FIT 2MM KEY (X2-MODEL-MOUNTING-SYSTEM-003).

Notes:

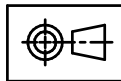
- 25 diameter cylinder, 75 long.
- Need tight tolerance on cutouts on ends to fit 2 mm key.
- Material: mild steel.

	NAME	DATE		
DRAWN	C.M. James	10/04/16	TITLE New Eichmann Cylinder	
CHECKED			DOCUMENT NO. X2-MODEL-MOUNTING-SYSTEM-001	
ENG APPR				
MGR APPR				
UNLESS OTHERWISE SPECIFIED DIMENSIONS ARE IN MILLIMETERS ANGULAR TOLERANCE ±0.1° DIMENSIONAL TOLERANCE ±0.1mm			SIZE A4	PROJECT Chris James PhD model REV 1
			FILE NAME: x2-m-m-system-001-1-eichmann-cylinder.dff	
			SCALE: AS SHOWN	WEIGHT: SHEET 1 OF 1

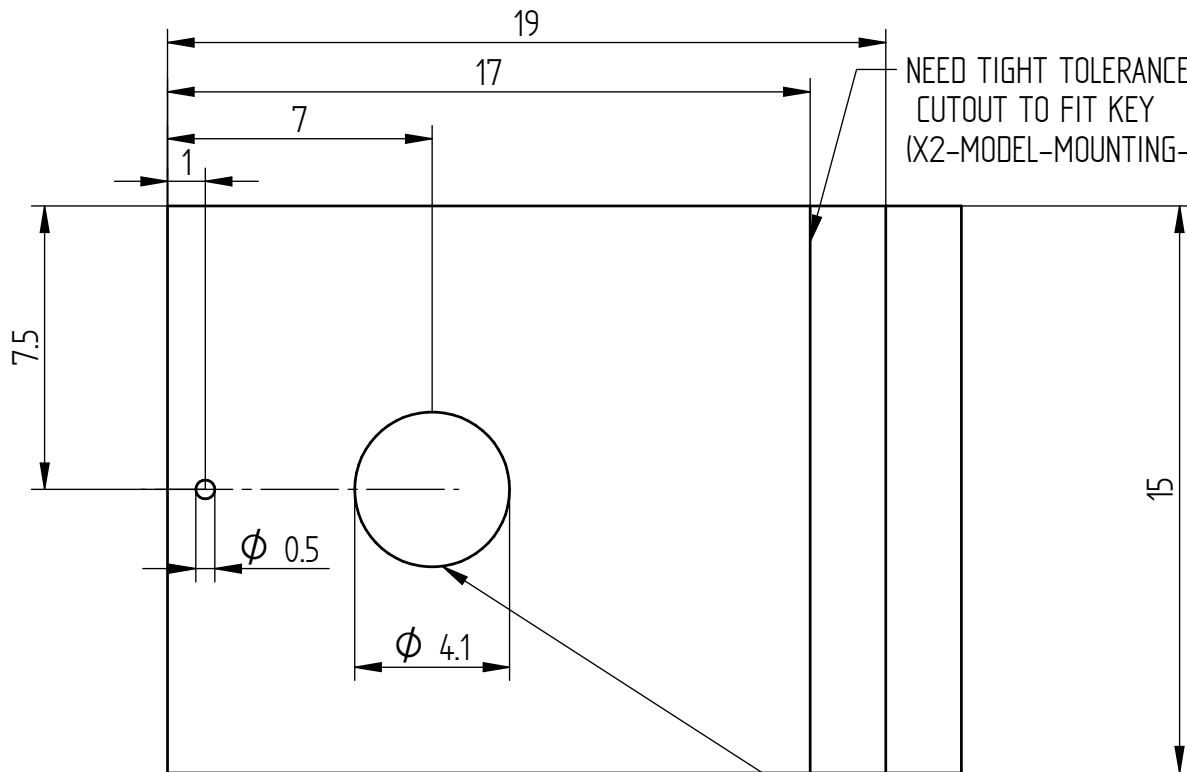


TOP VIEW (5:1)

DRAFTING STANDARD: AS1100 - 1992  
DO NOT SCALE

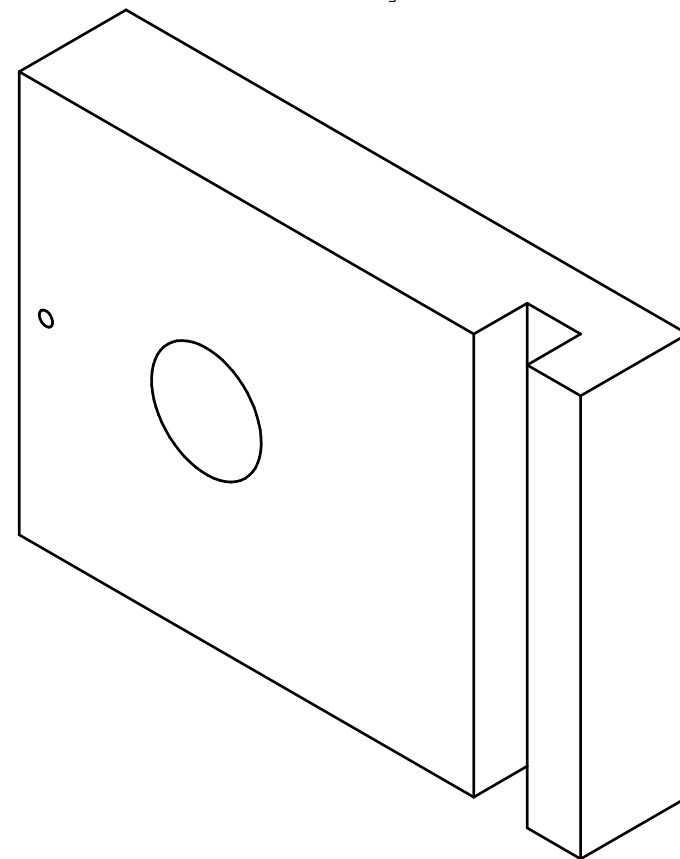


REVISION HISTORY			
REV	DESCRIPTION	DATE	APPROVED
0	New drawing by C.M. James.	25/03/14	
1	Updates to drawing to make it part of X2-MODEL-MOUNTING-SYSTEM drawing set.	03/04/16	



FRONT VIEW (5:1)

M4 TIGHT CLEARANCE HOLE



5:1

Notes:

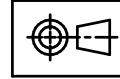
-20 long, 15 high. thickness of 4 is not essential, could be made slightly wider if only wider materials are available

- Material: stainless steel if available, could be made of aluminium or mild steel otherwise

- Need 2. One to fit either side of the model.

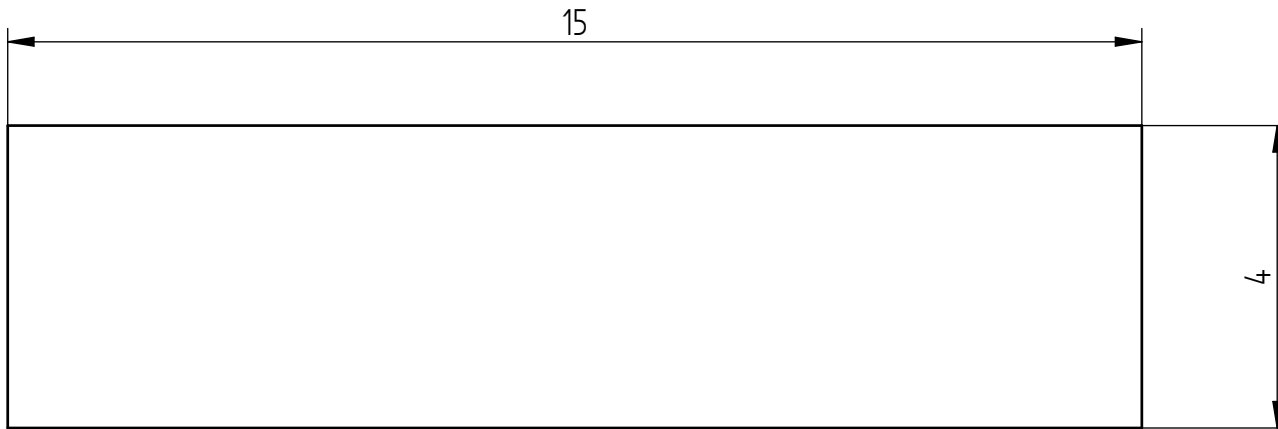
	NAME	DATE			
DRAWN	C.M. James	03/04/16			
CHECKED			TITLE: Aligning Tool for Eichmann Cylinder		
ENG APPR			DOCUMENT NO: X2-MODEL-MOUNTING-SYSTEM-002		
MGR APPR					
UNLESS OTHERWISE SPECIFIED DIMENSIONS ARE IN MILLIMETERS ANGULAR TOLERANCE $\pm 0.1^\circ$ DIMENSIONAL TOLERANCE $\pm 0.1\text{mm}$			SIZE	PROJECT	REV
			A4	Chris James PhD model	1
			FILE NAME: x2-m-m-system-002-1-aligning-tool.dft		
			SCALE: AS SHOWN	WEIGHT:	SHEET 1 OF 1

DRAFTING STANDARD: AS1100 - 1992  
DO NOT SCALE

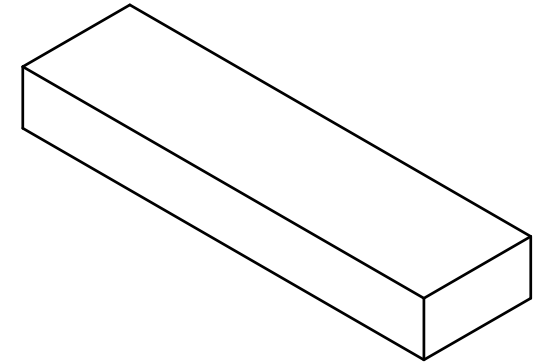


REVISION HISTORY

REV	DESCRIPTION	DATE	APPROVED
0	New drawing by C.M. James.	25/03/14	
1	Updates to drawing to make it part of X2-MODEL-MOUNTING-SYSTEM drawing set.	03/04/16	



TOP VIEW (10:1)



5:1



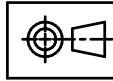
FRONT VIEW (10:1)

Notes:

- key needs to fit tightly into the groove on the other two parts, the cylinder (X2-MODEL-MOUNTING-SYSTEM-001) and the Aligning Tool (X2-MODEL-MOUNTING-SYSTEM-002).
- Material: not load bearing so stainless steel or aluminium is fine.
- Need 2 of these, one to fit either side of the model.

	NAME	DATE		
DRAWN	C.M. James	03/04/16	TITLE Key	
CHECKED			DOCUMENT NO. X2-MODEL-MOUNTING-SYSTEM-003	
ENG APPR			SIZE A4	PROJECT Chris James PhD model
MGR APPR			FILE NAME: x2-m-m-system-003-1-key.dft	REV 1
UNLESS OTHERWISE SPECIFIED DIMENSIONS ARE IN MILLIMETERS ANGULAR TOLERANCE ±0.1° DIMENSIONAL TOLERANCE ±0.1mm			SCALE: AS SHOWN	WEIGHT: SHEET 1 OF 1

DRAFTING STANDARD: AS1100 - 1992  
DO NOT SCALE

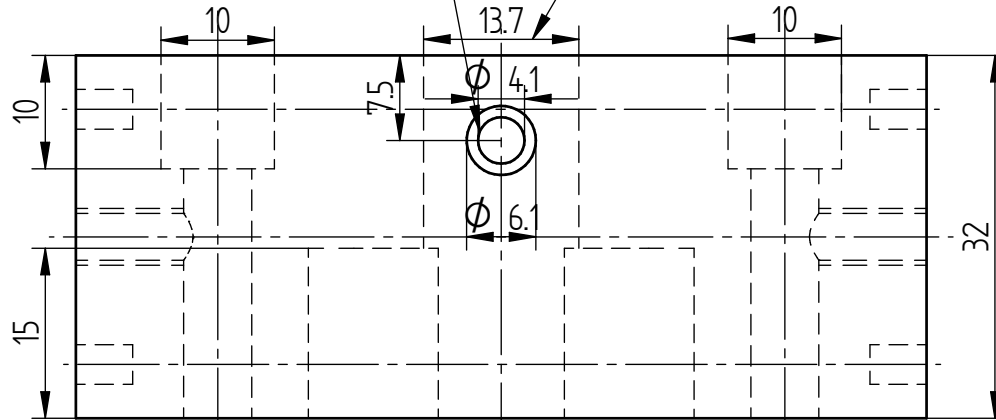


REVISION HISTORY

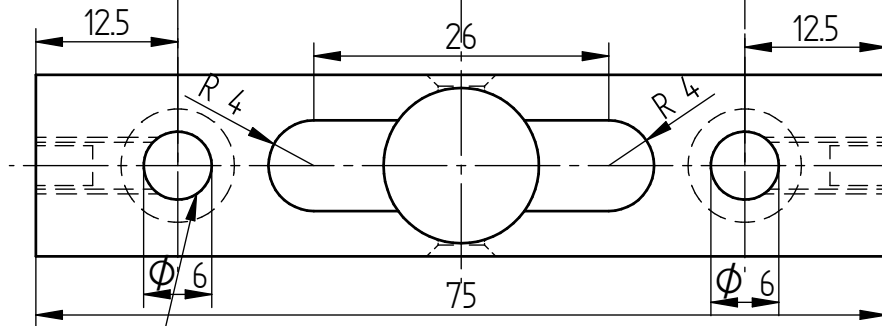
REV	DESCRIPTION	DATE	APPROVED
0	New drawing by C.M. James based on measurements of an existing part.	03/04/16	

VERY TIGHT M4 CLEARANCE HOLE WITH 45° COUNTERSINK (BOTH SIDES).

13.7 MM HOLE HAS A TIGHT FIT (PROBABLY H7/h6) WITH THE STING ADAPTER (X2-MODEL-MOUNTING-SYSTEM-005).



TOP VIEW (1.5:1)

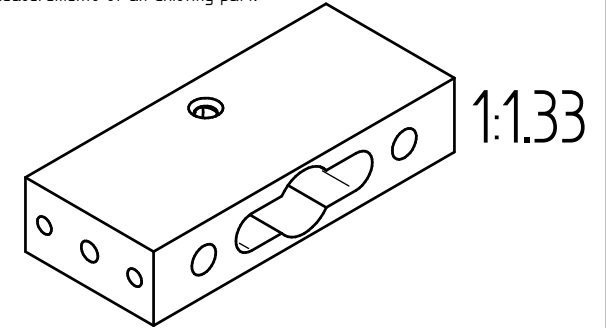


FRONT VIEW (1.5:1)

THIS APPEARS TO BE A VERY TIGHT M6 CLEARANCE HOLE FOR CONNECTION TO THE CYLINDER (X2-MODEL-MOUNTING-SYSTEM-001). (IN REALITY, IT IS PROBABLY SLIGHTLY LARGER THAN 6 MM.)

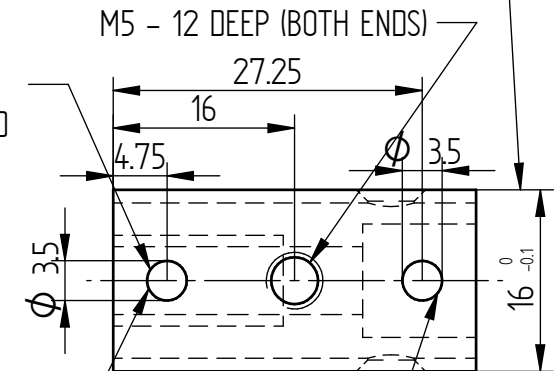
Notes:

- This drawing has been made based on measurements of an existing component.
- Material: Existing component appears to be steel.
- Part is symmetrical about the Front View in both directions.
- Hollow centre is for use with test models with inbuilt sensors.



SHOULD BE TOLERANCED DOWN TO FIT CYLINDER (X2-MODEL-MOUNTING-SYSTEM-001).

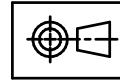
3 HOLES ARE FROM AN OLD ALIGNMENT SYSTEM AND COULD BE REMOVED FROM A NEW VERSION OF THIS PART.



BOTH ENDS  
SIDE VIEW (1.5:1)

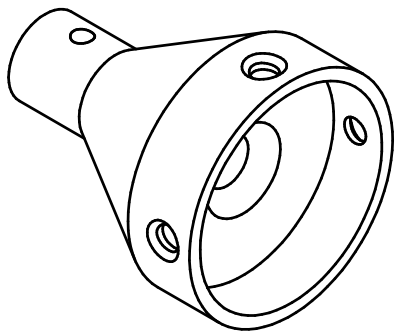
	NAME	DATE		
DRAWN	C.M. James	05/04/16	TITLE: Mounting Block	
CHECKED			DOCUMENT NO: X2-MODEL-MOUNTING-SYSTEM-004	
ENG APPR			SIZE: A4	PROJECT: Chris James PhD model
MGR APPR			FILE NAME: x2-m-m-system-004-0-mounting-block.dft	REV: 0
UNLESS OTHERWISE SPECIFIED DIMENSIONS ARE IN MILLIMETERS ANGULAR TOLERANCE ±0.1° DIMENSIONAL TOLERANCE ±0.1mm			SCALE: AS SHOWN	WEIGHT: SHEET 1 OF 1

DRAFTING STANDARD: AS1100 - 1992  
DO NOT SCALE

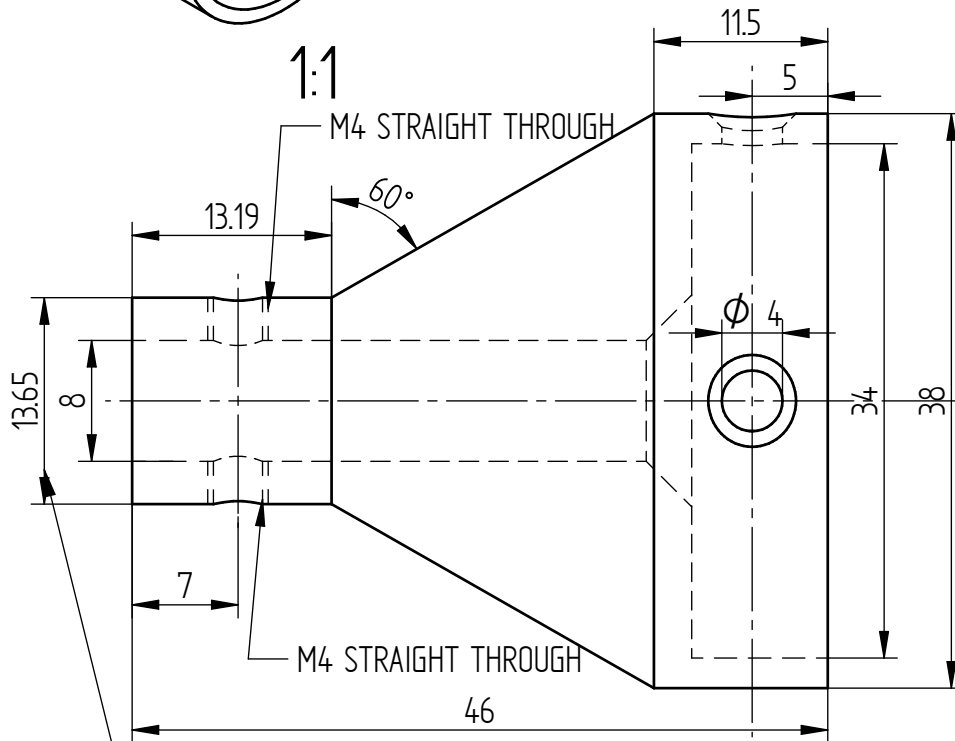


REVISION HISTORY

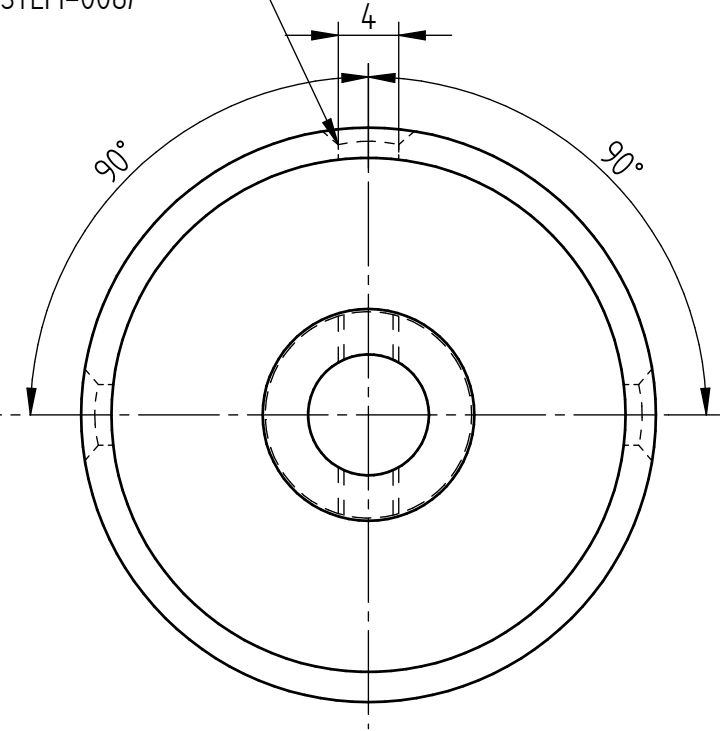
REV	DESCRIPTION	DATE	APPROVED
0	New drawing by C.M. James based on measurements of an existing part.	03/04/16	



3 x 4 mm HOLES WITH 45° COUNTERSINK FOR BOLTING THIS PIECE TO THE STING (X2-MODEL-MOUNTING-SYSTEM-006)



FRONT VIEW (2:1)



SIDE VIEW (2:1)

TIGHT FIT (PROBABLY H7/h6) BETWEEN THIS PART AND THE MOUNTING BLOCK (X2-MODEL-MOUNTING-SYSTEM-004)

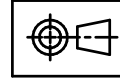
Notes:

- This drawing has been made based on measurements of an existing component.
- Material: Existing component appears to be made from steel.

NAME	DATE		
DRAWN C.M. James	10/04/16	TITLE Sting Adapter	
CHECKED		DOCUMENT NO. X2-MODEL-MOUNTING-SYSTEM-005	
ENG APPR		SIZE A4	PROJECT Chris James PhD model
MGR APPR		FILE NAME: x2-m-m-system-005-0-sting-adapter.dft	REV 0
UNLESS OTHERWISE SPECIFIED DIMENSIONS ARE IN MILLIMETERS		SCALE: AS SHOWN	WEIGHT:
ANGULAR TOLERANCE ±0.1°		SHEET 1 OF 1	
DIMENSIONAL TOLERANCE ±0.1mm			

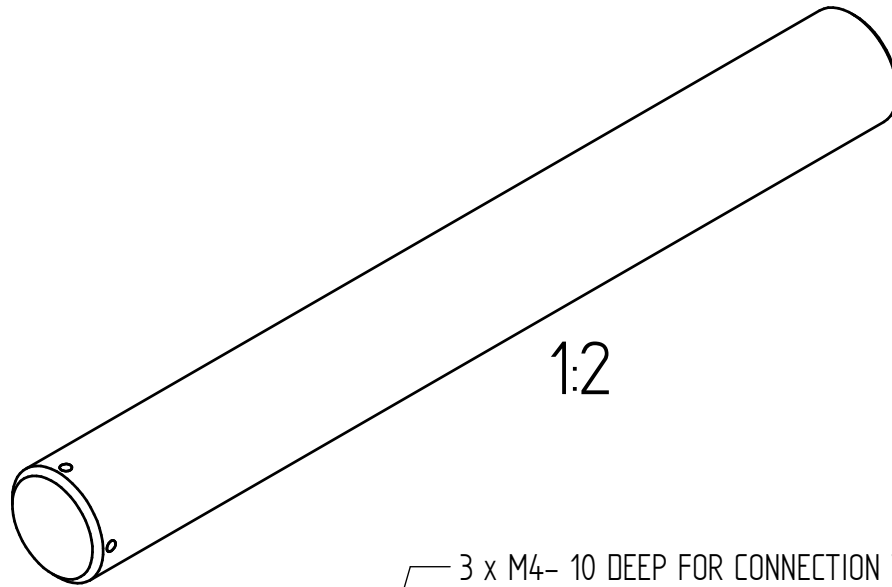


DRAFTING STANDARD: AS1100 - 1992  
DO NOT SCALE



REVISION HISTORY

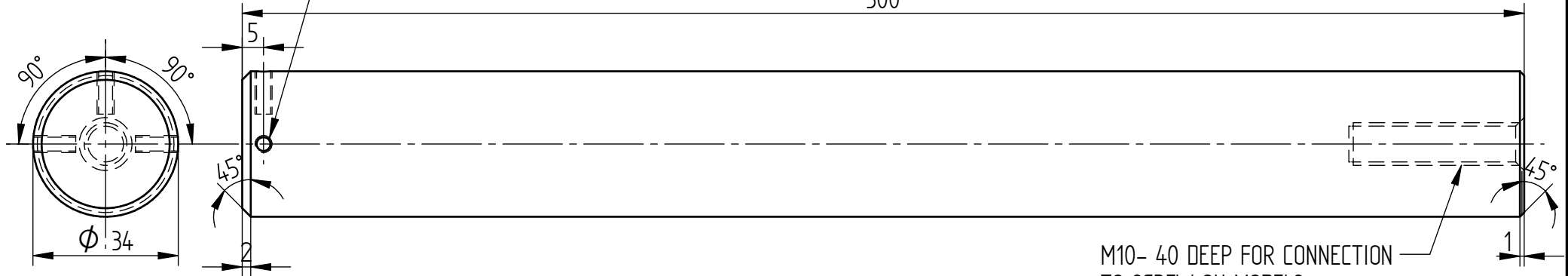
REV	DESCRIPTION	DATE	APPROVED
0	New drawing by C.M. James based on measurements of an existing part.	03/04/16	



1:2

3 x M4- 10 DEEP FOR CONNECTION TO THE STING ADAPTER (X2-MODEL-MOUNTING-SYSTEM-005)

300



SIDE VIEW  
(1:1.33)

FRONT VIEW (1:1.33)

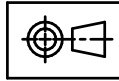
M10- 40 DEEP FOR CONNECTION TO SCREW ON MODELS.

Notes:

- This drawing has been made based on measurements of an existing component.
- Material: Existing component appears to be made from steel.
- A similar hollow sting for use with models with inbuilt sensors also exists and can be found on X2-MODEL-MOUNTING-SYSTEM-009.

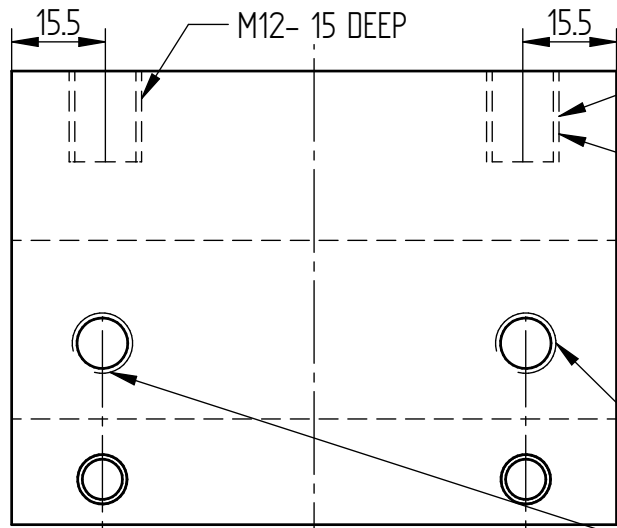
NAME	DATE	TITLE	
DRAWN C.M. James	10/04/16	Solid Sting	
CHECKED		DOCUMENT NO. X2-MODEL-MOUNTING-SYSTEM-006	
ENG APPR		SIZE A4	PROJECT Chris James PhD model
MGR APPR		FILE NAME: x2-m-m-system-006-0-solid-sting.dft	REV 0
UNLESS OTHERWISE SPECIFIED DIMENSIONS ARE IN MILLIMETERS ANGULAR TOLERANCE ±0.1° DIMENSIONAL TOLERANCE ±0.1mm		SCALE: AS SHOWN	WEIGHT: SHEET 1 OF 1

DRAFTING STANDARD: AS1100 - 1992  
DO NOT SCALE



REVISION HISTORY

REV	DESCRIPTION	DATE	APPROVED
0	New drawing by C.M. James based on measurements of an existing part.	03/04/16	
1	More detail of existing part added, and after dimensions were checked, the diameter of the large bore was changed from 33 to 34.	11/08/16	



TOP VIEW (1:1.25)

M12- 15 DEEP

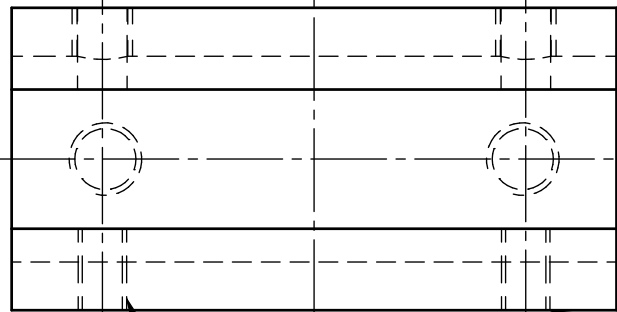
M12 HOLES ARE FOR CONNECTING THIS PART TO THE MODEL MOUNT (X2-MODEL-MOUNTING-SYSTEM-008)

A BOLT THROUGH THESE TOP M10 THREADED HOLES IS USED TO APPLY FRICTION TO THE SOLID STING (X2-MODEL-MOUNTING-SYSTEM-006)

M10 - THROUGH TOP

M10 - THROUGH TOP

A BOLT THROUGH THE TOP M8 CLEARANCE HOLE HERE THREADED INTO THE M8 BOTTOM THREADED HOLES CLAMPS THIS WHOLE PIECE TOGETHER.

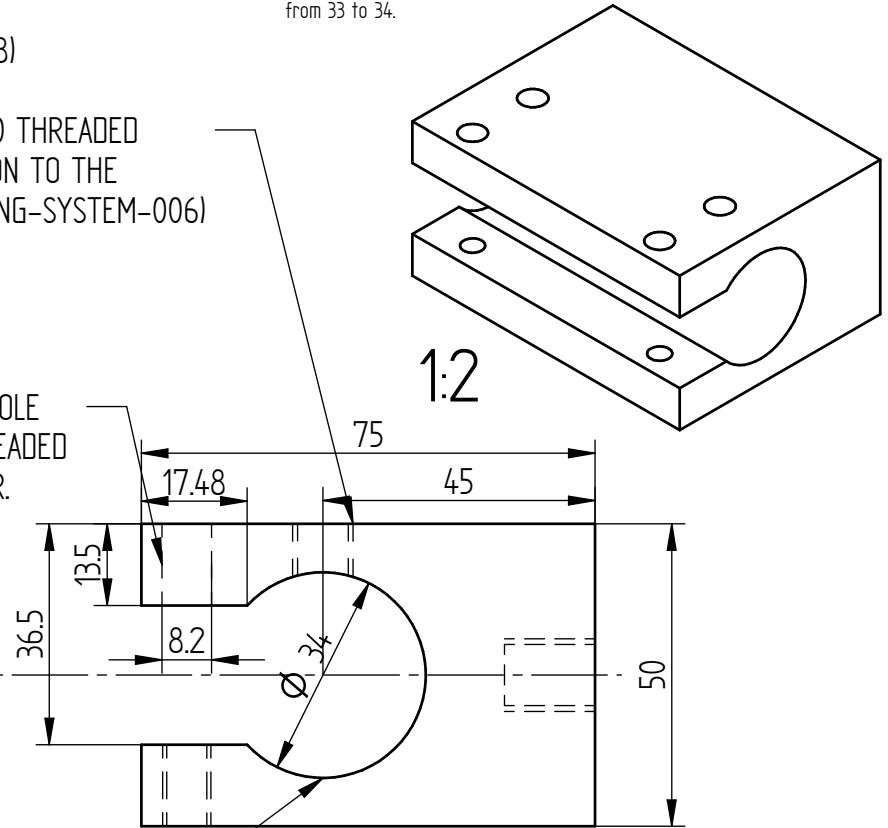


FRONT VIEW (1:1.25)

M8 - THROUGH BOTTOM

M8 - THROUGH BOTTOM

THE SOLID STING (X2-MODEL-MOUNTING-SYSTEM-006) MOUNTS THROUGH THIS CENTRE HOLE

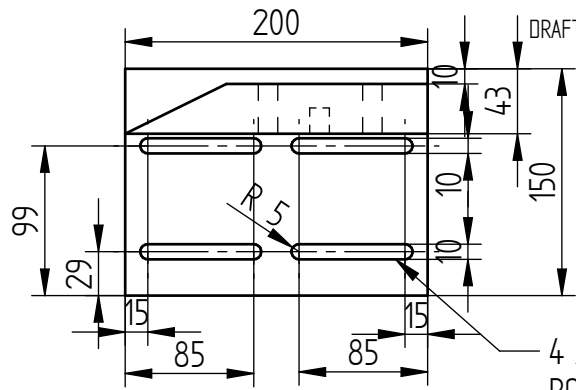


SIDE VIEW (1:1.25)

Notes:

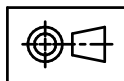
- This drawing has been made based on measurements of an existing component.
- Material: Existing component appears to be made from steel.
- Part is symmetrical about the Front View in both dimensions.

NAME	DATE	TITLE	
DRAWN C.M. James	11/08/16	Sting Clamp	
CHECKED		DOCUMENT NO. X2-MODEL-MOUNTING-SYSTEM-007	
ENG APPR		SIZE A4	PROJECT Chris James PhD model
MGR APPR		FILE NAME: x2-m-m-system-007-1-sting-clamp.dft	REV 1
UNLESS OTHERWISE SPECIFIED DIMENSIONS ARE IN MILLIMETERS		SCALE: AS SHOWN	WEIGHT:
ANGULAR TOLERANCE ±0.1°		SHEET 1 OF 1	
DIMENSIONAL TOLERANCE ±0.1mm			



TOP VIEW (1:5)

DRAFTING STANDARD: AS1100 - 1992  
DO NOT SCALE



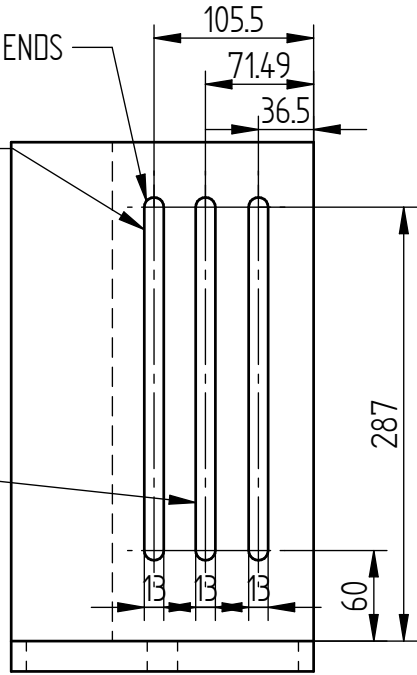
REVISION HISTORY			
REV	DESCRIPTION	DATE	APPROVED
0	New drawing by C.M. James based on measurements of an existing part.	03/04/16	

4 x 10 MM WIDE SLOTS WITH 5 MM RADIUS ROUNDED ENDS FOR CONNECTING THIS PART TO THE RAILS IN THE X2 DUMP TANK.

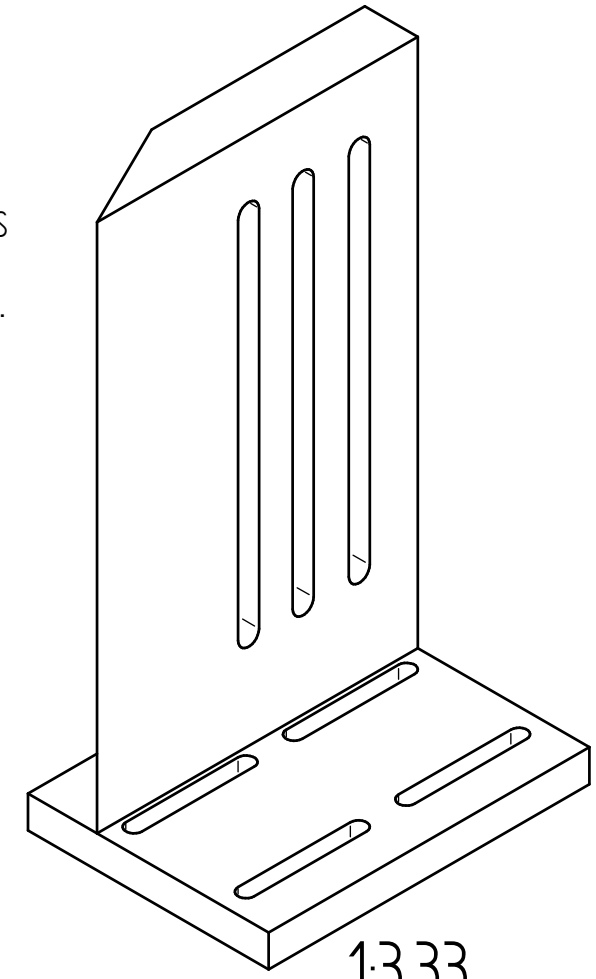
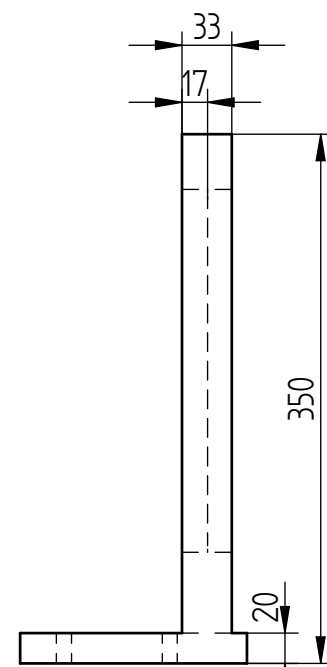
3 x 13 MM WIDE SLOTS WITH ROUNDED ENDS

FIRST AND THIRD SLOTS ARE HOLLOW AND ACT AS M12 CLEARANCE HOLES FOR MOUNTING THE STING CLAMP (X2-MODEL-MOUNTING-SYSTEM-007) TO THIS PART,

THE SECOND SLOT IS 17 MM DEEP AND IS USED FOR RUNNING CABLING FROM MODELS DOWN TO THE INSTRUMENT PANEL ON THE BOTTOM OF THE X2 DUMP TANK.



FRONT VIEW (1:5) SIDE VIEW (1:5)

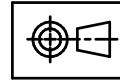


1:3.33

- Notes:
- This drawing has been made based on measurements of an existing component.
  - Material: Existing component appears to be made from steel.

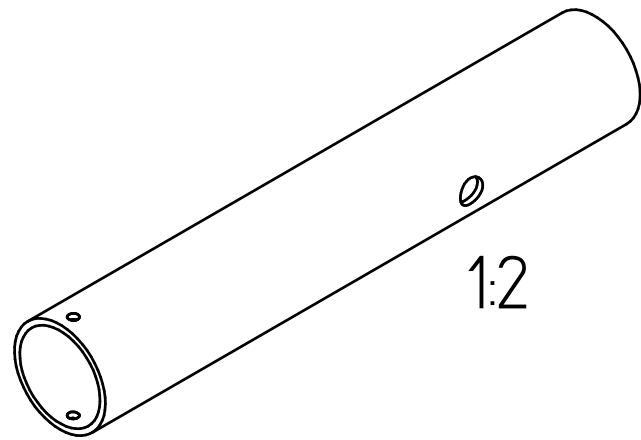
NAME	DATE		
DRAWN C.M. James	05/04/16	TITLE Model Mount	
CHECKED		DOCUMENT NO. X2-MODEL-MOUNTING-SYSTEM-008	
ENG APPR		SIZE A4 PROJECT Chris James PhD model REV 0	
MGR APPR		FILE NAME: x2-m-m-system-008-0-model-mount.dft	
UNLESS OTHERWISE SPECIFIED DIMENSIONS ARE IN MILLIMETERS ANGULAR TOLERANCE ±0.1° DIMENSIONAL TOLERANCE ±0.1mm		SCALE: AS SHOWN	WEIGHT: SHEET 1 OF 1

DRAFTING STANDARD: AS1100 - 1992  
DO NOT SCALE

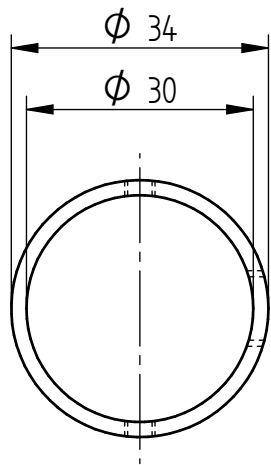


REVISION HISTORY

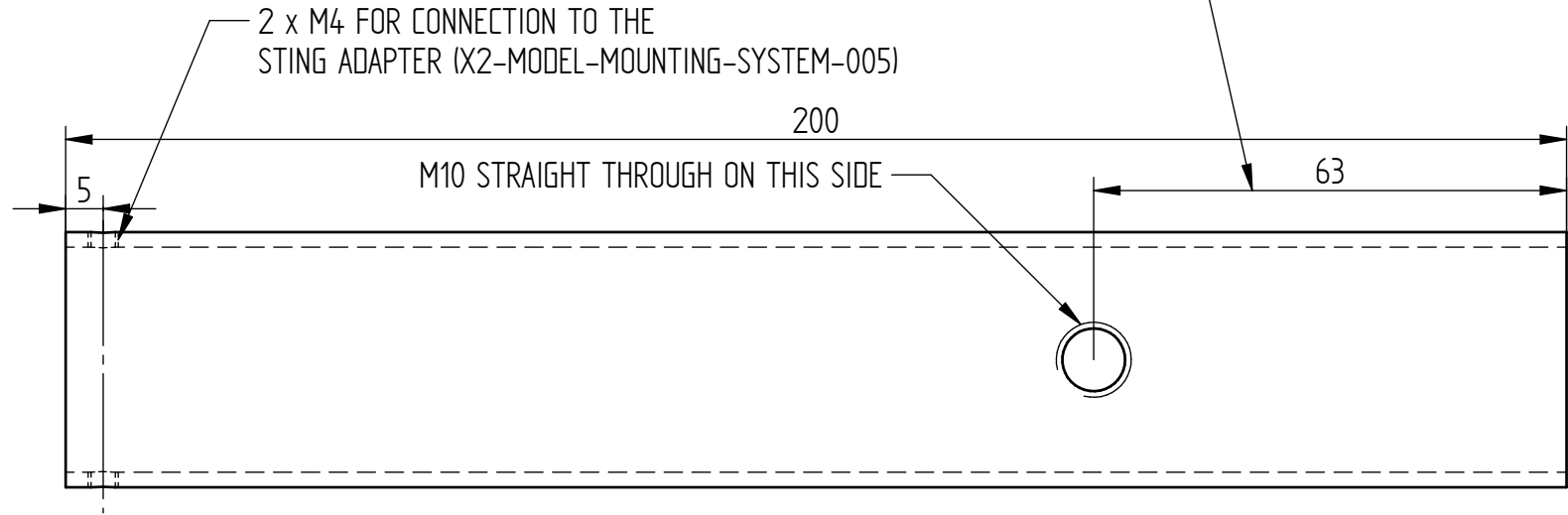
REV	DESCRIPTION	DATE	APPROVED
0	New drawing by C.M. James based on measurements of an existing part.	10/04/16	



THIS DIMENSION WAS NOT ABLE TO MEASURED ACCURATELY SO CANNOT BE GUARANTEED



SIDE VIEW (1:1)



FRONT VIEW (1:1)

Notes:

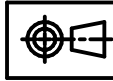
- This drawing has been made based on measurements of an existing component.
- Material: Existing component appears to be made from steel.
- This is the Hollow Sting for use with models with inbuilt sensors. A Solid Sting is shown on X2-MODEL-MOUNTING-SYSTEM-006.

NAME	DATE		
DRAWN C.M. James	10/04/16	TITLE Hollow Sting	
CHECKED		DOCUMENT NO. X2-MODEL-MOUNTING-SYSTEM-009	
ENG APPR		SIZE A4	PROJECT Chris James PhD model
MGR APPR		FILE NAME: x2-m-m-system-009-0-hollow-sting.dft	
UNLESS OTHERWISE SPECIFIED DIMENSIONS ARE IN MILLIMETERS		SCALE: AS SHOWN	WEIGHT:
ANGULAR TOLERANCE ±0.1°		SHEET 1 OF 1	
DIMENSIONAL TOLERANCE ±0.1mm			

## Appendix B

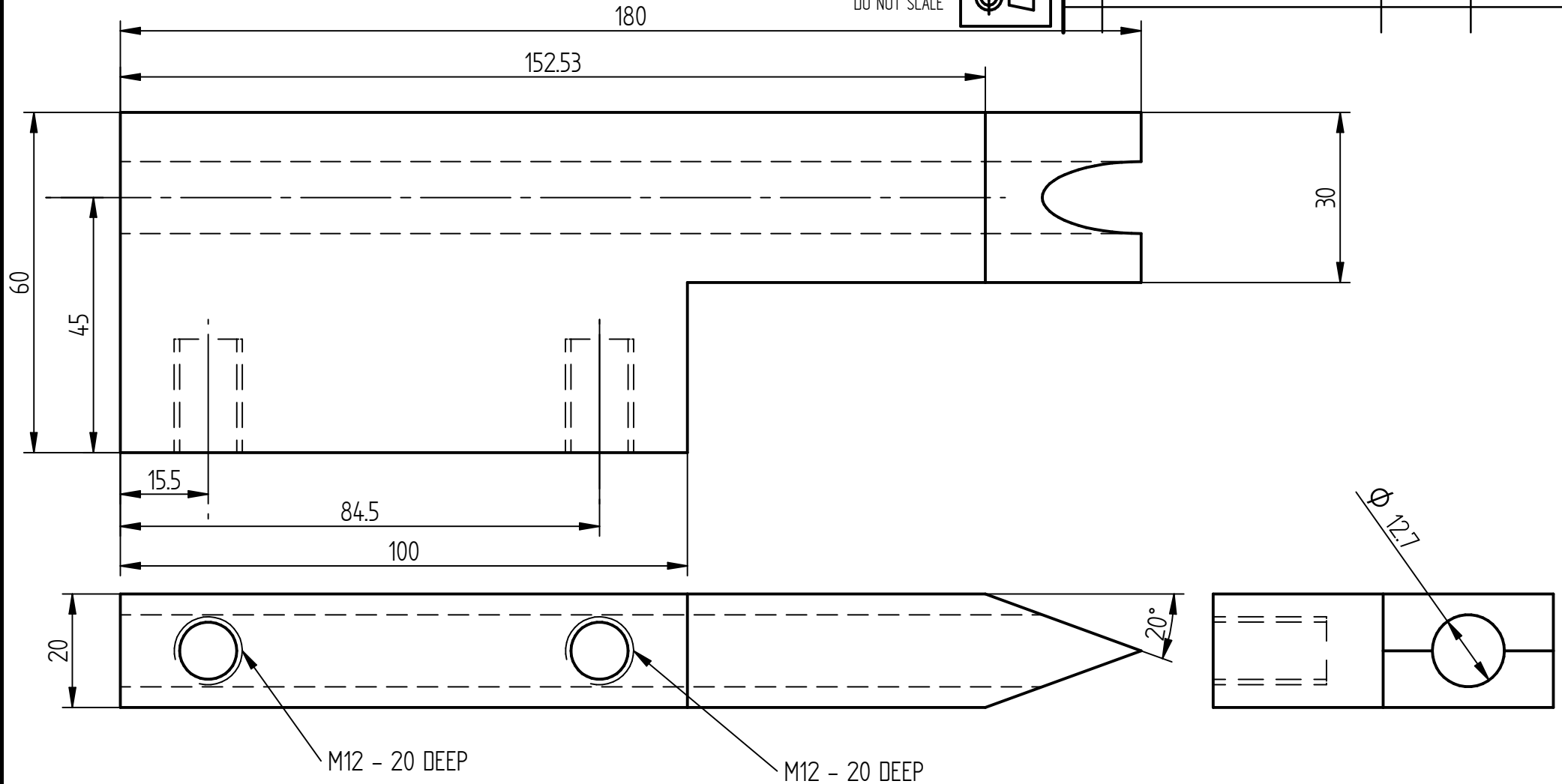
# Original Standalone Pitot Mount Drawing

DRAFTING STANDARD: AS1100 - 1992  
DO NOT SCALE



REVISION HISTORY

REV	DESCRIPTION	DATE	APPROVED



Notes:

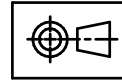
- made from 20 mm thick steel. Does not need to be stainless.
- lead dimensions 60 x 180
- 20 degree chamfer on the front edge, length does not need to be exactly what it is.
- Don't cut the holes until I can check on the model currently in the tunnel.
- Contact details: ph(internal) 54864, ph (mobile) 0423 229 601

NAME	DATE	TITLE	
DRAWN	uqcjame4	Standalone Mount	
CHECKED			
ENG APPR			
MGR APPR			
UNLESS OTHERWISE SPECIFIED DIMENSIONS ARE IN MILLIMETERS ANGULAR TOLERANCE ±0.1° DIMENSIONAL TOLERANCE ±0.1mm		SIZE A4	PROJECT Chris James PhD
		FILE NAME: standalone_mount.dft	REV 0
		SCALE: AS SHOWN	WEIGHT: SHEET 1 OF 1

## Appendix C

# Standalone Three Pitot Mount Drawings

DRAFTING STANDARD: AS1100 - 1992  
DO NOT SCALE



REVISION HISTORY

REV	DESCRIPTION	DATE	APPROVED
0	New drawing by C.M. James	04/09/15	

Item Number	Document Number	Revision number	Title	Material	Author	Quantity	Notes
1	X2-PMM-001	0	Standalone 3 Pitot Mount	Steel	C.M. James	1	To be made
2	X2-PMM-002	0	Standalone 3 Pitot Mount Backplate	Steel	C.M. James	1	To be made
3	X2-PIT-004	0	Pitot Tube Body	Stainless steel bar	D. Gildfind	3	To be supplied by Xlabs
4	X2-PIT-003-0	1	15 Deg Pitot Cone, 8 Hole	Stainless steel bar	D. Gildfind	3	To be supplied by Xlabs
5		N/A	M3 x 10 mm cap screw	Steel	C.M. James	4	
6		N/A	M6 x 5 mm grub screw	Steel	C.M. James	9	

Notes:

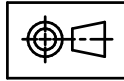
- Contact details: ph (internal) 54864, ph (mobile) 0413 642 000

	NAME	DATE		
DRAWN	C.M. James	04/09/15		
CHECKED				
ENG APPR			TITLE	
MGR APPR			Assembly Drawing (X2-PMM-000)	
UNLESS OTHERWISE SPECIFIED DIMENSIONS ARE IN MILLIMETERS ANGULAR TOLERANCE ±0.1° DIMENSIONAL TOLERANCE ±0.1mm			SIZE A4	PROJECT Chris James Pitot Mount Model
			FILE NAME: new_pcb_mount_model_assembly.dft	REV 0
			SCALE: AS SHOWN	WEIGHT: SHEET 1 OF 2

SOLID EDGE ACADEMIC COPY

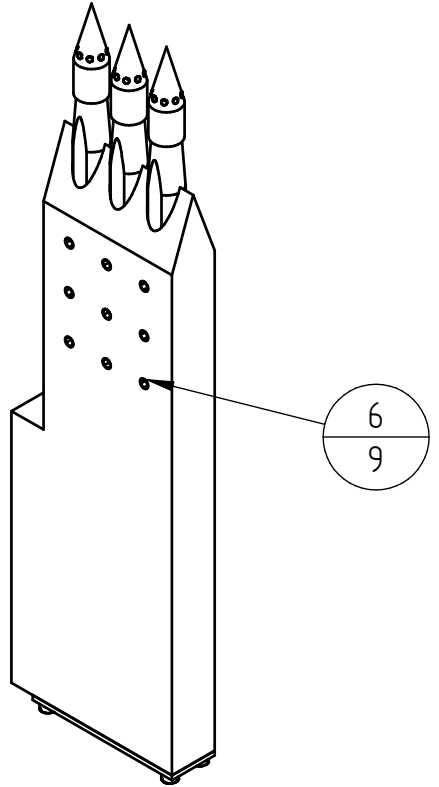
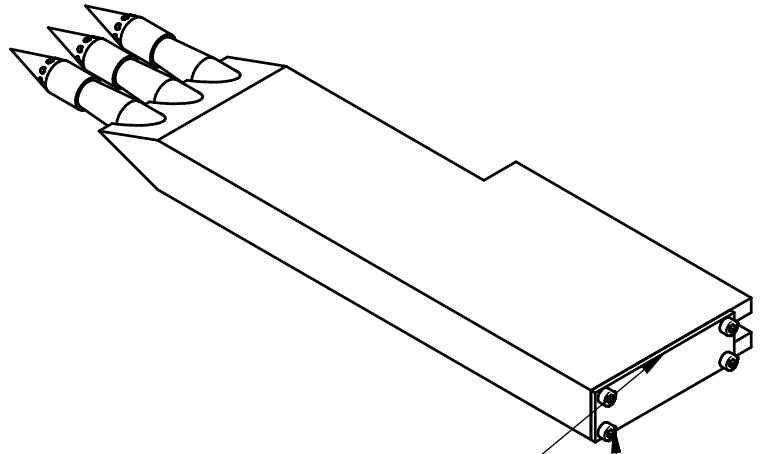
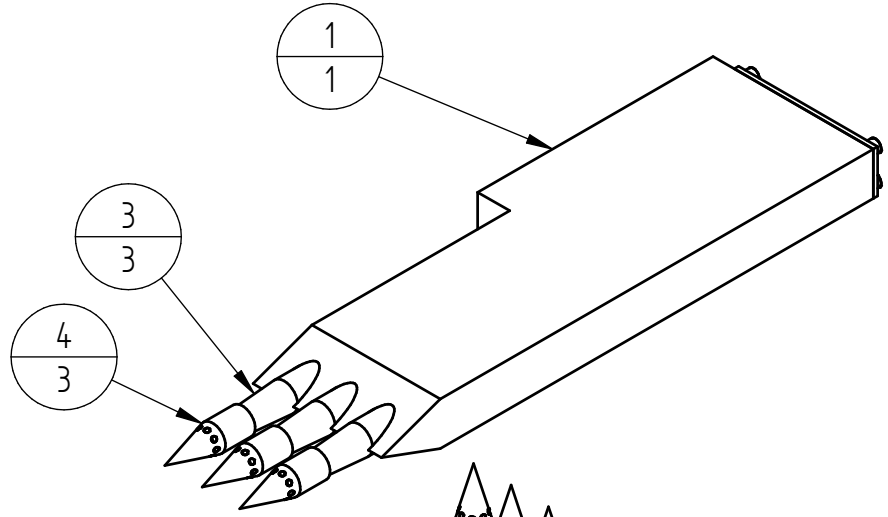


DRAFTING STANDARD: AS1100 - 1992  
DO NOT SCALE



REVISION HISTORY

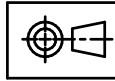
REV	DESCRIPTION	DATE	APPROVED
0	New drawing by C.M. James	04/09/15	



SOLID EDGE ACADEMIC COPY

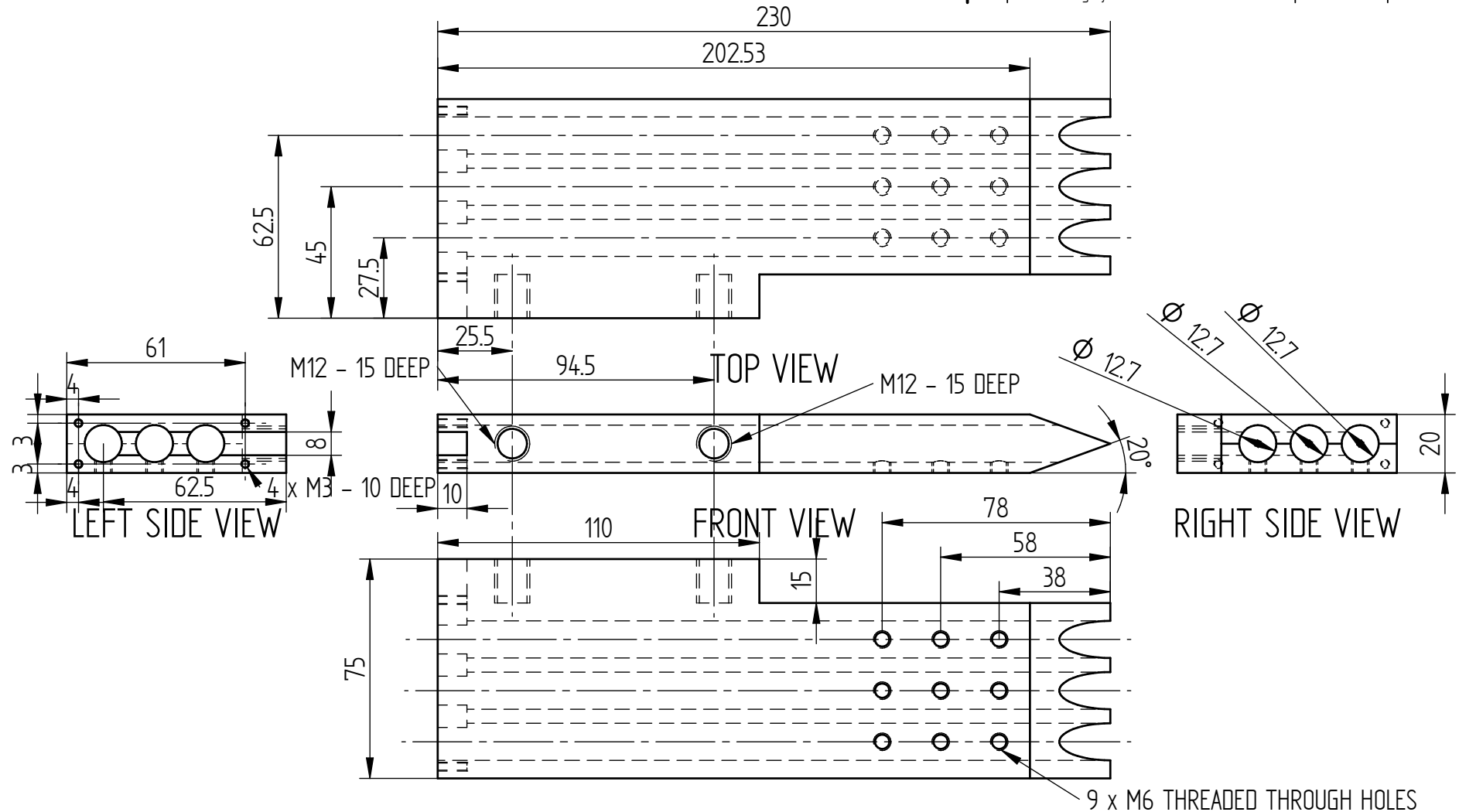
	NAME	DATE	TITLE	
DRAWN	C.M. James	04/09/15	Assembly Drawing (X2-PMM-000)	
CHECKED				
ENG APPR				
MGR APPR				
UNLESS OTHERWISE SPECIFIED DIMENSIONS ARE IN MILLIMETERS ANGULAR TOLERANCE ±0.1° DIMENSIONAL TOLERANCE ±0.1mm			SIZE A4	PROJECT Chris James Pitot Mount Model
			FILE NAME: new_pcb_mount_model_assembly.dft	REV 0
			SCALE: AS SHOWN	WEIGHT: SHEET 2 OF 2

DRAFTING STANDARD: AS1100 - 1992  
DO NOT SCALE



REVISION HISTORY

REV	DESCRIPTION	DATE	APPROVED
0	New drawing by C.M. James	04/09/15	



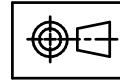
Notes:

- To be made from 20 mm thick steel. Does not need to be stainless.
- Leading dimensions 75 mm x 230 mm x 20 mm.
- 20 degree symmetrical chamfer on the front edge. Flat length (202.53) does not need to be exact to the drawing.
- 10 mm slot on back is NOT a through slot. Stops at left edge of half-most through hole.
- Contact details: ph (internal) 54864, ph (mobile) 0413 642 000

BOTTOM VIEW

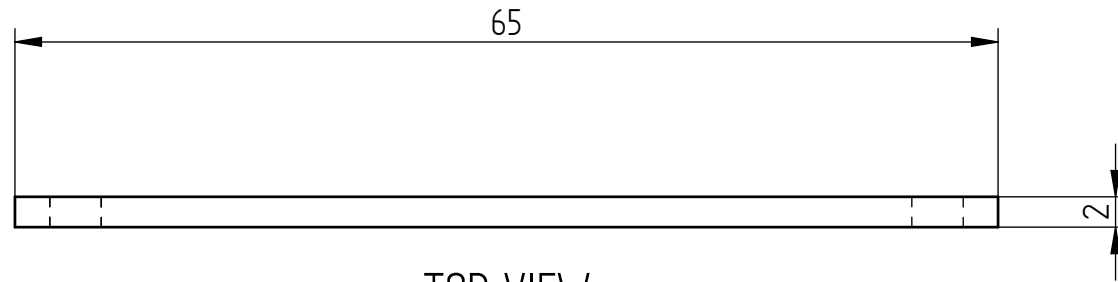
	NAME	DATE		
DRAWN	C.M. James	04/09/15		
CHECKED				
ENG APPR			TITLE Standalone 3 Pitot Mount (X2-PMM-001)	
MGR APPR				
UNLESS OTHERWISE SPECIFIED DIMENSIONS ARE IN MILLIMETERS ANGULAR TOLERANCE ±0.1° DIMENSIONAL TOLERANCE ±0.1mm			SIZE A4	PROJECT Chris James Pitot Mount Model
			FILE NAME: pcb_mount_model.dft	REV 0
			SCALE: AS SHOWN	WEIGHT: SHEET 1 OF 1

DRAFTING STANDARD: AS1100 - 1992  
DO NOT SCALE

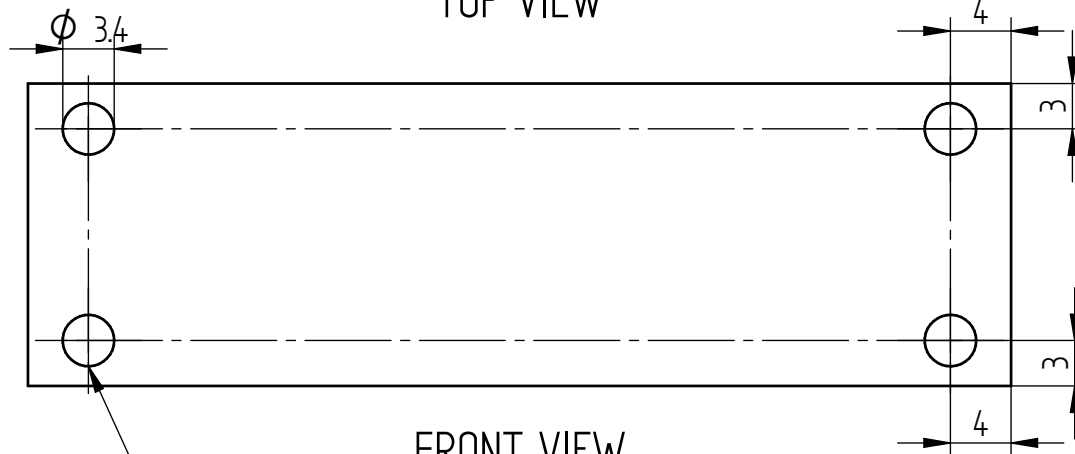


REVISION HISTORY

REV	DESCRIPTION	DATE	APPROVED
0	New drawing by C.M. James	04/09/15	

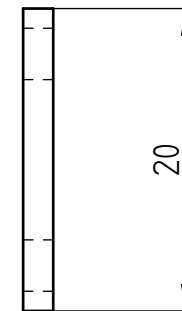


TOP VIEW



FRONT VIEW

4 x M3 medium clearance holes



SIDE VIEW

Notes:

- To be made from 2 mm thick steel. Does not need to be stainless.
- Leading dimensions 20 mm x 65 mm x 0 mm.
- Contact details: ph (internal) 54864, ph (mobile) 0413 642 000

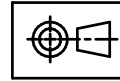
SOLID EDGE ACADEMIC COPY

	NAME	DATE		
DRAWN	C.M. James	07/09/15		
CHECKED				
ENG APPR			TITLE	
MGR APPR			Standalone 3 Pitot Mount Backplate (X2-PMM-002)	
UNLESS OTHERWISE SPECIFIED DIMENSIONS ARE IN MILLIMETERS ANGULAR TOLERANCE $\pm 0.1^\circ$ DIMENSIONAL TOLERANCE $\pm 0.1\text{mm}$			SIZE A4	PROJECT Chris James Pitot Mount Model
			FILE NAME: pcb_mount_backplate.dft	REV 0
			SCALE: AS SHOWN	WEIGHT: SHEET 1 OF 1

## Appendix D

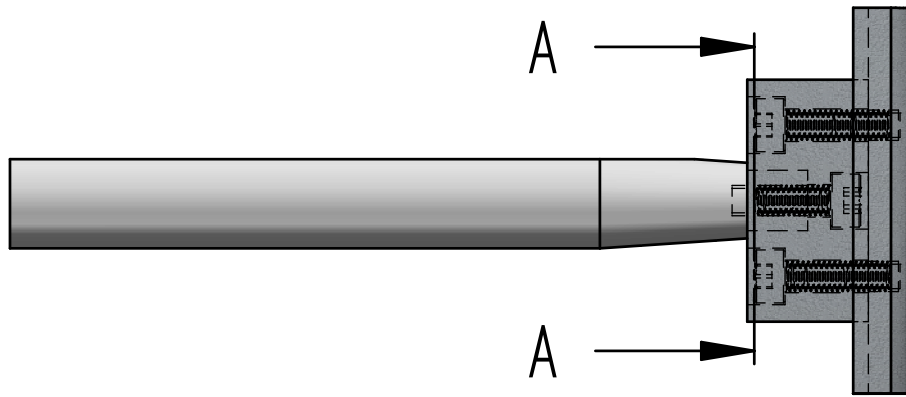
# Mini-cylinder Drawings

DRAFTING STANDARD: AS1100 - 1992  
DO NOT SCALE

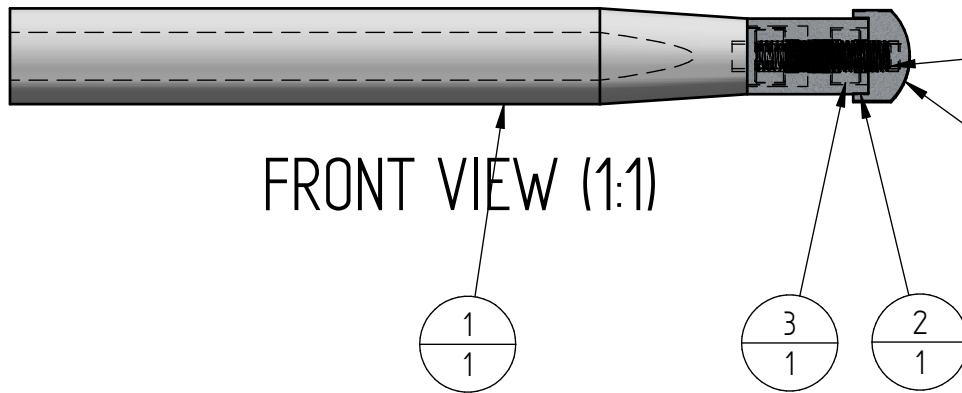


REVISION HISTORY

REV	DESCRIPTION	DATE	APPROVED
0	New drawing	28/03/16	n/a



TOP VIEW (1:1)

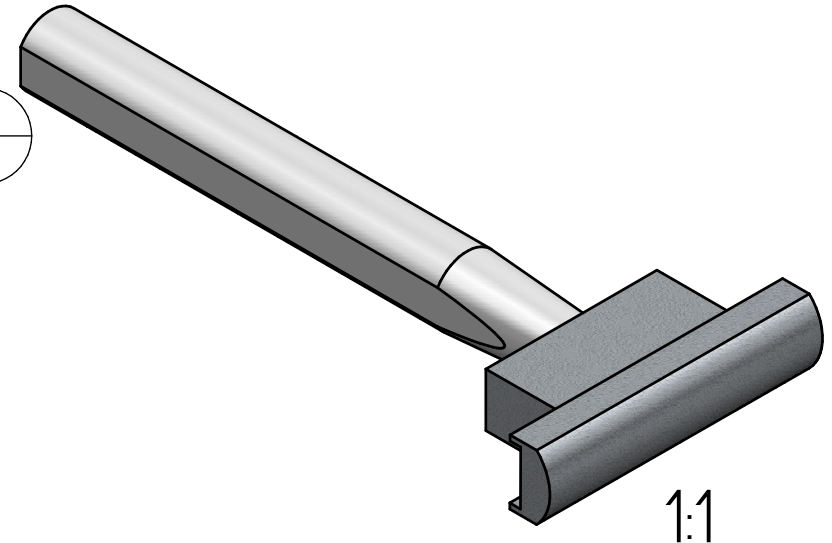


FRONT VIEW (1:1)

An Internal M4 x 10 mm cap screw is used to mount the Pitot Rake Mount Bracket (X2-PRM-002) to the Solid Pitot Rake Mount (X2-PRM-001).

2 x M4 x 14 mm cap screws are used to mount the Pitot Rake Mount Bracket (X2-PRM-002) to the 8.5 mm radius Eichmann Cylinder (X2-PRM-004).

SECTION A-A (1:1)



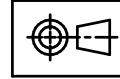
1:1

Notes:

- This is an example assembly showing X2-PRM-001 and X2-PRM-002 assembled with X2-PRM-004.
- The related Parts List can be found on Sheet 2.
- Contact details: ph(internal) 54864, ph (mobile) 0413 642 000

	NAME	DATE	TITLE	
DRAWN	C.M. James	28/03/16	Example Assembly (X2-PRM-000)	
CHECKED				
ENG APPR				
MGR APPR				
UNLESS OTHERWISE SPECIFIED DIMENSIONS ARE IN MILLIMETERS ANGULAR TOLERANCE $\pm 0.1^\circ$ DIMENSIONAL TOLERANCE $\pm 0.1\text{mm}$			SIZE A4	REV 0
			PROJECT Chris James Pitot Rake Models	
			FILE NAME: x2-prm-000-0-example-assembly.dft	
			SCALE: AS SHOWN	WEIGHT:

DRAFTING STANDARD: AS1100 - 1992  
DO NOT SCALE



REVISION HISTORY

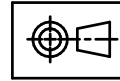
REV	DESCRIPTION	DATE	APPROVED
0	New drawing	28/03/16	n/a

Item Number	Document Number	Revision number	Title	Material	Author	Quantity	File Name (no extension)
1	X2-PRM-001	0	Solid Pitot Rake Mount	Stainless steel bar	C.M. James	1	solid_pitot_rake_mountl
2	X2-PRM-002	0	Pitot Rake Model Bracket	Steel	C.M. James	1	pitot_rake_model_bracket
3	N/A	N/A	M4 x 10 mm Cap Screw	Steel	C.M. James	1	M4 x 10 mm
4	X2-PRM-004	0	8.5 mm Radius Eichmann Cylinder	Stainless steel	C.M. James	1	8_5_radius_eichmann_cylinder_new
5	N/A	N/A	M4 x 14 mm Cap Screw	Steel	C.M. James	2	M4 x 14 mm

	NAME	DATE	TITLE	
DRAWN	C.M. James	28/03/16	Example Assembly (X2-PRM-000)	
CHECKED				
ENG APPR				
MGR APPR				
UNLESS OTHERWISE SPECIFIED DIMENSIONS ARE IN MILLIMETERS ANGULAR TOLERANCE ±0.1° DIMENSIONAL TOLERANCE ±0.1mm			SIZE A4	PROJECT Chris James Pitot Rake Models
			FILE NAME: x2-prm-000-0-example-assembly.dft	
			SCALE: AS SHOWN	WEIGHT: SHEET 2 OF 2

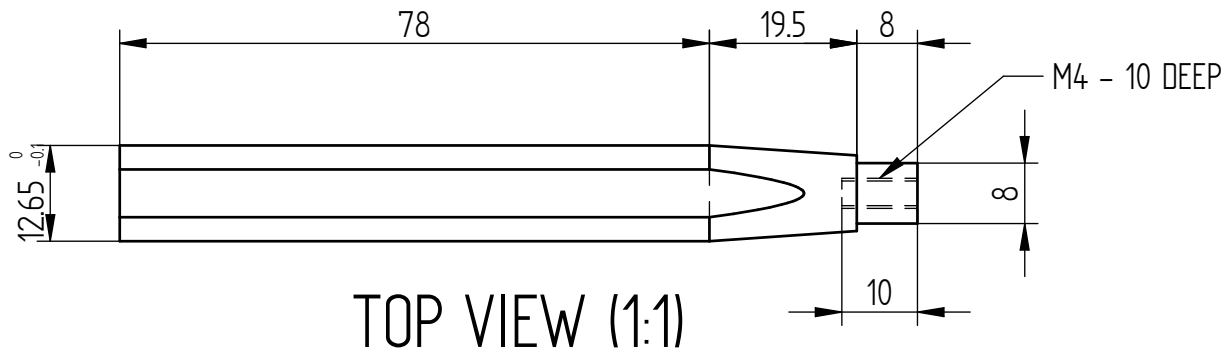
SOLID EDGE ACADEMIC COPY

DRAFTING STANDARD: AS1100 - 1992  
DO NOT SCALE

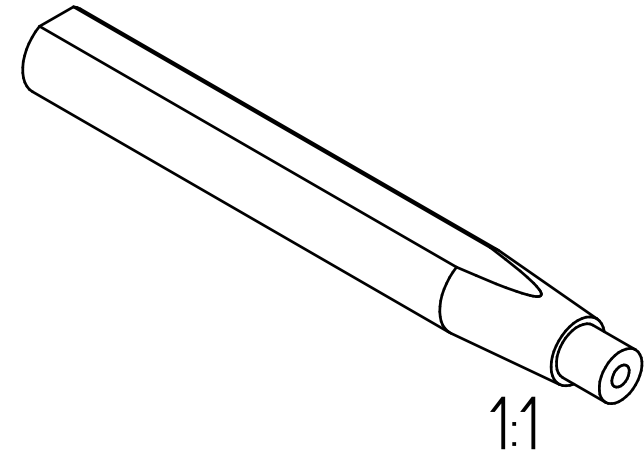


REVISION HISTORY

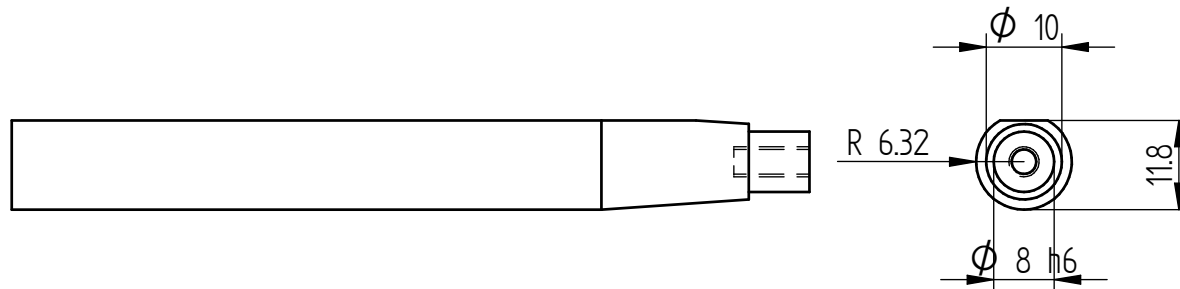
REV	DESCRIPTION	DATE	APPROVED
0	New drawing	28/03/16	n/a



TOP VIEW (1:1)



1:1



FRONT VIEW (1:1)

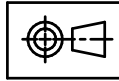
END VIEW (1:1)

Notes:

- Material: Stainless steel. Probably half inch bar.
- If necessary, tolerance down bar bore. Must fit inside X2 Pitot Rake. Check fit after completion.
- Dimension on flat does not need to be exact, it is just a flat section for grub screws.
- 8mm H7/h6 transition fit between this part and X2-PRM-002.
- Contact details: ph(internal) 54864, ph (mobile) 0413 642 000

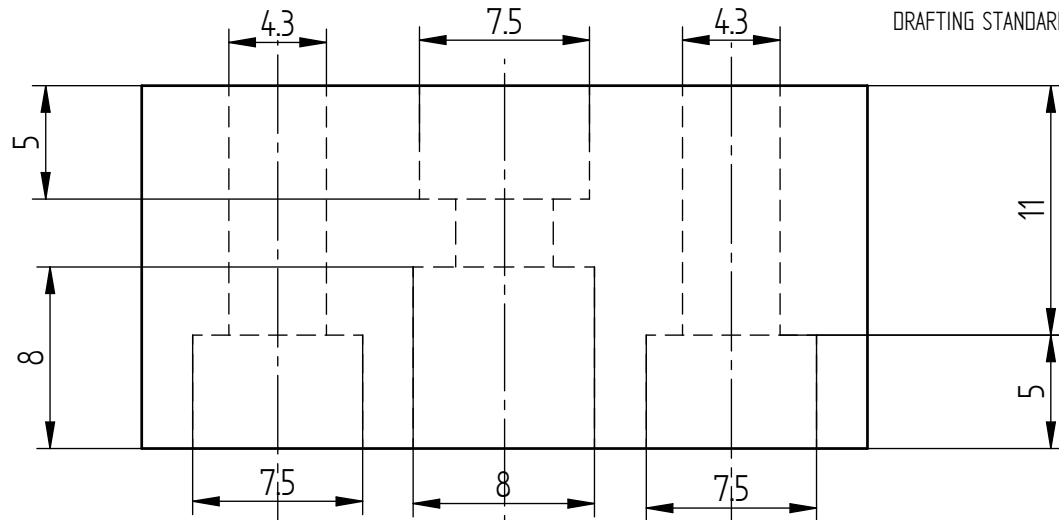
	NAME	DATE	TITLE	
DRAWN	C.M. James	28/03/16	Solid Pitot Rake Mount (X2-PRM-001)	
CHECKED				
ENG APPR				
MGR APPR				
UNLESS OTHERWISE SPECIFIED DIMENSIONS ARE IN MILLIMETERS ANGULAR TOLERANCE $\pm 0.1^\circ$ DIMENSIONAL TOLERANCE $\pm 0.1\text{mm}$			SIZE A4	PROJECT Chris James Pitot Rake Models FILE NAME: x2-prm-001-0-solid-pitot-rake-mount.dft SCALE: AS SHOWN
			REV 0	WEIGHT: SHEET 1 OF 1

DRAFTING STANDARD: AS1100 - 1992  
DO NOT SCALE

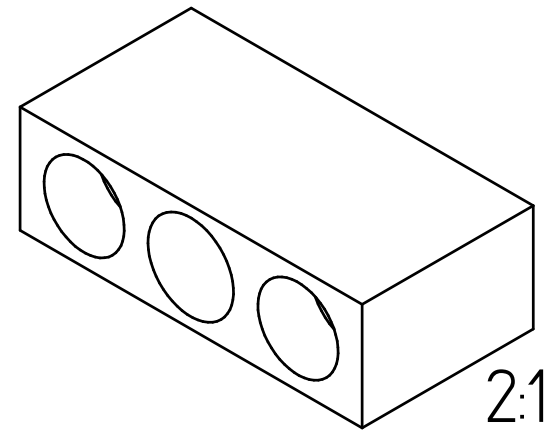


REVISION HISTORY

REV	DESCRIPTION	DATE	APPROVED
0	New drawing	28/03/16	n/a

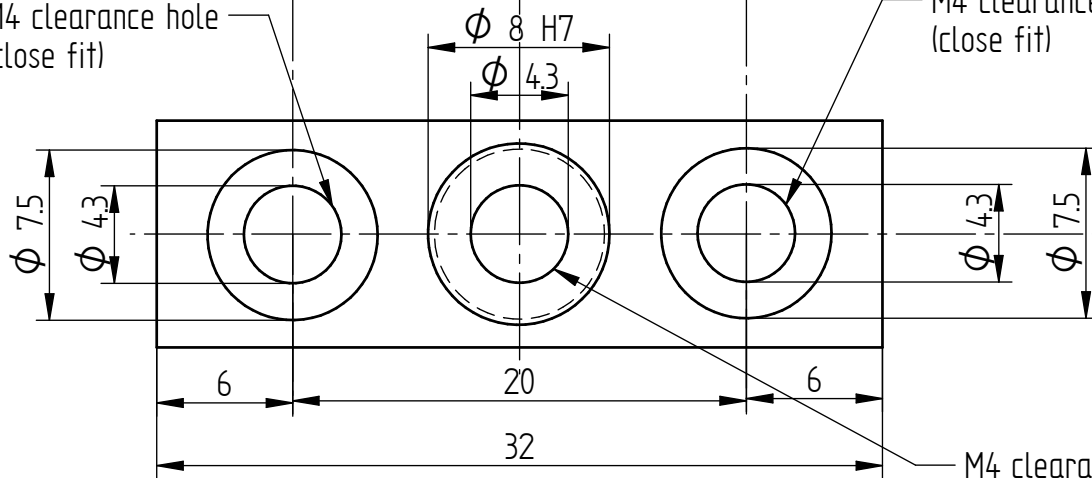


TOP VIEW (3:1)



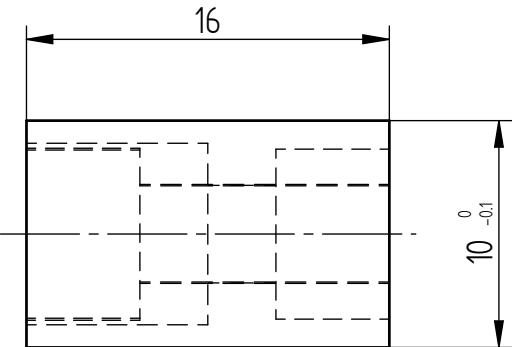
M4 clearance hole  
(close fit)

M4 clearance hole  
(close fit)



FRONT VIEW (3:1)

M4 clearance hole  
(close fit)



END VIEW (3:1)

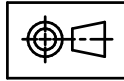
Notes:

- Material: Mild steel.
- Tolerance down 10 mm height for fit between this part and the models.
- 20 mm distance between M4 clearance holes is important for mounting this part to the models (X2-PRM-003, X2-PRM-004, X2-PRM-005).
- 8mm H7/h6 transition fit between this part and X2-PRM-001.
- Contact details: ph(internal) 54864, ph (mobile) 0413 642 000

	NAME	DATE		
DRAWN	C.M. James	28/03/16		
CHECKED				
ENG APPR			TITLE Pitot Rake Mount Bracket (X2-PRM-002)	
MGR APPR				
UNLESS OTHERWISE SPECIFIED DIMENSIONS ARE IN MILLIMETERS ANGULAR TOLERANCE $\pm 0.1^\circ$ DIMENSIONAL TOLERANCE $\pm 0.1\text{mm}$			SIZE A4	PROJECT Chris James Pitot Rake Models
			FILE NAME: x2-prm-002-0-pitot-rake-mount-bracket.dft	REV 0
			SCALE: AS SHOWN	WEIGHT: SHEET 1 OF 1

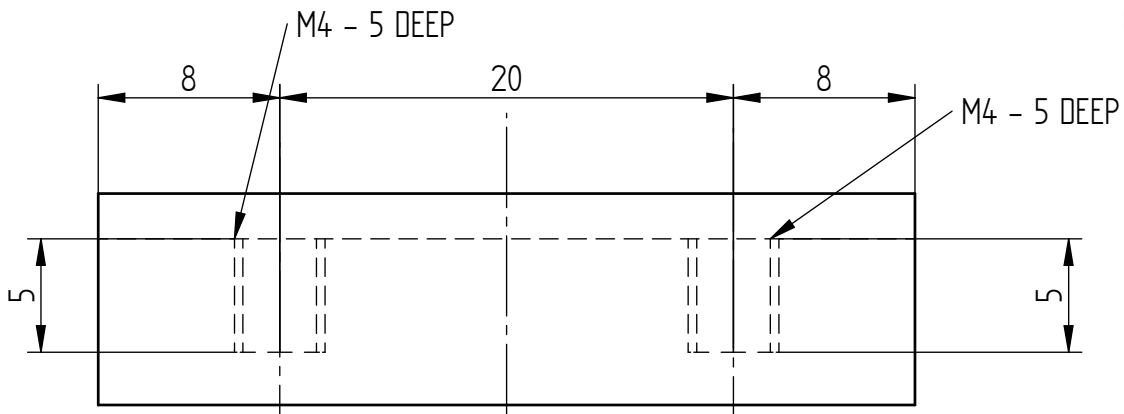


DRAFTING STANDARD: AS1100 - 1992  
DO NOT SCALE

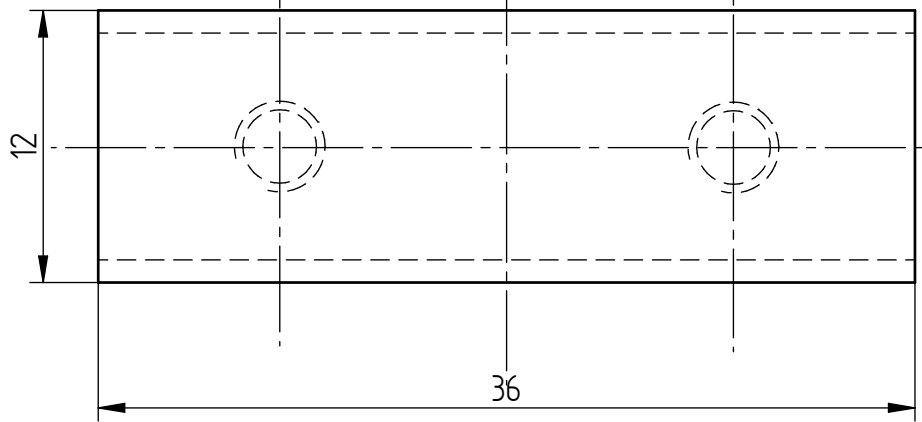


REVISION HISTORY

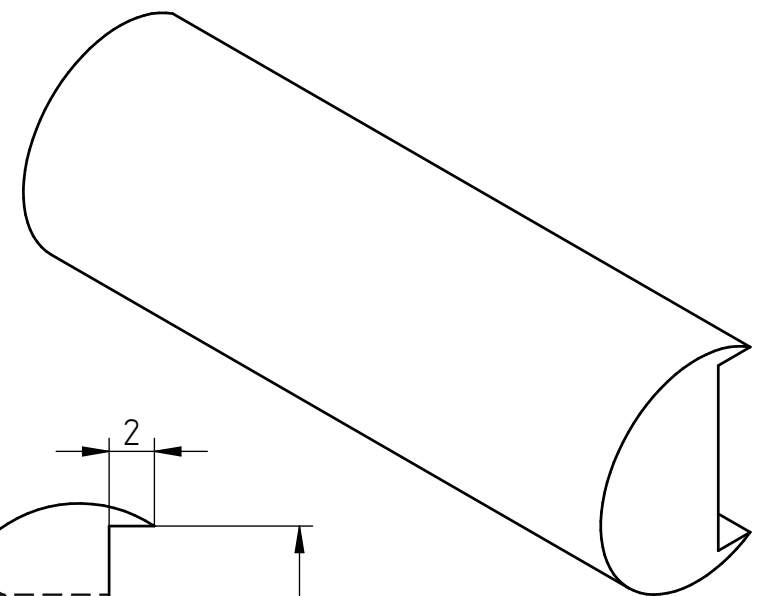
REV	DESCRIPTION	DATE	APPROVED
0	New drawing	28/03/16	n/a



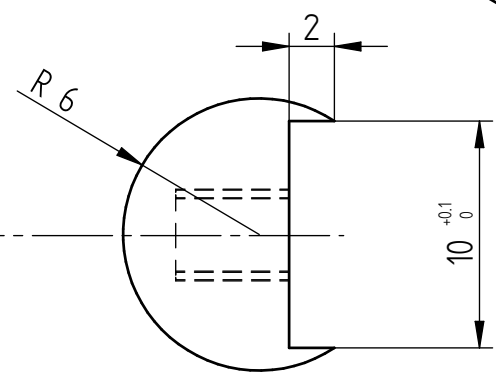
TOP VIEW (3:1)



FRONT VIEW (3:1)



3:1



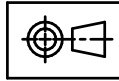
END VIEW (3:1)

Notes:

- Material: Mild steel. Was designed so it can be built from 6 mm radius bar.
- Tolerance up 10 mm cut out on back plate for fitting with mounting bracket.
- 20 mm distance between the M4 threaded holes is important for mounting this part to the the mounting bracket (X2-PRM-002).
- Contact details: ph (internal) 54864, ph (mobile) 0413 642 000

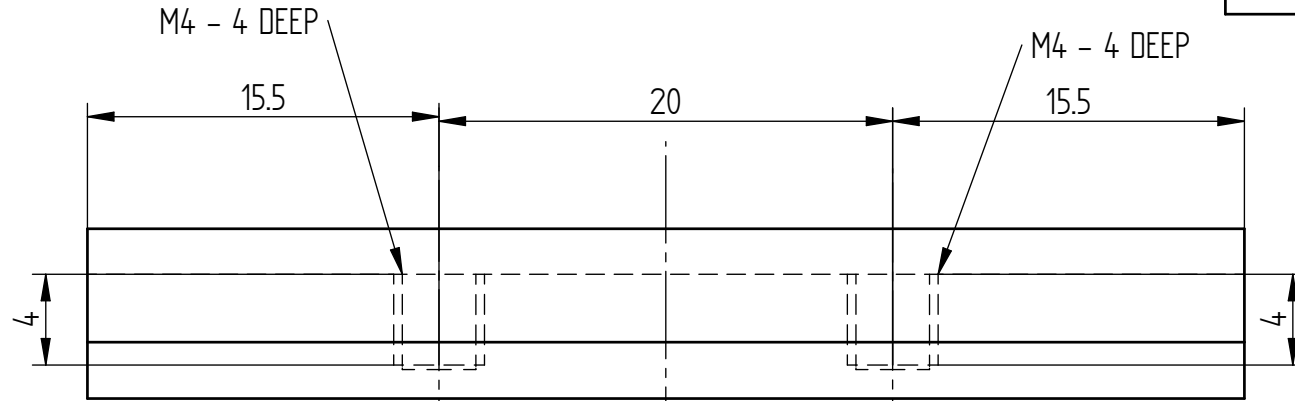
	NAME	DATE			
DRAWN	C.M. James	28/03/16			
CHECKED					
ENG APPR			TITLE		
MGR APPR			6mm Radius Cylinder (X2-PRM-003)		
UNLESS OTHERWISE SPECIFIED DIMENSIONS ARE IN MILLIMETERS ANGULAR TOLERANCE $\pm 0.1^\circ$ DIMENSIONAL TOLERANCE $\pm 0.1\text{mm}$			SIZE	PROJECT	REV
			A4	Chris James Pitot Rake Models	0
			FILE NAME: x2-prm-003-0-6-mm-radius-cylinder.dft		
			SCALE: AS SHOWN	WEIGHT:	SHEET 1 OF 1

DRAFTING STANDARD: AS1100 - 1992  
DO NOT SCALE

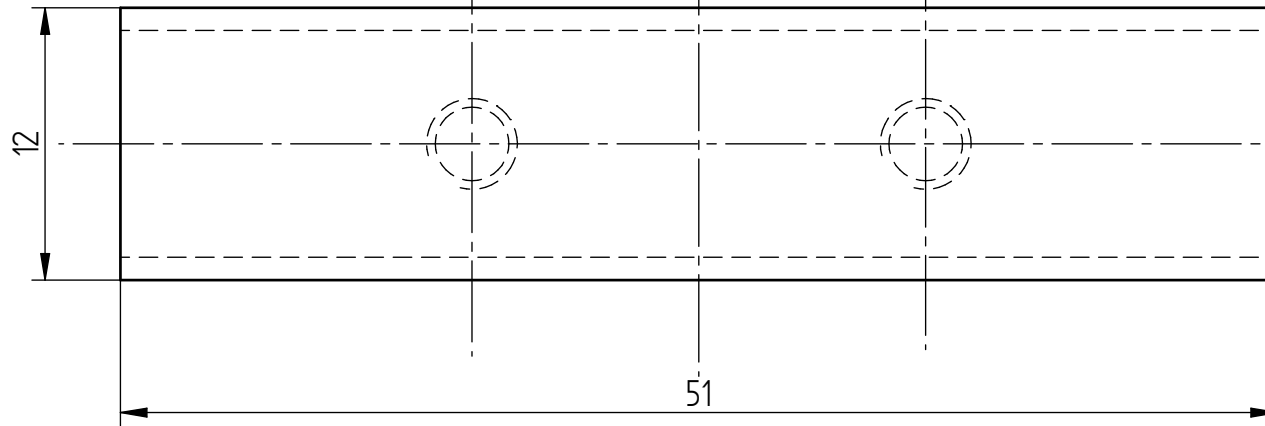


REVISION HISTORY

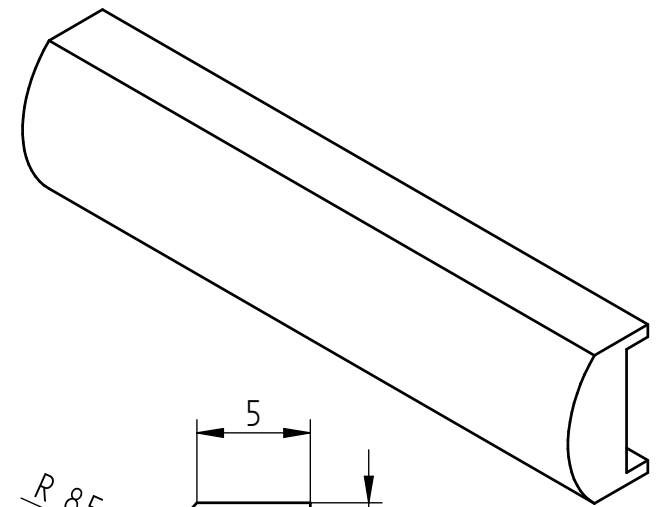
REV	DESCRIPTION	DATE	APPROVED
0	New drawing	28/03/16	n/a



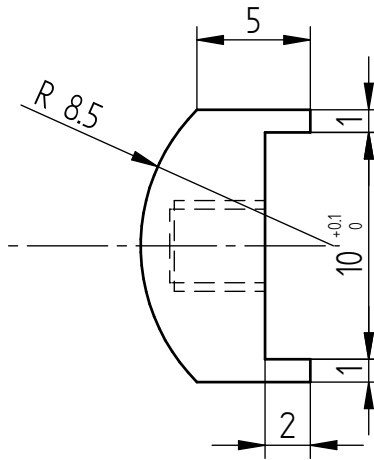
TOP VIEW (3:1)



FRONT VIEW (3:1)



2:1



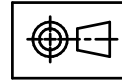
END VIEW (3:1)

Notes:

- Material: Mild steel.
- This is to be made if 16 mm steel bar is NOT available.
- Tolerance up 10 mm cut out on back plate for fitting with mounting bracket.
- 20 mm distance between the M4 threaded holes is important for mounting this part to the the mounting bracket (X2-PRM-002).
- Contact details: ph (internal) 54864, ph (mobile) 0413 642 000

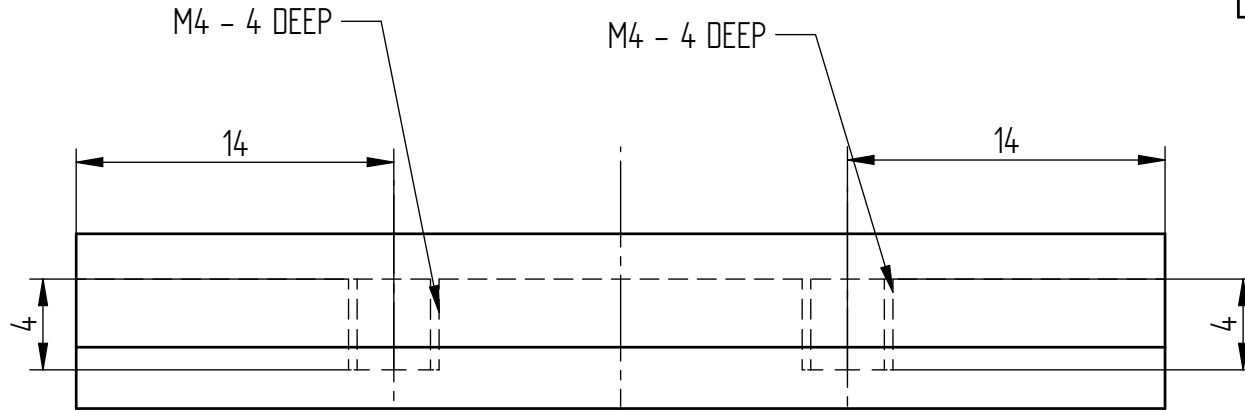
	NAME	DATE		
DRAWN	C.M. James	28/03/16		
CHECKED				
ENG APPR			TITLE	
MGR APPR			8.5 mm Radius Partial Cylinder (X2-PRM-004)	
UNLESS OTHERWISE SPECIFIED DIMENSIONS ARE IN MILLIMETERS ANGULAR TOLERANCE $\pm 0.1^\circ$ DIMENSIONAL TOLERANCE $\pm 0.1\text{mm}$			SIZE	PROJECT
			A4	Chris James Pitot Rake Models
			REV	0
			FILE NAME: X2-prm-004-0-8-5-mm-radius-cylinder.dft	
			SCALE: AS SHOWN	WEIGHT: SHEET 1 OF 1

DRAFTING STANDARD: AS1100 - 1992  
DO NOT SCALE

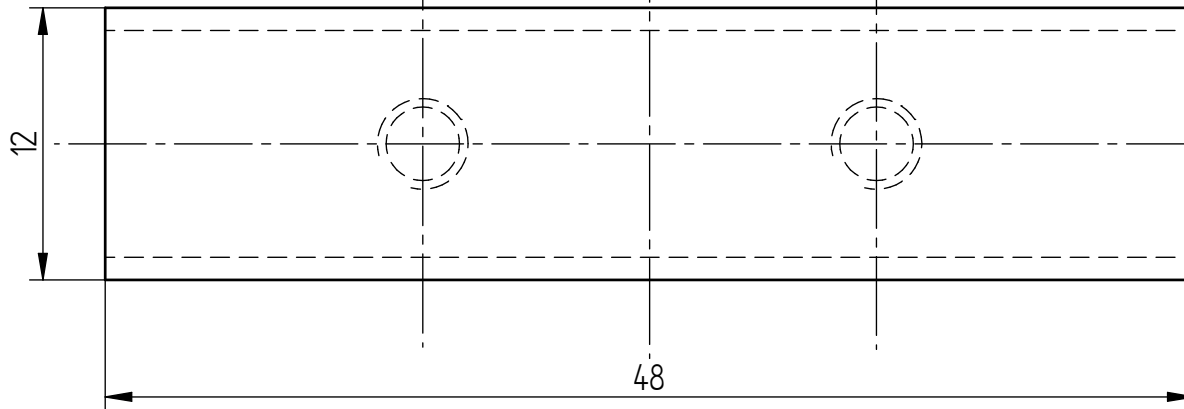


REVISION HISTORY

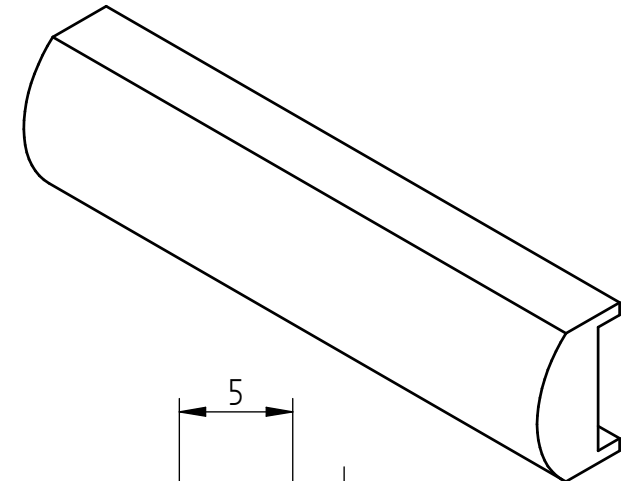
REV	DESCRIPTION	DATE	APPROVED
0	New drawing	28/03/16	n/a



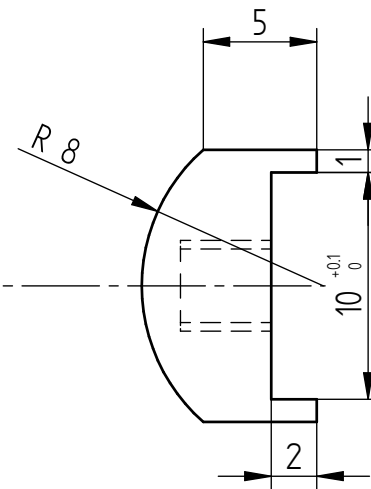
TOP VIEW (3:1)



FRONT VIEW (3:1)



2:1



END VIEW (3:1)

Notes:

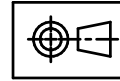
- Material: Mild steel. Cut from 16 mm steel bar if possible.
- This is to be built if 16 mm steel bar IS available.
- 20 mm distance between the M4 threaded holes is important for mounting this part to the the mounting bracket (X2-PRM-002).
- Tolerance up 10 mm cut out on back plate for fitting with mounting bracket.
- Contact details: ph (internal) 54864, ph (mobile) 0413 642 000

	NAME	DATE		
DRAWN	C.M. James	28/03/16		
CHECKED				
ENG APPR			TITLE	
MGR APPR			8 mm Radius Partial Cylinder (X2-PRM-005)	
UNLESS OTHERWISE SPECIFIED DIMENSIONS ARE IN MILLIMETERS ANGULAR TOLERANCE $\pm 0.1^\circ$ DIMENSIONAL TOLERANCE $\pm 0.1\text{mm}$			SIZE	PROJECT
			A4	Chris James Pitot Rake Models
			REV	0
			FILE NAME: x2-prm-005-0-8-mm-radius-cylinder.dft	
			SCALE: AS SHOWN	WEIGHT: SHEET 1 OF 1

## Appendix E

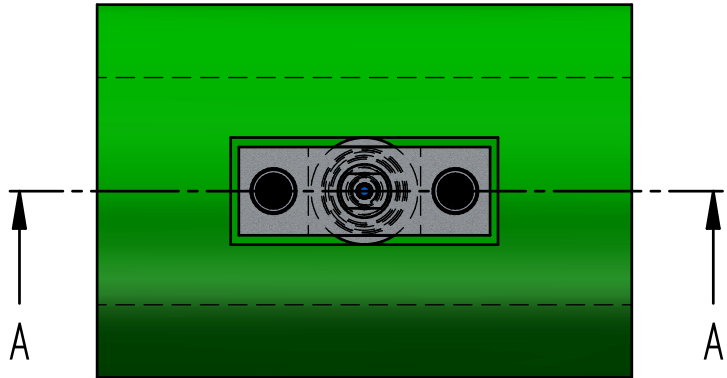
# New wall PCB Mount Drawings

DRAFTING STANDARD: AS1100 - 1992  
DO NOT SCALE

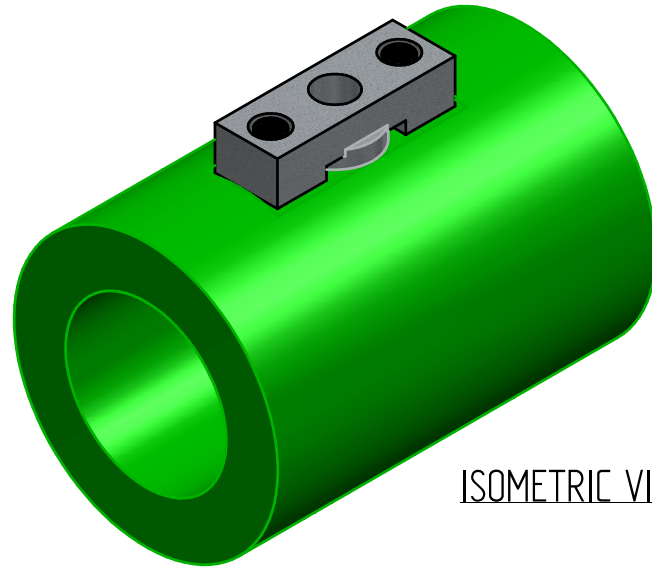
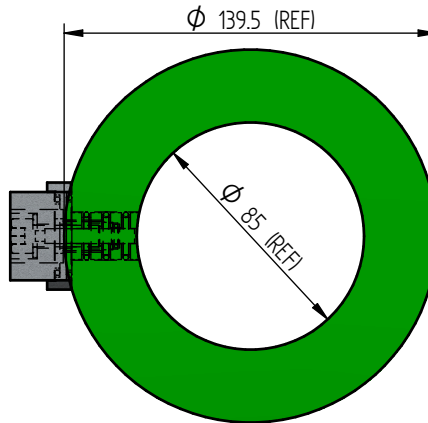


REVISION HISTORY

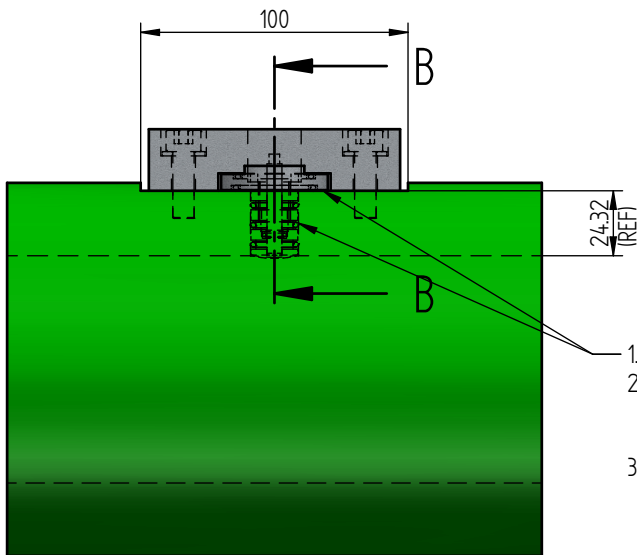
	DESCRIPTION	DATE	APPROVED
0	New drawing by D. Gildfind	15/01/2015	
1	New assembly drawing made by C.M. James to reflect changes made to x2-pcbmount-003.	28/08/2015	



1:2  
TOP VIEW



ISOMETRIC VIEW




SIDE VIEW

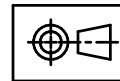
1. Bore out transducer hole to  $\phi 18 \pm 0.0025$
2. Plane tube down to a depth that brings the transducer mount inner face flush with the tube inner bore, WITHOUT o-rings installed.
3. If depth of removed material exceeds 3.5mm, thickness, consult with engineering.

- Notes:
1. See Sheet 2 for Sections A-A and B-B.
  2. See Sheet 3 for parts list.

PRINT ON A3 SHEETSIZE

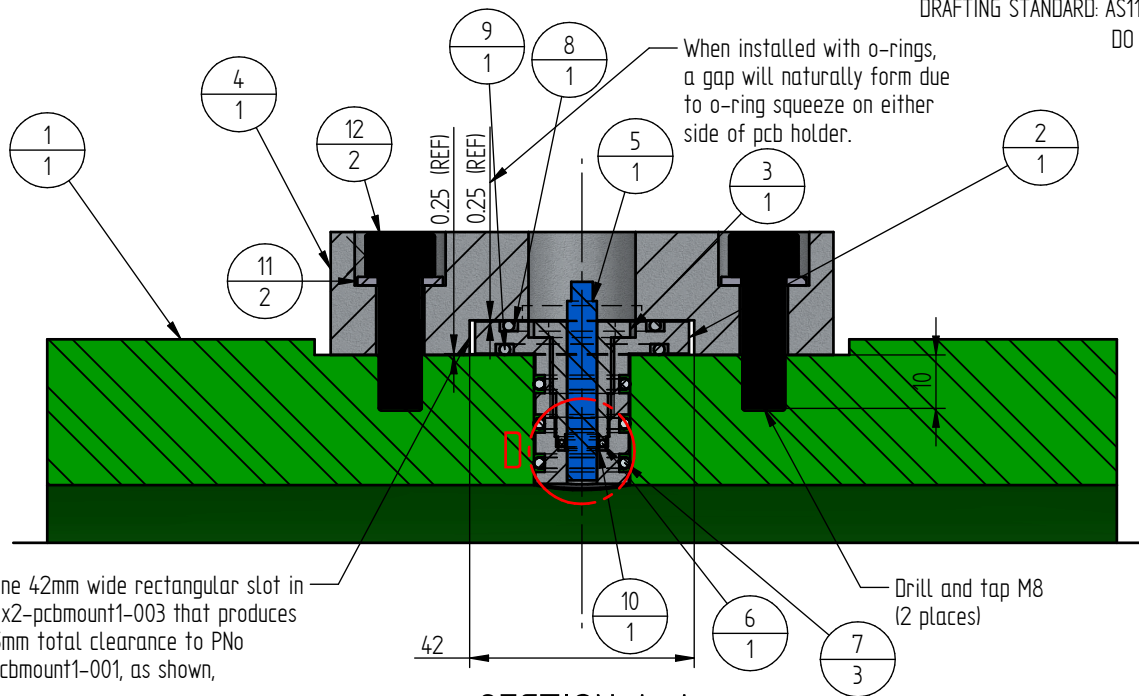
	NAME	DATE	CENTRE FOR HYPERSONICS THE UNIVERSITY OF QUEENSLAND		
DRAWN	C.M. James	24/08/15	 TITLE X2 pcb mount assembly		
CHECKED					
ENG APPR					
MGR APPR					
UNLESS OTHERWISE SPECIFIED DIMENSIONS ARE IN MILLIMETERS ANGULAR TOLERANCE $\pm 1.0^\circ$ DIMENSIONAL TOLERANCE $\pm 0.1\text{mm}$			SIZE A3	DWG NO x2-pcbmount1-000	REV 1
			FILE NAME: x2-pcbmount1-000-0-pcb-mount-assembly-drawing.dft	SCALE: AS SHOWN	WEIGHT: n/a
			SHEET 1 OF 3		

DRAFTING STANDARD: AS1100 - 1992  
DO NOT SCALE



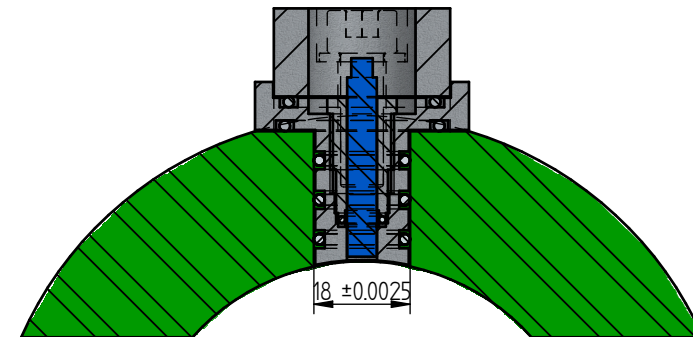
REVISION HISTORY

	DESCRIPTION	DATE	APPROVED
0	New drawing by D. Gildfind	15/01/2015	
1	New assembly drawing made by C.M. James to reflect changes made to x2-pcbmount-003.	28/08/2015	

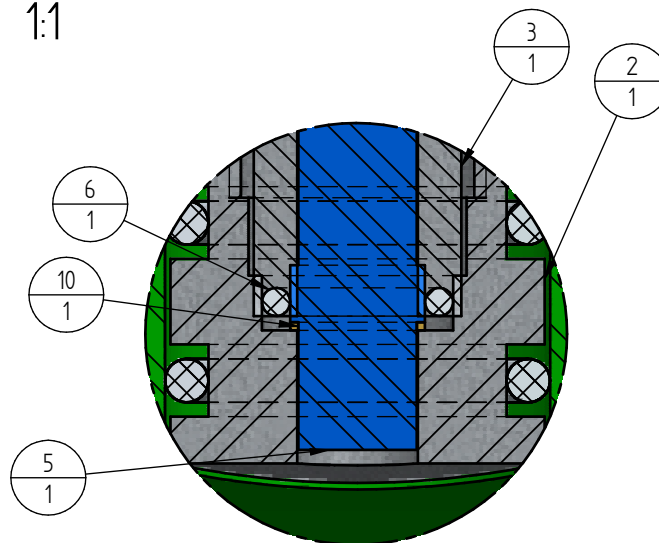


Machine 42mm wide rectangular slot in PNo. x2-pcbmount1-003 that produces a 0.5mm total clearance to PNo. x2-pcbmount1-001, as shown,

SECTION A-A  
1:1




SECTION B-B



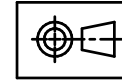
DETAIL D (SCALE 4:1)

PRINT ON A3 SHEETSIZE

SOLID EDGE ACADEMIC COPY

	NAME	DATE	CENTRE FOR HYPERSONICS THE UNIVERSITY OF QUEENSLAND	
DRAWN	C.M. James	24/08/15	 TITLE X2 pcb mount assembly	
CHECKED				
ENG APPR				
MGR APPR				
UNLESS OTHERWISE SPECIFIED DIMENSIONS ARE IN MILLIMETERS ANGULAR TOLERANCE ±1.0° DIMENSIONAL TOLERANCE ±0.1mm			SIZE <b>A3</b> DWG NO x2-pcbmount1-000	REV 1
SCALE: AS SHOWN			WEIGHT: n/a	SHEET 2 OF 3


DRAFTING STANDARD: AS1100 - 1992  
DO NOT SCALE



REVISION HISTORY

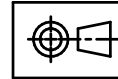
	DESCRIPTION	DATE	APPROVED
0	New drawing by D. Gildfind	15/01/2015	
1	New assembly drawing made by C.M. James to reflect changes made to x2-pcbmount-003.	28/08/2015	

Item Number	Document Number	Revision number	Title	Material	Author	Quantity
1	N/A	N/A	X2 acceleration tube section, O/D139.5mm, I/D 85mm	Steel	D. Gildfind	1
2	x2-pcbmount1-001	0	X2 PCB mount outer fitting	Stainless steel	D. Gildfind	1
3	x2-pcbmount1-002	0	PCB mount outer part	Stainless steel	D. Gildfind	1
4	x2-pcbmount-003	1	PCB tube holder	Stainless Steel, 316	C.M. James	1
5	112A22	N/A	PCB pressure transducer	Steel	D. Gildfind	1
6	BS006 o-ring	N/A	BS006 o-ring	Rubber	D. Gildfind	1
7	BS113	N/A	BS113 o-ring	Rubber	D. Gildfind	3
8	BS120	N/A	BS120 o-ring	Rubber	D. Gildfind	1
9	BS121	N/A	BS121 o-ring	Rubber	D. Gildfind	1
10	065A02 seal ring		065A02 seal ring	Brass, yellow brass	C.M. James	1
11	M8 washer		M8 washer	Steel	C.M. James	2
12	M8 x 25mm		M8 x 25mm	Steel	C.M. James	2

	NAME	DATE	CENTRE FOR HYPERSONICS THE UNIVERSITY OF QUEENSLAND	
DRAWN	C.M. James	24/08/15	 TITLE X2 pcb mount assembly	
CHECKED				
ENG APPR				
MGR APPR				
UNLESS OTHERWISE SPECIFIED DIMENSIONS ARE IN MILLIMETERS ANGULAR TOLERANCE ±1.0° DIMENSIONAL TOLERANCE ±0.1mm			SIZE <b>A3</b>	DWG NO x2-pcbmount1-000
			FILE NAME: x2-pcbmount1-000-0-pcb-mount-assembly-drawing.dft	REV 1
SCALE: AS SHOWN		WEIGHT: n/a	SHEET 3 OF 3	

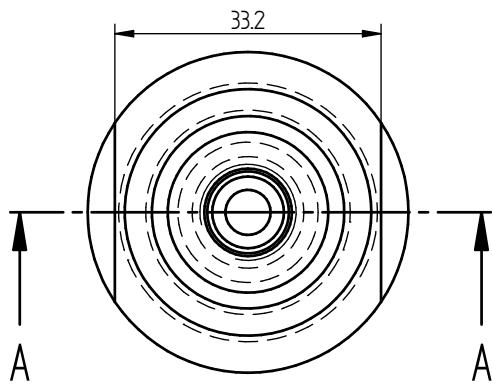
PRINT ON A3 SHEETSIZE  
SOLID EDGE ACADEMIC COPY

DRAFTING STANDARD: AS1100 - 1992  
DO NOT SCALE

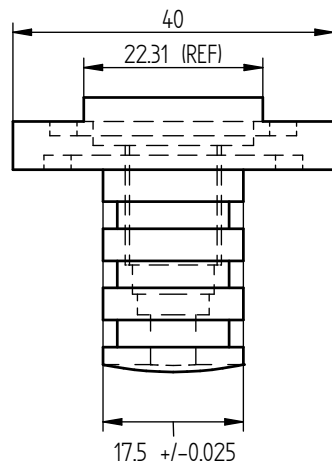
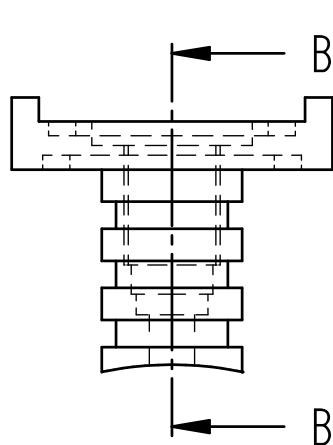


REVISION HISTORY

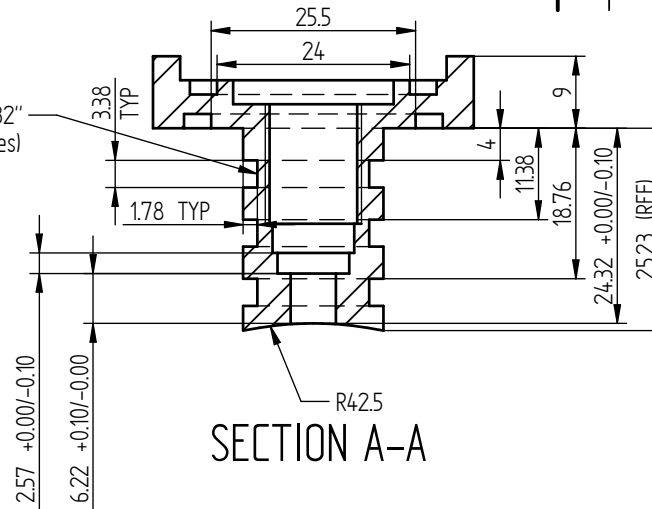
REV	DESCRIPTION	DATE	APPROVED
0	New drawing	15/01/2015	



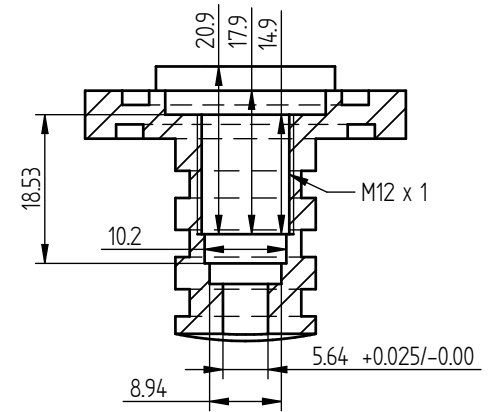
A A



Groove for 3/32" o-ring (5 places)




SECTION A-A



SECTION B-B

PRINT ON A3 SHEETSIZE

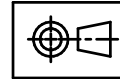
Notes:  
1. See Sheet 2 for isometric views.

	NAME	DATE	CENTRE FOR HYPERSONICS THE UNIVERSITY OF QUEENSLAND	
DRAWN	D. Gildfind	15/01/2015	 TITLE X2 pcb mount inner holder	
CHECKED				
ENG APPR				
MGR APPR				
UNLESS OTHERWISE SPECIFIED DIMENSIONS ARE IN MILLIMETERS ANGULAR TOLERANCE $\pm 1.0^\circ$ DIMENSIONAL TOLERANCE $\pm 0.1\text{mm}$			SIZE <b>A3</b>	DWG NO x2-pcbmount1-001
			REV 0	FILE NAME: x2-pcbmount1-001-0-pcb-holder-inner.dft
SCALE: AS SHOWN		WEIGHT: n/a	SHEET 1 OF 2	

SOLID EDGE ACADEMIC COPY



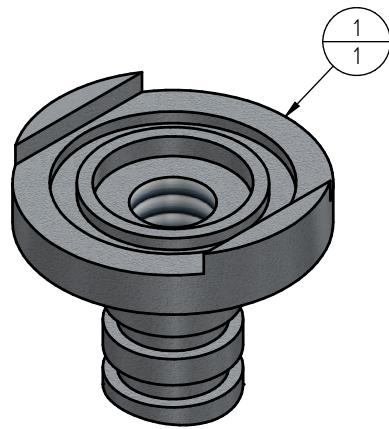
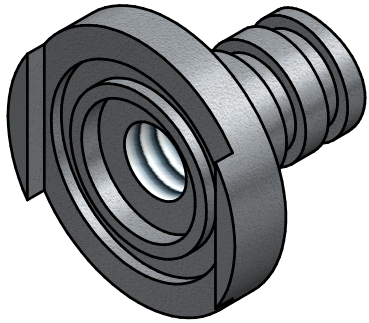
DRAFTING STANDARD: AS1100 - 1992  
DO NOT SCALE



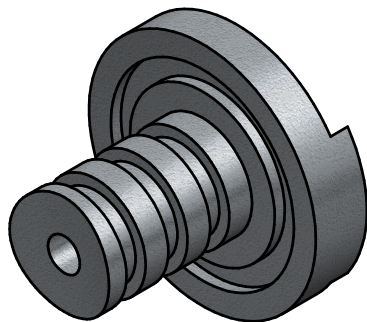
REVISION HISTORY

REV	DESCRIPTION	DATE	APPROVED
0	New drawing	15/01/2015	

PRINT ON A3 SHEETSIZE



1.5:1

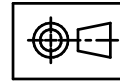


Item Number	Document Number	Revision number	Title	Material	Author	Quantity
1	x2-pcbmount1-001	0	X2 PCB mount outer fitting	Stainless steel	D. Gildfind	1

SOLID EDGE ACADEMIC COPY

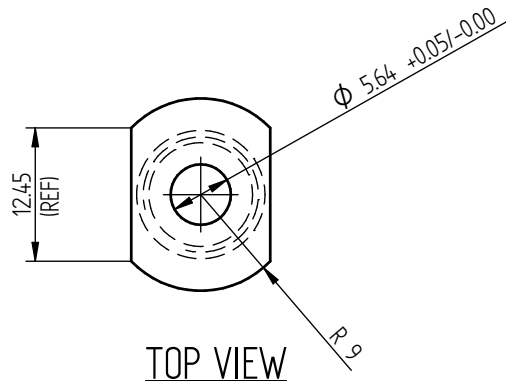
	NAME	DATE	CENTRE FOR HYPERSONICS THE UNIVERSITY OF QUEENSLAND		
DRAWN	D. Gildfind	15/01/2015	TITLE X2 pcb mount inner holder		
CHECKED					
ENG APPR					
MGR APPR					
UNLESS OTHERWISE SPECIFIED DIMENSIONS ARE IN MILLIMETERS ANGULAR TOLERANCE ±1.0° DIMENSIONAL TOLERANCE ±0.1mm			SIZE <b>A3</b>	DWG NO x2-pcbmount1-001	REV 0
			FILE NAME: x2-pcbmount1-001-0-pcb-holder-inner.dft		
			SCALE: AS SHOWN	WEIGHT: n/a	SHEET 2 OF 2

DRAFTING STANDARD: AS1100 - 1992  
DO NOT SCALE



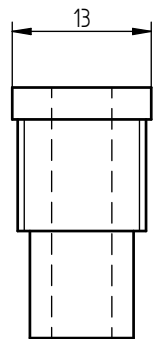
REVISION HISTORY

REV	DESCRIPTION	DATE	APPROVED
0	New drawing	15/01/2015	



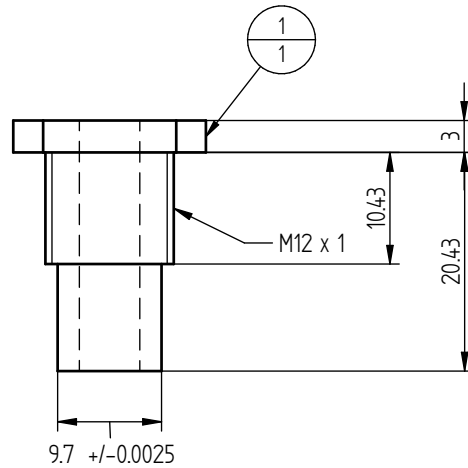
TOP VIEW

PRINT ON A3 SHEETSIZE

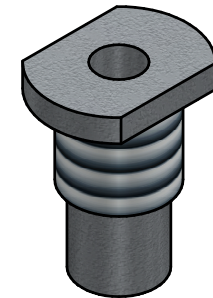
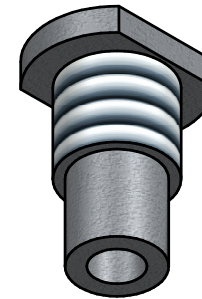


2:1

SIDE VIEW

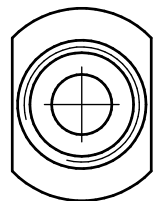


FRONT VIEW



2:1

ISOMETRIC VIEWS



VIEW FROM BELOW

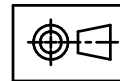
Item Number	Document Number	Revision number	Title	Material	Author	Quantity
1	x2-pcbmount1-002	0	PCB mount outer part	Stainless steel	D. Gildfind	1

	NAME	DATE	CENTRE FOR HYPERSONICS THE UNIVERSITY OF QUEENSLAND		
DRAWN	D. Gildfind	15/01/2015	TITLE X2 pcb mount outer holder		
CHECKED					
ENG APPR					
MGR APPR					
UNLESS OTHERWISE SPECIFIED DIMENSIONS ARE IN MILLIMETERS ANGULAR TOLERANCE $\pm 1.0^\circ$ DIMENSIONAL TOLERANCE $\pm 0.1\text{mm}$			SIZE A3	DWG NO x2-pcbmount1-002	REV 0
FILE NAME: x2-pcbmount1-002-0-pcb-holder-outer.dft					
SCALE: AS SHOWN		WEIGHT: n/a		SHEET 1 OF 1	

SOLID EDGE ACADEMIC COPY

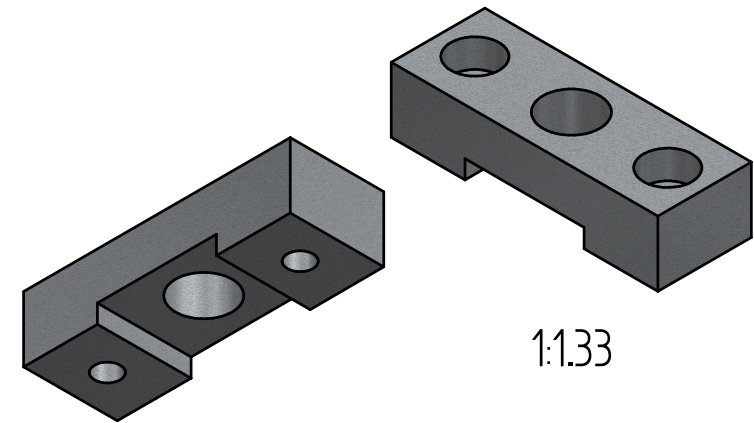
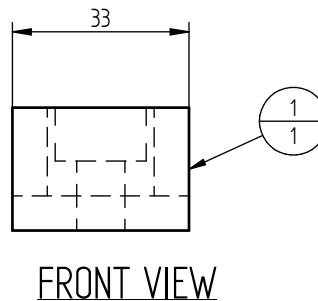
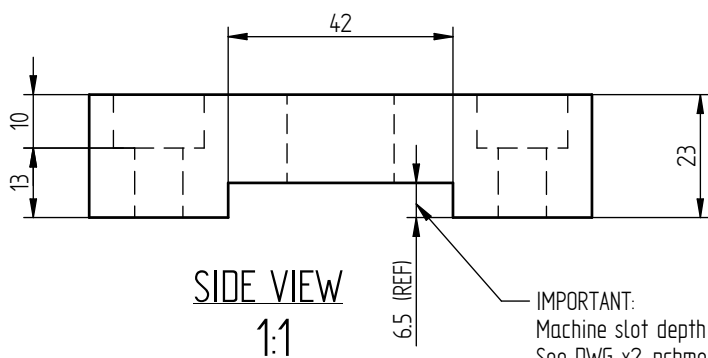
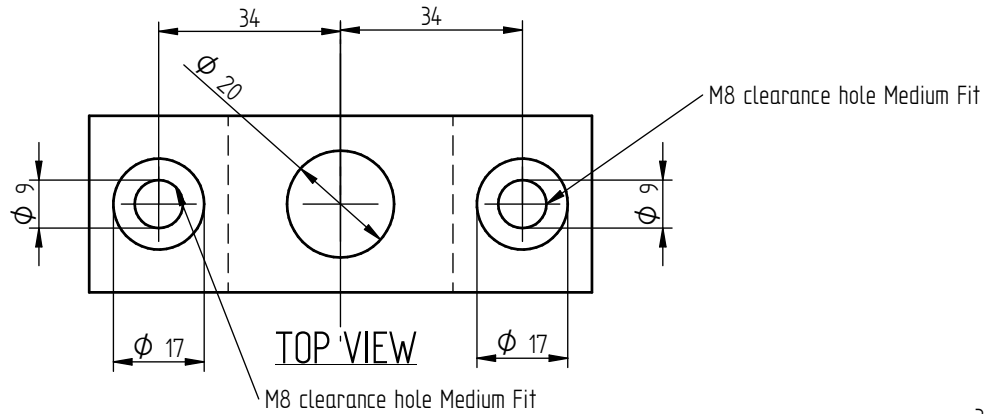
DRAFTING STANDARD: AS1100 - 1992  
DO NOT SCALE

PRINT ON A3 SHEETSIZE



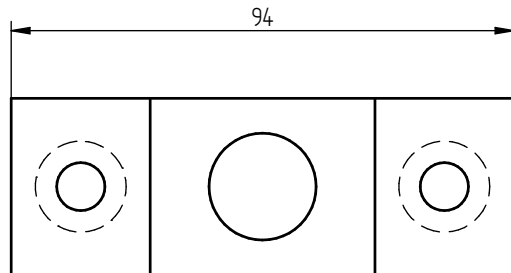
REVISION HISTORY

REV	DESCRIPTION	DATE	APPROVED
0	New drawing by D. Gildfind	15/01/2015	
1	Height of mount increased by 3 mm, bolt holes changed to M8, and material changed to 316 stainless steel to strengthen the piece by C.M. James.	24/08/2015	



1:1.33

ISOMETRIC VIEWS



BOTTOM VIEW

Item Number	Document Number	Revision number	Title	Material	Author	Quantity
1	x2-pcbmount-003	1	PCB tube holder	Stainless Steel, 316	C.M. James	1

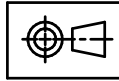
	NAME	DATE	CENTRE FOR HYPERSONICS THE UNIVERSITY OF QUEENSLAND			
DRAWN	C. M. James	24/08/15	TITLE X2 pcb mount tube holder			
CHECKED			SIZE A3 DWG NO x2-pcbmount1-003 REV 1			
ENG APPR			FILE NAME: x2-pcbmount1-003-0-pcb-tube-holder.dft			
MGR APPR			SCALE: AS SHOWN WEIGHT: n/a SHEET 1 OF 1			
UNLESS OTHERWISE SPECIFIED DIMENSIONS ARE IN MILLIMETERS ANGULAR TOLERANCE ±1.0° DIMENSIONAL TOLERANCE ±0.1mm						

SOLID EDGE ACADEMIC COPY

## Appendix F

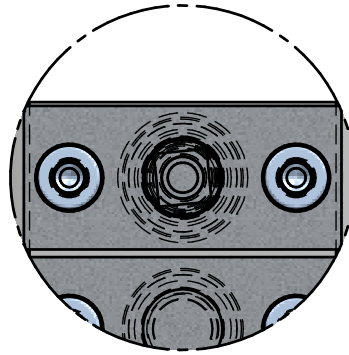
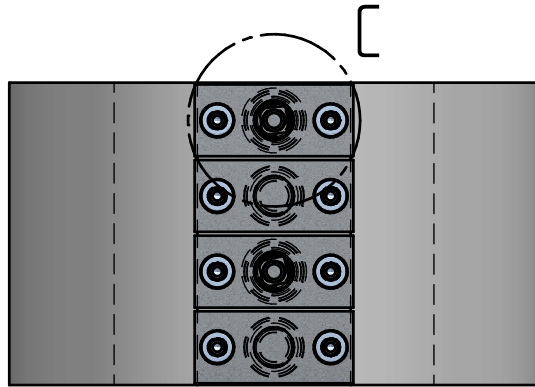
# Photodiode Mount PCB Mount Drawings

DRAFTING STANDARD: AS1100 - 1992  
DO NOT SCALE

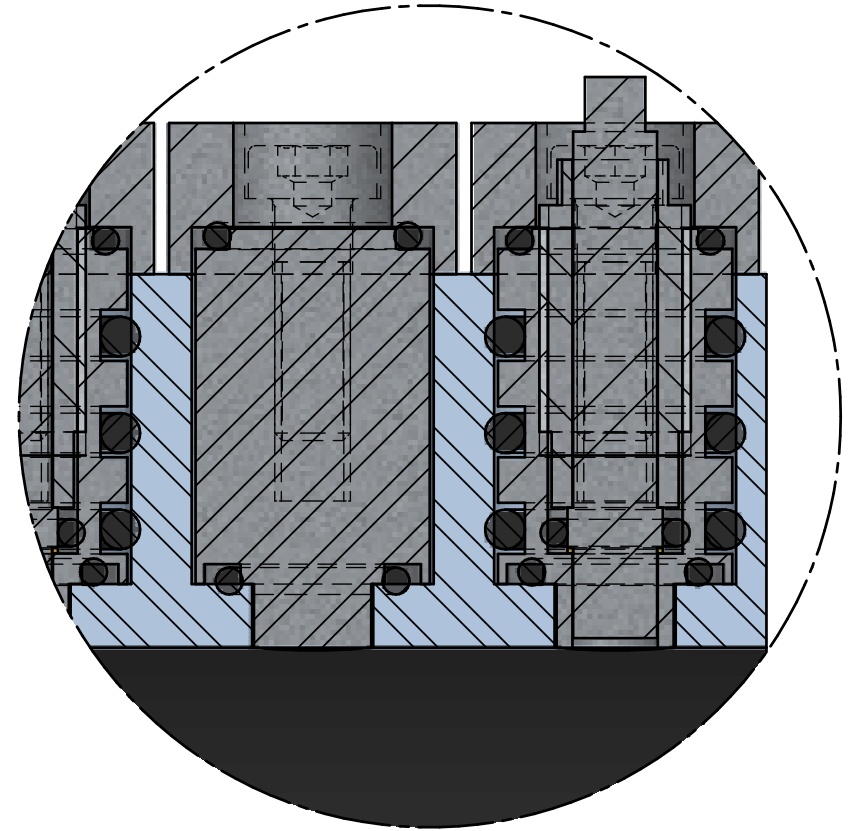


REVISION HISTORY

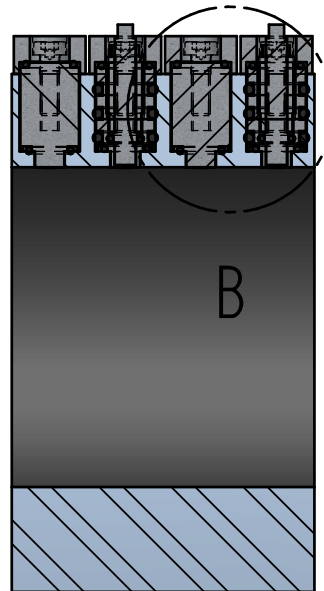
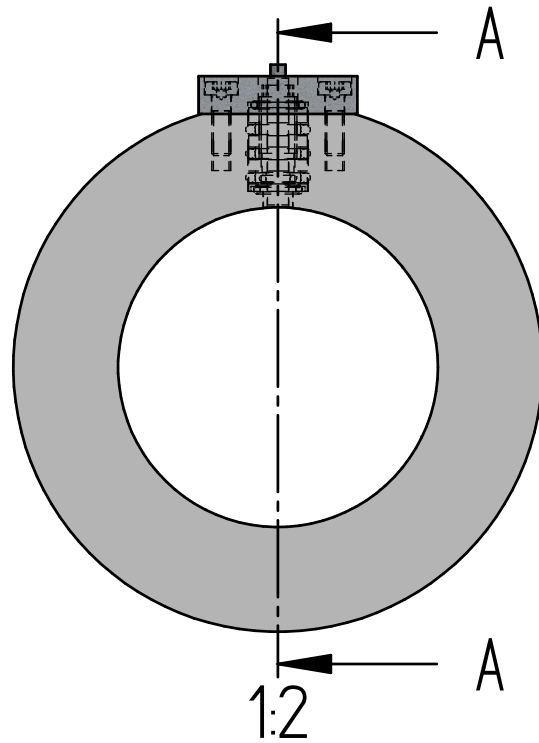
REV	DESCRIPTION	DATE	APPROVED
0	New drawing	17/11/15	n/a



DETAIL C (1:1)



DETAIL B (2:1)



SECTION A-A

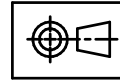
	NAME	DATE	TITLE	
DRAWN	C.M. James	18/11/15	Assembly Drawing (X2-PD-PCB-MOUNT-000)	
CHECKED				
ENG APPR				
MGR APPR				
UNLESS OTHERWISE SPECIFIED DIMENSIONS ARE IN MILLIMETERS ANGULAR TOLERANCE $\pm 0.1^\circ$ DIMENSIONAL TOLERANCE $\pm 0.1\text{mm}$			SIZE A4	PROJECT X2 Photodiode Mount PCB Mount
			FILE NAME: x2-pd-pcb-mount-000-assembly.dft	REV 0
			SCALE: AS SHOWN	WEIGHT: SHEET 1 OF 3

Notes:

- Contact details: ph (internal) 54864, ph (mobile) 0413 642 000

SOLID EDGE ACADEMIC COPY

DRAFTING STANDARD: AS1100 - 1992  
DO NOT SCALE



REVISION HISTORY

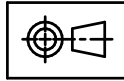
REV	DESCRIPTION	DATE	APPROVED
0	New drawing	17/11/15	n/a

Item Number	Document Number	Revision number	Title	Material	Author	Quantity
1	x2-pd-pcb-mount-001	0	X2 Photodiode Mount PCB Mount External Piece	Stainless steel	C.M. James	2
2	x2-pd-pcb-mount-002	0	X2 Photodiode Mount PCB Mount Internal Piece	Stainless steel	C.M. James	2
3	x2-pd-pcb-mount-003	0	X2 Photodiode Mount PCB Mount Mounting Bracket	Stainless steel	C.M. James	4
4	x2-pd-pcb-mount-004	0	X2 Photodiode Mount PCB Mount Blank Off	Stainless steel	C.M. James	2
5	x2-pd-pcb-mount-005	N/A	X2 Expansion Tube Representation	Steel	C.M. James	1
6	112A22	N/A	PCB pressure transducer	Steel	D. Gildfind	2
7	065A02 seal ring		065A02 seal ring	Brass, yellow brass	C.M. James	2
8	N/A	N/A	BS012 o-ring	Rubber	C.M. James	4
9	N/A	N/A	BS111 o-ring	Rubber	C.M. James	6
10	N/A	N/A	BS009 o-ring	Rubber	C.M. James	2
11	N/A	N/A	BS013 o-ring	Rubber	C.M. James	4
12			Hexagon socket head cap screw DIN 6912 - M5x16	Steel	uqcjame4	8

	NAME	DATE		
DRAWN	C.M. James	18/11/15		
CHECKED				
ENG APPR			TITLE	
MGR APPR			Assembly Drawing (X2-PD-PCB-MOUNT-000)	
UNLESS OTHERWISE SPECIFIED DIMENSIONS ARE IN MILLIMETERS ANGULAR TOLERANCE ±0.1° DIMENSIONAL TOLERANCE ±0.1mm			SIZE A4	PROJECT X2 Photodiode Mount PCB Mount
			FILE NAME: x2-pd-pcb-mount-000-assembly.dft	REV 0
			SCALE: AS SHOWN	WEIGHT:
			SHEET 2 OF 3	

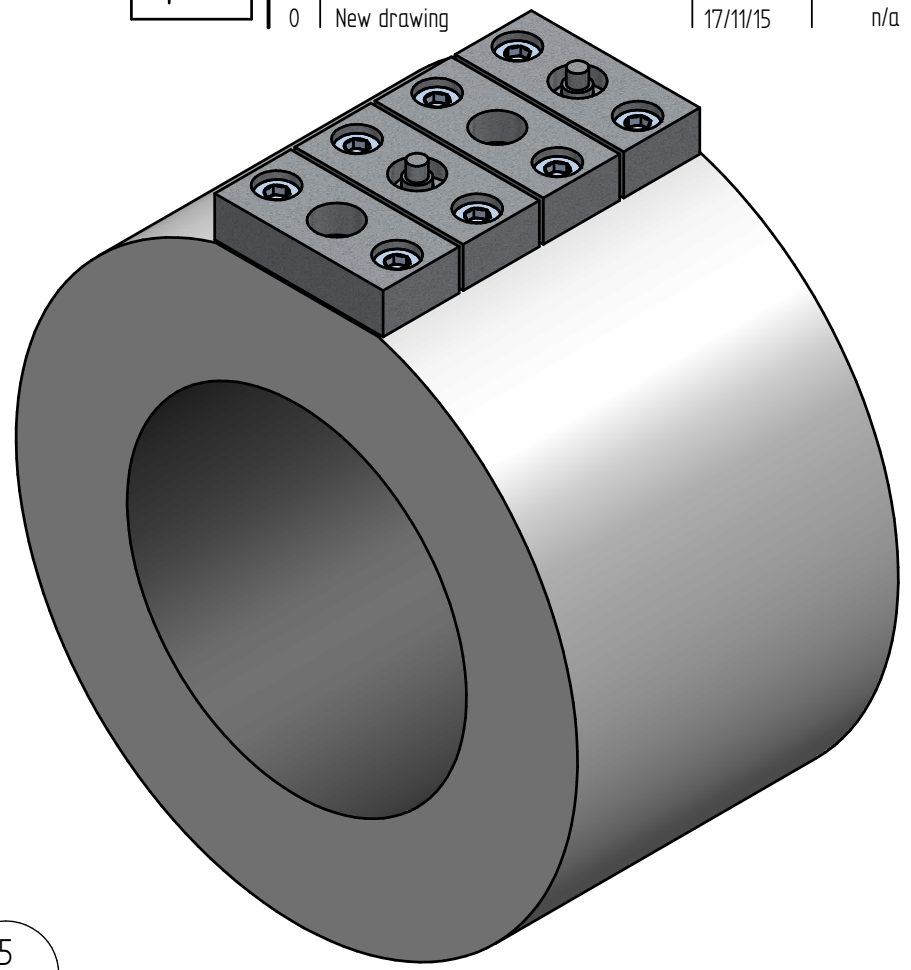
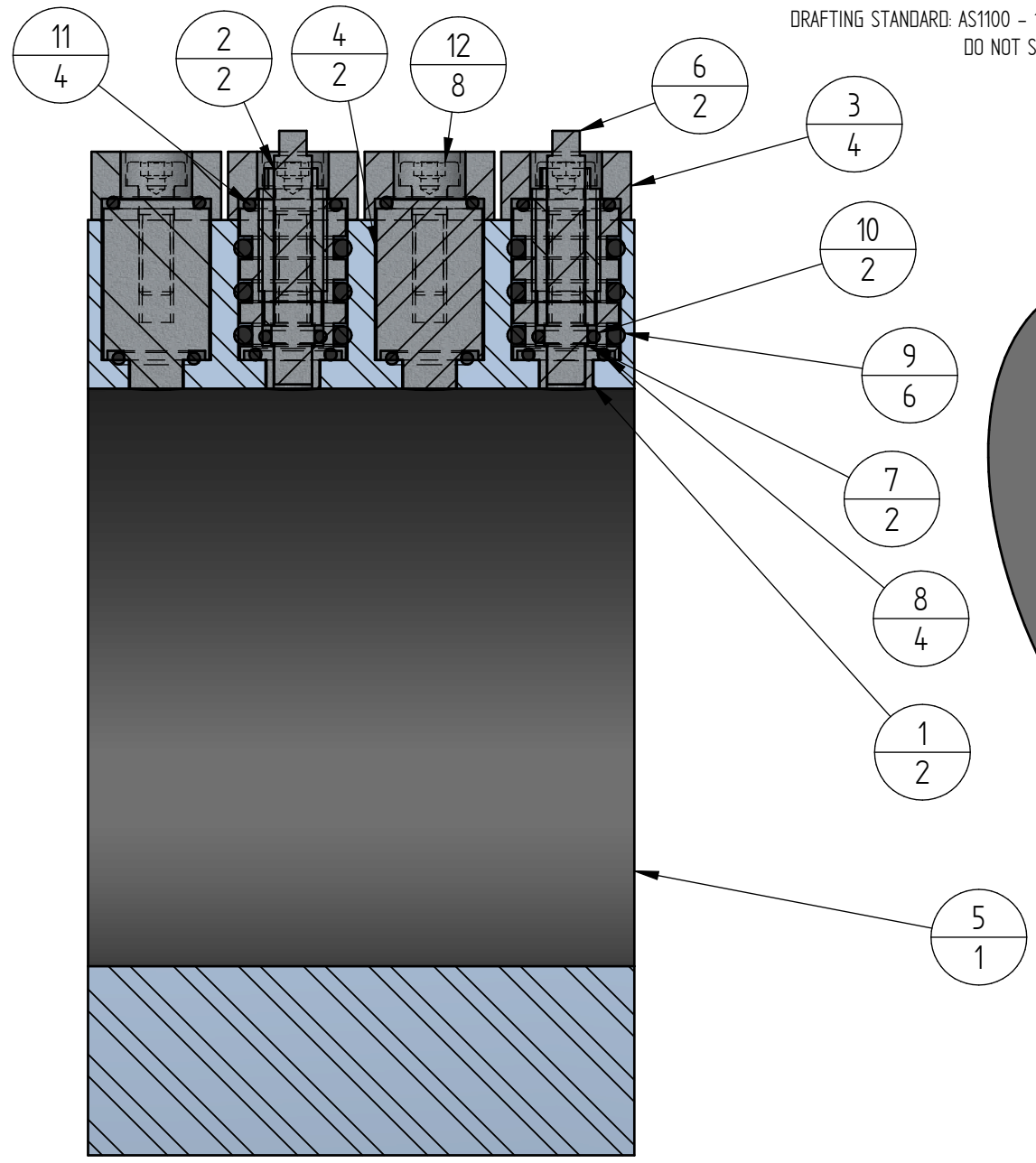
SOLID EDGE ACADEMIC COPY

DRAFTING STANDARD: AS1100 - 1992  
DO NOT SCALE



REVISION HISTORY

REV	DESCRIPTION	DATE	APPROVED
0	New drawing	17/11/15	n/a



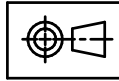
1:1.33

NAME	DATE	TITLE	
DRAWN	C.M. James	18/11/15	
CHECKED			
ENG APPR			
MGR APPR			
UNLESS OTHERWISE SPECIFIED DIMENSIONS ARE IN MILLIMETERS ANGULAR TOLERANCE ±0.1° DIMENSIONAL TOLERANCE ±0.1mm		SIZE A4	PROJECT X2 Photodiode Mount PCB Mount
		FILE NAME: x2-pd-pcb-mount-000-assembly.dft	REV 0
		SCALE: AS SHOWN	WEIGHT: SHEET 3 OF 3

SECTION A-A (1:1)

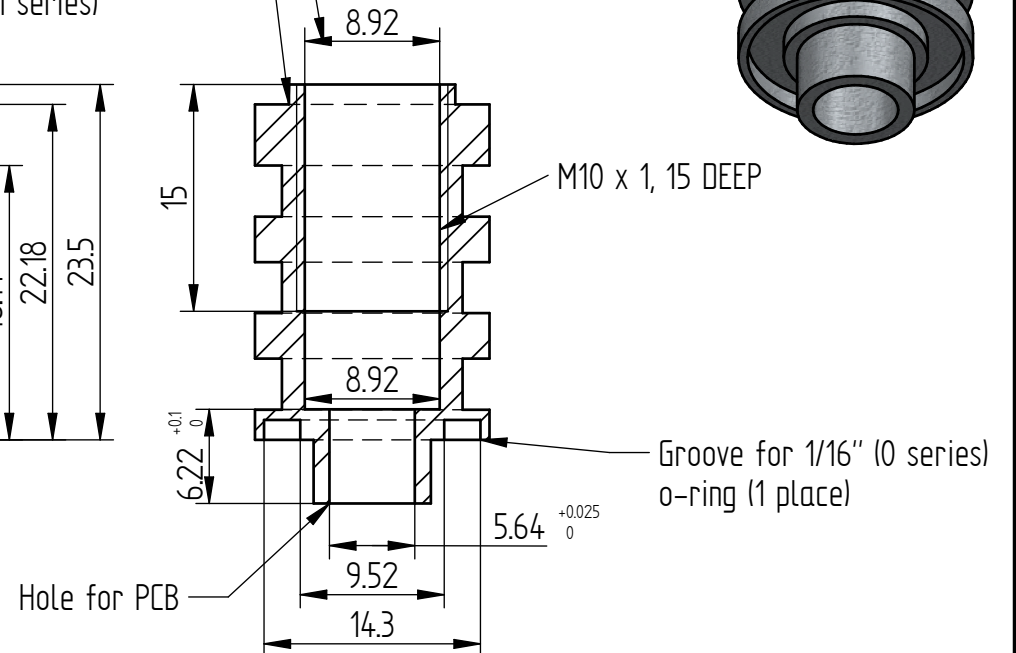
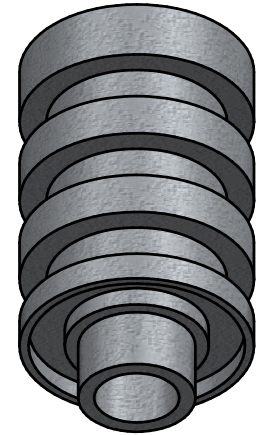
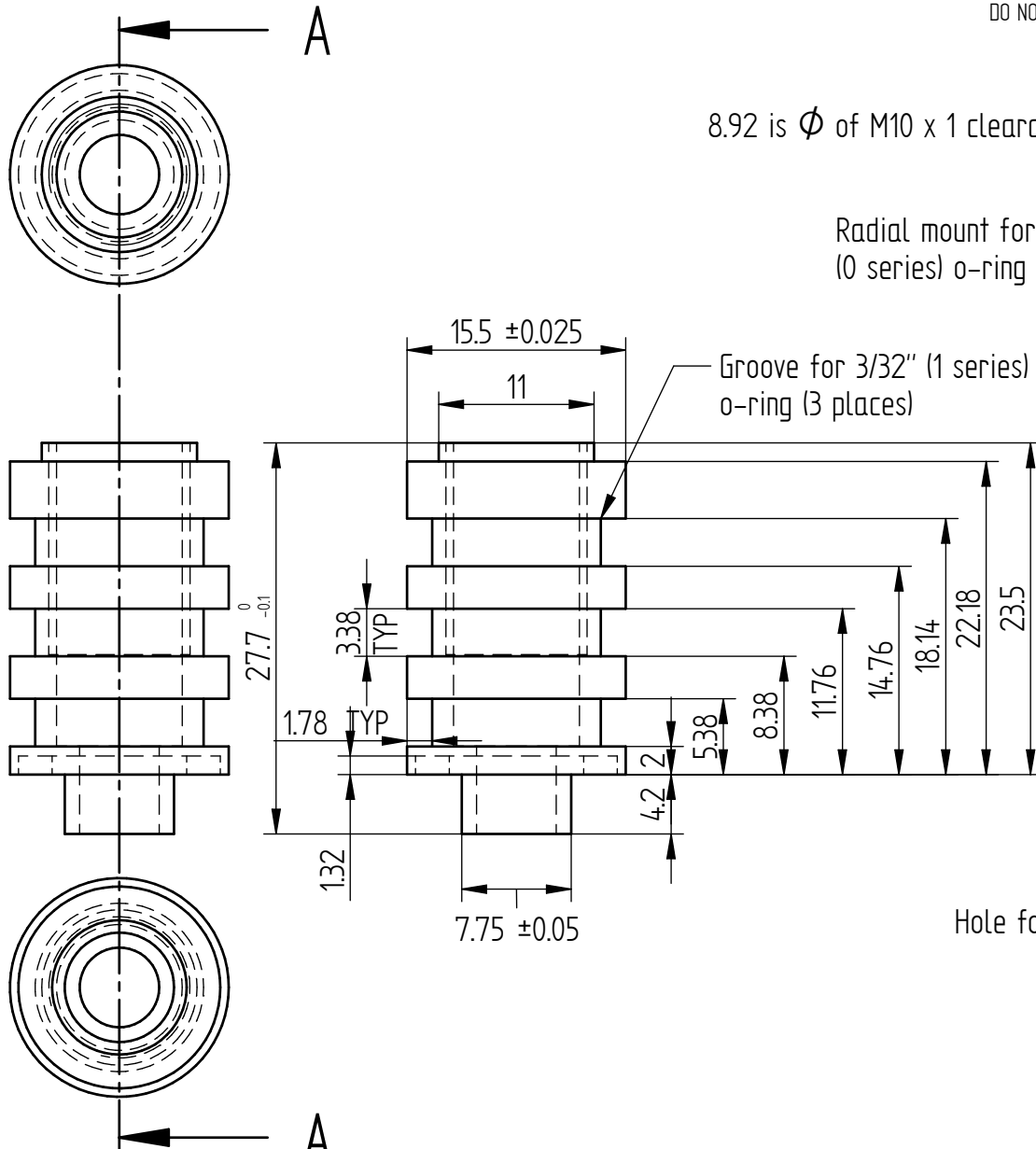
SOLIDWORKS ACADEMIC COPY

DRAFTING STANDARD: AS1100 - 1992  
DO NOT SCALE



REVISION HISTORY

REV	DESCRIPTION	DATE	APPROVED
0	New drawing	17/11/15	n/a



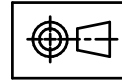
Notes:

- Material: Stainless steel.
- Contact details: ph (internal) 54864, ph (mobile) 0413 642 000

NAME	DATE	TITLE	
DRAWN C.M. James	17/11/15	PCB Mount External Piece (X2-PD-PCB-MOUNT-001)	
CHECKED		SIZE A4	PROJECT X2 Photodiode Mount PCB Mount
ENG APPR		FILE NAME: x2-pd-pcb-mount-001-external-piece.dft	REV 0
MGR APPR		SCALE: 2:1	WEIGHT:
UNLESS OTHERWISE SPECIFIED DIMENSIONS ARE IN MILLIMETERS ANGULAR TOLERANCE ±0.1° DIMENSIONAL TOLERANCE ±0.1mm		SHEET 1 OF 1	

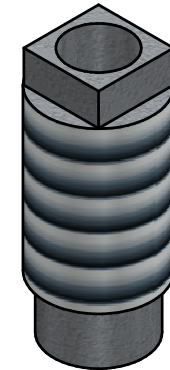
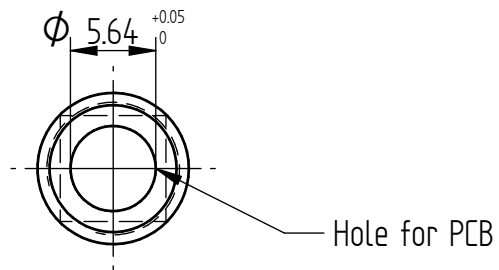
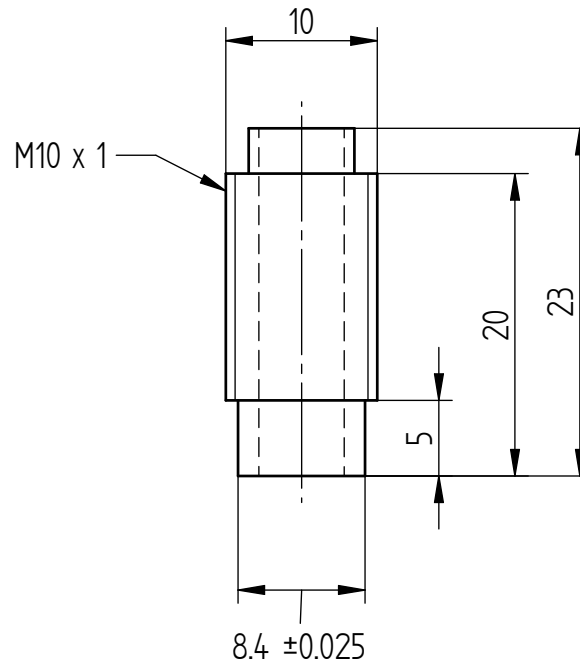
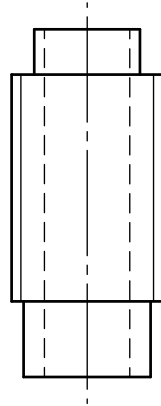
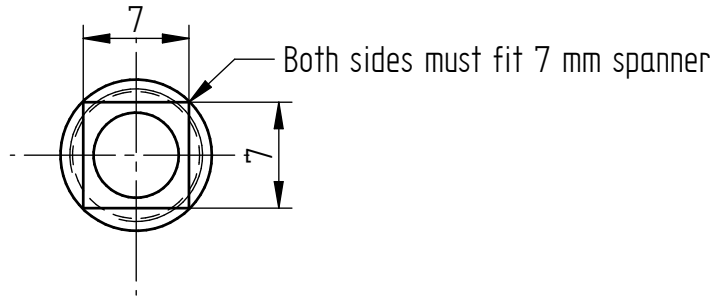


DRAFTING STANDARD: AS1100 - 1992  
DO NOT SCALE



REVISION HISTORY

REV	DESCRIPTION	DATE	APPROVED
0	New drawing	17/11/15	n/a

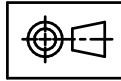


Notes:

- Material: Stainless steel.
- Contact details: ph (internal) 54864, ph (mobile) 0413 642 000

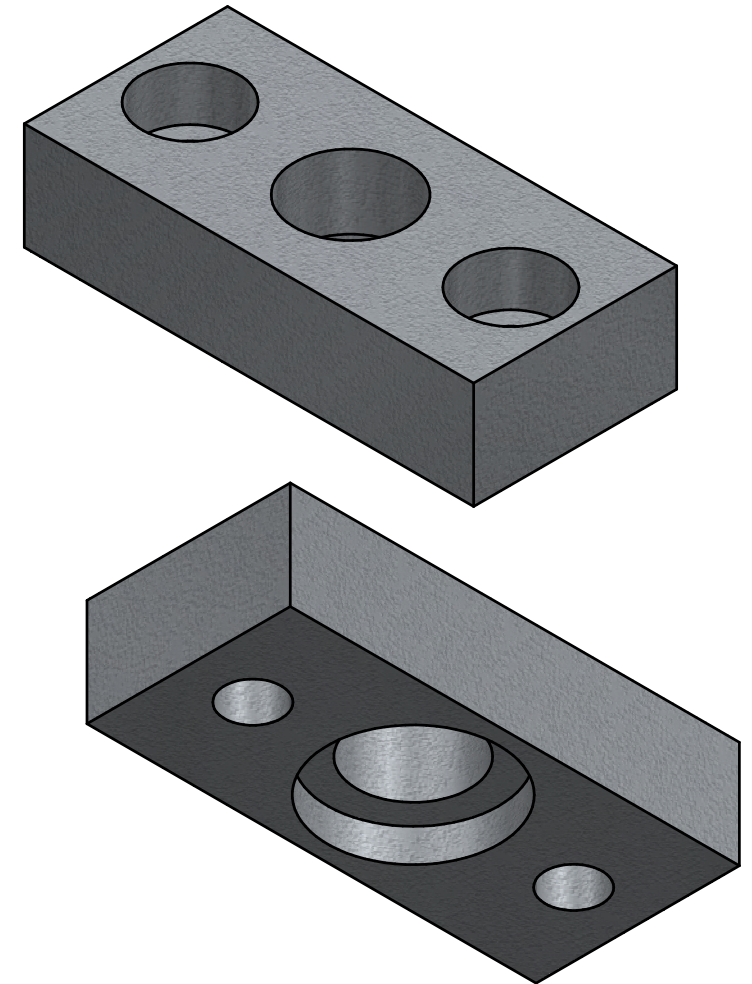
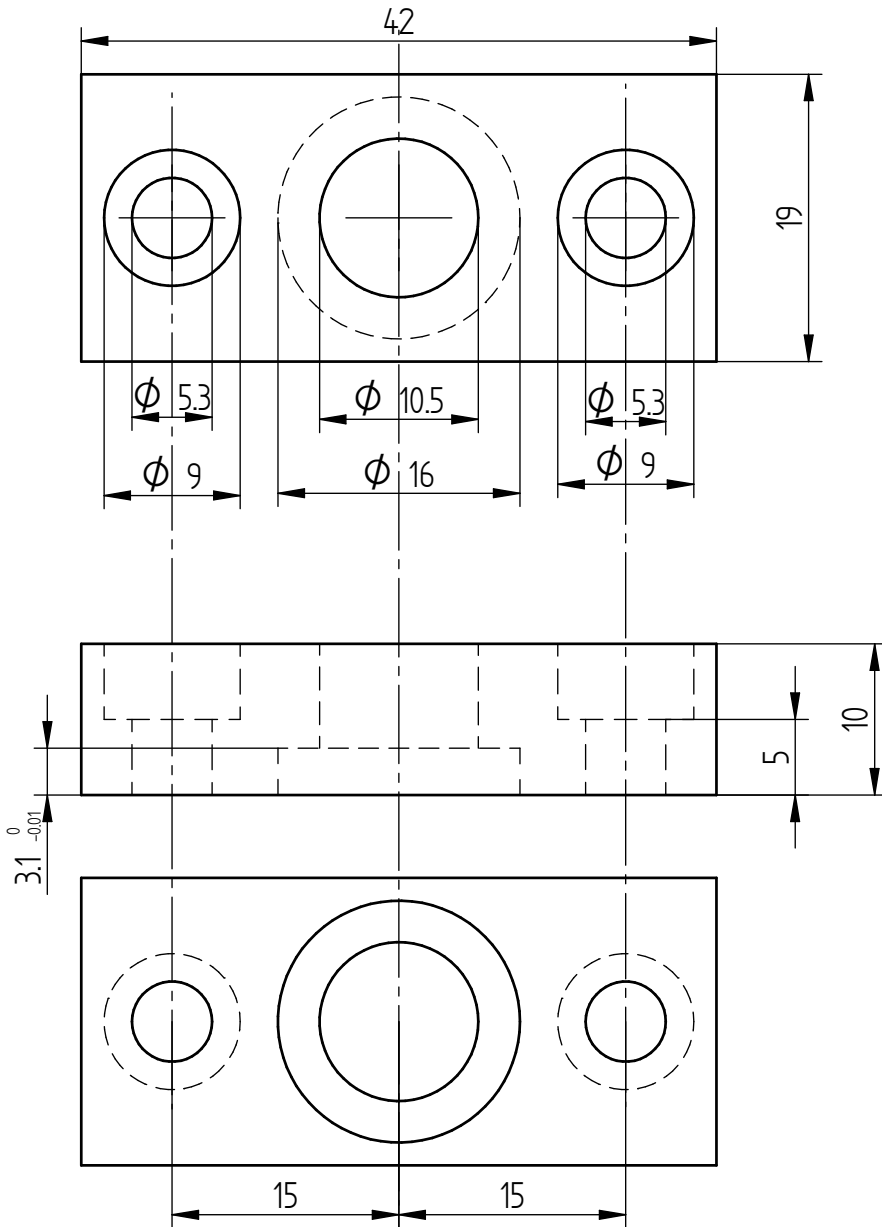
	NAME	DATE			
DRAWN	C.M. James	17/11/15			
CHECKED					
ENG APPR			TITLE		
MGR APPR			PCB Mount Internal Piece (X2-PD-PCB-MOUNT-002)		
UNLESS OTHERWISE SPECIFIED DIMENSIONS ARE IN MILLIMETERS ANGULAR TOLERANCE ±0.1° DIMENSIONAL TOLERANCE ±0.1mm			SIZE	PROJECT	REV
			A4	X2 Photodiode Mount PCB Mount	0
			FILE NAME: x2-pd-pcb-mount-002-internal-piece.dft		
			SCALE: 2:1	WEIGHT:	SHEET 1 OF 1

DRAFTING STANDARD: AS1100 - 1992  
DO NOT SCALE



REVISION HISTORY

REV	DESCRIPTION	DATE	APPROVED
0	New drawing	17/11/15	n/a

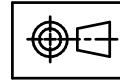


Notes:

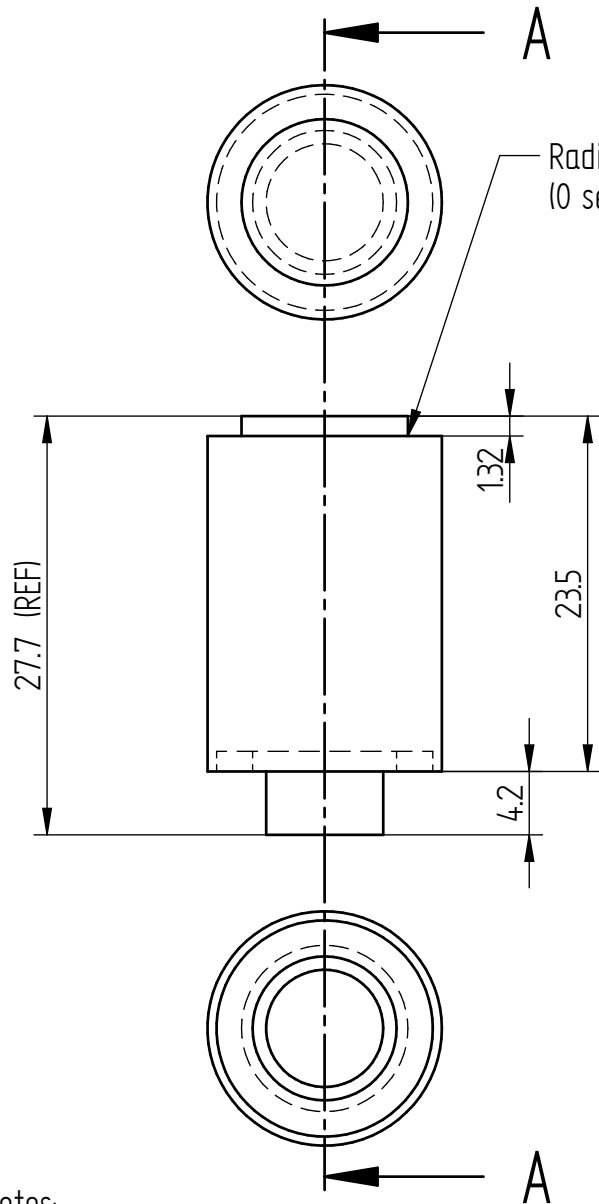
- Material: Stainless steel.
- Contact details: ph (internal) 54864, ph (mobile) 0413 642 000

	NAME	DATE			
DRAWN	C.M. James	17/11/15			
CHECKED					
ENG APPR			TITLE		
MGR APPR			PCB Mount Bracket (X2-PD-PCB-MOUNT-003)		
UNLESS OTHERWISE SPECIFIED DIMENSIONS ARE IN MILLIMETERS ANGULAR TOLERANCE $\pm 0.1^\circ$ DIMENSIONAL TOLERANCE $\pm 0.1$ mm			SIZE	PROJECT	REV
			A4	X2 Photodiode Mount PCB Mount	0
			FILE NAME: x2-pd-pcb-mount-003-bracket.dft		
			SCALE: 2:1	WEIGHT:	SHEET 1 OF 1

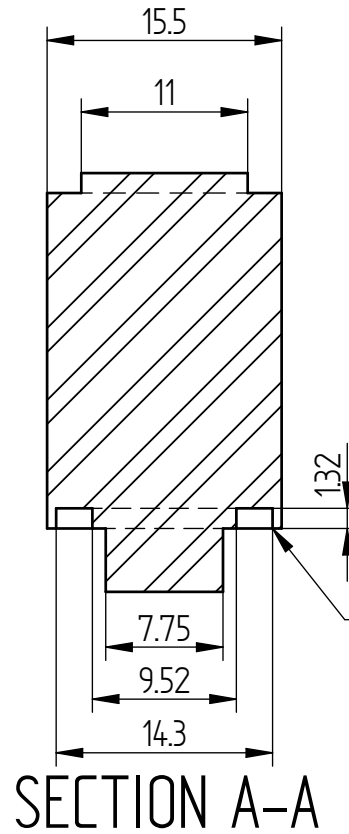
DRAFTING STANDARD: AS1100 - 1992  
DO NOT SCALE



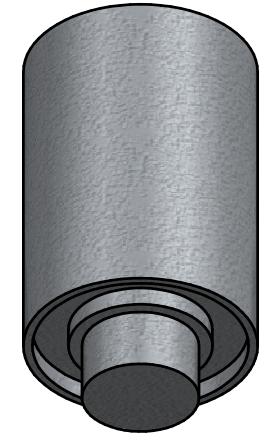
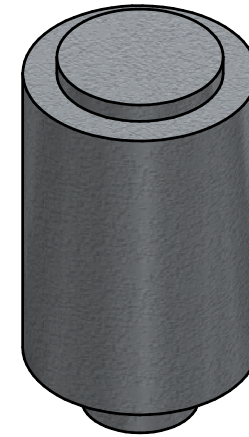
REVISION HISTORY			
REV	DESCRIPTION	DATE	APPROVED
0	New drawing	17/11/15	n/a



Radial mount for 1/16" (0 series) o-ring (1 place)



Groove for 1/16" (0 series) o-ring (1 place)

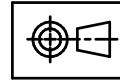


Notes:

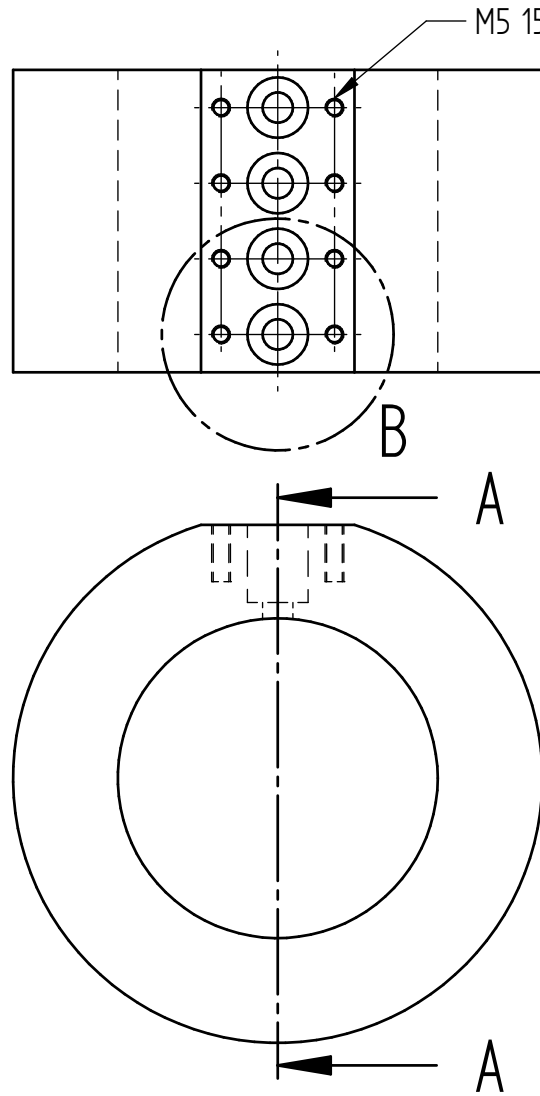
- Material: Stainless steel.
- Contact details: ph (internal) 54864, ph (mobile) 0413 642 000

	NAME	DATE	TITLE	
DRAWN	C.M. James	17/11/15	Plug (X2-PD-PCB-MOUNT-004)	
CHECKED				
ENG APPR				
MGR APPR				
UNLESS OTHERWISE SPECIFIED DIMENSIONS ARE IN MILLIMETERS ANGULAR TOLERANCE ±0.1° DIMENSIONAL TOLERANCE ±0.1mm			SIZE A4	PROJECT X2 Photodiode Mount PCB Mount
			FILE NAME: x2-pd-pcb-mount-004-plug.dft	REV 0
			SCALE: 2:1	WEIGHT: SHEET 1 OF 1

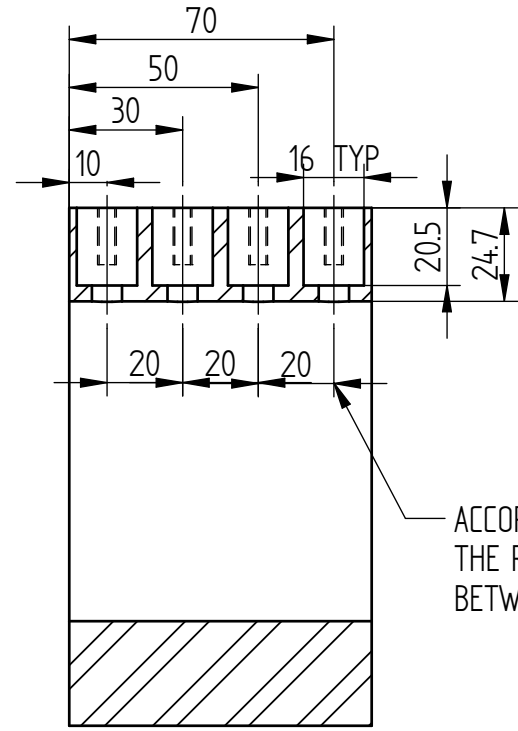
DRAFTING STANDARD: AS1100 - 1992  
DO NOT SCALE



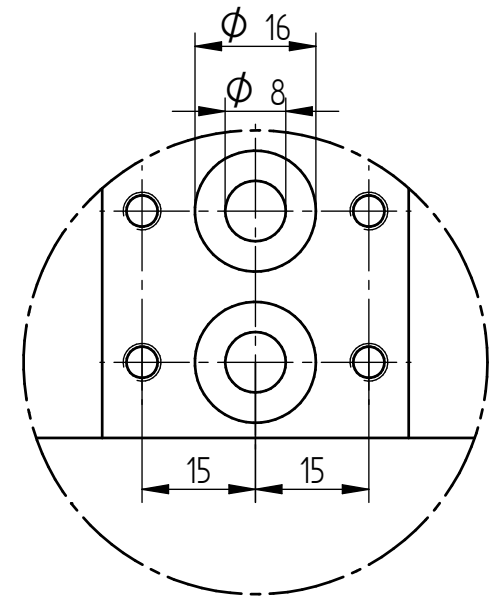
REVISION HISTORY			
REV	DESCRIPTION	DATE	APPROVED
0	New drawing	17/11/15	n/a



M5 15 DEEP (TYP, 8 HOLES).



SECTION A-A



DETAIL B (1:1)

ACCORDING TO ORIGINAL DRAWING,  
THE REFERENCE DIMENSION IS THE DISTANCE  
BETWEEN EACH CENTRELINE

- Notes:
- Material: Steel.
  - These are existing holes in the acceleration tube of the X2 expansion tube.
  - Tolerances of these existing holes cannot be guaranteed.
  - Can be accessed to re-measure if necessary.
  - Contact details: ph (internal) 54864, ph (mobile) 0413 642 000

	NAME	DATE		
DRAWN	C.M. James	18/11/15		
CHECKED				
ENG APPR			TITLE	
MGR APPR			Representative Tube Drawing (X2-PD-PCB-MOUNT-005)	
UNLESS OTHERWISE SPECIFIED DIMENSIONS ARE IN MILLIMETERS ANGULAR TOLERANCE $\pm 0.1^\circ$ DIMENSIONAL TOLERANCE $\pm 0.1\text{mm}$			SIZE A4	PROJECT X2 Photodiode Mount PCB Mount
			FILE NAME: x2-pd-pcb-mount-005-tube-piece.dft	REV 0
			SCALE: 1:2	WEIGHT: SHEET 1 OF 1

## Appendix G

# Calculating Experimental Shock Speed Uncertainty

This appendix details the procedure currently used for the calculation of expansion tube shock speed uncertainty in the Centre for Hypersonics at UQ. It is the procedure used by the shot analysis codes in the laboratory for the calculation of shock speed uncertainty, and it includes uncertainty and error from three different sources:

1. Distance uncertainty from the measured sensor locations and the physical size of each sensor.
2. Time uncertainty in ascertaining shock arrival on the sensors.
3. Sampling rate error from the clocking speed of the data acquisition system.

In a shock tube or expansion tube, a shock travels through the tube at shock speed  $V_s$ . Over the full length of the tube, depending on the strength of the facility driver and the severity of non-ideal effects such as low density shock tube (or ‘Mirels’) effects [106, 107, 108], wall friction, or heat losses, there may be attenuation of the shock and it will slow down as a function of distance ( $V_s(x)$ ), but as this analysis is interested in the *local* shock speed between two wall pressure sensors, this will not be considered here, and it will be assumed that  $V_s$  remains constant between the two sensors.

Consider a shock moving through the acceleration tube of an expansion tube at shock speed  $V_s$ . Just in front of the shock are two wall pressure sensors, ‘at1’ and ‘at2’, mounted at locations  $x_1$  and  $x_2$ , measured from a single datum point. This is shown in Fig. G.1, and constitutes time  $t_0$ .

At a certain time after  $t_0$  called  $t_1$ , the shock will pass pressure sensor ‘at1’. When this occurs, there will be a step increase in pressure at location  $x_1$ , which will be recorded by the sensor and later used to ascertain  $t_1$ . Similarly, at a certain time after  $t_1$  called  $t_2$ , the shock will pass pressure sensor ‘at2’, and the step increase in pressure seen at the location  $x_2$  will be recorded by sensor ‘at2’ and later used to ascertain  $t_2$ .

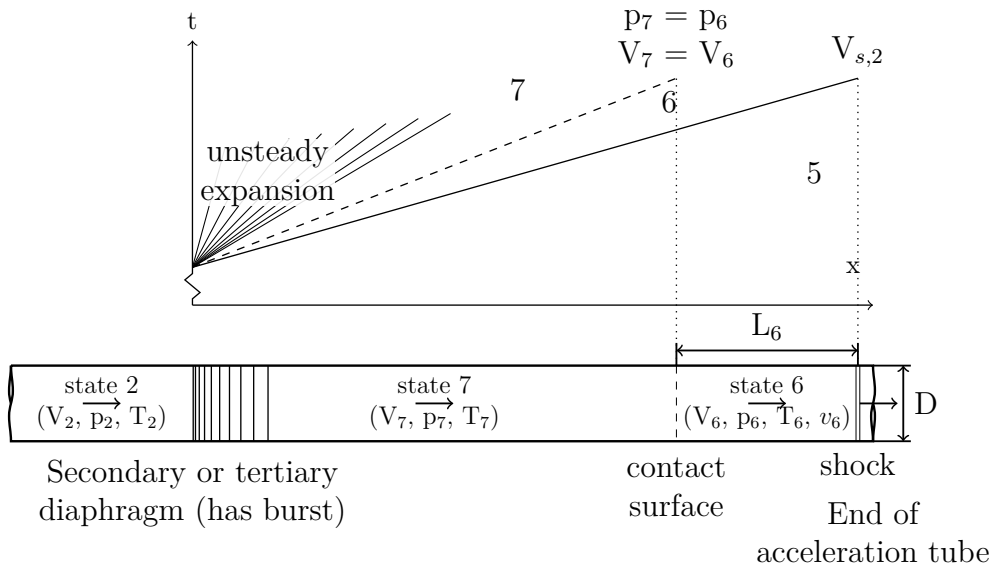


Figure G.1: Representation of a moving shock wave about to pass wall pressure sensors ‘at1’ and ‘at2’ in the X2 expansion tube. (Not to scale.)

Knowing the distance between the two sensors ( $x_2 - x_1$ ), and the time at which the shock passes both locations ( $t_1$  and  $t_2$ ), the nominal shock speed can be found as simply distance ( $\Delta x$ ) divided by time ( $\Delta t$ ):

$$V_s = \frac{x_2 - x_1}{t_2 - t_1} = \frac{\Delta x}{\Delta t} \tag{G.1}$$

Equation G.1, is a function of two distances ( $x_1$  and  $x_2$ ), and two times ( $t_1$  and  $t_2$ ). Therefore, to quantify the uncertainty, the uncertainties on both the distance and the time must be considered.

Three different types of distance uncertainty are considered:

1. Uncertainty in the measurement of the sensor locations ( $x_1$  and  $x_2$ ).
2. Uncertainty in the response of the pressure sensor due to the physical size of the sensor. (The pressure sensors used on X2 in the acceleration tube are 112A22 50 PSI pressure transducers from PCB Piezotronics with a sensor diameter of 5.54 mm [277].)

3. Uncertainty due to the shape of the shock not being planar like it is assumed.

These three uncertainties are encapsulated by a single distance uncertainty ( $\delta x_i$ ) of  $\pm 2.0 \times 10^{-3}$  m (2 mm) for each sensor location.

Therefore, because the distance uncertainties are independent measurements, the total distance uncertainty ( $\delta \Delta x$ ) for the shock speed calculation is:

$$\delta \Delta x = \sqrt{\delta x_1^2 + \delta x_2^2} \quad (\text{G.2})$$

One source of time uncertainty and one source of error are considered:

1. Time uncertainty in ascertaining shock arrival on the sensors.
2. Sampling rate error from the clocking speed of the data acquisition system.

Pressure transducers have a finite rise time to full signal ( $\leq 2.0 \mu\text{s}$  for the 112A22 pressure transducers used in X2's acceleration tube [277]) and the facility's data acquisition system is recording at a set clock speed (2.5 MHz for all sensors on X2, with most acceleration tube sensors also teed off into a 60 MHz card to reduce sampling rate error), meaning it can be difficult to ascertain exactly when the shock has passed each location. Two separate uncertainties are used to quantify this.

Firstly to remove any large uncertainties created by an automated process on what can sometimes be a relatively noisy signal, shock arrival times are found manually by a graphical interface which experimenters use to select shock arrival times for each signal. Instead of selecting a single time for shock arrival, experimenters are instructed to select the data point just before and just after when they believe the shock has arrived, giving a time range for shock arrival. The analysis code then finds both of the data points, calculates the midpoint, and adds a shock arrival uncertainty ( $\delta t_i$ ) to the data which is half of the distance between the original two points.

Secondly, to take into account the sampling rate error, an extra time uncertainty is added based on the size of a single sample ( $\delta t_{sr}$ ) to take into account the fact that the shock could arrive at any point in the sample. The size of a full sample instead of only half of a sample has been used as a conservative measure to take into account the fact that multiple samples are actually involved in the calculation process. Recently, acceleration tube pressure data (where shock speeds are often of the order of 10 km/s) has also been recorded on a high speed

National Instruments PXI-5105 card clocking at 60 MHz to reduce the sampling rate error on the acceleration tube shock speeds after it was found that the largest source of experimental uncertainty on these measurements was caused by the normal data acquisition system clocking at 2.5 MHz.

Therefore, because the time uncertainties are independent measurements, the total time uncertainty ( $\delta\Delta t$ ) for the shock speed calculation is:

$$\delta\Delta t = \sqrt{\delta t_1^2 + \delta t_2^2 + \delta t_{sr}^2} \quad (\text{G.3})$$

Now that total distance and time uncertainties ( $\delta\Delta x$  and  $\delta\Delta t$ ) are known, the total shock speed uncertainty ( $\delta V_s$ ) can be found using the uncertainty formula for the division of independent variables, which is shown below in the form appropriate for calculating the shock speed uncertainty:

$$\delta V_s = V_s \cdot \sqrt{\left(\frac{\delta\Delta x}{\Delta x}\right)^2 + \left(\frac{\delta\Delta t}{\Delta t}\right)^2} \quad (\text{G.4})$$



## Appendix H

# Setting Up and Running PITOT

PITOT forms part of the CFCFD code collection at UQ's Centre for Hypersonics [254], and as such, PITOT relies on installation of the accompanying Compressible Flow Python Library (cfpylib) to run. The latest version of the CFCFD code collection, instructions on how to obtain it, and the dependencies required to use it, can be found at the website found in the accompanying CFCFD reference [254] principally on the page titled 'Getting the codes and preparing to run them'. A page with separate specific instructions for PITOT also exists [293]. The authors have written an accompanying Makefile which can be used to install PITOT on a compatible Linux system with the correct dependencies installed. The authors use Ubuntu, and are aware that PITOT has been used on other Linux distributions as well. It is surely possible to manually install PITOT on a Macintosh or Windows system, but the authors cannot confirm this. The main obstacle would be getting PITOT to find and use CEA [197, 198] on the other operating systems.

PITOT is written in the Python programming language, and after it is installed, the most common way to run the program is to write a configuration file which conforms to Python syntax and then parse it to the overarching program by entering the line below into the terminal:

```
$ pitot.py --config_file=filename.cfg
```

Example annotated configuration files for various scenarios can be found in the examples folder of the CFCFD code collection covering both simple simulations and more complex ones using custom facilities, custom test gases, and other 'advanced' features. PITOT has been built to be modular and easy to script, and the configuration info can also be parsed to the program inside a Python script using a Python dictionary. Several different tools which make use of this have been created by the authors to perform tasks such as analysing air contamination or performing parametric studies of different fill pressures in the facility. These tools are included with the basic PITOT installation. The overall PITOT source code is open source and users can browse the code and make changes themselves if required.

## Appendix I

# Extra Information About PITOT

This appendix contains supplementary information about the PITOT program which was not deemed necessary to be included in the main text. Currently, it includes these things:

- Table I.1 detailing the notation of each state used inside the program. Associated diagrams expanding on these states can be found in Chapter 5 of the main text.
- Table I.2 detailing the basic inputs used in PITOT. It provides most of this inputs, but specific niche inputs are instead included as examples in the cfcfd repository [254].
- An annotated sample configuration file for a theoretical equilibrium air example.
- A Python file showing how to run the same PITOT configuration as the annotated configuration file from directly inside Python.

## I.1 State Details in PITOT

Table I.1: Description of the standard shock tunnel and expansion tube notation used by PITOT. *Note: Not all states are used for every simulation.*

State	Description
State 4i	Initial driver fill state for when custom driver conditions are simulated.
State 4	Primary driver gas at the diaphragm rupture condition. Taken to be a stagnation condition ( $M \approx 0$ ).
State 3s or (4" in the literature)	Primary driver gas after steady expansion to the throat Mach number. (Without an orifice plate it is a sonic throat [ $M = 1$ ], but orifice plates are used for some driver conditions, contracting the throat area, and resulting in a supersonic throat. If no throat is used to simulate a facility without an area change, this state will be the same as State 4 above)
State sd1	Secondary driver fill condition (pure He).
State sd2	Shocked secondary driver gas.
State 2r	Twice shocked secondary driver gas to simulate a reflected shock of user specified strength at the secondary diaphragm.
State sd3	State 3s unsteadily expanding into the secondary driver section.
State 1	Shock tube fill condition (test gas).
State 2	Shocked test gas.
State 2r	Twice shocked test gas to simulate a reflected shock of user specified strength at the secondary or tertiary diaphragm.
State 3	State 3s or State sd2 unsteadily expanding into the shock tube.
State 5	Acceleration tube fill condition (air).
State 6	Shocked accelerator gas.
State 7	Test gas unsteadily expanding into the acceleration tube
State 8	Nozzle exit condition after steady expansion through the nozzle.
State 10f	Frozen post shock condition at the stagnation point of the model.
State 10e	Equilibrium post shock condition at the stagnation point of the model.
State 10c	Post shock condition over at cone at a user-specified angle. (Default cone angle is $15^\circ$ .)
State 10wf	Frozen post shock condition behind a wedge at a user-specified angle.
State 10we	Equilibrium post shock condition behind a wedge at a user-specified angle.

## I.2 PITOT Configuration Details

Table I.2: Configuration details for PITOT

Parameter

Description	Choices	Default	Parameter
Facility	Expansion tube facility to simulate	x2 = the X2 expansion tube; x3 = the X3 expansion tube	x2
Test	Test case to run	fulltheory-shock = fully theoretical analysis, guessed shock speeds used to find solution; fulltheory-pressure = fully theoretical analysis, guessed shock speeds are found from set fill pressures; test = partially theoretical run where both shock speeds and fill pressures are specified based on tunnel data	fulltheory-pressure
Config	Expansion tube configuration to use	basic = no secondary driver, no nozzle; sec = with secondary driver, no nozzle; nozzle = with no secondary driver, nozzle; sec-nozzle = with secondary driver, nozzle	nozzle
Driver Gas	Driver gas composition to use	'He:0.80,Ar:0.20'; 'He:0.90,Ar:0.10'; 'He:1.0'; 'He:0.60,Ar:0.40' (all mole fractions)	'He:1.0'
Test Gas	Test gas to use	air; air5species; n2; titan; gasgiant_h215ne; gasgiant_h215he; gasgiant_h240ne; gasgiant_h285ne; gasgiant_h210he; gasgiant_h210ne	air
Vs1	Shock tube ('primary') shock speed (m/s)	Vs1 > 0	None
Vs2	Acceleration tube ('secondary') shock speed (m/s)	Vs2 > 0	None

Vsd	Secondary Driver shock speed (not needed if secondary driver isn't used)	$Vsd > 0$	None
p1	Shock tube fill pressure (Pa)	$p1 > 0$	None
p5	Acceleration tube fill pressure (Pa)	$p5 > 0$	None
psd1	Secondary driver fill pressure (Pa) (not needed if secondary driver isn't used)	$psd1 > 0$	None
Area ratio	Area ratio of the nozzle	$area\ ratio > 0$	2.5
Conehead	Switch to calculate pressure over a 15° conehead	n/a	False
Filename	Filename to save the result to	n/a	x2run.txt

## I.3 Sample PITOT Configuration File

Below is a Python based configuration file “high-speed-air-theory.cfg” for an equilibrium high enthalpy air condition in PITOT. After PITOT has been installed it can be parsed to the overarching program by entering the line below into the terminal:

```
$ pitot.py --config_file=filename.cfg
```

```
# high-speed-air-theory.cfg
# Example input file for pitot.
# Chris James (c.james4@uq.edu.au) 14/12/15
# This is a simple test of a fully theoretical high speed air condition.
# (Elise's Hayabusa entry air condition).
# I've tried to annotate this config file as much as I can so it will
# be useful to other people using the program.

#----- Start-up -----
# This is where the setup of the program is specified.

# Name of the output file (if required)
filename = 'high-speed-air-theory'

# Boolean statement controlling if pitot will clean up temporary files after running
# Use false unless you really want to clean everything up.

cleanup = True

# Testcase to run. There are three options:
# 'fulltheory-pressure' = a fully theoretical run where shock speeds are found from set fill pressures
# 'fulltheory-shock' = a fully theoretical run where fill pressures are found from set shock speeds
# 'experiment' = partially theoretical run where both shock speeds and fill pressures are specified based
# 'experiment-shock-tube-theory-acc-tube' = where the shock tube is specified from experiment (Vs1 and p1)
# 'theory-shock-tube-experiment-acc-tube' = where Vs1 is found from theory and the acc tube is found from

test = 'fulltheory-pressure'

# Solver to use. There are three options:
# 'eq' = equilibrium calculations using CEA code
# 'pg' = perfect gas solver
# "pg-eq" = a combination of pg and eq solvers, used for CO2 based gases. Sets state1 as a pg, but everyth

solver = 'eq'

# Mode that the program is run in. There are five options:
# 'printout' = normal run, prints out a summary to the screen, a txt file and a csv file at the end of the
# 'return' = simpler run, useful if pitot is to be used inside a bigger program. returns a set of values a
# the returned values are cfg, states, V and M, which are, the config dictionary, state dictionary, veloci
# 'cea-printout' = same as printout but does some cfcfd gas object printouts at the end
# 'txt-printout' = just does the txt file printout
# 'cea-txt-printout' = just the txt file printout but with cea style printouts too
# 'csv-printout' = just does the csv printout

mode = 'printout'
```

```
# Here you can specify how many steps are used for the various unsteady expansions

shock_tube_expansion_steps = 400

# need to use 800 - 1000 steps on the acceleration tube unsteady expansion to match the
# pressure across the contact surface properly, which is important.

acc_tube_expansion_steps = 1000

# Can specify your own bounds and initial guesses for the secant solver in
# the acceleration tube if you so desire

# for 'fulltheory-pressure' testcase:

#Vs2_lower =
#Vs2_upper =
#Vs2_guess_1 =
#Vs2_guess_2 =

# for 'fulltheory-shock' testcase: (all pressures in Pa)
#p5_lower = 5.0
#p5_upper = 2000.0
#p5_guess_1 = 10.0
#p5_guess_2 = 100.0

#----- Facility parameters -----
# This is where the facility parameters are specified.

# The facility to simulate. Currently there are two options:
# 'x2' = the x2 expansion tube
# 'x3' = the x3 expansion tube
# 'custom' = a custom facility where the driver configuration must be specified with a series of variables

facility = 'x2'

# Tunnel mode to use. There are three options:
# 'expansion-tube' = expansion tube mode
# 'nr-shock-tunnel' = non-reflected shock tunnel mode
# 'reflected-shock-tunnel' = reflected shock tunnel mode

tunnel_mode = 'expansion-tube'

# Secondary driver

secondary = False

# Nozzle

nozzle = True

# Piston in use (Only currently required for x2 facility). There are two main options,
# but this is generally also used to specify the driver condition, so other modes exist:
# 'lwp' or 'lwp-2mm' = lightweight piston. tuned 2mm diaphragm driver condition designed by David Gildfind
# 'ossp' = original single stage piston. designed by Michael Scott
# 'lwp-2.5mm' = tuned 2.5 mm diaphragm driver condition designed by David Gildfind
# 'lwp-2.5mm-isentropic' = isentropic compression version of tuned 2.5 mm diaphragm driver condition desig
```

```

# 'lwp-1.2mm' = tuned 1.2 mm diaphragm driver condition designed by David Gilfind
# 'lwp-2mm-new-paper' = new rupture conditions for 2mm diaphragm condition from the 2015 Gilfind et al Sho
# 'Sangdi-1.8MPa' = 1.8 MPa burst condition cold driver condition designed by Sangdi Gu, driver values fro
# 'Sangdi-2.2MPa' = 2.2 MPa burst condition cold driver condition designed by Sangdi Gu, driver values fro

piston = 'lwp-2mm-new-paper'

#----- Tunnel parameters -----

# Driver gas to use (by mole fraction). There are four options:
# Keep in mind, that the fourth option is normally only used for X3 facility.
# 'He:0.80,Ar:0.20'
# 'He:0.90,Ar:0.10'
# 'He:1.0'
# 'He:0.60,Ar:0.40'

driver_gas = 'He:1.0'

# Test gas to use (by mole fraction where mentioned). There are myriad options:
# Check the make_test_gas function in the main program for more info about the gases
# but the majority are mention below
# 'air'; 'air5species'; 'n2'; 'titan'; 'gasgiant_h215ne'; 'gasgiant_h215he';
# 'gasgiant_h240ne'; 'gasgiant_h285ne'; 'gasgiant_h210he'; 'gasgiant_h210ne';
# 'co2'; 'mars'; 'venus'; 'h2'
# NOTE: co2, mars and venus test gases only work with pg and pg-eq solvers

test_gas = 'air'

# Specified shock speeds (used for both the 'fulltheory-shock' and 'experiment' test cases)
# Units for shock speeds are m/s and should be inputted as floating point numbers
# Vsd, Vs1 and Vs2 are the names of the variables

# Specified fill pressures (used for both the 'fulltheory-pressure' and 'experiment' test cases)
# Units for fill pressures are Pa and should be inputted as floating point numbers
# psd, p1 and p5 are the names of the variables
# psd is secondary driver fill pressure (if used)
# p1 is shock tube fill pressure
# p5 is acceleration tube fill pressure (if used)

p1 = 13500.0 # Pa
p5 = 17.0 # Pa

#----- Final parameters -----
# Some parameters that control the solution

# Nozzle area ratio
# I used to generally use 2.5 (which was a value from Richard)
# BUT currently I've been using 5.64 (the geometric area ratio of the nozzle)

area_ratio = 5.64

# code for the pitot area ratio check mode

area_ratio_check = True
from numpy import arange
area_ratio_check_list = arange(2.0, 9.1, 0.1)

```



```
normalise_results_by = 'original value'

# Choose whether to expand expanding shocked test gas to the shock speed or
# the gas velocity behind the shock in the acceleration tube.
# 'flow-behind-shock' = expand shocked test gas to gas velocity behind shock in the acceleration tube
# 'shock-speed' = expand the shocked test gas to the shock speed in the acceleration tube
# I changed the default here to 'shock-speed' as that simulates the Mirels' Effect
# and would generally be correct for most high enthalpy test cases.

expand_to = 'shock-speed'

# Change the ratio of the expansion specified in the parameter above.
# Leave this value as a floating point 1.0 unless you know what you're doing,
# but it's used to tweak how far above or below the shock speed / gas velocity
# that the test gas is expanded to.

expansion_factor = 1.0

# Turns on the shock switch that is used for simulating scramjet conditions.
# In a scramjet condition in an expansion tube the secondary driver shock is
# driven faster than the shock in the test gas, creating a normal shock into
# the shock tube, instead of the usual unsteady expansion. The switch below turns
# that feature on (the code will try to look for the phenomena itself,
# but it won't always find it).
# NOTE: always make this false unless you know what it is!

shock_switch = False

# Turns on the code that calculates the conditions over a conehead placed in the test section.
# The conehead angle can be specified in degrees, but will default to 15 degrees if not specified.

conehead = True
conehead_angle = 15.0 # (degrees)

wedge = True
wedge_angle = 50.0 # degrees

# Turns on the code that calculates the conditions over a normal shock over a test model in the test section.

shock_over_model = True
all_total = True

make_one_line_summary = True
```

## I.4 Sample of PITOT scripted in Python

The Python code below is an example of how PITOT can be scripted from directly inside Python. The configuration data found in the dictionary below is exactly the same as the configuration data found in Appendix I.3 above, but this time PITOT can now be ran directly from Python by entering the command below into the terminal:

```
$ python pitot_scripting_example.py

#!/usr/bin/env python
"""
pitot_scripting_example.py
This example shows how the same PITOT configuration shown in high-speed-air-theory.cfg
could be ran from inside Python by using importing run_pitot and giving it the
configuration dictionary directly from inside Python.

Chris James (c.james4@uq.edu.au) - 28/02/16

"""

import sys, os
sys.path.append(os.path.expandvars("$HOME/e3bin")) # installation directory
sys.path.append("") # so that we can find user's scripts in current directory

from pitot import run_pitot

cfg = {'filename':'high-speed-air-theory', 'cleanup':True,
       'test':'fulltheory-pressure', 'solver':'eq',
       'mode':'printout', 'facility':'x2', 'tunnel_mode':'expansion-tube',
       'nozzle':True, 'secondary':False, 'piston':'lwp-2mm-new-paper',
       'driver_gas':'He:1.0', 'test_gas':'air', 'p1':13500.0, 'p5':17.0,
       'area_ratio':5.64, 'expand_to':'shock-speed', 'expansion_factor':1.0,
       'conehead':True, 'conehead_angle':15.0, 'wedge':True, 'wedge_angle':50.0,
       'shock_over_model':True, 'all_total':True}

run_pitot(cfg=cfg)
```

## Appendix J

# Hydrogen Safety

It is well known that hydrogen ( $H_2$ ) is a combustible gas, and therefore precautions must be taken when using a hydrogen based test gas for testing in the X2 expansion tube. This appendix presents some quick calculations to assess the danger of hydrogen combustion in the X2 expansion tube, as well as a procedure for using the gas safely.

Matheson Tri Gas, namesake of the *Matheson Gas Data Book* [294] give a very concise description of the Lower and Upper Explosive Limits for a combustible gas [295]:

*“The minimum concentration of a particular combustible gas or vapor necessary to support its combustion in air is defined as the Lower Explosive Limit (LEL) for that gas. Below this level, the mixture is too ‘lean’ to burn. The maximum concentration of a gas or vapor that will burn in air is defined as the Upper Explosive Limit (UEL). Above this level, the mixture is too ‘rich’ to burn. The range between the LEL and UEL is known as the flammable range for that gas or vapor.”*

In air, the Lower and Upper Explosive Limits for  $H_2$  are found to be 4% and 75% respectively (by volume). Therefore, it is important that any work done with hydrogen is done in a contained environment with the hydrogen kept outside of the flammable range whenever possible.

During testing on the X2 expansion tube,  $H_2$  is used in six different situations:

1. Above atmospheric pressure  $H_2$  gas in manifolds on the X2 expansion tube for mixing test gas. (Too rich to combust.)
2. Above atmospheric pressure  $H_2/He$  or  $H_2/Ne$  gas mixtures in manifolds on the X2 expansion tube for mixing test gas. (Too rich to combust.)

3. Diluted (with laboratory air) atmospheric pressure  $H_2$ ,  $H_2/He$ , or  $H_2/Ne$  mixtures in the shock tube, acceleration tube, dump tank and manifolds of the X2 expansion tube for pumping out through the exhaust system in the lab. (Too lean to combust.)
4. Below atmospheric pressure  $H_2/He$  or  $H_2/Ne$  in the shock tube and manifolds of the X2 expansion tube after the test gas has been filled before a shot. (Too rich to combust.)
5. Mixture of test gas ( $H_2/He$  or  $H_2/Ne$ ), air (from the acceleration tube), He (from primary and secondary driver tubes) in the shock tube, acceleration tube and dump tank of the X2 expansion tube after a shot. (Unsure whether this will be combustible or not, but contained in the tube itself regardless.)
6. Diluted (with air) Mixture of test gas ( $H_2/He$  or  $H_2/Ne$ ), air (from the acceleration tube), He (from primary and secondary driver tubes) in the shock tube, acceleration tube and dump tank of the X2 expansion tube after a shot. (Too lean to combust.)

In the list above it can be seen that when  $H_2$  is used in the X2 expansion tube, it is generally used in situations where it is either too lean or too rich to combust. Care must be taken when moving through the flammable range (from rich to lean) when diluting a test gas mixture to pump it out safely through the exhaust system, but the main risk is an explosion inside the tube after a shot has been done and air and  $H_2$  are interacting inside the tunnel. This is very unlikely to be dangerous (due to the fact that all proposed test gases contain 2 to 4 kPa of  $H_2$  which will be diluted by almost an atmosphere of inert driver gas after the shot, as well as dropping in pressure by approximately 20 times due to the large difference in volume between the shock tube and the whole tube and dump tank itself), but to be extremely conservative, a calculation was done in NASA's CEA program [198] for a Chapman-Jouget detonation of 1 kPa of  $H_2$  gas at 300 K with the stoichiometric amount of air. The output pressure and temperature were then used as inputs into the same calculation again to find the pressure and temperature if the original 'shocked' gas is hit by a reflected detonation wave. The final pressure and temperature were found to be 20 kPa and 2,576 K respectively, meaning that even in an extremely conservative scenario, a detonation inside the expansion tube will still lead to sub-atmospheric conditions in the tube.

The procedure written for using a test gas mixture which includes  $H_2$  in the X2 expansion tube can be found below:

Shock tube fill procedure:

1. Pump the shock tube and manifold down to vacuum.

2. Flush the shock tube and manifold with the diluent (He or Ne) if required. **Do not flush the shock tube with the test gas or pure H<sub>2</sub>.**
3. Open the test gas bottle while it is isolated from the manifold.
4. Isolate the vacuum pump and fill the shock tube to the required pressure.
5. Isolate the shock tube from the manifold.
6. Close the test gas bottle.
7. **Do not pump the test gas in the manifold out through the vacuum line. Wait until after the shot to remove it through the tube.**
8. Vent manifold up to atmospheric pressure (to go from being above the UEL to below the LEL) and seal it again until after the shot.

After shot procedure:

1. Immediately after the shot has been completed, open the sealed manifolds to the rest of the tube and vent the whole tube up to roughly 80 kPa to ensure the gas in the tube is below the LEL.
2. Wait for a few minutes.
3. Pump the tube down through the vacuum line to remove most of the now safe H<sub>2</sub>/He/air mixture.
4. Vent the whole tube up to roughly 80 kPa and then seal the tube again.
5. Wait for a few minutes again.
6. Pump the tube down again through the vacuum line to remove any remaining pockets of H<sub>2</sub>.

Mixing Procedure:

1. Clear area.
2. Seal off the whole expansion tube but leave it at atmospheric pressure. (It will be used for venting the H<sub>2</sub> gas into the expansion tube after mixing, so ensure no diaphragms are in place blocking the H<sub>2</sub> from expanding into the whole expansion tube.)

3. Isolate the expansion tube from the manifold.
4. Pump out the mix bottle through the manifold.
5. Flush the mix bottle with the diluent (He or Ne).
6. Pump out the manifold and the mix bottle again.
7. Open the H<sub>2</sub> bottle, while it is isolated from the manifold.
8. Isolate vacuum pumps from the manifold.
9. Fill the mix bottle to the required pressure with H<sub>2</sub>.
10. Close the mix bottle.
11. Vent the manifold into the expansion tube so that a mixture below the lean combustible limit of H<sub>2</sub> can be pumped out through the expansion tube's vacuum line.
12. Leave everything for a few minutes.
13. Pump the expansion tube down to 200 Pa or less.
14. Vent the manifold and expansion tube.
15. Pump the expansion tube down to 200 Pa or less again.
16. Isolate the tube from manifold. Keep pumping the manifold, vent tube and then seal at atmospheric pressure.
17. Open the diluent bottle (He/Ne) while isolated from manifold.
18. Fill manifold with diluent to above the pressure in the H<sub>2</sub> mix bottle (to ensure no H<sub>2</sub> is pushed into the manifold).
19. Open the mix bottle.
20. Fill the diluent to the required pressure.
21. Close the mix bottle.
22. Once again, just to be conservative, vent manifold into the tube at atmospheric pressure.
23. Pump down the tube.
24. Vent the tube, and vent the manifold.

- 
25. Write on the manifold the details of what has been mixed into the mix bottle and the data when it was done.
  26. **Finally, at the end of the experimental campaign a similar procedure should be used to empty the mix bottle so that a mixture containing  $H_2$  is not left lying around in the laboratory for another person (who may not be experienced in the handling of a test gas containing  $H_2$ ) to deal with.**

## Appendix K

# Stagnation Point Heat Flux Correlation Selection

Stagnation point axisymmetric convective heat flux was calculated using the equilibrium gas CFD correlation created by Sutton and Graves [289], which aimed to produce a generic equation which was applicable to all gas mixtures which would be of interest for planetary entry studies. Sutton and Graves' correlation [289] is valid for nine base gases (which include H<sub>2</sub>, He, and Ne) and mixtures of those base gases. The correlation was validated up to a stagnation enthalpy of 116.2 MJ/kg (roughly 15 km/s), but it has been used for gas giant entry calculations by Sutton [296] up to a flight speed of 47 km/s. Calculations performed here show that it agrees fairly well with the modern CFD results of Palmer et al. [71], which will be discussed later.

The simplest form of the correlation for the cold wall convective heat flux ( $q_{conv}$ ) in Sutton and Graves [289] comes from Equation 33 in the original work:

$$q_{conv} = K \sqrt{\frac{p_s}{R_n}} (h_s - h_w) \quad (\text{K.1})$$

where  $K$  is the convective heat transfer coefficient (in specified units),  $p_s$  is the stagnation pressure at the edge of the boundary layer,  $R_n$  is the vehicle or test model nose radius,  $h_s$  is the stagnation enthalpy at the edge of the boundary layer (basically,  $H_t$ ), and  $h_w$  is the wall enthalpy.

Using an equation for the stagnation pressure from Sutton [296]:

$$p_s = 0.952 \rho_\infty U_\infty^2 \quad (\text{K.2})$$

and also making the assumption that the kinetic part of the stagnation enthalpy is much larger than the static part (see Equation 6.1) and the wall enthalpy (i.e.  $\frac{U_\infty^2}{2} \gg (h - h_0) - h_w$ ),



the correlations are normally expressed in terms of the freestream density and velocity ( $\rho_\infty$  and  $U_\infty$ ), as was done in Sutton [296] and also more modern references such as Brandis and Johnston for Earth entry [297]:

$$q_{conv} = 0.487K \sqrt{\frac{\rho_\infty}{R_n}} U_\infty^3 \quad (\text{K.3})$$

K values for different base gases are provided in Table 2 of Sutton and Graves [289] in units of  $\text{kg/s-m}^{3/2}\text{-atm}^{1/2}$ , as well as set combinations of the base gases which were also calculated. Equation 44 of Sutton and Graves [289] provides an equation for finding the K value for an arbitrary mixture of the base gases, based on their individual mass fractions:

$$\frac{1}{K^2} = \sum \frac{c_{0,i}}{K_i^2} \quad (\text{K.4})$$

where  $c_0$  is the freestream mass fraction of the species. In Sutton and Graves [289], comparisons between Equation 44 and the results in Table 2 can be found in Figure 7, with comparisons for  $\text{H}_2/\text{He}$  mixtures found in Figure 7b.

For  $\text{H}_2$  and  $\text{He}$  in SI Units (but using original K values from Sutton and Graves [289]) this becomes:

$$K = \sqrt{\frac{1}{\frac{c_{0,\text{H}_2}}{K_{\text{H}_2}^2} + \frac{c_{0,\text{He}}}{K_{\text{He}}^2}}} \frac{1}{\sqrt{101.3 \times 10^3 \text{ Pa}}} = \sqrt{\frac{1}{\frac{c_{0,\text{H}_2}}{0.0395^2} + \frac{c_{0,\text{He}}}{0.0797^2}}} \frac{1}{\sqrt{101.3 \times 10^3}} \quad (\text{K.5})$$

where the final K value is now in  $\text{kg}^{1/2}/\text{m}$ . If the calculation is performed with neon instead of helium,  $K_{\text{Ne}} = 0.147,4 \text{ kg/s-m}^{3/2}\text{-atm}^{1/2}$  can be used instead of  $K_{\text{He}}$ .

Sutton also provides a simplified equation for K for gas giant entry mixtures [296] as Equation 9 of that work. However, comparing Sutton's [296] K value to the original work in Sutton and Graves [289], it appears that there must be an error in Sutton's [296] equation, as it predicts a larger K for a larger mass fraction of molecular hydrogen, whereas Table 2, Figure 7b, and Equation 44 in Sutton and Graves [289] all predict the opposite. This is shown in Fig. K.1 here where these different cases are compared. For this reason, and also the fact that it allows mixtures containing neon to be evaluated, the K equation from Sutton and Graves [289] (Equation K.5 in this work) has been used here.

To check the validity of the correlation from Sutton and Graves [289], it was decided to compare the results of the correlation to Palmer et al.'s CFD [71]. Calculations were performed

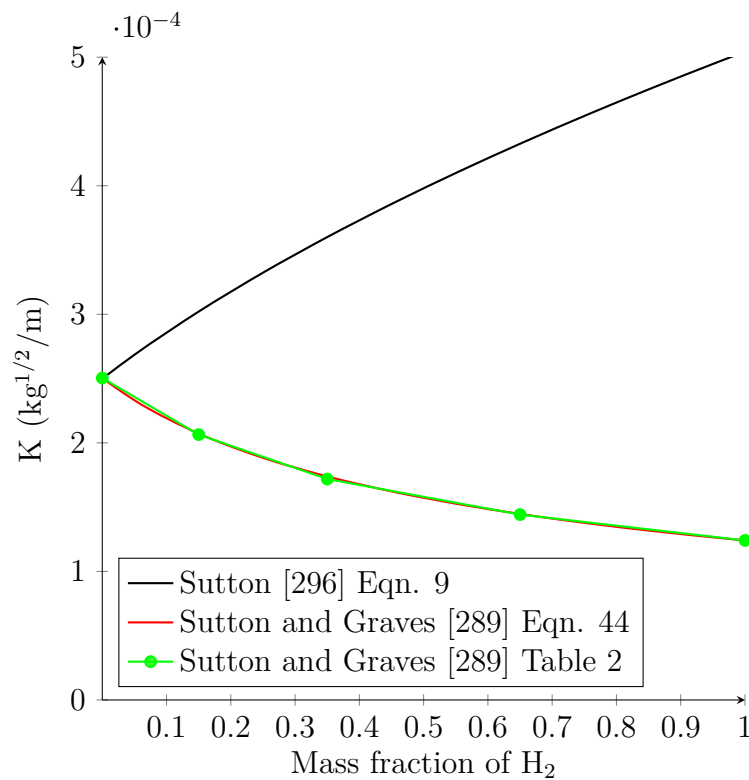


Figure K.1: Comparing the convective heat transfer coefficient ( $K$ ) in a  $H_2/He$  mixture between a simplified equation from Sutton [296] and the original work of Sutton and Graves [289].

for the Uranus and Saturn entry trajectory points found in Tables 4 and 8 of that work [71]. An 85% $H_2$ /15% $He$  gas composition was used for the Uranus entry conditions based on the work of Conrath et al. [273] and an 89% $H_2$ /11% $He$  gas composition was used for the Saturn entry conditions based on the work of Conrath et al. [274]. The nose radius for the proposed Uranus and Saturn entry probes were 0.38 m and 0.5 m respectively [68, 69, 70, 71]. The results can be found in Table K.1. It should be noted that the final Saturn trajectory point was for another trajectory, hence the very different time value.

Examining Table K.1 it can be seen that the correlation from Sutton and Graves [289] generally overestimates the convective heat flux, however, the minimum and maximum differences are 3.7% and 73% respectively. These are both very good results for a correlation which is almost half a century old now, is being used outside of its enthalpy limits, and is being used in a form which assumes that the wall enthalpy is negligible (when in reality the surface temperatures for these trajectory points are around 3,000 K to 4,000 K).

Sutton [296] included calculations of radiative heat flux for gas giant entry, but did not provide the base intensity matrix which was used to perform the calculations. For this reason, calculations provided here were performed using the SPECAIR [287, 288] results shown in

Table K.1: Comparison between stagnation point convective heat flux calculated by Palmer et al's CFD [71] and calculations performed here using the correlation from Sutton and Graves [289].

Planet	Time (s)	$q_{conv}$ (W/cm <sup>2</sup> )		% diff.
		Palmer et al. CFD [71]	Sutton and Graves [289]	
Uranus	34.5	542	563	4
Uranus	36.5	725	863	17
Uranus	42.5	1,942	4,166	73
Saturn	206	690	716	4
Saturn	272	790	951	19
Saturn	91.5	1,208	1,497	21

Fig. 7.9 in Section 7.4.4. These calculations were performed using equilibrium chemistry, which would not be true of the test conditions, only include line radiation from the Lyman and Balmer series (and any Neon contamination which falls within these regions), so continuum and molecular radiation are not included, but should give an order of magnitude indication of the radiative heat flux. The SPECAIR [287, 288] calculations were also performed using a 10 mm thick tangent slab, which is similar to the shock standoff of recent preliminary gas giant entry radiation experiments performed in X2 by Liu et al. [22]. The results were presented per cm<sup>3</sup> in Fig. 7.9, but were used here in their original cm<sup>2</sup> form. The radiative heat flux was calculated using an equation from Park [298] for calculating stagnation point radiative heat flux from simulated spectra over a specified wavelength range which is based on empirical results from Ried et al. [299]:

$$q_{rad}(\lambda_1 - \lambda_2) \equiv \int_0^{2\pi} \int_{\lambda_1}^{\lambda_2} I_\lambda d\lambda d\Omega \approx 2\pi 0.84 I(\lambda_1 - \lambda_2) \quad (\text{K.6})$$

where  $\lambda_1$  and  $\lambda_2$  are the lower and upper wavelength limits respectively,  $I$  is the radiance (measured in W/cm<sup>2</sup>-sr or equivalent units and often what is being referred to when the 'intensity' of radiation is discussed), and  $d\lambda$  and  $d\Omega$  represent integrations in wavelength and solid angle respectively.



**Titre:** Simulation du rayonnement de l'entrée atmosphérique sur les planètes gazeuses géantes

**Mots clés:** hypersonique, essais au sol, tube à expansion, tube à choc, entrée atmosphérique

**Résumé:** L'exploration des quatre planètes géantes gazeuses, Jupiter, Saturne, Neptune et Uranus, est importante pour comprendre l'évolution de notre système solaire et plus généralement de l'univers. Les sondes entrant dans l'atmosphère des géantes gazeuses ont des vitesses de 20 à 50 km/s, largement supérieures aux vitesses d'entrée atmosphérique sur les autres planètes du système solaire. Il s'agit d'un problème complexe car les conditions d'entrées sont brutales et les vitesses associées dépassent largement les capacités des installations d'essai au sol actuelles. Cette thèse examine la possibilité de simuler expérimentalement les conditions d'entrées proposées pour Uranus et Saturne à 22.3 et 26.9 km/s avec un tube d'expansion à piston libre. D'abord, la possibilité de simuler les conditions directement en recréant la vitesse d'entrée réelle a été étudiée.

Il a été trouvé qu'il était possible de simuler l'entrée d'Uranus mais seulement avec de grandes incertitudes. Pour cette raison, il a été proposé d'utiliser une substitution du gaz d'essai établie, dans lequel soit le pourcentage d'hélium dans l'atmosphère  $H_2/He$  est augmenté, soit l'hélium est remplacé par du néon, un gaz noble plus lourd. Cela permet de simuler uniquement les conditions post-choc des entrées. Théoriquement, il a été constaté que ces substitutions permettaient de simuler l'entrée Uranus ou Saturne, ce qui a été confirmé expérimentalement à l'aide d'hélium. Notant l'intérêt actuel d'envoyer des sondes d'entrée atmosphérique vers ces deux planètes, cette étude a démontré que les capacités expérimentales requises sont disponibles pour la réalisation d'expériences simulées avec les modèles d'essais.

**Title:** Radiation from Simulated Atmospheric Entry into the Gas Giants

**Keywords:** hypersonic, experimental, ground testing, expansion tube, shock tunnel, planetary entry

**Abstract:** Exploration of the four gas giant planets, Jupiter, Saturn, Uranus, and Neptune, is important for understanding the evolution of both our solar system and the greater universe. Due to their size, flight into the gas giants involves atmospheric entry velocities between 20 and 50 km/s. This is a complex issue because the entry conditions are harsh but the related velocities are mostly beyond the capabilities of current ground testing facilities. As such, this thesis examines the possibility of experimentally simulating proposed Uranus and Saturn entries at 22.3 and 26.9 km/s in a free piston driven expansion tube, the most powerful type of impulse wind tunnel. Initially, the possibility of simulating the conditions directly by re-creating the true flight velocity was investigated.

It was found to be possible to simulate the 22.3 km/s Uranus entry, but not without large uncertainties in the test condition. For this reason, it was proposed to use an established test gas substitution where the percentage of helium in the  $H_2/He$  atmosphere is increased, or the helium is substituted for the heavier noble gas neon. This allows just the post-shock conditions of the entries to be simulated. Theoretically it was found that these substitutions allowed both Uranus or Saturn entry to be simulated, which was confirmed experimentally using helium. Noting the current interest in sending atmospheric entry probes to both of these planets, this study has demonstrated that the required experimental capabilities are available for performing simulated experiments using test models.

